ÉCOLE DOCTORALE DES SCIENCES DE LA VIE ET DE LA SANTE

Laboratoire de bioimagerie et pathologies – LBP – CNRS UMR 7021

Équipe de recherche : Signalisation tumorale et cibles thérapeutiques

THÈSE

présentée par :

Chloé Bernhard

soutenue le 26 janvier 2024

pour obtenir le grade de : **Docteur de l'Université de Strasbourg**

Discipline : Biologie cellulaire et cancérologie

Hétérogénéité moléculaire et métabolique des gliomes de haut grade
Applications à l'évaluation de nouvelles thérapies

Thèse dirigée par :

Madame Monique DONTENWILL DR CNRS, UMR7021, Strasbourg

Rapporteurs :

Monsieur Thomas DAUBON DR CNRS, IBGC UMR5095, Bordeaux

Monsieur Stéphane DEDIEU PR, Medyc, UMR7369, Reims

Examinateur interne :

Madame Dominique GUENOT DR CNRS, IRFAC, U1113, Strasbourg

Membre invité

Monsieur Mohamed ELATI PR, CANTHER, UMR1277, U9020, Lille

A mes amours, ma famille et mes amis, et tout particulièrement à mon père,
à qui ce travail est dédié.

The most important factor in survival is neither intelligence nor strength but adaptability.
— Charles Darwin

REMERCIEMENTS

Ce manuscrit signe la fin de plus de trois années de travaux, de découvertes et de rencontres et je tiens à remercier ici toutes celles et ceux qui m'ont accompagnée et soutenue au cours de cette période.

Je tiens à exprimer tous mes remerciements aux membres du jury, qui ont accepté d'évaluer mon travail. Merci à Madame **Dominique Guenot**, Directeur de recherche au CNRS d'avoir accepté de présider le jury de ma thèse, à Monsieur **Thomas Daubon**, Directeur de recherche au CNRS et à Monsieur **Stéphane Dedieu**, Professeur de l'Université de Reims d'avoir accepté d'être rapporteurs de ce travail.

Je tiens à exprimer ma profonde gratitude envers **Monique Dontenwill** pour la confiance qu'elle m'a témoignée en m'accueillant dans son équipe, et pour m'avoir guidée tout au long de cette thèse, tout en me donnant l'opportunité de développer mon autonomie. Pour Lazare et moi, vous êtes incontestablement la personne la plus cool du laboratoire. Votre assurance et votre engagement professionnel sont une véritable source d'inspiration. Merci d'avoir été à l'écoute de mes idées, même les plus farfelues, et d'avoir pris le temps de m'expliquer et de me partager vos connaissances. Votre influence scientifique sur moi a été déterminante. Chaque échange d'idées avec vous m'a rendue plus forte. Je suis heureuse et honorée d'avoir été votre dernière doctorante.

Aux collaborateurs,

Un grand merci au Professeur **Mohamed Elati** pour m'avoir impliquée de manière significative dans un projet passionnant, unissant bio-informaticiens et biologistes pour décrypter la complexité des glioblastomes. Je suis reconnaissante pour la liberté d'expression et la confiance que vous m'avez accordées. Cette introduction au domaine de la bio-informatique a été une expérience enrichissante dans mon parcours. J'ai peut-être raté ma vocation de devenir bio-informaticienne, mais en tout cas, j'étais heureuse d'en découvrir plus via ce projet.

Je suis également très reconnaissante envers le Professeur **Izzie-Jacques Namer** pour la précieuse collaboration qui m'a permis de réaliser des analyses métabolomiques au sein de l'hôpital d'Hautepierre. Un remerciement vraiment spécial à **Hassiba Outilaft**, pour son aide et son soutien inestimable dans la réalisation de ces analyses. Nos journées à l'hôpital, remplies

de bonne humeur et de diverses discussions, ont été des moments agréables. Merci pour tout. Ne t'inquiète pas pour la fin de ta thèse, tu vas y arriver !

Un grand merci également à l'équipe des chimistes, le Professeur **Matteo Negroni** et **Alexis Verge**. Votre enseignement sur le domaine des lentivirus et la transduction des cellules souches cancéreuses a été extrêmement enrichissant. J'espère que vous parviendrez à développer des virus oncolytiques efficaces ! Alexis, un grand merci pour m'avoir aidé à rendre mes cellules colorées, les rendant plus belles et plus éclatantes que jamais.

Je tiens aussi à remercier le Professeur **Sylvie Fournel** et le Docteur **Stéphane Bellemin-Laponnaz** de m'avoir permis de travailler sur leur nouveau composé anticancéreux. Un grand merci à **Conor McCartin**, avec qui j'ai pu collaborer dès le master 2, pour sa disponibilité et sa sympathie.

Je tiens à exprimer ma gratitude à toute **l'équipe LBP** pour leur accompagnement durant ma thèse. Aux anciens, **Aude**, **Marina** et **Quentin**, merci d'avoir montré l'exemple. Un remerciement particulier à **Ombline**, avec qui j'ai partagé le même master, le même concours, et que j'ai retrouvée en thèse dans le même laboratoire! Merci pour toutes les fois où tu m'as apporté de l'aide, mais aussi simplement pour les bons moments que nous avons partagés. Je remercie également les petits derniers, **Yuri**, **Clémence**, **Chinar** et **Ronan** pour avoir insufflé une nouvelle énergie et bonne humeur au laboratoire. Yuri, bien que devenue ta tutrice sous la contrainte, c'était un plaisir. Je remercie également grandement **Chinar** pour son aide dans la réalisation de belles figures sur R mais aussi **Marlène** pour avoir veillé à la propreté de la salle de culture. Merci aussi pour les petites histoires de labo en mode 'on peut sortir le pop-corn', disait Mélissa. Nos pauses partagées entre étudiants, oscillant entre lamentations et bonnes vibes, resteront de bons souvenirs. Cette future équipe de jeunes chercheurs est prometteuse et me rend optimiste quant à l'avenir de la recherche. Je remercie également **Damien Reita** pour sa collaboration, sa sympathie et son aide dans l'analyse des données transcriptomiques. Je remercie **Sophie Martin** pour m'avoir supportée lors de mes élans de folie. Je tiens également à remercier le Professeur **Natacha Entz-Werle** pour son dévouement remarquable et sa contribution significative à la recherche sur les tumeurs cérébrales pédiatriques. J'aimerais particulièrement remercier **Sophie Foppolo** pour sa disponibilité, son aide, sa gentillesse, son écoute et son accompagnement pendant cette thèse. En tant que collègues de bureau, nous avons partagé beaucoup, et je te remercie particulièrement pour ton écoute attentive lorsque j'avais besoin d'extérioriser. Tu passes ton temps à remercier les autres autour de toi alors que c'est toi à qui on devrait dire mille fois merci.

J'aimerais également remercier **Ingrid** et **Adrien** pour leur présence rassurante en cas de besoin. Un merci également à **Tania** et **Jérôme** pour votre bonne humeur et l'énergie que vous avez apportée dans mon bureau au quotidien.

Un merci à « mes » étudiants que j'ai eu le plaisir d'encadrer : **Lisa**, **Minh**, **Yesim** et **Louan**. Je suis particulièrement reconnaissante envers Minh, pour sa gentillesse, son soutien et toutes ses attentions.

Je tiens également à remercier les enseignants que j'ai eu le plaisir de côtoyer et auprès desquels j'ai appris à enseigner, en particulier le Docteur **Thierry Chataigneau**, avec qui j'ai adoré dispenser les travaux pratiques de pharmacologie, et le Docteur **Anne Casset** pour sa bienveillance. Un merci également au Docteur **Emilie Sick**, dont j'ai toujours apprécié nos conversations furtives, pour m'avoir encouragé à enseigner et pour sa sympathie.

Je tiens également à exprimer ma reconnaissance envers toutes les associations qui se battent pour améliorer la recherche et faire évoluer le traitement du cancer, notamment la **Ligue contre le Cancer**, l'**INCA** et le **Rotary Club**.
J'aimerais remercier particulièrement les membres du Rotary Club pour leur précieuse contribution qui a rendu possible l'acquisition de différents équipements au sein de notre laboratoire, dont le Seahorse XFp. Grâce à votre soutien, j'ai pu développer une expertise sur cet appareil, qui m'a valu le surnom d'experte du Seahorse. Je me suis également réjouie de participer à vos actions de collecte de fonds. Bien que cela m'ait demandé de sortir de ma zone de confort, ces expériences m'ont permis de contribuer à cette cause qui me tient à cœur.

Je tiens également à remercier l'**équipe d'Agilent**, nos fournisseurs pour les analyses de flux extracellulaire, en particulier 'Monsieur Seahorse', comme Mélissa et moi aimions l'appeler, ainsi que l'équipe de support technique. Un grand merci pour votre réactivité face aux nombreux problèmes rencontrés. J'ai vraiment apprécié travailler avec cette technologie, mon seul regret est d'avoir du me contenter de ces petites microplaques.

Merci au Docteur **Jocelyn Céraline**, mon responsable de master, pour m'avoir rassuré sur mes capacités à entreprendre une thèse et m'avoir motivé. Je vous suis également reconnaissante pour le temps que vous m'avez accordé et pour votre soutien.

Mes remerciements les plus sincères à **Raphaël Schatz**,
Je ne te remercierai jamais assez pour l'aide et le réconfort que tu m'as apportés durant tant d'années, tant au niveau personnel que professionnel. Tu m'as permis d'avancer sereinement dans la vie et dans tous les projets que j'ai entrepris. Je te remercie de m'avoir guidée depuis mes débuts en recherche et de m'avoir épaulée tant de fois.

À mes amis,
Parmi eux, ceux qui ont partagé mon parcours depuis les années lycée, qui sont toujours présents aujourd'hui et pour qui j'ai beaucoup d'affection et qui occupent une place particulièrement spéciale : **Carole**, **Robin**, **Pierre**, **Martin** et **Yassine**. Ensuite, à mes amis arrivés plus tardivement dans ma vie, mais avec qui j'ai créé de belles amitiés et avec qui j'ai partagé des moments magiques et de complicité : **Alexis**, **Florian**, **Jamel**, **Joséphine**, **Lucas**, **Quentin** et **Tufan**. Je tiens également à remercier mes amis pharmaciens, **Gauthier** et **Ilias**, avec qui j'ai partagé des années d'études et dont notre amitié s'est précieusement conservée.
Plus que tout, merci à **Adèle** et **Camille**, des piliers essentiels à ma vie et cela, depuis de longues années, celles avec qui je partage tout. Bien que différentes, chacune de vous m'apporte quelque chose d'unique et de précieux à mes yeux. Adèle, tu es ma valeur sûre, mon repère. Camille, tu es mon rayon de soleil épicé. Merci à vous pour l'amour que vous me portez au quotidien et votre soutien inconditionnel.

À **Lazare Saladin**,
Ta présence et tes encouragements ont participé à mon épanouissement professionnel. Nos échanges, couvrant aussi bien la science que des sujets plus légers ou plus sérieux, ont rapidement renforcé notre relation et m'ont aidé à grandir personnellement. Je n'oublierai jamais le réconfort que tu m'as apporté, la complicité sincère et spéciale que nous avons partagée et ces rumeurs au labo qui nous ont particulièrement amusés.

À **Mélissa Messé**,
Ma plus belle rencontre au cours de cette folle aventure. J'ai eu de la chance de t'avoir dès le début et tu m'as beaucoup trop manqué à la fin... On a vécu des galères, des pleurs, mais surtout plus de rires et de confidences ! Nos moments au bureau, sous la hotte, et nos échanges constants étaient essentiels pour moi. Clairement, cette thèse n'aurait pas été la même sans toi. Merci pour ta gentillesse, ta générosité, et par-dessus tout, pour ton amitié.

À **Jules Nast,**

Je tiens à remercier Jules Nast pour l'accueil chaleureux qu'il m'a réservé dans sa vie et pour l'attention et l'amour qu'il m'a portée durant la dernière ligne droite de cette thèse. Ta présence à mes côtés a été un refuge paisible et réconfortant. Je te suis infiniment reconnaissante pour tous ces moments au paradis partagés, ainsi que pour ta compréhension et ta patience, surtout lors de ces soirées où, submergée par le stress, je t'ai parfois embêté. Merci pour toutes les émotions et sentiments profonds que tu éveilles en moi.

À **Doris** et **Charles**,

Ma mamy et mon papy, qui même s'ils ne comprennent pas ce que je fais depuis plusieurs années et attendent impatiemment que je finisse mes études, sont derrières moi et me soutiennent.

À **ma famille T**...

Isa, ma maman pétillante à la joie de vivre contagieuse, pour son soutien quotidien et sa présence rassurante dans mes moments de doute et de tourmente.

Cindy, ma sœur, à qui je dois tant et que j'aime tant. Merci de m'avoir guidée, de m'avoir aidée à relativiser dans les moments difficiles et de m'avoir donné confiance en moi à maintes reprises. Plus que tout, merci pour l'amour inconditionnel que tu m'apportes. Tu es ma plus grande force et ma plus grande fierté : c'est moi qui ai la chance d'avoir la meilleure des sœurs.

Romain, mon petit frère, merci pour tous ces éclats de rires, câlins partagés et notre complicité si précieuse.

À **Sylvain**, mon beau frère, qui selon ma sœur sait tout faire et qui, effectivement, a tant de fois répondu à mes appels. Je te remercie pour tout ce que tu as fait pour moi et ton dévouement envers ma sœur et notre famille.

À mon beau-père, **Jeff**, pour le rôle de beau-papoutch qu'il a pris avec amour dans ma vie.

J'aimerais également remercier mon neveu, **Victor**, pour ses bisous et le bonheur qu'il apporte dans notre famille.

Je chéris nos moments en famille, vous comptez tous énormément pour moi (même les « pièces rapportées »). Je vous suis infiniment reconnaissante pour votre présence constante et votre soutien. Sisi la famille!

Et enfin, une pensée profonde pour mon père, **Pierre**. Toi qui souhaitais me voir devenir architecte ou infirmière, j'espère que, malgré le chemin différent que j'ai choisi, tu es fier de moi, où que tu sois maintenant.

TABLE DES MATIÈRES

REMERCIEMENTS **1**
TABLE DES MATIÈRES **6**
LISTE DES FIGURES **8**
LISTE DES TABLEAUX **9**
LISTE DES ABRÉVIATIONS **10**

INTRODUCTION **16**

PARTIE 1 : LES GLIOMES DE HAUT GRADE **17**

1. Définition, épidémiologie et contexte 17
2. Classification de l'OMS 20
   2.1 Evolution de la classification de l'OMS 20
   2.2 Classification de l'OMS adoptée en 2021 21
3. Diagnostic et prise en charge thérapeutique 24
   3.1 Diagnostic 24
   3.2 Facteurs pronostiques 25
   3.3 Prise en charge thérapeutique 25
      3.3.1 Prise en charge du GB nouvellement diagnostiqué 25
      3.3.2 Prise en charge des symptômes 26
      3.3.3 Prise en charge des récidives 27
      3.3.4 Thérapie ciblée 27
      3.3.5 Dispositif TTF 28
4. Cellules souches de glioblastome 29
   4.1 Notion et caractéristiques 29
   4.2 Isolement et identification 30
   4.3 Fonctions pro-tumorigéniques 30
   4.4 Voies de signalisation 31
5. Échecs thérapeutiques 31
6. Vers de nouvelles stratégies thérapeutiques 34

PARTIE 2 : HÉTÉROGÉNÉITÉ ET PLASTICITÉ TUMORALE **38**

1. Concepts d'hétérogénéité et de plasticité tumorale 38
2. Modèles expliquant l'hétérogénéité des tumeurs 40
3. Hétérogénéité moléculaire des glioblastomes 40
4. Facteurs définissant l'hétérogénéité et la plasticité tumorale 45
   4.1 Génétique 45
   4.2 Réseaux de régulation génique 46
   4.3 Microenvironnement tumoral 47
      4.3.1 Niches 48
         4.3.1.1 Niches hypoxiques 48
         4.3.1.2 Niches invasives 49
         4.3.1.3 Niches périvasculaires 50
      4.3.2 Dialogue moléculaire et communication cellulaire 50
      4.3.3 Communication avec le stroma tumoral 51
5. Hétérogénéité et plasticité des cellules souches cancéreuses 52
6. Implication clinique et thérapeutique 54

PARTIE 3 : MÉTABOLISME TUMORAL ET APPROCHES THÉRAPEUTIQUES.. 56

1. Revue de la littérature 56
2. Reprogrammation et hétérogénéité métabolique des glioblastomes 92
3. Métabolisme des cellules souches de glioblastome 93
4. Quelques approches thérapeutiques 94

OBJECTIFS DE L'ÉTUDE 97

MATÉRIELS ET MÉTHODES 99

1. Lignées cellulaires 100
   - 1.1 Cellules souches de glioblastome 100
   - 1.2 Lignée commerciale U87MG et clones dérivés 100
2. Culture cellulaire 100
3. Analyse de l'expression génique 101
   - 3.1 Lignées de cellules souches de glioblastome 101
   - 3.2 Analyses différentielle des gènes et enrichissement 102
4. Analyse de l'activité d'un réseau de régulateurs spécifique des GB 102
5. Affectation de classes basées sur l'activité d'un réseau de régulateurs 102
6. Analyse de flux extracellulaire 103
7. Métabolomique 103
   - 7.1 Préparation des échantillons 103
   - 7.2 Spectroscopie RMN HR-MAS 104
   - 7.3 Analyse et statistiques 104
8. Agents pharmacologiques et réactifs 105
9. Incucyte 105
10. Test de sensibilité 106
11. Western Blot 106
12. NKX2.5 107
    - 12.1 Plasmides 107
    - 12.2 Transfection cellulaire 108
13. RT-qPCR 108

RÉSULTATS 110

Partie 1 : Hétérogénéité et plasticité moléculaire des glioblastomes : une exploration basée sur l'activité d'un réseau de régulateurs 111

- Contexte de l'étude 111
- Article 112
- Discussion et perspectives 143

Partie 2 : Hétérogénéité et plasticité moléculaire et métabolique des glioblastomes ; évaluation dans une cohorte de lignées de cellules souches 148

- Contexte de l'étude 148
- Article 149
- Données supplémentaires 180
- Discussion et perspectives 184

CONCLUSION GÉNÉRALE 192

RÉFÉRENCES 194

ANNEXES 213

LISTE DES FIGURES

Figure 1 : Caractéristiques des glioblastomes 19

Figure 2 : Caractéristiques histomoléculaires utilisées dans le diagnostic des gliomes diffus de haut grade 23

Figure 3 : Protocole de STUPP 26

Figure 4 : Les caractéristiques fonctionnelles des cellules souches de glioblastome 29

Figure 5 : Hétérogénéité et plasticité tumorale à l'origine de résistance aux traitements..... 34

Figure 6 : Hétérogénéité spatiotemporelle des glioblastomes..... 39

Figure 7 : Signature moléculaire des sous-types définis par *Verhaak et al.* en 2016..... 42

Figure 8 : Dynamique de l'hétérogénéité et de la plasticité des cellules de glioblastome..... 44

Figure 9 : Facteurs intrinsèques et environnementaux contribuant à la dynamique de l'écosystème des glioblastomes et favorisant l'hétérogénéité tumorale 46

Figure 10 : Divers processus affectant les cellules souches de glioblastome 53

Figure 11 : La bithérapie metformine/dichloroacétate inhibe efficacement la prolifération des cellules souches de glioblastome..... 180

Figure 12 : Résistance au témozolomide acquise des cellules souches de glioblastome suite à un traitement prolongé 181

Figure 13 : Absence d'effet du témozolomide sur le profil énergétique des cellules souches de glioblastome intrinsèquement résistantes..... 182

Figure 14 : Caractéristiques distinctives entre les cellules souches résistantes et sensibles au témozolomide 185

LISTE DES TABLEAUX

Tableau 1: Séquences d'impulsion et paramètres d'acquisition utilisées lors des expériences RMN HRMAS 105

Tableau 2 : Liste des anticorps utilisés pour Western Blot 107

Tableau 3 : Liste des primers utilisés pour la qPCR 109

Tableau 4 : Caractérisation des nouvelles sous-classes moléculaires des glioblastomes 147

LISTE DES ABRÉVIATIONS

2-DG	2-Deoxy-D-Glucose
3-BP	3-Bromopyruvate
3-BrOP	3-Bromo-2-oxopropionate-1-propyl ester
4-NB	4-Nitrobenzoate
5-ALA	5-Aminolevulinic Acid
ABC	ATP Binding Cassette
AC	Astrocyte-like
ACC	Acetyl-CoA Carboxylase
ACLY	ATP-Citrate Lyase
ACSS2	Acetyl-CoA Synthetase 2
ACSVL3	Acyl-CoA Synthetase Very Long-Chain Family Member 3
ADEMA	Algorithm to Determine Expected Metabolite level Alterations
AEO	Anhydrous Enol-Oxaloacetate
AKT	Protein Kinase B
ALDH	Aldehyde Dehydrogenase
α-KG	Alpha-Ketoglutarate
α-KGDH	α-Ketoglutarate Dehydrogenase
ALT	Alternative Lengthening of Telomeres
AMPK	AMP-Activated Protein Kinase
ARG	Arginase
ASPA	Aspartoacylase
ASS1	Argininosuccinate Synthase 1
ATP	Adenosine Triphosphate
ATRA	All-Trans Retinoic Acid
ATRX	Alpha-Thalassemia/Mental Retardation syndrome X-linked
BCAT1	Branched-Chain Amino Acid Transaminase 1
BCNU	1,3-Bis(2-chloroethyl)-1-nitrosourea
BDNF	Brain-Derived Neurotrophic Factor
β-FGF	Beta Fibroblast Growth Factor
BHE	Barrière Hémato-Encéphalique
BIT-100	BSA Insulin Transferrin
BMP	Protéines Morphogénétiques Osseuses
BSA	Bovine Serum Albumin
CAD	Carbamoyl-PhosphateSynthetase2,AspartateTranscarbamylase,Dihydroorotase
CAR	Chimeric Antigen Receptor
CCLE	Cancer Cell Line Encyclopedia
CCND1/E1	Cyclin D1/E1
CcO	Cytochrome c Oxidase
CD133	Prominin-1
CDK4/6	Cyclin Dependent Kinase 4/6

CDKN2A/B	Cyclin Dependent Kinase Inhibitor 2A/B
CEBPB/D	CCAAT/Enhancer Binding Protein Beta/Delta
CHK	Choline Kinase
CIMP	CpG Island Methylator Phenotype
CL	Classical
CL-A	Classical-Astrocyte
CL-B	Classical-Basal
CL-C	Classical-Ciliary-rich
cMET	MET proto-oncogene, receptor tyrosine kinase
co-TF	Co-transcription Factor
COX4-1	Cytochrome c Oxidase Subunit 4 Isoform 1
CpG	5'-Cytosine-phosphate-Guanine-3'
cPLA2	Cytoplasmic Phospholipase A2
CPMG	Carr-Purcell-Meiboom-Gill
CPT	Carnitine Palmitoyltransferase
CRISPR	Clustered Regularly Interspaced Short Palindromic Repeats
Cas9	CRISPR Associated Protein 9
CSC	Cellules Souches Cancéreuses
CSG	Cellules Souches de Glioblastome
CSN	Cellules Souches Neurales
CTSL	Cathepsine L
DCA	Dichloroacetate
DEGs	Differentially Expressed Genes
DepMap	Dependency Map
DGC	Differentiated Gblioblastoma Cells
DHAP	Dihydroxyacetone Phosphate
DHODH	Dihydroorotate Dehydrogenase
DIRs	Differentially Influenced Regulators
DMEMF12	Dulbecco's Modified Eagle Medium/F12
DMSO	Dimethyl Sulfoxide
ECAR	Taux d'Acidification Extracellulaire
ECL	Enhanced Chemiluminescence
EGF	Epidermal Growth Factor
EGFR(vIII)	Epidermal Growth Factor Receptor (variante III)
ELOVL	Elongation of Very Long Chain Fatty Acids
EMEM	Eagle's Minimum Essential Medium
EMT	Epithelial-Mesenchymal Transition
ENO	Enolase
ETC	Electron Transport Chain
FABP7	Fatty Acid Binding Protein 7
FADS2	Fatty Acid Desaturase 2
FAO	Fatty Acid Oxidation
FASN	Fatty Acid Synthase

FBS	Fetal Bovine Serum
FDA	Food and Drug Administration
FDR	False Discovery Rate
FGF-β	Fibroblast Growth Factor 2
FLT	18F-Fluorothymidine
G-CIMP	Glioma CpG Island Methylator Phenotype
G3P	Glyceraldehyde-3-Phosphate
G6PD	Glucose-6-Phosphate Dehydrogenase
GAPDH	Glyceraldehyde-3-Phosphate Dehydrogenase
GB/GBM	Glioblastome
GBCCL	Glioblastoma Cell Lines
GBM-cREG	Glioblastoma co-Regulatory
GBM-cREGMap	Glioblastoma Co-Regulatory Map
GBM-cREGNet	Glioblastoma co-Regulatory Network
GDH	Glutamate Dehydrogenase
GEO	Gene Expression Omnibus
GFAP	Glial Fibrillary Acidic Protein
GLDC	Glycine Decarboxylase
GLS	Glutaminase
GLUT	Glucose Transporter
GO	Gene Ontology
GPD1	Glycerol-3-Phosphate Dehydrogenase 1
GPI	Glucose-6-Phosphate Isomerase
GPM	Glycolytic, Pluri-metabolic
GRN	Gene Regulatory Network
GSC	Glioblastoma Stem Cell
GSH/GSSG	Reduced/Oxidized Glutathione
GTP	Guanosine Triphosphate
Gy	Gray (unité de mesure)
h-LICORN	Hybrid-Learning Co-Operative Regulation Networks
HD	Homozygous Deletion
HDAC	Histone Deacetylase
HGF	Hepatocyte Growth Factor
HIF	Hypoxia-Inducible Factor
HK	Hexokinase
HMG-CoA	Hydroxymethylglutaryl-CoA
HMGCR	Hydroxymethylglutaryl-CoA Reductase
HR-MAS NMR	High Resolution Magic Angle Spinning Nuclear Magnetic Resonance
HRP	Horseradish Peroxidase
HSQC	Heteronuclear Single Quantum Coherence
ID4	Inhibiteur de la Différenciation 4
IDH	Isocitrate Dehydrogenase
IDO	Indoleamine 2,3-Dioxygenase

IgG	Immunoglobuline G
IMP2	Insulin-Like Growth Factor 2 mRNA-Binding Protein 2
IMPDH	Inosine Monophosphate Dehydrogenase
IRM	Imagerie par Résonnance Magnétique
ITGA5	Integrin Alpha 5
Ivy GAP	Ivy Glioblastoma Atlas Project
KEGG	Kyoto Encyclopedia of Genes and Genomes
KO	Knockout
LDH	Lactate Dehydrogenase
LIMMA	Linear Models for Microarray Data
LncARN	Long Non-Coding RNA
MAPK	Mitogen-Activated Protein Kinase
MCT	Monocarboxylate Transporter
MDSCs	Myeloid-Derived Suppressor Cells
MES	Mesenchymal
MET	Metformine
MGMT	6-O-méthylguanine-ADN méthyltransférase
MKI67	Marker of Proliferation Ki-67
ML	Monolayer
MMF	Mycophenolate Mofetil
MMP	Métalloprotéases Matricielles
MMR	Mismatch Repair
MPA	Mycophenolic Acid
MPC	Mitochondrial Pyruvate Carrier
MPG	Méthylpurine Glycosylase
MRP	Multidrug Resistance-associated Protein
MTAP	5-Methylthioadenosine Phosphorylase
MTC	Mitochondrial
mTOR	Mechanistic Target Of Rapamycin kinase
MTX	Methotrexate
NAA	N-acétylaspartate
NAAG	N-acétylaspartylglutamate
$NADP^+$, NADPH	Oxidized, Reduced Nicotinamide Adenine Dinucleotide Phosphate
NADPH	Nicotinamide Adenine Dinucleotide Phosphate
NAMPT	Nicotinamide Phosphoribosyltransferase
NEU	Neural
NF1	Neurofibromin 1
NHE1	Sodium-Hydrogen Exchanger 1
NK(T)	Natural Killer (T)
NKX2-5	NK2 Homeobox 5
NL	Normal-Like
NNMT	Nicotinamide N-methyltransferase
NO	Nitric Oxide

NOS	Nitric Oxide Synthase
NPC	Neuronal Progenitor Cell
NS	Neurosphere
NTRK2	Neurotrophic Receptor Tyrosine Kinase 2
OCR	Taux de Consommation d'Oxygène
OMS	Organisation Mondiale de la Santé
OPC	Oligodendrocyte Progenitor Cell
OXPHOS	Oxidative Phosphorylation
P-gP	Glycoprotéine P
PARP	Poly(ADP-Ribose) Polymerase
PBS	Phosphate Buffered Saline
PCA	Principal Component Analysis
PCR	Polymerase Chain Reaction
PD-1	Programmed Death-1
PDGFR	Platelet Derived Growth Factor Receptor
PDH	Pyruvate Dehydrogenase
PDK1	Pyruvate Dehydrogenase Kinase 1
PDL-1	Programmed Death-Ligand 1
PDPK1	3-Phosphoinositide-Dependent Protein Kinase 1
PFK1	Phosphofructokinase-1
PGAM1	Phosphoglycerate Mutase 1
PGK1	Phosphoglycerate Kinase 1
PI3K	Phosphoinositide 3-Kinase
PINK1	PTEN Induced Kinase 1
PKM2	Pyruvate Kinase M2
PN	Proneural
PN-L	Proneural Low
PPI	Protein-Protein Interaction
PPP	Pentose Phosphate Pathway
PRMT5	Protein Arginine Methyltransferase 5
PTEN	Phosphatase and Tensin Homolog
pTERT	promoteur de TERT
PVDF	Polyvinylidene Difluoride
RMN	Résonance Magnétique Nucléaire
RNA	Acide Ribonucléique
RNA-Seq	RNA Sequencing
RNA18S	18S Ribosomal RNA
ROS	Reactive Oxygen Species
RT-qPCR	Real-Time Quantitative Polymerase Chain Reaction
SAM	S-Adenosyl Methionine
SCD	Stearoyl-CoA Desaturase
SHH	Sonic Hedgehog
SHMT2	Serine Hydroxymethyltransferase 2

siRNA	Small Interfering RNA
SLC1A5/ASCT2	Solute Carrier Family 1 Member 5/Alanine Serine Cysteine Transporter 2
SMPD1	Sphingomyelin Phosphodiesterase 1
SNC	Système Nerveux Central
SOAT1	Sterol O-Acyltransferase 1
SOD	Superoxyde Dismutase
SQSTM1	Sequestosome 1, p62
SREBP	Sterol Regulatory Element Binding Proteins
SVM	Support Vector Machine
TBST	Tris-Buffered Saline with Tween 20
TCA	Tricarboxylic Acid Cycle
TCGA	The Cancer Genome Atlas
TF	Transcription Factor
TFs/co-TFs	Transcription Factors/co-Transcription Factors
TGFRβR	TGFRβ receptor
TME	Tumor Microenvironment
TMZ	Temozolomide
TNIP1	TNFAIP3 Interacting Protein 1
TP53	Tumor Protein p53
TP63	Tumor Protein P63
TPI	Triosephosphate Isomerase
TPM	Transition Proneurale Mésenchymateuse
TTF	Tumour Treating Fields
UMAP	Uniform Manifold Approximation and Projection
UMPS	Uridine Monophosphate Synthetase
VDAC1	Voltage-Dependent Anion Channel 1
VEGF	Vascular Endothelial Growth Factor
WB	Western Blotting
wt	wild-type
XF	Extracellular flux

INTRODUCTION

PARTIE 1 : LES GLIOMES DE HAUT GRADE

1. Définition, épidémiologie et contexte

Les gliomes correspondent à des tumeurs primitives du système nerveux central (SNC) englobant une variété de tumeurs dérivant des cellules gliales, les cellules de soutien du tissu nerveux. Les gliomes sont divisés en gliomes diffus de l'adulte, gliomes diffus pédiatrique de bas grade, gliomes diffus de pédiatrique de haut grade et gliomes astrocytaires circonscrits. Les gliomes sont les formes les plus courantes de tumeurs cérébrales. Ces tumeurs résultent ainsi de la prolifération excessive de cellules gliales anormales : d'astrocytes (astrocytomes), d'oligodendrocytes (oligodendrogliomes) et d'épendymocytes (épendynomes). D'un point de vue épidémiologique, les tumeurs du système nerveux central représentent 1,6% des cancers diagnostiqués avec une incidence d'environ 3,5 pour 100 000 habitants. Ils surviennent à tout âge, mais le plus souvent il survient chez l'adulte, les hommes étant plus susceptibles que les femmes (avec une incidence de 3,9 et 3 pour 100 000 hommes et femmes respectivement) [1].

Les étiologies des gliomes sont encore mal comprises, mais certains facteurs de risque intrinsèques (prédisposition ou susceptibilité génétique) [2,3] et extrinsèques (environnementaux) ont été identifiés. Les seuls facteurs clairement associés au développement de ces tumeurs sont l'exposition à des doses élevées de rayonnements ionisants et la présence de mutations héréditaires de gènes à pénétrance élevée [1]. D'autres facteurs de risque tels que les déclencheurs viraux (cytomégalovirus humain) [4], l'âge adulte, l'IMC et l'activité physique à l'adolescence [5] et les antécédents familiaux de cancer [6] font actuellement l'objet de recherches approfondies. Cependant, dans la majorité des cas, les gliomes sont sporadiques, sans facteurs de risque connus.

L'avancée des recherches a permis d'approfondir la connaissance de la biologie des gliomes, laissant présager le développement de nouveaux outils diagnostiques et pronostiques ainsi que de nouvelles thérapies. Cependant, de nombreux travaux de recherche ont également révélé l'hétérogénéité et la complexité des gliomes. Ces tumeurs sont en effet caractérisées par une grande hétérogénéité, que ce soit au niveau de leur caractéristiques histologiques, génétiques ou moléculaires, leur topographie, leur âge de survenue, leur rapidité d'évolution ou de leur sensibilité aux thérapies.

Le terme « haut grade » fait référence au grade de malignité de ces tumeurs, regroupant les tumeurs gliales les plus agressives. Les gliomes de haut grade sont catégorisés de grade 3 ou 4 selon l'Organisation Mondiale de la Santé (OMS) et s'opposent aux gliomes de bas grade (1 et 2) [7]. Ce terme regroupe notamment les gliomes diffus de l'adulte de grade 3 (astrocytome IDH-muté, oligodendrogliomes) et de grade 4 (astrocytomes IDH-muté et glioblastomes IDH non mutés).

Dans cette thèse, nous nous sommes focalisé sur les glioblastomes (GB). Il s'agit de la tumeur maligne la plus courante du système nerveux central, représentant 49 % des tumeurs malignes. Les GB constituent également la majorité des gliomes (57,7 % des cas) et sont parmi les plus mortels et agressifs. Le taux d'incidence des GB est d'environ 3,23 pour 100 000 habitants par an, avec une survie relative à 5 ans de seulement 6,8% et une médiane de survie de 12 mois. Ce type de cancer touche davantage les personnes âgées de plus de 55 ans (90 % des cas) et est plus fréquent chez les hommes que chez les femmes (66,2 % des cas). Après le diagnostic, une survie moins favorable est observée chez les patients âgés de 40 ans ou plus, de sexe féminin, de race blanche et d'origine ethnique non hispanique. La plupart des patients décèdent dans les 15 à 18 mois suivant le traitement par chimioradiothérapie [8,9].

Les GB sont généralement classés comme des astrocytomes en raison de leur morphologie similaire à celle des astrocytes et caractérisés par des atypies cellulaires, une capacité invasive et diffuse, un haut niveau de prolifération (nombre de mitoses élevé), la présence de zones hypoxiques, nécrotiques et de pseudopalissades ainsi qu'une hyperplasie microvasculaire [7].

Les GB présentent une multitude de caractéristiques qui favorisent leur agressivité tumorale. Premièrement, leur hétérogénéité intrinsèque, qui se traduit par une diversité de cellules tumorales aux caractéristiques distinctes, rend le traitement particulièrement complexe. Deuxièmement, leur plasticité, qui leur permet de modifier leurs caractéristiques moléculaires et phénotypiques en réponse à des signaux du microenvironnement et qui contribue notamment à leur résistance aux traitements. Troisièmement, les GB sont généralement hautement prolifératifs et invasifs, infiltrant rapidement les tissus avoisinants et gênant la délimitation tumorale lors de la résection chirurgicale. En outre, l'agressivité des GB est exacerbée par la présence de cellules souches de GB (CSG). Ces cellules ont la capacité de s'auto-renouveler et de se différencier en diverses populations cellulaires cancéreuses. Elles sont également connues pour leur plasticité, ce qui leur permet d'adapter leur comportement en réponse à des signaux environnementaux, et pour leur résistance accrue aux thérapies [10]. L'angiogenèse aberrante et la formation de zones hypoxiques, voir nécrotiques, où l'approvisionnement en médicament

se complique, favorise également l'échappement thérapeutique ainsi que la croissance tumorale. Les GB subissent également de nombreuses modifications génétiques et épigénétique, qui conduisent à une hétérogénéité accrue et à l'acquisition de clones tumoraux résistants. Ces tumeurs peuvent modifier leur métabolisme énergétique pour s'adapter à des conditions en perpétuelle évolution et de s'adapter à des conditions appauvries en oxygène ou en nutriments. Enfin les GB sont capables d'éviter la destruction par les cellules du système immunitaire et de favoriser une inflammation qui favorise la croissance tumorale. Toutes ces caractéristiques font du GB, une tumeur particulièrement agressive, la recherche doit avancer et trouver des thérapies efficaces contre ce cancer particulièrement mortel (Figure 1).

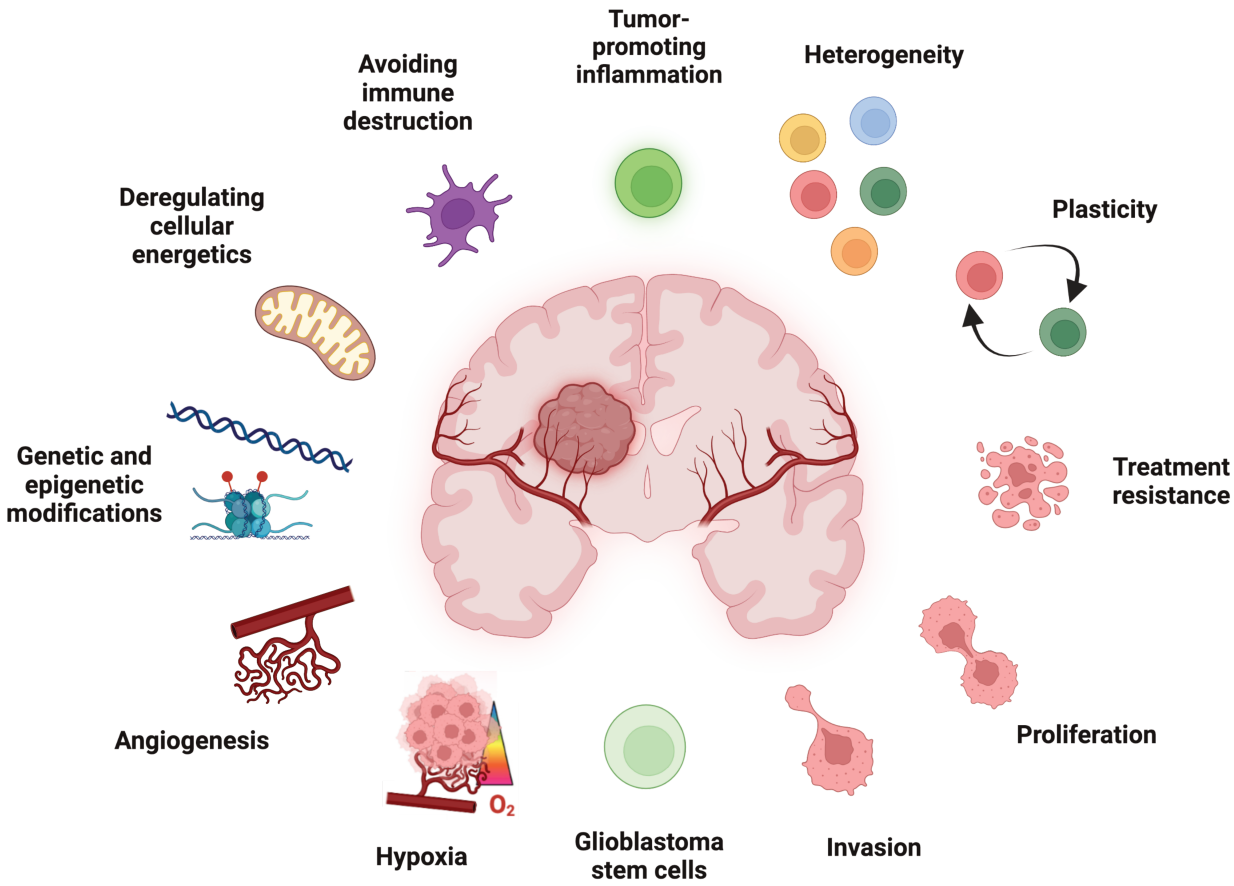

Figure 1 : Caractéristiques des glioblastomes

2. Classification de l'OMS

2.1 Evolution de la classification de l'OMS

Avant 2016, la classification des tumeurs cérébrales de l'OMS se basait exclusivement sur des critères histologiques. Le typage cellulaire jouait un rôle primordial. En effet, le diagnostic tenait compte de la ressemblance microscopique des cellules tumorales avec les cellules saines du tissu cérébral, de leur degré de différenciation, mais également de critères de malignité tels que la densité cellulaire, la présence d'atypies cytonucléaires, l'activité mitotique, la prolifération microvasculaire et la présence de nécrose.

En 2016, une nouvelle classification de l'OMS a été publiée, intégrant pour la première fois des critères moléculaires associés aux critères histologiques existants. Cette dernière a permis de définir des groupes plus homogènes en termes de pronostic et de prédiction de réponse au traitement [11]. En effet, l'avancée des recherches a identifié les mutations de l'isocitrate déshydrogénase 1 et 2 (IDH1 et IDH2) comme des biomarqueurs prédictifs d'une bonne réponse à la chimiothérapie de référence, le témozolomide (TMZ), utilisée dans le traitement des gliomes de haut grade [12,13] Ces mutations représentent également des biomarqueurs pronostiques d'une survie plus longue dans différents sous-types de gliomes. Cette découverte a nécessité le renouvellement de la classification des tumeurs du SNC afin de distinguer deux entités cliniques bien distinctes : les gliomes de haut grade IDH mutés des IDH non mutés [14].

Les progrès de la biologie moléculaire, notamment le séquençage de l'ADN à haut débit, le séquençage des ARN totaux et plus récemment le méthylome de l'ADN tumoral, ont permis d'affiner une fois de plus la classification des tumeurs cérébrales. En 2021, la cinquième édition de la classification OMS des tumeurs du système nerveux central a été publiée, dans laquelle les critères de diagnostic histomoléculaire (anomalies génétiques et épigénétiques) et de « grading » ont été affinés. Par ailleurs, l'une des améliorations majeures de la classification comprend la reconnaissance des gliomes diffus « de sous-type pédiatrique » (de bas ou haut grade) à distinguer des gliomes diffus de l'adulte, étant donné leur forte divergence.

2.2 Classification de l'OMS adoptée en 2021

La cinquième édition de la classification OMS des tumeurs du système nerveux central répertorie les gliomes dans la catégorie « Gliomes, tumeurs glioneuronales et tumeurs neuronales ».

Cette dernière est divisée en 6 familles :

- les gliomes diffus de type adulte,
- les gliomes diffus de bas grade de type pédiatrique,
- les gliomes diffus de haut grade de type pédiatrique,
- les gliomes astrocytaires circonscrits,
- les tumeurs glioneuronales et neuronales,
- les épendymomes.

Les gliomes diffus de type adulte englobent trois types :

- les astrocytomes IDH (isocitrate déshydrogénase) mutés,
- les oligodendrogliomes IDH mutés, 1p/19q codélétés (codélétion du bras court du chromosome 1 et bras long du chromosome 19),
- les GB IDH non mutés.

Comme énoncé précédemment certaines anomalies génétiques et épigénétiques sont associées aux critères histologiques afin d'aboutir à un diagnostic intégré des gliomes (Figure 2) [11]. Celles impliquées dans le diagnostic des gliomes diffus de l'adulte de haut grade sont décrites ci-dessous :

- *IDH1/IDH2* : Les gènes IDH codent pour des enzymes qui catalysent la conversion réversible de l'isocitrate en α-cétoglutarate. Les mutations entrainent un changement de l'activité catalytique de l'enzyme qui est alors capable de produire du 2-hydroxyglutarate, un oncométabolite [15]. Ces mutations sont généralement observées dans les gliomes de bas grade, prenant place à un stade précoce du développement tumoral [16]. On les retrouve également dans les oligodendrogliomes et dans les astrocytomes de haut grade. Comme énoncé précédemment, la présence de mutation au sein du gène *IDH* [12,13] a été identifié comme un biomarqueur prédictif d'une bonne réponse au TMZ et pronostique d'une survie plus longue dans différents sous-types de gliomes. Sur le plan clinique, les gliomes diffus de l'adulte de haut grade IDH mutés et

ceux IDH non mutés apparaissent comme deux entités bien distinctes. En effet, les gliomes de haut grade IDH non mutés (les plus fréquents) correspondent majoritairement à des gliomes dits « primaires » ou « *de novo* » qui prédominent chez les patients de plus de 55 ans. A l'inverse, les gliomes de haut grade IDH mutés, correspondent majoritairement à des gliomes dits « secondaires », c'est-à-dire survenant suite à des gliomes diffus de bas grade. Ces derniers apparaissent préférentiellement chez des patients plus jeunes dont la survie est généralement plus longue que celle des patients atteints de gliomes de haut grade *de novo*.

- Codélétion 1p/19q : La perte du bras court du chromosome 1 et la perte du bras long du chromosome 19 est une signature moléculaire des oligodendrogliomes et représente un facteur de bon pronostic étant associé à une meilleure réponse à la radio-chimiothérapie [17].

- *TP53* : *TP53* correspond à un gène suppresseur de tumeur, aussi appelé « gardien du génome ». La protéine p53 qui en découle correspond à un facteur de transcription qui régule de nombreux processus cellulaires tel que le cycle cellulaire, l'apoptose et l'autophagie. La présence de mutation au sein du gène *TP53* est une caractéristique des astrocytomes [18].

- Mutation p*TERT* : Le gène de la transcriptase inverse de la télomérase (*TERT*) est responsable du maintien des télomères dans les cellules germinales et souches. Ce gène est réexprimé dans la majorité des cancers humains dont les GB. La mutation du promoteur *TERT* (pTERT) est une altération moléculaire typique des GB permettant une surexpression de TERT, cette dernière a été corrélée à un mauvais pronostic des patients [19].

- *ATRX* : *ATRX* (*Alpha-Thalassemia / mental Retardation syndrome X-linked*) est un gène codant pour une protéine de remodelage de la chromatine. Les mutations au sein du gène *ATRX* ont été associée à la perte d'expression de cette protéine et à l'activation de la voie ALT (*Alternative Lengthening of Telomeres)*, une voie télomérase-indépendante de maintenance des télomères [20].

- +7/-10 : Le gain du chromosome 7 (trisomie 7) et la perte du chromosome 10 (monosomie 10) sont des anomalies chromosomiques typiques des GB.

- Amplification de l'*EGFR* : Les GB sont fréquemment caractérisés par une régulation positive du récepteur du facteur de croissance épidermique (EGFR). L'amplification du gène *EGFR* est retrouvée dans environ 60% des GB et est corrélée à un mauvais pronostic des patients [21,22]. Des mutations au sein du gène *EGFR* sont également retrouvées au sein des GB. Ces mutations peuvent entrainer la formation de récepteurs constitutivements actifs (EGFRvIII), retrouvés dans 10% des GB [23].

- *FUBP1* et *CIC* : Les mutations au sein des gènes *FUBP1* et *CIC* sont observées majoritairement dans les oligodendrogliomes [24].

- *CDKN2A* HD : La délétion homozygote de *CDKN2A (Cyclin Dependent Kinase Inhibitor 2A)* est présente dans de nombreux cancers, y compris les gliomes. Dans les astrocytomes IDH-mutées, elle permet de définir un grade 4 et annonce un mauvais pronostic [25].

	TYPE ADULTE *(> 25 ans)*			**Adolescents et Jeunes Adultes (AJA)** *(15-25 ans)*		**TYPE PÉDIATRIQUE** *(< 25 ans)*	
Type	Astrocytome IDH-muté	Oligodendrogliome IDH-muté 1p/19q-codelété	Glioblastome, IDH non-muté	Gliome diffus de la ligne médiane H3 K27-altéré	Gliome diffus hémisphérique H3 G34-muté	Gliome diffus pédiatrique de haut grade, H3 et IDH non-mutés	Gliome hémisphérique infantile
Altérations moléculaires	IDH1 /IDH2	IDH1 /IDH2 Codélétion 1p/19q	IDH1/IDH2 pTERT	Perte de H3K27Me3 ET H3K27 OU EZHIP OU EGFR	H3G34	IDH1/IDH2 H3	Famille des NTRK
	TP53 ATRX	pTERT CIC FUBP1	OU +7 -10 OU Amplification de l'EGFR	TP53 ACVR1 PDGFRα	ATRX TP53	PDGFRα MYCN EGFR Profil de méthylation	ALK ROS MET
Grade 2	Pas de CDKN2A HD Pas de PMV Pas de nécrose	Pas de PMV Index mitotique faible	Pas de grade 2	Pas de grade 2	Pas de grade 2	Pas de grade 2	Pas de grade 2
Grade 3	Pas de CDKN2A HD Pas de PMV Pas de nécrose Index mitotique élevé	PMV +/- nécrose Index mitotique élevé (≥ 6)	Pas de grade 3	Pas de grade 3	Pas de grade 3	Pas de grade 3	Pas de grade 3
Grade 4	CDKN2A HD OU PMV +/- nécrose	Pas de grade 4	Grade 4 seulement	Grade 4 seulement	Grade 4 seulement	Grade 4 seulement	Pas de grade 4

Figure 2 : Caractéristiques histomoléculaires utilisées dans le diagnostic des gliomes diffus de haut grade

Cette figure résume les caractéristiques histomoléculaires des gliomes diffus selon la nouvelle classification de l'OMS publiée en 2021. L'encadré rouge porte sur les gliomes diffus de haut grade de l'adulte [26]. 1p/19q : bras court du chromosome 1 et bras long du chromosome 19 ; +7/-10 : gain du chromosome 7 entier, perte du chromosome 10 entier ; ATRX : alpha-thalassemia/mental retardation, X-linked ; CIC : protéine Capicua ; CDKN2A HD : Cyclin Dependent Kinase Inhibitor 2A Homozygous Deletion ; EGFR : Epithelial growth factor receptor ; FUBP1 : Far Upstream Element Binding Protein 1 ; IDH : isocitrate déshydrogénase ; PMV : prolifération microvasculaire ; TP53 : tumor protein 53 ; TERTp : promoteur de TERT.

Les gliomes de haut grade peuvent être issus soit de la lignée astrocytaire pour les astrocytomes IDH mutés de grade 3 et 4 ainsi que les GB IDH non mutés, soit de la lignée oligodendrogliale pour les oligodendrogliomes de grade 3 IDH mutés, 1p/19q co-délétés. Dans le cas des astrocytomes IDH mutés, un nombre total de mitoses ≥ 2 permet de les classer en grade 3 et la présence d'une prolifération microvasculaire ou de zones nécrotiques en grade 4. Les astrocytomes IDH mutés présentant une délétion homozygote de *CDKN2A* sont également défini de grade 4 même en l'absence de prolifération microvasculaire ou de nécrose. Dans le cas des oligodendrogliomes IDH mutés, 1p/19q codélétés, un nombre de mitose ≥ 6 pour 10 champs à fort grossissement ou la présence d'une prolifération microvasculaire ou de nécrose permet de les classer de grade 3. Aucun grade 4 n'est défini pour ce type tumoral. Concernant les GB, ces derniers doivent présenter un gène *IDH* non muté (type sauvage) et au moins une des caractéristiques suivantes : une prolifération microvasculaire, une nécrose, une mutation du promoteur *TERT*, une amplification du gène *EGFR*, ou une altération combinée du nombre de copies des chromosomes 7 et 10 [7].

3. Diagnostic et prise en charge thérapeutique

3.1 Diagnostic

Une tumeur cérébrale doit être suspectée en présence de signes neurologiques d'apparition soudaine ou d'aggravation progressive. Il n'existe aucun symptôme spécifique des gliomes diffus de l'adulte. La symptomatologie dépend de la topographie et du volume tumorale. Lorsque la tumeur présente une taille importante ou que celle-ci entraîne un œdème important, les signes cliniques résultent d'une hypertension intracrânienne. L'apparition récente de symptômes cliniques tels que des céphalées, des déficits neurologiques (cognitifs, moteurs, visuels ou linguistiques) ou des crises d'épilepsie doit inciter à la réalisation d'une imagerie par résonance magnétique (IRM) [27]. Les gliomes diffus de haut grade prennent majoritairement place au niveau supratentorielle (dans 40% des cas au sein du lobe frontal) et plus rarement au niveau du tronc cérébral (5% des cas) ou du cervelet (<3% des cas) [28]. L'imagerie permet de révéler l'existence d'une tumeur cérébrale et sa localisation, mais seules des analyses histologiques et moléculaires du tissu tumoral (issu d'une biopsie ou de l'exérèse chirurgicale) permettent de confirmer son diagnostic précis. Ces analyses se basent sur les critères histologiques et moléculaires intégrés dans la classification des tumeurs du SNC de l'OMS précédemment décrite (Figure 2).

3.2 Facteurs pronostiques

Les facteurs cliniques de bon pronostic comprennent l'âge du patient < 60 ans, un index de Karnofsky (KPS) > 70, un score de Mini-Mental State Examination (MMSE) ≥ 27 et une localisation frontale de la tumeur [29]. L'index de KPS permet d'évaluer le degré d'autonomie et de dépendance du patient tandis que le MMSE permet d'évaluer leurs performances neurocognitives. Concernant les facteurs moléculaires de bon pronostic, ces derniers sont intégrés dans la classification de l'OMS de 2021 et comprennent : la présence de mutation au sein du gène *IDH*, la co-délétion 1p/19q, la délétion homozygote de *CDKN2A* [7]. La présence d'une infiltration de lymphocytes T cytotoxiques peut également être associée à une survie plus longue [30]. Le statut de méthylation du promoteur du gène *MGMT* (6-O-méthylguanine-ADN méthyltransférase) est un facteur prédictif de réponse au TMZ [31].

3.3 Prise en charge thérapeutique

3.3.1 Prise en charge du GB nouvellement diagnostiqué

Les gliomes de haut grade représentent un défi thérapeutique pour les oncologues. Malgré de nombreuses et diverses propositions thérapeutiques, s'appuyant sur des résultats précliniques encourageants, le traitement de référence des gliomes de haut grade n'a pas évolué depuis 2005. Ce dernier, nommé protocole STUPP, associe une résection chirurgicale à une radiothérapie et une chimiothérapie (témozolomide, TMZ) concomitante puis adjuvante durant une période de 6 mois [32]. Les améliorations des techniques chirurgicales ont permis un gain de survie des patients de quelques mois tout comme l'ajout de la chimiothérapie qui a permis d'allonger la survie médiane des patients à 14,6 mois, par rapport à 10,6 mois [33,34].

La résection chirurgicale de la tumeur doit être la plus complète possible tout en préservant les tissus sains avoisinants un maximum. La délimitation tumorale est problématique étant donné la grande capacité d'infiltration des cellules tumorales dans les tissus avoisinants, ces dernières pouvant se disséminer même à distance du site tumoral. Concernant la radiothérapie externe, celle-ci est mise en place dans un délai de 2 à 6 semaines suivant l'opération. Cette dernière délivre une dose totale de 60 Gray (Gy) en 30 fractions de 2 Gy avec une fraction par jour, 5 jours par semaine sur une période totale de 6 semaines [33]. Associé à la radiothérapie, le TMZ est administré *per os* à une dose de 75mg/m^2 quotidiennement pendant 6 semaines. Quatre semaines après la fin de la radiochimiothérapie, le TMZ est réintroduit en monothérapie

à une dose de 150–200 mg/m^2 avec une cure de 5 jours tous les mois sur une période totale de 6 mois (Figure 3).

Le TMZ est une chimiothérapie alkylante et représente le traitement standard des gliomes de haut grade. Il s'agit d'un composé triazène, une prodrogue dont le métabolite actif correspond au MTIC (3-methyl-(triazen-1-yl)imidazole-4-carboxamide). Le MTIC est ensuite rapidement converti en 5-aminoimidazole-4-carboxamide et en methyldiazonium. Ce dernier génère des adduits à l'ADN qui bloquent le cycle cellulaire et conduisent à la mort cellulaire. En effet, des alkylations en position O_6 et N_7 des guanines et N_3 des adénines provoquent des mésappariements entre les bases de l'ADN. Ces mésappariements sont pris en charge par le système de réparation Mismatch repair (MMR). Le système MMR va effectuer des cycles d'excision et de réinsertion afin de corriger les mésappariements de l'ADN mais certaines alkylations persistent. Cette réparation aberrante de l'ADN conduit les cellules tumorales à l'apoptose [35].

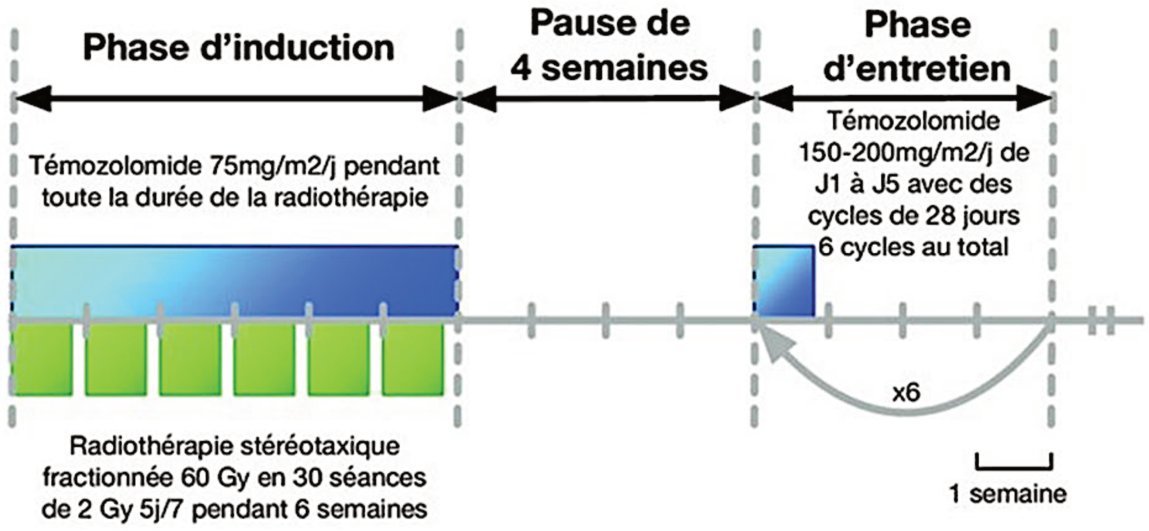

Figure 3 : Protocole de STUPP

3.3.2 Prise en charge des symptômes

Divers traitements symptomatiques, adaptés aux troubles des patients, sont généralement mis en place en postopératoire tels que les corticoïdes pour leurs effets anti-œdémateux, les anticonvulsivants, les anticoagulants en cas de pression intracrânienne, d'accident vasculaire cérébral et de thrombose veineuse profonde, les antiépileptiques en cas de crise d'épilepsie. Par ailleurs, une rééducation neuropsychologique, orthophonique ou encore une kinésithérapie peuvent être mis en place.

3.3.3 Prise en charge des récidives

Il n'existe aucun consensus sur la prise en charge thérapeutique des récidives des GB. Les options thérapeutiques restent limitées mais comprennent la réalisation d'une nouvelle résection tumorale, d'une nouvelle radiothérapie, la reprise d'un traitement au TMZ, la mise en place d'un traitement au bévacizumab (Avastin®), d'un dispositif TTF (*Tumor Treating Fields*) ou la mise en place de nouvelles thérapies telles que des agents alkylants (lomustine, carmustine, fotemustine, carboplatine ou procarbazine), un agent déstabilisateur des microtubules (vincristine).

La plupart du temps, les patients sont encouragés à intégrer un essai clinique [36]. L'abstention thérapeutique et/ou la mise en place de soins palliatifs peuvent également être discutés. La stratégie thérapeutique est ainsi déterminée lors d'une réunion de concertation multidisciplinaire et est personnalisée selon le profil de chaque patient [37].

3.3.4 Thérapie ciblée

Ces dernières années ont vu l'avènement de thérapies ciblées, mais aucune d'entre elles n'a permis une amélioration clinique significative des patients atteints de GB [38]. Seul le bévacizumab, un anticorps monoclonal dirigé contre le VEGF (*Vascular Endothelial Growth Factor*), a reçu une approbation par la *Food and Drug Administration* (FDA). Il est désormais indiqué en deuxième ligne pour les GB récidivants ou progressant rapidement en monothérapie. Dans les essais cliniques, l'ajout du bévacizumab au protocole STUPP a amélioré la survie sans progression, mais pas la survie globale des patients. Un effet anti-oedémateux a notamment été rapporté, soulignant son intérêt dans le cas d'œdème cérébral, principale morbidité des patients atteints de GB. De nombreux effets indésirables ont également été rapportés : thrombose artérielle et veineuse, hypertension, hémorragie cérébrale et altération de la cicatrisation des plaies [39]. Le bévacizumab est un anticorps anti-VEGF (Vascular Endothelial Growth Factor). Il se lie au VEGF, facteur clé de la vasculogenèse et de l'angiogenèse, inhibant de ce fait la liaison du VEGF à ses récepteurs, Flt-1 (VEGFR-1) et KDR (VEGFR-2), à la surface des cellules endothéliales. La neutralisation de l'activité biologique du VEGF altère la vascularisation tumorale d'où une inhibition temporaire de la croissance tumorale. L'effet est cependant grandement atténué en raison de la boucle autocrine VEGFR2-Neuropilin-1 au sein des CSG [40]. De plus, l'inhibition de la formation des vaisseaux causera une hypoxie qui, à long terme, facilitera le maintien ou l'expansion des populations de CSG [41–43].

De nombreux autres essais cliniques ont été entrepris pour évaluer l'efficacité de diverses thérapies ciblées. Ces essais ont exploré plusieurs axes de ciblage, notamment l'angiogenèse, la signalisation des CSG, l'autonomie de croissance, la migration des cellules tumorales, ainsi que le cycle cellulaire. Parmi les thérapies ciblées, les voies de signalisation des récepteurs à tyrosine kinase, comme celles des récepteurs EGFR, VEGF/VEGFR et PDGFR, sont les plus étudiées. L'imatinib (Glivec®), un inhibiteur de l'activité tyrosine kinase de plusieurs récepteurs (c-Kit, DDR1, DDR2, CSF-1R, PDGFRA et PDGFRB), ou encore le gefitinib (Iressa®) et l'erlotinib (Tarceva®), deux inhibiteurs des domaines tyrosines kinases de l'EGFR ont fait l'objet d'essais cliniques, utilisés seuls ou en association dans le traitement des gliomes récurrents. Des études de phase II ont examiné l'efficacité du cabozantinib (NCT00704288), un inhibiteur de tyrosine kinases à cibles multiples (MET, VEGFR2, FLT3, c-KIT, and RET), chez les patients atteints de GB progressifs, ainsi que celle de l'AMG 102 (Rilotumumab) (NCT01113398), un anticorps monoclonal dirigé contre le HGF (*Hepatocyte Growth Factor*), et de l'aflibercept (NCT00369590), un inhibiteur de VEGF, pour les GB récurrents [38].

Le cilengitide, un inhibiteur des intégrines αvβ3 et αvβ5, a été testé dans des études telles que l'essai NABTT 0306 et le CORE Study en combinaison avec le traitement standard pour les patients atteints de GB nouvellement diagnostiqués. Bien que des études précliniques aient montré que le cilengitide pourrait affecter à la fois les cellules tumorales et les cellules endothéliales, les résultats cliniques ont été décevants [44,45]. Plusieurs raisons peuvent expliquer cet échec. D'une part, la pharmacocinétique et notamment la demi-vie courte (de quelques heures) du cilengitide limitent ses propriétés chez les patients. D'autre part, aucun biomarqueur fiable n'a été identifié pour la stratification des patients [46,47].

3.3.5 Dispositif TTF

Le dispositif TTF (*Tumor Treating Fields*) est un appareil portable électronique composé d'électrodes capables de délivrer des champs électriques alternatifs de faible intensité et de fréquence intermédiaire (100 à 300 kHz), ces derniers perturbant la mitose des cellules cancéreuses en interférant avec les complexes septine et l'α/β-tubuline lors de la transition métaphase-anaphase du cycle cellulaire [48]. De plus, ce dispositif entraîne une interférence avec le métabolisme énergétique. En effet, la production de pyruvate, produit final de la glycolyse et carburant essentiel pour la respiration mitochondriale, est réduite lorsque les TTF sont appliqués [49]. En 2011, ce dispositif a été approuvé par la FDA pour le traitement du GB récurrent, puis en 2015 comme traitement adjuvant du GB nouvellement diagnostiqué [50,51].

4. Cellules souches de glioblastome

4.1 Notion et caractéristiques

Une des problématiques des GB qui complique leur prise en charge thérapeutique est la présence de cellules souches cancéreuses (CSC). Découvertes initialement en 2003 au sein des GB [52], les cellules souches de glioblastome (CSG) présentent de nombreuses similitudes avec les cellules souches neurales (CSN). Ces similitudes se manifestent en termes de propriétés, de localisation préférentielle, de voies de signalisation, de profils d'expression génique et de biomarqueurs. Tout comme les CSN, les CSG possèdent une capacité d'auto-renouvellement et un potentiel de différenciation ainsi que l'expression de marqueurs spécifiques aux cellules souches. Par ailleurs, tout comme les CSN, elles résident dans des microenvironnements particuliers favorables à leur survie et leur fonction, appelés « niches » [53]. L'auto-renouvellement, la prolifération persistante et la capacité à initier des tumeurs *in vivo* sont les caractéristiques fonctionnelles principales des CSG. D'autres traits incluent l'expression de marqueurs spécifiques aux cellules souches et un potentiel de différenciation. Toutefois, ces dernières caractéristiques, bien qu'importantes, ne définissent pas à elles seules le caractère souche des cellules (Figure 4). Dotées d'une grande plasticité et d'une capacité s'autorenouveler et à se propager, les CSG ont été impliquées dans l'initiation, le développement et la récidive des tumeurs [54–57].

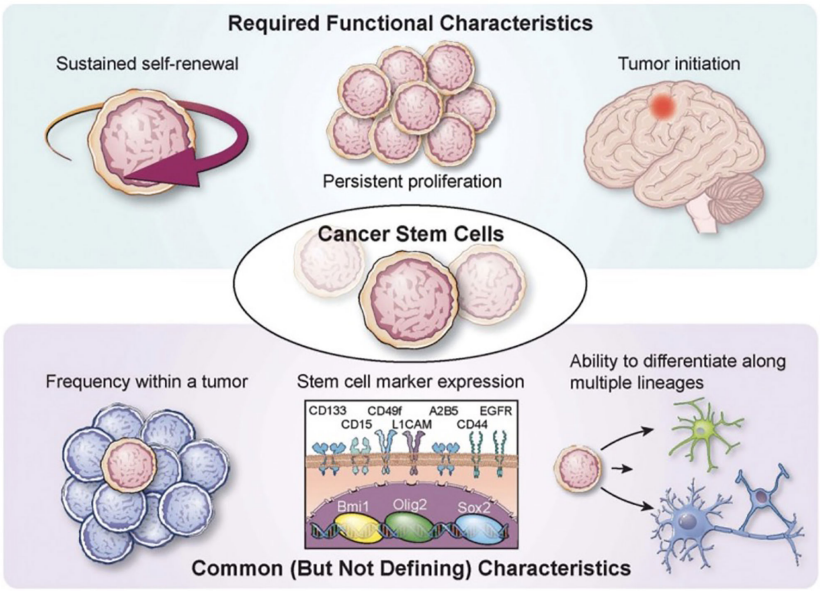

Figure 4 : Les caractéristiques fonctionnelles des cellules souches de glioblastome
Figure illustrant les caractéristiques fonctionnelles des cellules souches de glioblastome selon *Lathia et al*. [53] et illustré par *Piper et al.* [58].

4.2 Isolement et identification

L'isolement et l'identification des CSG sont des étapes cruciales pour étudier et comprendre la pathogenèse des GB. Historiquement, les techniques d'isolement se sont appuyées sur la cytométrie en flux en utilisant des marqueurs spécifiques tels que CD133. CD133, également connu sous le nom de Prominin-1, a été le premier marqueur utilisé pour identifier les CSC dans les tumeurs cérébrales humaines. Les cellules isolées avec ce marqueur, ont démontré leur capacité à former des neurosphères *in vitro* et à initier des tumeurs *in vivo* chez des souris immunodéprimées, engendrant des tumeurs qui reflètent la tumeur parentale d'origine [59].

Outre CD133, d'autres marqueurs de surface et médiateurs moléculaires ont été identifiés pour l'isolement et l'identification des CSG, tels que CD44, Musashi1, CD15, L1CAM, l'intégrine α6, Nestin, CD36, A2B5, LGR5, B23 et GPD1. La fiabilité de ces marqueurs est encore débattue dans la communauté scientifique. Il est important de noter que certains de ces marqueurs sont également exprimés par les CSN, ce qui peut compliquer leur utilisation exclusive pour l'identification des CSG [55].

Outre la recherche de marqueurs spécifiques des CSG, des progrès ont été accomplis grâce à la mise au point de conditions de culture *in vitro* favorisant l'enrichissement en populations cellulaires présentant des caractéristiques souches. En effet, les échantillons de GB post-chirurgie peuvent être cultivés *in vitro,* soit comme des cellules différenciées en monocouche adhérentes en présence de sérum, soit comme des neurosphères en suspension enrichies en CSG dans un milieu sans sérum contenant les facteurs de croissance EGF (*epidermal growth factor*) et FGF-β (*fibroblast growth factor 2*) [60].

Pour confirmer le caractère souche d'une cellule, il est recommandé de combiner l'évaluation de l'expression de plusieurs marqueurs avec d'autres caractéristiques fonctionnelles des CSG, telles que leur capacité à former des neurosphères *in vitro* et leur potentiel tumorigénique *in vivo* [53].

4.3 Fonctions pro-tumorigéniques

Les CSG seraient en grande partie responsables de certaines caractéristiques tumorales, telles que la prolifération, la maintenance et la récurrence des tumeurs [61]. De nombreux travaux de recherche ont révélé que les CSG sont plus agressives que les cellules non-CSG, même si les distinctions précises entre ces deux types cellulaires ne sont pas encore clairement

établies [62]. Selon de nombreuses études, les CSG jouent un rôle dans la promotion de l'angiogenèse tumorale [63,64], l'invasion tumorale [65] et l'évasion immunitaire [66], contribuant toutes aux échecs thérapeutiques. Elles peuvent également être appelées « cellules initiatrices de tumeur » étant capables d'initier la formation de tumeurs dans des modèles expérimentaux *in vivo* [53]. De nombreuses preuves suggèrent que la sous-population de CSG est probablement associée à une résistance aux thérapies standard et à la survenue des rechutes malignes [40,57,67].

4.4 Voies de signalisation

Les CSG sont régulées par plusieurs voies de signalisation, dont la voie Notch, la voie Wnt et la voie Sonic hedgehog (SHH). Ces voies jouent un rôle crucial dans la prolifération, la maintenance et la résistance des CSG aux thérapies. La voie Notch, par exemple, est essentielle pour la régulation des CSG. Elle peut être activée non seulement par des interactions avec l'endothélium, mais aussi par des protéines de la matrice extracellulaire comme la ténascine. De plus, la présence de nombreux récepteurs activateurs sur les CSG, tels que l'inhibiteur de la différenciation 4 (ID4) et la protéine de liaison aux acides gras 7 (FABP7), facilite le déclenchement de la signalisation Notch. La voie Wnt est un autre acteur majeur dans la régulation des CSG, influençant leurs caractéristiques de cellules souches, leur capacité à induire l'angiogenèse, ainsi que leur capacité de migration et d'invasion. Les mécanismes d'activation de cette voie sont variés, impliquant des processus génétiques et épigénétiques, et peuvent être à la fois canonique (voie β-caténine dépendante) ou non canonique (voies indépendantes de la β-caténine). Enfin, la voie SHH est également une voie importante au sein des CSG. Elle joue un rôle déterminant dans la résistance aux médicaments, en particulier en augmentant l'expression de la P-glycoprotéine et d'autres transporteurs ABC (ATP Binding Cassette). Ces voies de signalisation, parmi d'autres, soulignent la complexité des mécanismes qui régulent les CSG et offrent de nouvelles perspectives pour le développement de thérapies ciblées [68–70].

5. Échecs thérapeutiques

Les GB sont des tumeurs qui, en raison de leur forte résistance aux traitements, récidivent presque inévitablement. Malgré plus de 10 ans de recherche et de nombreux essais cliniques, les stratégies thérapeutiques n'ont toujours pas connu d'amélioration clinique significative.

Les raisons de ces échecs thérapeutiques sont multiples, notamment l'impossibilité d'effectuer une résection tumorale complète, l'hétérogénéité et la plasticité des GB avec une expression moléculaire variable des cibles thérapeutiques, la présence de CSG à fort potentiel tumorigène, les difficultés d'accès des médicaments aux cibles en raison de la barrière hémato-encéphalique ou de la complexité d'un réseau vasculaire tumoral dysfonctionnel, l'inactivation des drogues par l'acidification intra-tumorale et bien d'autres mécanismes de résistance aux traitements [71].

Lors de la prise en charge des patients atteints de GB, l'une des premières difficultés rencontrées est la réalisation d'une résection tumorale complète [65]. Les cellules cancéreuses présentent en effet une importante capacité d'infiltration dans les tissus avoisinants, compliquant la délimitation lors de la résection tumorale. Par ailleurs, certaines zones du cerveau ne peuvent être retirées sans altérer considérablement la qualité de vie des patients. 35% des patients nouvellement diagnostiqués sont considérés comme non opérables en raison de la localisation ou de la taille de la tumeur. Dans ces cas, une biopsie est recommandée pour établir un diagnostic. Lorsque la chirurgie est possible, la résection macroscopique est décrite comme un bon facteur pronostique [72]. Une méta-analyse a révélé que parmi 27 865 patients diagnostiqués avec un GB entre 2004 et 2013, les proportions pour une biopsie (patient non opérable), une résection partielle et une résection massive étaient respectivement de 28,5 %, 34,8 % et 36,8 % [73].

Un autre obstacle majeur est la BHE, qui limite l'accès des médicaments aux tumeurs. De nouvelles approches, telles que les nanoparticules ou la livraison par convection améliorée (CED), montrent des résultats précliniques et cliniques encourageants [74,75].

La nature complexe et variée des GB rend leur traitement particulièrement difficile. En effet, de manière générale, les échecs thérapeutiques des GB sont attribuables au caractère hautement hétérogène de ces tumeurs, composées de différentes populations cellulaires cancéreuses ayant des réponses variées aux traitements.

Les CSG sont souvent identifiées comme les principales responsables des échecs thérapeutiques, en raison de leur résistance accrue aux traitements anticancéreux, y compris à la radiothérapie [56] et à la chimiothérapie [57]. Cette résistance accrue peut être attribuée à (1) un état quiescent, rendant inefficaces les thérapies utilisées qui ciblent le cycle cellulaire [76], (2) une augmentation de l'efflux des médicaments par l'augmentation de transporteurs ABC

notamment MRP1 (*multidrug resistance-associated protein 1*) et P-gP (*permeability-glycoprotein*), (3) une capacité accrue à réparer l'ADN [56], (4) une régulation négative de l'apoptose ou inversement, une régulation positive des voies anti-apoptotiques [77,78], (5) une plus grande capacité de réserve mitochondriale [79] et (6) leur localisation au sein des niches hypoxiques [80].

Un des mécanismes de chimiorésistance fréquemment décrits dans les GB concerne la réparation de l'ADN endommagé par les agents chimiothérapeutiques. En effet, les dommages causés par le TMZ aux positions O6 et N7 des guanines peuvent être réparés par des enzymes spécifiques, tels que la O6-méthyl-guanine DNA méthyl transférase (MGMT) et la méthylpurine glycosylase (MPG). Des recherches ont mis en évidence une variabilité dans le profil de méthylation du promoteur du gène *MGMT* au sein des tumeurs de patients [81]. Théoriquement, cette information pourrait guider le choix du traitement chimiothérapeutique pour les GB, car la méthylation du promoteur du gène *MGMT* inhibe la production de la protéine MGMT, empêchant ainsi la réparation des dommages causés par le TMZ. Cependant, la détection du statut MGMT présente des limites et il n'existe pas de consensus actuel sur son utilisation en pratique clinique.

En complément des mécanismes de résistance déjà presentés auparavant, il est important de souligner que l'hétérogénéité et la dynamique évolutive des tumeurs contribuent également aux échecs thérapeutiques. Dès lors, deux mécanismes principaux permettent d'expliquer la résistance aux traitements : (1) la prolifération et la sélection au fil du temps de cellules intrinsèquement résistantes, et (2) l'adaptation dynamique des cellules tumorales à des phénotypes résistants. Dans le premier scénario, certaines cellules résistantes qui existent déjà au sein de la tumeur bénéficient d'avantages génétiques ou phénotypiques qui leur permettent de survivre aux traitements. Le second scénario fait appel au modèle d'évolution et de sélection clonale, où le traitement induit des mutations favorisant la résistance. Un autre mécanisme de résistance, la "résistance phénotypique adaptative", fait appel à la plasticité non génétique des cellules tumorales. Les cellules "persisters" peuvent survivre à la pression thérapeutique en adoptant des états résistants avec une réponse plus rapide que la sélection darwinienne. Ces cellules peuvent échapper au traitement en modifiant temporairement leur phénotype, par exemple en ajustant leur expression génique ou leur métabolisme. Ces changements sont réversibles - lorsque le traitement est arrêté, les persisters peuvent revenir à leur état phénotypique initial (Figure 5) [82].

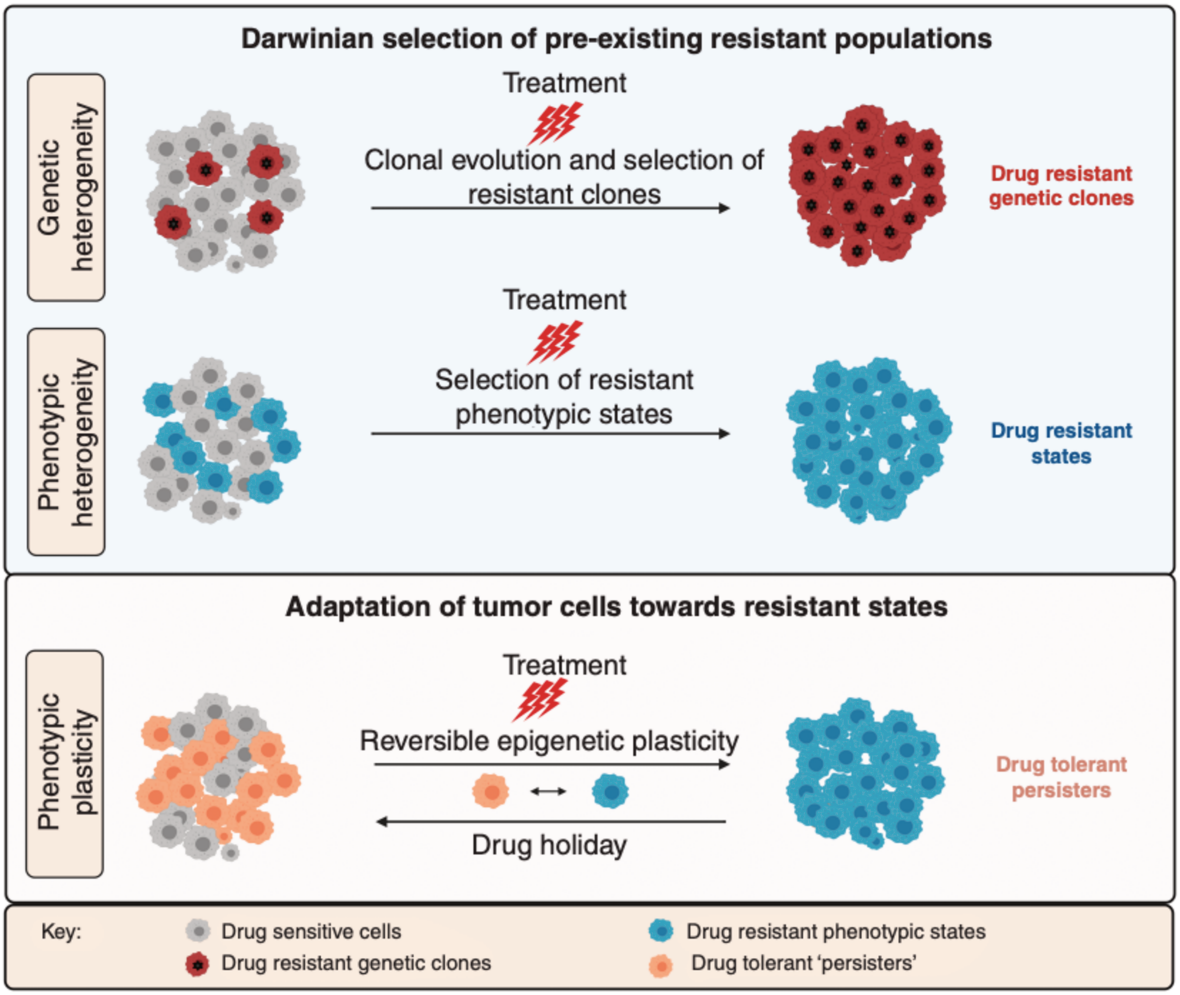

Figure 5 : Hétérogénéité et plasticité tumorale à l'origine de résistance aux traitements
Les tumeurs contiennent des cellules avec des sensibilités variables au traitement. Le traitement conduit à l'éradication des cellules sensibles aux médicaments. La résistance peut être entraînée par la sélection darwinienne de cellules résistantes préexistantes avec des caractéristiques génétiques ou phénotypiques avantageuses. Des clones génétiques hautement résistants peuvent également être acquis suite au traitement (c'est-à-dire, évolution et sélection clonales). La résistance adaptative est entraînée par des cellules persistantes tolérantes aux médicaments qui survivent au traitement et s'adaptent vers des états phénotypiques résistants. Les cellules persistantes peuvent revenir à leurs états phénotypiques initiaux et recréer l'hétérogénéité phénotypique lorsqu'elles sont libérées du traitement (c'est-à-dire, interruption du traitement). Ainsi, la résistance aux médicaments peut être le résultat d'une plasticité épigénétique réversible combinée à une expansion clonale irréversible [82].

6. Vers de nouvelles stratégies thérapeutiques

La recherche de nouvelles thérapies pour les GB s'est principalement axée sur les cibles moléculaires identifiées par des analyses génomiques à grande échelle, telles que celles du TCGA (*The Cancer Genome Atlas*). Des altérations moléculaires récurrentes dans des voies clés de la régulation cellulaire, de l'autophagie, de la réparation de l'ADN, de l'apoptose, de l'angiogenèse et des points de contrôle immunitaires ont été explorées comme cibles potentielles. Bien que des progrès aient été réalisés dans divers domaines thérapeutiques, y

compris la chirurgie, la radiothérapie et la chimiothérapie, les résultats cliniques restent insatisfaisants. De nos jours, les caractéristiques moléculaires des GB ne sont pas encore utilisées pour différencier les différentes stratégies de traitement disponibles. Néanmoins, de plus en plus d'essais cliniques intègrent désormais une évaluation génétique/épigénétique des tumeurs de patients dans leurs plans d'études. Le développement d'une médecine personnalisée est en cours, nécessitant non seulement l'identification de cibles spécifiques, mais également la sélection des patients susceptibles de répondre favorablement à ces traitements [38,83]. Ainsi, pour les implications futures, il est crucial de stratifier les patients en fonction de biomarqueurs pronostiques et prédictifs, tels que le niveau d'expression des cibles thérapeutiques au sein des cellules cancéreuses. Cette stratégie pourrait non seulement identifier les patients les plus susceptibles de répondre à une thérapie ciblée spécifique, mais aussi réduire les coûts [84].

Étant donné la plasticité des cellules cancéreuses, il convient également d'établir des approches combinatoires qui pourraient surmonter les mécanismes d'adaptation des cellules cancéreuses. Par exemple, le ciblage de la microglie, considéré comme un régulateur majeur de l'environnement tumoral, a été suggéré en combinaison avec des thérapies ciblées [85]. Des essais cliniques en cours, tels que NCT03743662, NCT03661723 et NCT04704154, combinent le bévacizumab ou d'autres thérapies ciblées aux inhibiteurs de points de contrôle immunitaire, ouvrant ainsi de nouvelles perspectives pour le traitement des GB.

Des essais cliniques ciblant simultanément différents effecteurs intracellulaires des voies de signalisation oncogéniques sont également à l'étude, avec une attention particulière portée aux inhibiteurs de PI3K et de mTOR. Il est également de plus en plus courant d'explorer des approches avec des inhibiteurs multi-kinases ou, de manière générale, des stratégies thérapeutiques multi-cibles. Les médicaments capables de cibler plusieurs nœuds critiques pour le développement et la progression des GB pourraient aider à contrer le manque d'efficacité et l'acquisition de résistance observés dans le cadre de monothérapie [86].

L'angiogenèse joue un rôle crucial dans le microenvironnement tumoral et fait l'objet d'une attention particulière dans la recherche de thérapies contre les GB. Les GB sont souvent caractérisés par une vascularisation importante, avec la formation de vaisseaux sanguins étroits et tortueux qui limitent l'efficacité de la chimiothérapie et favorisent le développement de la tumeur. Afin de réduire ces vaisseaux sanguins, de nombreux essais cliniques combinent actuellement une chimiothérapie avec un médicament anti-angiogénique. Le bévacizumab (Avastin®), un anticorps monoclonal dirigé contre le VEGF, est souvent utilisé dans ces essais.

Comme énoncé précédemment, ce médicament a été approuvé par la FDA pour le traitement en deuxième ligne des GB récidivants ou progressant rapidement en monothérapie.

En dehors de l'angiogenèse, d'autres stratégies thérapeutiques ciblant le microenvironnement tumoral sont également explorées. L'hypoxie et les facteurs induits par l'hypoxie (HIFs) sont des cibles particulièrement étudiées, étant donné que les GB sont des tumeurs très hypoxiques et que l'hypoxie joue un rôle majeur dans l'initiation, la progression, la résistance aux traitements, le maintien du phénotype souche et la récurrence des tumeurs [87].

D'autres approches en cours d'investigation comprennent les thérapies cellulaires et nouvelles immunothérapies, telles que la vaccination, les inhibiteurs des points de contrôle immunitaire, la thérapie T-cell, la thérapie NK, CAR T-cell, CAR NK, les cellules T gamma-delta, les cellules NKT, la thérapie cellulaire dendritique, la thérapie par les macrophages, la thérapie virale oncolytique et les inhibiteurs d'IDO [88]. Ces domaines de recherche sont en plein essor et pourraient apporter de nouvelles solutions dans la prise en charge thérapeutique des GB.

Les nanotechnologies sont également en cours de développement pour améliorer la délivrance de médicaments de manière plus spécifique et moins toxique. Elles sont particulièrement pertinentes pour le traitement des GB, où la BHE représente un défi majeur pour la délivrance de médicaments. Les nanoparticules, en raison de leur petite taille et de leurs propriétés modifiables, peuvent permettre le transport de médicaments à travers la BHE et une administration de traitements ciblés sur la tumeur, limitant ainsi la toxicité pour les tissus sains. Outre le développement de nouvelles thérapies, l'amélioration des méthodes de diagnostic et de suivi des patients est également un défi à relever dans la prise en charge des GB. Les progrès en nanotechnologie peuvent également contribuer dans ces domaines, en offrant des moyens plus efficaces et moins invasifs d'imagerie tumorale et de suivi de la réponse au traitement [89].

D'autres approches visant à exploiter les dérégulations métaboliques des cellules tumorales par rapport aux cellules saines sont également en cours d'exploration [90]. Ces approches anticancéreuses ciblant le métabolisme tumoral en cours d'étude sont abordées plus en détail dans la partie 3. La dérégulation du métabolisme énergétique est une caractéristique des cellules cancéreuses. Il est possible qu'une stratégie thérapeutique ciblant les dérégulations métaboliques des tumeurs soit plus efficace que le ciblage d'altérations génomiques spécifiques

dans une tumeur hétérogène comme le GB. De plus, les chimiothérapies utilisées actuellement dans le traitement des cancers présentent une forte toxicité. De nombreux effets secondaires sont observés : anémie, changements d'appétit, fatigue, perte de cheveux, nausées et vomissements. En les combinant à d'autres thérapies, il serait possible de limiter ces effets indésirables en diminuant les doses des agents chimiothérapeutiques tout en conservant une action anti-cancéreuse efficace [91]. De ce fait, des recherches intensives visent à identifier de nouvelles cibles thérapeutiques au sein du métabolisme tumoral. La compréhension des mécanismes et des voies métaboliques pro-tumorigéniques est nécessaire afin de définir les cibles thérapeutiques pertinentes et par la suite, de pouvoir proposer des thérapies combinées.

En conclusion, les progrès réalisés dans la compréhension des mécanismes moléculaires et cellulaires impliqués dans la pathogenèse des GB ont ouvert la voie à l'identification de nouvelles cibles thérapeutiques et au développement de nouvelles stratégies thérapeutiques. Cependant, l'importante hétérogénéité et la plasticité des GB continuent de poser des défis considérables, entravant notre capacité à améliorer significativement les résultats cliniques. Elles compliquent non seulement le choix du traitement, mais aussi le suivi de la progression de la maladie, car les différentes sous-populations de cellules tumorales peuvent réagir différemment aux thérapies et évoluer de manière indépendante. Les efforts de recherche et développement dans le domaine des GB doivent se poursuivre afin de déterminer les approches thérapeutiques les plus adaptées à chaque patient, en fonction des caractéristiques spécifiques de leur tumeur. En parallèle, les efforts de recherche se poursuivent pour identifier des marqueurs prédictifs de réponse aux traitements, avec pour objectif ultime d'optimiser la prise en charge des patients atteints de GB.

PARTIE 2 : HÉTÉROGÉNÉITÉ ET PLASTICITÉ TUMORALE

1. Concepts d'hétérogénéité et de plasticité tumorale

Les avancées en recherche ont révélé l'importante hétérogénéité des GB, que ce soit entre les différentes tumeurs de patients (hétérogénéité inter-tumorale) mais aussi au sein d'une même tumeur (hétérogénéité intra-tumorale). Cette hétérogénéité, observable à plusieurs niveaux, contribue à la complexité de ces tumeurs. Les GB sont caractérisés par une diversité de populations cellulaires et de microenvironnements (Figure 6). Ces différentes populations se distinguent par leurs morphologies uniques, des degrés variés d'aneuploïdie, des caractéristiques moléculaires distinctes, ainsi que par des profils géniques spécifiques. Ces caractéristiques sont étroitement liées au microenvironnement et varient selon un facteur spatio-temporel. Au fil de l'initiation et de la progression de la tumeur, ainsi que lors de récidives, les propriétés de la tumeur peuvent changer de façon significative. Cette dynamique est encore exacerbée sous la pression des thérapies [92].

L'hétérogénéité génétique, présente dans la majorité des cancers, découle d'une instabilité génomique caractéristique des cellules cancéreuses. Des mutations ponctuelles, des délétions, des amplifications, des translocations ou des inversions peuvent survenir de manière aléatoire pendant la réplication de l'ADN, conduisant à une diversité génétique. Cette dernière est souvent associée à une dérégulation épigénétique qui comprend des modifications du méthylome (modifications par méthylation de l'ADN), du transcriptome (modifications des ARN transcrits à partir de l'ADN) ainsi que des histones (modifications des protéines associées à l'ADN formant la chromatine). Ces modifications peuvent affecter l'expression génique et ainsi contribuer à l'hétérogénéité moléculaire. L'hétérogénéité moléculaire résultante se manifeste par une variété de protéines produites par les cellules tumorales, chacune ayant des fonctions distinctes. Cette diversité fonctionnelle ou phénotypique est illustrée par des variations dans la capacité des cellules cancéreuses à se diviser, à migrer, à envahir les tissus voisins, à résister aux traitements, ou encore par des variations dans l'expression de marqueurs membranaires. Les cellules cancéreuses peuvent, par exemple, exprimer des niveaux variables d'un récepteur spécifique, ce qui influence leur sensibilité à une thérapie ciblant ce récepteur. L'hétérogénéité spatiale du GB se manifeste par la coexistence de diverses zones tumorales. On distingue notamment le cœur de la tumeur et le bord invasif. La tumeur présente également des

zones hypoxiques et nécrotiques ainsi qu'une région de nécrose pseudopalissadique qui se distingue par une organisation en guirlande des cellules tumorales à la périphérie des régions nécrotiques. De plus, l'hyperplasie endothéliale, caractérisée par des lésions vasculaires, témoigne d'une prolifération accrue des cellules endothéliales. Enfin, la prolifération microvasculaire indique une augmentation du nombre de petits vaisseaux sanguins [92]. L'hétérogénéité spatiale est illustrée par la différence d'expression génique, d'altérations moléculaires et de variations du nombre de copies que l'on peut observer entre différentes zones topographiques d'une même tumeur [93,94].

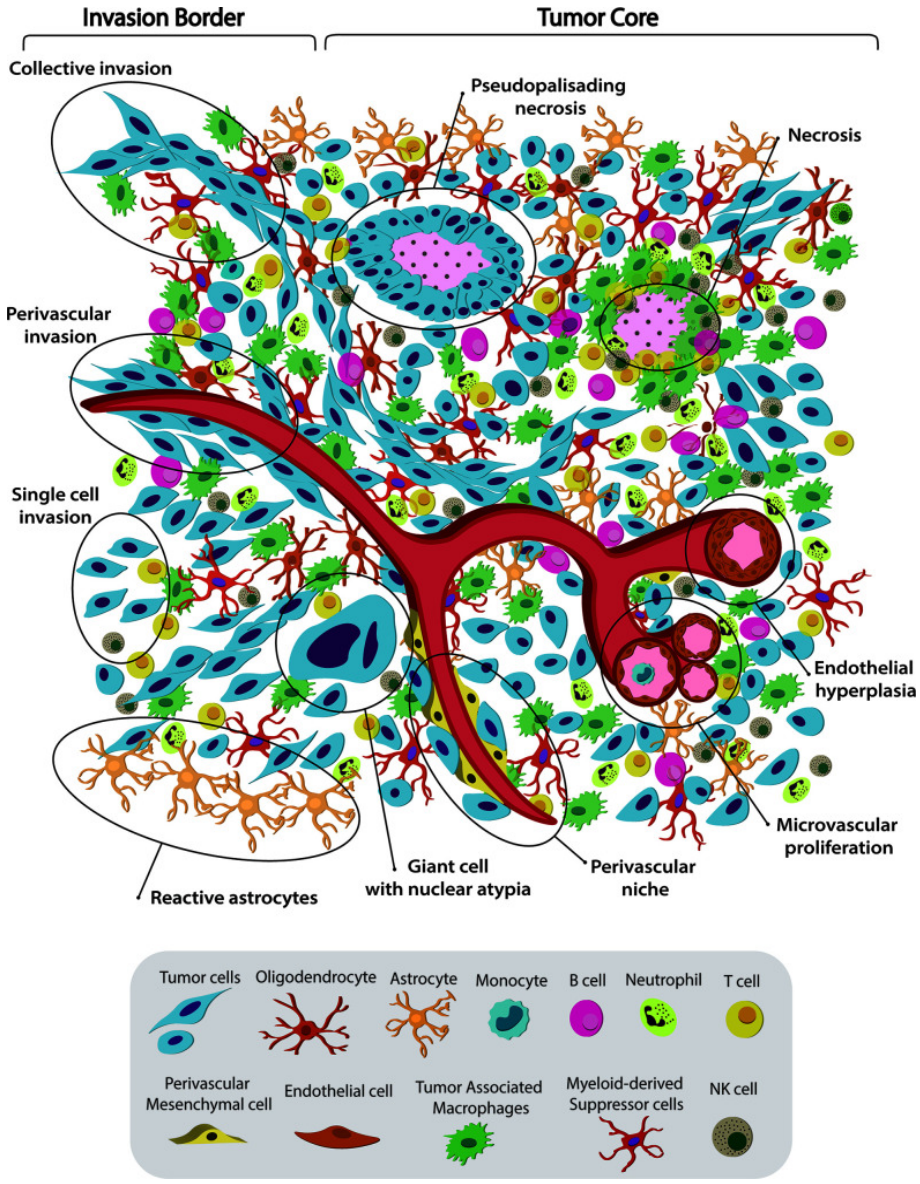

Figure 6 : Hétérogénéité spatiotemporelle des glioblastomes
Cette figure illustre les diverses populations cellulaires et microenvironnements qui composent les GB et évoluent selon une dynamique spatio-temporelle [92].

2. Modèles expliquant l'hétérogénéité des tumeurs

Plusieurs modèles ont été proposés pour expliquer l'hétérogénéité observée dans les tumeurs. Le modèle stochastique, également appelé modèle de l'évolution clonale, a été le premier à être décrit. Selon ce modèle, les cellules tumorales subissent des mutations stochastiques tout au long de l'expansion tumorale. Ces mutations peuvent conduire à la formation de clones tumoraux indépendants. Au fur et à mesure de l'évolution de la tumeur, certaines cellules acquièrent des mutations qui leur confèrent un avantage sélectif dans leur environnement, leur permettant de survivre et de proliférer de manière anarchique. Le modèle hiérarchique, quant à lui, repose sur une organisation hiérarchique des cellules tumorales, avec une minorité de cellules, les CSC, au sommet de la hiérarchie. Ces dernières possèdent un fort potentiel tumorigène, c'est-à-dire la capacité à initier la formation de tumeurs *in vivo*. Les CSC sont décrites comme étant plus résistantes aux thérapies et seraient ainsi responsables des récidives systématiques de GB. Elles sont capables de s'autorenouveler et de donner naissance, de manière asymétrique, à des cellules tumorales plus différenciées, contribuant ainsi au développement tumoral. D'autres modèles ont été décrits, tels que le modèle de coopération. Selon ce modèle, l'hétérogénéité intra-tumorale résulte d'une inter-coopération entre les cellules tumorales (souches et plus différenciées) et les cellules du microenvironnement (cellules endothéliales, cellules immunitaires, etc.). Ces dernières influencent le génotype et le phénotype des cellules tumorales. En outre, une perspective récente souligne la plasticité phénotypique non génétique, où l'hétérogénéité pourrait être issue d'états d'expression génique alternatifs, indépendamment des mutations, menant à divers comportements tumoraux. L'hétérogénéité des tumeurs pourrait ainsi résulter d'une coexistence de différentes cellules tumorales à haut potentiel tumorigénique, du phénomène d'évolution clonale marqué notamment par l'apparition de mutations stochastiques, ainsi que d'un réseau complexe d'interactions entre les cellules tumorales et leurs microenvironnements [95,96].

3. Hétérogénéité moléculaire des glioblastomes

Des classifications des GB basées sur des profils génétiques et moléculaires ont été élaborées pour stratifier les tumeurs. L'identification de signatures moléculaires est cruciale pour différencier les sous-types de GB et stratifier les patients. Ces signatures peuvent informer sur le comportement de la tumeur, notamment sa croissance, sa propagation et sa sensibilité aux thérapies.

Parmi ces classifications figure celle de *Phillips et al*. parue en 2006. Dans cette étude, les auteurs ont caractérisé trois sous-types de GB en se basant sur leurs ressemblances avec des cellules neurales à des étapes spécifiques de la neurogenèse. Les sous-types décrits comprennent le sous-type prolifératif, proneural et mésenchymateux. Le sous-type prolifératif manifeste une expression accrue de marqueurs associés à la prolifération cellulaire, tandis que le sous-type mésenchymateux démontre une expression élevée de marqueurs associés notamment à l'angiogenèse et à l'invasion tumorale. Le sous-type proneural, quant à lui, est caractérisé par l'expression de marqueurs de la lignée neuronale et a été associé à une survie plus longue par rapport aux deux autres. Cette étude a également souligné que les tumeurs ont tendance à évoluer vers le sous-type mésenchymateux lors de la récidive, suggérant une plasticité entre les sous-types tumoraux. Les résultats ont également suggéré l'implication des voies de signalisation Akt et Notch comme caractéristiques distinctives des gliomes de mauvais pronostic (sous-type prolifératif et mésenchymateux) par rapport aux gliomes de meilleur pronostic (sous-type proneural) [97].

En 2010, *Verhaak et al*. ont proposé une classification moléculaire basée sur l'analyse transcriptomique à grande échelle des GB à partir de la base de données TCGA. Cette analyse a révélé l'existence de signatures moléculaires permettant de définir quatre sous-types de GB adultes cliniquement pertinents : classique, mésenchymal, proneural et neural. Chaque sous-type présente une signature moléculaire distincte, c'est-à-dire un ensemble unique d'altérations génétiques et épigénétiques (Figure 7). Les GB classiques sont caractérisés par une amplification du chromosome 7 associée à une augmentation de l'expression d'EGFR et une perte du chromosome 10. Les GB mésenchymateux sont, quant à eux, caractérisés par la présence d'altérations aboutissant à une diminution de l'expression du gène *NF1*, soit par mutation, soit par délétion du locus 17q11.2. Des mutations sont également retrouvées au niveau du gène suppresseur de tumeurs *PTEN*. À l'inverse des GB classiques qui présentent une amplification de l'*EGFR* dans 90% des cas, celle-ci est absente au sein des GB mésenchymateux. Le sous-type mésenchymateux correspond aux formes de GB les plus agressives et les plus résistantes aux thérapies. Le sous-type proneural, lui, se caractérise par la présence d'une altération au niveau du gène *PDGFRA* entraînant sa surexpression, ainsi que par la présence de mutation du gène *IDH1* dans 40% des cas [21]. En 2017, le sous-type neural a été exclu de cette classification car il ne présentait pas de signature moléculaire tumorale spécifique et distincte [98].

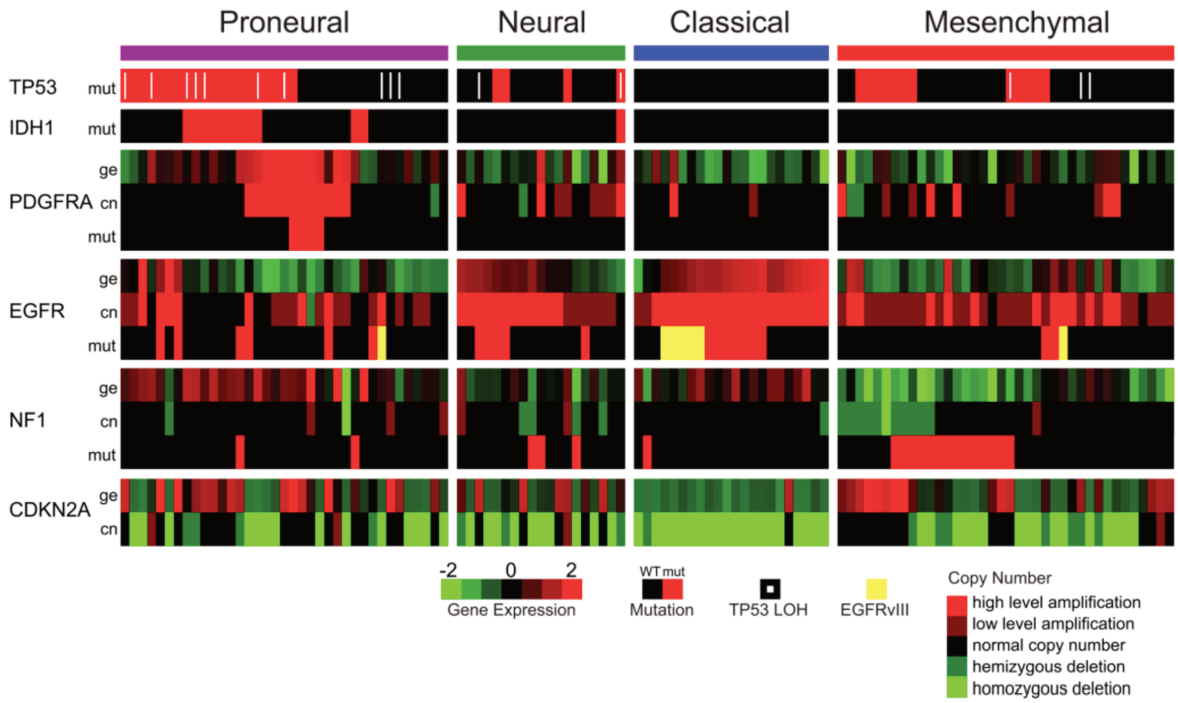

Figure 7 : Signature moléculaire des sous-types définis par *Verhaak et al.* en 2016.
Les données d'expression génique (ge), la présence ou non de mutation (mut) et les événements de nombre de copies (cn) sont représentés en fonction du sous-type proneural, neural, classique et mésenchymal [99]. EGFR : Epidermal Growth Factor Receptor ; EGFRvIII : Epidermal Growth Factor Receptor Variant III ; CDKN2A : Cyclin Dependent Kinase Inhibitor 2A ; LOH : Loss-of-Heterozygosity ; NF1 : Neurofibromin 1 ; PDGFRA : Platelet Derived Growth Factor Receptor Alpha ; IDH1 : Isocitrate Dehydrogenase 1. TP53 : Tumor Protein 53.

D'autres travaux de recherche ont révélé des distinctions notables dans les modifications épigénétiques entre les gliomes de haut grade primaires et secondaires [100,101]. En particulier, l'étude de *Noushmehr et al*. en 2010 a examiné la méthylation de promoteurs de gènes dans 272 GB issus du TCGA. Cette étude a révélé l'existence d'un sous-groupe de gliomes de haut grade caractérisé par une hyperméthylation au niveau de sous-groupes spécifiques d'îlots CpG. Ces gliomes, présentant le phénotype "méthylateur" CpG Island Methylator Phenotype (CIMP), sont classifiés comme appartenant au sous-type proneural selon la classification de Verhaak. De plus, ils sont étroitement associés à la présence de mutations *IDH1* et sont plus fréquemment observés dans les gliomes de bas grade [101]. Il est intéressant de noter que la valeur pronostique du phénotype CIMP semble surpasser celle de la méthylation du promoteur *MGMT* [102].

Dans une étude publiée en 2012, Sturm et ses collaborateurs ont proposé une classification plus détaillée des GB, en se basant sur des motifs spécifiques de méthylation de l'ADN. Ils ont ainsi identifié six groupes distincts de GB : K27, G34, IDH1, RTK I, RTK II et mésenchymateux [103]. Les groupes K27 et G34 regroupent principalement des GB pédiatriques et adolescents, et chaque sous-groupe est associé à des aberrations

chromosomiques, des mutations ou des amplifications génétiques spécifiques. Le groupe IDH1, quant à lui, présente une hyperméthylation globale de l'ADN. Le groupe RTK I est marqué par une amplification de *PDGFRA*, tandis que le groupe RTK II se caractérise par un gain du chromosome 7, une perte du chromosome 10, une perte de *CDKN2A* et une amplification de *EGFR*. Le groupe mésenchymateux, quant à lui, présente une incidence plus faible d'altérations génétiques typiques des GB par rapport aux autres sous-groupes. Il est à noter que bien qu'il y ait des similitudes avec la classification de Verhaak, la classification basée sur la méthylation de l'ADN ne correspond pas exactement aux sous-classes basées sur l'expression des gènes. Plus récemment, cette classification a été élargi pour englober presque toutes les tumeurs connues du système nerveux central [104].

En 2014, *Patel et al.* ont utilisé une analyse de l'ARN de cellules uniques pour identifier divers sous-types de GB présents dans une même tumeur. Ces expériences de séquençage d'ARN sur cellules uniques (*single-cell RNA-seq*) ont mis en évidence la présence de plusieurs sous-types cliniquement pertinents de GB (classique, proneural ou mésenchymateux) au sein d'une même tumeur [105].

En 2017, *Wang et al.* ont exploré les signatures moléculaires au sein des sous-types transcriptionnels décrits par Verhaak (proneural, mésenchymal, classique) ainsi que leur évolution tumorale, en comparant les tumeurs primaires à leurs récidives. Ces recherches ont révélé une hétérogénéité inter- et intra-tumorale au sein des GB et ont montré que le sous-type transcriptionnel reste le même dans 55% des récidives [98].

En 2019, Neftel et son équipe ont mis en évidence l'hétérogénéité des états cellulaires au sein des GB, offrant une nouvelle perspective sur la complexité intrinsèque de ces tumeurs. Dans des études précliniques sur des modèles animaux, ils ont démontré que les cellules individuelles de GB ont la capacité intrinsèque de moduler leur expression, adoptant ainsi différents états transcriptionnels. Par exemple, en utilisant des marqueurs tels que CD24 pour cibler des cellules similaires aux CSN, il a été démontré qu'une population cellulaire sélectionnée avec un état transcriptionnel spécifique, une fois implantée dans une souris, peut recréer la diversité des états observés avant le tri cellulaire. De plus, leurs travaux ont montré qu'un clone unique de cellules GB peut adopter plusieurs états transcriptionnels dans des modèles de xénogreffes dérivés de patients. Ils ont identifié quatre états cellulaires : cellules de type progéniteur neural (NPC), celles de type progéniteur oligodendrocytaire (OPC), celles de type astrocytaire (Astro) et celles de type mésenchymateux (Mes). Ces états, influencés par le

microenvironnement tumoral, sont associés à des altérations génétiques distinctes. Par ailleurs, la proportion des cellules entre ces états peut varier au fil de l'évolution de la tumeur et en réponse aux traitements, mettant en évidence la remarquable adaptabilité des GB (Figure 8Figure 8) [106].

Plus récemment, en 2021, Garofano et ses collègues ont également utilisé une approche multi-omique pour analyser des cellules individuelles de GB. Leur recherche a révélé l'existence de quatre sous-types distincts de GB, classés selon des critères neurodéveloppementaux (prolifératifs/progéniteurs *vs* neuronaux) et métaboliques (mitochondriaux *vs* glycolytiques/plurimétaboliques). Il a également été démontré que le GB mitochondrial était associé à un meilleur pronostic clinique [107].

Ces classifications illustrent bien l'hétérogénéité moléculaire des GB. Cependant, elles ont aussi mis en évidence une certaine fluidité entre les sous-types : un même GB peut présenter des caractéristiques de plusieurs sous-types, et un GB peut évoluer d'un sous-type à un autre au cours de sa progression ou en réponse aux thérapies.

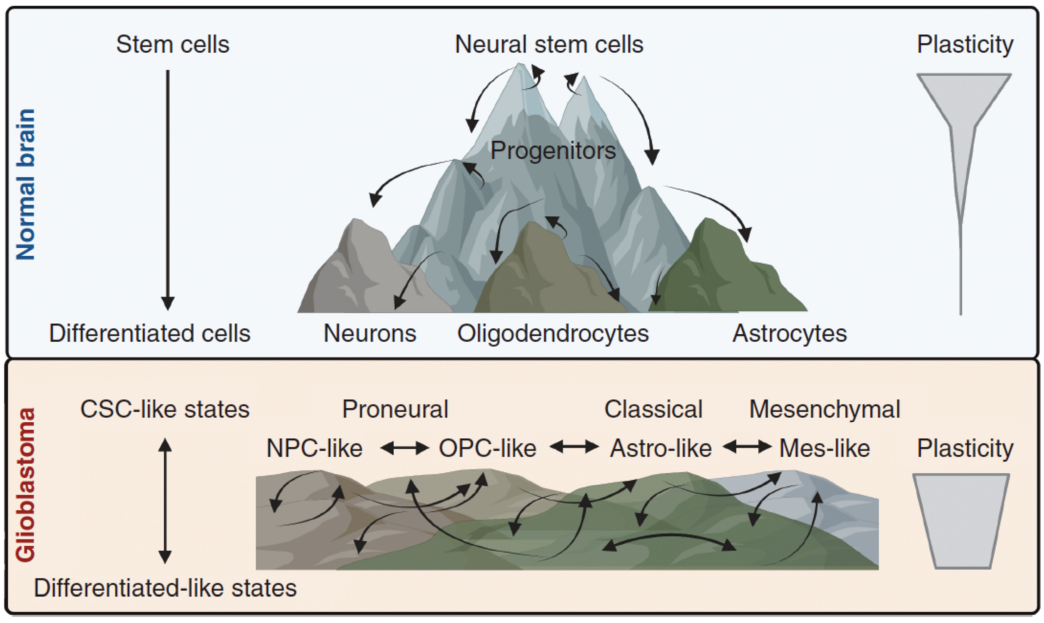

Figure 8 : Dynamique de l'hétérogénéité et de la plasticité des cellules de glioblastome
L'hétérogénéité et la plasticité des cellules de glioblastome diffèrent de l'organisation hiérarchique unidirectionnelle des cellules neurales, dans laquelle le processus de dédifférenciation reste très limité. À l'inverse, les glioblastomes se composent de populations de cellules tumorales diverses et dynamiques, où une grande plasticité est conservée, que ce soit entre les états de cellules souches cancéreuses (CSC-like) et des états plus différenciés (differentiated-like), mais également entre les sous-types proneural, classique et mésenchymal, ainsi qu'entre les cellules de type progéniteur neural (NPC), celles de type progéniteur oligodendrocytaire (OPC), celles de type astrocytaire (Astro) et celles de type mésenchymateux (Mes) [82].

Ces transitions d'états transcriptionnels commencent à être déchiffrées à l'aide de modélisation mathématique [108]. Cette avancée suggère que ces mécanismes de transition d'état pourraient ne pas être stochastiques, mais plutôt influencés et régulés par des facteurs tels que les signaux émanant du microenvironnement tumoral, la position spatiale des cellules au sein de la tumeur, et les modifications épigénétiques. Ces avancées sont d'autant plus pertinentes lorsqu'on les considère à la lumière d'autres études, telles que celles du projet Ivy Glioblastoma Atlas (Ivy GAP) et de l'atlas transcriptionnel anatomique de *Puchalski et al*., qui mettent en évidence un lien entre la localisation anatomique, l'histologie et les caractéristiques moléculaires [109]. Avec les progrès de la modélisation mathématique et la centralisation croissante de données histomoléculaires, il devient envisageable de prédire les trajectoires probables entre les différents états transcriptionnels des GB [108–110].

4. Facteurs définissant l'hétérogénéité et la plasticité tumorale

L'hétérogénéité et la plasticité tumorale sont influencées par une combinaison de facteurs à la fois intrinsèques et extrinsèques à la tumeur. Parmi les éléments intrinsèques, on compte le contexte génétique et épigénétique de la tumeur ainsi que son réseau transcriptionnel. Quant aux facteurs extrinsèques, ils sont principalement liés au microenvironnement tumoral. Celui-ci englobe les niches cellulaires, les interactions entre les cellules cancéreuses et leur environnement, notamment les interactions avec la matrice extracellulaire et les différentes sous-populations présentes dans le microenvironnement tumoral (Figure 9Figure 9Figure 9) [82].

4.1 Génétique

Les caractéristiques intrinsèques de la tumeur définissent directement l'hétérogénéité phénotypique et la plasticité intra-tumorale. Les altérations génétiques telles que l'amplification de l'*EGFR*, du *PDGFRA* et du *CDK4/6*, ainsi que les délétions ou les mutations inactivatrices de *TP53*, *PTEN*, *NF*1 et *CDKN2A/B* sont des déterminants clés de la variabilité entre les patients. Les tumeurs présentant une amplification de *PDGFRA* sont généralement enrichies en états similaires aux progéniteurs oligodendrocytaires (OPC-like), celles présentant une amplification de *CDK4* en états similaires aux progéniteurs neuronaux (NPC-like), et celles amplifiées en *EGFR* en états similaires aux astrocytes (Astro-like), tandis que les GB avec une perte de *NF1* contiennent des proportions plus élevées d'états mésenchymateux (MES-like) [106].

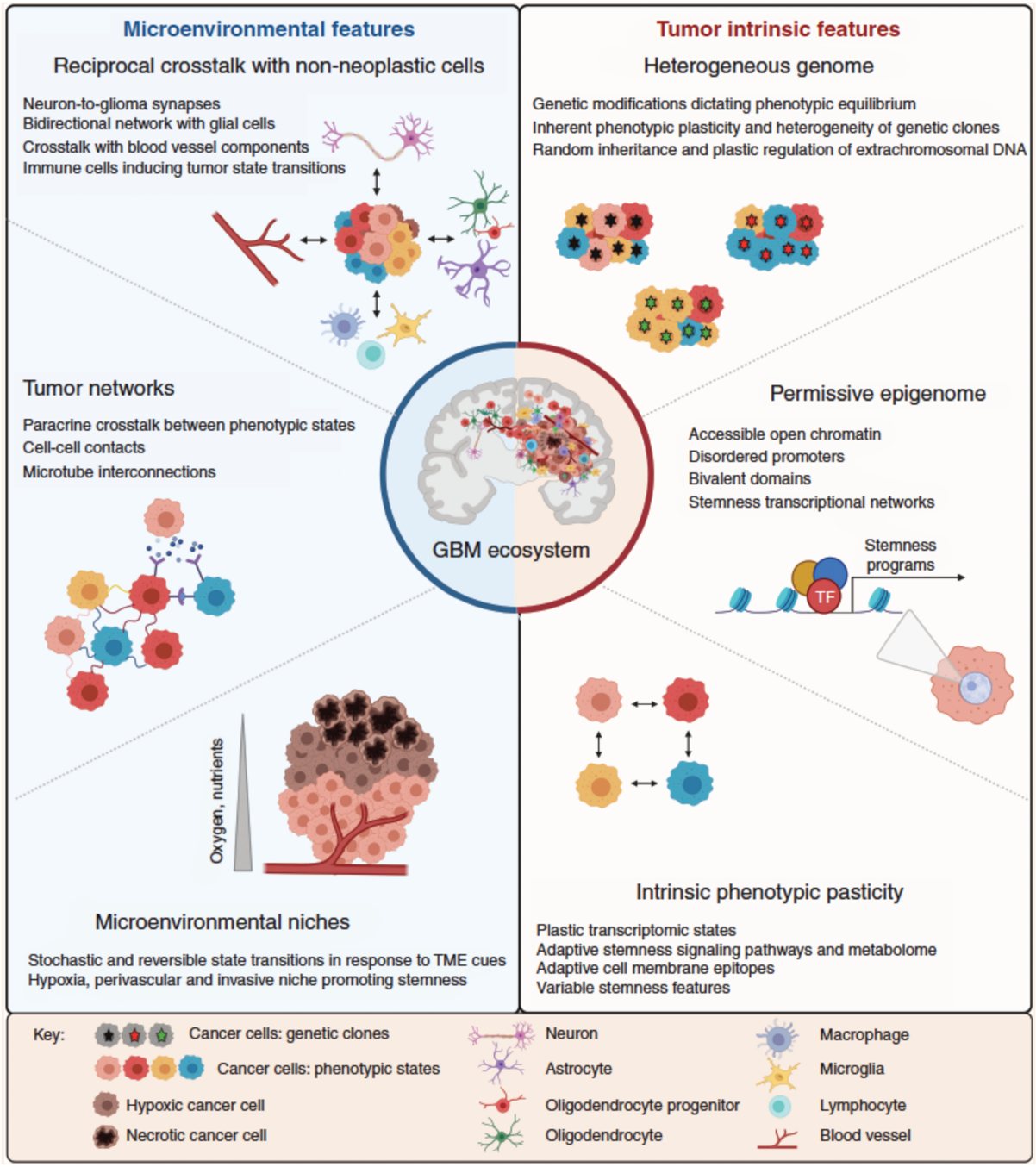

Figure 9 : Facteurs intrinsèques et environnementaux contribuant à la dynamique de l'écosystème des glioblastomes et favorisant l'hétérogénéité tumorale
La plasticité des cellules tumorales et l'équilibre des états phénotypiques sont déterminés par des caractéristiques intrinsèques à la tumeur ainsi que par des signaux extrinsèques provenant du microenvironnement tumoral [82].

4.2 Réseaux de régulation génique

Les mécanismes qui sous-tendent l'hétérogénéité phénotypique des tumeurs sont complexes et variés. Parmi ceux-ci, les réseaux de régulation génique, qui comprennent les facteurs de transcription et les cofacteurs modulant l'expression génique, semblent jouer un rôle majeur. Dans une étude menée par *Wu et al.* en 2020, l'analyse des réseaux de régulation génique de

différents sous-types de GB a démontré que ces sous-types présentent des profils uniques de facteurs de transcription et de régulateurs épigénétiques. Les chercheurs ont déterminé que SOX10 est un régulateur clé du sous-type RTK I. Sa répression induit une transition transcriptomique et phénotypique du sous-type RTK I vers le sous-type mésenchymateux, et cela s'opère *via* une modification d'un ensemble de régulateurs épigénétiques [111]. Ainsi, les mécanismes de régulation épigénétique et l'activité des facteurs de transcription s'avèrent être cruciaux dans la détermination du sous-type tumoral.

Les mécanismes épigénétiques, tels que la méthylation de l'ADN, les modifications des histones, le remodelage de la chromatine et les ARN non codants, en particulier les microARNs, modulent l'expression génique. Ces mécanismes épigénétiques contribuent souvent aux aberrations chromosomiques : par exemple, les régions génomiques amplifiées tendent à être hypométhylées, tandis que les régions subissant une perte du nombre de copies sont généralement hyperméthylées [112]. Un épigénome permissif favorise l'activation des zones transcriptionnelles responsables d'une reprogrammation vers la multipotence [113]. Cette reprogrammation peut être initiée par des voies oncogéniques, telles que la signalisation HGF/cMET [114], ou en réponse à des signaux du microenvironnement tumoral, comme l'hypoxie [115] et cela est souvent orchestré par le biais de régulateurs épigénétiques et d'ARN non codants. En effet, une étude publiée en 2021 a mis en évidence le rôle central de l'épigénome dans la détermination de l'hétérogénéité phénotypique des tumeurs. En procédant à une analyse multiomique de cellules individuelles provenant d'échantillons cliniques de gliomes primaires, combinant une étude du profil de méthylation de l'ADN, du transcriptome et du génotype, les chercheurs ont identifié une vaste diversité d'états cellulaires transcriptionnels dans les tumeurs. Cette diversité est souvent détectée indépendamment de l'hétérogénéité génétique mais est associée à des modifications du profil de méthylation de l'ADN [112].

4.3 Microenvironnement tumoral

Le microenvironnement est un acteur majeur, modulant notamment l'hétérogénéité spatiale et temporelle des tumeurs. Il façonne la diversité et la complexité des tumeurs en induisant des transitions dynamiques et réversibles au sein des cellules de GB en réponse aux variations environnementales [82,116]. Des facteurs tels que l'hypoxie [93,115,117,118], le pH [119] et la disponibilité des nutriments [120] sont décrits comme de puissants déclencheurs d'adaptations phénotypiques. Les GB hébergent des niches cellulaires distinctes, propices à l'émergence d'états cellulaires particuliers. Ainsi, certains microenvironnements sont

caractérisés par une prédominance de cellules présentant des traits phénotypiques uniques, tels qu'un état de quiescence [57], une capacité d'auto-renouvellement élevée [122,123], une adaptation aux conditions hypoxiques [42], ou une résistance accrue aux lésions de l'ADN induites par les radiations [56,124].

4.3.1 Niches

Le concept de niche a été initialement utilisé pour décrire les emplacements où les CSN normales sont localisées. Par la suite, ce terme a été employé pour caractériser les sites présentant la plus forte densité en CSG. On distingue principalement trois types de niches : les niches périvasculaires [125,126], invasives [127] et hypoxiques [128]. Récemment, une proposition d'unification des différents types de niches a vu le jour sous le terme "niche péri-artériolaire hypoxique", en analogie avec les niches de cellules souches hématopoïétiques de la moelle osseuse [126]. Ces niches regroupent divers types de cellules et des éléments de la matrice extracellulaire et fournissent des signaux biochimiques et mécaniques qui influencent la plasticité et l'hétérogénéité des CSG. De plus, elles modulent des mécanismes épigénétiques comme la méthylation de l'ADN et les modifications d'histones. Leur rôle est primordial dans la détermination du phénotype des CSG, influençant leur comportement et leur résistance thérapeutique. Ainsi, une stratégie visant à cibler ces niches pourrait ouvrir de nouvelles perspectives pour accroître la sensibilité des CSG aux traitements anticancéreux [129].

4.3.1.1 Niches hypoxiques

L'état d'oxygénation joue un rôle crucial dans la promotion de l'hétérogénéité et de la plasticité tumorale. Bien que les GB soient hautement vascularisés, ils contiennent d'importantes zones hypoxiques et nécrotiques. Cette dichotomie s'explique par des anomalies dans la formation des vaisseaux sanguins face à une croissance tumorale rapide [130]. Dans le cerveau sain, les niveaux d'oxygène fluctuent entre 12,5 % et 2,5 % (physioxie), tandis qu'ils peuvent chuter à 2,4 % ou même 0,1 % (hypoxie) dans les tissus tumoraux [131–133]. La capacité des cellules à s'adapter à ce microenvironnement hypoxique est régulée les facteurs de transcription appelés Facteurs Inductibles par l'Hypoxie (HIFs) tels que HIF-1α et HIF-2α [134]. Leur activité transcriptionnelle est associée à divers processus tumoraux, dont l'angiogenèse, l'adaptation métabolique, la migration et l'invasion des cellules tumorales, la clonogénicité et la résistance à la chimiothérapie [135–140]. Au cœur des GB, des zones comme les pseudopalisades, liées à l'hypoxie et la nécrose, sont ainsi enriches en CSG [93]. L'hypoxie induit des transitions phénotypiques réversibles chez les cellules de GB, les dotant des

caractéristiques de cellules souches, comme la capacité de former des neurosphères, l'auto-renouvellement, et l'expression de marqueurs spécifiques aux cellules souches [115]. L'hypoxie non seulement favorise le phénotype souche mais également l'expansion de sous-populations de CSG adaptées à ces conditions [156,157]. Les faibles niveaux d'oxygène poussent les CSG à passer d'un état prolifératif à un état quiescent, marqué par un arrêt cellulaire réversible en G0 [143]. Les CSG quiescentes posent un défi en oncologie, étant donné que ces cellules échappent aux systèmes de surveillance antitumorale et deviennent réfractaires aux traitements ciblant les cellules à prolifération rapide.

4.3.1.2 Niches invasives

Les niches invasives sont caractérisées par une croissance périvasculaire de cellules cancéreuses invasives le long des capillaires, entre l'endothélium et les astrocytes. Dotées d'une motilité remarquable, les cellules qui résident dans cette niche sont décrites comme responsables des récidives post-opératoires [144]. Des études suggèrent que la bordure invasive de la tumeur affiche des marqueurs de nature proneurale, alors que le cœur de la tumeur exprime davantage de marqueurs mésenchymateux [145]. Des analyses IRM de patients atteints de GB menées par *Nishikawa et al.* ont révélé que les tumeurs faiblement invasives à l'IRM montrent une expression prédominante de VEGF à leur périphérie. En outre, une forte concentration de CD44 dans cette région est liée à un phénotype des CSG hautement invasif et à un pronostic moins favorable [146]. Les processus de migration et d'invasion évoquent la transition épithélio-mésenchymateuse observée dans les carcinomes. Dans le contexte du GB, cette transition est décrite comme la transition proneurale-mésenchymateuse (TPM) [147]. Il a été constaté que la radiothérapie peut induire la TPM, suggérant ainsi qu'elle pourrait encourager l'apparition de phénotypes cellulaires plus agressifs et la formation de nouvelles zones tumorales [145]. La progression des CSG vers un phénotype invasif est dirigée par différents modulateurs incluant la N-cadhérine, l'intégrine α6 et les axes tels que Twist-Sox2, Snail, ZEB, STAT3, la périostine et NF-kB [148–150]. Les CSG se déplacent dans le parenchyme cérébral, décomposant la matrice extracellulaire en utilisant des enzymes tels que les métalloprotéinases MMP2, MMP9 et ADAMT2 [151,152]. La mobilité et l'invasion des CSG sont stimulées par des éléments solubles du microenvironnement tumoral, comme le TGF-β1 et l'adénosine. En effet, produit par la microglie ou par les cellules cancéreuses même, le TGF-β1 interagit avec le récepteur TGFRβ2 des CSG, stimulant leur invasion [153]. Sous l'effet de l'hypoxie, les CSG intensifient leur production d'adénosine. Une fois libérée dans l'espace extracellulaire, l'adénosine agit sur les CSG en se liant à leur récepteur adénosine A3, favorisant ainsi leur

migration et invasion [154]. Ainsi, la niche invasive présente des CSG qui exploitent divers signaux et mécanismes pour favoriser leur migration, leur invasion et, finalement, la récurrence tumorale post-opératoire.

4.3.1.3 Niches périvasculaires

Les niches périvasculaires se forment le long des capillaires où les CSG sont étroitement associées à l'endothélium, jouant un rôle crucial dans le maintien des propriétés souches des cellules cancéreuses [155]. Ce microenvironnement périvasculaire regroupe une variété de cellules, incluant les cellules cancéreuses, les cellules endothéliales, les péricytes, les astrocytes et les macrophages associés aux tumeurs. Ensemble, elles contribuent activement à la tumorigenèse [156]. Les cellules endothéliales, en particulier, fournissent des ligands et libèrent des modulateurs endogènes qui stimulent la signalisation des CSG *via* des voies comme Notch et l'oxyde nitrique [155,157]. De plus, diverses cellules du microenvironnement, y compris les cellules tumorales elles-mêmes, sécrètent l'angiopoïétine-1 (Ang-1) qui renforce l'interaction des CSG avec l'endothélium, facilitant ainsi leur invasion [158]. Les CSG libèrent également des facteurs pro-angiogéniques comme le VEGF, stimulant l'angiogenèse [63,159]. Elles expriment aussi L1CAM, une protéine d'adhésion, qui s'associe à l'intégrine αvβ3 de l'endothélium, renforçant leur caractère souche et l'angiogenèse [160,161]. Les CSG peuvent se transdifférenciées en cellules endothéliales et péricytes, un processus régulé par le facteur de transcription ETV2 et le TGF-β [65]. Cette transdifférenciation peut même être stimulée par des traitements comme la chimiothérapie [184] ou la radiothérapie [185]. De plus, au sein de ces niches périvasculaires, les cellules de GB peuvent s'organiser sous la forme de réseaux tubulaires appelés microtubes tumoraux. Ces microtubes tumoraux agissent comme des voies de communication entre des cellules éloignées et soutiennent différents processus tumoraux tels que la prolifération, l'invasion et la résistance aux thérapies [182].

4.3.2 Dialogue moléculaire et communication cellulaire

La communication moléculaire est essentielle à la structuration de l'écosystème du GB. L'étude de *Wang et al*. a récemment mis en lumière une interaction bénéfique à la croissance tumorale entre les CSG et les cellules tumorales différenciées. Les cellules différenciées libèrent le facteur BDNF, tandis que les CSG possèdent son récepteur, NTRK2. Cette interaction paracrine BDNF-NTRK2 est régulée en grande partie par le VGF. Ce dernier agit comme un intermédiaire entre les CSG et les cellules tumorales différenciées, soutenant la survie et le caractère souche des CSG. De plus, il stimule les cellules différenciées à produire

et libérer BDNF, consolidant la boucle de signalisation BDNF-NTRK2 [166]. Il a été établi que Gremlin1, produit par les CSG, joue un rôle essentiel dans la promotion de la prolifération tumorale et la préservation de la hiérarchie des GB. Gremlin1 agit comme un antagoniste des protéines morphogénétiques osseuses (BMP), qui sont connues pour stimuler la différentiation cellulaire. Spécifiquement exprimé par les CSG, Gremlin1 a pour objectif de les protéger des effets des BMPs endogènes. Cette protection se traduit par une inhibition de la différentiation, le maintien du phénotype souche et une augmentation de la croissance tumorale [167]. L'hétérogénéité spatiale au sein des tumeurs joue un rôle essentiel dans la résistance thérapeutique observée dans les GB. Une étude récente a mis en lumière une communication intracellulaire entre les cellules au cœur de la tumeur et celles situées à sa périphérie. Les cellules centrales démontrent une résistance thérapeutique accrue. De façon intéressante, ces cellules centrales influencent les cellules périphériques par une communication paracrine. Ce mécanisme de communication est initié par HDAC1, présent dans les cellules centrales, qui entraîne la sécrétion de la protéine soluble CD109. Cette protéine a pour effet d'amplifier le potentiel de malignité et de résistance aux traitements des cellules périphériques [168]. D'autres communications intratumorales ont été identifiées, notamment entre les cellules amplifiées en EGFRvIII et celles en EGFRwt. Les cellules avec une amplification de EGFRvIII libèrent des cytokines qui stimulent gp130 et EGFR chez les cellules voisines amplifiées en EGFRwt, favorisant ainsi la croissance tumorale [169]. En plus de la signalisation paracrine, les cellules de GB interagissent entre elles *via* des contacts directs, des exosomes et des microtubes tumoraux [164]. Ces réseaux tumoraux où les cellules sont connectées, présentent des voies d'expression génique associées au développement neurologique et à la progression tumorale. Il a été prouvé que, dans ces réseaux, les cellules connectées montrent une plus grande résistance à la radiothérapie [170].

4.3.3 Communication avec le stroma tumoral

L'interaction entre les cellules tumorales et le stroma tumoral s'est révélée être un élément clé dans la pathogenèse des GB, orchestrant non seulement leur évolution mais aussi leur plasticité. Cette communication implique divers composants du microenvironnement, notamment les cellules gliales, endothéliales, les péricytes, la microglie, les cellules immunitaires infiltrantes, et les neurones [171]. En dehors des interactions précédemment évoquées, notamment entre les CSG et l'endothélium vasculaire, il a également été démontré *in vitro* que les cellules de GB partagent entre elles des mitochondries et en reçoivent

d'astrocytes *via* les microtubes tumoraux. Ceci conduit à une augmentation de l'activité métabolique et de la tumorigénicité [172]. Par ailleurs, l'impact de l'activité neuronale sur la progression tumorale est de plus en plus reconnu, cette communication entre les neurones et les cellules de GB s'effectue *via* une interaction électrochimique dépendant des récepteurs AMPA [173]. L'importance croissante de la microglie dans la progression des GB est également documentée. Dans ce contexte, des analyses longitudinales comparant les tumeurs initiales aux récidives ont révélé que les changements propres aux cellules cancéreuses lors de la récidive sont accompagnés de modifications dans le microenvironnement. Notamment, une prédominance de macrophages M2 a été associé à une moindre efficacité de la radiothérapie et à une rechute rapide après traitement. Par ailleurs, l'hypermutation au sein des tumeurs a été corrélée à une augmentation du nombre de lymphocytes $CD8^+$ [98]. D'autres recherches ont indiqué que les transitions vers un phénotype mésenchymateux sont souvent influencées par des cytokines inflammatoires, telles que le TNFα, CCL5, CCL12 et G-CSF [124,174] ou encore l'Oncostatin M [175].

Ces découvertes soulignent l'interaction réciproque entre le microenvironnement et les cellules tumorales, suggérant de nouvelles approches thérapeutiques ciblant ces interconnexions.

5. Hétérogénéité et plasticité des cellules souches cancéreuses

Après avoir abordé l'hétérogénéité et la plasticité des GB de manière générale, il est crucial de comprendre comment ces concepts s'appliquent particulièrement aux CSG. Dotées d'une pluripotence leur conférant la capacité de se différencier en différents types cellulaires et d'une forte plasticité en réponse à des conditions environnementales hostiles, les CSG jouent un rôle majeur dans l'hétérogénéité et la dynamique tumorale. Plusieurs études ont révélé l'existence de différentes sous-populations de CSG au sein d'une même tumeur, chacune interagissant différemment avec son environnement et contribuant ainsi à l'hétérogénéité globale de la tumeur [176]. Sur le plan génomique, les CSG présentent une diversité de mutations et d'altérations épigénétiques, se manifestant par des phénotypes variés et une dynamique d'expression de leurs marqueurs [110]. À ce jour, aucun marqueur universel n'a été identifié pour ces cellules [55]. Moléculairement, deux sous-types sont classiquement décrits : les CSG mésenchymateuses et les CSG proneurales. D'un point de vue phénotypique, on différencie les CSG prolifératives des CSG quiescentes. Les CSG prolifératives et proneurales se localisent majoritairement dans des niches vascularisées. Ces cellules sont plus vulnérables aux

traitements comparées aux CSG quiescentes ou mésenchymateuses, et sont généralement associées à un meilleur pronostic clinique. En revanche, les CSG quiescentes et mésenchymateuses se localisent dans les niches hypoxiques et invasives. Ces dernières montrent une résistance accrue aux traitements et sont corrélées à un pronostic clinique défavorable [143,177,178]. Les caractéristiques des CSG sont influencées par des facteurs génétiques, épigénétiques, métaboliques, immunitaires et environnementaux (Figure 10) [53].

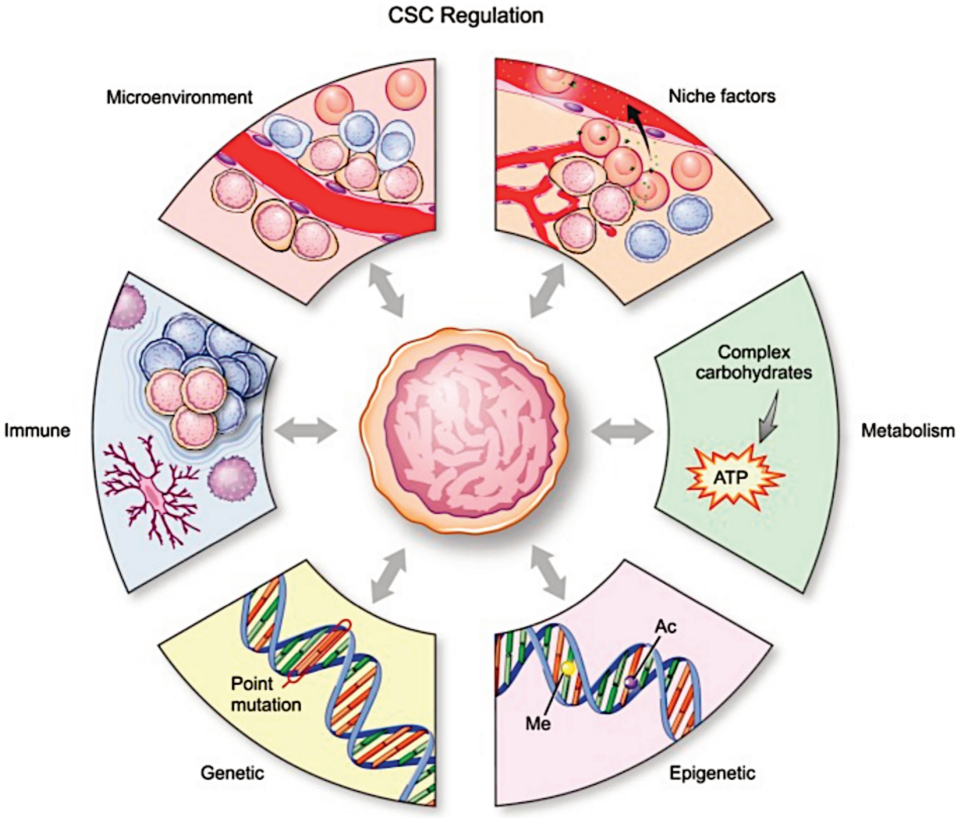

Figure 10 : Divers processus affectant les cellules souches de glioblastome
Il existe six mécanismes principaux par lesquels les cellules souches de glioblastome sont régulées : les altérations génétiques, épigénétiques et métaboliques, le microenvironnement tumoral, les niches, et le système immunitaire [70].

Les travaux récents de Niclou et ses collègues apportent un éclairage nouveau sur la plasticité des CSG. Ils ont démontré que les caractéristiques des CSG ne définissent pas une population distincte avec des propriétés fonctionnelles et des profils transcriptomiques spécifiques. Au contraire, ces caractéristiques représentent un état plastique, accessible à la majorité des cellules cancéreuses [110]. Cette adaptabilité se manifeste notamment au niveau de leur capacité à osciller entre un état souche et différencié [179]. De plus, elles peuvent également alterner entre des états actifs, contribuant à la croissance tumorale, et des états de quiescence ou de repos [143,178,180]. Leur flexibilité ne se limite pas à leur comportement, mais s'étend également à leur identité moléculaire, avec une capacité à transiter d'un sous-type

moléculaire à un autre [145]. Cette plasticité est en partie influencée par le microenvironnement tumoral et les thérapies employées. Par exemple, en réponse à la chimiothérapie, les cellules peuvent acquérir des caractéristiques souches [179,181]. Dans une autre étude, les auteurs ont observé qu'après une exposition à la radiothérapie, les CSG proneurales peuvent adopter des traits mésenchymateux [145]. Par ailleurs, dans des environnements hostiles, tels que des zones d'hypoxie ou d'acidification, les CSG montrent une plasticité remarquable en passant d'un état prolifératif à un état quiescent [143,180]. Grâce à une meilleure compréhension des mécanismes sous-jacents à la plasticité des cellules cancéreuses, nous pourrions développer de nouvelles approches pour traiter ces tumeurs [82]. Dans ce contexte, Niclou et ses collègues ont notamment suggéré que ces transitions d'état et l'hétérogénéité qui en résulte peuvent être prédites à l'aide de modèles mathématiques [110].

6. Implication clinique et thérapeutique

Les GB, par leur nature hétérogène et plastique, posent d'importants défis dans l'élaboration de thérapies efficaces. L'espoir réside donc dans la mise en place de nouvelles stratégies thérapeutiques personnalisées qui tiendront compte de l'hétérogénéité et de la plasticité des GB [110]. En dehors de la recherche de thérapies, la recherche de biomarqueurs spécifiques pouvant aider à stratifier les patients et à guider le choix des traitements est également en cours d'étude.

L'utilisation d'une médecine de précision, prenant en compte les variations génétiques individuelles, pourrait offrir des traitements plus ciblés et donc potentiellement plus efficaces. Cependant, à l'heure actuelle, de nombreuses études ont documenté la notion de « plasticité phénotypique adaptative ». La progression tumorale est historiquement attribuée à l'évolution darwinienne due à des mutations génétiques. Cependant, les recherches récentes suggèrent que la plasticité phénotypique non génétique, associée à des états d'expression génique alternatifs, principalement sous la dépendance de l'épigénétique, joue un rôle primordial dans la progression tumorale. Ainsi, il est nécessaire de prendre en compte l'évolution génétique mais également les transitions d'état non génétiques pour appréhender la complexité des GB [96].

La plateforme inTRINSiC ouvre de nouvelles perspectives en identifiant des régulateurs (facteurs de transcription) spécifiques à chaque sous-type de tumeur, qui pourraient être exploités comme cibles potentielles dans les thérapies anticancéreuses. En effet, les transitions d'état des cellules tumorales sont principalement régulées par des facteurs de transcription et des mécanismes épigénétiques. En ciblant ces éléments régulateurs clés, il serait possible de

contrer la plasticité phénotypique adaptative des tumeurs, ouvrant la voie à des traitements plus ciblés et potentiellement plus efficaces [182].

La majorité des recherches se sont focalisées sur les tumeurs primaires et ont permis de visualiser le paysage moléculaire des tumeurs naïves (avant tout traitement). Les études sur les tumeurs récidivantes sont moins nombreuses, malgré le fait que ce sont souvent ces tumeurs récurrentes, de plus en plus résistantes aux traitements, qui sont fatales pour les patients. Des recherches récentes ont comparé des tumeurs de patients avant et après traitement, révélant de grandes différences entre la tumeur initiale au moment du diagnostic et la récidive [183]. Pour parvenir à une compréhension robuste de la dynamique évolutive des GB, il est nécessaire de réaliser des études longitudinales et notamment un profilage multiomique sur de nombreux échantillons de tumeurs, à la fois primaires et récurrentes. Cela permettrait d'identifier les mécanismes clés qui jouent un rôle significatif dans la progression tumorale, la réponse au traitement ou la récidive des tumeurs. Par ailleurs, il est nécessaire d'aboutir à une standardisation de la façon dont les échantillons biologiques sont traités et analysés, afin de pouvoir garantir la fiabilité et la comparabilité des données recueillies [184].

Les CSG, souvent identifiées comme étant responsables des récidives, sont considérées comme des cibles pertinentes dans les stratégies anticancéreuses. Certaines études ont démontré que la suppression de CSG améliore la réponse au traitement par le TMZ et prolonge le délai de récidive et la survie des modèles animaux [57]. Une approche anticancéreuse consisterait à forcer les CSG à se différencier afin de les rendre non tumorigénique et éventuellement sensibles aux traitements habituels. Cependant, en raison de la plasticité bidirectionnelle, il devient crucial de cibler les divers états cellulaires au sein des GB ou encore de compléter des thérapies anti-CSG avec des stratégies inhibant la reprogrammation des cellules différenciées. De plus, des travaux récents montrent que les deux états cellulaires, souches et différenciés, sont interconnectés et qu'ils participent ensemble à la progression tumorale et à la résistance aux thérapies [166]. Ainsi, pour permettre une rémission à long terme du patient, il convient de cibler les deux états cellulaires, souche et différencié. Plutôt que de considérer ces cellules comme des entités uniques, il convient de les considérer comme des états dynamiques. L'objectif actuel est de mieux comprendre les mécanismes de plasticité des cellules cancéreuses, notamment leur adaptation à l'environnement et aux thérapies. Des traitements ciblant ces mécanismes pourraient être particulièrement prometteurs [184].

PARTIE 3 : MÉTABOLISME TUMORAL ET APPROCHES THÉRAPEUTIQUES

1. Revue de la littérature

La troisième partie de l'introduction de ma thèse se focalise sur le métabolisme tumoral et les approches thérapeutiques associées dans le contexte des GB. Elle s'appuie en grande partie sur une revue détaillée de la littérature sur le sujet que j'ai rédigée en tant que 1er auteur et publiée dans le journal International Journal of Molecular Science (IF 2023 : 6.2), intitulée « *Glioblastoma Metabolism: Insights and Therapeutic Strategies* ».

Cette revue s'inscrit dans le cadre des recherches récentes sur le métabolisme tumoral, désormais vu comme une source de cibles thérapeutiques prometteuses pour les thérapies anticancéreuses. Cette nouvelle approche est particulièrement prometteuse pour le traitement des GB. La revue présente ainsi une vue d'ensemble des altérations métaboliques observées dans les GB, avec un attention particulière portée aux CSG. Elle explore en profondeur les processus métaboliques spécifiques impliqués dans la pathogenèse des glioblastomes (GB), couvrant divers aspects du métabolisme tumoral, notamment le métabolisme du glucose, des acides aminés, des lipides, des nucléotides, du monocarbone, de la nicotinamide, ainsi que le cycle de l'acide citrique (TCA) et la chaîne de phosphorylation oxydative (OXPHOS). Pour chaque voie métabolique abordée, la revue décrit les approches thérapeutiques associées et met en lumière les résultats d'essais pré-cliniques et cliniques relatifs à ces stratégies. De plus, la revue traite de la complexité, de l'hétérogénéité et de la plasticité du métabolisme tumoral, en incluant les interactions métaboliques au sein du microenvironnement tumoral. Des stratégies d'associations thérapeutiques, combinant l'approche métabolique avec la radiothérapie, la chimiothérapie, les thérapies ciblées, l'immunothérapie, ainsi que les interventions diététiques sont également explorées. Dans le contexte de cette thèse, cette revue sert à la fois d'élément de contextualisation du projet, et de fondement pour l'investigation approfondie de l'hétérogénéité et de la plasticité métabolique des GB.

International Journal of
Molecular Sciences

MDPI

Review

Glioblastoma Metabolism: Insights and Therapeutic Strategies

Chloé Bernhard [1], Damien Reita [1,2], Sophie Martin [1], Natacha Entz-Werle [1,3] and Monique Dontenwill [1,*]

[1] UMR CNRS 7021, Laboratory Bioimaging and Pathologies, Tumoral Signaling and Therapeutic Targets, Faculty of Pharmacy, University of Strasbourg, 67405 lllkirch, France; chloe.bernhard@etu.unistra.fr (C.B.); damien.reita@chru-strasbourg.fr (D.R.); sophie.martin@unistra.fr (S.M.); natacha.entz-werle@chru-strasbourg.fr (N.E.-W.)
[2] Laboratory of Biochemistry and Molecular Biology, Department of Cancer Molecular Genetics, University Hospital of Strasbourg, 67200 Strasbourg, France
[3] Pediatric Onco-Hematology Unit, University Hospital of Strasbourg, 67098 Strasbourg, France
* Correspondence: monique.dontenwill@unistra.fr

Abstract: Tumor metabolism is emerging as a potential target for cancer therapies. This new approach holds particular promise for the treatment of glioblastoma, a highly lethal brain tumor that is resistant to conventional treatments, for which improving therapeutic strategies is a major challenge. The presence of glioma stem cells is a critical factor in therapy resistance, thus making it essential to eliminate these cells for the long-term survival of cancer patients. Recent advancements in our understanding of cancer metabolism have shown that glioblastoma metabolism is highly heterogeneous, and that cancer stem cells exhibit specific metabolic traits that support their unique functionality. The objective of this review is to examine the metabolic changes in glioblastoma and investigate the role of specific metabolic processes in tumorigenesis, as well as associated therapeutic approaches, with a particular focus on glioma stem cell populations.

Keywords: glioblastoma; metabolism; cancer stem cells; tumorigenic processes; therapy

Citation: Bernhard, C.; Reita, D.; Martin, S.; Entz-Werle, N.; Dontenwill, M. Glioblastoma Metabolism: Insights and Therapeutic Strategies. *Int. J. Mol. Sci.* **2023**, *24*, 9137. https://doi.org/10.3390/ijms24119137

Academic Editors: Bal Krishna Chaube and Shivendra Vikram Singh

Received: 6 April 2023
Revised: 10 May 2023
Accepted: 18 May 2023
Published: 23 May 2023

1. Introduction

Glioblastomas (GB) are highly malignant and among the most challenging cancers. The standard of care for the treatment of GB is still the Stupp protocol, which was first introduced in 2005. This protocol combines surgery, radiotherapy, and chemotherapy with temozolomide (TMZ) [1]. Although this treatment approach has been widely used, it fails to achieve long-term remission for patients, due in part to the molecular heterogeneity and plasticity of GB cells, including GB stem cells (GSCs). GB are characterized by a high degree of heterogeneity, whether in terms of their histological and molecular characteristics, cellular origin, topography, growth patterns, and sensitivity to therapy. This heterogeneity exists not only between different tumors (intertumoral heterogeneity), but also within the same tumor (intratumoral heterogeneity) [2,3]. In 2010, a large-scale transcriptomic analysis of GB revealed the presence of molecular signatures that define different clinically relevant subtypes of adult GB, including classical, mesenchymal, and proneural subtypes [4,5]. Later, the Neftel classification described the heterogeneity of different cellular states within a single tumor, distinguishing four major states (neural progenitor-like, oligodendrocyte progenitor-like, astrocyte-like, and mesenchymal-like) that are modulated by the microenvironment and favored by distinct genetic alterations. The proportion of cells in each state within a tumor can vary over the course of tumor evolution and under the pressure of treatments [6]. The search for new therapies for GB patients has predominantly centered around molecular targets discovered through comprehensive genomic analyses such as The Cancer Genome Atlas (TCGA). These targets are recurrent molecular alterations that disrupt important pathways that regulate growth, cell cycle, autophagy, DNA repair, apoptosis, angiogenesis, and immune checkpoints and are considered as potential therapeutic targets for GB treatment. Despite these efforts, no significant clinical improvement was

achieved, probably due to the significant intratumoral heterogeneity [7]. The interest in tumor metabolism has risen over the past decade. Indeed, targeting the tumor metabolism has proven promising, particularly for the elimination of GSCs [8]. Furthermore, combining conventional treatments with therapies targeting tumor metabolism may result in better care for GB patients, with lower doses of chemotherapy and fewer side effects, while still achieving effective anticancer results and potentially overcoming treatment resistance [9]. The understanding of protumorigenic metabolic mechanisms and pathways is necessary to define relevant therapeutic targets and subsequently to propose effective combination therapies. Advancements in research and technology have led to the identification of key differences between tissues and tumors that could be targeted in cancer therapy. However, research has also revealed the heterogeneity, complexity, and plasticity of tumor metabolism in both preclinical and clinical models [10].

2. Tumoral Metabolic Reprogramming

Reprogramming of metabolism in cancer is a multifaceted process driven by genetic and environmental factors. Tumoral metabolic reprogramming provides energy (ATP), precursors for macromolecules (carbohydrates, lipids, proteins, and nucleic acids), and reducing equivalents essential for the extensive proliferative activity of cancer cells. Alterations in glycolysis, Oxidative Phosphorylation (OXPHOS), the Pentose Phosphate Pathway (PPP), lipids, amino acids and nucleotides metabolism have been observed (Figure 1) [11,12]. Moreover, cancer cells adapt to their environment by reprogramming their cellular metabolism, which allows them to grow, survive and proliferate in a constantly changing environment [13].

GB cells primarily rely on glucose as their metabolic fuel, but they can also utilize amino acids such as glutamine and glutamate, lipids such as fatty acids and lipid droplets [14], and other sources such as acetate [15], depending on the genetic background and the tumor microenvironment. For example, GB cells expressing constitutively active AKT are totally glucose dependent [16]. Glucose can either undergo aerobic glycolysis leading to lactate formation or be oxidized in the mitochondria through the Tricarboxylic Acid Cycle (TCA), both of which are energy-producing pathways. The TCA cycle provides reducing equivalents that supply the function of the respiratory chain, the site of massive ATP energy production. In contrast, the conversion of pyruvate into lactate (aerobic glycolysis) yields only a small amount of energy. Beyond energy needs, cancer cells need to generate biomass. Thus, in GB, metabolic intermediates of glycolysis are shunted to the Pentose Phosphate Pathway but also to the serine and lipid biosynthetic pathways. The upregulation of the Pentose Phosphate Pathway stimulates the nucleotide synthesis which is essential for DNA replication and repair, but also to produce reducing equivalents (NADPH) supporting redox homeostasis and lipid biosynthesis [17]. The TCA cycle, supplied with glucose and alternative fuels such as glutamate, fatty acids, acetate, and ketones, provides energy intermediates and anabolic precursors [15,18,19].

The metabolic changes in GB are attributed to mutations in tumor-suppressor genes and oncogenes, as well as the influence of the surrounding microenvironment. The relationship between metabolic and molecular reprogramming is complex and interdependent [20,21]. Oncogenic signaling pathways (such as PI3K-AKT-mTOR, MYC, and Ras) or the inactivation of tumor-suppressor genes (such as TP53) have been demonstrated to modulate tumor metabolism [22]. The PI3K-AKT-mTOR signaling pathway plays a crucial role in regulating tumor metabolism, including promoting glycolysis and anabolic metabolism of nucleotides, lipids, and proteins, and is frequently aberrantly activated in GB. mTOR regulates cell growth, translation, and the initiation of autophagy [23]. Hypoxia and hypoxia-inducible factors (HIFs) also play a crucial role in promoting metabolic reprogramming in cancer cells as well as in stemness and therapy resistance [24,25].

Since metabolism plays a pivotal role in GB tumorigenesis and progression, it presents a valuable avenue for exploring potential therapeutic approaches in treating GB.

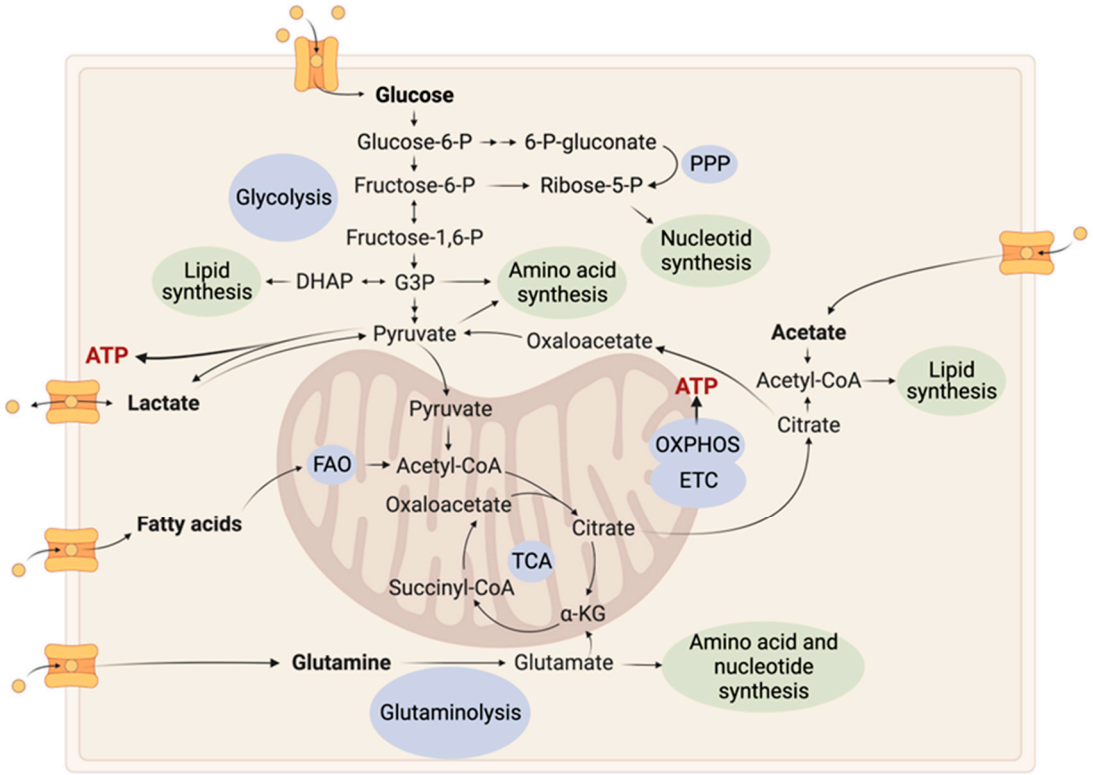

Figure 1. Active metabolic pathways in glioblastoma. Cancer cells exhibit a variety of metabolic changes, including increased glycolysis leading to lactate production and glutaminolysis, which provides energy for the TCA cycle. Metabolic nutrients are highlighted in bold. Metabolic intermediates are channeled into nucleic acid, amino acid, and lipid biosynthetic pathways. These metabolic pathways are intricately connected [10,18]. α-KG: α-Ketoglutarate; ATP: Adenosine Triphosphate; DHAP: Dihydroxyacetone Phosphate; ETC: Electron Transport Chain; FAO: Fatty Acid Oxidation; G3P: Glyceraldehyde-3-Phosphate; OXPHOS: Oxidative Phosphorylation; P: Phosphate; PPP: Pentose Phosphate Pathway; TCA: Tricarboxylic Acid Cycle. Figure created with BioRender.com.

2.1. Glucose Metabolism

The Warburg effect, also known as aerobic glycolysis, is a metabolic feature commonly found in cancer cells. This metabolic change is characterized by increased glucose uptake and consumption, resulting in an increase in lactate production, even in the presence of oxygen [10]. Aerobic glycolysis produces less energy than oxidative metabolism, but allows cancer cells to rapidly convert available resources into biomass (lipids, nucleotides, and amino acids) [17]. This is also critical for the survival and proliferation of cancer cells under hypoxic conditions [20,26]. Lactate production is accompanied by the production of protons, both of which pass through the extracellular environment via monocarboxylate (MCT 1,4) and Na^+/H^+ type 1 (NHE1) transporters, respectively. This leads to the acidification of the microenvironment and the development of an immunosuppressive environment, promoting the growth and invasion of cancer cells [27,28]. Lactate can also trigger angiogenesis by being imported into endothelial cells [20]. The Warburg effect results from an increase in the transcription of genes coding for Glucose Transporters (GLUT) and glycolysis-associated enzymes, making them potential targets for therapy (Figure 2) [29].

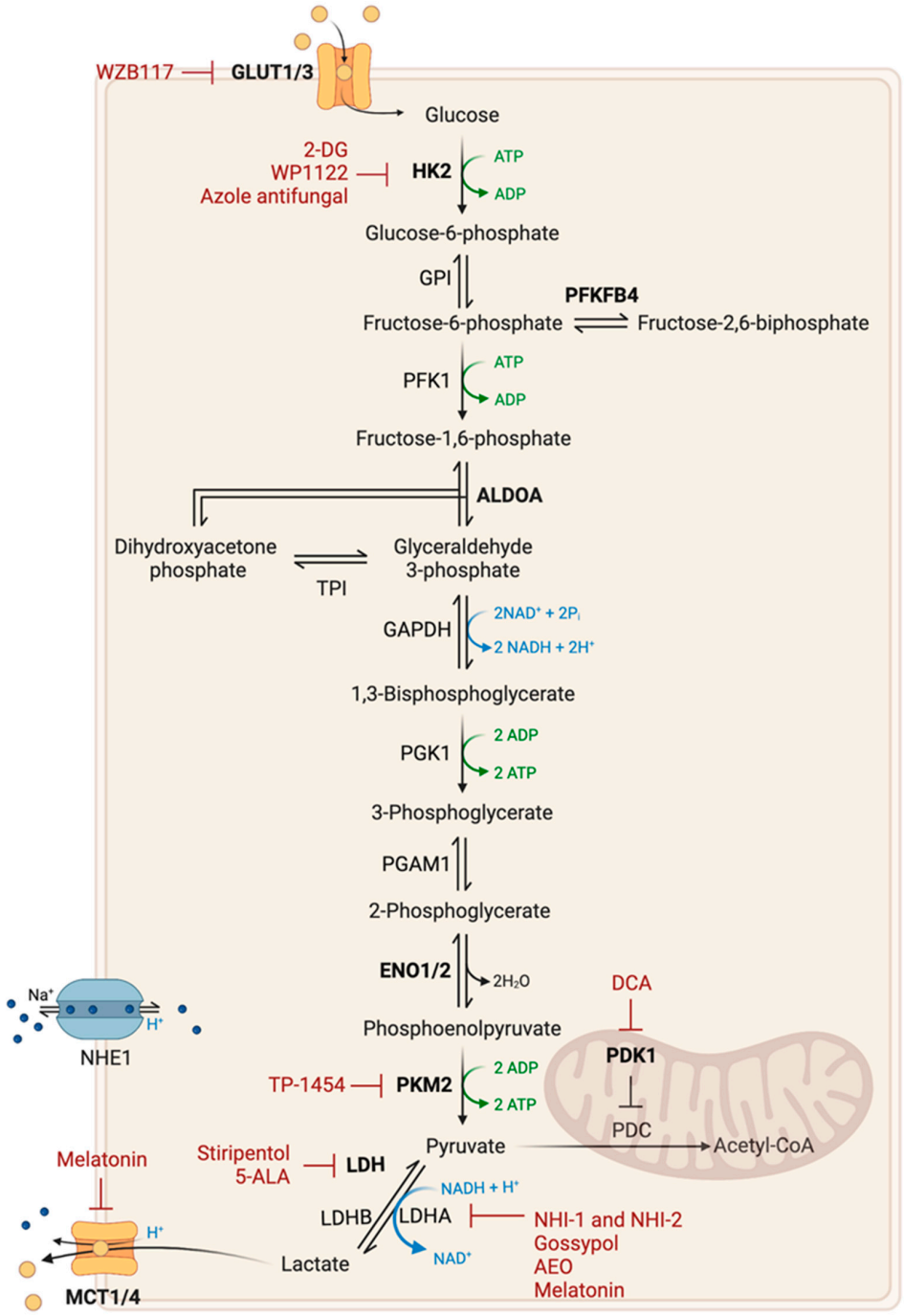

Figure 2. Warburg effect and related therapy. The Warburg effect, a hallmark of cancer metabolism, refers to metabolic reprogramming in cancer cells towards increased glucose uptake, glycolysis, and lactate production, even in the presence of oxygen. The most critical enzymes and transporters involved in this process are highlighted in bold and potential therapies in red. Targeting these enzymes and transporters is a potential strategy in cancer therapy. ADP: Adenosine Diphosphate; ATP: Adenosine Triphosphate; AEO: Anhydrous Enol-Oxaloacetate; 5-ALA: 5-Aminolevulinic Acid; 2-DG: 2-Deoxyglucose; ENO: Enolase; GAPDH: Glyceraldehyde-3-Phosphate Dehydrogenase; GLUT: Glucose Transporter; HK: Hexokinase; LDH: Lactate Dehydrogenase; MCT: Monocarboxylate Transporter; NAD^+/NADH,H^+ Oxidized/reduced Nicotinamide Adenine Dinucleotide; NHE1: Sodium-Hydrogen Exchanger 1; PGAM1: Phosphoglycerate Mutase 1; PFK1: Phosphofructokinase-1; PGK1: Phosphoglycerate Kinase 1; PKM2: Pyruvate Kinase M2; TPI: Triosephosphate Isomerase. Figure created with BioRender.com.

The use of 2-Deoxyglucose (2-DG) has shown potential as a cytotoxic agent in cancer treatment due to its ability to inhibit glycolysis and disrupt cellular metabolism. A phase II clinical trial found that 2-DG was both safe and well tolerated in GB patients [30,31]. However, its short half-life and adverse effects limit its therapeutic potential. To address these issues, novel analogues and prodrugs of 2-DG have been developed. One such analogue, WP1122, has demonstrated promising results in preclinical studies. WP1122 releases 2-DG and has a longer half-life, good oral bioavailability and is well tolerated in animal models. WP1122 has completed a phase I clinical trial (NCT05195723) and is planned to enter in clinical trial for the treatment of GB patients [32]. The future perspectives for 2-DG and its analogues in anticancer therapy lie in their potential synergistic effects when combined with other potent cytotoxic agents.

Other potential targets are GLUT1 and GLUT3 isoforms, which are commonly overexpressed in GB [33]. GLUT1 isoform is crucial for glucose transport across the blood–brain barrier, and GLUT3 isoform is mainly expressed in neurons and overexpressed in GSCs and has a higher affinity for glucose and has been linked to poor prognosis in GB patients [34,35]. Silencing of *GLUT3* in GSCs [35], as well as *GLUT1* silencing or pharmacological inhibition of GLUT1 using WZB117 [36], reduced tumor formation in vivo. Metabolic dependency on GLUT3 has been observed in some classical and proneural GB subtypes, driven by an abnormal $\alpha v\beta 3$ integrin expression [37]. Moreover, GLUT3 expression has been linked to bevacizumab resistance [38]. A recent study revealed that histone deacetylase 2 knockdown resulted in the suppression of GLUT3 expression by upregulating miR-3189, leading to an antitumorigenic effect [39]. Currenly, there are few GLUT inhibitors and no GLUT3 specific inhibitors, and their efficacy in GB and potential toxicity to normal cells have not been extensively studied [33].

Another therapeutic approach involves targeting glycolytic-associated enzymes. Many glycolytic enzymes are upregulated in cancer cells, and some have been identified as crucial for tumor growth, such as Hexokinase 2 (HK2), aldolase A (ALDOA), pyruvate dehydrogenase kinase 1 (PDK1), Pyruvate Kinase M2 (PKM2), 6-phosphofructo-2-kinase/fructose-2,6-biphosphatase 4 (PFKFB4) and Enolase 1 and 2 (ENO1 and ENO2) [40,41]. HK2 plays a significant role in the inhibition of mitochondria-mediated apoptosis and has been linked to tumor grade and poor prognosis in GB [42]. Depletion of HK2 in GB xenograft models decreased tumor proliferation and angiogenesis but increased tumor invasion [42]. The inhibition of HK2 in cancer therapy may be doubted due to its non-specificity and systemic toxicity, as well as the fact that tumors expressing HK2 can also express HK1 [9]. However, ketoconazole and posaconazole, members of the azole class of antifungals, have been identified as inhibitors of tumor metabolism that target the HK2-associated gene signature. This treatment has been shown to induce apoptotic cell death in vitro and reduce tumor growth in vivo in GB models [43]. These promising results have led to the initiation of phase I clinical trials (NCT04869449 and NCT04825275) in patients with brain tumors. PFKFB4 has been identified as another critical enzyme for the maintenance of GSCs, and its high expression is correlated with poor prognosis in GB patients [40]. The final step in glycolysis is catalyzed by Pyruvate Kinase (PK). Normally, the PKM2 isoform is only expressed in embryonic tissues and adult stem cells. In cancer, however, PKM2 is overexpressed, leading to a reprogramming of glucose utilization. PKM2 has a lower affinity for phosphoenolpyruvate (PEP) compared to PKM1, resulting in low enzymatic activity, allowing the metabolic intermediates produced upstream to be used for biosynthetic processes [44]. PKM2 has the ability to directly bind to histone H3 and induce its phosphorylation, thereby enabling the expression of genes such as *CCND1* (Cyclin D1) and *MYC*. There is a correlation between the phosphorylation levels of histone H3, the levels of nuclear PKM2, the grade of malignancy, and the patient's prognosis [45]. Additionally, under oxidative stress, PKM2 can be translocated into mitochondria and prevent apoptosis by phosphorylating Bcl-2 [46]. Recently, TP-1454, a compound that activates PKM2, entered a phase I clinical trial and is currently being evaluated in combination therapy for patients with solid progressive tumors (NCT04328740). A study has shown that trametinib (a MEKK

inhibitor) specifically targets the PKM2/c-MYC pathway, leading to the suppression of glycolysis and growth in glioma cells. A phase II clinical trial (NCT03919071) is currently recruiting newly diagnosed high-grade glioma patients who have undergone radiation therapy to evaluate the effectiveness of a combined treatment of trametinib and dabrafenib (a MAPK inhibitor) [47]. Enolase is another crucial enzyme, catalyzing the formation of PEP. Enolase activity is determined by three genes: *ENO1*, ubiquitously expressed; *ENO2*, expressed only in neural tissue; and *ENO3*, expressed in muscle tissue. An analysis of TCGA data revealed that some GB exhibit homozygous deletions in *ENO1*, resulting in the abnormal expression of ENO2. This highlights a metabolic vulnerability of GB cells lacking *ENO1*, in which *ENO2* deletion has inhibited the growth, survival and tumorigenic properties of cancer cells [48]. PDK1 is another promising target for anticancer therapy, as it has been demonstrated to play a critical role in the survival of GSCs. PDK1 functions as a negative regulator of pyruvate dehydrogenase (PDH), reducing the supply of acetyl-CoA in the mitochondria and thus leading to a decrease in oxidative mitochondrial metabolism [49]. Dichloroacetate (DCA), usually used to treat lactic acidosis, has been shown to reverse the Warburg effect by inhibiting PDK1. This activates mitochondrial PDH and thus increases the flow of pyruvate into the mitochondria, leading to membrane depolarization, an increase in mitochondrial reactive oxygen species (ROS) levels, and ultimately the induction of apoptosis. DCA is particularly noteworthy in its ability to enhance radiation sensitivity. Indeed, in animal models of GB, DCA has been shown to improve survival when combined with radiotherapy [50]. Although phase I (NCT01111097) and phase II (NCT00540176) clinical trials have been conducted, clinical data on its efficiency remain lacking. However, preliminary results have shown that this drug crosses the blood–brain barrier and is well tolerated by patients.

Lactate Dehydrogenase (LDH) is a major enzyme that catalyzes the interconversion of pyruvate to lactate. There are two types of LDH found in cancers: LDH-A, involved in the Warburg effect, catalyzes the conversion of pyruvate to lactate; and LDH-B catalyzes the reverse reaction, i.e., the conversion of lactate to pyruvate. LDH-A is overexpressed in GB, particularly in hypoxic and invasive areas. Overexpression of LDHA has been linked to tumor initiation, maintenance and progression, as well as poor prognosis in many types of cancer, including decreased survival in GB patients treated with radiotherapy [51,52]. In vitro studies have shown that LDH-A inhibitors, such as NHI-1 and NHI-2, affect the maintenance of GSCs, inhibit cell differentiation and induce apoptosis processes [53]. More recently, research has demonstrated that lactate fuels GB anaplerosis by replenishing the TCA cycle in absence of glucose through LDH-B activity [54]. A metabolic cooperation between glycolytic and oxidative cancer cells has also been described. Cells under hypoxic conditions overexpress LDH-A, exhibiting glycolytic phenotype that produce large amounts of lactate and secretes it into the microenvironment. More distant oxidative cells that overexpress LDH-B uptake lactate and convert it to pyruvate to fuel the TCA cycle. The combined ablation of both LDH isoforms, but not just one, has been shown to decreased tumor growth, improved mouse survival, and increased sensitivity to radiotherapy. In addition, the anti-epileptic drug stiripentol has been shown to inhibit the activity of both LDH isoforms and has been proven to effectively decrease the growth of GB [55]. Another promising compound in this regard is gossypol, a natural polyphenolic drug, which targets the Bcl-2 protein family and various dehydrogenases, including aldehyde dehydrogenases (ALDH) and LDH-A. Gossypol has been shown to inhibit the growth and induce cell death of TMZ-resistant GB cells, including GSC, with increased sensitivity [56]. Clinical trials evaluating gossypol for the treatment of GB have been conducted. Different patient responses have been observed, including tumor stability for over seven months of treatment (phase I: NCT00390403; phase II: NCT00540722) [57]. One therapeutic approach for inhibiting glycolysis involves the use of 5-Aminolevulinic Acid (5-ALA), a natural heme precursor that accumulates in GB tumors to a greater extent than in healthy cells. 5-Aminolevulinic Acid has been shown that 5-ALA can impair glycolysis by inhibiting LDH, leading to cell death. The use of 5-ALA as an adjuvant for visualization of high-grade

gliomas was approved by the Food and Drug Administration (FDA) in 2017 and has since become a common tool for guiding brain cancer resection. 5-ALA's potential as a cancer treatment could improve the therapeutic care for GB patients [58]. Melatonin has been demonstrated to impact glycolysis in GSCs leading to cell death by repressing LDH-A and MCT4 expression, resulting in reduced lactate production and decreased intracellular pH and ATP levels. Additionally, this approach caused an increase in ROS and blockage of cell cycle progression, ultimately resulting in cell death [59]. Recently, researchers have developed a novel approach to target GB cells by using therapeutic nanoparticles. These nanoparticles are designed to penetrate the blood–brain barrier and specifically recognize the membrane components of GB cells. Upon entering the tumor, lactate oxidase within the nanoparticles converts lactate into pyruvic acid and hydrogen peroxide. Pyruvic acid blocks histone expression and induces cell cycle arrest, while hydrogen peroxide generates singlet oxygen to kill GB cells through a reaction with a delivered photosensitizer [60]. Recent studies have demonstrated the potential of oxaloacetate, a TCA cycle metabolite, to suppress the Warburg effect in GB [61]. Treatment with oxaloacetate resulted in reduced tumor growth and increased survival in animal models of implanted GB [62]. These results led to the initiation of a clinical trial with Anhydrous Enol-Oxaloacetate (AEO) oral administration in combination with standard therapy for newly diagnosed GB patients (NCT04450160).

In summary, the Warburg effect, lactate production, overexpression of Glucose Transporters and glycolysis-associated enzymes are important features of cancer cell metabolism that offer potential targets for therapy, particularly in certain GB subtypes with specific metabolic vulnerabilities.

2.2. Amino Acid Metabolism

2.2.1. Glutamine Metabolism

Reprogrammed glutamine metabolism is essential for the survival and proliferation of cancer cells, providing TCA cycle intermediates, nucleotides, amino acids, and fatty acids biosynthesis, regulating redox homeostasis, and modulating α-KG levels involved in DNA and histone demethylation. Reprogrammed glutamine metabolism stimulates the synthesis of glutathione, which helps fight against oxidative stress [63] and was correlated to an increased capacity of resistance to radio- and chemo-therapies [64]. As a result, targeting glutamine metabolism has emerged as a promising therapeutic strategy in many cancers, including GB (Figure 3).

Glutamine enters cells via the SLC1A5/ASCT2 transporters and is converted to glutamate within the mitochondria via an oxidative deamination reaction catalyzed by glutaminases (GLS). This reaction converts glutamine to glutamate and ammonia. Glutamate is then converted to α-KG by glutamate dehydrogenase (GDH), replenishing TCA cycle intermediates [65]. Glutamine can also be converted into pyruvate by the malic enzyme to fuel TCA cycle or produce lactate. GB cells are able to use microenvironment-derived glutamate to generate glutamine through the expression of glutamine synthetase [15,19]. Regarding circulating glutamine, it does not represent a major fuel for the TCA cycle. Low expression of glutamine synthetase has been linked to improved prognosis in GB patients, with an average survival time that is two-fold longer [66]. Overexpression of this enzyme has been found in GSC populations [67]. Some cancer cells are extremely sensitive to glutamine deprivation [68], while other cells are insensitive due to autonomous glutamine production via glutamine synthetase expression [67].

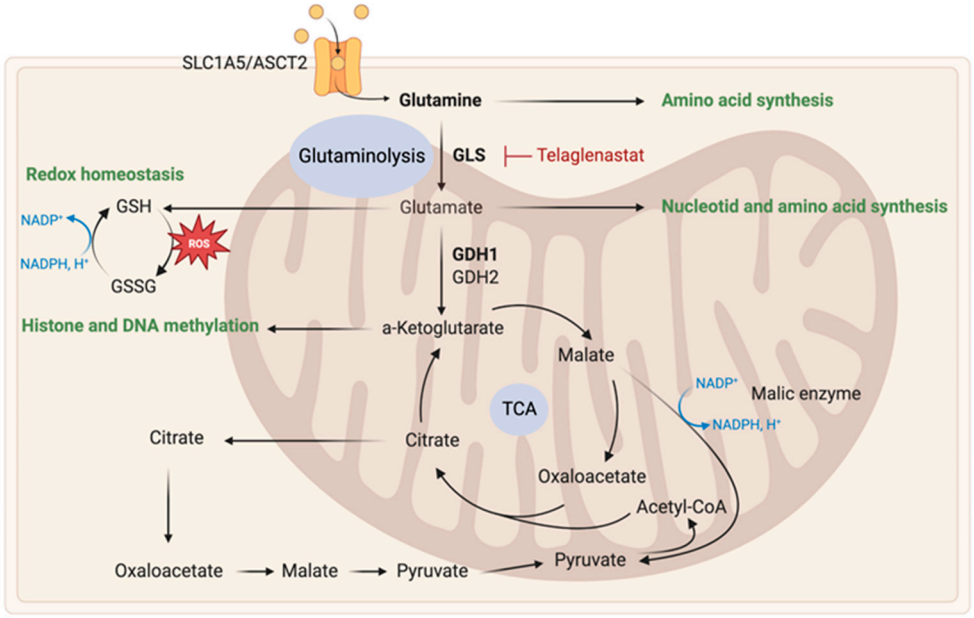

Figure 3. Glutamine metabolism pathways and processes in tumorigenesis and related therapy. Reprogrammed glutamine metabolism is involved in tumorigenic processes, which are highlighted in green. Reprogrammed glutamine metabolism supplies essential components for nucleotides, amino acids, and fatty acids biosynthesis, drives the TCA cycle, and maintains redox balance, as well as influencing epigenetic modifications through modulation of α-KG levels. Cancer cells take up glutamine via the transporter ASCT2/SLC1A5, which is then converted into glutamate by glutaminase. The conversion of glutamate to α-ketoglutarate by glutamate dehydrogenase fuels the TCA cycle. In GB, therapeutic targets are highlighted in bold and therapy in red. $NADP^+$/$NADPH,H^+$: Oxidized/reduced Nicotinamide Adenine Dinucleotide Phosphate; GLS: Glutaminase; GDH1/2: Glutamate Dehydrogenase 1/2; GSH/GSSG: Reduced/oxidized Glutathione; SLC1A5/ASCT2: Solute Carrier Family 1 Member 5/Alanine Serine Cysteine Transporter 2, member 5; TCA: Tricarboxylic Acid Cycle. Figure created with BioRender.com.

Glutaminase inhibition (GLS) as a therapeutic strategy has been proposed in many cancers. This approach was able to decrease GB growth in both in vitro and in vivo models [69]. The mesenchymal GB subtype [70] and those with aberrant c-MYC signaling [71] are particularly sensitive to GLS inhibition. Moreover, GLS plays a role in resistance to mTOR inhibitors, and dual inhibition of mTOR and GLS in vivo synergistically slowed GB growth [72]. A phase II clinical trial evaluating telaglenastat, a GLS inhibitor, in combination with poly(ADP-ribose) polymerases (PARPs) inhibitor, talazoparib, has been completed in advanced/metastatic solid tumors patients (NCT03875313).

Another potential therapeutic target is glutamate dehydrogenase (GDH). In GB, GDH expression is upregulated and correlates with poor patient prognosis. Inhibition of GDH decreased tumor proliferation in various in vitro and in vivo models [73]. Recently, researchers distinguished the two existing GDH isoforms (GDH1 and GDH2) and showed a correlation between strong GDH2 expression and improved patient prognosis. In vitro, overexpression of GDH2 leads to a significant decrease in proliferation, migration and clonogenicity of GB cells. It seems that it is GDH1, but not GDH2, that should be targeted in anticancer strategies [74].

Overall, targeting glutamine metabolism presents a potential avenue for developing effective therapies for GB and other cancers [68].

2.2.2. Arginine Metabolism

Arginine is an amino acids actively metabolized by tumor cells to facilitate tumor progression and immunosuppression. L-arginine is a crucial component of the urea cycle

and plays a role in modulating both immune function and tumor metabolism. Arginine is catalyzed by two enzymes: Arginase 1 (ARG1), which converts L-arginine into urea and ornithine; and cytokine-inducible Nitric Oxide synthase (NOS) which converts L-arginine into citrulline and Nitric Oxide (NO). In GB, arginine metabolism is altered, characterized by an upregulation of amino acid transporters CAT-1 and the Arginase enzymes, particularly ARG II located in the mitochondria. Additionally, there is a downregulation of key enzymes responsible for endogenous arginine synthesis, such as Argininosuccinate Synthase 1 (ASS1). Potential therapeutic strategies targeting arginine metabolism include targeting the Arginase enzyme and arginine depletion therapy (Figure 4).

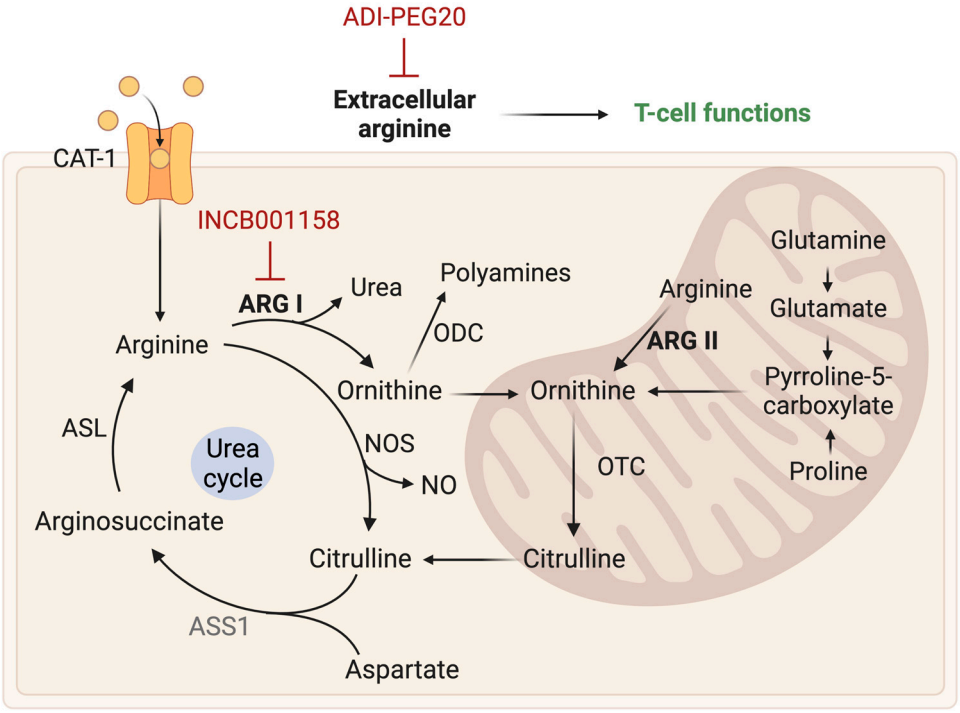

Figure 4. Arginine metabolism and related therapies. In glioblastoma, alterations in arginine metabolism are observed, characterized by an increase in arginine uptake, elevated arginase 2 (ARG II) levels, and a decrease in Argininosuccinate Synthase 1 (ASS1), an enzyme responsible for endogenous arginine synthesis. Therapeutic targets for GB are highlighted in bold, and therapies in red. The latter approach has shown promising results in ASS1-deficient glioblastomas. ADI-PEG20: Pegylated Arginine Deaminase; ASS1: Argininosuccinate Synthase 1; ARG: Arginase; ASL: Argininosuccinate Lyase; NO: Nitric Oxide; NOS: Nitric Oxide Synthase; ODC: Ornithine Decarboxylase; OTC: Ornithine Transcarbamylase. Figure created with BioRender.com.

Depleting extracellular arginine has been established as an effective treatment approach for cancers exhibiting deficiencies in arginine metabolism and dependence on exogenous sources. However, the arginine deficiency in the tumor microenvironment inhibits T-cell function, promoting immunosuppression. Thus, targeting arginine metabolism may present a dilemma between deprivation and replenishment.

Some GB tumors exhibit a deficiency in *ASS1*. These tumors account for 20% of all GB cases and are particularly sensitive to arginine deprivation. Depleting arginine using pegylated arginine deiminase (ADI-PEG20) has been shown to reduce tumor growth in vitro and in vivo [75]. The phase I study on recurrent high-grade gliomas showed promising results with ADI-PEG20 in combination with chemotherapy [76,77]. Targeting the Arginase enzyme has also been evaluated in clinical trials. INCB001158, an Arginase inhibitor, has completed a phase I/II clinical trial in combination with chemotherapy for the treatment of advanced solid tumors (NCT03314935). Further research is needed to determine the most effective strategy to target arginine metabolism in GB.

2.3. Lipid Metabolism

GB cells are surrounded by a lipid-rich environment, and lipid metabolism plays a critical role in the development and progression of GB. Lipids comprise a heterogeneous group of organic compounds, including fatty acids, triglycerides, phospholipids and cholesterol. Tumor reprogramming of lipid metabolism involves alterations in import/export pathways, lipid catabolism including Fatty Acid Oxidation (FAO), as well as alterations in de novo lipid synthesis pathways such as lipogenesis and cholesterol synthesis. Numerous potential therapeutic strategies targeting lipid metabolism have been investigated for the treatment of GB (Figure 5) [78].

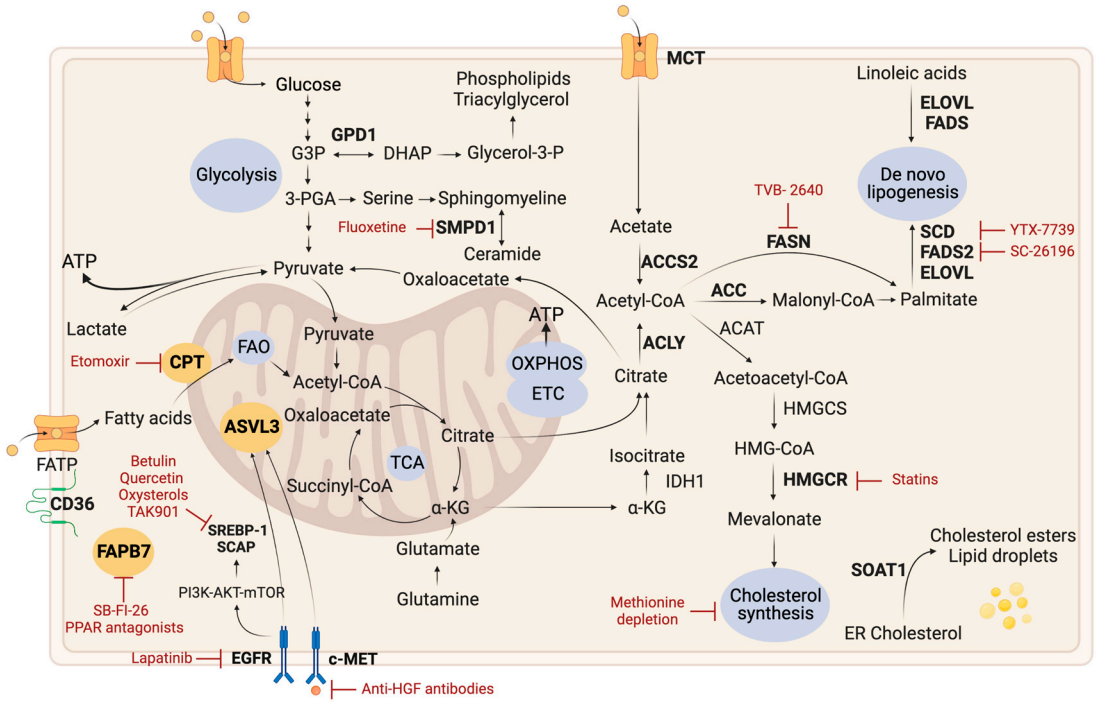

Figure 5. Lipid metabolism and associated therapies. In glioblastoma, alterations occur in multiple lipid biosynthesis and degradation pathways, including de novo lipogenesis, Fatty Acid Oxidation, cholesterol metabolism, and other lipid-related pathways. This figure highlights potential therapeutic targets in lipid metabolism that are highlighted in bold, as well as several therapies that target lipid-associated pathways, which are highlighted in red. ACC: Acetyl-CoA Carboxylase; ACCS2: Acetyl-CoA Synthetase 2; ACAT: Acetyl-CoA Acetyltransferase; α-KG: α-Ketoglutarate; ATP: Adenosine Triphosphate; CPT: Carnitine Palmitoyltransferase; DHAP: Dihydroxyacetone Phosphate; ETC: Electron Transport Chain; EGFR: Epidermal Growth Factor Receptor; ELOVL: Elongation of Very Long Chain Fatty Acids; ER: Endoplasmic Reticulum; FADs: Long-Chain Acyl-CoA Dehydrogenases; FAO: Fatty Acid Oxidation; FAPB7: Fatty Acid Binding Protein 7; FASN: Fatty Acid Synthase; FATP: Fatty Acid Transport Protein; G3P: Glyceraldehyde-3-Phosphate; GPD1: Glycerol-3-Phosphate Dehydrogenase 1; HGF: Hepatocyte Growth Factor; HMG-CoA: Hydroxymethylglutaryl-CoA; HMGCR: Hydroxymethylglutaryl-CoA Reductase; HMGCS: Hydroxymethylglutaryl-CoA Synthase; IDH1: Isocitrate Dehydrogenase 1; MCT: Monocarboxylate Transporters; OXPHOS: Oxidative Phosphorylation; P: Phosphate; PPAR: Peroxisome Proliferator-Activated Receptors; SCAP: SREBP-Cleavage-Activating Protein; SCD: Stearoyl-CoA Desaturase; SREBP-1: Sterol Regulatory Element Binding Proteins; SMPD1: Sphingomyelin Phosphodiesterase 1; SOAT1: Sterol O-Acyltransferase 1; TCA: Tricarboxylic Acid Cycle. Figure created with BioRender.com.

2.3.1. Lipid Droplets

In GB, lipid biosynthetic activity is accompanied by an accumulation of lipid droplets, which are particularly overexpressed in GSCs. These droplets contain large quantities

of neutral lipids, triglycerides, and/or cholesterol esters, representing an important energy reserve that can be used in response to metabolic stress [79]. Furthermore, as these droplets are not detectable in healthy tissue, they have the potential to serve as a diagnostic biomarker for GB [80]. Interestingly, researchers have discovered that glucose deprivation can lead to the binding of choline kinase (CHK) alpha 2 to lipid droplets, which promotes lipid droplet lipolysis, increased FAO, and brain tumor growth [81]. Therefore, CHK alpha 2 is a promising therapeutic target for GB.

2.3.2. De Novo Lipogenesis

Lipid biosynthetic activity is required to promote membrane biogenesis and to produce lipid signaling molecules that support the important proliferative activity of cancer cells [82]. Two main sources are used for de novo fatty acid synthesis: acetyl-CoA and acetate. Acetyl-CoA can be synthesized either from citrate through ATP-citrate lyase (ACLY) or acetate through acetyl-CoA synthetase 2 (ACSS2). This requires NADPH-reducing equivalents, which may be generated by the enzymatic activity of the malic enzyme or isocitrate dehydrogenase 1 (IDH1) or through the PPP or the serine and glycine metabolism pathways. De novo lipid synthesis is followed by an ATP-dependent acetyl-CoA carboxylation by acetyl-coA carboxylase (ACC), a limiting step, generating malonyl-CoA. Fatty acid synthase (FASN) then catalyzes the synthesis of palmitate from seven molecules of malonyl-CoA and one molecule of acetyl-CoA while consuming 7 molecules of ATP and 14 of NADPH. Acetate is a major fuel for the TCA cycle through the activity of the enzyme acetyl-CoA synthetase 2 (ACSS2) which generates acetyl-CoA. In GB, higher expression levels of ACSS2 are associated with higher tumor grade and lower survival rates. In mice, injection of *ACSS2* shRNA in GB cells significantly inhibits tumor growth [15]. ACSS2 expression appears to be critical for promoting GB viability and tumor growth by increasing the processes of mitochondrial TCA cycle and lipogenesis. In vitro, ACSS2 knockdown has led to the inhibition of self-renewal and the induction of cell death in GSCs [15]. In GB cell models, forced expression of EGFRvIII resulted in increased de novo lipogenesis and was correlated with increased tumor growth. This effect was reversed by inhibiting the ACC enzyme using siRNA [83]. Another potential GB therapeutic target includes the enzyme FASN. FASN expression was correlated with tumor grade and its inhibition resulted in anticancer effects in different in vitro models. Cerulenin and orlistat, drugs used in the treatment of obesity, inhibit FASN and showed anticancer activity in different GB cell models [84,85]. Further study on GSCs showed that cerulenin-mediated inhibition of FASN decreased proliferation, migration and expression of stem cell markers and increased the expression of GFAP, a marker of differentiation [86]. Thus, it appears that fatty acid synthesis plays a major role in the maintenance of GSCs. Currently, FASN inhibitors have already completed clinical trials in many cancers, including GB in combination with bevacizumab (NCT03032484, phase II). Rich JN and colleagues discovered that GSCs rely on polyunsaturated fatty-acid synthesis to maintain the integrity of their cellular membranes. By targeting the key enzyme elongation of very long chain fatty acids 2 (ELOVL2), involved in this process, researchers disrupted EGFR signaling and slowed down GSC proliferation [87]. Another targets for GSCs are stearoyl-CoA desaturase (SCD) or fatty acid desaturase 2 (FADS2) [88,89]. Targeting these pathways was found to increase palmitate accumulation and enhance TMZ sensitivity. YTX-7739, an SCD inhibitor, has been shown to be effective in treating GSCs either alone or in combination with TMZ by triggering lipotoxicity and impairing DNA damage repair. Interestingly, the study also revealed that aberrant MEK/ERK signaling and AMP-activated protein kinase (AMPK) repression are involved in SCD inhibitor sensitivity, while activation of AMPK determines treatment resistance [88].

2.3.3. Fatty Acid Oxidation

Inhibition of FAO has also emerged as a promising therapeutic strategy for cancer treatment. FAO fuels cancer growth by generating ATP and NADPH. In GB, overexpression

of fatty acid transporters has been observed such as the carnitine palmitoyltransferase (CPT) transporters, CPT1A and CPT1C, playing a key role in the transport of long-chain fatty acids from the cytoplasm into the mitochondria. Fatty acid binding protein 7 (FABP7) have also been identified as a potential marker for GSCs [90]. In different models of GB, both in vitro and in vivo, CPT1 inhibition using etomoxir [91], or FABP7 inhibition using SB-FI-26 or PPAR antagonists, have showed anticancer activity [79,92]. Recent research has linked high levels of mitochondrial FAO enzymes (CPT1A, CPT2, and ACAD9, the acyl-CoA dehydrogenase family member 9) to poor prognosis in recurrent GB patients. The study also revealed that inhibiting FAO metabolism reduces the expression of the immune checkpoint protein CD47, which is highly expressed in GSCs, and hinders tumor growth. Preclinical experiments have demonstrated that the combination of etomoxir, an inhibitor of FAO metabolism, and anti-CD47 antibodies effectively decreased GB growth [93].

2.3.4. Cholesterol Metabolism

Cancer cells have a higher dependency on cholesterol compared to healthy cells for their survival and proliferation. Cholesterol can be obtained from the microenvironment or synthesized de novo by cancer cells. In healthy tissue, astrocytes rely on de novo synthesis, whereas GB cells inhibit their own synthesis and instead exhibit a higher dependence on exogenous cholesterol. This dependence is supported by an upregulation of low density lipoprotein receptors (LDLRs), which facilitate cholesterol uptake by GB cells. Both synthetic liver X receptors (LXR) agonists and statins, which block the activity of HMG-CoA reductase, have been suggested as potential anticancer agents due to their ability to modulate cholesterol metabolism [94].

GB cells have shown to be sensitive to LXR agonist-dependent cell death. Oxysterols are derivatives of cholesterol that serve as endogenous ligands for LXRs. The activation of LXRs promotes cholesterol efflux via sterol transporters, and inhibits cholesterol uptake by promoting LDLR degradation. This negative feedback system plays an essential role in maintaining cholesterol homeostasis. In a study, the authors showed that LXR-623, a LXRα-partial/LXRβ-full agonist selectively induced cell death in GB cells, leading to tumor regression and increased survival in animal model. This approach specifically targets the dysregulated cholesterol homeostasis in cancer cells, without affecting healthy cells [95].

A study showed that GSC populations exhibit overexpression of HMG-CoA reductase (HMGCR) and other components of the mevalonate pathway, which are required for de novo cholesterol synthesis [96]. Statins can inhibit HMGCR activity and thus de novo cholesterol synthesis. A phase II clinical trial (NCT02029573) investigated the efficacy of atorvastatin in combination with standard treatment in newly diagnosed GB patients. Although atorvastatin was well tolerated, it did not result in a significant clinical improvement. Interestingly, the trial identified high LDL levels as an important independent prognostic factor of poor cancer-related outcomes in the study cohort [97].

In addition to its role in de novo cholesterol synthesis, the mevalonate pathway is also involved in the prenylation of proteins. Farnesyl pyrophosphate (FPP) and geranylgeranyl pyrophosphate (GGPP) are precursors of cholesterol in this pathway and are implicated in the prenylation and activation of oncogenic proteins such as Ras and Rho. These proteins are crucial for the development and progression of cancers. Therefore, inhibiting the mevalonate pathway using farnesyl transferase inhibitors (FTIs) or geranylgeranyl transferase inhibitors (GGTIs) is a potential therapeutic approach for treating GB and other cancers [98–101].

In conclusion, in various in vitro and in vivo models, blocking cholesterol absorption or de novo biosynthesis has demonstrated anticancer effects [94].

2.3.5. Other Lipid-Related Pathways

Methionine depletion was found to decrease the proliferation and increase cell death of GSCs. The depletion led to global DNA demethylation, reduced expression of stem cell

markers, and decreased cholesterol synthesis through an alteration of the SREBF2-FOXM1 and ACA43 axis [102].

Some lipid-related proteins are highly expressed in GB but not detected in healthy glial cells. One such protein is very long-chain acyl-CoA synthetase homolog 3 (ACSVL3), which adds coenzyme A to fatty acids required for their β-oxidation. ACSVL3 expression is particularly upregulated in GSCs through the EGFR, HGF/c-MET, and AKT signaling pathways. Targeting ACSVL3, which is upregulated in GSCs, may be a promising therapeutic approach for GB [103,104].

Another study has identified sphingomyelin phosphodiesterase 1 (SMPD1), an enzyme that regulates the conversion of sphingomyelin to ceramide, as a drug target in GB. Fluoxetine has been found to inhibit SMPD1 activity and kill GB cells, inhibiting EGFR signaling and activating lysosomal stress. Combining fluoxetine with TMZ has led to complete tumor regression in mice [105].

Oncogenic pathways promote the expression of Sterol Regulatory Element-Binding Proteins (SREBPs), a family of transcription factors that regulate cholesterol and fatty acid metabolism, including lipogenesis. The SREBP-1a protein can activate different target genes involved in lipid synthesis while SREBP-1c mainly regulates fatty acid metabolism, for example by regulating FASN. The SREBP-2 protein mainly regulates the transcription of genes related to cholesterol metabolism, such as the genes encoding HMGCR and LDLR. The EGFR-PI3K-AKT pathway is a signaling pathway that regulates lipid biosynthesis. Indeed, it increases glucose uptake in cancer cells, thus promoting N-glycosylation of the SCAP protein, which is involved in the proteolytic cleavage activation of the SREBP-1 protein. In vivo, lapatinib-mediated inhibition of EGFR-PI3K-AKT signaling [106] or inhibition of the SCAP N-glycolysation [107] decreased tumor growth in EGFRvIII overexpressing GB models. Other molecules that impair the synthesis, maturation or activity of SREBP (e.g., betulin, quercetin or oxysterols) showed anticancer activity on GB cells [108]. A recent study investigated the effects of TAK901, an Aurora kinase inhibitor, on GB both in vitro and in vivo. The results showed that TAK901 reduced self-renewal and migration capacity of GSCs and induced cell cycle arrest and apoptosis by altering SREBP1-mediated lipid metabolism [109]. Impairment of cholesterol esterification through inhibition of sterol O-acyltransferase 1 (SOAT1) has also led to inhibition of SREBP-1 regulated fatty acid synthesis, impacting tumor growth in GB [110].

A study showed that GPD1, a member of the NAD-dependent glycerol-3-phosphate dehydrogenase family, is expressed specifically in dormant GSCs responsible for tumor relapse after chemotherapy. GPD1 plays a critical role in carbohydrate and lipid metabolism by catalyzing the reversible conversion of Dihydroxyacetone Phosphate and NADH to glycerol-3-phosphate and NAD^+. Dormant GSCs upregulate the glycerophospholipid metabolism pathway that is dependent on GPD1, as well as the taurine and hypotaurine pathway, which both contribute to lipid metabolism and help to maintain GSC dormancy and stress resistance. Inhibiting GPD1 resulted in impaired GSCs maintenance and prolonged animal survival, making it a promising therapeutic target for treating GB [111].

Recent studies have shown that CD36 is selectively used by GSCs to promote their maintenance. Furthermore, CD36 expression is negatively correlated with patient prognosis and is an informative biomarker for malignancy. CD36 is a scavenger receptor that plays a crucial role in sensing danger-associated molecular patterns and oxidized lipoproteins. Therefore, CD36 has the potential to serve as both a biomarker for clinical diagnosis/prognosis and a promising target for cancer therapy [112].

AMPK is a ubiquitous enzyme which serves as a metabolic checkpoint, linking growth factor signaling to cell metabolism, partly through the negative regulation of mTOR. In EGFRvIII-expressing GB, the 5-Aminoimidazole-4-carboxamideribonucleotide (AICAR), an AMPK agonist, reduced tumor growth mainly through the inhibition of cholesterol and fatty acid synthesis [113].

Overall, lipid metabolism, including de novo lipogenesis, FAO, cholesterol metabolism and others lipid-related pathways, plays a crucial role in the growth and survival of GB cells, and targeting these pathways may represent potential therapeutic options [79].

2.4. Nucleotide Metabolism

Targeting nucleotide metabolism is a potential therapeutic strategy in the treatment of GB (Figure 6). Nucleotides and deoxynucleotides are essential building blocks of DNA, RNA, and ribosomes. There are also involved in energy metabolism (ATP, GTP) and main coenzymes (NAD^+, $NADP^+$, FAD, CoA), making them crucial for cellular signaling. These molecules are generated through two primary pathways: de novo synthesis and nucleotide salvage pathways. De novo synthesis of purines or pyrimidines requires ribose, amino acids, and significant amounts of energy, while nucleotide salvage pathways require less energy and use pre-formed purines or pyrimidines from nucleotide catabolism.

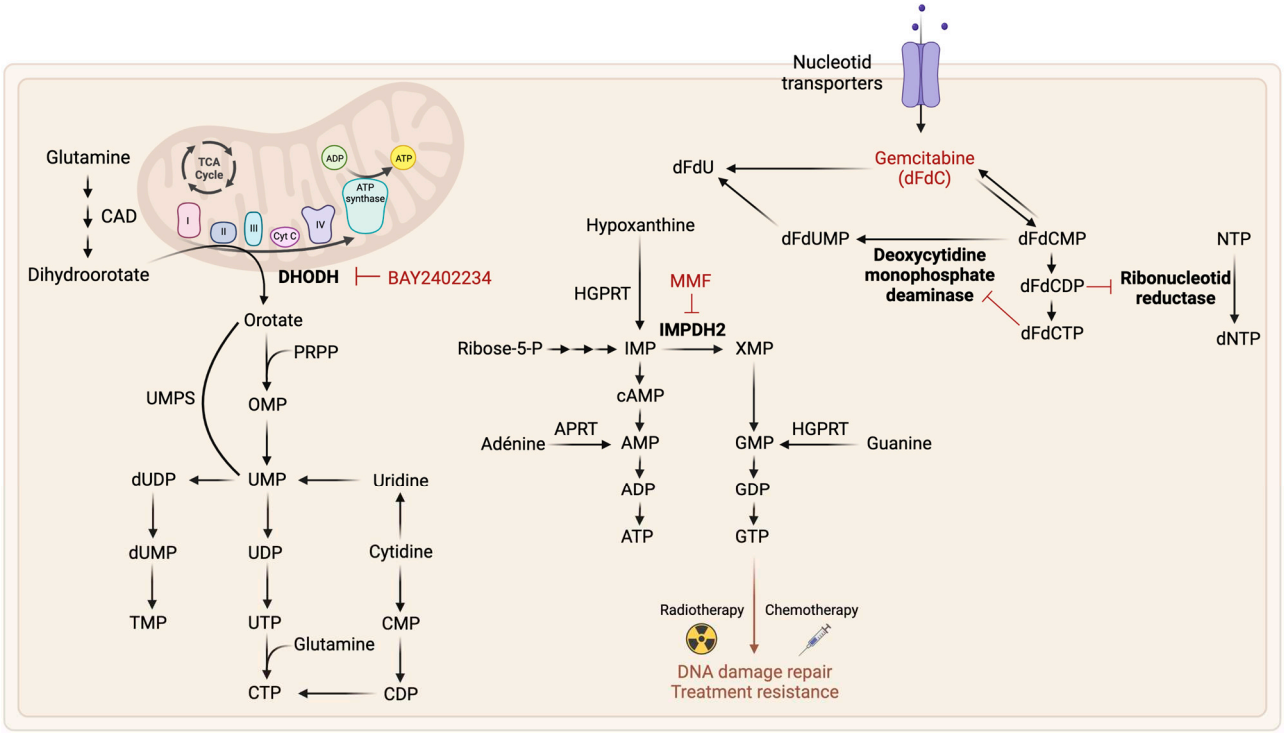

Figure 6. Nucleotide metabolism and associated therapies. This figure highlights potential therapeutic targets in nucleotide metabolism that are highlighted in bold, as well as several therapies that target nucleotide-associated pathways, which are highlighted in red. ADP: Adenosine Diphosphate; AMP: Adenosine Monophosphate; APRT: Adenosine Phosphoribosyltransferase; ATP: Adenosine Tri-phosphate; cAMP: Cyclic Adenosine Monophosphate; CAD: Carbamoyl-Phosphate Synthetase 2, Aspartate Transcarbamylase, and Dihydroorotase; CDP: Cytidine Diphosphate; CMP: Cytidine Monophosphate; CTP: Cytidine Triphosphate; DHODH: Dihydroorotate Dehydrogenase; DNA: Deoxyribonucleic Acid; dFdC: Difluoro-deoxy-cytidine; dFdCDP: Difluoro-deoxy-cytidine Diphosphate; dFdCMP: Difluoro-deoxy-cytidine Monophosphate; dFdCTP: Difluoro-deoxy-cytidine Triphosphate; dFdUMP: Difluoro-deoxy-uridine Monophosphate; dFdU: Difluoro-deoxy-uridine; dUDP: Deoxyuridine Diphosphate; dUMP: Deoxyuridine Monophosphate; GDP: Guanosine Diphosphate; GMP: Guanosine Monophosphate; GTP: Guanosine Triphosphate; HGPRT: Hypoxanthine-Guanine Phosphoribosyltransferase; IMP: Inosine Monophosphate; IMPDH2: Inosine Monophosphate Dehydrogenase 2; MMF: Mycophenolate mofetil; dNTP: Deoxynucleotide Triphosphate; NTP: Nucleotide Triphosphate; OMP: Orotidine Monophosphate; PRPP: Phosphoribosyl Pyrophosphate; TMP: Thymidine Monophosphate; UDP: Uridine Diphosphate; UMP: Uridine Monophosphate; UTP: Uridine Triphosphate; UMPS: Uridine Monophosphate Synthetase.

The salvage pathway is the primary source of pyrimidines for differentiated or quiescent cells, while proliferating cells are expected to rely more on de novo synthesis to meet their increased pyrimidine requirements. One study showed that a subpopulation of GSCs is sensitive to the inhibition of de novo pyrimidine synthesis [114], highlighting its potential therapeutic targeting in GB treatment. Enzymes necessary for the de novo biosynthesis of pyrimidines, such as dihydroorotate dehydrogenase (DHODH) and uridine monophosphate synthase (UMPS), are overexpressed in GB cell lines and patient tumors. DHODH inhibition impaired GB cell proliferation, including those resistant to TMZ. Interestingly, in vivo, inhibition of DHODH did not affect pyrimidine levels in healthy brain cells, emphasizing the activity of the pyrimidine salvage pathway in these cells [115,116]. A recent study found that BAY2402234, a drug that inhibits the DHODH pathway, successfully suppressed the growth of GSCs in vitro and reduced GB growth in human GB xenograft models [117]. Another study also found that GSCs depend on de novo pyrimidine synthesis and linked a metabolic aberration to driver mutations. Indeed, EGFR or PTEN mutations activated carbon influx through pyrimidine synthesis. Targeting enzymes involved in pyrimidine synthesis, such as CAD protein (carbamoyl-phosphate synthetase 2, aspartate transcarbamylase, and dihydroorotase) and DHODH, inhibited GSC survival and self-renewal and reduced tumor growth in rodent models. Inhibition of both tumor-specific driver mutations and DHODH activity demonstrated sustained inhibition of pyrimidine synthesis and tumorigenic capacity. The study suggests a potential therapeutic approach for precision medicine by targeting metabolic reprogramming and driver mutations concomitantly to completely inhibit specific pathway [118]. The activity of the pyrimidine salvage pathway in GB, highlighting by increased localization of radiolabeled tracer 18F-fluorothymidine (FLT) within the tumor, suggests potential prognostic value. However, further research is needed to fully understand the mechanisms underlying pyrimidine salvage pathway activity in GB, and to develop effective strategies for targeting this pathway [119].

Both the de novo and salvage pathways for purine synthesis have been identified in GB. De novo purines synthesis depends on c-MYC and plays an essential role in cell proliferation and the maintenance of GSCs tumorigenic properties [120]. A study demonstrated that intracellular levels of purines, particularly guanosine, are linked to radiation resistance due to the resulting GTP synthesis. In GB, the rate-limiting enzyme for de novo guanosine synthesis, inosine monophosphate dehydrogenase (IMPDH2), is upregulated, resulting in increased GTP biosynthesis, which is associated with a poor prognosis. Mycophenolic acid (MPA) and its prodrug mycophenolate mofetil (MMF) are FDA-approved inhibitor of GTP synthesis. Inhibiting GTP synthesis can sensitize GB cells to radiation by disrupting DNA repair. On the other hand, purines administration in radiosensitive models has been shown to lead to acquired resistance to radiotherapy [121]. Further research has found that the ciliary protein ARL13B interacts with IMPDH2 and contributes to chemoresistance by inhibiting the purine salvage pathway. It has been demonstrated that MMF can inhibit the ARL13B-IMPDH2 interaction, which enhances the effectiveness of TMZ [122]. Purine salvage pathway activity has also been observed in GB, including the hypoxanthine salvage pathway, which has been correlated with anti-folate resistance [121].

The potential of inhibiting nucleotide metabolism as a therapeutic strategy for GB treatment is currently being evaluated. One approach involves using gemcitabine, a cytidine analogue that has shown promising results in the treatment of solid tumors, including high-grade gliomas. Gemcitabine integrates into the DNA of proliferating cells and inhibits ribonucleotide reductase, thus hindering DNA synthesis. Since gemcitabine can pass through the blood–brain barrier, it can accumulate in brain tumors. A phase II clinical trial combining gemcitabine with radiotherapy in high-grade glioma patients demonstrated its efficacy [123]. However, the short half-life, side effects, and chemoresistance of gemcitabine have been reported [124].

In conclusion, the inhibition of nucleotide metabolism and the use of nucleotide-based therapies represent a promising avenue for the development of new GB treatments.

2.5. Monocarbon Metabolism

In GB, monocarbon units are essential for nucleotide synthesis, methylation reactions, and maintenance of redox potential, supporting tumor growth [125]. Metabolic vulnerabilities have been identified in certain conditions involving one-carbon metabolism. In poorly vascularized tumor regions, cancer cells depend on serine and glycine metabolism for survival, highlighted by high levels of mitochondrial serine hydroxymethyltransferase (SHMT2) and glycine decarboxylase (GLDC). SHMT2 inhibits PKM2 activity, reducing oxygen consumption and creating a metabolic state that promotes the use of upstream metabolic intermediates. GLDC inhibition impaired cancer cells survival with high SHMT2 levels due to an excess of glycine, not metabolized by GLDC, which is thus converted to toxic molecules (aminoacetone and methylglyoxal). Therefore, SHMT2 plays a crucial role in the adaptation of cancer cells to tumor microenvironment, while also rendering them vulnerable to inhibition of the glycine cleavage system [126].

Another metabolic vulnerability involves 5-methylthioadenosine phosphorylase (MTAP). Homologous deletions of *MTAP* are found in 40% of GB cases, resulting in a dependence of cancer cells on Protein Arginine Methyltransferase 5 (PRMT5). In these *MTAP*-deficient cancer cells, inhibition of PRMT5 inhibits tumor growth [127]. Other studies have demonstrated that PRMT5 inhibition effectively suppressed tumor growth in both differentiated GB cells and GSCs [125] and prolonged the survival of patient-derived xenograft models [128]. A phase I clinical trial is ongoing to evaluate the value of a PRMT5 inhibitor in treating solid tumors, including GB (NCT02783300).

One possible approach to target monocarbon metabolism is through dietary intervention. Studies have shown that a low methionine diet can reduce circulating antioxidant and nucleotide levels, and enhance the sensitivity of tumors to radio- and chemo-therapy. Therefore, implementing a low methionine diet may represent a promising adjunctive therapy for GB treatment [129].

Folate is an important source of one-carbon units. Anti-folate drugs, such as methotrexate (MTX) and pemetrexed, have shown promising results in GB and are being considered as a therapeutic option in combination with other treatments. They have been found to be selectively toxic to GSCs but not to normal fibroblasts or neural stem cells. In an in vivo experiment, MTX alone failed to show anti-GSC effects but enhanced the effects of CEP1347, an inducer of GSC differentiation. Combining anti-folate drugs with cytotoxic and differentiation therapies could lead to a new and effective way to eliminate GSCs, offering a promising treatment for GB patients [130].

2.6. Nicotinamide Metabolism

Pharmacological inhibition of nicotinamide phosphoribosyltransferase (NAMPT), an enzyme essential for NAD^+ biosynthesis has shown promising results in cancer therapy by repressing glycolytic phenotype [131]. Further, a study showed increased sensitivity of MYC-amplified GB models to glycolysis inhibition mediated by NAMPT inhibitor, highlighting a metabolic vulnerability in these tumor subtypes [132].

The modulation of DNA methylation is crucial for cancer cells and nicotinamide metabolism plays a fundamental role in this process. Nicotinamide N-methyltransferase (NNMT) was among the most consistently overexpressed metabolic genes in GB compared to healthy brain tissue and is implicated in methionine metabolism. NNMT was preferentially expressed in mesenchymal GSCs. The depletion of S-adenosyl methionine (SAM), a methyl donor generated from methionine, by NNMT leads to lower levels of methionine, SAM, and nicotinamide, but higher levels of oxidized NAD^+ in GSCs compared to differentiated tumor cells. Targeting NNMT expression reduced the proliferation and self-renewal of mesenchymal GSCs, and reduced tumor growth in vivo. The results showed also that NNMT could be a potential therapeutic target for GB by disrupting the oncogenic DNA hypomethylation [133].

2.7. TCA Cycle

Inhibiting the TCA cycle, which is essential for both catabolic and anabolic functions necessary for tumor growth, is a promising strategy for effective cancer therapy.

CPI-613 is a first-in-class drug that targets the TCA cycle. Specifically, it is a lipoate analogue that inhibits two major TCA cycle enzyme complexes, α-ketoglutarate dehydrogenase (α-KGDH) and pyruvate dehydrogenase (PDH), leading to accelerated and inefficient consumption of nutrient stores in cancer cells [134]. Although the exact mechanism by which CPI-613 exerts its anticancer effects is not fully understood, it has demonstrated promising results in phase I and II clinical trials for various types of cancer (NCT01832857) and was evaluating in phase III clinical trials for other malignancies (NCT03504410, NCT03504423). These findings suggest that targeting GB metabolism could be achieved through a novel class of TCA-targeted therapy, such as CPI-613. However, further research is needed to confirm its effectiveness in GB [135].

IDH catalyzes the oxidative decarboxylation of isocitrate to α-ketoglutarate and is involved in multiple cellular functions, such as glucose sensing, lipogenesis, glutamine catabolism, and defense against ROS and radiation [136,137]. Mutations in *IDH* occur early in tumorigenesis and are specific to tumors, providing an attractive therapeutic target in gliomas. The new WHO classification excludes the diagnosis of GB in the presence of *IDH* mutations. Nevertheless, in vitro studies have shown that targeting IDH1 wild-type could be a potential strategy to sensitize cells to radiation therapy. Knockdown of wild-type *IDH1* in GB cells resulted in decreased levels of NADPH, deoxynucleotides, and antioxidants, demonstrating the potential of IDH1 targeting as a therapeutic approach for GB [138].

2.8. Electron Transport Chain and Oxidative Phosphorylation

Analysis of patient high-grade gliomas revealed that 43% of tumors contained at least one mitochondrial DNA alterations in genes encoding complexes I, III and/or IV of the respiratory chain [139]. Strong expression of cytochrome c oxidase (CcO), a terminal enzyme in the respiratory chain, has been correlated with poor patient outcomes [140]. Further research on CcO has demonstrated that COX4-1 (an isoform of CcO subunit 4) is involved in cell proliferation, repression of ROS production, increased expression of stem cell markers, and self-renewal of GSCs [141]. Additionally, inhibition of the respiratory chain or depletion of mitochondrial DNA in cancer cells increases CD133 expression, a stem cell marker [142].

Studies have shown that OXPHOS inhibition leads to the downregulation of insulin-like growth factor 2 mRNA-binding protein 2 (IMP2), resulting in the inhibition of GSC maintenance. A strong correlation was observed between IMP2 expression, self-renewal of CGC, and decreased survival in animal models [143]. Induction of MPC1 expression may be a potential therapeutic strategy for GB, as it has been linked to increased chemosensitivity to TMZ [144].

Metformin, an anti-diabetic drug, has shown promise as a therapeutic option for GB, with multiple anticancer effects including the inhibition of complex I of the respiratory chain, activation of AMPK, suppression of the mTORC1 pathway, alteration of mitochondrial biosynthetic pathways, and stimulation of the immune system [145–147]. Metformin has been shown to reduce cell viability, proliferation, and migration, increase apoptosis, disrupt epithelial-mesenchymal transition, increase the production of ROS and negatively impact mitochondrial membrane potential and biogenesis in certain GB cell lines, including GSCs [148,149]. Notably, metformin has demonstrated higher antiproliferative activity on CD133-expressing subpopulations, suggesting a certain level of selectivity towards GSCs [150]. Clinical trials evaluating metformin in GB have been conducted, including a completed study on low dose TMZ plus metformin or placebo in patients with recurrent or refractory GB (NCT03243851). Phase II clinical trials are currently in progress to assess the effectiveness of metformin in combination with chemotherapy, radiotherapy, ketogenic diet, and/or paxalisib (PI3K/mTOR inhibitor) in GB patients [151].

2.9. Transporters and Ion Channels

In GB, a decrease in the expression of the mitochondrial pyruvate transporters MPC1 and MPC2 has been observed. This leads to a decrease in the flow of pyruvate into the mitochondria and an increase in glycolytic activity and compensatory pathways that maintain fuel oxidation in the TCA cycle, such as glutaminolysis, FAO, and branched chain amino acid pathways [152]. A decrease in MPC1 expression has been associated with a poor response to TMZ in GB [144]. Thus, inducing the expression of MPC1 could represent a potential therapeutic strategy for GB.

The voltage-dependent anion channel 1 (VDAC1), a mitochondrial protein controlling cell energy, metabolic homeostasis and apoptosis, is one of the relevant targets in GB. Depleting VDAC1 expression using short interfering RNA inhibit GB growth and tumor growth in xenograft mouse models. VDAC1 depletion also reversed oncogenic properties and altered transcription factors, leading to tumor cell differentiation into neuron- and astrocyte-like cells [153].

3. Complexity, Heterogeneity, and Plasticity of Tumor Metabolism

Tumor metabolism is a complex and dynamic process, characterized by heterogeneity and plasticity. The metabolic heterogeneity of GB is due to a combination of intrinsic factors such as tissue of origin and genetics, as well as extrinsic factors such as the patient's metabolism and the microenvironment [13]. Different microenvironments and cell subpopulations in GB lead to metabolic diversity, and cancer cells evolve over time in response to a constantly changing environment, highlighting the notion of metabolic complexity and flexibility.

3.1. Metabolic Heterogeneity and Plasticity

This heterogeneity has been demonstrated through a multitude of studies in xenograft models or from resected patient tumors using ^{13}C or multi-omics approaches [154]. Garofano et al. employed a multi-omics computational approach to analyze single GB cells and patient tumors and identified four subtypes of GB based on neurodevelopmental (proliferative/progenitor vs. neuronal) and metabolic (mitochondrial vs. glycolytic/plurimetabolic) criteria. This study revealed that different subpopulations of GB cells exhibit distinct metabolic profiles, with some being dependent on OXPHOS and others relying on aerobic glycolysis, amino acid metabolism, and lipid metabolism and showed that mitochondrial GB was associated with a more favorable clinical outcome [155]. Another multi-omics study defined a new classification of GB based on the tumor immune landscape, which effectively predicts patient outcome and defines specific lipid metabolism for each subtype [156]. Recent research has highlighted the metabolic heterogeneity of GB, with GSCs and non-GSCs exhibiting distinct metabolic profiles. GSCs are characterized by lower lipid droplet accumulation and a distinct lipid metabolism, with decreased levels of neutral lipids and increased polyunsaturated fatty acid production [157]. Other studies showed that cancer cells in nutrient-deprived regions metabolize droplet lipids more extensively [158], while cancer cells in oxygen-deprived regions exhibit a more glycolytic profile [55]. Further research has revealed metabolic heterogeneity even within the GSC population. One study showed that mesenchymal and proneural GSCs have different metabolic profiles and responses to metabolic-related therapies. The study found that mesenchymal GSCs were more glycolytic and less responsive to metformin, while proneural GSCs were less invasive, metabolized glucose through the Pentose Phosphate Pathway, and were more responsive to metformin. These results suggest the importance of considering metabolic heterogeneity in future clinical trials, as targeting glycolysis may be an effective strategy for inhibiting mesenchymal tumor cells, while proneural cells may respond better to OXPHOS inhibition [159]. Metabolic plasticity enables cells to adapt to various environmental factors, such as fluctuations in nutrient and oxygen availability, oxidative stress, and therapeutic interventions. One example of this plasticity was highlighted in an in vitro study which demonstrated that the inhibition of coenzyme Q biosynthesis with 4-nitrobenzoate (4-NB)

significantly increased the cholesterol content in glioma cells, leading to decreased oxygen levels, reduced plasma membrane fluidity, and stabilization of HIF-1α, thereby increasing glycolysis [160]. This study revealed metabolic plasticity and the interconnection between OXPHOS metabolism, glycolysis, and cholesterol metabolism. The ability of tumor cells to adapt their metabolism highlights the importance of understanding metabolic changes in cancer in order to develop therapies that impair tumor cell adaptation.

3.2. Metabolic Interactions in the Tumor Microenvironment

In addition to metabolic heterogeneity within tumors, cancer cells have been found to engage in cooperative metabolic interactions to meet their metabolic requirements. This cooperation can occur between different cancer cells as well as between cancer cells and stromal cells. For example, glycolytic and oxidative cancer cells, even located far from each other, have shown to mutualize their energy resources [55]. There is also evidence of cooperation between cancer cells and endothelial cells to promote neoangiogenesis, ensuring the availability of essential nutrients and oxygen to cancer cells [161]. The immune cells have also demonstrated their ability to regulate tumor metabolism and cooperate with cancer cells. M2 macrophages have shown to secrete interleukin-6 (IL-6), promoting the phosphorylation of Phosphoglycerate Kinase 1 (PGK1) in tumor cells mediated by 3-phosphoinositide-dependent protein kinase 1 (PDPK1). This phosphorylation facilitates glycolysis, leading to increased tumor cell proliferation and tumorigenesis [162]. A metabolic symbiotic relationship between cancer cells and myeloid-derived suppressor cells (MDSCs) has also been described, where lactate produced by cancer cells can sustain MDSCs, which play a role in creating an immunosuppressive microenvironment that impacts both innate and adaptive immunity [163]. In conclusion, the metabolic interactions between cancer cells and surrounding cells play a crucial role in regulating tumor metabolism and can have protumorigenic effects. Further research should explore these interactions in order to develop innovative cancer treatment strategies.

4. Combination of Therapies

4.1. Metabolic-Related Therapy

Metabolic-related therapy has been considered as a promising approach for cancer treatment due to the metabolic alterations present in cancer cells. However, its efficacy as a single therapy has been limited. Combining metabolic therapy with other treatments has shown greater potential. Despite the potential benefits, the metabolic plasticity and heterogeneity of cancer cells can result in therapeutic resistance and undermine the effectiveness of metabolic therapy. To overcome these challenges, it is essential to comprehend the underlying mechanisms of metabolic heterogeneity and plasticity in cancer cells and to determine the metabolic dependencies and preferences of different cancer subtypes, as well as the compensatory metabolic mechanisms.

A study conducted by Yang and colleagues shed light on the metabolic plasticity of GB cells in response to downregulation of mitochondrial pyruvate transporters carriers MPC1 and MPC2. This resulted in a decrease in the transport of pyruvate into the mitochondria, thereby activating alternative sources of fuel, such as glutaminolysis, branched-chain amino acid pathways, and FAO, for the TCA cycle [152]. The concurrent inhibition of MPC and GDH led to a significant inhibition of tumor growth compared to the use of either inhibition separately [140]. This underscores the importance of taking into account the adaptability of GB cells when designing therapeutic strategies.

Due to the metabolic plasticity of cancer cells, dual inhibition of tumor bioenergetics has been proposed as a relevant therapeutic approach. The dual inhibition of glycolysis and OXPHOS was investigated on GB tumorspheres. The combination of 2-DG and metformin resulted in a decrease in the invasive properties of cancer cells, prolonged survival in a mouse model, and led to a downregulation of stemness- and epithelial mesenchymal transition-related genes [164]. Targeting ATP synthesis through triple therapy with targeted inhibitors of the TCA cycle, phospholipids, and glycolysis (EPIC-0412, AACOCF3,

and 2-DG) has also been found to inhibit tumor growth both in vitro and in vivo [165]. These results suggest that multiple inhibition of cellular bioenergetics may be a promising approach for GB treatment that requires further clinical evaluation.

The value of combining metabolic-targeted therapies was also demonstrated by Hoang-Minh et al., who found that *FABP7* knockout increased the sensitivity of GSCs to pharmacological inhibition of glycolysis induced by 2-DG [79]. The dual inhibition of glycolysis and FAO pathways, using DCA and ranolazine, has also shown inhibitory effects on tumor growth and increased survival in an orthotopic xenograft model [166]. The therapeutic potential of inhibiting both CPT1A and glucose-6-phosphate dehydrogenase (G6PD), critical enzymes for FAO and the PPP, respectively, was also evaluated. The combination of etomoxir and DHEA, inhibitors of CPT1A and G6PD, respectively, resulted in decreased viability, ATP levels, and expression of genes associated with stemness and invasiveness, and showed inhibitory effects on tumor growth and increased survival in a mouse model [167]. Another study revealed that the combination of cytoplasmic phospholipase A2 (*cPLA2*) knockdown and metformin impair mitochondrial energy metabolism in primary GB cells, and reduced tumor growth and prolonged survival in a patient-derived xenograft model [168]. A recent study found that the loss of branched-chain amino acid transaminase 1 (BCAT1) in GB leads to a metabolic vulnerability that can be targeted with α-ketoglutarate (AKG). The combination of BCAT1 inhibitor gabapentin and AKG was found to be synthetically lethal in patient-derived GB tumors both in vitro and in vivo. The loss of BCAT1 resulted in an imbalance of NAD^+/NADH ratio and impaired OXPHOS, nucleotide biosynthesis, and mTORC1 activity. The combination of BCAT1 loss and AKG treatment led to mitochondrial dysfunction, cellular building block depletion, and cell death, providing a targetable metabolic vulnerability in GB and a potential therapeutic strategy to improve treatment outcomes [169].

4.2. Metabolic Therapies and Radiotherapy

Metabolic therapies and radiotherapy have been shown to be a promising combination in treating GB. Resistance to radiotherapy has been linked to high glycolytic states and increased mitochondrial reserve capacity [170].

Inhibition of glycolysis has been shown to radiosensitize GB cells in various in vitro and in vivo models, either through knockdown of *HK2* [171], use of 2-DG [30] or DCA [50]. Additionally, depletion of glutathione (via GLS inhibition), NAD^+ (via ascorbate use and PARPs inhibition) or inhibition of IDH or nucleotide metabolism can also result in radiosensitization of GB cells [9].

The repair of radiation-induced DNA damage is a barrier to the efficacy of radiotherapy, and these DNA repair mechanisms are dependent on NAD^+, a cofactor used by the key enzymes of the DNA repair pathways such as PARPs. Inhibiting PARPs is a therapeutic strategy being evaluated for the treatment of GB.

Other strategies to limit the availability of NAD^+ have been tested, such as the inhibition of nicotinamide phosphoribosyltransferase (NAMPT). NAMPT is a rate-limiting enzyme for NAD^+ recovery. NAMPT was clinically tested as a monotherapy but the trial was prematurely abandoned due to a narrow therapeutic index [172].

The IDH1 enzyme, which is overexpressed in GB, plays a role in the biosynthesis of NADPH, a critical reducing agent. Depletion of NADPH results in oxidative stress, which makes the cells more susceptible to radiation-induced DNA damage. By inhibiting wild-type IDH1, NADPH levels can be decreased, thus increasing the sensitivity of GB cells to radiation therapy, as demonstrated in various in vitro and in vivo studies [138].

Since the effects of radiotherapy on DNA are largely due to ROS (O_2^-, H_2O_2, OH^-), a relevant therapeutic strategy is to increase the levels of ROS within cancer cells or to decrease the levels of antioxidants. In order to increase the levels of ROS, it is possible to act on the metabolism of glutamine, which is involved in the production of mitochondrial ROS through its oxidation in the TCA cycle. Glutamine metabolism plays a key role in the maintenance of redox homeostasis due to its role in the synthesis of glutathione,

a major antioxidant. GLS inhibitors have been tested in IDH-mutated GB, which are known to be highly dependent on glutaminase for survival. CB-839, a GLS inhibitor, has been shown to sensitize cells to oxidative stress and radiotherapy in both in vitro and in vivo models [173]. CB-839 is currently being tested in combination with radiotherapy and TMZ in a phase I clinical trial for patients with IDH-mutated diffuse or anaplastic astrocytoma (NCT03528642). Ascorbic acid has been shown to increase ROS in cancer cells. The combination of TMZ, radiotherapy and ascorbic acid is currently being evaluated in a phase II clinical trial for the treatment of GB (NCT02344355) [174].

The combination of radiotherapy and the arginine-depleting agent ADI-PEG20 has been found to greatly improve treatment outcome of GB, resulting in a durable and complete response, with an extended disease-free survival in a GB model. ADI-PEG20 enhances the sensitivity of GB cells to radiation by generating cytotoxic peroxynitrites, which are nitrogen-based free radicals with potent cellular toxicity. Additionally, ADI-PEG20 promotes the infiltration of immune cells into the tumors and shifts the anti-inflammatory phenotype of these cells to a pro-inflammatory one. This leads to an increased in DNA damage and in a more aggressive immune response against the tumors [175].

Finally, the combination of radiotherapy and nucleotide metabolism inhibitors is another therapeutic strategy used in many cancers. Gemcitabine, a nucleoside analogue, has been tested in clinical trials in combination with radiotherapy for the treatment of high-grade gliomas. A phase II trial in patients with newly diagnosed GB showed a radiosensitizing effect of gemcitabine [123]. In some studies, gemcitabine has shown the ability to act synergistically with radiotherapy but also with other chemotherapeutic agents (e.g., paclitaxel, cisplatin, carboplatin). However, a short half-life, side effects and chemoresistance have been described [124].

In conclusion, the combination of metabolic therapies with radiotherapy has shown promising results. Inhibition of glycolysis, IDH or nucleotide metabolism, NAD^+ depletion, use of ascorbic acid or ADI-PEG20 are some of the strategies that have been evaluated on GB.

4.3. Metabolic Therapies and Chemotherapy

TMZ induces remodeling of the respiratory chain [176] and has been shown to increase fatty acid uptake in GSCs [177]. In wild-type TP53 GB cells, TMZ induces an upregulation of TP53 which leads to a repression of PINK1 (PTEN-induced putative kinase 1) and subsequent mitophagy. An increase in mitochondrial mass after TMZ treatment has been observed, which is thought to be dependent on AMPK-mediated signaling. Inhibition of mitochondrial fusion process in GB cells sensitizes them to TMZ [178].

Inhibition of glycolysis has been demonstrated to enhance the efficacy of chemotherapy in high-grade glioma models. This effect has been observed both in vitro, through *HK2* knockdown [42], and in vivo, through local administration of 3-bromopyruvate (3-BP) [179]. A combination of the glycolysis inhibitor 3-bromo-2-oxopropionate-1-propyl ester (3-BrOP) and carmustine was shown to have a synergistic effect against GSCs under hypoxic conditions, which are highly resistant to standard chemotherapy agents such as TMZ or carmustine. This combination reduced the ability of GSCs to form neurospheres in vitro and to inhibit tumor growth in vivo [180]. The combination of 2-DG and l,3-bis(2-chloroethyl)-1-nitrosourea (BCNU) was found to increase the sensitivity of GB cells by regulating glycolysis, ROS, and Endoplasmic Reticulum stress pathways, resulting in increased energy deficiency, oxidative stress, and apoptosis [181]. A recent study revealed that the combination of TMZ and metformin effectively suppressed the proliferation and induced apoptosis of both glioma cells and GSCs. This treatment downregulated the AKT-mTOR signaling pathway while enhancing AMPK activation, reduced tumor growth in vitro and in vivo, and making it a promising therapeutic option for advanced GB [182]. Moreover, the combination of TMZ with energy metabolism inhibitors, gossypol and phenformin, resulted in significant impairment of energy production, viability, stemness, and invasiveness in GSC lines compared to TMZ monotherapy or gossypol-phenformin dual therapy [183].

The combination of the FAO inhibitor etomoxir with TMZ has also been studied. The study found that GB tissues had a higher expression of FAO-related genes compared to healthy brain tissue, and that the combination of etomoxir and TMZ had a more pronounced effect in reducing cell viability, stemness, and invasiveness, and in improving survival outcomes in mouse xenograft model [184]. A study showed that the accumulation of saturated fatty acids, particularly palmitate, combined with TMZ treatment improves its efficacy against GB cells. The inhibition of SCD and/or FADS2 enhances palmitate accumulation and increases TMZ efficacy. The combination therapy was effective against recurrent GB cells [89].

Moreover, a study has revealed that a long non-coding RNA (lncRNA), TP73-AS1, is overexpressed in primary GB patient samples and its expression in tumors is correlated with poor patient prognosis. TP73-AS1 promotes TMZ resistance through the regulation of metabolic genes such as *ALDH1*. The *ALDH1* gene, which encodes type 1 aldehyde dehydrogenases, is overexpressed in GSCs and has been implicated in tumorigenesis as well as in TMZ resistance [185]. Clinical trials combining an ALDH inhibitor (disulfiram) and copper with radio-chemotherapy for GB are underway (NCT02715609).

In conclusion, several metabolic approaches have been explored in combination with chemotherapy for the treatment of GB. These include targeting glycolysis, OXPHOS and fatty acid metabolism. This has shown promising results in preclinical studies and further investigation is warranted to determine their potential as effective treatments for GB.

4.4. Metabolic and Targeted Therapies

Targeted therapies, such as bevacizumab and PI3K-AKT-mTOR inhibitors have shown to have an impact on tumor metabolism. A study showed that treatment with bevacizumab led to a metabolic adaptation toward anaerobic metabolism, increasing glycolytic activity, lactate production, and decreasing TCA cycle metabolites in orthotopic GB models. The treatment also resulted in a decrease in glutathione levels, indicating oxidative stress within the tumors [186]. Currently, bevacizumab is the only approved targeted therapy for the management of relapsed GB; however, its combination with the standard protocol has not shown significant clinical benefits. Further research exploring the combination of bevacizumab with glycolytic inhibitors may be worthwhile [187].

The PI3K-AKT-mTOR pathway is a promising strategy for GB therapy as it plays a crucial role in regulating cell proliferation, metabolism, and survival. However, therapies targeting this pathway, either alone or in combination with radiochemotherapy, have demonstrated limited clinical efficacy. In this context, a study showed that inhibition of mTOR signaling can protect glioma cells from hypoxia-induced cell death in an autophagy-independent manner [188]. Therapy resistance to mTOR inhibition may be due to a metabolic adaptation in the tumor cells. A study showed that mTOR-targeted therapy led to an increase in the levels of GLS and glutamate, and that inhibiting GLS in conjunction with the treatment sensitized cells to mTOR inhibitors in various in vitro and in vivo models [72]. As previously mentioned, a phase II clinical trial evaluating telaglenastat, a GLS inhibitor, in combination with PARP inhibitor, talazoparib, has been completed in advanced/metastatic solid tumors patients (NCT03875313).

In conclusion, targeted therapies have been shown to have a significant impact on tumor metabolism. The combination of bevacizumab with glycolytic inhibitors may offer promising results, while the limited efficacy of therapies targeting the PI3K-AKT-mTOR pathway may be improved through glutaminase inhibition. Further research is necessary to fully explore these treatment options.

4.5. Metabolic Therapies and Immunotherapy

The tumor microenvironment of GB is highly immunosuppressive, limiting the effectiveness of immunotherapies. Lactate, produced through the Warburg effect in cancer cells, plays a significant role in establishing an immunosuppressive environment. Targeting

lactate metabolism by inhibiting glycolysis or lactate export could improve the efficacy of immunotherapies for GB [189].

Combining immunotherapy with metabolic therapies has shown promise in treating GB. For example, the combination of T-cell therapy with a metabolism-modulating drug, liposomal avasimibe, has demonstrated improved antitumor efficacy in mouse models of GB [190]. Another example is the inhibition of the enzyme indoleamine 2,3 dioxygenase 1 (IDO1), which is frequently expressed in GB and leads to the inhibition of T lymphocytes' cytotoxic functions. Inhibition of IDO has increased GB's sensitivity to checkpoint inhibitors in various in vivo models [191]. However, early clinical trials incorporating the combination of immunotherapy and IDO inhibition were unsuccessful in the treatment of melanoma and pancreatic cancer. A recent study investigated the combination of anti-PD-1 immunotherapy with a novel glutamate modulator, BHV-4157, in a mouse model of GB. The results showed better survival when using BHV-4157 in combination with anti-PD1 immunotherapy. The concentration of glutamate in the tumor environment decreased, and there was an increase in $CD4^+$ T cells, major players in the adaptive immune response, and a decrease in regulatory immune cells within the tumor. These findings suggest that glutamate in GB has a role in immunosuppression and provide a basis for further exploring combinatorial approaches for GB treatment [192].

4.6. Diet Interventions

Diet is a crucial environmental factor that modulates tumor metabolism, and emerging evidence suggests that dietary interventions could influence the therapeutic response of cancer patients. For instance, fasting for 48 h prior to radio- and chemotherapy has been shown to increase survival in GB xenograft models [193]. In addition, calorie-restricted ketogenic diets have been associated with a robust increase in $CD8^+$ T cells, a key player in the antitumor adaptive immune response, as well as a decrease in the immune checkpoint ligand, PDL-1, highlighting the role of diet in immune defense against cancer [194]. Furthermore, low-methionine diets have been found to limit monocarbon metabolism, increase circulating antioxidant and nucleotide levels, and sensitize tumors to radio- and chemotherapies [129]. The calorie-restricted ketogenic diet and intermittent fasting remain the most extensively studied practices to date. A recent clinical trial, the RGO2 trial (NCT01754350), investigated the effects of these two dietary interventions on patients with recurrent GB undergoing radiotherapy. While the results indicated that a ketogenic diet or intermittent fasting practice leads to significant metabolic changes in patient serum samples, no significant differences were found in progression-free survival or overall survival. However, the caloric intake of the control group was not controlled and was lower than expected, leading to a potential bias in the results. Future research is needed to define the optimal protocols for fasting and restrictive diets, including the composition, intensity, and duration of dietary interventions, to ensure a favorable benefit-to-risk ratio for cancer patients [195]. Overall, dietary interventions have shown potential in modulating tumor metabolism and improving the therapeutic response of cancer patients, but further research is needed to determine the optimal protocols for their clinical application.

5. Discussion and Perspectives

Significant advancements in the field of cancer metabolism have provided new avenues for the treatment of GB, a highly aggressive brain tumor that remains challenging to treat effectively. Two key discoveries have driven interest in targeting tumor metabolism for anticancer strategies: the regulation of metabolic enzymes by oncogenes and tumor-suppressor genes, and the identification of specific mutations in genes encoding metabolic enzymes involved in tumorigenesis. Examples of such mutations include the succinate dehydrogenase mutation, linked to the development of paragangliomas [196], and the *IDH* mutations, commonly found in gliomas and serving as important diagnostic, prognostic, and predictive biomarkers for a favorable response to TMZ in glioma patients [10].

GB initiation and progression involve significant metabolic reprogramming to support rapid cell division and growth. Alterations in oncogenes and tumor-suppressor genes drive changes in the expression of key metabolic enzymes and transporters, leading to altered metabolism in cancer cells. Metabolic characteristics can directly impact signaling pathways and therapeutic responses [20]. The tumor microenvironment plays a pivotal role in shaping the metabolic profile of GB, as factors such as tumor growth, angiogenesis activation, hypoxic zone formation, and nutrient deprivation contribute to metabolic alterations. These changes enable cancer cells to adapt and meet their demands in response to the changing microenvironment. Moreover, GB cells may switch to compensatory or more efficient metabolic pathways in response to therapy.

Recent advances in cancer metabolism research have led to the development of a limited number of clinical trials, summarized in Table 1. Concurrently, Figure 7 highlights the most advanced metabolic-targeted therapies for GB. Many approaches are still under investigation in preclinical studies, and no significant clinical improvement has been achieved thus far. The efficacy of metabolic-targeted therapy relies on factors such as target metabolic pathway expression and cell plasticity. Cancer cells can utilize different metabolic pathways and adapt to changing environmental conditions or therapy, rendering a single metabolic pathway-targeting approach potentially insufficient. Furthermore, drug specificity and the use of targeted metabolic pathways by healthy cells, such as immune cells, must be taken into account, as inhibiting these pathways may cause undesirable side effects. While preclinical studies show promise, clinical trials are necessary to determine the safety and efficacy of these treatments for GB.

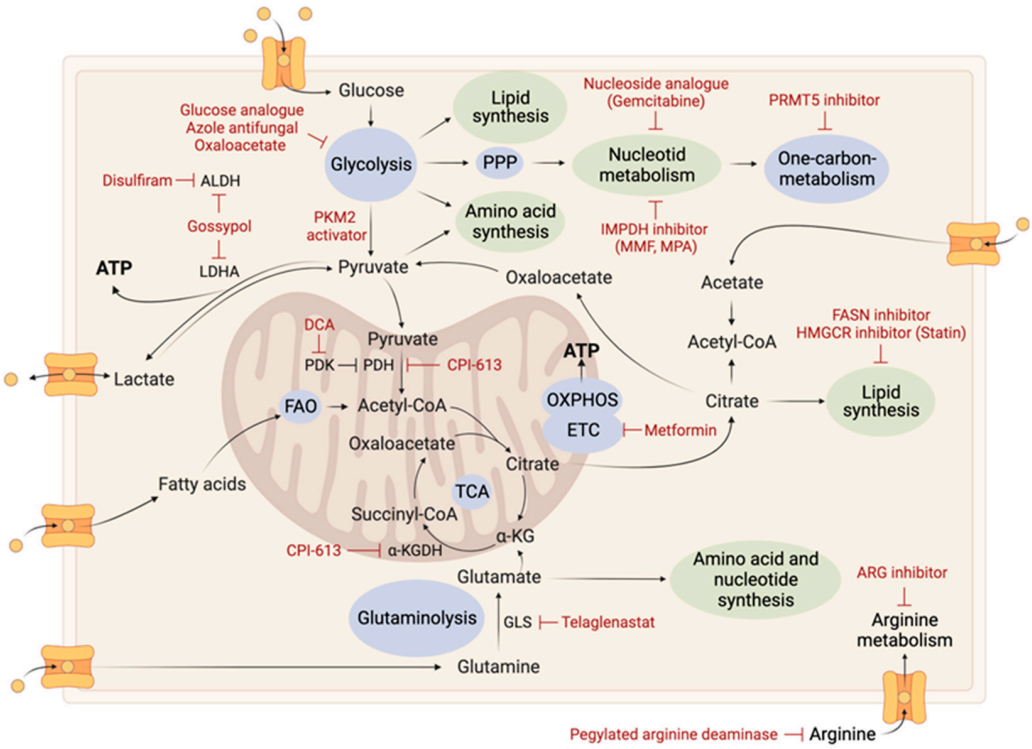

Figure 7. Advanced metabolic-targeted therapy in glioblastoma. α-KG: α-Ketoglutarate; ARG: Arginase; ATP: Adenosine Triphosphate; DCA: Dichloroacetate; ETC: Electron Transport Chain; FAO: Fatty Acid Oxidation; FASN: Fatty Acid Synthase; HMGCR: Hydroxymethylglutaryl-CoA Reductase; IMPDH: Inosine Monophosphate Dehydrogenase; MPA: Mycophenolic acid; MMF: Mycophenolate mofetil; OXPHOS: Oxidative Phosphorylation; PKM2: Pyruvate Kinase M2; PRMT5: Protein Arginine Methyltransferase 5; TCA: Tricarboxylic Acid Cycle. Figure created with BioRender.com.

Table 1. Main Clinical Trials in Metabolic Targeting for Glioblastoma Therapy.

Therapy	Mechanism	Trial Phase	Study Participants/Therapeutic Strategy	References
2-Deoxy-D-Glucose	Glucose analogue	I/II	Newly diagnosed GB patients treated with 2-DG in combination with radiotherapy	[30,31]
WP1122	Glucose analogue	I	Healthy volunteers	NCT05195723
Ketoconazole Posaconazole	HK2 inhibitor	I I	GB patients scheduled for radiotherapy	NCT04869449 NCT04825275
TP-1454	PKM2 activator	I	Patients with progressive solid tumors, treated with TP-1454 alone or in combination with immunotherapy	NCT04328740
Dichloroacetate	PDK1 inhibitor	I II	Recurrent GB Newly diagnosed and recurrent GB	NCT01111097 NCT00540176
Gossypol	Bcl-2 protein family and dehydrogenases inhibitor	I II	Newly diagnosed GB treated in combination with TMZ with or without radiotherapy Progressive or recurrent GB	NCT00390403 NCT00540722
Anhydrous Enol-Oxaloacetate (AEO)	Oxaloacetate pro-drug	II	Newly diagnosed GB treated in combination with standard therapy	NCT04450160
Telaglenastat	GLS inhibitor	I/II	Advanced/metastatic solid tumors patients in combination with talazoparib (PARPs inhibitor)	NCT03875313
ADI-PEG20	Pegylated arginine deiminase	I	Recurrent high-grade gliomas in combination with chemotherapy	[76,77]
INCB001158	Arginase inhibitor	I/II	Advanced solid tumors in combination with chemotherapy	NCT03314935
TVB-2640	FASN inhibitor	II	Recurrent GB in combination with bevacizumab	NCT03032484
Atorvastatin	HMG-CoA reductase inhibitor	II	Newly diagnosed GB patients treated in combination with radiotherapy and temozolomide	NCT02029573
Gemcitabine	Nucleoside analogue	II	High-grade glioma patients treated in combination with radiotherapy	[123]
GSK3326595	PRMT5 inhibitor	I	GB	NCT02783300
CPI-613	TCA-targeted therapy	II	Solid tumor	NCT01832857
Metformin	AMPK activator, complex I respiratory chain inhibitor	II II	Recurrent or refractory GB treated with low TMZ plus metformin Newly diagnosed IDH wild-type GB patients with the OXPHOS+ signature in combination with standard therapy	NCT03243851 NCT04945148
Ascorbic Acid	Cofactor, antioxidant	II	Newly diagnosed GB treated in combination with the standard therapy	NCT02344355
Disulfiram	ALDH inhibitor	I/II	Patients with presumed GB treated with disulfiram and copper before surgery and during adjuvant chemoradiotherapy	NCT02715609

The intricate relationships between metabolic pathways, as well as the connections between metabolic and cell signaling pathways, warrant further investigation. Signaling pathways that modulate tumor metabolism have not been fully described in this review.

For example, HIF-2α, a transcription factor activated in response to hypoxia, reprograms cellular metabolism and has been shown to maintain stemness [197]. Unfortunately, a phase II clinical trial showed no significant responses to HIF-2α inhibitors in recurrent GB patients (NCT03216499). Further studies are needed to fully evaluate HIF-2α inhibitors' potential, especially in combination therapy. Autophagy, which is upregulated during stress conditions such as limited nutrient and oxygen availability, as well as in response to anticancer therapy, also requires further investigation. Although not a metabolic pathway in the strictest sense, autophagy is closely linked to cellular metabolism. As a catabolic process, it recycles cellular components, providing energy and building blocks for the cell, and confers a survival advantage to glioma cells in the hostile conditions of the tumor microenvironment. Autophagy can also regulate pro-growth signaling and metabolic rewiring of cancer cells, further supporting tumor growth. However, the use of autophagy inhibitors in GB treatment remains challenging [198]. Additional areas deserving further exploration include the role of the tumor microenvironment in shaping tumor metabolism, the crosstalk between cancer cells and stromal cells, and the underlying mechanisms of therapeutic resistance, particularly those related to metabolic-targeted therapies. Moreover, the involvement of epigenetic regulation and non-coding RNA regulators in GB metabolism presents another area deserving of deeper examination.

Despite numerous targeted therapies evaluated in clinical trials, the limited progress achieved in treating GB can be attributed to intratumoral heterogeneity, inadequate patient classification, and the crucial role of GSCs in therapy resistance and tumor relapse.

Novel therapeutic approaches based on the identification of metabolic vulnerabilities or the inhibition of multiple targets simultaneously may hold promise for improving treatment options for GB patients. Combination therapy, including metabolic therapies alongside radiotherapy, chemotherapy, immunotherapy, and targeted therapies, also shows potential in addressing GB's therapeutic challenges. The challenges ahead include determining which metabolic pathways to target in each patient's tumor, identifying pharmacological targets, and understanding how cancer cells modulate their metabolic strategy. To advance our understanding of GB and identify novel treatment strategies, continued investigation into the complex interplay between metabolic and molecular pathways, the tumor microenvironment, and therapeutic resistance is crucial.

Author Contributions: Conceptualization, C.B. and M.D.; writing—original draft preparation, C.B.; writing—review and editing, C.B., D.R., S.M., N.E.-W. and M.D.; visualization, C.B., D.R., S.M., N.E.-W. and M.D.; supervision, M.D.; project administration, M.D. All authors have read and agreed to the published version of the manuscript.

Funding: C.B. was a recipient of a PhD grant from the French Ministry of Higher Education, Research and Innovation. This research was supported by the ITI Innovec (IdEx (ANR-10-IDEX-0002) and SFRI (ANR-20-SFRI-0012)).

Informed Consent Statement: Informed consent was obtained from all subjects involved in the study.

Acknowledgments: The authors would like to acknowledge the Ligue contre le Cancer for its long lasting support of the team and the French Ministry of Higher Education, Research, and Innovation (MSRI).

Conflicts of Interest: The authors declare no conflict of interest.

References

1. Stupp, R.; Mason, W.P.; van den Bent, M.J.; Weller, M.; Fisher, B.; Taphoorn, M.J.B.B.; Belanger, K.; Brandes, A.A.; Marosi, C.; Bogdahn, U.; et al. Radiotherapy plus Concomitant and Adjuvant Temozolomide for Glioblastoma. *N. Engl. J. Med.* **2005**, *352*, 987–996. [CrossRef]
2. Jiang, Y.; Uhrbom, L. On the Origin of Glioma. *Ups. J. Med. Sci.* **2012**, *117*, 113–121. [CrossRef] [PubMed]
3. Ostrom, Q.T.; Bauchet, L.; Davis, F.G.; Deltour, I.; Fisher, J.L.; Langer, C.E.; Pekmezci, M.; Schwartzbaum, J.A.; Turner, M.C.; Walsh, K.M.; et al. The Epidemiology of Glioma in Adults: A State of the Science Review. *Neuro Oncol.* **2014**, *16*, 896–913. [CrossRef]

4. Verhaak, R.G.W.; Hoadley, K.A.; Purdom, E.; Wang, V.; Qi, Y.; Wilkerson, M.D.; Miller, C.R.; Ding, L.; Golub, T.; Mesirov, J.P.; et al. Integrated Genomic Analysis Identifies Clinically Relevant Subtypes of Glioblastoma Characterized by Abnormalities in PDGFRA, IDH1, EGFR, and NF1. *Cancer Cell* **2010**, *17*, 98–110. [CrossRef]
5. Wang, Q.; Hu, B.; Hu, X.; Kim, H.; Squatrito, M.; Scarpace, L.; DeCarvalho, A.C.; Lyu, S.; Li, P.; Li, Y.; et al. Tumor Evolution of Glioma-Intrinsic Gene Expression Subtypes Associates with Immunological Changes in the Microenvironment. *Cancer Cell* **2017**, *32*, 42–56.e6. [CrossRef]
6. Neftel, C.; Laffy, J.; Filbin, M.G.; Hara, T.; Shore, M.E.; Rahme, G.J.; Richman, A.R.; Silverbush, D.; Shaw, M.L.; Hebert, C.M.; et al. An Integrative Model of Cellular States, Plasticity, and Genetics for Glioblastoma. *Cell* **2019**, *178*, 835–849.e21. [CrossRef] [PubMed]
7. Cruz Da Silva, E.; Mercier, M.-C.; Etienne-Selloum, N.; Dontenwill, M.; Choulier, L. A Systematic Review of Glioblastoma-Targeted Therapies in Phases II, III, IV Clinical Trials. *Cancers* **2021**, *13*, 1795. [CrossRef] [PubMed]
8. Garnier, D.; Renoult, O.; Alves-Guerra, M.-C.C.; Paris, F.; Pecqueur, C. Glioblastoma Stem-Like Cells, Metabolic Strategy to Kill a Challenging Target. *Front. Oncol.* **2019**, *9*, 118. [CrossRef]
9. Zhou, W.; Wahl, D.R. Metabolic Abnormalities in Glioblastoma and Metabolic Strategies to Overcome Treatment Resistance. *Cancers* **2019**, *11*, 1231. [CrossRef]
10. Vander Heiden, M.G.; Cantley, L.C.; Thompson, C.B. Understanding the Warburg Effect: The Metabolic Requirements of Cell Proliferation. *Science* **2009**, *324*, 1029–1033. [CrossRef]
11. Libby, C.J.; Tran, A.N.; Scott, S.E.; Griguer, C.; Hjelmeland, A.B. The Pro-Tumorigenic Effects of Metabolic Alterations in Glioblastoma Including Brain Tumor Initiating Cells. *Biochim. Biophys. Acta Rev. Cancer* **2018**, *1869*, 175–188.
12. Deshmukh, R.; Allega, M.F.; Tardito, S. A Map of the Altered Glioma Metabolism. *Trends Mol. Med.* **2021**, *27*, 1045–1059. [CrossRef] [PubMed]
13. Faubert, B.; Solmonson, A.; DeBerardinis, R.J. Metabolic Reprogramming and Cancer Progression. *Science* **2020**, *368*, eaaw5473. [CrossRef]
14. Yang, K.; Rich, J.N. A Delicate Initiation: Lipolysis of Lipid Droplets Fuels Glioblastoma. *Mol. Cell* **2021**, *81*, 2686–2687. [CrossRef]
15. Mashimo, T.; Pichumani, K.; Vemireddy, V.; Hatanpaa, K.J.; Singh, D.K.; Sirasanagandla, S.; Nannepaga, S.; Piccirillo, S.G.; Kovacs, Z.; Foong, C.; et al. Acetate Is a Bioenergetic Substrate for Human Glioblastoma and Brain Metastases. *Cell* **2014**, *159*, 1603–1614. [CrossRef] [PubMed]
16. Elstrom, R.L.; Bauer, D.E.; Buzzai, M.; Karnauskas, R.; Harris, M.H.; Plas, D.R.; Zhuang, H.; Cinalli, R.M.; Alavi, A.; Rudin, C.M.; et al. Akt Stimulates Aerobic Glycolysis in Cancer Cells. *Cancer Res.* **2004**, *64*, 3892–3899. [CrossRef]
17. Lunt, S.Y.; Vander Heiden, M.G. Aerobic Glycolysis: Meeting the Metabolic Requirements of Cell Proliferation. *Annu. Rev. Cell Dev. Biol.* **2011**, *27*, 441–464. [CrossRef]
18. Maher, E.A.; Marin-Valencia, I.; Bachoo, R.M.; Mashimo, T.; Raisanen, J.; Hatanpaa, K.J.; Jindal, A.; Jeffrey, F.M.; Choi, C.; Madden, C.; et al. Metabolism of [U-13C]Glucose in Human Brain Tumors in Vivo. *NMR Biomed.* **2012**, *25*, 1234–1244. [CrossRef]
19. Wise, D.R.; Thompson, C.B. Glutamine Addiction: A New Therapeutic Target in Cancer. *Trends Biochem. Sci.* **2010**, *35*, 427–433. [CrossRef]
20. Agnihotri, S.; Zadeh, G. Metabolic Reprogramming in Glioblastoma: The Influence of Cancer Metabolism on Epigenetics and Unanswered Questions. *Neuro Oncol.* **2016**, *18*, 160–172. [CrossRef]
21. El Khayari, A.; Bouchmaa, N.; Taib, B.; Wei, Z.; Zeng, A.; El Fatimy, R. Metabolic Rewiring in Glioblastoma Cancer: EGFR, IDH and Beyond. *Front. Oncol.* **2022**, *12*, 901951. [CrossRef]
22. Park, J.H.; Pyun, W.Y.; Park, H.W. Cancer Metabolism: Phenotype, Signaling and Therapeutic Targets. *Cells* **2020**, *9*, 2308. [CrossRef]
23. Masui, K.; Tanaka, K.; Akhavan, D.; Babic, I.; Gini, B.; Matsutani, T.; Iwanami, A.; Liu, F.; Villa, G.R.; Gu, Y.; et al. MTOR Complex 2 Controls Glycolytic Metabolism in Glioblastoma through FoxO Acetylation and Upregulation of C-Myc. *Cell Metab.* **2013**, *18*, 726–739. [CrossRef] [PubMed]
24. Li, Z.; Bao, S.; Wu, Q.; Wang, H.; Eyler, C.; Sathornsumetee, S.; Shi, Q.; Cao, Y.; Lathia, J.; McLendon, R.E.; et al. Hypoxia-Inducible Factors Regulate Tumorigenic Capacity of Glioma Stem Cells. *Cancer Cell* **2009**, *15*, 501–513. [CrossRef]
25. Heddleston, J.M.; Li, Z.; McLendon, R.E.; Hjelmeland, A.B.; Rich, J.N. The Hypoxic Microenvironment Maintains Glioblastoma Stem Cells and Promotes Reprogramming towards a Cancer Stem Cell Phenotype. *Cell Cycle* **2009**, *8*, 3274–3284. [CrossRef]
26. DeBerardinis, R.J.; Lum, J.J.; Hatzivassiliou, G.; Thompson, C.B. The Biology of Cancer: Metabolic Reprogramming Fuels Cell Growth and Proliferation. *Cell Metab.* **2008**, *7*, 11–20. [CrossRef] [PubMed]
27. Fukumura, D.; Xu, L.; Chen, Y.; Gohongi, T.; Seed, B.; Jain, R.K. Hypoxia and Acidosis Independently Up-Regulate Vascular Endothelial Growth Factor Transcription in Brain Tumors in Vivo. *Cancer Res.* **2001**, *61*, 6020–6024. [PubMed]
28. de la Cruz-López, K.G.; Castro-Muñoz, L.J.; Reyes-Hernández, D.O.; García-Carrancá, A.; Manzo-Merino, J. Lactate in the Regulation of Tumor Microenvironment and Therapeutic Approaches. *Front. Oncol.* **2019**, *9*, 1143. [CrossRef]
29. Moreno-Sánchez, R.; Rodríguez-Enríquez, S.; Marín-Hernández, A.; Saavedra, E. Energy Metabolism in Tumor Cells. *FEBS J.* **2007**, *274*, 1393–1418. [CrossRef] [PubMed]
30. Dwarakanath, B.; Singh, D.; Banerji, A.; Sarin, R.; Venkataramana, N.; Jalali, R.; Vishwanath, P.; Mohanti, B.; Tripathi, R.; Kalia, V.; et al. Clinical Studies for Improving Radiotherapy with 2-Deoxy-D-Glucose: Present Status and Future Prospects. *J. Cancer Res. Ther.* **2009**, *5*, 21. [CrossRef]

31. Singh, D.; Banerji, A.K.; Dwarakanath, B.S.; Tripathi, R.P.; Gupta, J.P.; Mathew, T.L.; Ravindranath, T.; Jain, V. Optimizing Cancer Radiotherapy with 2-Deoxy-D-Glucose: Dose Escalation Studies in Patients with Glioblastoma Multiforme. *Strahlenther. Onkol.* **2005**, *181*, 507–514. [CrossRef]
32. Priebe, W.; Zielinski, R.; Fokt, I.; Felix, E.; Radjendirane, V.; Arumugam, J.; Tai Khuong, M.; Krasinski, M.; Skora, S. EXTH-07. design and evaluation of wp1122, an inhibitor of glycolysis with increased cns uptake. *Neuro Oncol.* **2018**, *20*, vi86. [CrossRef]
33. Labak, C.M.; Wang, P.Y.; Arora, R.; Guda, M.R.; Asuthkar, S.; Tsung, A.J.; Velpula, K.K. Glucose Transport: Meeting the Metabolic Demands of Cancer, and Applications in Glioblastoma Treatment. *Am. J. Cancer Res.* **2016**, *6*, 1599–1608.
34. Christensen, D.R.; Calder, P.C.; Houghton, F.D. GLUT3 and PKM2 Regulate OCT4 Expression and Support the Hypoxic Culture of Human Embryonic Stem Cells. *Sci. Rep.* **2015**, *5*, 17500. [CrossRef] [PubMed]
35. Flavahan, W.A.; Wu, Q.; Hitomi, M.; Rahim, N.; Kim, Y.; Sloan, A.E.; Weil, R.J.; Nakano, I.; Sarkaria, J.N.; Stringer, B.W.; et al. Brain Tumor Initiating Cells Adapt to Restricted Nutrition through Preferential Glucose Uptake. *Nat. Neurosci.* **2013**, *16*, 1373–1382. [CrossRef] [PubMed]
36. Shibuya, K.; Okada, M.; Suzuki, S.; Seino, M.; Seino, S.; Takeda, H.; Kitanaka, C. Targeting the Facilitative Glucose Transporter GLUT1 Inhibits the Self-Renewal and Tumor-Initiating Capacity of Cancer Stem Cells. *Oncotarget* **2015**, *6*, 651–661. [CrossRef]
37. Cosset, É.; Ilmjärv, S.; Dutoit, V.; Elliott, K.; von Schalscha, T.; Camargo, M.F.; Reiss, A.; Moroishi, T.; Seguin, L.; Gomez, G.; et al. Glut3 Addiction Is a Druggable Vulnerability for a Molecularly Defined Subpopulation of Glioblastoma. *Cancer Cell* **2017**, *32*, 856–868.e5. [CrossRef]
38. Kuang, R.; Jahangiri, A.; Mascharak, S.; Nguyen, A.; Chandra, A.; Flanigan, P.M.; Yagnik, G.; Wagner, J.R.; De Lay, M.; Carrera, D.; et al. GLUT3 Upregulation Promotes Metabolic Reprogramming Associated with Antiangiogenic Therapy Resistance. *JCI Insight* **2017**, *2*, e88815. [CrossRef]
39. Kwak, S.; Park, S.-H.; Kim, S.-H.; Sung, G.-J.; Song, J.-H.; Jeong, J.-H.; Kim, H.; Ha, C.H.; Kim, S.W.; Choi, K.-C. MiR-3189-Targeted GLUT3 Repression by HDAC2 Knockdown Inhibits Glioblastoma Tumorigenesis through Regulating Glucose Metabolism and Proliferation. *J. Exp. Clin. Cancer Res.* **2022**, *41*, 87. [CrossRef]
40. Goidts, V.; Bageritz, J.; Puccio, L.; Nakata, S.; Zapatka, M.; Barbus, S.; Toedt, G.; Campos, B.; Korshunov, A.; Momma, S.; et al. RNAi Screening in Glioma Stem-like Cells Identifies PFKFB4 as a Key Molecule Important for Cancer Cell Survival. *Oncogene* **2012**, *31*, 3235–3243. [CrossRef]
41. Sanzey, M.; Abdul Rahim, S.A.; Oudin, A.; Dirkse, A.; Kaoma, T.; Vallar, L.; Herold-Mende, C.; Bjerkvig, R.; Golebiewska, A.; Niclou, S.P. Comprehensive Analysis of Glycolytic Enzymes as Therapeutic Targets in the Treatment of Glioblastoma. *PLoS ONE* **2015**, *10*, e0123544. [CrossRef]
42. Wolf, A.; Agnihotri, S.; Micallef, J.; Mukherjee, J.; Sabha, N.; Cairns, R.; Hawkins, C.; Guha, A. Hexokinase 2 Is a Key Mediator of Aerobic Glycolysis and Promotes Tumor Growth in Human Glioblastoma Multiforme. *J. Exp. Med.* **2011**, *208*, 313–326. [CrossRef] [PubMed]
43. Agnihotri, S.; Mansouri, S.; Burrell, K.; Li, M.; Mamatjan, Y.; Liu, J.; Nejad, R.; Kumar, S.; Jalali, S.; Singh, S.K.; et al. Ketoconazole and Posaconazole Selectively Target HK2-Expressing Glioblastoma Cells. *Clin. Cancer Res.* **2019**, *25*, 844–855. [CrossRef]
44. Christofk, H.R.; Vander Heiden, M.G.; Harris, M.H.; Ramanathan, A.; Gerszten, R.E.; Wei, R.; Fleming, M.D.; Schreiber, S.L.; Cantley, L.C. The M2 Splice Isoform of Pyruvate Kinase Is Important for Cancer Metabolism and Tumour Growth. *Nature* **2008**, *452*, 230–233. [CrossRef] [PubMed]
45. Yang, W.; Xia, Y.; Hawke, D.; Li, X.; Liang, J.; Xing, D.; Aldape, K.; Hunter, T.; Alfred Yung, W.K.; Lu, Z. PKM2 Phosphorylates Histone H3 and Promotes Gene Transcription and Tumorigenesis. *Cell* **2012**, *150*, 685–696. [CrossRef]
46. Liang, J.; Cao, R.; Wang, X.; Zhang, Y.; Wang, P.; Gao, H.; Li, C.; Yang, F.; Zeng, R.; Wei, P.; et al. Mitochondrial PKM2 Regulates Oxidative Stress-Induced Apoptosis by Stabilizing Bcl2. *Cell Res.* **2017**, *27*, 329–351. [CrossRef] [PubMed]
47. Gao, M.; Yang, J.; Gong, H.; Lin, Y.; Liu, J. Trametinib Inhibits the Growth and Aerobic Glycolysis of Glioma Cells by Targeting the PKM2/c-Myc Axis. *Front. Pharmacol.* **2021**, *12*, 760055. [CrossRef]
48. Muller, F.L.; Colla, S.; Aquilanti, E.; Manzo, V.E.; Genovese, G.; Lee, J.; Eisenson, D.; Narurkar, R.; Deng, P.; Nezi, L.; et al. Passenger Deletions Generate Therapeutic Vulnerabilities in Cancer. *Nature* **2012**, *488*, 337–342. [CrossRef]
49. Larrieu, C.M.; Storevik, S.; Guyon, J.; Pagano Zottola, A.C.; Bouchez, C.L.; Derieppe, M.-A.; Tan, T.Z.; Miletic, H.; Lorens, J.; Tronstad, K.J.; et al. Refining the Role of Pyruvate Dehydrogenase Kinases in Glioblastoma Development. *Cancers* **2022**, *14*, 3769. [CrossRef]
50. Shen, H.; Hau, E.; Joshi, S.; Dilda, P.J.; McDonald, K.L. Sensitization of Glioblastoma Cells to Irradiation by Modulating the Glucose Metabolism. *Mol. Cancer Ther.* **2015**, *14*, 1794–1804. [CrossRef]
51. Valvona, C.J.; Fillmore, H.L.; Nunn, P.B.; Pilkington, G.J. The Regulation and Function of Lactate Dehydrogenase A: Therapeutic Potential in Brain Tumor. *Brain Pathol.* **2016**, *26*, 3–17. [CrossRef]
52. Kim, J.; Han, J.; Jang, Y.; Kim, S.J.; Lee, M.J.; Ryu, M.J.; Kweon, G.R.; Heo, J.Y. High-Capacity Glycolytic and Mitochondrial Oxidative Metabolisms Mediate the Growth Ability of Glioblastoma. *Int. J. Oncol.* **2015**, *47*, 1009–1016. [CrossRef] [PubMed]
53. Daniele, S.; Giacomelli, C.; Zappelli, E.; Granchi, C.; Trincavelli, M.L.; Minutolo, F.; Martini, C. Lactate Dehydrogenase-A Inhibition Induces Human Glioblastoma Multiforme Stem Cell Differentiation and Death. *Sci. Rep.* **2015**, *5*, 15556. [CrossRef]
54. Guyon, J.; Fernandez-Moncada, I.; Larrieu, C.; Bouchez, C.; Chouleur, T.; Espedal, H.; Røsland, G.; Daher, B.; Barre, A.; Dartigues, B. Specific Expression of Lactate Dehydrogenases in Glioblastoma Controls Intercellular Lactate Transfer to Promote Tumor Growth and Invasion. *Res. Sq.* **2021**. [CrossRef]

55. Guyon, J.; Fernandez-Moncada, I.; Larrieu, C.M.; Bouchez, C.L.; Pagano Zottola, A.C.; Galvis, J.; Chouleur, T.; Burban, A.; Joseph, K.; Ravi, V.M.; et al. Lactate Dehydrogenases Promote Glioblastoma Growth and Invasion via a Metabolic Symbiosis. *EMBO Mol. Med.* **2022**, *14*, e15343. [CrossRef] [PubMed]
56. Kim, H.Y.; Lee, B.I.; Jeon, J.H.; Kim, D.K.; Kang, S.G.; Shim, J.K.; Kim, S.Y.; Kang, S.W.; Jang, H. Gossypol Suppresses Growth of Temozolomide-Resistant Glioblastoma Tumor Spheres. *Biomolecules* **2019**, *9*, 595. [CrossRef]
57. Fiveash, J.B.; Chowdhary, S.A.; Peereboom, D.; Mikkelsen, T.; Nabors, L.B.; Lesser, G.J.; Rosenfeld, M.R.; Ye, X.; Grossman, S.A. NABTT-0702: A Phase II Study of R-(-)-Gossypol (AT-101) in Recurrent Glioblastoma Multiforme (GBM). *J. Clin. Oncol.* **2009**, *27*, 2010. [CrossRef]
58. Grigalavicius, M.; Ezzatpanah, S.; Papakyriakou, A.; Raabe, T.T.H.; Yannakopoulou, K.; Theodossiou, T.A. 5-ALA Is a Potent Lactate Dehydrogenase Inhibitor but Not a Substrate: Implications for Cell Glycolysis and New Avenues in 5-ALA-Mediated Anticancer Action. *Cancers* **2022**, *14*, 4003. [CrossRef]
59. Fernandez-Gil, B.I.; Otamendi-Lopez, A.; Bechtle, A.; Vazquez-Ramos, C.A.; Qosja, N.; Suarez-Meade, P.; Sarabia-Estrada, R.; Jentoft, M.E.; Guerrero-Cázares, H.; Escames, G.; et al. Melatonin Treatment Triggers Metabolic and Intracellular PH Imbalance in Glioblastoma. *Cells* **2022**, *11*, 3467. [CrossRef]
60. Lu, G.; Wang, X.; Li, F.; Wang, S.; Zhao, J.; Wang, J.; Liu, J.; Lyu, C.; Ye, P.; Tan, H.; et al. Engineered Biomimetic Nanoparticles Achieve Targeted Delivery and Efficient Metabolism-Based Synergistic Therapy against Glioblastoma. *Nat. Commun.* **2022**, *13*, 4214. [CrossRef] [PubMed]
61. Ijare, O.; Conway, D.; Cash, A.; Baskin, D.; Pichumani, K. CBMT-49. Oxaloacetate Alters Glucose Metabolism in Glioblastoma: 13C Isotopomer Study. *Neuro Oncol.* **2019**, *21*, vi43–vi44. [CrossRef]
62. Ruban, A.; Berkutzki, T.; Cooper, I.; Mohar, B.; Teichberg, V.I. Blood Glutamate Scavengers Prolong the Survival of Rats and Mice with Brain-Implanted Gliomas. *Investig. New Drugs* **2012**, *30*, 2226–2235. [CrossRef]
63. Natarajan, S.K.; Venneti, S. Glutamine Metabolism in Brain Tumors. *Cancers* **2019**, *11*, 1628. [CrossRef] [PubMed]
64. Kucharzewska, P.; Christianson, H.C.; Belting, M. Global Profiling of Metabolic Adaptation to Hypoxic Stress in Human Glioblastoma Cells. *PLoS ONE* **2015**, *10*, e0116740. [CrossRef] [PubMed]
65. DeBerardinis, R.J.; Mancuso, A.; Daikhin, E.; Nissim, I.; Yudkoff, M.; Wehrli, S.; Thompson, C.B. Beyond Aerobic Glycolysis: Transformed Cells Can Engage in Glutamine Metabolism That Exceeds the Requirement for Protein and Nucleotide Synthesis. *Proc. Natl. Acad. Sci. USA* **2007**, *104*, 19345–19350. [CrossRef]
66. Rosati, A.; Poliani, P.L.; Todeschini, A.; Cominelli, M.; Medicina, D.; Cenzato, M.; Simoncini, E.L.; Magrini, S.M.; Buglione, M.; Grisanti, S.; et al. Glutamine Synthetase Expression as a Valuable Marker of Epilepsy and Longer Survival in Newly Diagnosed Glioblastoma Multiforme. *Neuro Oncol.* **2013**, *15*, 618–625. [CrossRef]
67. Tardito, S.; Oudin, A.; Ahmed, S.U.; Fack, F.; Keunen, O.; Zheng, L.; Miletic, H.; Sakariassen, P.Ø.; Weinstock, A.; Wagner, A.; et al. Glutamine Synthetase Activity Fuels Nucleotide Biosynthesis and Supports Growth of Glutamine-Restricted Glioblastoma. *Nat. Cell Biol.* **2015**, *17*, 1556–1568. [CrossRef]
68. Obara-Michlewska, M.; Szeliga, M. Targeting Glutamine Addiction in Gliomas. *Cancers* **2020**, *12*, 310. [CrossRef]
69. Cheng, T.; Sudderth, J.; Yang, C.; Mullen, A.R.; Jin, E.S.; Mates, J.M.; DeBerardinis, R.J. Pyruvate Carboxylase Is Required for Glutamine-Independent Growth of Tumor Cells. *Proc. Natl. Acad. Sci. USA* **2011**, *108*, 8674–8679. [CrossRef]
70. Oizel, K.; Chauvin, C.; Oliver, L.; Gratas, C.; Geraldo, F.; Jarry, U.; Scotet, E.; Rabe, M.; Alves-Guerra, M.C.; Teusan, R.; et al. Efficient Mitochondrial Glutamine Targeting Prevails over Glioblastoma Metabolic Plasticity. *Clin. Cancer Res.* **2017**, *23*, 6292–6305. [CrossRef] [PubMed]
71. Wise, D.R.; Deberardinis, R.J.; Mancuso, A.; Sayed, N.; Zhang, X.-Y.X.Y.; Pfeiffer, H.K.; Nissim, I.; Daikhin, E.; Yudkoff, M.; McMahon, S.B.; et al. Myc Regulates a Transcriptional Program That Stimulates Mitochondrial Glutaminolysis and Leads to Glutamine Addiction. *Proc. Natl. Acad. Sci. USA* **2008**, *105*, 18782–18787. [CrossRef] [PubMed]
72. Tanaka, K.; Sasayama, T.; Irino, Y.; Takata, K.; Nagashima, H.; Satoh, N.; Kyotani, K.; Mizowaki, T.; Imahori, T.; Ejima, Y.; et al. Compensatory Glutamine Metabolism Promotes Glioblastoma Resistance to MTOR Inhibitor Treatment. *J. Clin. Investig.* **2015**, *125*, 1591–1602. [CrossRef] [PubMed]
73. Zhang, J.; Wang, G.; Mao, Q.; Li, S.; Xiong, W.; Lin, Y.; Ge, J. Glutamate Dehydrogenase (GDH) Regulates Bioenergetics and Redox Homeostasis in Human Glioma. *Oncotarget* **2016**, *5*, 1–12. [CrossRef]
74. Franceschi, S.; Corsinovi, D.; Lessi, F.; Tantillo, E.; Aretini, P.; Menicagli, M.; Scopelliti, C.; Civita, P.; Pasqualetti, F.; Naccarato, A.G.; et al. Mitochondrial Enzyme GLUD2 Plays a Critical Role in Glioblastoma Progression. *EBioMedicine* **2018**, *37*, 56–67. [CrossRef] [PubMed]
75. Przystal, J.M.; Hajji, N.; Khozoie, C.; Renziehausen, A.; Zeng, Q.; Abaitua, F.; Hajitou, A.; Suwan, K.; Want, E.; Bomalaski, J.; et al. Efficacy of Arginine Depletion by ADI-PEG20 in an Intracranial Model of GBM. *Cell Death Dis.* **2018**, *9*, 1192. [CrossRef]
76. Hall, P.E.; Lewis, R.; Syed, N.; Shaffer, R.; Evanson, J.; Ellis, S.; Williams, M.; Feng, X.; Johnston, A.; Thomson, J.A.; et al. A Phase I Study of Pegylated Arginine Deiminase (Pegargiminase), Cisplatin, and Pemetrexed in Argininosuccinate Synthetase 1-Deficient Recurrent High-Grade Glioma. *Clin. Cancer Res.* **2019**, *25*, 2708–2716. [CrossRef]
77. Hou, X.; Chen, S.; Zhang, P.; Guo, D.; Wang, B. Targeted Arginine Metabolism Therapy: A Dilemma in Glioma Treatment. *Front. Oncol.* **2022**, *12*, 3484. [CrossRef]
78. Broadfield, L.A.; Pane, A.A.; Talebi, A.; Swinnen, J.V.; Fendt, S.-M. Lipid Metabolism in Cancer: New Perspectives and Emerging Mechanisms. *Dev. Cell* **2021**, *56*, 1363–1393. [CrossRef]

79. Hoang-Minh, L.B.; Siebzehnrubl, F.A.; Yang, C.; Suzuki-Hatano, S.; Dajac, K.; Loche, T.; Andrews, N.; Schmoll Massari, M.; Patel, J.; Amin, K.; et al. Infiltrative and Drug-resistant Slow-cycling Cells Support Metabolic Heterogeneity in Glioblastoma. *EMBO J.* **2018**, *37*, e98772. [CrossRef]
80. Guo, D. Lipid Droplets, Potential Biomarker and Metabolic Target in Glioblastoma. *Intern. Med. Rev.* **2017**, *3*. [CrossRef]
81. Liu, R.; Lee, J.-H.; Li, J.; Yu, R.; Tan, L.; Xia, Y.; Zheng, Y.; Bian, X.-L.; Lorenzi, P.L.; Chen, Q.; et al. Choline Kinase Alpha 2 Acts as a Protein Kinase to Promote Lipolysis of Lipid Droplets. *Mol. Cell* **2021**, *81*, 2722–2735.e9. [CrossRef] [PubMed]
82. Guo, D.; Bell, E.H.; Chakravarti, A. Lipid Metabolism Emerges as a Promising Target for Malignant Glioma Therapy. *CNS Oncol.* **2013**, *2*, 289–299. [CrossRef]
83. Jones, J.E.C.; Esler, W.P.; Patel, R.; Lanba, A.; Vera, N.B.; Pfefferkorn, J.A.; Vernochet, C. Inhibition of Acetyl-CoA Carboxylase 1 (ACC1) and 2 (ACC2) Reduces Proliferation and De Novo Lipogenesis of EGFRvIII Human Glioblastoma Cells. *PLoS ONE* **2017**, *12*, e0169566. [CrossRef] [PubMed]
84. Zhao, W.; Kridel, S.; Thorburn, A.; Kooshki, M.; Little, J.; Hebbar, S.; Robbins, M. Fatty Acid Synthase: A Novel Target for Antiglioma Therapy. *Br. J. Cancer* **2006**, *95*, 869–878. [CrossRef]
85. Grube, S.; Dünisch, P.; Freitag, D.; Klausnitzer, M.; Sakr, Y.; Walter, J.; Kalff, R.; Ewald, C. Overexpression of Fatty Acid Synthase in Human Gliomas Correlates with the WHO Tumor Grade and Inhibition with Orlistat Reduces Cell Viability and Triggers Apoptosis. *J. Neurooncol.* **2014**, *118*, 277–287. [CrossRef] [PubMed]
86. Yasumoto, Y.; Miyazaki, H.; Vaidyan, L.K.; Kagawa, Y.; Ebrahimi, M.; Yamamoto, Y.; Ogata, M.; Katsuyama, Y.; Sadahiro, H.; Suzuki, M.; et al. Inhibition of Fatty Acid Synthase Decreases Expression of Stemness Markers in Glioma Stem Cells. *PLoS ONE* **2016**, *11*, e0147717. [CrossRef]
87. Gimple, R.C.; Kidwell, R.L.; Kim, L.J.Y.; Sun, T.; Gromovsky, A.D.; Wu, Q.; Wolf, M.; Lv, D.; Bhargava, S.; Jiang, L.; et al. Glioma Stem Cell–Specific Superenhancer Promotes Polyunsaturated Fatty-Acid Synthesis to Support EGFR Signaling. *Cancer Discov.* **2019**, *9*, 1248–1267. [CrossRef]
88. Eyme, K.M.; Sammarco, A.; Jha, R.; Mnatsakanyan, H.; Pechdimaljian, C.; Carvalho, L.; Neustadt, R.; Moses, C.; Alnasser, A.; Tardiff, D.F.; et al. Targeting de Novo Lipid Synthesis Induces Lipotoxicity and Impairs DNA Damage Repair in Glioblastoma Mouse Models. *Sci. Transl. Med.* **2023**, *15*, eabq6288. [CrossRef]
89. Parik, S.; Fernández-García, J.; Lodi, F.; De Vlaminck, K.; Derweduwe, M.; De Vleeschouwer, S.; Sciot, R.; Geens, W.; Weng, L.; Bosisio, F.M.; et al. GBM Tumors Are Heterogeneous in Their Fatty Acid Metabolism and Modulating Fatty Acid Metabolism Sensitizes Cancer Cells Derived from Recurring GBM Tumors to Temozolomide. *Front. Oncol.* **2022**, *12*, 4708. [CrossRef]
90. Morihiro, Y.; Yasumoto, Y.; Vaidyan, L.K.; Sadahiro, H.; Uchida, T.; Inamura, A.; Sharifi, K.; Ideguchi, M.; Nomura, S.; Tokuda, N.; et al. Fatty Acid Binding Protein 7 as a Marker of Glioma Stem Cells. *Pathol. Int.* **2013**, *63*, 546–553. [CrossRef] [PubMed]
91. Lin, H.; Patel, S.; Affeck, V.S.; Wilson, I.; Turnbull, D.M.; Joshi, A.R.; Maxwell, R.; Stoll, E.A.; Affleck, V.S.; Wilson, I.; et al. Fatty Acid Oxidation Is Required for the Respiration and Proliferation of Malignant Glioma Cells. *Neuro Oncol.* **2017**, *19*, 43–54. [CrossRef] [PubMed]
92. De Rosa, A.; Pellegatta, S.; Rossi, M.; Tunici, P.; Magnoni, L.; Speranza, M.C.; Malusa, F.; Miragliotta, V.; Mori, E.; Finocchiaro, G.; et al. A Radial Glia Gene Marker, Fatty Acid Binding Protein 7 (FABP7), Is Involved in Proliferation and Invasion of Glioblastoma Cells. *PLoS ONE* **2012**, *7*, e52113. [CrossRef] [PubMed]
93. Jiang, N.; Xie, B.; Xiao, W.; Fan, M.; Xu, S.; Duan, Y.; Hamsafar, Y.; Evans, A.C.; Huang, J.; Zhou, W.; et al. Fatty Acid Oxidation Fuels Glioblastoma Radioresistance with CD47-Mediated Immune Evasion. *Nat. Commun.* **2022**, *13*, 1511. [CrossRef]
94. Ahmad, F.; Sun, Q.; Patel, D.; Stommel, J.M. Cholesterol Metabolism: A Potential Therapeutic Target in Glioblastoma. *Cancers* **2019**, *11*, 146. [CrossRef]
95. Villa, G.R.; Hulce, J.J.; Zanca, C.; Bi, J.; Ikegami, S.; Cahill, G.L.; Gu, Y.; Lum, K.M.; Masui, K.; Yang, H.; et al. An LXR-Cholesterol Axis Creates a Metabolic Co-Dependency for Brain Cancers. *Cancer Cell* **2016**, *30*, 683–693. [CrossRef] [PubMed]
96. Wang, X.; Huang, Z.; Wu, Q.; Prager, B.C.; Mack, S.C.; Yang, K.; Kim, L.J.Y.; Gimple, R.C.; Shi, Y.; Lai, S.; et al. MYC-Regulated Mevalonate Metabolism Maintains Brain Tumor–Initiating Cells. *Cancer Res.* **2017**, *77*, 4947–4960. [CrossRef] [PubMed]
97. Altwairgi, A.K.; Alghareeb, W.A.; AlNajjar, F.H.; Alhussain, H.; Alsaeed, E.; Balbaid, A.A.O.; Aldanan, S.; Orz, Y.; Alsharm, A.A. Atorvastatin in Combination with Radiotherapy and Temozolomide for Glioblastoma: A Prospective Phase II Study. *Investig. New Drugs* **2021**, *39*, 226–231. [CrossRef]
98. Lo, H.-W. Targeting Ras-RAF-ERK and Its Interactive Pathways as a Novel Therapy for Malignant Gliomas. *Curr. Cancer Drug Targets* **2010**, *10*, 840–848. [CrossRef]
99. Ma, Y.; Gong, Y.; Cheng, Z.; Loganathan, S.; Kao, C.; Sarkaria, J.N.; Abel, T.W.; Wang, J. Critical Functions of RhoB in Support of Glioblastoma Tumorigenesis. *Neuro Oncol.* **2015**, *17*, 516–525. [CrossRef]
100. Al-Koussa, H.; El Atat, O.; Jaafar, L.; Tashjian, H.; El-Sibai, M. The Role of Rho GTPases in Motility and Invasion of Glioblastoma Cells. *Anal. Cell. Pathol.* **2020**, *2020*, 9274016. [CrossRef]
101. Yanae, M.; Tsubaki, M.; Satou, T.; Itoh, T.; Imano, M.; Yamazoe, Y.; Nishida, S. Statin-Induced Apoptosis via the Suppression of ERK1/2 and Akt Activation by Inhibition of the Geranylgeranyl-Pyrophosphate Biosynthesis in Glioblastoma. *J. Exp. Clin. Cancer Res.* **2011**, *30*, 74. [CrossRef] [PubMed]
102. Yokogami, K.; Kikuchi, T.; Watanabe, T.; Nakatake, Y.; Yamashita, S.; Mizuguchi, A.; Takeshima, H. Methionine Regulates Self-Renewal, Pluripotency, and Cell Death of GIC through Cholesterol—RRNA Axis. *BMC Cancer* **2022**, *22*, 1351. [CrossRef] [PubMed]

103. Sun, P.; Xia, S.; Lal, B.; Shi, X.; Yang, K.S.; Watkins, P.A.; Laterra, J. Lipid Metabolism Enzyme ACSVL3 Supports Glioblastoma Stem Cell Maintenance and Tumorigenicity. *BMC Cancer* **2014**, *14*, 401. [CrossRef] [PubMed]
104. Pei, Z.; Sun, P.; Huang, P.; Lal, B.; Laterra, J.; Watkins, P.A. Acyl-CoA Synthetase VL3 Knockdown Inhibits Human Glioma Cell Proliferation and Tumorigenicity. *Cancer Res.* **2009**, *69*, 9175–9182. [CrossRef]
105. Bi, J.; Khan, A.; Tang, J.; Armando, A.M.; Wu, S.; Zhang, W.; Gimple, R.C.; Reed, A.; Jing, H.; Koga, T.; et al. Targeting Glioblastoma Signaling and Metabolism with a Re-Purposed Brain-Penetrant Drug. *Cell Rep.* **2021**, *37*, 109957. [CrossRef] [PubMed]
106. Guo, D.; Prins, R.M.; Dang, J.; Kuga, D.; Iwanami, A.; Soto, H.; Lin, K.Y.; Huang, T.T.; Akhavan, D.; Hock, M.B.; et al. EGFR Signaling Through an Akt-SREBP-1–Dependent, Rapamycin-Resistant Pathway Sensitizes Glioblastomas to Antilipogenic Therapy. *Sci. Signal.* **2009**, *2*, ra82. [CrossRef]
107. Cheng, C.; Ru, P.; Geng, F.; Liu, J.; Yoo, J.Y.; Wu, X.; Cheng, X.; Euthine, V.; Hu, P.; Guo, J.Y.; et al. Glucose-Mediated N-Glycosylation of SCAP Is Essential for SREBP-1 Activation and Tumor Growth. *Cancer Cell* **2015**, *28*, 569–581. [CrossRef]
108. Sassi, K.; Nury, T.; Samadi, M.; Fennira, F.B.-A.; Vejux, A.; Lizard, G. Cholesterol Derivatives as Promising Anticancer Agents in Glioblastoma Metabolic Therapy. In *Gliomas*; Exon Publications: Brisbane, Australia, 2021; pp. 97–120.
109. Zhan, X.; Qiu, R.; He, Y.; Zhao, Z.; Huang, M.; Liu, Q.; Zhi, F.; Long, W. The Aurora Kinase Inhibitor TAK901 Inhibits Glioblastoma Growth by Blocking SREBP1-Mediated Lipid Metabolism. *Cancers* **2022**, *14*, 5805. [CrossRef]
110. Geng, F.; Cheng, X.; Wu, X.; Yoo, J.Y.; Cheng, C.; Guo, J.Y.; Mo, X.; Ru, P.; Hurwitz, B.; Kim, S.-H.; et al. Inhibition of SOAT1 Suppresses Glioblastoma Growth via Blocking SREBP-1–Mediated Lipogenesis. *Clin. Cancer Res.* **2016**, *22*, 5337–5348. [CrossRef]
111. Rusu, P.; Shao, C.; Neuerburg, A.; Acikgöz, A.A.; Wu, Y.; Zou, P.; Phapale, P.; Shankar, T.S.; Döring, K.; Dettling, S.; et al. GPD1 Specifically Marks Dormant Glioma Stem Cells with a Distinct Metabolic Profile. *Cell Stem Cell* **2019**, *25*, 241–257.e8. [CrossRef] [PubMed]
112. Hale, J.S.; Otvos, B.; Sinyuk, M.; Alvarado, A.G.; Hitomi, M.; Stoltz, K.; Wu, Q.; Flavahan, W.; Levison, B.; Johansen, M.L.; et al. Cancer Stem Cell-Specific Scavenger Receptor CD36 Drives Glioblastoma Progression. *Stem Cells* **2014**, *32*, 1746–1758. [CrossRef]
113. Guo, D.; Hildebrandt, I.J.; Prins, R.M.; Soto, H.; Mazzotta, M.M.; Dang, J.; Czernin, J.; Shyy, J.Y.-J.; Watson, A.D.; Phelps, M.; et al. The AMPK Agonist AICAR Inhibits the Growth of EGFRvIII-Expressing Glioblastomas by Inhibiting Lipogenesis. *Proc. Natl. Acad. Sci. USA* **2009**, *106*, 12932–12937. [CrossRef] [PubMed]
114. Laks, D.R.; Ta, L.; Crisman, T.J.; Gao, F.; Coppola, G.; Radu, C.G.; Nathanson, D.A.; Kornblum, H.I. Inhibition of Nucleotide Synthesis Targets Brain Tumor Stem Cells in a Subset of Glioblastoma. *Mol. Cancer Ther.* **2016**, *15*, 1271–1278. [CrossRef] [PubMed]
115. Echizenya, S.; Ishii, Y.; Kitazawa, S.; Tanaka, T.; Matsuda, S.; Watanabe, E.; Umekawa, M.; Terasaka, S.; Houkin, K.; Hatta, T.; et al. Discovery of a New Pyrimidine Synthesis Inhibitor Eradicating Glioblastoma-Initiating Cells. *Neuro Oncol.* **2020**, *22*, 229–239. [CrossRef]
116. Lafita-Navarro, M.C.; Venkateswaran, N.; Kilgore, J.A.; Kanji, S.; Han, J.; Barnes, S.; Williams, N.S.; Buszczak, M.; Burma, S.; Conacci-Sorrell, M. Inhibition of the de Novo Pyrimidine Biosynthesis Pathway Limits Ribosomal RNA Transcription Causing Nucleolar Stress in Glioblastoma Cells. *PLOS Genet.* **2020**, *16*, e1009117. [CrossRef] [PubMed]
117. Spina, R.; Mills, I.; Ahmad, F.; Chen, C.; Ames, H.M.; Winkles, J.A.; Woodworth, G.F.; Bar, E.E. DHODH Inhibition Impedes Glioma Stem Cell Proliferation, Induces DNA Damage, and Prolongs Survival in Orthotopic Glioblastoma Xenografts. *Oncogene* **2022**, *41*, 5361–5372. [CrossRef]
118. Wang, X.; Yang, K.; Wu, Q.; Kim, L.J.Y.Y.; Morton, A.R.; Gimple, R.C.; Prager, B.C.; Shi, Y.; Zhou, W.; Bhargava, S.; et al. Targeting Pyrimidine Synthesis Accentuates Molecular Therapy Response in Glioblastoma Stem Cells. *Sci. Transl. Med.* **2019**, *11*, eaau4972. [CrossRef]
119. Nikaki, A.; Angelidis, G.; Efthimiadou, R.; Tsougos, I.; Valotassiou, V.; Fountas, K.; Prasopoulos, V.; Georgoulias, P. 18F-Fluorothymidine PET Imaging in Gliomas: An Update. *Ann. Nucl. Med.* **2017**, *31*, 495–505. [CrossRef]
120. Wang, X.; Yang, K.; Xie, Q.; Wu, Q.; Mack, S.C.; Shi, Y.; Kim, L.J.Y.; Prager, B.C.; Flavahan, W.A.; Liu, X.; et al. Purine Synthesis Promotes Maintenance of Brain Tumor Initiating Cells in Glioma. *Nat. Neurosci.* **2017**, *20*, 661–673. [CrossRef]
121. Zhou, W.; Yao, Y.; Scott, A.J.; Wilder-Romans, K.; Dresser, J.J.; Werner, C.K.; Sun, H.; Pratt, D.; Sajjakulnukit, P.; Zhao, S.G.; et al. Purine Metabolism Regulates DNA Repair and Therapy Resistance in Glioblastoma. *Nat. Commun.* **2020**, *11*, 3811. [CrossRef]
122. Shireman, J.M.; Atashi, F.; Lee, G.; Ali, E.S.; Saathoff, M.R.; Park, C.H.; Savchuk, S.; Baisiwala, S.; Miska, J.; Lesniak, M.S.; et al. De Novo Purine Biosynthesis Is a Major Driver of Chemoresistance in Glioblastoma. *Brain* **2021**, *144*, 1230–1246. [CrossRef] [PubMed]
123. Metro, G.; Fabi, A.; Mirri, M.A.; Vidiri, A.; Pace, A.; Carosi, M.; Russillo, M.; Maschio, M.; Giannarelli, D.; Pellegrini, D.; et al. Phase II Study of Fixed Dose Rate Gemcitabine as Radiosensitizer for Newly Diagnosed Glioblastoma Multiforme. *Cancer Chemother. Pharmacol.* **2010**, *65*, 391–397. [CrossRef] [PubMed]
124. Bastiancich, C.; Bastiat, G.; Lagarce, F. Gemcitabine and Glioblastoma: Challenges and Current Perspectives. *Drug Discov. Today* **2018**, *23*, 416–423. [CrossRef] [PubMed]
125. Banasavadi-Siddegowda, Y.K.; Welker, A.M.; An, M.; Yang, X.; Zhou, W.; Shi, G.; Imitola, J.; Li, C.; Hsu, S.; Wang, J.; et al. PRMT5 as a Druggable Target for Glioblastoma Therapy. *Neuro Oncol.* **2018**, *20*, 753–763. [CrossRef]
126. Kim, D.; Fiske, B.P.; Birsoy, K.; Freinkman, E.; Kami, K.; Possemato, R.L.; Chudnovsky, Y.; Pacold, M.E.; Chen, W.W.; Cantor, J.R.; et al. SHMT2 Drives Glioma Cell Survival in Ischaemia but Imposes a Dependence on Glycine Clearance. *Nature* **2015**, *520*, 363–367. [CrossRef]

127. Kryukov, G.V.; Wilson, F.H.; Ruth, J.R.; Paulk, J.; Tsherniak, A.; Marlow, S.E.; Vazquez, F.; Weir, B.A.; Fitzgerald, M.E.; Tanaka, M.; et al. MTAP Deletion Confers Enhanced Dependency on the PRMT5 Arginine Methyltransferase in Cancer Cells. *Science* **2016**, *351*, 1214–1218. [CrossRef]
128. Sachamitr, P.; Ho, J.C.; Ciamponi, F.E.; Ba-Alawi, W.; Coutinho, F.J.; Guilhamon, P.; Kushida, M.M.; Cavalli, F.M.G.; Lee, L.; Rastegar, N.; et al. PRMT5 Inhibition Disrupts Splicing and Stemness in Glioblastoma. *Nat. Commun.* **2021**, *12*, 979. [CrossRef]
129. Gao, X.; Sanderson, S.M.; Dai, Z.; Reid, M.A.; Cooper, D.E.; Lu, M.; Richie, J.P.; Ciccarella, A.; Calcagnotto, A.; Mikhael, P.G.; et al. Dietary Methionine Influences Therapy in Mouse Cancer Models and Alters Human Metabolism. *Nature* **2019**, *572*, 397–401. [CrossRef]
130. Okada, M.; Suzuki, S.; Togashi, K.; Sugai, A.; Yamamoto, M.; Kitanaka, C. Targeting Folate Metabolism Is Selectively Cytotoxic to Glioma Stem Cells and Effectively Cooperates with Differentiation Therapy to Eliminate Tumor-Initiating Cells in Glioma Xenografts. *Int. J. Mol. Sci.* **2021**, *22*, 11633. [CrossRef]
131. Tan, B.; Young, D.A.; Lu, Z.-H.; Wang, T.; Meier, T.I.; Shepard, R.L.; Roth, K.; Zhai, Y.; Huss, K.; Kuo, M.-S.; et al. Pharmacological Inhibition of Nicotinamide Phosphoribosyltransferase (NAMPT), an Enzyme Essential for NAD+ Biosynthesis, in Human Cancer Cells. *J. Biol. Chem.* **2013**, *288*, 3500–3511. [CrossRef]
132. Tateishi, K.; Iafrate, A.J.; Ho, Q.; Curry, W.T.; Batchelor, T.T.; Flaherty, K.T.; Onozato, M.L.; Lelic, N.; Sundaram, S.; Cahill, D.P.; et al. Myc-Driven Glycolysis Is a Therapeutic Target in Glioblastoma. *Clin. Cancer Res.* **2016**, *22*, 4452–4465. [CrossRef]
133. Jung, J.; Kim, L.J.Y.; Wang, X.; Wu, Q.; Sanvoranart, T.; Hubert, C.G.; Prager, B.C.; Wallace, L.C.; Jin, X.; Mack, S.C.; et al. Nicotinamide Metabolism Regulates Glioblastoma Stem Cell Maintenance. *JCI Insight* **2017**, *2*, e90019. [CrossRef] [PubMed]
134. Stuart, S.D.; Schauble, A.; Gupta, S.; Kennedy, A.D.; Keppler, B.R.; Bingham, P.M.; Zachar, Z. A Strategically Designed Small Molecule Attacks Alpha-Ketoglutarate Dehydrogenase in Tumor Cells through a Redox Process. *Cancer Metab.* **2014**, *2*, 4. [CrossRef] [PubMed]
135. Zachar, Z.; Marecek, J.; Maturo, C.; Gupta, S.; Stuart, S.D.; Howell, K.; Schauble, A.; Lem, J.; Piramzadian, A.; Karnik, S.; et al. Non-Redox-Active Lipoate Derivates Disrupt Cancer Cell Mitochondrial Metabolism and Are Potent Anticancer Agents in Vivo. *J. Mol. Med.* **2011**, *89*, 1137–1148. [CrossRef] [PubMed]
136. Huang, J.; Yu, J.; Tu, L.; Huang, N.; Li, H.; Luo, Y. Isocitrate Dehydrogenase Mutations in Glioma: From Basic Discovery to Therapeutics Development. *Front. Oncol.* **2019**, *9*, 506. [CrossRef]
137. Calvert, A.E.; Chalastanis, A.; Wu, Y.; Hurley, L.A.; Kouri, F.M.; Bi, Y.; Kachman, M.; May, J.L.; Bartom, E.; Hua, Y.; et al. Cancer-Associated IDH1 Promotes Growth and Resistance to Targeted Therapies in the Absence of Mutation. *Cell Rep.* **2017**, *19*, 1858–1873. [CrossRef]
138. Wahl, D.R.; Dresser, J.; Wilder-Romans, K.; Parsels, J.D.; Zhao, S.G.; Davis, M.; Zhao, L.; Kachman, M.; Wernisch, S.; Burant, C.F.; et al. Glioblastoma Therapy Can Be Augmented by Targeting IDH1-Mediated NADPH Biosynthesis. *Cancer Res.* **2017**, *77*, 960–970. [CrossRef] [PubMed]
139. Lloyd, R.E.; Keatley, K.; Littlewood, D.T.J.; Meunier, B.; Holt, W.V.; An, Q.; Higgins, S.C.; Polyzoidis, S.; Stephenson, K.F.; Ashkan, K.; et al. Identification and Functional Prediction of Mitochondrial Complex III and IV Mutations Associated with Glioblastoma. *Neuro Oncol.* **2015**, *17*, 942–952. [CrossRef]
140. Griguer, C.E.; Cantor, A.B.; Fathallah-Shaykh, H.M.; Gillespie, G.Y.; Gordon, A.S.; Markert, J.M.; Radovanovic, I.; Clement-Schatlo, V.; Shannon, C.N.; Oliva, C.R. Prognostic Relevance of Cytochrome c Oxidase in Primary Glioblastoma Multiforme. *PLoS ONE* **2013**, *8*, e61035. [CrossRef] [PubMed]
141. Oliva, C.R.; Markert, T.; Gillespie, G.Y.; Griguer, C.E. Nuclear-Encoded Cytochrome c Oxidase Subunit 4 Regulates BMI1 Expression and Determines Proliferative Capacity of High-Grade Gliomas. *Oncotarget* **2015**, *6*, 4330–4344. [CrossRef]
142. Griguer, C.E.; Oliva, C.R.; Gobin, E.; Marcorelles, P.; Benos, D.J.; Lancaster, J.R.; Gillespie, G.Y. CD133 Is a Marker of Bioenergetic Stress in Human Glioma. *PLoS ONE* **2008**, *3*, e3655. [CrossRef]
143. Janiszewska, M.; Suvà, M.L.; Riggi, N.; Houtkooper, R.H.; Auwerx, J.; Clément-Schatlo, V.; Radovanovic, I.; Rheinbay, E.; Provero, P.; Stamenkovic, I.; et al. Imp2 Controls Oxidative Phosphorylation and Is Crucial for Preserving Glioblastoma Cancer Stem Cells. *Genes Dev.* **2012**, *26*, 1926–1944. [CrossRef] [PubMed]
144. Chai, Y.; Wang, C.; Liu, W.; Fan, Y.; Zhang, Y. MPC1 Deletion Is Associated with Poor Prognosis and Temozolomide Resistance in Glioblastoma. *J. Neurooncol.* **2019**, *144*, 293–301. [CrossRef]
145. Iliopoulos, D.; Hirsch, H.A.; Struhl, K. Metformin Decreases the Dose of Chemotherapy for Prolonging Tumor Remission in Mouse Xenografts Involving Multiple Cancer Cell Types. *Cancer Res.* **2011**, *71*, 3196–3201. [CrossRef] [PubMed]
146. Griss, T.; Vincent, E.E.; Egnatchik, R.; Chen, J.; Ma, E.H.; Faubert, B.; Viollet, B.; DeBerardinis, R.J.; Jones, R.G. Metformin Antagonizes Cancer Cell Proliferation by Suppressing Mitochondrial-Dependent Biosynthesis. *PLoS Biol.* **2015**, *13*, e1002309. [CrossRef] [PubMed]
147. Mazurek, M.; Litak, J.; Kamieniak, P.; Kulesza, B.; Jonak, K.; Baj, J.; Grochowski, C. Metformin as Potential Therapy for High-Grade Glioma. *Cancers* **2020**, *12*, 210. [CrossRef]
148. Yang, S.H.; Li, S.; Lu, G.; Xue, H.; Kim, D.H.; Zhu, J.-J.; Liu, Y. Metformin Treatment Reduces Temozolomide Resistance of Glioblastoma Cells. *Oncotarget* **2016**, *7*, 78787–78803. [CrossRef]
149. Feng, S.-W.; Chang, P.-C.; Chen, H.-Y.; Hueng, D.-Y.; Li, Y.-F.; Huang, S.-M. Exploring the Mechanism of Adjuvant Treatment of Glioblastoma Using Temozolomide and Metformin. *Int. J. Mol. Sci.* **2022**, *23*, 8171. [CrossRef]

150. Würth, R.; Pattarozzi, A.; Gatti, M.; Bajetto, A.; Corsaro, A.; Parodi, A.; Sirito, R.; Massollo, M.; Marini, C.; Zona, G.; et al. Metformin Selectively Affects Human Glioblastoma Tumor-Initiating Cell Viability. *Cell Cycle* **2013**, *12*, 145–156. [CrossRef]
151. Ohno, M.; Kitanaka, C.; Miyakita, Y.; Tanaka, S.; Sonoda, Y.; Mishima, K.; Ishikawa, E.; Takahashi, M.; Yanagisawa, S.; Ohashi, K.; et al. Metformin with Temozolomide for Newly Diagnosed Glioblastoma: Results of Phase I Study and a Brief Review of Relevant Studies. *Cancers* **2022**, *14*, 4222. [CrossRef] [PubMed]
152. Yang, C.; Ko, B.; Hensley, C.T.; Jiang, L.; Wasti, A.T.; Kim, J.; Sudderth, J.; Calvaruso, M.A.; Lumata, L.; Mitsche, M.; et al. Glutamine Oxidation Maintains the TCA Cycle and Cell Survival during Impaired Mitochondrial Pyruvate Transport. *Mol. Cell* **2014**, *56*, 414–424. [CrossRef] [PubMed]
153. Arif, T.; Krelin, Y.; Nakdimon, I.; Benharroch, D.; Paul, A.; Dadon-Klein, D.; Shoshan-Barmatz, V. VDAC1 Is a Molecular Target in Glioblastoma, with Its Depletion Leading to Reprogrammed Metabolism and Reversed Oncogenic Properties. *Neuro Oncol.* **2017**, *19*, 951–964. [CrossRef] [PubMed]
154. Mohan, A.A.; Tomaszewski, W.H.; Haskell-Mendoza, A.P.; Hotchkiss, K.M.; Singh, K.; Reedy, J.L.; Fecci, P.E.; Sampson, J.H.; Khasraw, M. Targeting Immunometabolism in Glioblastoma. *Front. Oncol.* **2021**, *11*, 696402. [CrossRef] [PubMed]
155. Garofano, L.; Migliozzi, S.; Oh, Y.T.; D'Angelo, F.; Najac, R.D.; Ko, A.; Frangaj, B.; Caruso, F.P.; Yu, K.; Yuan, J.; et al. Pathway-Based Classification of Glioblastoma Uncovers a Mitochondrial Subtype with Therapeutic Vulnerabilities. *Nat. Cancer* **2021**, *2*, 141–156. [CrossRef] [PubMed]
156. Wang, L.-B.; Karpova, A.; Gritsenko, M.A.; Kyle, J.E.; Cao, S.; Li, Y.; Rykunov, D.; Colaprico, A.; Rothstein, J.H.; Hong, R.; et al. Proteogenomic and Metabolomic Characterization of Human Glioblastoma. *Cancer Cell* **2021**, *39*, 509–528.e20. [CrossRef] [PubMed]
157. Shakya, S.; Gromovsky, A.D.; Hale, J.S.; Knudsen, A.M.; Prager, B.; Wallace, L.C.; Penalva, L.O.F.; Brown, H.A.; Kristensen, B.W.; Rich, J.N.; et al. Altered Lipid Metabolism Marks Glioblastoma Stem and Non-Stem Cells in Separate Tumor Niches. *Acta Neuropathol. Commun.* **2021**, *9*, 101. [CrossRef]
158. Cabodevilla, A.G.; Sánchez-Caballero, L.; Nintou, E.; Boiadjieva, V.G.; Picatoste, F.; Gubern, A.; Claro, E. Cell Survival during Complete Nutrient Deprivation Depends on Lipid Droplet-Fueled β-Oxidation of Fatty Acids. *J. Biol. Chem.* **2013**, *288*, 27777–27788. [CrossRef]
159. Seliger, C.; Meyer, A.-L.; Leidgens, V.; Rauer, L.; Moeckel, S.; Jachnik, B.; Proske, J.; Dettmer, K.; Rothhammer-Hampl, T.; Kaulen, L.D.; et al. Metabolic Heterogeneity of Brain Tumor Cells of Proneural and Mesenchymal Origin. *Int. J. Mol. Sci.* **2022**, *23*, 11629. [CrossRef]
160. Liparulo, I.; Bergamini, C.; Bortolus, M.; Calonghi, N.; Gasparre, G.; Kurelac, I.; Masin, L.; Rizzardi, N.; Rugolo, M.; Wang, W.; et al. Coenzyme Q Biosynthesis Inhibition Induces HIF-1α Stabilization and Metabolic Switch toward Glycolysis. *FEBS J.* **2021**, *288*, 1956–1974. [CrossRef]
161. Sonveaux, P.; Copetti, T.; De Saedeleer, C.J.; Végran, F.; Verrax, J.; Kennedy, K.M.; Moon, E.J.; Dhup, S.; Danhier, P.; Frérart, F.; et al. Targeting the Lactate Transporter MCT1 in Endothelial Cells Inhibits Lactate-Induced HIF-1 Activation and Tumor Angiogenesis. *PLoS ONE* **2012**, *7*, e33418. [CrossRef]
162. Zhang, Y.; Yu, G.; Chu, H.; Wang, X.; Xiong, L.; Cai, G.; Liu, R.; Gao, H.; Tao, B.; Li, W.; et al. Macrophage-Associated PGK1 Phosphorylation Promotes Aerobic Glycolysis and Tumorigenesis. *Mol. Cell* **2018**, *71*, 201–215.e7. [CrossRef]
163. Di Ianni, N.; Musio, S.; Pellegatta, S. Altered Metabolism in Glioblastoma: Myeloid-Derived Suppressor Cell (MDSC) Fitness and Tumor-Infiltrating Lymphocyte (TIL) Dysfunction. *Int. J. Mol. Sci.* **2021**, *22*, 4460. [CrossRef]
164. Kim, E.H.; Lee, J.-H.; Oh, Y.; Koh, I.; Shim, J.-K.; Park, J.; Choi, J.; Yun, M.; Jeon, J.Y.; Huh, Y.M.; et al. Inhibition of Glioblastoma Tumorspheres by Combined Treatment with 2-Deoxyglucose and Metformin. *Neuro Oncol.* **2017**, *19*, 197–207. [CrossRef] [PubMed]
165. Yang, S.; Zhao, J.; Cui, X.; Zhan, Q.; Yi, K.; Wang, Q.; Xiao, M.; Tan, Y.; Hong, B.; Fang, C.; et al. TCA-Phospholipid-Glycolysis Targeted Triple Therapy Effectively Suppresses ATP Production and Tumor Growth in Glioblastoma. *Theranostics* **2022**, *12*, 7032–7050. [CrossRef] [PubMed]
166. McKelvey, K.J.; Wilson, E.B.; Short, S.; Melcher, A.A.; Biggs, M.; Diakos, C.I.; Howell, V.M. Glycolysis and Fatty Acid Oxidation Inhibition Improves Survival in Glioblastoma. *Front. Oncol.* **2021**, *11*, 633210. [CrossRef] [PubMed]
167. Kim, S.J.; Park, S.J.; Park, J.; Cho, H.J.; Shim, J.-K.; Seon, J.; Choi, R.J.; Yoon, S.-J.; Moon, J.H.; Kim, E.H.; et al. Dual Inhibition of CPT1A and G6PD Suppresses Glioblastoma Tumorspheres. *J. Neurooncol.* **2022**, *160*, 677–689. [CrossRef]
168. Zhan, Q.; Yi, K.; Cui, X.; Li, X.; Yang, S.; Wang, Q.; Fang, C.; Tan, Y.; Li, L.; Xu, C.; et al. Blood Exosomes-Based Targeted Delivery of CPLA2 SiRNA and Metformin to Modulate Glioblastoma Energy Metabolism for Tailoring Personalized Therapy. *Neuro Oncol.* **2022**, *24*, 1871–1883. [CrossRef]
169. Zhang, B.; Peng, H.; Zhou, M.; Bao, L.; Wang, C.; Cai, F.; Zhang, H.; Wang, J.E.; Niu, Y.; Chen, Y.; et al. Targeting BCAT1 Combined with α-Ketoglutarate Triggers Metabolic Synthetic Lethality in Glioblastoma. *Cancer Res.* **2022**, *82*, 2388–2402. [CrossRef]
170. Vlashi, E.; Lagadec, C.; Vergnes, L.; Matsutani, T.; Masui, K.; Poulou, M.; Popescu, R.; Della Donna, L.; Evers, P.; Dekmezian, C.; et al. Metabolic State of Glioma Stem Cells and Nontumorigenic Cells. *Proc. Natl. Acad. Sci. USA* **2011**, *108*, 16062–16067. [CrossRef]
171. Vartanian, A.; Agnihotri, S.; Wilson, M.R.; Burrell, K.E.; Tonge, P.D.; Alamsahebpour, A.; Jalali, S.; Taccone, M.S.; Mansouri, S.; Golbourn, B.; et al. Targeting Hexokinase 2 Enhances Response to Radio-Chemotherapy in Glioblastoma. *Oncotarget* **2016**, *7*, 69518–69535. [CrossRef]

172. Sampath, D.; Zabka, T.S.; Misner, D.L.; O'Brien, T.; Dragovich, P.S. Inhibition of Nicotinamide Phosphoribosyltransferase (NAMPT) as a Therapeutic Strategy in Cancer. *Pharmacol. Ther.* **2015**, *151*, 16–31. [CrossRef] [PubMed]
173. McBrayer, S.K.; Mayers, J.R.; DiNatale, G.J.; Shi, D.D.; Khanal, J.; Chakraborty, A.A.; Sarosiek, K.A.; Briggs, K.J.; Robbins, A.K.; Sewastianik, T.; et al. Transaminase Inhibition by 2-Hydroxyglutarate Impairs Glutamate Biosynthesis and Redox Homeostasis in Glioma. *Cell* **2018**, *175*, 101–116.e25. [CrossRef] [PubMed]
174. Castro, M.; Carson, G.; McConnell, M.; Herst, P. High Dose Ascorbate Causes Both Genotoxic and Metabolic Stress in Glioma Cells. *Antioxidants* **2017**, *6*, 58. [CrossRef]
175. Hajji, N.; Garcia-Revilla, J.; Soto, M.S.; Perryman, R.; Symington, J.; Quarles, C.C.; Healey, D.R.; Guo, Y.; Orta-Vázquez, M.L.; Mateos-Cordero, S.; et al. Arginine Deprivation Alters Microglial Polarity and Synergizes with Radiation to Eradicate Non-Arginine-Auxotrophic Glioblastoma Tumors. *J. Clin. Investig.* **2022**, *132*, e142137. [CrossRef]
176. Oliva, C.R.; Nozell, S.E.; Diers, A.; McClugage, S.G.; Sarkaria, J.N.; Markert, J.M.; Darley-Usmar, V.M.; Bailey, S.M.; Gillespie, G.Y.; Landar, A.; et al. Acquisition of Temozolomide Chemoresistance in Gliomas Leads to Remodeling of Mitochondrial Electron Transport Chain. *J. Biol. Chem.* **2010**, *285*, 39759–39767. [CrossRef]
177. Caragher, S.; Miska, J.; Shireman, J.; Park, C.H.; Muroski, M.; Lesniak, M.S.; Ahmed, A.U. Temozolomide Treatment Increases Fatty Acid Uptake in Glioblastoma Stem Cells. *Cancers* **2020**, *12*, 3126. [CrossRef]
178. Wang, N.; Huang, R.; Yang, K.; He, Y.; Gao, Y.; Dong, D. Interfering with Mitochondrial Dynamics Sensitizes Glioblastoma Multiforme to Temozolomide Chemotherapy. *J. Cell. Mol. Med.* **2022**, *26*, 893–912. [CrossRef] [PubMed]
179. Wicks, R.T.; Azadi, J.; Mangraviti, A.; Zhang, I.; Hwang, L.; Joshi, A.; Bow, H.; Hutt-Cabezas, M.; Martin, K.L.; Rudek, M.A.; et al. Local Delivery of Cancer-Cell Glycolytic Inhibitors in High-Grade Glioma. *Neuro Oncol.* **2015**, *17*, 70–80. [CrossRef]
180. Yuan, S.; Wang, F.; Chen, G.; Zhang, H.; Feng, L.; Wang, L.; Colman, H.; Keating, M.J.; Li, X.; Xu, R.-H.; et al. Effective Elimination of Cancer Stem Cells By a Novel Drug Combination Strategy. *Stem Cells* **2013**, *31*, 23–34. [CrossRef]
181. Sun, X.; Fan, T.; Sun, G.; Zhou, Y.; Huang, Y.; Zhang, N.; Zhao, L.; Zhong, R.; Peng, Y. 2-Deoxy-D-Glucose Increases the Sensitivity of Glioblastoma Cells to BCNU through the Regulation of Glycolysis, ROS and ERS Pathways: In Vitro and In Vivo Validation. *Biochem. Pharmacol.* **2022**, *199*, 115029. [CrossRef]
182. Yu, Z.; Zhao, G.; Xie, G.; Zhao, L.; Chen, Y.; Yu, H.; Zhang, Z.; Li, C.; Li, Y. Metformin and Temozolomide Act Synergistically to Inhibit Growth of Glioma Cells and Glioma Stem Cells in Vitro and in Vivo. *Oncotarget* **2015**, *6*, 32930–32943. [CrossRef]
183. Park, H.H.; Park, J.; Cho, H.J.; Shim, J.-K.; Moon, J.H.; Kim, E.H.; Chang, J.H.; Kim, S.Y.; Kang, S.-G. Combinatorial Therapeutic Effect of Inhibitors of Aldehyde Dehydrogenase and Mitochondrial Complex I, and the Chemotherapeutic Drug, Temozolomide against Glioblastoma Tumorspheres. *Molecules* **2021**, *26*, 282. [CrossRef] [PubMed]
184. Shim, J.-K.; Choi, S.; Yoon, S.-J.; Choi, R.J.; Park, J.; Lee, E.H.; Cho, H.J.; Lee, S.; Teo, W.-Y.; Moon, J.H.; et al. Etomoxir, a Carnitine Palmitoyltransferase 1 Inhibitor, Combined with Temozolomide Reduces Stemness and Invasiveness in Patient-Derived Glioblastoma Tumorspheres. *Cancer Cell Int.* **2022**, *22*, 309. [CrossRef]
185. Mazor, G.; Levin, L.; Picard, D.; Ahmadov, U.; Carén, H.; Borkhardt, A.; Reifenberger, G.; Leprivier, G.; Remke, M.; Rotblat, B. The LncRNA TP73-AS1 Is Linked to Aggressiveness in Glioblastoma and Promotes Temozolomide Resistance in Glioblastoma Cancer Stem Cells. *Cell Death Dis.* **2019**, *10*, 246. [CrossRef] [PubMed]
186. Fack, F.; Espedal, H.; Keunen, O.; Golebiewska, A.; Obad, N.; Harter, P.N.; Mittelbronn, M.; Bähr, O.; Weyerbrock, A.; Stuhr, L.; et al. Bevacizumab Treatment Induces Metabolic Adaptation toward Anaerobic Metabolism in Glioblastomas. *Acta Neuropathol.* **2015**, *129*, 115–131. [CrossRef]
187. Keunen, O.; Johansson, M.; Oudin, A.; Sanzey, M.; Rahim, S.A.A.; Fack, F.; Thorsen, F.; Taxt, T.; Bartos, M.; Jirik, R.; et al. Anti-VEGF Treatment Reduces Blood Supply and Increases Tumor Cell Invasion in Glioblastoma. *Proc. Natl. Acad. Sci. USA* **2011**, *108*, 3749–3754. [CrossRef]
188. Divé, I.; Klann, K.; Michaelis, J.B.; Heinzen, D.; Steinbach, J.P.; Münch, C.; Ronellenfitsch, M.W. Inhibition of MTOR Signaling Protects Human Glioma Cells from Hypoxia-Induced Cell Death in an Autophagy-Independent Manner. *Cell Death Discov.* **2022**, *8*, 409. [CrossRef]
189. Romero-Garcia, S.; Moreno-Altamirano, M.M.B.; Prado-Garcia, H.; Sánchez-García, F.J. Lactate Contribution to the Tumor Microenvironment: Mechanisms, Effects on Immune Cells and Therapeutic Relevance. *Front. Immunol.* **2016**, *7*, 52. [CrossRef] [PubMed]
190. Hao, M.; Hou, S.; Li, W.; Li, K.; Xue, L.; Hu, Q.; Zhu, L.; Chen, Y.; Sun, H.; Ju, C.; et al. Combination of Metabolic Intervention and T Cell Therapy Enhances Solid Tumor Immunotherapy. *Sci. Transl. Med.* **2020**, *12*, eaaz6667. [CrossRef] [PubMed]
191. Wainwright, D.A.; Chang, A.L.; Dey, M.; Balyasnikova, I.V.; Kim, C.K.; Tobias, A.; Cheng, Y.; Kim, J.W.; Qiao, J.; Zhang, L.; et al. Durable Therapeutic Efficacy Utilizing Combinatorial Blockade against IDO, CTLA-4, and PD-L1 in Mice with Brain Tumors. *Clin. Cancer Res.* **2014**, *20*, 5290–5301. [CrossRef]
192. Medikonda, R.; Choi, J.; Pant, A.; Saleh, L.; Routkevitch, D.; Tong, L.; Belcaid, Z.; Kim, Y.H.; Jackson, C.M.; Jackson, C.; et al. Synergy between Glutamate Modulation and Anti–Programmed Cell Death Protein 1 Immunotherapy for Glioblastoma. *J. Neurosurg.* **2022**, *136*, 379–388. [CrossRef] [PubMed]
193. Safdie, F.; Brandhorst, S.; Wei, M.; Wang, W.; Lee, C.; Hwang, S.; Conti, P.S.; Chen, T.C.; Longo, V.D. Fasting Enhances the Response of Glioma to Chemo- and Radiotherapy. *PLoS ONE* **2012**, *7*, e44603. [CrossRef] [PubMed]
194. Kanarek, N.; Petrova, B.; Sabatini, D.M. Dietary Modifications for Enhanced Cancer Therapy. *Nature* **2020**, *579*, 507–517. [CrossRef]

195. Voss, M.; Wagner, M.; von Mettenheim, N.; Harter, P.N.; Wenger, K.J.; Franz, K.; Bojunga, J.; Vetter, M.; Gerlach, R.; Glatzel, M.; et al. ERGO2: A Prospective, Randomized Trial of Calorie-Restricted Ketogenic Diet and Fasting in Addition to Reirradiation for Malignant Glioma. *Int. J. Radiat. Oncol.* **2020**, *108*, 987–995. [CrossRef]
196. Astuti, D.; Latif, F.; Dallol, A.; Dahia, P.L.M.; Douglas, F.; George, E.; Sköldberg, F.; Husebye, E.S.; Eng, C.; Maher, E.R. Gene Mutations in the Succinate Dehydrogenase Subunit SDHB Cause Susceptibility to Familial Pheochromocytoma and to Familial Paraganglioma. *Am. J. Hum. Genet.* **2001**, *69*, 49–54. [CrossRef]
197. Nusblat, L.M.; Tanna, S.; Roth, C.M. Gene Silencing of HIF-2α Disrupts Glioblastoma Stem Cell Phenotype. *Cancer Drug Resist.* **2020**, *3*, 199. [CrossRef]
198. Simpson, J.E.; Gammoh, N. The Impact of Autophagy during the Development and Survival of Glioblastoma. *Open Biol.* **2020**, *10*, 200184. [CrossRef] [PubMed]

2. Reprogrammation et hétérogénéité métabolique des glioblastomes

La reprogrammation métabolique, caractéristique clé des cancers, permet aux cellules cancéreuses de produire l'énergie (ATP) et les biomolécules nécessaires, comme les nucléotides, acides aminés, lipides et glucides, pour soutenir leur prolifération rapide. Dans les GB, des altérations sont observées dans diverses voies métaboliques, y compris la glycolyse, l'oxydation et la synthèse de lipides, ainsi que dans le métabolisme des acides aminés et des nucléotides [185,186]. L'effet Warburg, où les cellules cancéreuses privilégient la glycolyse aérobie même en présence d'oxygène, est particulièrement notable [187]. Ce phénomène favorise une production rapide d'ATP et de macromolécules, tout en adaptant les cellules à un environnement hypoxique. Cependant, la chaîne respiratoire mitochondriale reste fonctionnelle dans les GB, indiquant une utilisation mixte de la glycolyse aérobie et d'autres voies métaboliques [188,189].

La glycolyse aérobie joue un rôle central dans la transformation métabolique des cellules cancéreuses, influencée par des changements épigénétiques et par l'activité d'oncogènes. Dans les GB, le glucose métabolisé par la glycolyse produit du pyruvate, qui peut être converti en lactate ou bien acheminé vers les mitochondries pour entrer dans le cycle TCA. Ce cycle, suivi d'OXPHOS, génère une quantité significative d'énergie [190]. En plus du glucose, les cellules GB métabolisent d'autres substrats, tels que les acides aminés et les lipides, et la glutaminolyse est souvent exploitée pour alimenter le cycle TCA par anaplérose [191–193]. Les intermédiaires de la glycolyse et du cycle TCA peuvent être détournés vers des voies biosynthétiques pour contribuer à la production de biomasse nécessaire à la croissance cellulaire.

Une analyse approfondie des données du TCGA a révélé que les tissus cérébraux sains présentent principalement une signature OXPHOS, tandis que les tumeurs cérébrales tendent à afficher une signature glycolytique. Cependant, le profil métabolique des GB peut être très divers, comme l'ont montré de nombreuses études utilisant des modèles de xénogreffes ou des tumeurs de patients, s'appuyant sur des approches utilisant le ^{13}C [188,194,195] ou des méthodes multi-omiques [107,196]. Les tumeurs du sous-type mésenchymateux, particulièrement invasives, manifestent une importante activité de glycolyse [189]. Une étude a introduit une classification innovante des GB basée sur le paysage immunitaire tumoral, avec des implications pronostiques, et révélant une hétérogénéité significative dans le métabolisme lipidique des différents sous-types [196]. Des études d'IRM sur des patients ont également révélé une hétérogénéité entre les tumeurs primaires et les tumeurs récurrentes [197].

L'hétérogénéité intra-tumorale des GB est également bien documentée. En utilisant une approche multi-omique, Garofano et ses collègues ont identifié des sous-types distincts de GB tels que le sous-type mitochondrial et le sous-type glycolytique plurimétabolique. En effet, ils ont découvert qu'au sein des tumeurs, certaines cellules de GB privilégient l'OXPHOS, tandis que d'autres favorisent la glycolyse aérobie, le métabolisme des acides aminés et des lipides. Il a été démontré que le sous-type mitochondrial de GB est associé à un meilleur pronostic clinique [107]. D'autres recherches ont montré que les cellules cancéreuses dans des régions pauvres en nutriments métabolisent davantage les gouttelettes lipidiques [198], tandis que celles dans des zones pauvres en oxygène présentent un profil plus glycolytique [199] et accumulent des lipides [200]. Par ailleurs, une étude comparative a révélé que les cellules de GB à croissance rapide privilégient la glycolyse aérobie, alors que celles à croissance plus lente favorisent l'OXPHOS et possèdent une concentration élevée en lipides, qu'elles métabolisent en l'absence de glucose. Les cellules à croissance plus lente se sont révélées plus résistantes aux traitements et présentent une plus grande capacité d'invasion [194]. D'autres travaux ont mis en évidence que, par rapport aux cellules de GB à faible potentiel de motilité, celles à fort potentiel de motilité présentent un métabolisme énergétique accru, une production élevée de ROS, une charge mitochondriale importante, et sont enrichies en voies antioxydantes, notamment en glutathion [201].

L'hétérogénéité des GB est influencée par des facteurs variés, incluant des caractéristiques moléculaires propres aux tumeurs et les conditions uniques du microenvironnement. Les cellules tumorales, dotées d'une plasticité métabolique, s'adaptent aux variations environnementales, telles que les fluctuations de disponibilité en nutriments et en oxygène, le stress oxydatif, et les réponses aux traitements thérapeutiques. Cette capacité d'adaptation leur permet de survivre et de proliférer dans un environnement en perpétuelle évolution [193,202–204].

3. Métabolisme des cellules souches de glioblastome

Poursuivant notre exploration du métabolisme des GB, nous allons maintenant nous pencher spécifiquement sur les caractéristiques métaboliques des CSG. Ces cellules résident dans des niches spécifiques, souvent caractérisées par des conditions environnementales défavorables. Pour survivre et prospérer dans ces milieux hostiles, les CSG ont développé une adaptabilité métabolique remarquable, leur permettant de fonctionner efficacement tant dans des conditions

aérobies qu'hypoxiques [42,125]. Cette flexibilité métabolique leur permet de basculer entre des phénotypes oxydatifs et glycolytiques en fonction des besoins [205,206].

Le consensus actuel suggère que, bien que les CSG soient métaboliquement flexibles, elles privilégient principalement OXPHOS pour la production d'ATP. À l'opposé, les cellules de GB différenciées tendent à dépendre davantage de la glycolyse aérobie [79,202]. Selon l'étude de *Vlashi et al.*, les CSG sont décrites comme moins glycolytiques, consommant moins de glucose et produisant moins de lactate que les cellules filles différenciées. Elles présentent également une plus grande capacité de réserve mitochondriale, leur conférant une plus grande radiorésistance [79]. De la même manière que les CSN en état de quiescence, les CSG à croissance lente s'appuient sur l'oxydation des acides gras et l'OXPHOS pour leur métabolisme énergétique [194,207,208].

Des études récentes ont mis en évidence une hétérogénéité métabolique significative entre deux sous-types de CSG dans les GB : les sous-types proneural et mésenchymateux. Les CSG mésenchymateuses se distinguent par leur agressivité, leur résistance à la radiothérapie, et une prédominance de la voie glycolytique, caractérisée notamment par une expression élevée des gènes liés à l'enzyme aldehyde déshydrogénase (ALDH). L'inhibition de l'ALDH1A3 a spécifiquement réduit la croissance des CSG mésenchymateuses, sans affecter les CSG proneurales. De plus, une transition des CSG proneurales vers le type mésenchymateux a été observée après une radiothérapie, transition qui peut être empêchée par l'inhibition de l'ALDH1A3, soulignant ainsi son rôle potentiel dans la pathogenèse des GB [177]. Des études complémentaires ont confirmé cette divergence métabolique, soulignant que les CSG mésenchymateuses sont plus glycolytiques et moins sensibles à la metformine, tandis que les CSG proneurales, moins invasives, favorisent le métabolisme du glucose *via* la voie du phosphate de pentose et sont plus sensibles à la metformine [209].

4. Quelques approches thérapeutiques

L'évolution des recherches sur le métabolisme tumoral ouvre des perspectives prometteuses pour le développement de stratégies thérapeutiques contre le GB [90].

Parmi ces avancées, la documentation de la co-existence des états glycolytiques et OXPHOS au sein des tumeurs [189], ainsi que la dépendance des CSG au métabolisme mitochondriale et leur sensibilité accrue aux traitements ciblant les mitochondries [210,211] représente des avancées significatives. En ciblant la glycolyse, il est désormais envisagé que

les CSG pourraient être épargnées. De plus, l'approche consistant à cibler une seule voie énergétique s'est avérée produire des effets antitumoraux limités [79]. Cette limitation est due à l'hétérogénéité intrinsèque et à la plasticité métabolique des cellules tumorales, qui peuvent activer des voies métaboliques alternatives en réponse à l'inhibition d'une voie spécifique. Par conséquent, une stratégie thérapeutique qui cible simultanément plusieurs voies métaboliques, en particulier la glycolyse et la respiration mitochondriale, apparaît comme une approche plus globale et efficace pour cibler la tumeur dans son ensemble [212,213].

D'autres avancées ont été réalisé concernant les CSG, notamment la découverte de leur importante capacité de réserve mitochondriale, qui est corrélée à une résistance accrue à la radiothérapie [79]. Le dichloroacétate (DCA), un médicament habituellement utilisé pour traiter l'acidose lactique, a montré un potentiel notable dans la réduction de cette capacité de réserve mitochondriale des CSG. En inversant l'effet Warburg, le DCA favorise le flux de pyruvate vers les mitochondries, entraînant une dépolarisation de la membrane mitochondriale et une augmentation des concentrations d'espèces réactives de l'oxygène (ROS), ce qui déclenche l'apoptose des cellules tumorales. L'efficacité anticancéreuse du DCA a été démontrée tant *in vitro* qu'*in vivo*, soulignant son potentiel thérapeutique dans le traitement des GB [214,215].

La metformine, médicament pour le diabète de type 2, a montré des effets anticancéreux en inhibant le complexe I mitochondrial, en altérant les voies de biosynthèse des mitochondries et en activant AMPK. Ce médicament a également démontré des effets anticancéreux *in vitro* et in vivo, offrant une nouvelle piste thérapeutique pour le GB [216–218].

De manière intéressante, la combinaison de DCA et de MET produit un effet synergique sur les CSG, réduisant la croissance tumorale *in vitro* et *in vivo* [219] en augmentant notamment le stress oxydatif au sein des GB [220]. Cette approche ainsi que d'autres approches thérapeutiques visant à induire ou augmenter le stress oxydatif au sein des GB pourraient s'avérer prometteuses [221].

L'effet Warburg, caractéristique des cancers, a stimulé des recherches intensives sur l'enzyme LDHA en tant que cible potentielle pour les stratégies anticancéreuses. Les lactates déshydrogénases, LDHA et LDHB, spécifiquement exprimées dans les tissus des GB, jouent un rôle crucial dans l'interconversion du pyruvate et du lactate. Il a été démontré que l'inhibition simultanée de LDHA et LDHB est plus efficace que l'inhibition de chacune de ces enzymes individuellement, inhibant ainsi la croissance des GB tant *in vitro* qu'*in vivo*. Cette double inhibition favorise une augmentation de OXPHOS dans les cellules LDHA/B KO. Dans ce contexte, le stiripentol, un médicament antiépileptique, a montré sa capacité à inhiber l'activité

des deux isoformes de LDH, réduisant efficacement la croissance des GB [199]. L'approche combinée ciblant LDHA et LDHB s'avère donc particulièrement prometteuse pour augmenter la sensibilité des GB à divers traitements thérapeutiques tels que la radiothérapie, la chimiothérapie et d'autres thérapies ciblant les mitochondries [199].

La combinaison de différentes stratégies thérapeutiques, ciblant des vulnérabilités métaboliques des cellules tumorales, représente une approche prometteuse pour surmonter la résistance aux traitements et améliorer les résultats cliniques des patients atteints de GB.

OBJECTIFS DE L'ÉTUDE

L'hétérogénéité et la plasticité moléculaire des cellules tumorales du GB représentent des obstacles majeurs à la mise au point de thérapies efficaces. Actuellement, le traitement des GB, combinant chirurgie et radio-chimiothérapie, reste insuffisant pour assurer une rémission à long terme des patients. Les GB se distinguent par la coexistence de populations cellulaires diverses, parmi lesquelles les CSC, bien que minoritaires, jouent un rôle crucial dans la pathogenèse des GB. Ces cellules se situent principalement à proximité des vaisseaux sanguins ou dans des régions hypoxiques, et sont à l'origine de diverses populations tumorales différenciées formant la masse tumorale. À cette hétérogénéité cellulaire et moléculaire s'ajoute une hétérogénéité métabolique, la dérégulation du métabolisme étant une caractéristique fondamentale des cancers.

Au sein du laboratoire, la thématique « tumeurs cérébrales adultes et microenvironnement » se concentre sur l'étude de l'intégrine $\alpha5\beta1$, un senseur clé du microenvironnement et notamment de la matrice extracellulaire. Nos résultats soulignent son importance dans l'agressivité des GB, tout en mettant en évidence son expression hétérogène, tant *in vitro* qu'*in vivo* et chez les patients. Cette recherche s'inscrit dans une approche plus globale visant à comprendre comment l'expression d'une cible thérapeutique peut varier dans différentes conditions et souligne l'importance d'une classification précise des tumeurs pour améliorer l'efficacité de thérapies ciblées.

Dans ce contexte, les objectifs de ma recherche sont les suivants :

- Proposer une nouvelle classification de l'hétérogénéité moléculaire des GB, en collaboration avec des bioinformaticiens, pour mieux comprendre la diversité et la complexité de ces tumeurs.
- Caractériser l'hétérogénéité et la plasticité métabolique de modèles de CSG, en mettant l'accent sur la manière dont les changements environnementaux influencent leur métabolisme.
- Établir des liens entre les aspects moléculaires et métaboliques des GB, en particulier en ce qui concerne la résistance aux traitements, afin d'identifier de nouvelles cibles et stratégies thérapeutiques potentielles.

Ces objectifs visent à approfondir notre compréhension des mécanismes sous-jacents régissant la pathogenèse des GB, et à contribuer au développement de thérapies plus ciblées et efficaces.

MATÉRIELS ET MÉTHODES

1. Lignées cellulaires

1.1 Cellules souches de glioblastome

Les lignées cellulaires NCH644 et NCH421k, des cellules souches de gliome dérivées de patients, nous ont été fournies par le Pr. Herold-Mende [222]. Les lignées cellulaires 5706 et 3731, également des cellules de type souche de gliome dérivées de patients, nous ont été fournies par le Dr. Ahmed Idbaih. Pour finir, les lignées cellulaires TC7 et TC22, dérivées de deux xénogreffes de GB de patients, ont été établies dans notre laboratoire.

1.2 Lignée commerciale U87MG et clones dérivés

En plus des lignées de cellules souches dérivés de patients, nous avons utilisé la lignée cellulaire U87MG, une lignée cellulaire adhérente de GB fournie par American Type Culture Collection (ATCC, LGC Standards Sarl, Molsheim, France) et deux lignées clonales résistantes au TMZ dérivées de U87MG, précédemment établies au sein du laboratoire par un traitement à long terme de TMZ à 50 µM : U87MG R50 et U87MG R50 OFF. La lignée clonale U87MG R50 a été cultivée en continu dans un milieu contenant 50 µM de TMZ tandis que la lignée U87MG R50 OFF a été mise hors de pression du TMZ après deux mois de traitement.

2. Culture cellulaire

Nous avons cultivé une cohorte de 10 lignées de cellules souches de gliomes dérivées de patients dans un milieu de cellules souches (culture de neurosphères) ou un milieu de différenciation (culture de cellules adhérentes) en normoxie (21% O_2) ou en hypoxie (1% O_2). Pour cela, un incubateur multi-gaz 255L (HERACell VI0S 250i, ThermoFischer) est utilisé, permettant de moduler les taux d'oxygène. Les lignées NCH644, NCH421k, 5706 et 3731 ont été cultivées en condition de neurosphères en utilisant le milieu Eagle modifié de Dulbecco avec le DMEM/F-12 (milieu de culture Eagle modifié de Dulbecco/mélange de nutriments F-12) suplémenté de GlutaMAX™ (DMEMF12, GlutaMAX™, Gibco™), complété par de la BSA Insulin Transferrin (BIT-100) (20%) (Provitro), des facteurs de croissance EGF (20 ng/mL) (Reliatech) et β-FGF (20 ng/mL) (Reliatech). Les lignées TC7 et TC22 ont été cultivées en condition de neurosphère en utilisant DMEMF12, GlutaMAX™ (Gibco™), supplémenté avec du B27™ (2%) (Provitro), des facteurs de croissance EGF (20 ng/mL) (Reliatech) et β-FGF (20 ng/mL) (Reliatech). Ces cellules ont été cultivées en monocouche avec le milieu DMEM/F12 + GlutaMAX™ (Gibco™) complété par 10% (vol/vol) de sérum de veau fœtal

(SVF) (Gibco™). La lignée cellulaire U87MG et les clones dérivées ont été cultivées en monocouche dans un milieu MEM (Minimum Essential Medium Eagle) supplémenté avec 10% (vol/vol) de SVF (Gibco™), 1% de pyruvate de sodium (Gibco™) et 1% d'acides aminés non essentiels (Gibco™) et dans un milieu pour cellules souches utilisant DMEMF12+GlutaMAX™ (Gibco™) complété par du B27™ (2%) (Provitro), des facteurs de croissance EGF (20 ng/mL) (Reliatech) et β-FGF (20 ng/mL) (Reliatech).

3. Analyse de l'expression génique

3.1 Lignées de cellules souches de glioblastome

Chaque lignée de CSG a été cultivée dans différentes conditions expérimentales : souche, différenciée, hypoxique. Après une exposition prolongée à ces conditions de culture, les cellules ont été transférées dans des flacons T75 et cultivées pendant trois jours avant la récolte pour la préparation des culots cellulaires. Les échantillons ont été traités selon les protocoles standards de préparation d'ARN. L'ARN total a été extrait en utilisant le kit approprié, avec une étape subséquente de vérification de la qualité et de la quantité de l'ARN.

Pour les lignées NCH644 et NCH421k, dans les conditions souche et différenciée, l'ARN total a été isolé et des cibles d'ADNc monocaténaires biotinylées ont été préparées en utilisant le kit d'expression Ambion WT (#4411974) et le kit de marquage terminal Affymetrix GeneChip® WT (#900671), conformément aux instructions fournies par les fabricants. Les ADNc ont été hybridés sur des puces GeneChip® Human Gene 2.0 ST (Affymetrix), ciblant plus de 40 000 transcrits RefSeq et environ 11 000 LncARN. Les puces ont été traitées et analysées en utilisant les équipements et les logiciels Affymetrix. Les données brutes ont ensuite été analysées et traitées en utilisant le logiciel Affymetrix Expression Console version 1.4.1 avec les paramètres RMA par défaut.

Pour les autres lignées cellulaires et conditions expérimentales, des séquençages d'ARN ont été réalisées au sein de la plateforme GenomEast de l'Institut de Génétique et de Biologie Moléculaire et Cellulaire. La préparation des librairies a été effectuée en s'appuyant sur le guide de référence TruSeq Stranded mRNA – PN 1000000040498. À partir de 500 ng d'ARN total, les librairies RNA-Seq ont été générées en utilisant le kit TruSeq Stranded mRNA Library Prep et les IDT for Illumina – TruSeq RNA UD Indexes (96 index, pour 96 échantillons) (Illumina, San Diego, USA), en respectant les instructions du fabricant. Après purification de l'ARN messager par des billes magnétiques liées à des oligos poly-T, la fragmentation a été induite par

des cations divalents à 94°C pendant 2 minutes. Les fragments d'ARN clivés ont été transcrits en ADNc monocaténaire par une transcriptase inverse utilisant des amorces aléatoires. La spécificité des brins a été obtenue en remplaçant le dTTP par du dUTP lors de la synthèse du deuxième brin de cADN, en utilisant la DNA Polymerase I et la RNase H. Après adjonction d'une base 'A' et la ligation d'un adaptateur sur les fragments d'ADNc double brin, les produits ont été purifiés et enrichis par PCR (30 sec à 98°C; (10 sec à 98°C, 30 sec à 60°C, 30 sec à 72°C) × 12 cycles; 5 min à 72°C) pour créer la librairie de cRNA. Les amorces PCR en excès ont été éliminées par purification avec les billes SPRI select (Beckman-Coulter, Villepinte, France). La qualité et la quantité des librairies d'ADNc finales ont été vérifiées par électrophorèse capillaire. Le séquençage a été réalisé sur un séquenceur Illumina HiSeq 4000, produisant des lectures simples de 50 bases. L'analyse des images et le décodage des bases ont été effectués à l'aide du RTA version 2.7.7 et du bcl2fastq version 2.20.0.422.

3.2 Analyses différentielle des gènes et enrichissement

Pour l'analyse différentielle des gènes, les gènes ayant un log2FC supérieur à 1,5 ont été considérés comme significativement up-régulés, tandis que ceux ayant un log2FC inférieur à -1,5 ont été considérés comme significativement down-régulés. L'analyse d'enrichissement des gènes a été réalisée à l'aide du logiciel EnrichR. Les listes de gènes régulés ont été soumises à EnrichR pour identifier les voies biologiques et les processus associés. Les résultats ont été filtrés en fonction de la valeur p et du score combiné pour identifier les voies les plus pertinentes. Nous avons utilisé un seuil de valeur p ajustée inférieure à 0,05.

4. Analyse de l'activité d'un réseau de régulateurs spécifique des GB

Nous avons utilisé l'outil GBM-cReg, développé lors de nos recherches précédentes, pour une analyse approfondie du paysage régulateur dans diverses conditions expérimentales, en utilisant des données transcriptomiques. Cet outil emploie la fonction CoRegQuery avec le GBM-CoRegNet pour calculer l'influence des régulateurs dans le jeu de données entrant. L'influence de chaque régulateur est classifiée comme positive ou négative, offrant ainsi un aperçu de leur impact sur l'expression génique.

5. Affectation de classes basées sur l'activité d'un réseau de régulateurs

Des classes moléculaires basées sur l'activité d'un réseau de régulateurs spécifique des GB ont été attribuées à nos modèles d'étude en utilisant un modèle de Machine à Vecteurs de Support

(SVM). Ce modèle SVM a préalablement été entraîné sur une méta-cohorte de 1612 tumeurs de patients) et a par la suite été utilisé pour analyser les données des CSG dans diverses conditions expérimentales. Ce modèle évalue l'influence des régulateurs et attribue des classes aux échantillons individuels en fonction de leurs profils transcriptomiques. Lorsque le modèle SVM attribue des probabilités inférieures à 75%, ces échantillons sont catégorisés comme « Mixtes », indiquant une activité régulatrice complexe de l'échantillon qui ne correspond pas clairement à une classe spécifique.

6. Analyse de flux extracellulaire

Afin d'étudier le profil énergétique et la contribution des voies énergétiques (glycolyse et OXPHOS) de nos cellules, un analyseur Seahorse XFp (Seahorse Bioscience) a été utilisé. Cette appareil permet l'analyse en temps réel des taux de consommation d'oxygène (OCR) et des taux d'acidification extracellulaire (ECAR) de cellules souches ou adhérentes cultivées *in vitro* dans des microplaques. La veille de l'analyse, les cartouches XFp ont été hydratées dans de l'eau stérile dans un incubateur sans CO_2 à 37 °C. Le jour de l'analyse, les cellules ont été ensemencées sur les microplaques de culture Seahorse XFp (Agilent®) préalablement coatées au Cell-Tak à 22,4 µg/mL (Corning®) à raison de 60 000 cellules/puits dans leur milieu de culture spécifique. Après 45 minutes, le milieu a été remplacé par le milieu Seahorse XF DMEM (Agilent 103575-100) complété par 10mM de glucose (Agilent 103577-100), 2mM de glutamine (Agilent 103579-100) et 1mM de pyruvate de sodium (Agilent 103578-100). Les cellules ont été équilibrées dans un incubateur sans CO_2 jusqu'à leur analyse. L'eau stérile des cartouches a été remplacé par le calibrant (Aligent®) et les cartouches ont été replacées au sein d'un incubateur sans-CO_2 45 minutes à 1 heure avant analyse. Après ce délai écoulé, les cartouches ont été chargées avec les inhibiteurs métaboliques selon les instructions du fabricant. Les valeurs d'OCR et d'ECAR ont été obtenues au fil du temps dans chaque puits, au niveau basal, puis après injection des inhibiteurs métaboliques. Les données ont été analysées en utilisant Agilent Seahorse Analytics.

7. Métabolomique

7.1 Préparation des échantillons

Les cellules ont été ensemencées et incubées en normoxie ou en hypoxie pendant une semaine. Après une semaine, les cellules ont été collectées, comptées et centrifugées à 300g pendant 5

minutes. Des culots cellulaires d'environ 2 à 10 millions de cellules ont été lavés dans du Phosphate Buffered Saline (PBS), puis centrifugés à 300 g pendant 10 minutes à 4°C. Les culots secs ont été conservés à -80°C jusqu'à leur analyse. Quatre culots cellulaires à différents passages ont été préparés à partir des différentes lignées de cellules souches cultivées en normoxie. Deux culots ont été préparés pour les lignées cellulaires adhérentes cultivées en normoxie ainsi que les lignées cellulaires de type souche cultivées en hypoxie. Les cellules ont été transférées dans des inserts jetables HR-MAS Kel-f pré-pesés de 25 µL. Les inserts scellés ont ensuite été pesés pour déterminer la masse du culot, puis le volume des inserts a été complété avec de l'oxyde de deutérium (D_2O). Les inserts ont ensuite été stockés à -20°C jusqu'à l'analyse.

7.2 Spectroscopie RMN HR-MAS

Les expériences de RMN HR-MAS ont été réalisées sur un spectromètre Bruker Avance III fonctionnant à une fréquence protonique de 500,13 MHz, équipé d'une sonde HRMAS à triple résonance (^{1}H, ^{13}C, ^{31}P). La température a été maintenue à 277 K pendant toute la durée de l'acquisition afin de réduire la dégradation des cellules. Toutes les expériences ont été réalisées sur des échantillons tournant à 3502 Hz. Les paramètres des séquences utilisées sont décrits (Tableau 1). Les spectres ont été normalisés par rapport à la masse de chaque échantillon et étalonnés en utilisant une quantité définie de lactate comme référence.

7.3 Analyse et statistiques

L'identification des métabolites a été effectuée à partir de profils ^{1}H unidimensionnels et a été approfondie à l'aide de profils ^{1}H-^{13}C HSQC bidimensionnels. L'analyse en composantes principales (PCA) a été utilisée pour évaluer l'homogénéité des ensembles de données de RMN HR-MAS et exclure les valeurs aberrantes techniques ou biologiques (hors de l'intervalle de confiance de 95%). Une PCA a ensuite été utilisée pour identifier les principales sources de variance au sein des ensembles de données et les différences métabolomiques entre les échantillons. Des analyses statistiques multivariées ont été réalisées à l'aide d'une analyse PCA et de l'algorithme ADEMA. En outre, des analyses multivariées ont été réalisées à l'aide de l'algorithme ADEMA. L'algorithme ADEMA est basé sur l'information mutuelle et calcule les changements de niveau attendus pour chaque métabolite par rapport à une condition donnée, prend en compte plusieurs métabolites en même temps et est basé sur l'information mutuelle (MI). Le taux de fausse découverte (FDR) a été contrôlé à un niveau de 5%.

	^{1}H CPMG	^{13}C HSQC-2D
Temps de relaxation (D1 ; sec)	2	1,5
Champ RF présaturation (Hz)	50	50
Durée d'acquisition (AQ ; sec)	2,3396351	F2: 0,146; F1: 0,006
Échantillonnage	32768	F2 : 8192 ; F1 : 256
Largeur de spectre (SW ; ppm)	14,0019	F2: 14,0019 ; F1 : 165,65
Nombre de scans fictifs (DS)	4	64
Nombre de scans (NS)	1024	272
Durée d'expérience (EXPT)	1 h 16 min 38 sec	1 jour 8 h 45 min
Nombre de boucles (L4)	328	NA
Temps d'interpulse (µs)	143	NA

Tableau 1: Séquences d'impulsion et paramètres d'acquisition utilisées lors des expériences RMN HRMAS

8. Agents pharmacologiques et réactifs

Le témozolomide (TMZ) (réf. #T2577 ; Sigma Aldrich) a été préparé en le dissolvant dans du DMSO pour obtenir une concentration de 100 mM. Il a ensuite été conservé à -20°C jusqu'à son utilisation. Dans toutes les expériences menées, la concentration finale de DMSO dans le milieu de culture n'a jamais dépassé 0,1%.

L'oligomycine (réf. #75351), la roténone (réf. #R8875), l'antimycine A (réf. #A8674) et le FCCP (réf. #C2920) ont été achetés auprès de Sigma Aldrich. L'oligomycine et le FCCP ont été dissous dans du DMSO pour obtenir des solutions mères à 10 mM. L'antimycine A et la roténone ont été dissoutes respectivement dans de l'éthanol à 70% et 100% pour obtenir des solutions mères à 1 mM. L'ensemble des solutions a été stocké à -20°C et conservé pendant 2 mois.

La metformine (MET) (réf. #317240) et le dichloroacétate (DCA) (réf. #347795) ont été achetés auprès de Sigma Aldrich et ont été dissous dans les milieux de culture spécifiques à chaque lignée cellulaire pour obtenir une concentration de 10 mM.

9. Incucyte

Pour les expériences normoxiques et hypoxiques, les cellules ont été incubées dans un incubateur multi-gaz à CO_2 (HERACell VI0S 250i, ThermoFischer) et suivies par une évaluation microscopique en temps réel en utilisant la technologie Incucyte®. 3000 cellules souches/puits ou 15000 cellules adhérentes/puits ont été ensemencées dans une plaque 96 puits

et cultivées pendant 6 jours dans un incubateur à 37°C, 5% CO_2 en normoxie (20% O_2) ou en hypoxie (1% O_2). Les tests de prolifération cellulaire ont été réalisés par analyse en temps réel IncuCyte. La confluence des cellules adhérentes et la surface (mm^2) de la neurosphère ont été suivies avec un système d'analyse de cellules vivantes IncuCyte™ Zoom. La technologie IncuCyte® a pris des images toutes les 4 heures, la surface et la confluence cellulaire ont été mesurées puis normalisées au temps zéro. La signification statistique de la croissance tumorale du jour 0 au jour 6 a été analysée par des tests t appariés. La signification statistique entre les conditions normoxiques et hypoxiques a été réalisée à l'aide de tests t non appariés. $P < 0,05$ a été considéré comme significatif, *$P < 0,05$, **$P < 0,01$, ***$P < 0,001$, ****$P < 0,0001$. Les résultats sont présentés sous forme de moyenne et la barre d'erreur représente l'erreur standard de la moyenne (SEM). Graphpad Prism Version 8 a été utilisé pour analyser les données.

10. Test de sensibilité

Les tests de drogues ont été effectués par analyse en temps réel IncuCyte. Les cellules ont été ensemencées en présence ou en l'absence de différentes thérapies, seules ou en association. Concernant les tests de sensibilité au TMZ, le TMZ a été dilué dans le milieu spécifique à la lignée et les cellules ont été traitées avec des concentrations croissantes de TMZ (12,5, 25, 50 et 100 µM). Les cellules ont été placées (à raison de 3000 cellules par puits d'une plaque à 96 puits) directement en l'absence (contrôle DMSO) ou en présence de différentes concentrations de TMZ. La dynamique de croissance des CSG en réponse au TMZ a été évaluée à l'aide de la technologie Incucyte.

11. Western Blot

Les cellules ont été lysées dans un tampon d'échantillon Laemmli (Biorad) complété par du b-mercaptoéthanol à 5 % et les protéines ont été fractionnées par SDS-PAGE (20 %), transférées sur une membrane PVDF (GE Healthcare, Velizy, France), qui a été bloquée avec du lait écrémé à 5 % (p/v) dans du PBST pendant 1 h à température ambiante, sondée avec un anticorps primaire dans une solution de blocage pendant une nuit à 4 °C, incubés avec des anticorps secondaires conjugués à la peroxydase de raifort (HRP) (GE Healthcare) pendant 1 h à température ambiante et le signal chimioluminescent a été détecté à l'aide du système de chimioluminescence améliorée (ECL™ Prime Western Blotting System, GE Healthcare Bioscience) avec un analyseur ImageQuant™ LAS 4000 (GE Healthcare). La quantification des images non saturées a été réalisée à l'aide du logiciel ImageJ (National institutes of Health,

Bethesda, MD, USA). Pour chaque expérience, 3 lysats provenant de différentes cultures cellulaires ont été utilisés. Les protéines a-tubuline ou la GAPDH ont été utilisées comme contrôle de charge pour tous les échantillons. Les anticorps utilisées pour ces expériences sont décrits (Tableau 2).

Protéine cible	Fournisseur	Référence	Espèce	Dilution
α-Tubulin	Sigma-Aldrich	T9026	Mouse	1/3000
CD133	Biolegend	372802	Mouse	1/1000
EGFR	Ozyme	D38B1	Rabbit	1/1000
GAPDH	Millipore	MAB374	Mouse	1/3000
GFAP	Merck	MAB360	Mouse	1/1000
HK2	Proteintech	22029-1-AP	Rabbit	1/5000
Integrin α5	Cell Signaling	D7B7G	Rabbit	1/1000
LDHA	Proteintech	19987-1-AP	Rabbit	1/5000
NKX2-5	Cell Signaling	E1Y8H	Rabbit	1/1000
OCT4	Cell signaling	2750S	Rabbit	1/1000
SOX2	Cell Signaling	2748S	Rabbit	1/1000
IgG-HRP anti-mouse	Promega	W4018	Goat	1/10000
IgG-HRP anti-rabbit	Promega	W4028	Goat	1/10000

Tableau 2 : Liste des anticorps utilisés pour Western Blot

12. NKX2.5

12.1 Plasmides

Des plasmides codant pour la protéine d'intérêt NKX2.5 ont été acquis auprès de la société Proteintech. Pour produire une quantité suffisante de plasmides pour nos expériences, nous avons procédé à leur amplification par transformation bactérienne. Les plasmides ont été introduits dans des bactéries compétentes par choc thermique. Les bactéries transformées ont ensuite été cultivées sur un milieu sélectif contenant l'antibiotique pour sélectionner uniquement les bactéries transformées. Suite à la croissance des colonies bactériennes, l'extraction des plasmides a été effectuée à l'aide d'un kit d'extraction d'ADN standard selon les instructions du fabricant. Les plasmides extraits ont ensuite été quantifiés et leur qualité a été vérifiée par électrophorèse sur gel d'agarose après digestion avec des enzymes de restriction.

12.2 Transfection cellulaire

La transfection cellulaire consiste à introduire un ou plusieurs fragments d'ADN exogènes dans les cellules. La technique repose sur l'inclusion de plasmides dans des liposomes, qui vont ainsi pouvoir rentrer dans la cellule par endocytose ou par fusion du liposome avec la membrane plasmique. L'expression du matériel transfecté n'est que transitoire car le plasmide ne s'intègre pas au génome de la cellule. Les cellules ont été ensemencées dans des plaques 6 puits à raison de 0,5.106cellules/puit. Elles sont transfectées 24h après ensemencement, avec l'agent de transfection lipofectamine 2000 (ThermoFisher) dans un milieu Opti-MEM™ I Reduced-Serum Medium (Thermo Fisher Scientific). Les cellules ont été transfectées avec le plasmide NKX2.5 ou le plasmide vide. Un contrôle avec du milieu optiMEM seul ainsi qu'un contrôle lipofectamine seul ont été réalisées. Les cellules sont ensuite incubées pendant 24h. Le plasmide pcDNA3.1(+) NKX2.5 et pcDNA3.1(+) pneg ont été commandé sur ProteoGenix ou produit par transformation bactérienne et amplification

13. RT-qPCR

Les cellules sont ensemencées dans une plaque 6 puits avec une densité de 0,5 million de cellules par puits et sont cultivées dans un milieu optiMEM pur, ou supplémenté de lipofectamine 2000 (Thermofisher), du plasmide négatif (5 µg) ou du plasmide NKX2.5 (5 µg), pendant une période de 24 heures. Les cellules sont ensuite lavées avec du PBS 1X puis lysées avec 350 µl de tampon RLT provenant du kit d'extraction (RNEasy Plus Mini Kit, Qiagen). La procédure RNeasy est une technologie bien établie pour la purification de l'ARN. Cette technologie associe les propriétés de liaison sélective d'une membrane à base de silice à la rapidité de la technologie microspin. Les échantillons biologiques sont d'abord lysés et homogénéisés en présence d'un tampon contenant du guanidine-thiocyanate fortement dénaturant (tampon RLT), qui inactivera immédiatement les RNAses pour assurer la purification d'un ARN intact. De l'éthanol est ajouté pour fournir des conditions de liaison appropriées, et l'échantillon est ensuite appliqué sur une colonne de spin mini RNeasy, où l'ARN total se lie à la membrane et les contaminants sont efficacement éliminés par lavage. L'ARN de haute qualité est ensuite élue dans 100 µl d'eau. La quantité d'ARN extraite est ensuite déterminée par spectrophotométrie UV-Visible, en utilisant le NanoDrop™One (ThermoFisher). La transcription inverse est ensuite réalisée avec le kit iScript™ Reverse Transcription Supermix (BioRad), en utilisant 1 µg d'ARN. Les échantillons sont ensuite placés dans un thermocycleur (T100, Biorad) pour la réaction de transcription inverse selon le

programme iScript : une phase de priming (5 minutes à 25°C), une activation de la transcriptase inverse (46 minutes à 46°C) et une inactivation de la transcriptase inverse (1 minute à 95°C). La qPCR (PCR quantitative ou PCR en temps réel) est effectuée en utilisant un mélange réactionnel comprenant les amorces spécifiques (Tableau 3) et le SYBR GreenTM comme réactif. Pour chaque puits d'une plaque optique MicroAmpTM de 96 puits (Applied BiosystemsTM), 15 µl de ce mélange sont déposés. L'ADNc, préalablement obtenu par transcription inverse, est dilué 5 fois avec de l'eau exempte de RNase. Ensuite, 5 µl de cette solution diluée sont ajoutés à chaque puits, permettant d'atteindre une concentration finale de 50 ng par puits. La qPCR est effectuée à l'aide du StepOnePlus^{TM} (4376357, Thermofisher) et du logiciel StepOneTM (v2.3). L'ARN18S a été utilisé comme contrôle endogène.

Gène cible	Fabriquant	Référence	Amorces/Transcrit détecté
RNA18S	Invitrogen Thermo Fisher	426826 Y4744 (D03) 426826 Y4744 (D04)	5'-TGTGGTGTTGAGGAAAGCAG-3' 3'-TCCAGACCATTGGCTAGGAC-5'
GAPDH	Invitrogen Thermo Fisher	710832 L3872 (H11) 710832 L3872 (H12)	5'-GTCACCAGGGCTGCTTTTAACTCT-3' 3'-GGAATCATATTGGAACATGTAAACCAT-5'
GPI	Qiagen	PPH00897C	NM_000175.3
HK2	Qiagen	PPH00983B	NM_000189.4
LDHA	Qiagen	PPH02047H	NM_005566.3
TPI1	Qiagen	PPH02051A	NM_000365.5

Tableau 3 : Liste des primers utilisés pour la qPCR

RÉSULTATS

Partie 1 : Hétérogénéité et plasticité moléculaire des glioblastomes : une exploration basée sur l'activité d'un réseau de régulateurs

Contexte de l'étude

Afin de mieux comprendre l'hétérogénéité et la plasticité moléculaire des GB, un projet collaboratif avec l'équipe du Professeur Elati, expert en bioinformatique au laboratoire CANTHER de Lille, a été entrepris. L'hétérogénéité et la plasticité des tumeurs sont deux défis majeurs en neuro-oncologie. Ces phénomènes contribuent significativement à la malignité prononcée et à la résistance aux thérapies de ces tumeurs. Le projet a débuté par une analyse approfondie des données transcriptomiques extraites de la base de données CCLE 2019Q1, qui porte sur des dizaines de lignées cellulaires de GB. Une approche par biologie des systèmes, orchestrée par l'équipe de bioinformaticiens de Lille (équipe CANTHER), a permis de tisser un réseau de régulateurs et de co-régulateurs hautement spécifiques au GB, dévoilant un paysage moléculaire complexe. En exploitant les profils d'expression génique, nous avons réussi à prédire l'activité des régulateurs, déterminant s'ils sont actifs (indiqués en rouge) ou inactifs (marqués en bleu), ainsi que l'influence des régulateurs sur leurs gènes cibles, notamment en termes de répression ou d'activation de leur transcription. En intégrant l'analyse de milliers d'échantillons de tumeurs de patients grâce à la base de données GlioVis, une classification innovante des GB en sept sous-classes a été établie, chaque sous-classe se distinguant par des activités régulatrices propres, ainsi que par des caractéristiques moléculaires et biologiques uniques.

A co-regulatory influence map of glioblastoma heterogeneity and plasticity

Chloé Bernhard*[1], Konstantinos Geles*[2], Geoffrey Pawlak*[2], Silvia Anna Ciafrè[3], Wajdi Dhifli[2], Aurélien Dispot[2], Christel Herold-Mende[4], Maria Kondratova[2], Sophie Martin[1], Mélissa Messé[1], Damien Reita[1,5], David Tulasne[2], Isabelle Van Seuningen[2], Monique Dontenwill[1#], Mohamed Elati[2#@]

1. UMR7021 CNRS, University of Strasbourg, Illkirch, France
2. Univ. Lille, CNRS, Inserm, CHU Lille, UMR9020-U1277 – CANTHER – Cancer Heterogeneity Plasticity and Resistance to Therapies, Lille F-59000, France
3. Dept. of Biomedicine and Prevention, University of Rome "Tor Vergata", Rome, Italy
4. Division of Neurosurgical Research, Department of Neurosurgery, Heidelberg University Hospital, 69120 Heidelberg, Germany
5. Department of Cancer Molecular Genetics, Laboratory of Biochemistry and Molecular Biology, University Hospital of Strasbourg, 67200 Strasbourg, France

In preparation for submission

** These authors contributed equally to the work*

 # These authors co-supervised the study

@ To whom correspondence should be addressed.

ABSTRACT

We present GBM-cRegMap, an online resource offering a comprehensive co-regulatory influence network perspective on Glioblastoma (GBM) heterogeneity and plasticity. By leveraging representation learning algorithms, we derived two components: GBM-CoRegNet, a highly specific co-regulatory network of tumor cells, and GBM-CoRegMap, a unified network influence map comprising 1612 tumors from 16 studies. By applying GBM-cRegMap, we illustrated the synergy between the two components by refining GBM molecular classification, pinpointing potential key regulators, and aligning the transcriptional profiles of tumors and in vitro models. By amalgamating a vast dataset, we validated proneural (PN)-mesenchymal (MES) axis and identified three subclasses within the classical (CL) tumours (astrocyte-like (CL-A), epithelial basal-like (CL-B), and ciliary-rich (CL-C)) as well as a neural normal-like subclass (NL). As a widely applicable closed loop, spanning preclinical models to tumors and back, GBM-cRegMap has been provided to the GBM research community as an easy-to-use web tool (https://gbm.cregmap.com).

INTRODUCTION

Glioblastoma (GBM), the most common and aggressive brain and central nervous system malignancy, represents a significant challenge in neuro-oncology. Accounting for 48.6% of malignant brain tumors

and 57.7% of all gliomas, GBMs is among the most lethal and aggressive forms of cancer. Despite standard therapy (Stupp protocol, which combines surgery, chemotherapy, and radiotherapy), most patients succumb within 15 to 18 months[1]. Intrinsically, GBMs exhibit highly heterogeneous histopathology and molecular characteristics. Current approaches struggle to capture the full complexity of GBM, often leading to an incomplete understanding and limited therapeutic options. The diversity of GBM is multi-faceted, encompassing population heterogeneity, intra-tumoral heterogeneity, tumor plasticity, and the influence of the microenvironment and therapy. These facets, which impact clinical outcomes and tumor progression, require comprehensive exploration. This heterogeneity underscores the need for a comprehensive and in-depth understanding of the molecular landscape of GBM to develop more effective therapeutic strategies.

Past research has attempted to classify GBM into subtypes based on bulk gene expression profiling with varying degrees of success. The Philips group first defined three major tumor subsets: proneural, mesenchymal, and proliferative[2]. Later, Verhaak et al.[3] proposed a classification encompassing four subtypes: proneural (PN), neural (NEU), classical (CL), and mesenchymal (MES), which was subsequently revised to three subtypes, excluding the Neural subtype[4]. Further nuances in GBM classification arise from considering additional parameters, such as the glioma CpG island methylator phenotype (G-CIMP). More recent single-cell studies have revealed additional layers of intra-tumoral heterogeneity due to the co-existence of immune cells, as well as plasticity of transcriptional programs within the same tumor. Neftel et al.[6] deconvolute the phenotypic states of GBM cells into four major lineage-specific cellular identities: astrocyte-like (AC), mesenchymal-like (MES), neural progenitor cell-like (NPC) and oligodendrocyte progenitor cell-like (OPC). The Lavarone group[7] uncovered based on the most active pathways four states along two axes, a metabolic axis including mitochondrial (MTC), and glycolytic/pluri-metabolic (GPM) and a neurodevelopmental axis including proliferative/progenitor (PPR) and neuronal (NEU) states. However, despite ultimately proposing the same number of subtypes, the four classification schemas are largely non-overlapping, failed to predict survival and inform on pharmacologic vulnerability. Except, the MES subtype has been reproducibly identified across the different studies, with the worse prognosis.

These observations imply that promising route for dissecting GBM heterogeneity is to understand the gene regulatory networks (GRN) that give rise to different molecular subtypes and cell states. GRN provides a conceptual modelling framework and toolkit for abstracting, inferring, integrating, and interpreting data representing these complex biological systems. To date, computational approaches that have proven successful are those that allow for the reverse-engineered construction of context-specific GRN (e.g., ARACNe[8] and LICORN[9,10] using a bulk-transcriptome and SCENIC[11] using single-cell data). A second key breakthrough in regulatory network exploration made possible by CoRegNet[12,13] and VIPER[14] was the consideration of the activity of regulators, rather than just their

expression, based on evaluations of the expression of target genes, with the aim of detecting master regulators. In the context of GBM, numerous recent studies have relied on the inference of PN/MES subtype-specific regulatory networks, mostly from TCGA patient or single-cell data. Using SCENIC, three important transcriptional factors have been identified: *FOSL2*, *CEBPB*, and *EPAS1*, which are dominant in mesenchymal cells[15]. Similarly, previous studies using ARACNE have confirmed that *CEBPB* and *STAT3,* the master regulators, cooperate with *FOSL2* to mediate PN to MES transition[16].

Therefore, we argue that the application of omics and systems biology approaches has significantly contributed to GBM research. However, the field now faces a challenge in that data and knowledge are distributed across numerous studies and databases. Each study showed a notable increase in data size, complexity, and specificity. Consequently, fostering collaboration among biologists necessitates a concerted effort to centralize data from these investigations into an easily accessible and intuitive system-level approach. Centralization serves as a crucial prerequisite for constructing comparable and comprehensive oncological system models. To tackle this challenge, we introduced GBM-cRegMap, a robust web-based tool designed to allow researchers to rapidly access a unified co-regulatory influence network view of GBM cancer. GBM-cRegMap delves into representation learning, a pivotal aspect of machine learning, in which algorithms extract significant patterns from raw data and transform them into more interpretable, accessible, and shared representations. The GBM-cRegMap tool incorporates the workflow illustrated in Fig. 1A, integrating data from over 20 transcriptome studies of tumors and cell lines (Supplementary Table S1). The GBM-cRegMap tool enables users to explore similarities and differences between subtypes, identify possible core regulators, detect rare subtypes, align tumors with cell line transcriptomic profiles, and define new targets associated with different tumor states and plasticity. The GBM-cRegMap boasts an intuitive interface that is accessible to users without expertise in bioinformatics. For all generated networks and plots, users can run various annotations, add new data, and download the raw data necessary to reproduce the plots in future analyses or publications. The wide range of computational network biology, machine learning, visualization, bioinformatics software, and resources required to achieve this are listed in Supplementary Table S2.

We validated the utility of this tool by proposing an alternative description of GBM cancer heterogeneity based on regulatory network activities that are detectable across cohorts. Additionally, we identified new targets associated with different tumor states, plasticity, and resistance to therapy, showcasing the versatility and significance of GBM-cRegMap in advancing our understanding of GBM at the system level.

RESULTS

Representation Learning and Evaluation of GBM-cRegMap Reference Components.

Using h-LICORN, we first generated a gene regulatory network (GRN) from the transcriptome of 42 GBM cancer cell lines from CCLE 2019Q1 with a curated list of regulators composed of transcription factors (TFs) and co-factors (co-TFs) (n = 2,375). We used transcriptomes from GBM tumor-derived cell lines to strengthen the signal specific to GBM cells and to prevent the introduction of possible bias due to the use of less homogeneous transcriptomic data from GBM tumors containing the contribution of non-specific signals and signals associated with the tumor microenvironment. The resulting GRN was composed of 539 co-regulators (Supplementary Table S3), 8269 target genes and 32360 regulatory interactions were significantly enriched in validated TF-gene interactions and transcription factor-binding sites ($p < 1e\text{-}100$). Based on the shared targets of each pair of TFs/co-TFs (Supplementary Table S4), the GBM-GRN was transformed into a co-regulatory network (GBM-CoRegNet) using the CoRegNet package[13]. GBM-CoRegNet (Fig. 2A) contains 2171 co-operativity interactions enriched in PPIs ($p < 1e\text{-}100$). Moreover, the functional enrichment analysis unveiled a substantial enrichment (adjusted p-value < 0.01) of biological processes related to GBM within the identified TFs/co-TFs. These processes include neuron differentiation (GO:0030182), mesenchymal cell differentiation (GO:0048762), central nervous system development (GO:0007417), as well as aspects of the GBM microenvironment such as cellular response to Hypoxia (GO:0071456) and cellular response to oxidative stress (GO:0034599). Additionally, core pathways implicated in GBM, including NOTCH, Wnt, and PTEN/PI3K/Akt, exhibited significant enrichment. Furthermore, many regulators with the largest number of target genes, such as *CCND1*, *SOX2*, *GATA3*, *MYC*, *SNAI2*, *MEF2C*, *FOSL2*, *CEBPB*, and *EPAS1*, have already been shown to be associated with GBM[4,6,15,16]. This demonstrates that the inferred GBM-CoRegNet is biologically representative.

Next, we compiled a GBM meta-cohort from 16 GBM tumor cohorts (Supplementary Table S3) and computed sample-independent gene regulatory influences using the inferred GBM-GRN (see Methods). Although the 2021 WHO-CNS[17] edition no longer classifies IDH-mutant gliomas as GBM, we included these tumors in our cohort to comprehensively explore the molecular landscape of high-grade gliomas. The resulting meta-cohort influence data achieved both significant feature reduction and sample size augmentation (single GBM bulk expression cohort: <500 samples x $\simeq 18000$ features vs. meta-cohort influence data: 1612 samples × 539 features). Because of its greater sensitivity, as well as its ability to capture both local and global relationships[18], we use Uniform Manifold Approximation and Projection (UMAP)[19] to visualize the meta-cohort influence data in two-dimensional embedded space, hereafter denoted as "GBM-CoRegMap". To ensure that the resulting GBM-CoRegMap simulates tumor heterogeneity and does not result from potential confounding factors, we annotated samples according

to Verhaak subtypes using their published gene expression classifier. Fig. 2B-C, shows that GBM-CoRegMap successfully removed batch effects and recapitulated the state-of-the-art heterogeneity of GBM. Furthermore, in comparison to gene expression, an influence-based Verhaak subtypes classifier achieved a 33% average increase in cross-batch prediction performance, as evaluated using area under curve measure (AUC) with the PAMR (prediction analysis for microarrays) classifier (Supplementary Table S5). Consistent with the GBM literature[4,6], the subtype showing the highest homogeneity were the MES and the lowest were the CL and NEU subtypes, as shown in Fig. 2C, pointing to the need for refinement of the Verhaak classification. The large sample size of the GBM-CoRegMap allows for greater statistical power in subtype identification and minimizes sampling bias[20].

A Meta-Cohort Analysis of 1612 Tumors Refines GBM Molecular Classification into Seven Classes with Biological and Clinical Relevance.

GBM-cRegMap-based unsupervised clustering resulted in seven distinct molecular classes (Fig. 2C-D). These classes were named according to Verhaak's prior subtyping. These seven molecular classes exhibited varying sample sizes, with the following distribution: 17% proneural (PN), 6% proneural-low proliferative (PN-L), 11% normal-like neural (NL), 18% classical-astrocyte-like (CL-A), 9% classical-basal-like (CL-B), 14% classical-cilia-rich (CL-C), and 25% mesenchymal (MES). We initiated our analysis by characterizing the GBM-cRegMap classes at both transcriptomic (Fig. 3A, Supplementary Tables S6-7) and genomic (Fig. 3C) levels, leading to the identification of associated pathways and biological processes (Fig. 3B-D). Subsequently, we examined the cellular state as described by Neftel et al.[7] single cell study (Fig. 3D), cellular immune components of the tumor microenvironment (TME) (Fig. 3D-F), and clinical outcome (Fig. 3E).

The PN, PN-L, and NL subclasses are primarily characterized by attributes of developmental processes, including proneural, gliogenesis, and neural signatures. The PN and PN-L subclasses comprised the majority of the PN_Verhaak tumors, indicating a further subdivision of the proneural subtype into two distinct entities[4].They also correlated as progenitor cell states (NPC- and OPC-like), as described by Neftel et al.[7]. The PN subclass is enriched in cellular division and mitotic cell cycle pathways, expressing the highest levels of proliferation markers *MKI67* and *DLGAP5*. In contrast, PN-L exhibited a low proliferative state. Both subclasses exhibited a high frequency of *TP53* mutations (> 59%) compared with the other subtypes (0–32%). *PDGFRA* mutations were almost exclusive to the PN subclass (PN: 16%, PN-L: 0%), whereas mutations in IDH1 were more frequent in PN-L (PN-L: 52%, PN:14%). The NL subclass comprised 42% of NEU_Verhaak subtype, harboring a distinct cluster of GBM with a 'normal-like' transcriptomic profile enriched in neuron developmental-associated pathways and neurogliomal synaptic communication. We identified common genes signature with the newly identified ‘normal-like’ IDH-WT subtype by Nguyen et al.[21], such as *SLC32A1* (vesicular gamma-

aminobutyric acid transporter) and *SYT5* (synaptotagmin 5). We identified mutations in *PTEN* in 57% of our NL cases. Moreover, mutations in *STAG2* were more frequent in this subgroup, observed in 21% of cases. While *STAG2* deficiency characterizes only a small subset, increasing preclinical evidence supports its role as a driver of tumor formation and resistance to standard therapies. This finding is particularly noteworthy given the growing body of preclinical evidence suggesting that *STAG2* mutations may play a critical role in tumor formation and treatment resistance[22,23]. Our identification of this mutation within the NL subclass underscores the need for further investigation of its role and potential as a therapeutic target. The CL-A, CL-B, and CL-C subclasses comprised the majority of CL_Verhaak tumors. These three subclasses showed similarity to the genetic patterns of the Classical Verhaak subgroup with high *EGFR* alteration rate and lower rate of *TP53* for CL-A and CLA-B (Fig. 3C). In contrast to the CL-A subclass, the CL-B and CL-C are distributed orthogonally across the Verhaak subtypes. More importantly, these three subclasses define previously unknown GBM subtypes that reveal the tumor microenvironment and metabolic, mutational, and clinical information. The CL-A subclass enriched in an astrocyte-like meta-signature (Fig. 3D, Cellular State score[24]), cell migration signature, and pronounced activation of the *EGFR*, Sonic hedgehog, and MAPK signaling pathways (Fig. 3A). It also showed upregulation of *MEOX2* homeobox TF and fatty acid synthesis genes (*ELOVL2, ACSL3, PLA2G5*), and high expression of the stem cell markers NES and Notch (Fig. 3A). The CL-B demonstrates enrichment in factors associated with stem cell survival (*SERPINB3*, *NANOG*, *SALL4*), the coagulation pathway, keratinization, and cell-cell adhesion (Fig. 3A) – features commonly expressed in basal squamous epithelial cells[25–27]. Moreover, its enrichment in the oxidative phosphorylation (OXPHOS) pathway signature might associate CL-B with a mitochondrial subtype that could be potentially treated with specific mitochondrial inhibitors[28]. Notably, pseudo-epithelial and epithelial morphologies, although uncommon in GBM, are acknowledged as subtypes in the 2021 WHO classification of CNS tumors and are potentially associated with poorer prognoses[29]. Unlike CL-A and CL-C, CL-B did not overexpress EGFR and exhibited a lower mutation rate (CL-A: 41%, CL-B: 21%, CL-C: 32%); instead, it showed an increased mutation rate of *FLG* (CL-A: 14%, CL-B: 26%, CL-C: 13%) and an exclusive mutation rate of *NRAS* (4%) and *PPARG* (2%). The CL-C (cilia-rich) subclass was notably enriched in unexpected processes linked to cilia, including cilia assembly, movement, and organization, along with OXPHOS, lipid metabolism, and dopamine metabolic processes (Fig. 3A-B-D, Supplementary Table S7). The transcriptional CL-C landscape is further shaped by the activation of pivotal cell signaling pathways, such as *STAT3* and *RPS6KA1*, and epigenetic regulators, such as *HDAC1, HDAC5, CBX4, and SUV39H2*. Prominent genes upregulated in this subtype, including *DDIT4L* and *LGR6* (known to facilitate DNA repair and chemoresistance[30,31]) and *ETNPPL* (a negative regulator of glioma growth[32]), further characterize the CL-C subclass. Unlike the other two classical subclasses, CL-C exhibited a lower proliferative signature ($p < 0.01$) and increased mutation rates of *TP53* (CL-A: 14%, CL-B: 19%, CL-C: 32%) and *DNAH9* (CL-C: 7%). In Parkinson's disease, the primary cilium plays a pivotal role in mediating cellular reactions to oxidative stress, thereby supporting

the survival of dopamine neurons[33]. Recent studies have linked suppressed ciliogenesis in glioma stem cells (GSCs) to continuous self-renewal, while restoring ciliogenesis shifts GSCs towards the differentiation state, suggesting that cilium-targeting could be a potential treatment for GSCs proliferation[34]. Finally, the MES subclass strongly aligns with the MES_Verhaak subtype, the Lavarone and the single-cell MES-like state. This alignment reflects reported mesenchymal identity features, such as an increased mutation rate and reduced NF1 expression[3]. The MES subclass is enriched in the epithelial-mesenchymal transition (EMT) and immune-associated pathways. It also showed a preference for glycolysis/hypoxia-related functions and lipid metabolism, but showed no enrichment for the OXPHOS signature (Fig. 3A-B-D, Supplementary Table S7).

To characterize the cellular components of the TME in each GBM subclass, we inferred the fraction of cellular states and stromal/immune cells using GBMdeconvoluteR[24] and consequently tumor cell purity by applying PUREE[35]. PN is enriched with neural-progenitor-like (NPC) cells, while the PN-L subclass is associated with the presence of oligodendrocytes. CL-A was enriched in astrocyte-like cells (AC). Similarly, the activated dendritic cell gene signature was significantly greater in the CL-B subtype, suggesting that this subtype may benefit from dendritic cell vaccines. CL-C is enriched in mast cells. MES is associated with macrophage, monocyte, and immune cell infiltrations. The NL subclass was associated with the presence of B cells, in line with a previous study[21], suggesting a distinct immunological profile for NL gliomas (Fig. 3D). NL and MES had the lowest tumor purity, followed, in increasing order, by PN-L, CL-B, and CL-C, whereas CL-A and PN showed the highest tumor purity (Fig. 3F).

To determine the impact of our GBM refined classification on clinical outcomes, we used the log-rank test and compared the results with Verhaak's classification (Fig. 3E). In terms of overall survival, the best outcome was associated with the PN-L subclass (Fig. 3E, $p<0.001$). By contrast, the CL-C subclass, along with MES and CL-A, was associated with the worst outcomes. Although Verhaak's and Lavarone's classifications categorized CL-B, and CL-C subclasses as CL and MTC respectively, our subdivision highlighted a clear difference in the overall survival distribution between these two subclasses. We also confirmed previously reported associations with sex and age (Supplementary Table S8), such as the MES subclass being overrepresented in male samples, while the median age of the patients was shown to be lower for the PN and PN-L subclasses than for the others. Interestingly, CL-A did not show gender differences with respect to other subclasses.

To study the subclass switch resulting from tumor progression, we examined 96 matched primary and recurrent GBM samples. The evolutionary trajectory of recurrent GBM (Fig.3G, Supplementary Table S9) was marked by a significant decrease (~80%) in the CL-A class (from 14.9% to 3%), followed by 43% of the CL-C class (from 20.9% to 11.9%), and an even greater increase in the NL class, more than

80% (from 3% to 22.4%). The MES class was mainly stable (following previously identified rates), showing a lower increase of ~20% (from 22.4% to 26.9%), and the PN class remained stable, with an even lower increase of 7% (from 20.9% to 22.4%). Approximately 60% of recurrent NL samples were derived mainly from the CL-B and CL-C classes.

Definition of GBM Subclass-Specific Differential Subnetworks and Corresponding Cell Line Repertoires

To gain insight into subtype-specific active co-regulatory networks, first, differentially influent regulators (DIRs) were inferred using the Seurat::findmarker function[18] with the default Wilcoxon rank-sum test (Fig.4A, Supplementary Table S10). We then took advantage of publicly available data[36] regarding the effect of CRISPR-Cas9-mediated knockout (AVANA 19Q4 DepMap data) of the selected regulators on our defined GBM-derived cell lines for each subclass (Fig. 4B). CoRegQuery was assigned with high confidence and robustness (Supplementary Table S11) a specific class to 27 of 42 GBM Cancer Cell Lines (GBCCL), revealing a heterogeneous pattern of subclasses across the GBM cell line panel (Fig. 4C). The PN co-regulatory subnetwork confirmed their high-proliferation state, visible on transcriptomic analysis, composed of cell cycle, survival, and proliferation markers such as *CCND1*, *CDC6*, *FOXM1*, *BIRC5*, *and E2F7*. In addition, several regulators with unexplored roles in the PN subtype (e.g., *PA2G4*, *DEPDC1*, *ATAD2*, and *TFAP2C*) have been identified, which are predominantly involved in cell division, cell cycle, and proliferation. The PN-L class is characterized by high activity of transcriptional regulators implicated in the negative regulation of DNA-templated transcription, such as *SALL2*, *ZNF704*, *GBX2*, and *CREB3L4*, with an expected downregulation of PN cell cycle regulation and proliferation-associated TF-co-TFs. CRISPR-Cas9 AVANA 19Q4 analysis showed a greater dependence on *ZNF536*, *HOXA2*, and *PBX4* for PN cell lines. The NL co-regulated subnetwork comprised *PRDM16*, *SP100*, *TNIP1*, *ZFP3*, *MEIS3*, *POU3F3*, *SNCA*, *ZNF704*, *TRB23*, and *ZNF711* regulators. Genes such as *PRDM16* and *MEIS3* are instrumental in cell-lineage development and fate decisions. *PRDM16*, in particular, is linked to stem cell maintenance and cellular differentiation[37]. *SP100* and *SNCA* correlate with reduced malignancy in GBM cell line[38,39] hinting their potential role in mitigating malignancy within this class. Moreover, in the NL class, *SMAD3* has emerged as a regulator associated with favorable prognosis. Its inhibition, coupled with the stimulation of the neurogliomal circuit, accelerates tumor progression[40]. Unsurprisingly, *SNAI2*, *PAX8*, *FOSL2*, *EPAS1*, *RUNX2*, *and EGFR* were associated with the top-ranking influence score for MES-specific regulators, but also with the top dependency scores, highlighting their known roles in the mesenchymal state. Note that the user can explore any gene viability score using the GBM-CoRegMap tab, as well as the calculated influence scores. As an example, we here used MES TF *SNAI2* (Fig. 4D). Further data established the role of the hypoxic tumor microenvironment in MES GBM, which is suggested by the inclusion of *EPAS1* in the MES co-regulated subnetwork, and of *CEBPD*, recently identified as a master transcription factor for hypoxia-regulated genes in GBM[41].

Unlike the Proneural/Mesenchymal axis, few TFs/co-TFs have been characterized as key regulators of Verhaak-Classical tumors. Our analysis revealed that the CL-A co-regulated subnetwork included epigenetic modifiers, such as *DLX1* and *HDAC10*, as well as *NKX2-2* and *GLIS1* (Fig. 4A, Supplementary Table S10). CRISPR-Cas9 analysis confirmed the crucial roles of *HDAC10*, *ZNF671*, and *ZNF181* in this class (Fig. 4B). The CL-B co-regulated subnetwork includes *HDAC10*, *PRAME*, *PPARG*, *SALL1*, and *STAT6*. CRISPR-Cas9 analysis confirmed that the main regulators of CL-B were *LBX2*, *HES4*, and *PITX1*. Notably, the CL-B subclass features high activity of the transcription factor *PPARG*, a master metabolic regulator implicated in tumor stromal-epithelial crosstalk and carcinogenesis[42]. Furthermore, the CL-B class relies heavily on *PRAME* regulator (Fig. 4B), an oncoprotein linked to advanced tumor stages and poor prognosis, underlining its clinical relevance[43]. The CL-C co-regulated subnetwork included *PAX6*, *HDAC5*, *POU3F2*, *SOX2*, *NKX2-5*, *EBF4*, and *GLIS2*. CRISPR-Cas9 analysis (Fig. 4B) showed that the main regulators of CL-C were *PAX6*, *POU3F2*, and *ZNF580*. Within this subclass, *SOX2* exerts a significant regulatory influence, maintaining the ability of bidirectional conversion between stem and differentiated states, thus promoting the aggressiveness of this subclass[44].

Phenotypic Plasticity upon GSC Differentiation and Chemotherapy Treatment

At the cellular level, the malignant characteristics of GBM are largely attributed to the GBM stem cells (GSCs). These cells, endowed with stem-like properties, can self-renew, generate diverse cancerous cell populations, and initiate tumors in vivo[45]. The GSC lines NCH644 and NCH421k, when cultured as neurospheres (NS), a condition that preserves their stem-like state, as evidenced by the expression of stem cell markers such as SOX2, CD133, and Nestin, were found to align with the PN subclass and CL-B/C, respectively. The predicted molecular subclass of NCH644 in the stem state is consistent with previous work described by Herold-Mende et al.[46] (Fig. 5A). However, upon differentiation induced by FBS, a distinct shift in the regulatory networks was observed. After differentiation, NCH644 may shift to the MES subclass, whereas NCH421k moves to the CL-C subclass. This transformation was evident not only at the regulatory network level, but also in their phenotypic features (Fig. 5B). When cultured in monolayer conditions followed by differentiation, as evidenced by the expression of the differentiation marker GFAP, NCH644 cells displayed astrocytic traits and significant ITGA5 expression, a mesenchymal marker not found in NCH421k cells. Moreover, differentiated NCH421k cells, which belong to the CL-C subclass characterized by a low proliferation signature, exhibited reduced proliferation compared to NCH644 cells (Fig. 5C). This study highlights the plasticity of GSCs during differentiation, and the correlation between specific subclasses and phenotypic features[46].

Next, we utilized the CoRegQuery function to examine transcriptomic data obtained from our previous work[47], where we compared the untreated U87MG cell line with its TMZ-resistant variants, U87MG-R50 (continuously exposed to 50 μM TMZ) and U87MG-OFF (post-TMZ removal), to gain insight into

the regulatory mechanisms behind treatment resistance. We found that the TFs/co-TFs influence the network in U87MG-OFF cells more closely resembled that of naive U87MG cells, potentially due to both being cultured without TMZ, in contrast to the U87MG-R50 cells grown with TMZ (Fig. 6A). In response to TMZ treatment and the resistance phenotype, the activated subnetwork included MDM2, CDKN2B, NKX2-5, CCNE1, AJUBA, and TP63. Conversely, the repressed subnetwork included PAX8, EGFR, AHR, SMAD3, CCND1, and FOSL1 (Fig. 6B). Regulatory network analyses identified MDM2 as one of the most deregulated regulators between TMZ-resistant and TMZ-sensitive cell lines, highlighting elevated MDM2 activity in TMZ-resistant cell lines compared to that in TMZ-sensitive cell lines. This observation aligns with that of a previous study that highlighted MDM2's role in TMZ resistance via the p53 pathway[47]. Our findings emphasize the potential of MDM2 as a therapeutic target in GBM and underscore the importance of regulatory network analyses for understanding therapy resistance. To highlight GBM-cRegMap capabilities, we further provided experimental evidence showing that GBM-cRegMap can accurately measure the regulator activity, even for proteins whose encoding gene differential expression was not detected. For this purpose, we focused on two genes: PAX8 and EGFR. Notably, the mRNA expression of these two genes did not differ among the three cell lines. However, by inferring the influence of proteins (TFs/co-TFs) based on the expression of their context-specific targets through regulator network analysis, we detected distinct variations in the activity of these regulators (Fig. 6B-C). Further Western blot analysis revealed that both PAX8 and EGFR protein levels were repressed in U87MG-R50 cells (Fig. 6D-E). Thus, GBM-cRegMap successfully predicted regulator activity, underscoring its utility and precision. Moreover, in line with previous research by Slatter et al. (2014)[48], which demonstrated that a reduction in PAX8 expression led to a decrease in glioma cell growth in vitro, our findings revealed that the U87MG R50 cell line exhibited lower PAX8 activity and protein expression, in part linked to a consequent decline in cell proliferation[47].

DISCUSSION

GBM, characterized by its high heterogeneity and plasticity, is highly resistant to treatment, leading to poor patient prognosis. We introduced GBM-cRegMap, a powerful web-based tool to provide researchers with rapid access to a unified co-regulatory influence network view of GBM cancer. Many of the software tools we used are based on techniques originating in artificial intelligence (AI), especially representation learning: H-LICORN[9], CoRegNet[13], LatNet[49] and Seurat[50] (Fig. 1). Using the H-LICORN algorithm and the CoRegNet package, we presented the first GBM-specific co-regulatory network, inferred without any a priori knowledge. More specifically, we convert the inferred GRN into a co-operativity network of transcription factors and cofactors (TFs/co-TFs; co-activators and co-repressors). A major reason for focusing on co-operative TFs/co-TFs is that disease phenotypes, including disease progression and treatment response phenotypes, have been shown to be maintained

by small groups of TFs and co-TFs[16]. Compared to other approaches, we used transcriptomes from GBM tumor-derived cell lines for the first time to produce a more reliable GRN and prevent the introduction of possible bias due to the use of less homogeneous transcriptomic data from GBM tumors containing the contribution of non-specific signals and signals associated with the tumor microenvironment. Notably, many of the regulators forming part of the network were previously associated with GBM and/or neural differentiation, emphasizing the biological representativity of the inferred GBM-CoRegNet. Subsequently, we demonstrated that it was also relevant to build a harmonized tumor heterogeneity map, GBM-CoRegMap, that encompasses a meta-cohort analysis of 1612 tumors from 16 studies. We showed that GBM-CoRegMap successfully removed batch effects and recapitulated the state-of-the-art heterogeneity of GBM. More importantly, our comprehensive GBM-CoRegMap led to a novel molecular classification of GBM into seven distinct classes, which aligns well with previous reports. Each subtype is uniquely defined by the activity of a regulatory network, which reveals distinct biological and clinical implications. We confirmed and expanded our knowledge about the proneural (PN) and mesenchymal (MES) subtypes and distinguished three classical-like subtypes (CL-A: astrocyte-like, CL-B: epithelial basal-like, CL-C: ciliary-rich), as well as NL (normal-like) and low-proliferative PN-L (Proneural-Low) subtypes. The discovery of distinct subtypes of classical GBM, such as CL-C with ciliary-rich features and CL-B with epithelial traits, highlights unique molecular and biological processes. The poor prognosis of the CL-C subtype, linked to its ciliary characteristics, underscores the potential of primary cilia in GBM oncogenesis and resistance to therapy. This finding suggests that targeting cilia-associated pathways could be crucial, particularly for treating challenging subtypes, such as CL-C. Our study supports the existence of the normal-like (NL) subtype identified by Nguyen in 2020[21] which encompasses 49% of the NEU_Verhaak subtype. The NL subtype is characterized by a “normal” transcriptomic profile that is enriched in neuron developmental-associated pathways. Additionally, we discovered alterations in the tumor suppressor gene PTEN in 57% of NL cases, along with a higher frequency of STAG2 mutations in this subtype, underscoring its distinct tumor characteristics. It should be noted that increasing evidence supports the notion that some GBs hijack neuronal mechanisms to fuel their own growth [51]. This finding challenges the earlier perspective of Wang et al.[4], who suggested that the neural subtype defined by Verhaak might lack a tumor-specific signature, thereby questioning its classification as a distinct tumor subtype.

The CoRegMap tab is also empowered by downstream analyses, such as annotation of the map with molecular subtype, tumor purity, regulator influence, copy number variation, somatic mutations, clinical data, or gene essentiality scores. Additionally, it enables alignment and colocalization of patient-derived cell models within the reference tumor heterogeneity map. We aligned the cell lines with the tumor subtypes, aiding clinical translation. While many cell lines were classified as mixed using Verhaak gene expression classifiers, our approach successfully classified them. Supervised

classification assigns 27 Cancer Cell Lines to GBM-cRegMap subtypes with high confidence. However, some limitations of this study persist. The cell line classification mainly covers MES, PN, and CL-C, necessitating other cell models for recapturing classes, such as CL-A, CL-B, and PN-L. Our classification system also facilitates TF/coTF inferences for each subtype. Based on our analysis of the influence and dependency scores, we identified the pivotal regulators for each subclass. Key regulators of the PN subclass are ZNF536, HOXA2, and PBX4. ZNF671, ZNF181, and HDAC10 were prominent in the CL-A subclass. The CL-B subclass is regulated by LBX2, HES4, and PITX1, whereas the CL-C subclass is regulated by PAX6, POU3F2, and ZNF580. Notably, in the MES subclass, the master regulators CEBPB and SNAI2 were highly active, consistent with our expectations. Moreover, the MES subtype shows a distinct influence from the tumor microenvironment, as indicated by the activity of hypoxia-related regulators, such as EPAS1 and CEBPD. This suggests a significant impact of hypoxic conditions on these tumors.

The online GBM-cRegMap tool empowers GBM research and clinical communities to incorporate their transcriptomic data via the CoRegQuery function, deepening our understanding of GBM's multi-faceted landscape. Our study underscores two key applications of the GBM-cRegMap. First, we characterized GSC heterogeneity and plasticity upon differentiation. Second, we explored the phenotypic plasticity of differentiated GBM cells in response to treatment. This analysis emphasizes the utility of the tool for tracking the adaptability of tumor cells during and after treatment, which is vital for understanding the mechanisms underlying treatment resistance and tumor recurrence. A notable finding is the activation of the MDM2 regulator, which corroborates with previous research[47].

In conclusion, we provide a new comprehensive tool to study the co-regulatory networks driving the heterogeneity and plasticity of GBM cancer. GBM-cRegMap has a significant potential to aid in patient stratification and opens enormous possibilities for characterizing suitable therapeutic targets for the molecular heterogeneity of GBM.

MATERIALS AND METHODS

GBM-cRegMap development

Transcriptome public data collection. The transcriptomic and clinical outcome data of GBM tumors were collected from GlioVis[52] including 16 datasets with a total of 1612 samples (Supplementary Table S1). Further cell-line transcriptomic data were downloaded from the Cancer Dependency Map (DepMap)[36] and GEO, including 12 datasets with 42 commercial cell lines, xx stem cells, and xx normal brain samples (Supplementary Table S1). For consistency, all gene identifiers were transformed into HGNC (HUGO Gene Nomenclature Committee (HGNC) symbols. All of the above datasets were also classified using the Verhaak classifier from the GlioVis web application. The RNA-seq datasets that

had been downloaded from the GEO database were normalized using the edgeR[53] R package, with TMM normalization and log transformed counts per million. Microarray data were normalized using the standard workflow of the limma[54] R package.

Regulatory elements and interactions public data collection. A list of regulators containing 2,375 genes from two different sources (1,639 transcription factors (TF) with experimentally validated DNA binding specificity[55] and 752 transcription cofactors (TcoF) with experimental validation information[56] was utilized. The regulation evidence (TF-Target) list included 2,269,717 interactions retrieved using a wide range of bioinformatics tools and databases (listed in Supplementary Table S2) from 1) ChIP-seq data downloaded directly from the ChEA2 database; 2) human transcription factor binding site (TFBS) models, in the form of position weight matrices (PWM), recovered with MotifDB R/Bioconductor. The promoter sequences were scanned for these TFBS using the PWMEnrich R/Bioconductor package, and 3) the TF-Target list was completed using the tftargets R package and evidence from databases (*e.g.,* TRED, ITFP, ENCODE, BEDOPS, TRRUST). The co-operative evidence (TF-TF) list included 1,257,053 protein-protein interactions (PPI) interactions from various PPI databases (*e.g.,* BioGrid, HIPPIE, STRING, and HPRD) obtained with the iRefR R package.

Gene regulatory network inference. gene regulatory networks were inferred using the CoRegNet Bioconductor package[13]. Starting from transcriptomic data and a list of human regulators, CoRegNet uses the hLICORN algorithm[9] to capture regulatory interactions between regulators and target genes in four steps: (1) Transcriptomic data is discretized into values of -1, 0 and 1 according to per-gene distribution. Genes present in the transcriptomic dataset were split into regulators and target genes, and only those with a minimum support of non-zero values after discretization were retained. (2) A frequent itemset algorithm identifies potential sets of co-activators and co-inhibitors among regulators. (3) For each target gene, a list of candidate co-activator and co-inhibitor sets (GRN) was selected according to a regulatory program (association rule) metric. (4) Each GRN candidate for each gene was scored based on the regression between the expression of GRN set regulators and the expression of the gene concerned. For each gene, the top ten GRN candidates, according to the R2 score, were retained. CoRegNet can then be used to select the best GRN for each gene based on interaction evidence data. Regulatory and co-operativity evidence was incorporated into each candidate GRN with an integrative selection algorithm, yielding an R2 score for each of the integrated datasets. The GRN with the highest merged score was selected. CoRegNet builds a co-regulatory network GBM-CoRegNet from the GRNs obtained, by setting a co-operativity relationship between a pair of regulators TFi and TFj if they have a minimum of five target genes in common and the relationship is significant ($p =< 0.01$) according to the Jaccard similarity co-efficient formula:$\frac{TFi \cap TFj}{TFi \cup TFj}$.

Network-based regulatory influence signal quantification. The regulatory network structure provides the set of activated and repressed genes under reference conditions. Based on this structure, we can capture the influence of each regulator, which is a latent signal of the regulator activity in each sample based on its observed effect on downstream entities. For each regulator, a Welch t-test was performed to compare the distribution of activated Ar and repressed Ir genes. The influence of regulator r is computed as follows:

$$Influence(r) = \frac{\overline{E(A^r)} - \overline{E(I^r)}}{\sqrt{\frac{\mu_{A^r}^2}{A^r} + \frac{\mu_{I^r}^2}{I^r}}}$$

where $E(A^r)$ and $E(I^r)$ are the expression of the activated and repressed genes in the samples, respectively. $E(A^r)$ and $E(I^r)$ are their respective means, and μA^r and μI^r are their standard deviations. A regulator is active only when it activates A^r and represses I^r as expected by the regulatory network model. This is reflected by a positive welch t-test value. Thus, the higher the value of $Influence(r)$ the more the regulator r is active in the sample. In this work, we compute the $Influence$ of a regulator only if it at least has five or more activated or five or more repressed genes. It is worth noting that due to the tight thresholds used in the network construction, it is possible that some local gene networks get filtered and thus some regulators could have either of their activated or repressed target gene sets with less than five genes. In this case, we fill the smaller set (having less than 5 target genes) with the target genes for which that regulator has the highest R2 regression score. This allows us to capture the $Influence$ values for a maximum number of regulators. In addition, for some regulators the expression values of some of its target genes could be missing in some tumor samples for which we want to compute the influence. In this case, we estimate the missing expression values with the LatNet method[49] using as a reference dataset the cell lines expression. It can occur that the expression of some target genes cannot be estimated for a particular sample making the computation of the influence of a regulator not possible. In this (rare) case, the missing influence value for that sample is assigned the median of the obtained influence values for that regulator on the other samples.

Seurat Clustering. cRegMap subclass computation was performed with the Seurat R package[50] according to a modularity optimization-based clustering approach. The smart local moving (SLM) graph clustering algorithm was applied to a shared nearest neighbor graph (SNN) plotted from the influence data. When using the Seurat package, before clustering, the Seurat:: ScaleData function was used with default parameters to scale the influential data. Seurat::RunPCA was called with 20 PCs, and all other parameters were set at default values. Clustering with the Seurat package was performed on all calculated principal components using the Seurat::FindNeighbors function with default parameters,

followed by the Seurat::FindClusters function with a specified resolution of 0.8 resulting in seven clusters.

Mapping and annotating query datasets. Mapping and annotating query datasets involve a multistep process. Initially, CoRegQuery utilized GBM-CoRegNet to compute the regulatory influences of the input dataset. Subsequently, a Support Vector Machine (SVM) model was employed to classify the query samples. We utilized the e1071 R package[57], implementing an SVM with a radial kernel and a **one**-vs-rest strategy for multiclass classification. The SVM model was trained based on the influences and classifications derived from the tumor cohort. In the next step, CoRegQuery employs the Seurat::ProjectUMAP function to project the query dataset samples into (Uniform Manifold Approximation and Projection) coordinates of GBM-CoRegMap. The Seurat function identifies the nearest reference sample neighbors and their distances for each query sample and performs a UMAP projection by supplying the calculated neighbor set along with the UMAP model previously computed in GBM-CoRegMap.

The GBM-cRegMap webserver. GBM-cRegMap is written in the R language and uses the functions of several widely used packages (Supplementary Table S2) available from Bioconductor and CRAN based on the Golem [58] framework. This framework simplifies the development and deployment of a stable and robust web application using R Shiny[59]. A plotly graphics system is used to generate interactive visualizations, with interactions enabled by brushing or clicking on them in the Shiny framework. GBM-cRegMap is released on Docker[60] with all packages necessary to prevent update conflicts. The GBM-cRegMap web application was deployed with Google Cloud Run and is publicly available from https://blca.cregmap.com. The GBM-cRegMap user interface includes three main tabs: “CoRegNet,” “CoRegMap” and “CoRegQuery.” With the "CoRegNet" tab, the GBM-CoRegNet network was visualized via a Shiny applet in the R package visNetwork[61]. The CoRegNet network representations are intuitively understandable by biologists (Fig. 2A). They also facilitate the integration of several layers of information over the nodes and edges. This tab is designed to allow users to explore the co-regulatory network and to identify core active co-regulators in a single sample (e.g., cell line) or a particular phenotype (e.g., tumor subtype) for further analysis. The "CoRegMap" tab displays an interactive UMAP plot of the regulatory influence signal matrix with the Seurat R package. The "CoRegMap" tab also allows users to annotate samples with several items of information, including molecular subtype, influence of the regulator, copy number variation, somatic mutations, clinical data and a CRISPR/Cas9 screen-based DepMap gene essentiality score for the survival/proliferation of cell lines. Finally, query datasets can be mapped to GBM-cRegMap references with the “CoRegQuery” tab. GBM-cRegMap allows users to easily upload their expression datasets or retrieve expression datasets from the Gene Expression Omnibus (GEO). As input, expression data can be uploaded in CSV format, or as a GEO series ID, also known as GEO accession code, which is used by BLCA-cRegMap to extract

the gene expression dataset and experimental information from GEO. GBM-cRegMap calculates, in a few seconds, the influence of regulators on the new data, displaying the results in the reference GBM-CoRegNet and GBM-CoRegMap using the machine learning procedure of mapping and annotating the query dataset.

Characterization of GBM-cRegMap subclasses

Functional enrichment analysis of DEGs. For microarray gene expression analysis, the linear models for microarray data (LIMMA) R package[54] was used, and P-values were adjusted using the Benjamini-Hochberg method. For RNA-seq data gene expression analysis, the edgeR[53] R package was used followed by limma-voom[62] and standard differential expression (DE) analysis. Gene Ontology (GO) enrichment analysis was performed using the R packages clusterProfiler[63] and enrichR[64]. Ontologies with a padj<0.01 and gene counts of more than five were examined. Furthermore, the Kyoto Encyclopedia of Genes and Genomes (KEGG), Molecular Signatures Database (MSigDB), and REACTOME pathway databases were searched for enriched terms using the R package msigdbr[65].

Analysis of genomic alterations. Somatic mutations were analyzed using the GBM-TCGA dataset. The TCGAbiolinks R package[66] was used to download mutation annotation files (MAF) aligned against the hg38 sequence, and analysis was performed using the R package maftools[67].

Cellular components deconvolution and Tumor purity scores. The TCGA-GBM dataset was used to identify the tumor purity of each sample and the abundance of cellular populations with respect to the GBM-cRegMap classification. Using the PUREE[35] (pan-cancer tumor purity estimation) web server, the purity score for each sample of the dataset was calculated and displayed as boxplots for each class. Utilizing the GBMdeconvoluteR[24] web-server, the various immune and stromal cell populations were estimated per sample, and the resulting values were averaged per GBM-cRegMap subclass.

Survival analysis. Survival analyses were performed using the R package survminer[68], overall survival was calculated using the Kaplan-Meier method, and the log-rank test was used to compare survival curves.

Classification of cell lines. CoRegQuery assigned a specific class with high confidence (SVM posterior probability > 0.75) to 27 out of 42 GBM Cancer Cell Lines (GBCCL) (Fig. 4, Supplementary Table S11), revealing a heterogeneous pattern of subclasses across the GBM cell line panel. We assessed the robustness of our method by analyzing transcriptomic data from multiple independent datasets for a single-cell line. These datasets were generated using various transcriptomic profiling techniques, including microarray and RNA-seq, and sourced from six distinct datasets (Supplementary Table S9). The classification outcomes were fundamentally consistent across different profiling techniques and

datasets, underscoring the reliability of our classification approach. When we explored the PubMed citation status of the studied GBCCL (Supplementary Table S11), we revealed a bias, with only five (150> citations each) out of the 27 cell lines being used extensively by the scientific community. Our classification system aligns with the literature for these 5 cell lines. For instance, U87MG, a well-known mesenchymal GBCCL, was assigned to the MES subclass, LN229 to the PN subclass, and T98G, known to be dependent on Oxidative Phosphorylation[69], to the CL-B class. Normal brain samples (GSE15824 n=2 and GSE15209 n=6) were consistently categorized as NL.

Identification and validation of sub-class specific regulators. For the identification of differentially influential regulators (DIRs), the Wilcoxon rank-sum test from Seurat R package was used, and in each cluster identification was performed utilizing the Seurat::FindAllMarkers function (cutoff: min.pct: 0.25 and logfc.threshold: 0.20), p-value adjustment was performed using Bonferroni correction. Additional ranking of DIRs was determined using the Wilcoxon-Mann-Whitney test between the average CERES dependency score of the cell lines assigned to the subclass versus the average dependency score of the rest. The CERES dependency score[70] of the cell lines was acquired using R package depmap[36].

In-house data generation investigating phenotypic plasticity.

Cell lines, culture and conditions. The U87MG GBM cell line was obtained from the American Type Culture Collection (LGC Standards Sarl; Molsheim, France). Two TMZ-resistant clonal lines were established in our laboratory by exposing the U87MG parent line to 50 µM TMZ for extended periods: U87MG R50 and U87MG R50 OFF. U87MG R50 cells were continuously cultured in a medium supplemented with 50 µM TMZ, while U87MG R50 OFF was relieved of TMZ pressure after a two-month treatment period. TMZ (cat #T2577; Sigma Aldrich) was prepared as a 100mM stock solution in DMSO and stored at 4°C until use. These cell lines were routinely cultured in Eagle's Minimum Essential Medium (EMEM) with 10% heat-inactivated fetal bovine serum (FBS), 1% sodium pyruvate, and 1% non-essential amino acids at 37°C with 5% CO_2. Glioma stem-like cells NCH644 and NCH421k were provided by Dr. Christel Herold-Mende[46]. Cells were cultured in Dulbecco's modified Eagle's medium (DMEM) supplemented with Nutrient Mixture F-12 and GlutaMAX™ (DMEMF12+GlutaMAX™, Gibco™). These cells were cultured under serum-free conditions as neurospheres (NS) to maintain a stem-like state, and the medium was further enhanced with Bovine Serum Albumin (BSA), Insulin Transferrin (BIT-100, 20%) (Provitro), Epidermal Growth Factor (EGF, 20 ng/mL), and Fibroblast Growth Factor (20 ng/mL) (Reliatech). Differentiation was induced by culturing the cells in DMEM/F12 + GlutaMAX™ medium (Gibco™) supplemented with 10% (vol/vol) FBS (Gibco™) or all-trans retinoic acid (ATRA). Cultures were maintained at 37°C in a humidified

atmosphere containing 5% CO_2. Periodic authentication of all cell lines was conducted by Multiplexion GmbH, coupled with regular testing for mycoplasma contamination, to ensure culture integrity.

RNAseq data. Transcriptomic analyses of the U87, U87MG R50, and U87MG R50 OFF cell lines were based on previously reported data[47]. For the NCH644 and NCH421k lines in both stem-like and differentiated states, total RNA was isolated, and biotinylated single-strand cDNA targets were prepared using the Ambion WT Expression Kit (Cat #4411974) and Affymetrix GeneChip® WT Terminal Labeling Kit (Cat #900671) according to the manufacturer's guidelines. The cDNAs were hybridized onto GeneChip® Human Gene 2.0 ST arrays (Affymetrix) targeting over 40,000 RefSeq transcripts and approximately 11,000 lncRNAs. The chips were processed and scanned using Affymetrix equipment and software. Raw data were then analyzed and processed using Affymetrix Expression Console software version 1.4.1 with default RMA settings.

Western blotting analysis. glioma cell lines NCH421k and NCH644 were cultured as neurospheres (NS) for stem-like conditions and as monolayers (ML) in differentiated conditions in the presence of all-trans retinoic acid (ATRA). Cells were lysed with Laemmli sample buffer (60mM Tris-HCl pH 6.8, 20% glycerol, 2% SDS, 0.01% bromophenol blue, and 5%-mercaptoethanol) (Bio-Rad) and heated at 95°C for 10 min. Proteins were separated using precast gradient 4-20% SDS-PAGE gels (Bio-Rad) and transferred to PVDF membranes (GE Healthcare). The membranes were blocked with 5% nonfat milk in Tris-buffered saline with 0.1% Tween-20 (TBST) for 1 h at room temperature and then incubated overnight with primary antibodies against EGFR (4267S, Cell Signaling), PAX8 (10336, Proteintech), GAPDH (MAB374, Millipore), α-tubulin (T9026, Sigma Aldrich), GFAP (MAB360, Millipore), OCT4 (2750S, Cell Signaling), CD133 (372802, Biolegend), Nestin (MAB5326, Millipore), and ITGA5 (D7B7G, Cell Signaling) diluted in TBST with 5% nonfat milk at 4°C. After washing with TBST, membranes were incubated with horseradish peroxidase (HRP)-conjugated anti-mouse and anti-rabbit secondary antibodies diluted in TBST with 5% nonfat milk at room temperature for 1 h. The blots were visualized using an enhanced chemiluminescence (ECL) system with an ImageQuant™ LAS 4000 analyzer (GE Healthcare).

Proliferation assays. To assess cell proliferation, spheroids were generated using the hanging drop method. A cell suspension of 2000 differentiated cells per 20 µL growth medium supplemented with 20% methyl cellulose (Sigma Aldrich, M0262) was placed on the inner surface of a petri dish cover. After 48 h, each spheroid was transferred to a poly L-lysine-coated 24-well plate (one sphere per well). Spheroid size was monitored over the course of 1 week at 37°C. Microscopic images of spheroids were captured at 4X magnification on days 0 and 6.

Immunofluorescence assays. Cells were fixed with ice-cold methanol for 10 min. After fixation, the cells were incubated overnight at 4°C with the primary antibody PAX8 Proteintech #10336-1-AP

(1:50). The cells were then incubated with a goat anti-rabbit AF488 secondary antibody (1:500) at room temperature for 2 h. The expression of PAX8 in the U87MG, U87MG R50, and U87MG R50 OFF cell lines was observed and analyzed under a fluorescence microscope.

Acknowledgements. This work was supported by grants from Institut National du Cancer INCa (PL-Bio project n°2017-145), the French National Research Agency ANR (Greener Project ANR-20-CE20-0028 and the ANR AI_PhD@Lille program). CB received a doctoral fellowship from the French Ministry of Higher Education, Research, and Innovation (MESRI) and MM a doctoral fellowship from CNRS (MITI 80 PRIME program).

Competing interests. The authors declare that they have no known competing financial interests or personal relationships that could have influenced the work reported in this study.

Data availability. The public data used in this study were acquired from GEO (https://www.ncbi.nlm.nih.gov/geo/), DepMap (https://depmap.org/portal/download/all/), GlioVis (http://gliovis.bioinfo.cnio.es), and TCGA (https://portal.gdc.cancer.gov/). Other data supporting the findings of this study are available through the online GBM-cRegMap tool, associated Github (xxx), and corresponding author upon request.

Code availability. The GBM-cRegMap web application was deployed with Google Cloud Run and is publicly available at https://gbm.cregmap.com. The source code is available in Github (xxx).

Ethical Compliance: All procedures performed in studies involving human participants were in accordance with the ethical standards of the institutional and/or national research committee and with the 1964 Helsinki Declaration and its later amendments or comparable ethical standards.

REFERENCES

1. Ostrom, Q. T., Cioffi, G., Waite, K., Kruchko, C. & Barnholtz-Sloan, J. S. CBTRUS Statistical Report: Primary Brain and Other Central Nervous System Tumors Diagnosed in the United States in 2014–2018. *Neuro-Oncology* **23**, iii1–iii105 (2021).
2. Gilbertson, R. J. High-grade glioma: can we teach an old dogma new tricks? *Cancer Cell* **9**, 147–148 (2006).
3. Verhaak, R. G. W. *et al.* Integrated Genomic Analysis Identifies Clinically Relevant Subtypes of Glioblastoma Characterized by Abnormalities in PDGFRA, IDH1, EGFR, and NF1. *Cancer Cell* **17**, 98–110 (2010).
4. Wang, Q. *et al.* Tumor Evolution of Glioma-Intrinsic Gene Expression Subtypes Associates with Immunological Changes in the Microenvironment. *Cancer Cell* **32**, 42-56.e6 (2017).
5. Olar, A. & Aldape, K. D. Using the molecular classification of glioblastoma to inform personalized treatment. *The Journal of Pathology* **232**, 165–177 (2014).
6. Lasorella, A. & Iavarone, A. The making of the glioblastoma classification. *Br J Cancer* **125**, 4–6 (2021).
7. Neftel, C. *et al.* An Integrative Model of Cellular States, Plasticity, and Genetics for Glioblastoma. *Cell* **178**, 835-849.e21 (2019).
8. Margolin, A. A. *et al.* ARACNE: an algorithm for the reconstruction of gene regulatory networks in a mammalian cellular context. *BMC bioinformatics* **7 Suppl 1**, S7 (2006).
9. Elati, M. *et al.* LICORN: learning co-operative regulation networks from gene expression data. *Bioinforma. Oxf. Engl* **23**, 2407–14 (2007).
10. Chebil, I., Nicolle, R., Santini, G., Rouveirol, C. & Elati, M. Hybrid method inference for the construction of co-operative regulatory network in human. *IEEE Trans. Nanobioscience* **13**, 97–103 (2014).
11. Aibar, S. *et al.* SCENIC: single-cell regulatory network inference and clustering. *Nature Methods* **14**, 1083–1086 (2017).
12. Nicolle, R., Elati, M. & Radvanyi, F. Network Transformation of Gene Expression for Feature Extraction. in *2012 11th International Conference on Machine Learning and Applications* 108–113 (IEEE, 2012). doi:10.1109/ICMLA.2012.27.
13. Nicolle, R., Radvanyi, F. & Elati, M. CoRegNet: reconstruction and integrated analysis of co-regulatory networks. *Bioinforma. Oxf. Engl* **31**, 3066–8 (2015).
14. Alvarez, M. J. *et al.* Functional characterization of somatic mutations in cancer using network-based inference of protein activity. *Nature Genetics* **48**, 838–847 (2016).
15. Xiong, A., Zhang, J., Chen, Y., Zhang, Y. & Yang, F. Integrated single-cell transcriptomic analyses reveal that GPNMB-high macrophages promote PN-MES transition and impede T cell activation in GBM. *EBioMedicine* **83**, 104239 (2022).
16. Carro, M. S. *et al.* The transcriptional network for mesenchymal transformation of brain tumours. *Nature* **463**, 318–325 (2010).
17. Louis, D. N. *et al.* The 2021 WHO Classification of Tumors of the Central Nervous System: a summary. *Neuro-Oncology* **23**, 1231–1251 (2021).
18. Becht, E. *et al.* Dimensionality reduction for visualizing single-cell data using UMAP. *Nature Biotechnology* **37**, 38–44 (2019).
19. McInnes, L., Healy, J., Saul, N. & Großberger, L. UMAP: Uniform Manifold Approximation and Projection. *Journal of Open Source Software* **3**, 861 (2018).
20. Kerry, S. M. & Bland, J. M. Sample size in cluster randomisation. *BMJ (Clinical research ed.)* **316**, 549 (1998).
21. Nguyen, H. D. *et al.* A machine learning analysis of a 'normal-like' IDH-WT diffuse glioma transcriptomic subgroup associated with prolonged survival reveals novel immune and neurotransmitter-related actionable targets. *BMC Med* **18**, 280 (2020).
22. El Beaino, M. *et al.* Loss of Stag2 cooperates with EWS-FLI1 to transform murine Mesenchymal stem cells. *BMC cancer* **20**, 3 (2020).
23. Shen, C.-H. *et al.* Loss of cohesin complex components STAG2 or STAG3 confers resistance to BRAF inhibition in melanoma. *Nature Medicine* **22**, 1056–1061 (2016).
24. Ajaib, S. *et al.* GBMdeconvoluteR accurately infers proportions of neoplastic and immune cell populations from bulk glioblastoma transcriptomics data. *Neuro-Oncology* **25**, 1236–1248 (2023).

25. Kawai, S. *et al.* Generation of a lung squamous cell carcinoma three-dimensional culture model with keratinizing structures. *Scientific Reports* **11**, 24305 (2021).
26. Saidak, Z. *et al.* Squamous Cell Carcinoma Antigen-encoding Genes SERPINB3/B4 as Potentially Useful Markers for the Stratification of HNSCC Tumours. *Anticancer Research* **38**, 1343–1352 (2018).
27. Magnus, N., Gerges, N., Jabado, N. & Rak, J. Coagulation-related gene expression profile in glioblastoma is defined by molecular disease subtype. *Journal of Thrombosis and Haemostasis* **11**, 1197–1200 (2013).
28. Garofano, L. *et al.* Pathway-based classification of glioblastoma uncovers a mitochondrial subtype with therapeutic vulnerabilities. *Nature Cancer* **2**, 141–156 (2021).
29. Rodriguez, F. J., Scheithauer, B. W., Giannini, C., Bryant, S. C. & Jenkins, R. B. Epithelial and pseudoepithelial differentiation in glioblastoma and gliosarcoma: A comparative morphologic and molecular genetic study. *Cancer* **113**, 2779–2789 (2008).
30. Ho, K.-H. *et al.* A Key Role of DNA Damage-Inducible Transcript 4 (DDIT4) Connects Autophagy and GLUT3-Mediated Stemness To Desensitize Temozolomide Efficacy in Glioblastomas. *Neurotherapeutics* **17**, 1212–1227 (2020).
31. Cheng, Y. *et al.* LGR6 promotes glioblastoma malignancy and chemoresistance by activating the Akt signaling pathway. *Experimental and Therapeutic Medicine* **22**, 1364 (2021).
32. Leventoux, N. *et al.* Transformation Foci in IDH1-mutated Gliomas Show STAT3 Phosphorylation and Downregulate the Metabolic Enzyme ETNPPL, a Negative Regulator of Glioma Growth. *Sci Rep* **10**, 5504 (2020).
33. Bae, J.-E. *et al.* Primary cilia mediate mitochondrial stress responses to promote dopamine neuron survival in a Parkinson's disease model. *Cell Death & Disease* **10**, 952 (2019).
34. Goranci-Buzhala, G. *et al.* Cilium induction triggers differentiation of glioma stem cells. *Cell Reports* **36**, 109656 (2021).
35. Revkov, E., Kulshrestha, T., Sung, K. W.-K. & Skanderup, A. J. PUREE: accurate pan-cancer tumor purity estimation from gene expression data. *Communications Biology* **6**, 394 (2023).
36. Gatto, L. & Killian, T. depmap: Cancer Dependency Map Data Package. (2022).
37. Chuikov, S., Levi, B. P., Smith, M. L. & Morrison, S. J. Prdm16 promotes stem cell maintenance in multiple tissues, partly by regulating oxidative stress. *Nature Cell Biology* **12**, 999–1006 (2010).
38. Held-Feindt, J., Hattermann, K., Knerlich-Lukoschus, F., Mehdorn, H. M. & Mentlein, R. SP100 reduces malignancy of human glioma cells. *Int J Oncol* **38**, 1023–1030 (2011).
39. Song, Y.-C. *et al.* Proteogenomic characterization and integrative analysis of glioblastoma multiforme. *Oncotarget* **8**, 97304–97312 (2017).
40. Chakraborty, C. *et al.* Rewiring of the promoter-enhancer interactome and regulatory landscape in glioblastoma orchestrates gene expression underlying neurogliomal synaptic communication. *Nature Communications* **14**, 6446 (2023).
41. Mao, X. *et al.* CEBPD is a master transcriptional factor for hypoxia regulated proteins in glioblastoma and augments hypoxia induced invasion through extracellular matrix-integrin mediated EGFR/PI3K pathway. *Cell Death & Disease* **14**, 269 (2023).
42. Cheng, H. S., Yip, Y. S., Lim, E. K. Y., Wahli, W. & Tan, N. S. PPARs and Tumor Microenvironment: The Emerging Roles of the Metabolic Master Regulators in Tumor Stromal-Epithelial Crosstalk and Carcinogenesis. *Cancers* **13**, (2021).
43. Li, J. *et al.* Clinicopathological and Prognostic Significance of PRAME Overexpression in Human Cancer: A Meta-Analysis. *BioMed research international* **2020**, 8828579 (2020).
44. Lopez-Bertoni, H. *et al.* Sox2 induces glioblastoma cell stemness and tumor propagation by repressing TET2 and deregulating 5hmC and 5mC DNA modifications. *Signal Transduction and Targeted Therapy* **7**, 37 (2022).
45. Lathia, J. D., Mack, S. C., Mulkearns-Hubert, E. E., Valentim, C. L. L. & Rich, J. N. Cancer stem cells in glioblastoma. *Genes & Development* **29**, 1203–1217 (2015).
46. Podergajs, N. *et al.* Expansive growth of two glioblastoma stem-like cell lines is mediated by bFGF and not by EGF. in *Radiology and Oncology* vol. 47 330–337 (Association of Radiology and Oncology, 2013).
47. Sani, S. *et al.* Temozolomide-Acquired Resistance Is Associated with Modulation of the Integrin Repertoire in Glioblastoma, Impact of α5β1 Integrin. *Cancers* **14**, 369 (2022).
48. Hung, N. *et al.* Increased paired box transcription factor 8 has a survival function in Glioma. *BMC Cancer* **14**, 159 (2014).

49. Dhifli, W., Puig, J., Dispot, A. & Elati, M. Latent network-based representations for large-scale gene expression data analysis. *BMC Bioinformatics* **19**, (2019).
50. Hao, Y. *et al.* Dictionary learning for integrative, multimodal and scalable single-cell analysis. *Nat Biotechnol* (2023) doi:10.1038/s41587-023-01767-y.
51. Venkataramani, V. *et al.* Glioblastoma hijacks neuronal mechanisms for brain invasion. *Cell* **185**, 2899-2917.e31 (2022).
52. Bowman, R. L., Wang, Q., Carro, A., Verhaak, R. G. W. & Squatrito, M. GlioVis data portal for visualization and analysis of brain tumor expression datasets. *Neuro Oncol* **19**, 139–141 (2017).
53. Robinson, M. D., McCarthy, D. J. & Smyth, G. K. edgeR: a Bioconductor package for differential expression analysis of digital gene expression data. *Bioinformatics* **26**, 139–140 (2010).
54. Ritchie, M. E. *et al.* limma powers differential expression analyses for RNA-sequencing and microarray studies. *Nucleic Acids Research* **43**, e47–e47 (2015).
55. Lambert, S. A. *et al.* The Human Transcription Factors. *Cell* **172**, 650–665 (2018).
56. Schmeier, S., Alam, T., Essack, M. & Bajic, V. B. TcoF-DB v2: update of the database of human and mouse transcription co-factors and transcription factor interactions. *Nucleic Acids Res* **45**, D145–D150 (2017).
57. Meyer, D. *et al.* e1071: Misc Functions of the Department of Statistics, Probability Theory Group (Formerly: E1071), TU Wien. (2022).
58. Fay, C., Guyader, V., Rochette, S. & Girard, C. *golem: A Framework for Robust Shiny Applications*. (2023).
59. Chang, W. *et al.* shiny: Web Application Framework for R. (2023).
60. Merkel, D. Docker: Lightweight Linux Containers for Consistent Development and Deployment. *Linux J.* **2014**, (2014).
61. B.V., A. & Contributors, T. B. visNetwork. Network Visualization using « vis.js. *Library* (2022).
62. Law, C. W., Chen, Y., Shi, W. & Smyth, G. K. voom: Precision weights unlock linear model analysis tools for RNA-seq read counts. *Genome Biol* **15**, R29 (2014).
63. Wu, T. *et al.* clusterProfiler 4.0: A universal enrichment tool for interpreting omics data. *The Innovation* **2**, 100141 (2021).
64. Kuleshov, M. V. *et al.* Enrichr: a comprehensive gene set enrichment analysis web server 2016 update. *Nucleic Acids Res* **44**, W90-97 (2016).
65. Dolgalev, I. *msigdbr: MSigDB Gene Sets for Multiple Organisms in a Tidy Data Format*. (2022).
66. Mounir, M. *et al.* New functionalities in the TCGAbiolinks package for the study and integration of cancer data from GDC and GTEx. *PLoS Comput Biol* **15**, e1006701 (2019).
67. Mayakonda, A., Lin, D. C., Assenov, Y., Plass, C. & Koeffler, H. P. Maftools: efficient and comprehensive analysis of somatic variants in cancer. *Genome Res* **28**, 1747–56 (2018).
68. Kassambara, A., Kosinski, M., Biecek, P. & Fabian, S. survminer: Drawing Survival Curves using 'ggplot2'. (2021).
69. Oppermann, H., Schnabel, L., Meixensberger, J. & Gaunitz, F. Pyruvate attenuates the anti-neoplastic effect of carnosine independently from oxidative phosphorylation. *Oncotarget* **7**, 85848–85860 (2016).
70. Meyers, R. M. *et al.* Computational correction of copy number effect improves specificity of CRISPR-Cas9 essentiality screens in cancer cells. *Nat Genet* **49**, 1779–1784 (2017).

Figure legend

Figure 1. GBM-cRegMap workflow. The GBM-cRegMap tool features three main elements within its user interface: CoRegNet, CoRegMap, and CoRegQuery. Leveraging representation learning algorithms, we derive two components GBM-CoRegNet and GBM-CoRegMap. GBM-CoRegNet is a highly specific co-regulatory network of tumor cells featuring 539 transcription factors/co-factors and their 8269 target genes. We used the hybrid-learning co-operative regulatory networks (H-LICORN) algorithm that integrates data-mining methods with numerical linear regression to efficiently infer a context-specific GRN[9] using a more uniform transcriptomic dataset from GBM cancer cell lines. LICORN stands out in that regard, considering the co-operativity between co-regulators and incorporating it into the model, bringing it closer to the biological reality compared to other approaches. More specifically, we convert the inferred GRN into a co-operativity network of transcription factors and cofactors (TFs/co-TFs; co-activators and co-repressors). The CoRegNet tab allows users to investigate and evaluate the extent to which phenotype(s) of interest (e.g., tumor subtypes, wild-type vs treated cell lines), each characterized by a set of active co-regulators, are colocalized in the reference GBM-CoRegNet network using an intuitive visualization powered by Shiny. Second feature is GBM-CoRegMap, a unified influence map comprising 1612 tumors from 16 studies, which is enhanced by downstream analysis data, such as annotation of the map with molecular subtype, tumor purity, regulator influence, copy number variation, somatic mutations, clinical data, or gene essentiality scores. Additionally, it enables the possible alignment and colocalization of patient-derived cell models within the reference tumor heterogeneity map. Finally, "CoRegQuery" assists in analyzing query datasets, even when few samples are profiled, using GBM-cRegMap synergetic compounds. As input, user can upload expression datasets or simply providing a GEO (Gene Expression Omnibus) series ID. GBM-cRegMap swiftly calculates regulator influences for new data, presenting results in GBM-CoRegNet compound and allows to further investigate selected co-regulators, interactions and systems for relevance to the study. Furthermore, a supervised machine learning procedure enhances the tool's efficiency in predicting the localization of the query dataset samples within the GBM-CoRegMap. This ensures consistent comparison of tumor transcriptional patterns, facilitating potential exploration into tumor heterogeneity as well as the adaptability of the studied phenotypes.

Figure 2. CoRegMap view of glioblastoma heterogeneity. (A) Co-operativity network inferred from the transcriptome of 42 GBM cancer-derived cell lines (GBM-CoRegNet). Nodes represent transcription factors and cofactors (TFs/co-TFs). Node size is proportional to the number of targets of the TF/coTF. The co-regulatory interactions between nodes are indicated as follows: protein-protein interactions with published evidence are shown in blue, transcriptional regulation interactions with published evidence are shown in red and interactions defined solely by the H-LICORN algorithm are shown in gray. (B) UMAP visualization of the meta-cohort of 1629 tumors showing the difference of using the transcriptomic (top) and influence (bottom) data of the different datasets. It is evident that the influence data produce a batch effect-free meta-cohort versus the original RNA expression values. (C) UMAP visualization of the GBM-cRegMap meta-cohort using sample annotation colors derived from the Verhaak classification (top) and GBM-cRegMap unsupervised clustering (bottom). (D) Alluvial plot displaying the GBM-cRegMap metacohort samples with the state-of-the-art classification of glioblastoma (Verhaak classification on the left) and their corresponding classification proposed by GBM-cRegMap (on the right).

Figure 3. Molecular and clinical characteristics of GBM-cRegMap classes. (A) Heatmap of RNA-seq scaled expression data of the TCGA-GBM (n=522) dataset displaying the biologically relevant gene

signatures for each GBM-cRegMap class. On columns the samples are grouped per GBM-cRegMap class and on rows hierarchical clustering has been used while separating each gene signature per class. The colors indicate high (red) and low (green) levels of relative expression. (B) Dot plot with significantly enriched Gene Ontology Biological Processes for each GBM-cRegMap class derived from clusterProfiler R package. Only GO/BPs presenting an adjusted p-value <0.05 were considered, P-values were adjusted with the Benjamini-Hochberg method. (C) Oncoplot showing the most important genomic alterations associated with cRegMap classes. The available data from TCGA-GBM dataset were used. With red squares are indicated the highest alteration rate values per gene for each class. (D) Heatmap displaying the cellular state score using the GBMdeconvoluteR tool and the metabolic gene signature scores using the singscore R package. Asterisks are used to showcase the highest score per row. (E) Overall survival curve stratified by cRegMap class. Survival analysis is performed with the Kaplan-Meier method, using the R package survival. Kaplan-Meier curves were generated from the available meta-cohort clinical data of 1110 patients. (F) Boxplot displaying tumor cell purity scores for each cRegMap class of the TCGA-GBM samples that were obtained using the PUREE (pan-cancer tumor purity estimation) webserver.

Figure 4. GBM Subclass-Matched Cell Line Repertoires and Specific Differential Subnetworks. (A) Visualization of 27 GBM cell lines as predicted by SVM-based classification within the coordinates of GBM-CoRegMap using CoRegQuery. Dotted lines connect a GBM CCLE sample to another sample of the same cell line from a different dataset. (B) Left panels: GBM-CoRegNet visualization for each of the predicted subclasses. Node color (red: high; blue: low) indicates the influence of the corresponding TF/coTF (as a proxy of TF/coTF activity) and the intensity of the color indicates the strength of the signal. Node labels of important TFs and co-TFs associated with the subclass are provided. Right panels: impact on cell viability (CERES dependency score) analysis. For each regulator, there are two vertical values, the gray dot is the average CERES score for the cell lines not assigned to the subclass and the colored dot is the average CERES score in cell lines assigned to the subclass. The dotted horizontal line displays the viability threshold. (C) Heatmap showing the top 10 Differentially Influenced regulators for each subclass, color values representing the scaled relative influences. (D) GBM-CoRegMap example plots of the various metadata that can be visualized using the GBM-cRegMap tool. The top plot shows the SNAI2 regulatory influence while visualizing the topology of various cell lines, while the bottom plot shows the SNAI2 CRISPR dependency scores for the same cell lines.

Figure 5: Glioblastoma stem cells plasticity upon differentiation. (A) GBM-cRegMap meta-cohort visualization projecting the GBM-CoRegQuery results from transcriptomic data of NCH644 and NCH421k under stem-like state “S” and differentiated state “D”. All conditions were tested in triplicates. (B) Representative phase contrast images of NCH644 and NCH421k cells showing cellular morphology and differential protein marker expression using western blotting under neurosphere (NS) and monolayer, differentiated (ML) conditions. (C) Assessment of proliferative capacity differences between NCH644 and NCH421k under differentiated states after 6 days of culture. Representative images show cell morphology of differentiated cells on day 0 and day 6. The graph represents the average fold increase in sphere size at day 6 (n=6).

Figure 6: Plasticity in response to chemotherapy Temozolomide. (A) GBM-cRegMap meta-cohort visualization projecting the GBM-CoRegQuery results from transcriptomic data (three replicates each) of U87MG naïve cell lines and TMZ-resistant cells, U87MG R50 and U87MG R50 OFF. (B) Corresponding CoRegNet influence networks. Node color (red = high; blue = low) indicates the influence of the corresponding TF/coTF and the intensity of the color indicates the strength of the

influence. Node size and edge color follow the same patterns as indicated in Fig.2 A. (C) Heatmap showing top Differentially Influenced Regulators (DIRs) for each cell line, color values representing the scaled relative influences. (D) Detection of PAX8 and EGFR protein in U87MG, U87MG R50, and U87MG R50 OFF by western blotting (representative blot), and their predicted activity based on the regulatory network (coloured dots under the WB), along with quantitative analysis (n=7) of their relative protein expression (upper graphs). (E) Detection of PAX8 protein by immunofluorescence assays in U87MG, U87MG R50, and U87MG R50 OFF cell lines.

Supplementary Tables

Table S1: Transcriptomic datasets used to generate gbm.cregmap reference compounds. Related to Fig.1.

Table S2: Software, tools and resources required to develop GBM-cRegMap. Related to Fig.1.

Table S3: GBM-CoRegNet regulators. Related to Fig.2A.

Table S4: GBM-coRegNet co-regulators pairs. Related to Fig.2A.

Table S5: Cross-study prediction performance.

Table S6: Differentially expressed genes (DEGs) analysis. Related to Fig.3A.

Table S7: Functional enrichment analysis of the GBM-cRegMap subclasses. Related to Fig.3B.

Table S8: Gender and age differences in GBM-cRegMap subclasses.

Table S9: Subclass switching of primary/recurrent pairs. Related to Fig.3G.

Table S10: Differentially influent regulators (DIRs) analysis. Related to Fig.4A.

Table S11: Classification of glioblastoma cell lines. Related to Fig.4C.

Table S12: Classification of stem cells. Related to Fig.5A-B.

Figure 1

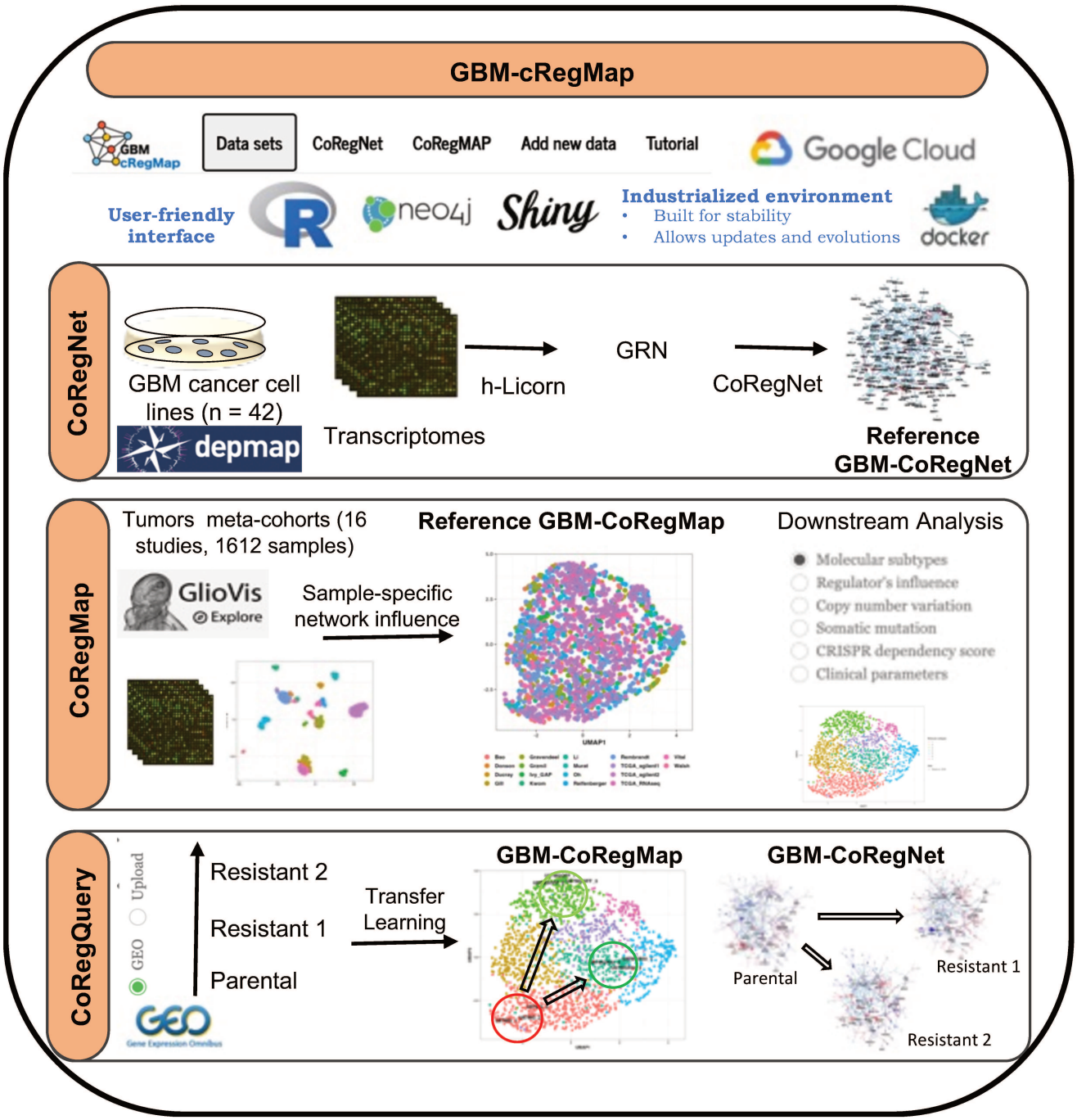
GBM-cRegMap
GBM cRegMap
Data sets
CoRegNet
CoRegMAP
Add new data
Tutorial
Google Cloud
User-friendly interface
neo4j
Shiny
Industrialized environment
• Built for stability
• Allows updates and evolutions
docker
CoRegNet
GBM cancer cell lines (n = 42)
depmap
Transcriptomes
h-Licorn
GRN
CoRegNet
Reference GBM-CoRegNet
CoRegMap
Tumors meta-cohorts (16 studies, 1612 samples)
GlioVis Explore
Sample-specific network influence
Reference GBM-CoRegMap
Downstream Analysis
Molecular subtypes
Regulator's influence
Copy number variation
Somatic mutation
CRISPR dependency score
Clinical parameters
CoRegQuery
Upload
GEO
Resistant 2
Resistant 1
Parental
Transfer Learning
GBM-CoRegMap
GBM-CoRegNet
Parental
Resistant 1
Resistant 2

Figure 2

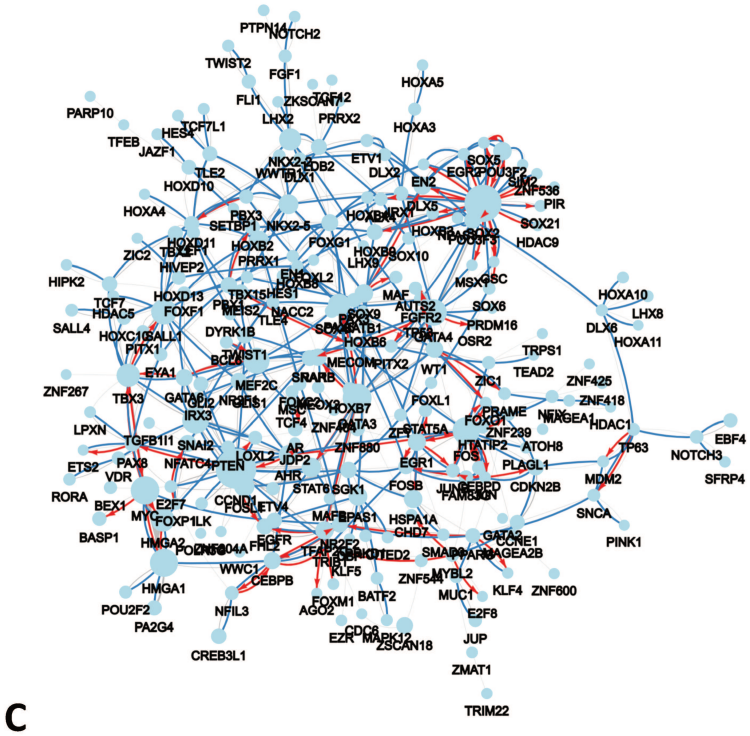
A
PTPN14
NOTCH2
TWIST2
FGF1
HOXA5
FLI1
ZKSCAN1
TCF12
PARP10
LHX2
PRRX2
HOXA3
TCF7L1
TFEB
HES1
JAZF1
ETV1
SOX5
TLE2
DLX2
EGR2
POU3F2
SUZ2
HOXD10
DLX1
EN2
ZNF536
HOXA4
PBX3
DLX5
PIR
SETBP1
NKX2-5
HOXB3
SOX21
HOXD11
HOXB2
FOXG1
SOX2
HDAC9
ZIC2
PRRX1
LHX9
SOX10
HIPK2
HIVEP2
HOXB8
MSX1
GSC
HOXA10
HOXD13
MEIS2
NACC2
SOX6
LHX8
TCF7
FOXF1
FGFR2
SALL4
HDAC5
PRDM16
DLX6
HOXA11
DYRK1B
GATA4
OSR2
TRPS1
PITX1
TWIST1
TEAD2
EYA1
SRARB
WT1
ZIC1
ZNF425
ZNF267
MEF2C
ZNF418
TBX3
FOXL1
PRAME
HDAC1
LPXN
IRX3
TCF4
FOXO1
MAGEA1
EBF4
TGFB1I1
ZNF239
NOTCH3
SNAI2
ZNF880
ATOH8
TP63
ETS2
PAX8
LOXL2
JDP2
EGR1
PLAGL1
SFRP4
VDR
AHR
FOS
MDM2
RORA
STAT6
SGK1
FOSB
CDKN2B
BEX1
E2F7
CCND1
FOSL1
ETV4
SNCA
MYC
FOXP1
HSPA1A
BASP1
CHD7
PINK1
HMGA2
EGFR
CCNE1
WWC1
CEBPB
KLF5
MYBL2
HMGA1
ZNF544
KLF4
ZNF600
POU2F2
NFIL3
AGO2
FOXM1
BATF2
MUC1
E2F8
PA2G4
CDC6
JUP
CREB3L1
ZSCAN18
ZMAT1
TRIM22
B
UMAP2
UMAP1
10
0
-10
-20
-10
0
10
5.0
2.5
0.0
-2.5
-2
0
2
4
Bao
Donson
Ducray
Gill
Gravendeel
Grzmil
Ivy_GAP
Kwom
Li
Murat
Oh
Reifenberger
Rembrandt
TCGA_agilent1
TCGA_agilent2
TCGA_RNAseq
Vital
Walsh
C
UMAP2
UMAP1
Verhaak
Classical
Mesenchymal
Neural
Proneural
Molecular subtypes
PN
PN-L
NL
CL-A
CL-B
CL-C
MES
Data
Tumors (n= 1612)
D
Proneural
Classical
Neural
Mesenchymal
PN
PN-L
CL-A
CL-B
NL
CL-C
MES

Figure 3

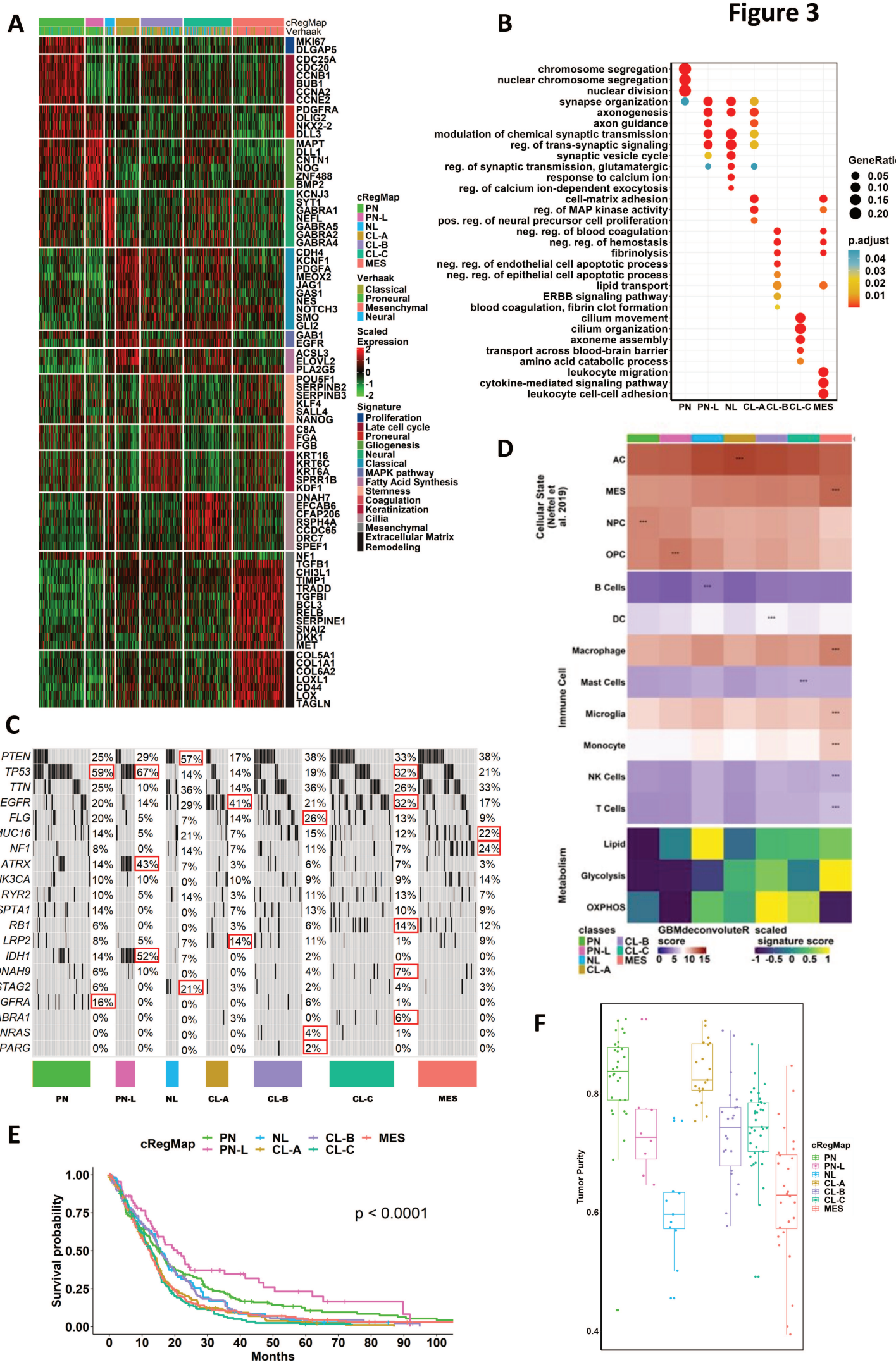
A
cRegMap
Verhaak
MKI67
DLGAP5
CDC25A
CDC20
CCNB1
BUB1
CCNA2
CCNE2
PDGFRA
OLIG2
NKX2-2
DLL3
MAPT
DLL1
CNTN1
NOG
ZNF488
BMP2
KCNJ3
SYT1
GABRA1
NEFL
GABRA5
GABRA2
GABRA4
CDH4
KCNF1
PDGFA
MEOX2
JAG1
GAS1
NES
NOTCH3
SMO
GLI2
GAB1
EGFR
ACSL3
ELOVL2
PLA2G5
POU5F1
SERPINB2
SERPINB3
KLF4
SALL4
NANOG
C8A
FGA
FGB
KRT16
KRT6C
KRT6A
SPRR1B
KDF1
DNAH7
EFCAB6
CFAP206
RSPH4A
CCDC65
DRC7
SPEF1
NF1
TGFB1
CHI3L1
TIMP1
TRADD
TGFBI
BCL3
RELB
SERPINE1
SNAI2
DKK1
MET
COL5A1
COL1A1
COL6A2
LOXL1
CD44
LOX
TAGLN
cRegMap
PN
PN-L
NL
CL-A
CL-B
CL-C
MES
Verhaak
Classical
Proneural
Mesenchymal
Neural
Scaled Expression
2
1
0
-1
-2
Signature
Proliferation
Late cell cycle
Proneural
Gliogenesis
Neural
Classical
MAPK pathway
Fatty Acid Synthesis
Stemness
Coagulation
Keratinization
Cilia
Mesenchymal
Extracellular Matrix Remodeling
B
chromosome segregation
nuclear chromosome segregation
nuclear division
synapse organization
axonogenesis
axon guidance
modulation of chemical synaptic transmission
reg. of trans-synaptic signaling
synaptic vesicle cycle
reg. of synaptic transmission, glutamatergic
response to calcium ion
reg. of calcium ion-dependent exocytosis
cell-matrix adhesion
reg. of MAP kinase activity
pos. reg. of neural precursor cell proliferation
neg. reg. of blood coagulation
neg. reg. of hemostasis
fibrinolysis
neg. reg. of endothelial cell apoptotic process
neg. reg. of epithelial cell apoptotic process
lipid transport
ERBB signaling pathway
blood coagulation, fibrin clot formation
cilium movement
cilium organization
axoneme assembly
transport across blood-brain barrier
amino acid catabolic process
leukocyte migration
cytokine-mediated signaling pathway
leukocyte cell-cell adhesion
PN PN-L NL CL-A CL-B CL-C MES
GeneRatio
0.05
0.10
0.15
0.20
p.adjust
0.04
0.03
0.02
0.01
C
PTEN 25% 29% 57% 17% 38% 33% 38%
TP53 59% 67% 14% 14% 19% 32% 21%
TTN 25% 10% 36% 14% 36% 26% 33%
EGFR 20% 14% 29% 41% 21% 32% 17%
FLG 20% 5% 7% 14% 26% 13% 9%
MUC16 14% 5% 21% 7% 15% 12% 22%
NF1 8% 0% 14% 7% 11% 7% 24%
ATRX 14% 43% 7% 3% 6% 7% 3%
PIK3CA 10% 10% 0% 10% 9% 9% 14%
RYR2 10% 5% 14% 3% 11% 13% 7%
SPTA1 14% 0% 0% 7% 13% 10% 9%
RB1 6% 0% 0% 3% 6% 14% 12%
LRP2 8% 5% 7% 14% 11% 1% 9%
IDH1 14% 52% 7% 0% 2% 0% 0%
DNAH9 6% 10% 0% 0% 4% 7% 3%
STAG2 6% 0% 21% 3% 2% 4% 3%
PDGFRA 16% 0% 0% 0% 6% 1% 0%
GABRA1 0% 0% 0% 3% 0% 6% 0%
NRAS 0% 0% 0% 0% 4% 1% 0%
PPARG 0% 0% 0% 0% 2% 0% 0%
PN PN-L NL CL-A CL-B CL-C MES
D
Cellular State (Neftel et al. 2019)
AC
MES
NPC
OPC
Immune Cell
B Cells
DC
Macrophage
Mast Cells
Microglia
Monocyte
NK Cells
T Cells
Metabolism
Lipid
Glycolysis
OXPHOS
classes
PN
PN-L
NL
CL-A
CL-B
CL-C
MES
GBMdeconvoluteR scaled score
0 5 10 15
signature score
-1 -0.5 0 0.5 1
E
cRegMap
PN
PN-L
NL
CL-A
CL-B
CL-C
MES
Survival probability
1.00
0.75
0.50
0.25
0.00
p < 0.0001
0 10 20 30 40 50 60 70 80 90 100
Months
F
Tumor Purity
0.8
0.6
0.4
cRegMap
PN
PN-L
NL
CL-A
CL-B
CL-C
MES

Figure 4

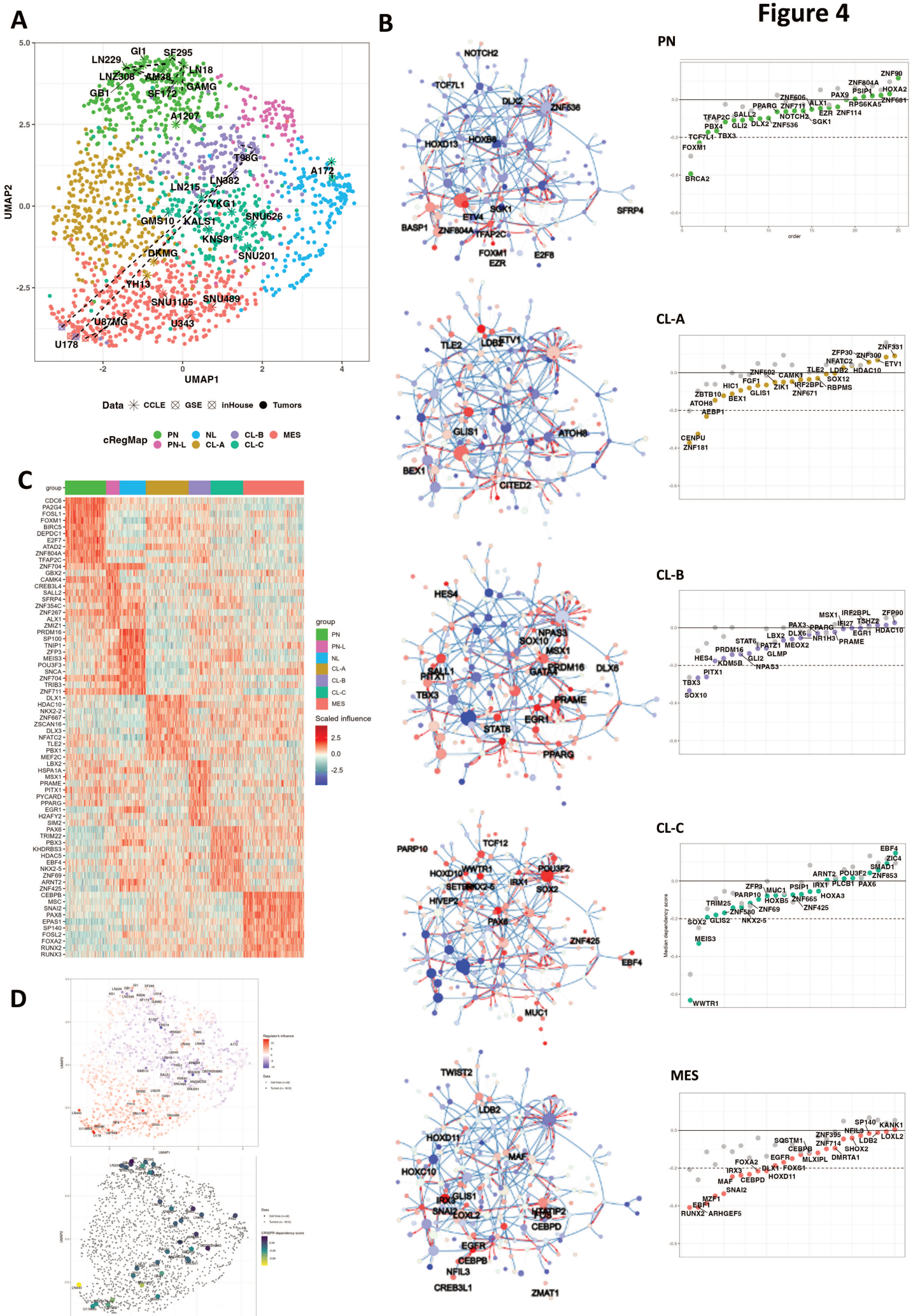
A
B
C
D
PN
CL-A
CL-B
CL-C
MES
UMAP1
UMAP2
Data CCLE GSE inHouse Tumors
cRegMap PN PN-L NL CL-A CL-B CL-C MES
group
Scaled influence
Median dependency score
order

Figure 5

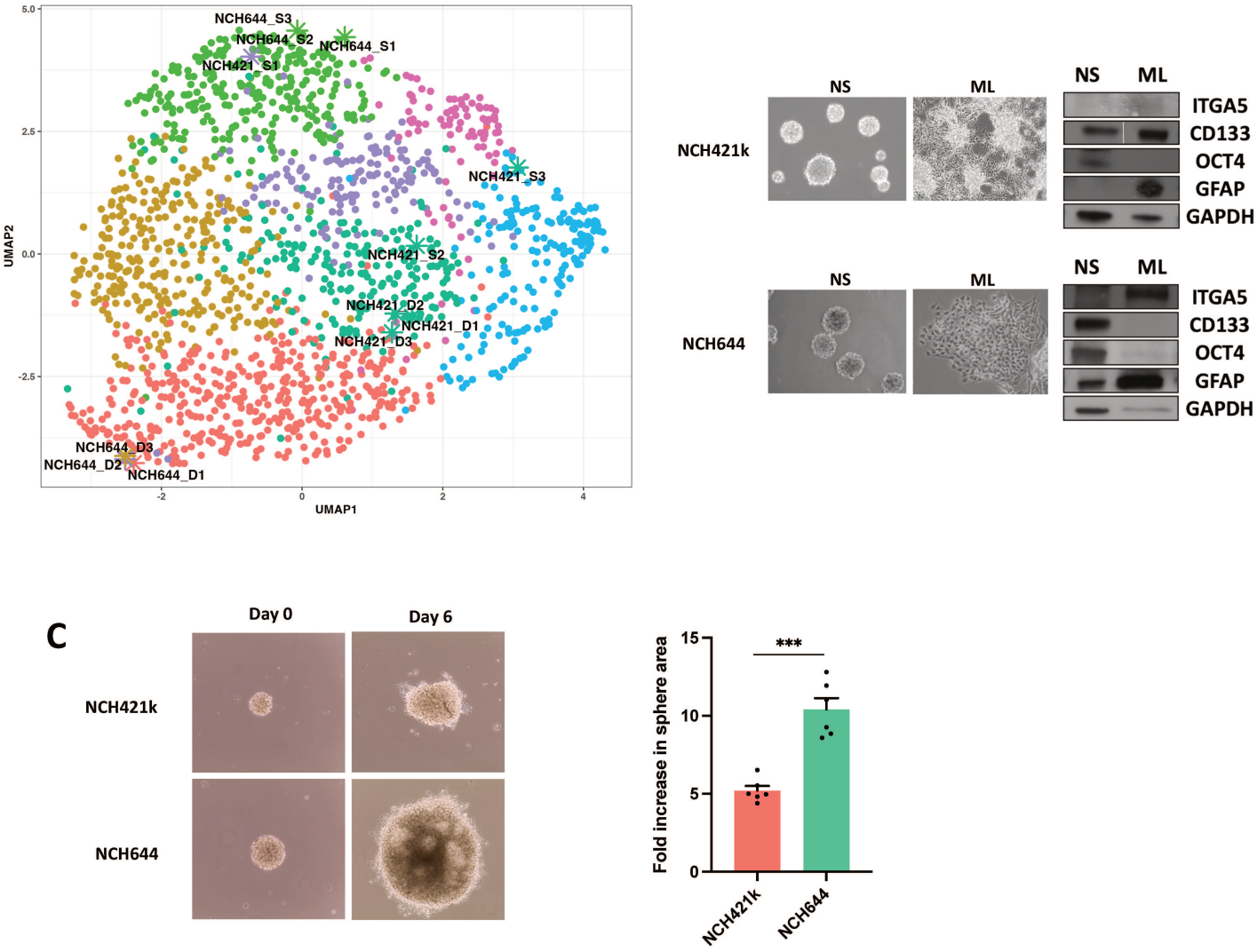
A
NCH644_S3
NCH644_S2
NCH644_S1
NCH421_S1
NCH421_S3
NCH421_S2
NCH421_D2
NCH421_D1
NCH421_D3
NCH644_D3
NCH644_D2
NCH644_D1
UMAP1
UMAP2
B
NS
ML
NCH421k
NCH644
ITGA5
CD133
OCT4
GFAP
GAPDH
C
Day 0
Day 6
NCH421k
NCH644
Fold increase in sphere area
***

Figure 6

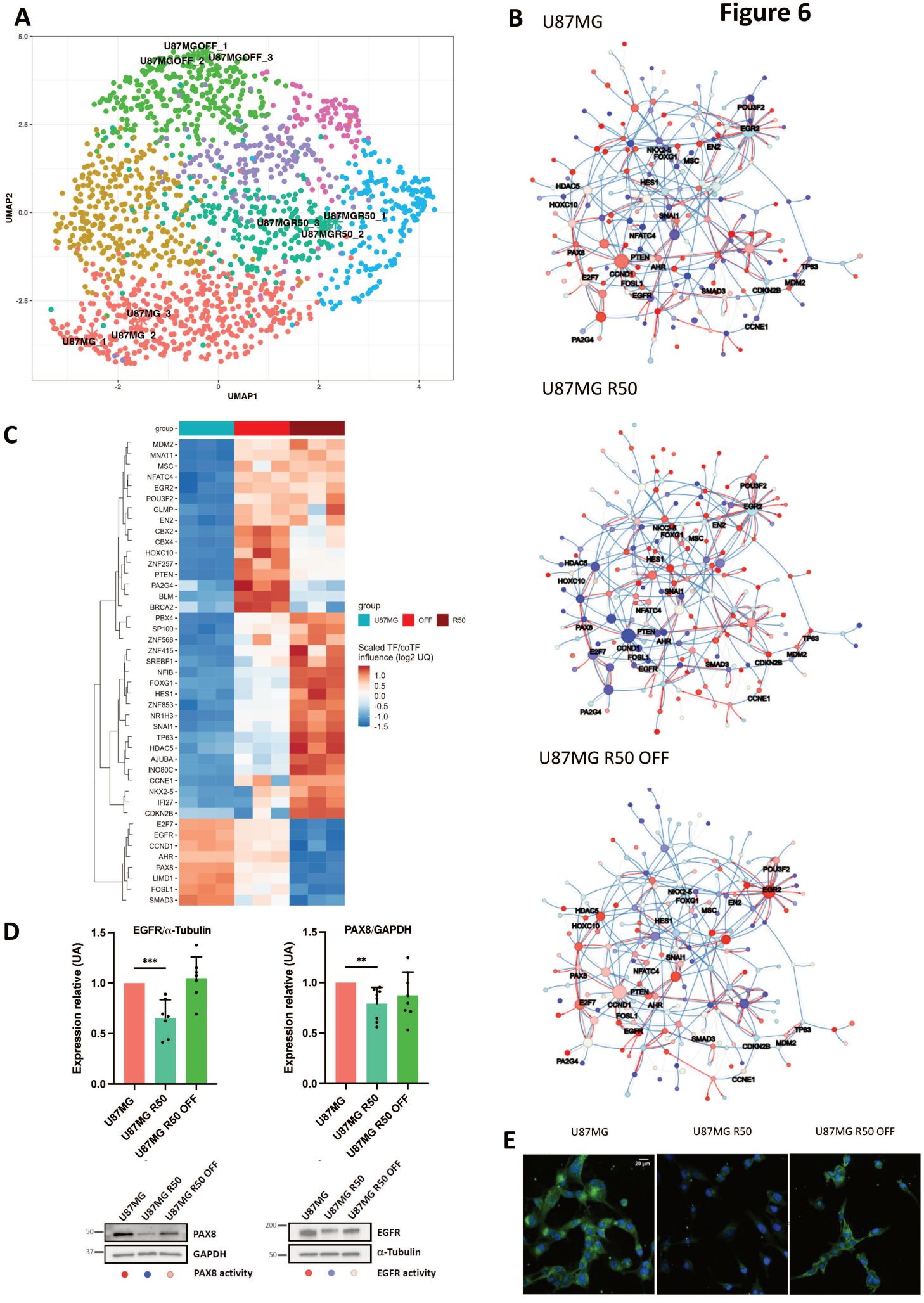
A
U87MGOFF_1
U87MGOFF_2
U87MGOFF_3
U87MGR50_1
U87MGR50_3
U87MGR50_2
U87MG_3
U87MG_2
U87MG_1
UMAP1
UMAP2
B
U87MG
U87MG R50
U87MG R50 OFF
C
group
U87MG
OFF
R50
Scaled TF/coTF influence (log2 UQ)
D
EGFR/α-Tubulin
PAX8/GAPDH
Expression relative (UA)
U87MG
U87MG R50
U87MG R50 OFF
PAX8
GAPDH
PAX8 activity
EGFR
α-Tubulin
EGFR activity
E
U87MG
U87MG R50
U87MG R50 OFF

Discussion et perspectives

En étroite collaboration avec le laboratoire CANTHER de Lille, notre projet interdisciplinaire a réuni des bioinformaticiens et des biologistes pour disséquer la complexité et la plasticité des GB. Nous avons adopté une approche bioinformatique, combinant biologie des systèmes et apprentissage automatique, pour développer deux outils en ligne : GBM-cRegNet, un réseau de régulateurs et co-régulateurs spécifiques des GB, et cRegMAP, une cartographie des GB, définissant sept sous-classes basées sur des profils régulateurs distincts. Ces nouvelles classes ont été caractérisées à différents niveaux, que ce soit en termes d'activité du réseau de régulateurs, d'expression génique, d'altérations moléculaires, de caractéristiques biologiques et cliniques (Tableau 4). Ces outils permettent non seulement de visualiser la diversité des GB mais également d'étudier en profondeur l'activité régulatrice de chaque sous-classe.

Alors que la plupart des études antérieures reposent sur des tailles de cohortes limitées, notre approche a permis d'intégrer 1612 tumeurs de patients provenant de 16 études différentes dans notre méta-cohorte. L'analyse de cette méta-cohorte a conduit à une nouvelle classification des GB en sept classes. Par rapport à la classification de Verhaak [21], notre approche a permis de distinguer trois sous-types classiques, CL-A : Astrocyte-like, CL-B : Epithelial Basal-like, CL-C : Cilia-rich. Nous avons également distingué la classe PN (Proneural), PN-L (Proneural-Low, à faible prolifération), MES (Mesenchymal) ainsi que le sous-type NL (Normal-like). Les tumeurs IDH-mutées ainsi que les gliomes au phénotype G-CIMP n'ont pas été exclus de l'étude afin d'avoir une vision globale du paysage moléculaire des gliomes de haut grade. Toutes les tumeurs IDH-mutées se retrouvent dans les classes PL-L (52%), PN (14%) et NL (7%), ces classes correspondent à celles associées à un meilleur pronostic des patients. L'identification de nouveaux sous-types tumoraux comme le sous-type CL-C, avec des caractéristiques associées aux cils, et le CL-B, avec des caractéristiques épithéliales, indique la présence de processus moléculaires et biologiques spécifiques au sein de ces classes. L'identification et la caractérisation de la classe CL-C représentent une avancée majeure, étant l'une des classes de plus mauvais pronostic. Des preuves croissantes suggèrent que les cils primaires pourraient être impliqués dans divers processus tumoraux et dans la résistance thérapeutique [223]. Une étude a montré que les patients atteints de gliome avec une forte expression génique liée aux cils primaires avaient un moins bon pronostic [224]. Notre étude soutient l'existence du sous-type « neural » décrit par Verhaak en 2010 [21], ainsi que du sous-

type « normal-like » identifié par Nguyen en 2020 [225]. Nous avons notamment identifié au sein de notre classe NL la surexpression de certains gènes de la signature du sous-type normal-like de Nguyen (SLC32A1 et SYT5) [225]. Nous avons également mis en lumière la présence d'altérations moléculaires dans le gène suppresseur de tumeurs PTEN dans 57% des tumeurs NL, ainsi qu'une fréquence plus élevée de mutations STAG2 dans ce sous-type. Ces découvertes soulignent la malignité du sous-type NL et la présence de caractéristiques tumorales distinctes. De plus, de plus en plus de preuves montrent que les cellules cancéreuses peuvent acquérir des caractéristiques neuronales [226,227]. Ces observations remettent en question la perspective antérieure de *Wang et al.*, qui suggéraient que le sous-type neural, initialement défini par Verhaak, ne présentait pas de signature tumorale spécifique, remettant ainsi en question sa classification en tant que sous-type tumoral distinct [98]. Ainsi, des preuves croissantes soutiennent que ce sous-type tumoral, malgré son profil transcriptomique 'normal-like', doit être reconnu comme une entité tumorale distincte.

Notre étude a permis d'identifier des régulateurs clés pour chaque sous-classe de GB. Dans le sous-type PN, les régulateurs principaux sont ZNF536, HOXA2 et PBX4. Pour la sous-classe CL-A, les régulateurs dominants sont ZNF671, ZNF181 et HDAC10. Dans la sous-classe CL-B, les facteurs clés incluent LBX2, HES4 et PITX1, tandis que dans la sous-classe CL-C, ce sont PAX6, POU3F2 et ZNF580. Concernant la sous-classe MES, CEBPB et SNAI2 se distinguent comme régulateurs principaux, ce qui correspond aux descriptions existantes dans la littérature scientifique. De plus, le sous-type MES révèle une interaction spécifique avec l'environnement tumoral, marquée par l'activité de régulateurs associés à l'hypoxie, tels qu'EPAS1 et CEBPD. Des thérapies ciblées visent spécifiquement certains de ces régulateurs. EPAS1, également connu sous le nom de HIF-2α, est un facteur de transcription ciblé dans de nombreuses études sur les GB. Des inhibiteurs de HIF-2α sont actuellement en développement pour traiter divers cancers, en particulier ceux affectés par des conditions hypoxiques. Par ailleurs, le panobinostat, un inhibiteur pan-HDAC, agit sur plusieurs HDACs, notamment HDAC10, un régulateur essentiel de la sous-classe CL-A, et HDAC5, important dans la sous-classe CL-B.

La plateforme en ligne GBM-cReg, grâce à sa fonctionnalité CoRegQuery, facilite l'intégration de nouvelles données transcriptomiques. Cet outil permet aux chercheurs d'analyser une variété d'échantillons, qu'ils proviennent de modèles *in vitro*, *in vivo*, ou de tumeurs prélevées sur des patients, en exploitant leurs données transcriptomiques obtenues par des technologies telles que le RNAseq ou les puces à ADN Affymetrix. Cette analyse des

réseaux de régulateurs apporte une dimension innovante à la recherche fondamentale, pouvant faciliter la compréhension des mécanismes pro-tumoraux. En effet, cet outil pourrait permettre d'identifier les régulateurs essentiels impliqués dans la plasticité tumorale, réagissant à des facteurs variés du microenvironnement, que ce soit en réponse à des thérapies, des variations de nutriments ou d'oxygène, ou lors de processus de différenciation ou de dédifférentiation cellulaire. La comparaison des profils régulateurs entre des lignées cellulaires naturellement sensibles à une thérapie spécifique et celles résistantes, soit de manière intrinsèque, soit acquise, à ces mêmes thérapies, pourrait permettre d'approfondir la compréhension des mécanismes de résistance aux traitements. Dans notre étude, nous avons notamment observé une augmentation de l'activité du régulateur MDM2 dans les deux lignées de GB résistantes au TMZ dérivées de la lignée U87MG. Des recherches préalablement conduites dans notre laboratoire avaient révélé qu'une inhibition de MDM2 pouvait effectivement renverser la résistance au TMZ observée dans ces mêmes lignées [228].

Alors que de nombreuses lignées cellulaires ont été classées comme 'mixtes' selon la classification de Verhaak, notre méthodologie innovante marque une évolution significative, nous permettant d'assigner avec un haut degré de confiance une classe spécifique à chaque lignée. Cela constitue une avancée importante vers une meilleure compréhension et classification des GB et de nos modèles d'étude.

Malgré des progrès significatifs, notre étude présente certaines limitations. Parmi celles-ci, le biais de sélection des échantillons, les contraintes liées à la détection des transcrits, l'absence de données fonctionnelles directes (nos analyses se basent sur les niveaux d'ARN plutôt que sur les protéines ou les activités cellulaires), les biais algorithmiques, et les biais d'interprétation. Notre approche, fondée sur des prédictions in silico issues de données transcriptomiques, déduit l'influence des régulateurs à partir des niveaux de transcrits détectés, ce qui introduit certains biais. La qualité et l'hétérogénéité des données peuvent affecter la fiabilité des résultats. Nos modèles cellulaires actuels se concentrent principalement sur les sous-types MES, PN et CL-C des GB, soulignant ainsi le besoin de développer de nouveaux modèles pour mieux représenter d'autres classes telles que CL-A, CL-B et PN-L. Ces modèles supplémentaires sont essentiels pour une compréhension plus approfondie des spécificités de ces classes. De plus, l'absence de données cliniques détaillées dans notre méta-cohorte, en particulier sur les traitements des patients, limite les implications cliniques de cet outil.

Les recherches futures pourraient enrichir l'outil GBM-cReg en intégrant des données sur les traitements des patients, augmentant ainsi la pertinence clinique de cette nouvelle classification. L'élargissement des lignées cellulaires utilisées pour la construction du réseau pourrait offrir une vue plus complète des différents régulateurs impliqués dans la pathogenèse des GB. Actuellement, l'outil ne permet pas un accès direct aux gènes cibles de chaque régulateur ni à l'impact de ces régulateurs sur ces gènes, qu'il soit positif ou négatif. L'intégration future de cette fonctionnalité pourrait permettre aux chercheurs d'accéder rapidement aux informations sur les gènes activés ou réprimés par un régulateur donné. Étant donné que le ciblage direct d'un facteur de transcription n'est pas toujours réalisable, une stratégie alternative pourrait consister à viser les gènes cibles de ce dernier, offrant ainsi de nouvelles perspectives pour le développement de traitements anticancéreux.

Les informations sur la biologie des tumeurs de GB sont dispersées à travers de nombreuses bases de données et études. Le développement d'outils comme GBM-cReg, qui a permis l'intégration de données transcriptomiques provenant de 16 études, représente un progrès important dans cette direction. Pour améliorer significativement la recherche sur les GB, il est essentiel de centraliser et d'exploiter conjointement les données biologiques et cliniques.

Ainsi, cet outil innovant ouvre des horizons prometteurs pour la compréhension de l'hétérogénéité et de la plasticité des tumeurs, pour l'élucidation des mécanismes pro-tumoraux, et également pour l'identification de nouvelles cibles thérapeutiques potentielles ainsi que la stratification des patients. En conclusion, notre étude marque un progrès significatif dans la compréhension de la nature complexe du GB. En combinant des méthodes informatiques de pointe avec des données expérimentales approfondies, nous ouvrons de nouvelles perspectives pour une meilleure compréhension et un traitement plus efficace du GB.

Classe	MES	CL-A	PN	CL-C	NL	CL-B	PN-L
Cohort proportion	25,4%	17,9%	17,2%	13,6%	11,0%	9,2%	5,6%
Signature	Mesenchymal Hypoxia-dependant	Classical Astrocyte-like	Proneural	Ciliary-rich Classical Low proliferative	Neural-like	Classical Hypercoagulation Epithelioid-like	Proneural G-CIMP IDH-mut
Median survival (months) [IC 95%]	12 [11 -13]	12 [11-14]	15 [13-17]	13 [11-14]	16 [14-18]	15 [14-18]	21 [14-42]
2-years survival [IC 95%]	84% [79-88]	80% [73-85]	66% [58-72]	84% [77-89]	70% [58-78]	70% [60-77]	59% [44-70]
Top 10 influent regulators	CEBPB MSC SNAI2 PAX8 EPAS1 SP140 FOSL2 FOXA2 RUNX2 RUNX3	DLX1 HDAC10 NKX2-2 ZNF667 ZSCAN16 DLX3 NFATC2 TLE2 PBX1 MEF2C	CDC6 PA2G4 FOSL1 FOXM1 BIRC5 DEPDC1 E2F7 ATAD2 ZNF804A TFAP2C	PAX6 TRIM22 PBX3 KHDRBS3 HDAC5 EBF4 NKX2-5 ZNF69 ARTNT2 ZNF425	PRDM16 SP100 TNIP1 ZFP3 MEIS3 POU3F3 SNCA ZNF704 TRIB3 ZNF711	LBX2 HSPA1A MSX1 PRAME PiTX1 PYCARD PPARG EGR1 H2AFY2 SIM2	ZNF704 GBX2 CAMK4 CREB3L4 SALL2 SFRP4 ZNF354C ZNF267 ALX1 ZMIZ1
Influent genes expressed	DKK1 COL1A1 COL3A1 TAGLN CD44 IL6 CCL2 MMP7 CCL7 NNMT VDR TLR2 ITAG5	EGFR CPNE4 MEOX2 NOS2 ELOVL2 SEC61G NPY2R ARSJ KLHL4 KCNF1 PDGFA NES DNMT3A	ERBB3 DLL3 TMSB15A PDGFRA RAB3C TOP2A KIF15 MKI67 BUB1 RRM2 CCNE2 CDK1 CDC6	DDIT4L LGR6 ETNPPL EGFR DRC1 RSPH1 RSPH4A CST3 DNAI2 SMAD1/9 STAT3 RPS6KA1 TP53INP1	CCK VSNL1 SYNPR NEFM CREG2 MAL2 SV2B TMEM125 SYT13 NEFL SYT1 CALM1 PACSIN1	ACSM3 SERPINB3 FGB PRR15L SERPINA7 CTCFL TYR SERPINB4 KRT family C8A C8B FGA FGB	LUZP2 KLRC2 GALNT13 SUSD5 SH3GL2 CDH18 IRX2 FERMT1 VWC2 MSTN TMEFF2 EPHB1 MYOT
Molecular alterations	PTEN (39%) TP53 (23%)	EGFR (42%) PTEN (23%) MUC16 (36%)	TP53 (58%) PTEN (27%) EGFR (22%) PDGFRA (19%)	PTEN (33%) EGFR (33%) TP53 (30%)	PTEN (53%) EGFR (27%) STAG2 (21%)	PTEN (38%) EGFR (20%)	TP53 (68%) IDH1 (55%) ATRX (41%) PTEN (27%)
Cell Markers	Microglia	Vascular endothelial cell, astrocyte	Oligodendrocyte, neural stem cell	Ciliated cell, astrocyte	Glutamatergic neuron, glial cell	Eosinophil, (pseudo)epithelial cell	Neuron, oligodendrocyte
Metabolism	Glycolysis +++ Lipid ++ OXPHOS -	Glycolysis ++ OXPHOS + Lipid -	OXPHOS - Glycolysis --- Lipid ---	OXPHOS ++ Lipid + Glycolysis -	Lipid +++ OXPHOS + Glycolysis -	OXPHOS +++ Glycolysis ++ Lipid +	Lipid - Glycolysis --- OXPHOS ---
Cellular state	MES	AC	NPC				OPC
Immune cell	Microglia Macrophages Monocytes NK cells T cells			Mast cells	B-cells	Dendritic cells	

Tableau 4 : Caractérisation des nouvelles sous-classes moléculaires des glioblastomes

Partie 2 : Hétérogénéité et plasticité moléculaire et métabolique des glioblastomes ; évaluation dans une cohorte de lignées de cellules souches

Contexte de l'étude

L'hétérogénéité et la plasticité représentent des défis majeurs en oncologie, jouant un rôle clé dans la résistance thérapeutique des GB. Cette étude se focalise sur l'exploration de l'hétérogénéité métabolique et moléculaire des CSG, ainsi que sur leur plasticité en réponse à la différenciation cellulaire et à l'hypoxie. Nous examinons également comment ces facteurs influencent la résistance au TMZ. Notre approche intégrée vise à cartographier le paysage métabolique et moléculaire des CSG, pour mieux comprendre leur capacité d'adaptation et de résistance au TMZ dans divers environnements mais également afin de déceler des vulnérabilités thérapeutiques. Pour cela, nous avons entretenu une cohorte de lignées de CSG dérivées de patients disponibles au laboratoire. Ces dernières ont été cultivées dans différents microenvironnements afin de mimer ce qui pourrait se passer *in vivo*. Des conditions de culture optimisées permettent de maintenir leurs propriétés souches et de les cultiver sous forme de neurosphères. D'autres conditions permettent d'induire et de maintenir la différenciation des cellules, en les cultivant en monocouche de cellules adhérentes. Les conditions de culture ont également varié entre la normoxie (21 % O_2) et l'hypoxie (1 % O_2) pour simuler l'hétérogénéité du microenvironnement tumoral. L'utilisation de la technologie Incucyte nous a permis d'analyser en temps réel la dynamique de croissance des neurosphères ou des cellules différenciées, ainsi que leur réactivité au TMZ et à d'autres thérapies. Les profils transcriptomiques de chaque lignée ont été établis sous différentes conditions de culture et intégrés dans GBM-cReg (*Bernhard et al.,* BioRxiv) pour déterminer la classe de GB basée sur l'activité régulatrice et caractériser l'activité de chaque régulateur du réseau. En parallèle, le métabolome de chaque lignée et condition a été caractérisé par spectroscopie RMN HRMAS. Les analyses métabolomiques, notamment *via* ADEMA, ont permis d'analyser la reprogrammation métabolique en réponse à la différenciation ou à l'hypoxie et de comparer les lignées résistantes aux sensibles. L'outil MetaboAnalyst a été utilisé pour intégrer les données transcriptomiques et métabolomiques, offrant une vision multiomique de la biologie des CSG. Ainsi, cette approche méthodologique multiparamétrique nous a permis de générer une base de données détaillée sur la biologie des CSG, allant de leurs profils métaboliques et transcriptomiques à l'activité du réseau de régulateurs et leur réponse à divers traitements.

Metabolism Landscape and Molecular Heterogeneity are Linked to Chemotherapy Resistance in Glioblastoma Stem Cells

Chloé Bernhard[1], Mélissa Messe[1], Sophie Foppolo[1], Damien Reita[1,2], Salmanli Chinar[1], Hassiba Outilfalt[3], Geoffrey Pawlak[4], Herold-Mende Christel[5], Idbaih Ahmed[6], Namer Izzie[3], Mohamed Elati[4], and Monique Dontenwill[1]

1. UMR7021 CNRS, University of Strasbourg, Illkirch, France
2. Department of Molecular Cancer Genetics, Molecular Oncology & Pharmacogenetics, University Hospital of Strasbourg, 67000 Strasbourg, France
3. ICANS | Institut cancérologie Strasbourg Europe, Strasbourg, France
4. Univ. Lille, CNRS, Inserm, CHU Lille, UMR9020-U1277 – CANTHER, Lille F-59000, France
5. Department of Neurosurgery, University Clinic, Heidelberg, Germany
6. Sorbonne University, Inserm, CNRS, UMR S 1127, Brain Institute, ICM, AP-HP, University Hospitals La Pitié Salpêtrière - Charles Foix, Neurology Department 2-Mazarin, F-75013 Paris, France

Keywords: glioblastoma; glioblastoma stem cell; metabolism; heterogeneity; plasticity; chemoresistance

ABSTRACT

Glioblastoma (GB) remains one of the most challenging malignancies in oncology, largely due to its pronounced resistance to standard treatments, including temozolomide (TMZ). This study delves into the metabolic and molecular heterogeneity of GB stem cells (GSCs), as well as their plasticity in response to cellular differentiation and hypoxia, and its correlation with TMZ resistance. Utilizing extracellular flux analysis, metabolomics, transcriptomics, and regulators network activity analysis, we have uncovered significant insights into the metabolic and molecular landscape of GSCs, particularly in the context of TMZ resistance. Our findings reveal that glycolytic GSCs, especially under normoxic and hypoxic conditions, exhibit enhanced resistance to TMZ. This resistance is associated with distinct metabolic and molecular characteristics, including lower levels of N-acetylaspartate (NAA) and increased activity of PINK1, a key transcription factor involved in mitophagy. Furthermore, our study indicates that GSCs may acquire TMZ resistance through the differentiation process, associated with deregulation of pathways related to autophagy, and oxidative stress management. Overall, this study underscores the potential role of autophagy and oxidative stress response in mediating TMZ resistance and open new avenues for the development of targeted therapeutic strategies to overcome TMZ resistance in both GSCs and differentiated GB cells (DGCs), highlighting potential therapeutic pathways and targets for future research.

INTRODUCTION

Glioblastomas (GBs) are the most frequent and devastating primary malignant brain tumors. Despite the implementation of the Stupp protocol in 2005 - comprising maximal surgical resection followed by concomitant and adjuvant temozolomide (TMZ) chemotherapy and radiotherapy - survival outcomes remain bleak [1]. Most patients relapse and no significant clinical improvement has been achieved despite extensive clinical trials of new therapeutic proposals [2]. The recurrence of GB is almost a certainty, highlighting the failure of existing therapeutic measures and underscoring the urgency for alternative strategies. A major factor contributing to this therapeutic failure is the complex heterogeneity and plasticity of GBs. GB contain differentiated GB cells (DGCs) that constitute the main bulk of the tumor, but also GB stem cells (GSCs) which are particularly problematic due to their abilities to self-renew and to differentiate into various cancer cell lineages. Their roles in initiating and sustaining tumor growth, as well as their higher resistance to conventional therapies, make them key players in therapeutic resistance and overall tumor recurrence [3]. Recent work has demonstrated an interconnection between the two cellular states, stem and differentiated, involved in tumour progression and resistance to therapies [4]. On the molecular front, GBs can be categorized into four major subtypes with implications for clinical outcomes : pro-neural, neural, classical, and mesenchymal [5]. Different molecular subtypes can be found globally within the same tumour, highlighting the intra-tumoral heterogeneity of GB [6]. This heterogeneity extends to the tumor metabolism. In 2021, Garofano et al. [7] identified four distinct GB subtypes using a multi-omic approach, categorized into neurodevelopmental and metabolic types, specifically mitochondrial and glycolytic/plurimetabolic. The study revealed that patients with the mitochondrial subtype had a more favorable clinical prognosis. Additionally, other research has shown that GSCs demonstrate remarkable metabolic plasticity, adapting to different nutritional and oxygen conditions within the tumor microenvironment [8]. While GSCs are metabolically flexible, they primarily utilize oxidative phosphorylation (OXPHOS) for ATP generation, in contrast to DGCs that mainly utilize aerobic glycolysis [9,10]. Recent research in cancer treatment suggest that metabolic pathways in tumor cells could serve as actionable therapeutic targets. This has led to the burgeoning field of metabolic therapy, which offers a glimmer of hope in the otherwise grim context of GB treatment [11]. Our study aims to investigate the molecular and metabolic state of GSCs under different conditions, including stem and differentiated state as well as in hypoxia, to provide a comprehensive understanding that may inform the development of targeted therapeutic approaches for GB. We focus on the molecular and metabolic heterogeneity and plasticity of GSCs, exploring how these traits correlate with TMZ resistance. Our comprehensive analysis employed advanced technologies such as Seahorse XF real-time metabolic profiling and HRMAS NMR spectroscopy, underscoring the link between metabolic features and drug sensitivity. Additionally, we utilized the GBM-cRegMap tool (Bernhard and al, BioRxiv) to identify key regulators potentially involved in TMZ resistance in both GSCs and differentiated GSCs, offering new insights into the molecular complexity of GB. This study not only enhances our

understanding of the metabolic dynamics in GB but also opens new avenues for targeted therapeutic interventions aimed at overcoming drug resistance in this devastating disease.

MATERIALS AND METHODS

Cell lines

NCH644 and NCH421k cell lines are patient-derived GSCs provided by Pr. Herold-Mende[12]. 5706 and 3731 cell lines are patient-derived GSCs provided by Dr Ahmed Idbaih. TC7 and TC22 GSCs are derived from two patient-derived GB xenografts and were established in the laboratory of Bioimaging and Pathologies [13].

Cell Culture

We cultured a cohort of 6 patient-derived GSCs lines in stem cell medium (neurospheres) or differentiation medium (adherent cell culture) in normoxia (21% O_2) or hypoxia (1% O_2). NCH644, NCH421k, 5706 and 3731 lines were cultured in neurosphere condition using Dulbecco's Modified Eagle medium with nutrient Mixture F-12 and GlutaMAX™ (DMEMF12+GlutaMAX™, Gibco™), supplemented with BSA Insulin Transferrin (BIT-100) (20%) (Provitro), EGF (20 ng/mL) (Reliatech) and β-FGF (20 ng/mL) (Reliatech) growth factors. TC7 and TC22 lines were cultured in neurosphere condition using DMEMF12+GlutaMAX™ (Gibco™), supplemented with B27™ (2%) (Provitro), EGF (20 ng/mL) (Reliatech) and β-FGF (20 ng/mL) growth factors (Reliatech). These cells were cultured in monolayer condition using DMEM/F12 + GlutaMAX™ medium (Gibco™) supplemented with 10% (vol/vol) fetal bovine serum (FBS) (Gibco™).

Seahorse metabolic flux analysis

Energy production and pathways (glycolysis and OXPHOS) were evaluated through Seahorse XFp analysis. Real-time analysis of oxygen consumption rates (OCR) and extracellular-acidification rates (ECAR) of stem-like or adherent cells were assessed in vitro using the Seahorse XFp analyzer (Seahorse Bioscience). XFp flux cartridges were hydrated in XF Calibrant overnight at 37 °C. Cells were plated at 60 000 cells/well into the lineage-specific medium on Seahorse XFp culture microplates (Agilent®) coated with Cell-Tak at 22.4 µg/mL (Corning®) to ensure adherence. After 45 minutes, media was changed into Seahorse XF DMEM medium (Agilent 103575-100) supplemented with 10 mM glucose (Agilent 103577-100), 2 mM glutamine (Agilent 103579-100) and 1 mM Sodium pyruvate (Agilent 103578-100). Cells were equilibrated in a humidified non-CO_2 incubator until the start of the assay. Flux cartridges were loaded with Oligomycin (1.5 µM) and Rotenone/Antimycin A (0.5 µM each) according to manufacturer's instructions. Oxygen consumption rate and basal extracellular acidification rate values were obtained over time in each well, at basal level and after injection of oligomycin and rotenone/antimycin A mixture. Data were analyzed using Agilent Seahorse Analytics. All results were normalized to input cell numbers.

Metabolomic

Culture and sample preparation for metabolomic analysis

Cells were seeded and incubated in normoxia (21% O_2) or hypoxia (1% O_2) for one week. After one week, cells were collected, counted and centrifuged at 300 g for 5 minutes. Cell pellets of about 2-10 million cells were washed in Phosphate Buffered Saline (PBS), then centrifuged at 300 g for 10 min at 4°C. The dry pellets were stored at -80°C until analysis. Four cell pellets at different passages were prepared from the different stem-like cell lines grown under normoxic conditions. For the adherent cell lines under normoxic conditions and the stem-like cell lines under hypoxic conditions, 2 pellets each were prepared. Cells were transferred to pre-weighed 25 µL disposable HR-MAS Kel-f inserts. The sealed inserts were then weighed to determine the pellet mass, then the volume of the inserts was completed with deuterium oxide (D_2O). Inserts were then stored at -20°C until analysis.

HR-MAS NMR Spectroscopy

HR-MAS NMR experiments were performed on a Bruker Avance III spectrometer operating at a proton frequency of 500.13 MHz, equipped with a triple-resonance (^{1}H, ^{13}C, ^{31}P) HRMAS probe. The temperature was maintained at 277 K throughout the acquisition time in order to reduce cell degradation. All experiments were conducted on samples spinning at 3502 Hz. Detailed NMR experimental parameters are provided in the following table. The spectra were normalised to the weight of each sample and calibrated using a defined amount of lactate as a reference.

	^{1}H CPMG	^{13}C HSQC-2D
Relaxation time (D1 ; sec)	2	1,5
Presaturation RF field (Hz)	50	50
Acquisition time (AQ ; sec)	2,3396351	F2: 0,146; F1: 0,006
Sampling	32768	F2 : 8192 ; F1 : 256
Spectrum width (SW ; ppm)	14,0019	F2: 14,0019 ; F1 : 165,65
Number of dummy scans (DS)	4	64
Number of scans (NS)	1024	272
Duration of experiment (EXPT)	1 h 16 min 38 sec	1 jour 8 h 45 min
Number of loops (L4)	328	NA
Interpulse time (µs)	143	NA

Table 1: Detailed NMR experimental parameters

Metabolomic profiling data analysis and statistics

Metabolite identification was conducted using one-dimensional ^{1}H profiles and and further investigated using two-dimensional ^{1}H-^{13}C HSQC profiles. Principal component analysis (PCA) was used to assess HR-MAS NMR datasets homogeneity and exclude technical or biological outliers (out of the 95% confidence interval). Then, PCA was used to identify primary sources of variance within the datasets and metabolomic difference between samples. To achieve a more detailed understanding, we used the Algorithm to Determine Expected Metabolite level Alterations (ADEMA) [14]. This algorithm, which

is based on mutual information, considers metabolite quantification values and incorporates metabolic pathway information either unidirectionally or bidirectionally, with reference to the Kyoto Encyclopedia of Genes and Genomes (KEGG) [15,16] and Salway's work [17]. Unlike conventional methods that analyze individual metabolite concentrations, ADEMA evaluates changes in groups of metabolites between two experimental sets. This provides insights into collective biomarkers and allows for the prediction of expected changes in individual metabolite levels based on the metabolic network topology considered. The false discovery rate (FDR) was controlled at a 5% level to mitigate the risk of Type I errors. Various groups of metabolites related to metabolic pathways were analyzed in our study : Taurine HypoTaurine Allocystathionine Methionine Aspartate Serine ; Aspartate Asparagine Acetate Threonine N-acetylaspartate N-Acetylaspartylglutamic acid ; Aspartate Lysine N-acetyl-L-lysine ; Acetate Threonine Allocystathionine Methionine ; Glucose Acetate Hydroxybutyrate ; Aspartate Threonine Isoleucine ; Glucose Serine Glycine ; Glucose Valine Isoleucine Leucine ; Glucose Lactate ; Valine Lactate Alanine ; Glucose Myoinositol Scylloinositol ; Ascorbate Glutathione Glycine Glutamate ; Glutamate GABA Proline Histidine ; Aspartate Adenosine Succinate Fumarate ; Glutamate Glutamine Glycine ; Glutamate Arginine Glycine TotalCreatine Ornithine ; Creatine Phosphocreatine TotalCreatine ; Aspartate Arginine Ornithine ; Ethanolamine Choline Glycerophosphocholine Phosphocholine TotalCholine ; Glycerophosphocholine Phosphocholine ; Choline Betaine Glycine ; Serine Glycerol Phenylalanine Tyrosine. Statistical evaluations were conducted using Graphpad Prism 8.0 and MetaboAnalyst 5.0 [18].

Pharmacological agents

Temozolomide (TMZ) (Ref. #T2577, Sigma-Aldrich) was prepared by dissolving it in DMSO to a concentration of 100 mM and then stored at -20°C until use. In all experiments conducted, the final concentration of DMSO in the culture medium did not exceed 0.1%. Oligomycin (Ref. #75351), rotenone (Ref. #R8875), and antimycin A (Ref. #A8674) were purchased from Sigma-Aldrich. Oligomycin was dissolved in DMSO to create 10 mM stock solutions. Antimycin A was dissolved in 70% ethanol to obtain a 1 mM stock solution. Rotenone was dissolved in 100% ethanol to prepare a 1 mM stock solution. All stock solutions were stored at -20°C and were stable for up to 2 months.

Proliferation and chemotherapy sensitivity assays

For normoxic and hypoxic experiments, cells were incubated in a Thermo Scientific Heracell 250i CO_2 incubator (ThermoFischer) and followed by the real-time microscopic assessment using Incucyte® technology. 3000 stem-like cells/well or 15000 adherent cells/well were seeded in a 96-well plate and cultured during 6 days in an incubator at 37°C, 5% CO_2 in normoxia (21% O_2) or in hypoxia (1% O_2). Cell proliferation assays were performed by IncuCyte real-time analysis. Cell confluency of adherent cells and surface area (mm^2) of neurosphere was followed with an IncuCyte^{TM} Zoom Live Cell Analysis system. The IncuCyte® technology took images every 4 hours, surface area and cell confluence was

measured then normalized at time zero. Statistical significance for the tumour growth from day 0 to day 6 was analysed by paired t-tests. Statistical significance between the normoxic and hypoxic conditions was performed using unpaired t-tests. $P < 0.05$ was considered to be significant, and $*P < 0.05$, $**P < 0.01$, $***P < 0.001$, $****P < 0.0001$. Results are shown as mean and the error bar represents the standard error of mean (SEM). GraphPad Prism 8.0 was used to analyze the data.

Transcriptomic analyses

Transcriptomic analyses for the NCH644 and NCH421k in stem-like and differentiated state were based on methods and data previously reported (Bernhard et al., BioRxiv). For other transcriptomic analyses, RNA-Seq experiments were conducted. Library preparation was performed at the GenomEast platform at the Institute of Genetics and Molecular and Cellular Biology using the TruSeq Stranded mRNA Reference Guide – PN 1000000040498. RNA-Seq libraries were generated from 500 ng of total RNA using the TruSeq Stranded mRNA Library Prep Kit and IDT for Illumina – TruSeq RNA UD Indexes (96 Indexes, 96 Samples) (Illumina, San Diego, USA), according to the manufacturer's instructions. Briefly, following purification with poly-T oligo-attached magnetic beads, the mRNA was fragmented using divalent cations at 94°C for 2 minutes. The cleaved RNA fragments were then reverse transcribed into first-strand cDNA using reverse transcriptase and random primers. Strand specificity was achieved by replacing dTTP with dUTP during second-strand cDNA synthesis using DNA Polymerase I and RNase H. Following the addition of a single 'A' base and subsequent adapter ligation onto double-stranded cDNA fragments, the products were purified and enriched with PCR (30 sec at 98°C; (10 sec at 98°C, 30 sec at 60°C, 30 sec at 72°C) x 12 cycles; 5 min at 72°C) to create the cDNA library. Surplus PCR primers were further removed by purification using SPRI select beads (Beckman-Coulter, Villepinte, France), and the final cDNA libraries were checked for quality and quantified using capillary electrophoresis. The libraries were sequenced on an Illumina HiSeq 4000 sequencer, producing single-end 50-base reads. Image analysis and base calling were performed using RTA version 2.7.7 and bcl2fastq version 2.20.0.422.

Regulator Network Analysis.

The GBM-cRegMap tool, as previously developed by Bernhard et al. (BioRxiv), was utilized for a thorough analysis of the regulatory landscape under a range of experimental conditions, employing transcriptomic data. This tool employs the CoRegQuery function within the GBM-cRegNet to determine the influence of regulators in the input dataset. It categorizes the influence of each regulator as either positive or negative, thereby offering insights into their respective impacts on gene expression.

Support Vector Machine Model for Class Assignment

A Support Vector Machine (SVM) model, previously trained on a meta-cohort, was employed to analyze the GSC data under various experimental conditions. This model evaluates the influence of regulators

and assigns classes to individual samples based on their transcriptomic profiles. When the SVM model assigns class probabilities below 75%, these samples are categorized as 'Mixed', indicating a complex regulatory pattern that does not clearly fit into a single class. This categorization is essential for recognizing the diverse molecular profiles present in GSC lines.

Enrichment Analysis

Enrichr (https://maayanlab.cloud/Enrichr/) is a comprehensive web-server hosting a variety of datasets [19]. For our study, we utilized the Reactome 2022, KEGG 2021 Human, BioPlanet 2019, MSigDB Hallmark 2020, GO Biological Process 2023 datasets. We established a statistical significance threshold of less than 0.05**.**

Integrative omics was performed using MetaboAnalyst 5.0 [18]. Both transcriptomics and metabolomics data underwent individual statistical assessments through the "General Statistical Analysis and Visualization" feature in MetaboAnalyst. For a combined pathway evaluation, we identified metabolites and transcripts that exhibited significant changes (based on an adjusted p-value<0.05 and a log2 fold changes >1). We submitted the log2 fold changes of both metabolic transcripts and metabolites, ensuring the correct species (homo sapiens) was chosen. The algorithm parameters set were: Enrichment analysis using the "Hypergeometric test", Topology measure set to "Degree Centrality", and the Integration method as "Combine query". We exported result tables and overview diagrams for both "Metabolic Pathways—Metabolites Only" and "Metabolic Pathways—Integrated". Additionally, we created volcano plots utilizing the ggplot2 package in R (version 4.0.2, from the Free Software Foundation's GNU project, Boston, MA, USA).

RT-qPCR Analysis

U87MG were seeded in a 6-well plate at a density of 0.5 million cells per well and cultured in pure OptiMEM medium, or supplemented with Lipofectamine 2000 (ThermoFisher), negative control plasmid (5 µg), or NKX2.5 plasmid (5 µg) for a period of 24 hours. The cells were then washed with 1X PBS and lysed with 350 µL of RLT buffer from the extraction kit (RNEasy Plus Mini Kit, Qiagen). The RNeasy procedure is a well-established technology for RNA purification. This technology combines the selective binding properties of a silica-based membrane with the speed of microspin technology. Biological samples are first lysed and homogenized in the presence of a buffer containing highly denaturing guanidine-thiocyanate (RLT buffer), which immediately inactivates RNases to ensure the purification of intact RNA. Ethanol is added to provide appropriate binding conditions, and the sample is then applied to an RNeasy mini spin column, where total RNA binds to the membrane and contaminants are efficiently removed by washing. High-quality RNA is then eluted in 30 µL of water. The quantity of extracted RNA is then determined by UV-Visible spectrophotometry, using the NanoDrop™One (ThermoFisher). Reverse transcription is then performed using the iScript™ Reverse Transcription Supermix kit (BioRad), using 1 µg of RNA. The samples are then placed in a thermocycler

(T100, BioRad) for the reverse transcription reaction according to the iScript program: a priming phase (5 minutes at 25°C), reverse transcriptase activation (46 minutes at 46°C), and reverse transcriptase inactivation (1 minute at 95°C). qPCR (quantitative PCR or real-time PCR) is performed using a reaction mixture including specific primers (Table 1) and SYBR GreenTM as a reagent. For each well of a 96-well MicroAmpTM optical plate (Applied BiosystemsTM), 15 µl of this mixture are deposited. The cDNA, previously obtained by reverse transcription, is diluted 5 times with RNase-free water. Then, 5 µl of this diluted solution is added to each well, reaching a final concentration of 50 ng per well. qPCR is performed using the StepOnePlusTM (4376357, Thermofisher) and StepOneTM software (v2.3). RNA18S was used as an endogenous control.

Genes	Manufacturer	Reference	Primers/Transcript detected
RNA18S	Invitrogen Thermo Fisher	426826 Y4744 (D03) 426826 Y4744 (D04)	5'-TGTGGTGTTGAGGAAAGCAG-3' 3'-TCCAGACCATTGGCTAGGAC-5'
GAPDH	Invitrogen Thermo Fisher	710832 L3872 (H11) 710832 L3872 (H12)	5'-GTCACCAGGGCTGCTTTTAACTCT-3' 3'-GGAATCATATTGGAACATGTAAACCAT-5'
GPI	Qiagen	PPH00897C	NM_000175.3
HK2	Qiagen	PPH00983B	NM_000189.4
LDHA	Qiagen	PPH02047H	NM_005566.3
TPI1	Qiagen	PPH02051A	NM_000365.5

Table 2 : List of Primers Used for qPCR

RESULTS

GSCs Metabolic Profile is Heterogeneous

Our primary goal was to elucidate the metabolic diversity among GSC lines under normoxic conditions (Fig. 1). Using Seahorse XF technology for real-time metabolic profiling, we observed distinct oxygen consumption rates (OCR) and extracellular acidification rates (ECAR), revealing distinct mitochondrial and glycolytic activities (Fig. 1A). The NCH421k line demonstrated the highest mitochondrial respiration, with an OCR of 115.7 pmol/min (± 20.9), while the TC7 line had a markedly lower OCR of 50.2 pmol/min (±12.1), harboring the less oxidative phenotype. Conversely, ECAR data revealed the TC7 line as the most glycolytically active, with an ECAR of 42.9 mpH/min (± 13.0), in contrast to the 5706 line, which had the lowest at 25.7 mpH/min (± 1.8). Real-Time ATP Rate Assays further underscored these metabolic variations across the GSC lines (Fig. 1B). For example, the NCH421k cell line demonstrated a high metabolic activity, characterized by the highest ATP production rate observed at 545.0 pmol/min. In contrast, the 5706 cell line exhibited the lowest rate at 298.4 pmol/min, indicating a more quiescent state. Variations in glycolytic and mitochondrial ATP production rates were also noted, with the TC7 line showing the highest glycolytic ATP rate (261.4 ± 49.9 pmol/min) and the NCH421k line the highest mitochondrial ATP production (397.9 ± 49.9 pmol/min). We used the Seahorse XF ATP Rate Index, calculated as the ratio of mitochondrial ATP production rate to glycolytic ATP production

rate, as a robust metric for distinguishing metabolic phenotypes (Fig. 1C). We categorized the GSC lines into two distinct metabolic groups: oxidative cells, which primarily depend on oxidative phosphorylation, as indicated by an XF ATP Rate Index greater than 1 (including NCH421k, TC22, and 3731 lines), and glycolytic cells, which mainly rely on glycolysis, as indicated by an XF ATP Rate Index less than 1 (comprising 5706, NCH644, and TC7 lines). To complement our Seahorse XF analyses, we performed metabolomic study using HRMAS NMR spectroscopy (Fig. 1D). Our comparative analysis of glycolytic and oxidative cells revealed distinct metabolites with statistically significant concentration differences, showing that allocystathionine, N-acetyl-L-lysine, N-acetylaspartate (NAA), and N-acetylaspartylglutamic acid (NAAG) levels are higher, while alanine and taurine levels are lower in oxidative GSCs compared to glycolytic GSCs.

To further substantiate these findings and gain deeper insights, we employed the ADEMA algorithm for network comparison to compare glycolytic and oxidative GSCs. This advanced analysis highlighted pronounced differences in several key metabolic pathways, including glycolysis, the TCA (tricarboxylic acid) cycle, glutaminolysis, amino acid metabolism, oxidative stress response, and phospholipid metabolism (Fig. 2). Specifically, in glycolytic GSC lines, there was an expected upregulation of glucose and lactate levels, indicative of enhanced glycolytic activity, accompanied by decreased levels of metabolites related to phospholipid metabolism, such as NAA and choline. Additionally, we noticed a decrease in glutamine levels in glycolytic GSCs, indicating a lesser reliance on glutamine and glutaminolysis. This reduction in glutamine, vital for glutathione synthesis, corresponded with lower glutathione levels. Variations in amino acid profiles suggest distinct divergences in amino acid biosynthesis and catabolism pathways. In glycolytic GSCs, the pathways of alanine, glycine, and proline are downregulated, while those of lysine and leucine are upregulated compared to oxidative GSCs. Ascorbate levels are upregulated while myoinositol and glutathione are downregulated in glycolytic GSCs compared to oxidative GSC, suggesting divergent redox status and distinct strategies in managing oxidative stress. The decreased levels of creatine in glycolytic lines may reflect a lower capacity for energy storage or an increased consumption of energy reserves. The pathway most significantly altered between the two groups, as identified by ADEMA analysis, involved aspartate, threonine, NAA, and N-acetylaspartylglutamic acid. Overall, these results corroborate our Seahorse findings and highlight the complexity and heterogeneity in metabolic profiles across GSC lines.

GSCs Plasticity Is Accompanied by Metabolic Reprogramming

In GB, stem-like cells and more differentiated cells (DGC) coexist within a tumor. This complexity is further influenced by environmental conditions, such as hypoxia. Indeed, GSCs are known to reside preferentially in hypoxic niches or perivascular niches. Understanding how GSCs adapt their metabolism in these varied contexts is essential, as it plays a crucial role in their ability to survive, grow, and resist treatments. We therefore evaluated GSCs metabolism in hypoxia as well as after

differentiation. To induce differentiation, GSCs were grown in a medium enriched with FBS and without EGF and β-FGF growth factors. This culture condition induced a shift to a differentiated state, previously confirmed by observing an increase in the glial marker GFAP (data not shown).

To investigate the bioenergetic changes accompanying differentiation, we performed Seahorse ATP Real-Time Rate Assays and metabolomic analyses (Fig. 3A-D). The ATP Rate Assays revealed a general increase in ATP production rates (significant for the TC22, 3731, and NCH644) following differentiation (Fig. 3A). This suggests that DGCs are more metabolically active than their GSC counterparts. Four of the six GSC lines exhibited a glycolytic phenotype after differentiation, as indicated by a glycolytic index greater than 50%. Specifically, glycolytic index increased for NCH421k, 3731 and NCH644 but decreased for the 5706 cell line (Fig. 3B). Metabolomic data, analyzed through principal component analysis (PCA), revealed a distinct metabolic shift between stem-like and differentiated states across all cell lines (Fig. 3C). This shift was particularly evident in the positioning of glycerophosphocholine on the PC1 axis, suggesting a considerable change in its concentration between the two cellular states and indicating that its associated metabolic pathways are integral to the metabolic reprogramming upon differentiation. Additionally, ADEMA was employed to characterize the metabolic reprogramming of each GSC upon differentiation, revealing distinct metabolic fingerprints for each cell line (Fig. 3D). Notably, ADEMA predicted an elevation in lactate levels post-differentiation in the 3731 line, confirming its heightened glycolytic activity and a decrease in 5706 cell line, confirming reduced glycolytic activity (Fig. 3D). While DGCs are generally characterized as more glycolytic than their GSC counterparts, our study reveal a notable variability in glycolysis reprogramming after differentiation. Moreover, our results indicate that metabolic plasticity of GSCs is not determined by the initial metabolic profile under stem state : glycolytic GSCs may become more or less glycolytic after differentiation, and a similar pattern is observed in oxidative GSCs.

Turning to hypoxia-induced bioenergetic changes, we cultured GSCs under neurosphere conditions in a hypoxic environment (1% O_2) for 3 days, followed by metabolic assays (Fig. 3E). We found that hypoxia typically impaired ATP production rates across all GSC lines, thereby hindering oxidative phosphorylation. In oxidative GSC lines such as NCH421k and TC22, hypoxia notably promoted glycolysis, leading to increased lactate production. In contrast, the glycolytic NCH644 cell line exhibited reduced glycolytic activity under hypoxic conditions, a finding corroborated by HRMAS NMR spectroscopy (data not shown). These results indicate varied metabolic responses to hypoxia among GSC populations. Particularly, oxidative GSCs demonstrate a higher degree of metabolic plasticity in response to hypoxic stress. This observation could have significant implications for the survival and treatment resistance of various GSC populations within the hypoxic tumor microenvironment.

Overall, our analysis underscores that metabolic reprogramming is a hallmark of GSCs, particularly evident under in vitro conditions designed to mimic in vivo environments such as hypoxia and

differentiation. Our findings confirm the inherent metabolic heterogeneity within GSC populations, highlighting their capacity to adapt and reprogram metabolically in response to environmental cues.

Glycolytic GSCs are more resistant to TMZ

We then aimed to characterize the chemotherapy sensitivity or resistance to TMZ in a 6-day treatment assay conducted under the conditions used above, namely normoxic GSCs (21% O_2), hypoxic GSCs (1% O_2), and differentiated GSCs in normoxic conditions (21% O_2). We observed significant variations in drug sensitivity among GSC lines (Fig. 4A). Under normoxic conditions, oxidative GSC lines were sensitive to TMZ at concentrations as low as 12.5 μM, while glycolytic lines exhibited higher resistance to TMZ, revealing a direct correlation between metabolism features and TMZ sensitivity under normoxic conditions (Fig. 4A). The general response to TMZ across GSC lines was largely unchanged in hypoxia (Fig. 4B). Although increased glycolytic ATP production was observed in some cell lines (NCH421k and TC22) under hypoxic conditions (Fig. 3D), this did not correspond to heightened TMZ resistance as might be expected from the results obtained in normoxia. This indicates that TMZ resistance is complex and cannot be solely attributed to the metabolic state of the cells. Interestingly, all GSCs appeared resistant to TMZ after undergoing differentiation (Fig. 4C) generally coupled to a decrease in proliferation. In normoxia, the metabolic distinctions between glycolytic and oxidative GSCs closely align with those between TMZ-resistant and TMZ-sensitive lines. Analysis of Figure 2, therefore also provide the metabolomic landscape of TMZ resistant versus TMZ sensitive GSC. Results thus indicate that TMZ-resistant GSCs exhibit increased glucose and lactate levels, along with a decrease in NAA-associated pathways, compared to TMZ-sensitive GSCs. In addition, the significant inverse correlation between NAA levels and TMZ resistance (p-value $3x10^{-7}$) , suggests NAA potential as a biomarker for TMZ sensitivity in GB.

Identification of Key Regulators Potentially Involved in TMZ Resistance in GSCs

We developed recently the GBM-cRegMap tool to investigate the molecular complexity and plasticity of GB (Bernhard and al, BioRxiv). GBM-cRegMap depicts a regulator/coregulator network highly specific for GB and predicts the influence of each network node as either positive or negative on target gene expression. With this tool, we were able to propose 7 subclasses of GB with distinct regulator network activities. In this study, we integrated transcriptomic data from GSC lines cultivated under various experimental conditions into the GBM-cRegMap tool. The classification of each cell line in the 7 subclasses is shown in supplementary data Table 1. A posterior probability calculation with Support Vector Machine (SVM) employed for each transcriptomic data set revealed that, for each GSC, there is a dispersion across multiple molecular classes, consistent with the molecular intratumoral heterogeneity of GSCs [20]. We then compared network regulator activities between Glycolytic/TMZ-Resistant and

OXPHOS/TMZ-Sensitive GSCs in order to identify potential therapeutic vulnerabilities. Among the 526 regulators/coregulators examined, 206 demonstrated statistically significant differential activation between the two groups, with 161 regulators reaching high significance (p-value < 0.01) (Fig. 5A, Supplementary Table 2).

The top 20 regulators with positive influence in the resistant and negative influence in the sensitive GSCs include ZNF239, FOXM1, CCNK, ZNF737, ZNF681, ZNF93, JDP2, ZFP90, BIRC5, PINK1, SAV1, FOXS1, ZNF22, MAP2K3, MDM2, CHAMP1, ZNF354C, ARID3A, ALX1, and CENPU (Fig. 5). Notably, regulators such as FOXS1 [21], FOXM1 [22], MAP2K3 [23], and MDM2 [24] have been previously linked to increased TMZ resistance. The PTEN-induced mitochondrial kinase 1 (PINK1) regulator is of particular interest because it is intricately involved in key processes related to cellular metabolism, mitochondrial function, and the regulation of oxidative stress response. PINK1 overexpression increases OCR, decreases glycolysis and is linked to a more favorable prognostic in GB [25]. However, PINK1-related mitophagy has also been linked to drug tolerant persister lung cancer cells and poor prognosis [26]. Our results suggest a potential role for PINK1 activation in GSCs TMZ resistance which warrants further studies.

At the opposite, we identified regulators with positive influence in TMZ-sensitive GSCs and negative influence in the TMZ-resistant GSCs including BCL6, FOXG1, HOXB2, NFE2L3, GLIS2, GATA4, FOXO4, PAX3, PLAG1, ZNF471, MECOM, ZFP30, DMRTA1, NFIA, KCTD1, ZNF502, MEIS2, KANK1, TEAD2, ZIC2 and NKX2.5 (Fig. 5). Among them, we identified NKX2.5, a transcription factor normally involved in cardiac development but with recent implications in cancer. In particular, a recent study has shown that its activation by an lncRNA suppresses the Warburg effect by repressing ERB2 in hepatocellular carcinomas [27]. We showed that NKX2.5 overexpression in GB U87MG decreases glycolytic enzymes but, in contrast with PINK1, it also decreases OCR (Fig. 6).

Using GBM-cRegMap (Bernhard et al., BioRxiv), mapping a meta-cohort of 1,612 patient tumors in 7 subclasses, we observed distinct regulation of PINK1 and NKX2.5 in different GB subclasses. Generally, we observed high activity of PINK1 and an absence of NKX2.5 activity in the proneural (PN) subtype. In contrast, the classical-C (CL-C) subtype typically exhibited high activity of NKX2.5 while PINK1 was repressed (Fig. 5B).

Altogether, results suggest that metabolic players such as PINK1 and NKX2.5 may have complex roles in GSC resistance to TMZ with influence in specific subclasses of GB. Further investigations are warranted to fully understand their role in GB pathogenesis.

Identification of Key Regulators Potentially Involved in TMZ-Resistance of Differentiated GSCs

We showed above that in vitro differentiation of GSCs led to TMZ resistance (Fig. 4C), We thus specifically evaluated metabolic and molecular changes in TC22 and 3731 lines, classified as oxidative TMZ-sensitive GSCs but as oxidative and glycolytic TMZ-resistant DGC respectively (Fig. 3A) These lines exhibit the most pronounced acquired TMZ resistance upon differentiation (Fig. 4A, C).

As shown in the metabolomic analysis (Fig. 3D), a significant upregulation of metabolites such as 2-hydroxybutyrate, allocystathionine, ascorbate, asparagine, betaine, ethanolamine, glutathione, lysine, methionine, and N-acetyl-L-lysine was noted upon differentiation for both cell lines. Many of them are known to dysregulate methylation process (allocystathionine, methionine) [28] or to enhance antioxidant programs (ascorbate and glutathione) [29,30] and may play roles in acquired TMZ resistance.

Transcriptomic data of both cell lines in stem and differentiated states were compared, revealing 1384 genes commonly upregulated after differentiation (log2FC>1) (Supplementary Table 3). Enrichment analysis using EnrichR of these commonly upregulated genes post-differentiation indicated that they are primarily associated with Phagosome, Extracellular Matrix Organization, Interferon Gamma Response, and Epithelial Mesenchymal Transition (Fig. 7, Supplementary Table 3). The upregulation of phagosome-related genes suggests a potential link with autophagy processes. Among these genes, LAMP1 (Lysosomal Associated Membrane Protein 1) and CTSL (Cathepsin L), which are directly involved in lysosomal processes crucial for autophagy, and are significantly upregulated in both cell lines after differentiation [31].

To gain deeper insights in the reprogramming of pathways in these two cell lines as they transitioned from a TMZ-sensitive to a TMZ-resistant state, we integrated metabolomic and transcriptomic data using MetaboAnalyst (Supplementary Table 4). This analysis encompassed each metabolite and transcript that demonstrated statistically significant divergence between TMZ-sensitive GSCs and their TMZ-resistant differentiated counterparts, along with their log2 fold changes. This comprehensive approach revealed significant enrichment in specific pathways, identified using the Homo sapiens KEGG pathway library. Metabolically, we observed significant deregulation in pathways such as glycerolipid and glycerophospholipid metabolism, nitrogen metabolism, lysine degradation, inositol phosphate metabolism, ether lipid metabolism, and the phosphatidylinositol signaling system. On a molecular level, significant changes were identified in pathways directly related to cellular stress response, including autophagy and mitophagy. Additionally, our analysis uncovered reprogramming in key processes like focal adhesion, actin cytoskeleton regulation, and tight junction pathways, which are essential for cell adhesion, communication, and interaction with the extracellular matrix. Further analysis revealed substantial modifications in several critical signaling pathways, including MAPK,

HIF-1, Wnt, p53, Ras, Hippo, PI3K-Akt, mTOR, and FoxO. Many of these pathways play vital roles in cellular stress responses and maintaining cellular homeostasis. The enhanced functionality of these pathways likely contributes to the cells' increased capacity to manage oxidative stress induced by TMZ, a key factor in the development of resistance.

In our investigation of GSCs' acquired resistance to TMZ post-differentiation, we utilized the GBM-cRegMap tool to pinpoint key regulatory elements involved in this adaptation (Supplementary Table 5). Among the 136 regulators that commonly influence the two resistant DGC lines positively, 88 exhibited highly divergent activities between the resistant differentiated state and their TMZ-sensitive stem cell counterparts (p-value < 0.01) (Fig. 8). Notably, several of these regulators, such as CEBPD [32], HDAC1 [33], SNAI2 [34], SOX9 [35], and HES1 [36], have been previously linked to TMZ resistance. Key autophagy-related gene SQSTM1 [37,38] and CEBPD [32] are of particular interest, potentially shielding against oxidative stress and promoting cancer survival. The identification of these key regulatory elements, which are activated during the transition to a TMZ-resistant state upon differentiation, not only deepens our understanding of GB's adaptive mechanisms but also opens up potential pathways for targeted therapy to counteract drug resistance in DGCs.

We observed that among all the resistant GSCs (5706, NCH644, and TC7), 117 regulators consistently showed a positive influence (Supplementary Table 6). Regarding the differentiated TC22 and 3731 lines, both characterized by pronounced TMZ resistance, both shared 136 positively influencing regulators (Supplementary Table 7). Interestingly, our analysis unveiled a distinct pattern of regulatory activation between the two resistant populations (stem and differentiated). Indeed, only 13 regulators were found to be common in positively influencing both resistant GSCs and DGCs, highlighting different molecular targets between the two GB populations.

These findings not only shed light on the complex interplay between molecular and metabolic reprogramming in GB, but also reveal key molecular pathways and regulatory networks potentially implicated in TMZ resistance. Overall, they highlight the potential role of autophagy, oxidative stress responses, and mitochondrial dynamics in mediating this resistance, thereby opening new and promising pathways for the development of targeted therapeutic strategies to overcome TMZ resistance in both GSCs and DGCs.

DISCUSSION

Our study has unveiled the intricate metabolic landscape and molecular heterogeneity of GSCs, revealing a notable association between molecular and metabolic features and TMZ resistance.

We found that the distinct metabolic profiles of GSCs, characterized by varying degrees of oxidative phosphorylation and glycolysis, are correlated with their sensitivity to TMZ. Specifically, glycolytic

GSCs defined in normoxic conditions demonstrated heightened resistance to TMZ, both in normoxic and hypoxic environments. This resistance is accompanied by increased glucose and lactate levels and a decrease in NAA-associated pathways. Significantly, our results suggest the potential of NAA as a predictive biomarker for TMZ resistance, evidenced by a strong inverse correlation between NAA levels and TMZ resistance (p-value $3x10^{-7}$). Additionally, our analysis revealed a significant increase in total choline in TMZ-resistant cell lines compared to sensitive ones (p-value < 0.006), aligning with recent studies that identified choline elevation as a tumor biomarker, while NAA reduction was indicative of alteration of healthy neuronal tissue. In this study, the ratio of choline to NAA serves as a specific tumor biomarker in vivo. Moreover, recent research indicates that an increase in NAA levels is associated with oxidative stress, characterized by elevated nitric oxide production and a decrease in antioxidant capacity [39]. GSCs with high NAA levels could therefore be more responsive to TMZ treatment due to their increased susceptibility to oxidative stress. The specific role of NAA in GB and its relationship with TMZ resistance necessitates further investigation, especially in light of these new insights.

The identification of key molecular regulators, through our novel GBM-cRegMap tool, provides insights into the underlying mechanisms of TMZ resistance in GSC population, highlighting potential therapeutic targets. These regulators, including PINK1 and NKX2.5, offer promising avenues for future research aimed at overcoming chemotherapy resistance in GB. PINK1, emerging as a potential key factor involved in TMZ resistance, is a putative mitochondrial serine/threonine kinase, which protects cells against oxidative stress induced apoptosis. Its enhanced activity in resistant GSCs indicating increased mitochondrial quality control through the induction of the mitophagy process, thereby potentially improving oxidative stress response and attenuating the apoptotic signals induced by TMZ. This concept aligns with prior research indicating the significance of TMZ-induced mitochondrial DNA damage [40]. Given that dysfunctional mitochondria are known producers of reactive oxygen species, PINK1's role in facilitating mitophagy becomes crucial in reducing oxidative stress. The glycolytic phenotype observed in TMZ-resistant GSCs may represent an adaptive mechanism to ensure continued energy production when mitochondrial function is compromised. This observation of PINK1's involvement highlights a nuanced interplay between mitochondrial dynamics and cellular energy pathways in the context of chemoresistance.

The heterogeneity of GSCs is further highlighted under conditions that mimic the tumor microenvironment, such as hypoxia and differentiation, where GSCs demonstrate remarkable adaptability in their metabolic reprogramming. In our study, we have observed that differentiated GB cells generally exhibit a glycolytic phenotype. This aligns with previous studies indicating that GSCs, when cultured in vitro, have a metabolism distinct from their differentiated counterparts, with the latter being more glycolytic than the GSCs [9]. Interestingly, in our cohort, we noted variability in this trend; some GSCs became more glycolytic post-differentiation, while others did not, indicating that increased glycolysis post-differentiation is not a universal characteristic of all GSCs.

This plasticity has profound implications for cancer treatment, particularly with regard to the development of resistance to treatments like TMZ. Interestingly, in our cohort of GSCs, all DGCs appear resistant to TMZ. To further understand this phenomenon, we focused on the metabolic and molecular plasticity of those GSCs which exhibited the most pronounced acquired resistance to TMZ post-differentiation.

We observed a notable upregulation in metabolites such as 2-hydroxybutyrate, allocystathionine, ascorbate, asparagine, betaine, ethanolamine, glutathione, lysine, methionine, and N-acetyl-L-lysine. These changes suggest potential roles of this metabolites in acquired TMZ resistance, possibly through dysregulation of methylation programs or upregulation of antioxidant programs. Notably, allocystathionine, methionine, lysine, and betaine play a pivotal role in methylation processes, suggesting enhanced methylation capacity post-differentiation or alteration of DNA methylation patterns, thereby changing gene expression profiles. Allocystathionine might also reflect an upregulation in transsulfuration pathways, influencing detoxification and DNA repair mechanisms. Recently, elevated asparagine levels have been associated with metabolic adaptability in GSCs, enhancing their invasiveness and therapy resistance [41]. The increase in N-acetyl-L-Lysine suggests enhanced lysine acetylation events, which may influence processes such as DNA repair, gene expression and protein stability, potentially offering resistance mechanisms to agents like TMZ [42]. The upregulation of potent antioxidants, ascorbate and glutathione, suggests an enhanced ability of differentiated resistant cells to counteract oxidative stress, which might mitigate TMZ-induced oxidative damage [29,30]. Furthermore, the increased ethanolamine levels could reflect changes in phospholipid metabolism, potentially affecting membrane composition and fluidity, thereby influencing drug uptake or efflux [43].

Our findings suggest that the modulation of autophagy plays a critical role in combating TMZ resistance. Autophagy, a biological process essential for degrading and recycling damaged or superfluous cellular components, can have divergent effects in cancer, either supporting cancer cell survival or inducing cell death. The precise mechanisms by which autophagy impacts GB cells remain to be fully elucidated [44–46]. It has been shown that modulating autophagy, either through induction or inhibition, directly affects GB cell metabolism, disrupting mitochondrial respiratory chain function and mitochondrial dynamics [46].

The role of oxidative stress, particularly ROS levels, is also crucial in regulating cellular homeostasis and autophagy activation. Studies have revealed that in TMZ-sensitive cells, an increase in ROS induced by treatment activates autophagy, leading to cell death. Conversely, in resistant cells, this increase in ROS is absent, preventing autophagy activation. Artificially increasing oxidative stress has been shown to reactivate autophagy and restore TMZ sensitivity [44].

These observations suggest that autophagy, mitochondrial dynamics, and oxidative stress could be strategic targets to counter TMZ resistance. Given that autophagy can promote either cell survival or death, modulating autophagy using pharmacological inhibitors, such as chloroquine, or inducers, like rapamycin, has garnered significant attention [45].

Using our cREGMAP tool, we analyzed the plasticity of regulator activity between the stem-sensitive condition and its resistant differentiated counterparts. Among the regulators that positively influence the two resistant DGC lines, SQSTM1, also known as p62, an autophagy-related protein, is of particular interest. The role of p62/SQSTM1 in glioma progression is not fully elucidated; however, its expression correlates with poor patient outcomes [38], and p62 has been shown to promote proliferation, invasion, and mesenchymal transition in GB [47]. Furthermore, it is posited that in GSCs, p62 may influence invasive behavior by modulating energy metabolism and mitochondrial function [37]. Additionally, p62 may contribute to cancer progression by providing a defense against cell death induced by oxidative stress [48].

Overall, our understanding of these pathways not only sheds light on the resilience and adaptability of GB cells but also opens new avenues for developing targeted therapies to overcome TMZ resistance. By targeting key adaptive mechanisms, particularly in the autophagy, we can potentially disrupt the cellular processes contributing to resistance, offering a promising strategy in GB treatment.

However, it is important to acknowledge the limitations of our study, primarily the in vitro nature of the experiments and the use of specific cell lines. Future research, including in vivo studies and exploration of therapeutic targets, is necessary. Such studies could provide further insights into the complex interplay between metabolic reprogramming, environmental conditions, and drug resistance in GB, ultimately contributing to the development of more effective treatment strategies for this challenging malignancy.

The plasticity of GSCs presents both challenges and opportunities in the development of anticancer therapies. The molecular and metabolic adaptations of GSCs, in response to changing environmental conditions or treatments, can lead to treatment resistance. However, this adaptability also opens avenues for developing therapeutic strategies aimed at disrupting the equilibrium of cancer cells. We have uncovered complex nuances in the metabolic and molecular profiles of GSCs, especially in their response to differentiation or hypoxia. This adaptability underscores the challenges in developing effective therapies. Nevertheless, through modeling and network analysis, we can anticipate this plasticity, paving the way for potentially more effective combined therapies against GB.

To delve into the clinical applications of cancer metabolism, a precise understanding of the metabolic pathways in human tumors is required. Caution is warranted when extrapolating in vitro results to the

in vivo context. Primary tumor cells undergo significant genomic and gene expression changes when adapted to in vitro cell culture [49], potentially losing the influence of their original microenvironment on their metabolism.

Overall, our work provides a comprehensive view of the heterogeneity and metabolic and molecular plasticity of GSCs. This offers significant insights for the development of targeted, personalized therapeutic strategies to overcome treatment resistance in GBs. In conclusion, our research not only advances the understanding of GSC metabolism and its impact on chemotherapy resistance but also lays the groundwork for developing more effective, personalized treatments for GB, potentially improving outcomes for patients afflicted with this aggressive cancer.

REFERENCES

1. Stupp, R.; Mason, W.P.; van den Bent, M.J.; Weller, M.; Fisher, B.; Taphoorn, M.J.B.B.; Belanger, K.; Brandes, A.A.; Marosi, C.; Bogdahn, U.; et al. Radiotherapy plus Concomitant and Adjuvant Temozolomide for Glioblastoma. *N. Engl. J. Med.* **2005**, *352*, 987–996, doi:10.1056/NEJMoa043330.
2. Cruz Da Silva, E.; Mercier, M.-C.; Etienne-Selloum, N.; Dontenwill, M.; Choulier, L. A Systematic Review of Glioblastoma-Targeted Therapies in Phases II, III, IV Clinical Trials. *Cancers (Basel).* **2021**, *13*, 1795, doi:10.3390/cancers13081795.
3. Mattei, V.; Santilli, F.; Martellucci, S.; Delle Monache, S.; Fabrizi, J.; Colapietro, A.; Angelucci, A.; Festuccia, C. The Importance of Tumor Stem Cells in Glioblastoma Resistance to Therapy. *Int. J. Mol. Sci.* **2021**, *22*, 3863, doi:10.3390/ijms22083863.
4. Wang, X.; Prager, B.C.; Wu, Q.; Kim, L.J.Y.Y.; Gimple, R.C.; Shi, Y.; Yang, K.; Morton, A.R.; Zhou, W.; Zhu, Z.; et al. Reciprocal Signaling between Glioblastoma Stem Cells and Differentiated Tumor Cells Promotes Malignant Progression. *Cell Stem Cell* **2018**, *22*, 514-528.e5, doi:10.1016/j.stem.2018.03.011.
5. Verhaak, R.G.W.; Hoadley, K.A.; Purdom, E.; Wang, V.; Qi, Y.; Wilkerson, M.D.; Miller, C.R.; Ding, L.; Golub, T.; Mesirov, J.P.; et al. Integrated Genomic Analysis Identifies Clinically Relevant Subtypes of Glioblastoma Characterized by Abnormalities in PDGFRA, IDH1, EGFR, and NF1. *Cancer Cell* **2010**, *17*, 98–110, doi:10.1016/j.ccr.2009.12.020.
6. Neftel, C.; Laffy, J.; Filbin, M.G.; Hara, T.; Shore, M.E.; Rahme, G.J.; Richman, A.R.; Silverbush, D.; Shaw, M.L.; Hebert, C.M.; et al. An Integrative Model of Cellular States, Plasticity, and Genetics for Glioblastoma. *Cell* **2019**, *178*, 835-849.e21, doi:10.1016/j.cell.2019.06.024.
7. Garofano, L.; Migliozzi, S.; Oh, Y.T.; D'Angelo, F.; Najac, R.D.; Ko, A.; Frangaj, B.; Caruso, F.P.; Yu, K.; Yuan, J.; et al. Pathway-Based Classification of Glioblastoma Uncovers a Mitochondrial Subtype with Therapeutic Vulnerabilities. *Nat. Cancer* **2021**, *2*, 141–156, doi:10.1038/s43018-020-00159-4.
8. Badr, C.E.; Silver, D.J.; Siebzehnrubl, F.A.; Deleyrolle, L.P. Metabolic Heterogeneity and Adaptability in Brain Tumors. *Cell. Mol. Life Sci.* **2020**, *77*, 5101–5119, doi:10.1007/s00018-020-03569-w.
9. Vlashi, E.; Lagadec, C.; Vergnes, L.; Matsutani, T.; Masui, K.; Poulou, M.; Popescu, R.; Della Donna, L.; Evers, P.; Dekmezian, C.; et al. Metabolic State of Glioma Stem Cells and Nontumorigenic Cells. *Proc. Natl. Acad. Sci. U. S. A.* **2011**, *108*, 16062–16067, doi:10.1073/pnas.1106704108.
10. Kant, S.; Kesarwani, P.; Prabhu, A.; Graham, S.F.; Buelow, K.L.; Nakano, I.; Chinnaiyan, P. Enhanced Fatty Acid Oxidation Provides Glioblastoma Cells Metabolic Plasticity to Accommodate to Its Dynamic Nutrient Microenvironment. *Cell Death Dis.* **2020**, *11*, 253, doi:10.1038/s41419-020-2449-5.
11. Bernhard, C.; Reita, D.; Martin, S.; Entz-Werle, N.; Dontenwill, M. Glioblastoma Metabolism: Insights and Therapeutic Strategies. *Int. J. Mol. Sci.* **2023**, *24*, 9137, doi:10.3390/ijms24119137.
12. Campos, B.; Wan, F.; Farhadi, M.; Ernst, A.; Zeppernick, F.; Tagscherer, K.E.; Ahmadi, R.; Lohr, J.; Dictus, C.; Gdynia, G.; et al. Differentiation Therapy Exerts Antitumor Effects on Stem-like Glioma Cells. *Clin. Cancer Res.* **2010**, *16*, 2715–2728, doi:10.1158/1078-0432.CCR-09-1800.
13. Blandin, A.F.; Noulet, F.; Renner, G.; Mercier, M.C.; Choulier, L.; Vauchelles, R.; Ronde, P.; Carreiras, F.; Etienne-Selloum, N.; Vereb, G.; et al. Glioma Cell Dispersion Is Driven by A5 Integrin-Mediated Cell-Matrix and Cell-Cell Interactions. *Cancer Lett.* **2016**, *376*, 328–338, doi:10.1016/j.canlet.2016.04.007.
14. Cicek, A.E.; Bederman, I.; Henderson, L.; Drumm, M.L.; Ozsoyoglu, G. ADEMA: An Algorithm to Determine Expected Metabolite Level Alterations Using Mutual Information. *PLoS Comput. Biol.* **2013**, *9*, doi:10.1371/journal.pcbi.1002859.
15. Kanehisa, M.; Goto, S.; Sato, Y.; Kawashima, M.; Furumichi, M.; Tanabe, M. Data, Information, Knowledge and Principle: Back to Metabolism in KEGG. *Nucleic Acids Res.* **2014**, *42*, D199–D205, doi:10.1093/nar/gkt1076.
16. Kanehisa, M. KEGG: Kyoto Encyclopedia of Genes and Genomes. *Nucleic Acids Res.* **2000**, *28*, 27–30, doi:10.1093/nar/28.1.27.
17. Mesquita, I.; Rodrigues, F. Cellular Metabolism at a Glance. In; 2018; pp. 3–27.
18. Chong, J.; Wishart, D.S.; Xia, J. Using MetaboAnalyst 4.0 for Comprehensive and Integrative Metabolomics Data Analysis. *Curr. Protoc. Bioinforma.* **2019**, *68*, doi:10.1002/cpbi.86.
19. Xie, Z.; Bailey, A.; Kuleshov, M. V.; Clarke, D.J.B.; Evangelista, J.E.; Jenkins, S.L.; Lachmann, A.; Wojciechowicz, M.L.; Kropiwnicki, E.; Jagodnik, K.M.; et al. Gene Set Knowledge Discovery with Enrichr. *Curr. Protoc.* **2021**, *1*, doi:10.1002/cpz1.90.
20. Dirkse, A.; Golebiewska, A.; Buder, T.; Nazarov, P. V.; Muller, A.; Poovathingal, S.; Brons, N.H.C.C.; Leite, S.; Sauvageot, N.; Sarkisjan, D.; et al. Stem Cell-Associated Heterogeneity in Glioblastoma Results from Intrinsic Tumor Plasticity Shaped by the Microenvironment. *Nat. Commun.* **2019**, *10*, 1–16, doi:10.1038/s41467-019-09853-z.
21. Xue, B.-Z.; Xiang, W.; Zhang, Q.; Wang, H.-F.; Zhou, Y.-J.; Tian, H.; Abdelmaksou, A.; Xue, J.; Sun, M.-X.; Yi, D.-Y.; et al. CD90low Glioma-Associated Mesenchymal Stromal/Stem Cells Promote

Temozolomide Resistance by Activating FOXS1-Mediated Epithelial-Mesenchymal Transition in Glioma Cells. *Stem Cell Res. Ther.* **2021**, *12*, 394, doi:10.1186/s13287-021-02458-8.
22. Guo, L.; Wu, Z. FOXM1-Mediated NUF2 Expression Confers Temozolomide Resistance to Human Glioma Cells by Regulating Autophagy via the PI3K/AKT/MTOR Signaling Pathway. *Neuropathology* **2022**, *42*, 430–446, doi:10.1111/neup.12824.
23. Hsu, J.B.-K.; Lee, T.-Y.; Cheng, S.-J.; Lee, G.A.; Chen, Y.-C.; Le, N.Q.K.; Huang, S.-W.; Kuo, D.-P.; Li, Y.-T.; Chang, T.-H.; et al. Identification of Differentially Expressed Genes in Different Glioblastoma Regions and Their Association with Cancer Stem Cell Development and Temozolomide Response. *J. Pers. Med.* **2021**, *11*, doi:10.3390/jpm11111047.
24. Sato, A.; Sunayama, J.; Matsuda, K.; Seino, S.; Suzuki, K.; Watanabe, E.; Tachibana, K.; Tomiyama, A.; Kayama, T.; Kitanaka, C. MEK-ERK Signaling Dictates DNA-Repair Gene MGMT Expression and Temozolomide Resistance of Stem-Like Glioblastoma Cells via the MDM2-P53 Axis. *Stem Cells* **2011**, *29*, 1942–1951, doi:10.1002/stem.753.
25. Agnihotri, S.; Golbourn, B.; Huang, X.; Remke, M.; Younger, S.; Cairns, R.A.; Chalil, A.; Smith, C.A.; Krumholtz, S.-L.; Mackenzie, D.; et al. PINK1 Is a Negative Regulator of Growth and the Warburg Effect in Glioblastoma. *Cancer Res.* **2016**, *76*, 4708–4719, doi:10.1158/0008-5472.CAN-15-3079.
26. Li, Y.; Chen, H.; Xie, X.; Yang, B.; Wang, X.; Zhang, J.; Qiao, T.; Guan, J.; Qiu, Y.; Huang, Y.-X.; et al. PINK1-Mediated Mitophagy Promotes Oxidative Phosphorylation and Redox Homeostasis to Induce Drug-Tolerant Persister Cancer Cells. *Cancer Res.* **2023**, *83*, 398–413, doi:10.1158/0008-5472.CAN-22-2370.
27. Chen, G.; Jiang, J.; Wang, X.; Feng, K.; Ma, K. LncENST Suppress the Warburg Effect Regulating the Tumor Progress by the Nkx2-5/ErbB2 Axis in Hepatocellular Carcinoma. *Comput. Math. Methods Med.* **2021**, *2021*, 1–12, doi:10.1155/2021/6959557.
28. Sanderson, S.M.; Gao, X.; Dai, Z.; Locasale, J.W. Methionine Metabolism in Health and Cancer: A Nexus of Diet and Precision Medicine. *Nat. Rev. Cancer* **2019**, *19*, 625–637, doi:10.1038/s41568-019-0187-8.
29. Traverso, N.; Ricciarelli, R.; Nitti, M.; Marengo, B.; Furfaro, A.L.; Pronzato, M.A.; Marinari, U.M.; Domenicotti, C. Role of Glutathione in Cancer Progression and Chemoresistance. *Oxid. Med. Cell. Longev.* **2013**, *2013*, 1–10, doi:10.1155/2013/972913.
30. Ye, P.; Mimura, J.; Okada, T.; Sato, H.; Liu, T.; Maruyama, A.; Ohyama, C.; Itoh, K. Nrf2- and ATF4-Dependent Upregulation of XCT Modulates the Sensitivity of T24 Bladder Carcinoma Cells to Proteasome Inhibition. *Mol. Cell. Biol.* **2014**, *34*, 3421–3434, doi:10.1128/MCB.00221-14.
31. Debnath, J.; Gammoh, N.; Ryan, K.M. Autophagy and Autophagy-Related Pathways in Cancer. *Nat. Rev. Mol. Cell Biol.* **2023**, *24*, 560–575, doi:10.1038/s41580-023-00585-z.
32. Lin, H.-Y.; Lim, S.-W.; Hsu, T.-I.; Yang, W.-B.; Huang, C.-C.; Tsai, Y.-T.; Chang, W.-C.; Ko, C.-Y. CCAAT/Enhancer-Binding Protein Delta Regulates Glioblastoma Survival through Catalase-Mediated Hydrogen Peroxide Clearance. *Oxid. Med. Cell. Longev.* **2022**, *2022*, 1–16, doi:10.1155/2022/4081380.
33. Hanisch, D.; Krumm, A.; Diehl, T.; Stork, C.M.; Dejung, M.; Butter, F.; Kim, E.; Brenner, W.; Fritz, G.; Hofmann, T.G.; et al. Class I HDAC Overexpression Promotes Temozolomide Resistance in Glioma Cells by Regulating RAD18 Expression. *Cell Death Dis.* **2022**, *13*, 293, doi:10.1038/s41419-022-04751-7.
34. Liao, H.; Bai, Y.; Qiu, S.; Zheng, L.; Huang, L.; Liu, T.; Wang, X.; Liu, Y.; Xu, N.; Yan, X.; et al. MiR-203 Downregulation Is Responsible for Chemoresistance in Human Glioblastoma by Promoting Epithelial-Mesenchymal Transition via SNAI2. *Oncotarget* **2015**, *6*, 8914–8928, doi:10.18632/oncotarget.3563.
35. Garros-Regulez, L.; Aldaz, P.; Arrizabalaga, O.; Moncho-Amor, V.; Carrasco-Garcia, E.; Manterola, L.; Moreno-Cugnon, L.; Barrena, C.; Villanua, J.; Ruiz, I.; et al. MTOR Inhibition Decreases SOX2-SOX9 Mediated Glioma Stem Cell Activity and Temozolomide Resistance. *Expert Opin. Ther. Targets* **2016**, *20*, 393–405, doi:10.1517/14728222.2016.1151002.
36. Liu, Z.-H.; Dai, X.-M.; Du, B. Hes1: A Key Role in Stemness, Metastasis and Multidrug Resistance. *Cancer Biol. Ther.* **2015**, *16*, 353–359, doi:10.1080/15384047.2015.1016662.
37. Galavotti, S.; Bartesaghi, S.; Faccenda, D.; Shaked-Rabi, M.; Sanzone, S.; McEvoy, A.; Dinsdale, D.; Condorelli, F.; Brandner, S.; Campanella, M.; et al. The Autophagy-Associated Factors DRAM1 and P62 Regulate Cell Migration and Invasion in Glioblastoma Stem Cells. *Oncogene* **2013**, *32*, 699–712, doi:10.1038/onc.2012.111.
38. Ieni, A.; Pizzimenti, C.; Broggi, G.; Caltabiano, R.; Germanò, A.; Barbagallo, G.; Vigneri, P.; Giuffrè, G.; Tuccari, G. Immunoexpression of P62/SQSTM1/Sequestosome-1 in Human Primary and Recurrent IDH1/2 Wild-type Glioblastoma: A Pilot Study. *Oncol. Lett.* **2022**, *24*, 336, doi:10.3892/ol.2022.13456.
39. Surendran, S.; Bhatnagar, M. Upregulation of N-Acetylaspartic Acid Induces Oxidative Stress to Contribute in Disease Pathophysiology. *Int. J. Neurosci.* **2011**, *121*, 305–309, doi:10.3109/00207454.2011.558225.
40. Oliva, C.R.; Nozell, S.E.; Diers, A.; McClugage, S.G.; Sarkaria, J.N.; Markert, J.M.; Darley-Usmar, V.M.;

Bailey, S.M.; Gillespie, G.Y.; Landar, A.; et al. Acquisition of Temozolomide Chemoresistance in Gliomas Leads to Remodeling of Mitochondrial Electron Transport Chain. *J. Biol. Chem.* **2010**, *285*, 39759–39767, doi:10.1074/jbc.M110.147504.

41. Thomas, T.M.; Miyaguchi, K.; Edwards, L.A.; Wang, H.; Wollebo, H.; Aiguo, L.; Murali, R.; Wang, Y.; Braas, D.; Michael, J.S.; et al. Elevated Asparagine Biosynthesis Drives Brain Tumor Stem Cell Metabolic Plasticity and Resistance to Oxidative Stress. *Mol. Cancer Res.* **2021**, *19*, 1375–1388, doi:10.1158/1541-7786.MCR-20-0086.
42. Hu, M.; He, F.; Thompson, E.W.; Ostrikov, K. (Ken); Dai, X. Lysine Acetylation, Cancer Hallmarks and Emerging Onco-Therapeutic Opportunities. *Cancers (Basel).* **2022**, *14*, 346, doi:10.3390/cancers14020346.
43. Calzada, E.; Onguka, O.; Claypool, S.M. Phosphatidylethanolamine Metabolism in Health and Disease. In; 2016; pp. 29–88.
44. Dico, A. Lo; Salvatore, D.; Martelli, C.; Ronchi, D.; Diceglie, C.; Lucignani, G.; Ottobrini, L. Intracellular Redox-Balance Involvement in Temozolomide Resistance-Related Molecular Mechanisms in Glioblastoma. *Cells* **2019**, *8*, 1315, doi:10.3390/cells8111315.
45. Yan, Y.; Xu, Z.; Dai, S.; Qian, L.; Sun, L.; Gong, Z. Targeting Autophagy to Sensitive Glioma to Temozolomide Treatment. *J. Exp. Clin. Cancer Res.* **2016**, *35*, 23, doi:10.1186/s13046-016-0303-5.
46. Kriel, J.; Müller-Nedebock, K.; Maarman, G.; Mbizana, S.; Ojuka, E.; Klumperman, B.; Loos, B. Coordinated Autophagy Modulation Overcomes Glioblastoma Chemoresistance through Disruption of Mitochondrial Bioenergetics. *Sci. Rep.* **2018**, *8*, 10348, doi:10.1038/s41598-018-28590-9.
47. Pölönen, P.; Jawahar Deen, A.; Leinonen, H.M.; Jyrkkänen, H.-K.; Kuosmanen, S.; Mononen, M.; Jain, A.; Tuomainen, T.; Pasonen-Seppänen, S.; Hartikainen, J.M.; et al. Nrf2 and SQSTM1/P62 Jointly Contribute to Mesenchymal Transition and Invasion in Glioblastoma. *Oncogene* **2019**, *38*, 7473–7490, doi:10.1038/s41388-019-0956-6.
48. Umemura, A.; He, F.; Taniguchi, K.; Nakagawa, H.; Yamachika, S.; Font-Burgada, J.; Zhong, Z.; Subramaniam, S.; Raghunandan, S.; Duran, A.; et al. P62, Upregulated during Preneoplasia, Induces Hepatocellular Carcinogenesis by Maintaining Survival of Stressed HCC-Initiating Cells. *Cancer Cell* **2016**, *29*, 935–948, doi:10.1016/j.ccell.2016.04.006.
49. Lee, J.; Kotliarova, S.; Kotliarov, Y.; Li, A.; Su, Q.; Donin, N.M.; Pastorino, S.; Purow, B.W.; Christopher, N.; Zhang, W.; et al. Tumor Stem Cells Derived from Glioblastomas Cultured in BFGF and EGF More Closely Mirror the Phenotype and Genotype of Primary Tumors than Do Serum-Cultured Cell Lines. *Cancer Cell* **2006**, doi:10.1016/j.ccr.2006.03.030.

Figure legend

Figure 1. Metabolic heterogeneity in GSC lines under normoxic conditions
(A) Energy Map depicting both Oxygen Consumption Rates (OCR) and Extracellular Acidification Rates (ECAR) for different GSC lines. (B) Glycolytic and mitochondrial ATP production rates among the GSC lines. (C) XF ATP Rate Index, serving as a metric for distinguishing metabolic phenotypes among the GSC lines. All Seahorse data are represented as means from at least three independent experiments ± SEM. (D) Metabolomic characterization of GSC lines: The heatmap of intracellular metabolite profiles is plotted using absolute concentrations. Statistical significance between oxidative and glycolytic GSC metabolite concentration are highlighted (*P<0.05).

Figure 2. Metabolic Network Heterogeneity between GSC Populations: ADEMA Analysis Reveals Distinct Metabolic Pathways Between Glycolytic and Oxidative GSCs
Using ADEMA network analysis, this figure contrasts the metabolic profiles of glycolytic TMZ-resistant and oxidative TMZ-sensitive GSCs. Red and green boxes indicate metabolites with increased or decreased levels in glycolytic versus oxidative GSCs, based on HR-MAS NMR data. Gray boxes show no significant change. Key findings include higher glucose, lactate, and choline levels in resistant lines, and reduced NAA-associated pathways, underscoring distinct metabolic signatures linked to TMZ resistance.

Figure 3. GSCs Metabolic Plasticity in Response to Differentiation or Hypoxia
(A) Histograms illustrate ATP production rates, detailing the contributions of mitochondrial activity and glycolysis in both stem-like and differentiated states of GSCs. (B) The glycolytic index, indicating the proportion of ATP production from glycolysis, classifies cells as predominantly glycolytic (glycolytic index > 50%) or primarily oxidative. These assessments were conducted using real-time ATP assays with the Agilent Seahorse XFp Analyzer. (C) Principal Component Analysis comparing metabolomic profiles of stem-like and differentiated GSCs. Scores for Principal Components 1 (PC1) and 2 (PC2), illustrating the variance and separation between stem and differentiated condition. (D) Results from the Algorithm to Determine Expected Metabolite level Alterations (ADEMA) analysis, depicting changes in metabolic pathways upon differentiation. Red indicates upregulation, and green indicates downregulation of metabolite levels after differentiation. (E) Energetic metabolic changes in response to hypoxia in GSCs. Histograms illustrate ATP production rates in GSCs as well as the contributions of mitochondrial activity and glycolysis to energy production. Data, collected using the Seahorse XFp extracellular flux analyzer, compare ATP production in GSCs after 3 days under normoxic (21% O_2) and hypoxic (1% O_2) conditions. The results demonstrate the metabolic flexibility of oxidative cells, which enhance glycolysis in response to hypoxic stress. Statistical significance is indicated as *P < 0.05, **P < 0.01, ***P < 0.001, ****P < 0.0001.

Figure 4. TMZ Sensitivity Assays in GSCs Under Various Conditions
This figure presents the outcomes of TMZ sensitivity assays in GSCs under normoxic (A), hypoxic (B), and differentiated conditions (D). Over a six-day period, cell proliferation and chemotherapy response were evaluated using IncuCyte® real-time microscopic analysis. The assays demonstrate distinct patterns of tumor growth and response to TMZ in each condition. Statistical significance between treated conditions and control is indicated as *P < 0.05, **P < 0.01, ***P < 0.001, ****P < 0.0001. Results, shown as mean ± SEM, underscore the differential sensitivity of GSCs to TMZ across various environmental settings.

Figure 5. Divergent regulatory network activity between TMZ-resistant and TMZ-sensitive GSC
(A) This heatmap illustrates the differentially influenced regulators across various GSC cell lines, with color values indicating the scaled relative influences. The analysis distinctly highlights the disparity in regulator activity between TMZ-resistant (marked in red) and TMZ-sensitive GSCs. Statistical significance was established with a p-value threshold of <0.01, emphasizing the highly divergent regulator activities between these two groups. (B) Influence of PINK1 (left) and NKX2.5 (right) on the cREGMAP meta-cohort of 1612 patients, revealing divergent activities between these two regulators in GB tumors.

Figure 6 : NKX2.5 overexpression impaired energy metabolism
(A) Western Blot Analysis of NKX2.5 and HK2 Expression in U87MG Cells: This blot illustrates the expression levels of NKX2.5 and HK2 proteins in U87MG cells where NKX2.5 has been overexpressed. Four conditions are shown: control (untreated), lipofectamine only, negative control plasmid, and NKX2.5 plasmid transfection. (B) Transcriptional Repression of Glycolytic Genes by NKX2.5: RT-qPCR analysis showing the transcriptional repression of glycolytic genes (HK2, GPI, TPI, GAPDH, LDHA) in U87MG cells upon overexpression of NKX2.5. (C) Energy Map of OCR and ECAR in U87MG Cells: This map depicts both Oxygen Consumption Rates (OCR) and Extracellular Acidification Rates (ECAR), comparing the energetic profiles of U87MG cells transfected with a negative control plasmid to those overexpressing NKX2.5. (D) Mitochondrial Stress Test Results: Data from the Agilent Mitostress test comparing U87MG cells transfected with a negative control plasmid to those overexpressing NKX2.5, highlighting the impact of NKX2.5 overexpression on mitochondrial function.

Figure 7. Enrichment analysis of commonly upregulated genes after differentiation in TMZ-acquired resistant differentiated GSCs

Figure 8. Comparative Analysis of Regulatory Network Activity in TMZ-Sensitive GSC and their TMZ-resistant differentiated counterparts
This heatmap compares the regulatory network activity between two GSC lines that are initially TMZ-sensitive in their stem-like state and become TMZ-resistant upon differentiation. Color values indicate the scaled relative influences of regulators, highlighting the significant shifts in regulatory network activity associated with the differentiation process and acquired TMZ resistance. This comparative analysis underscores the dynamic nature of regulatory networks in response to cellular differentiation.

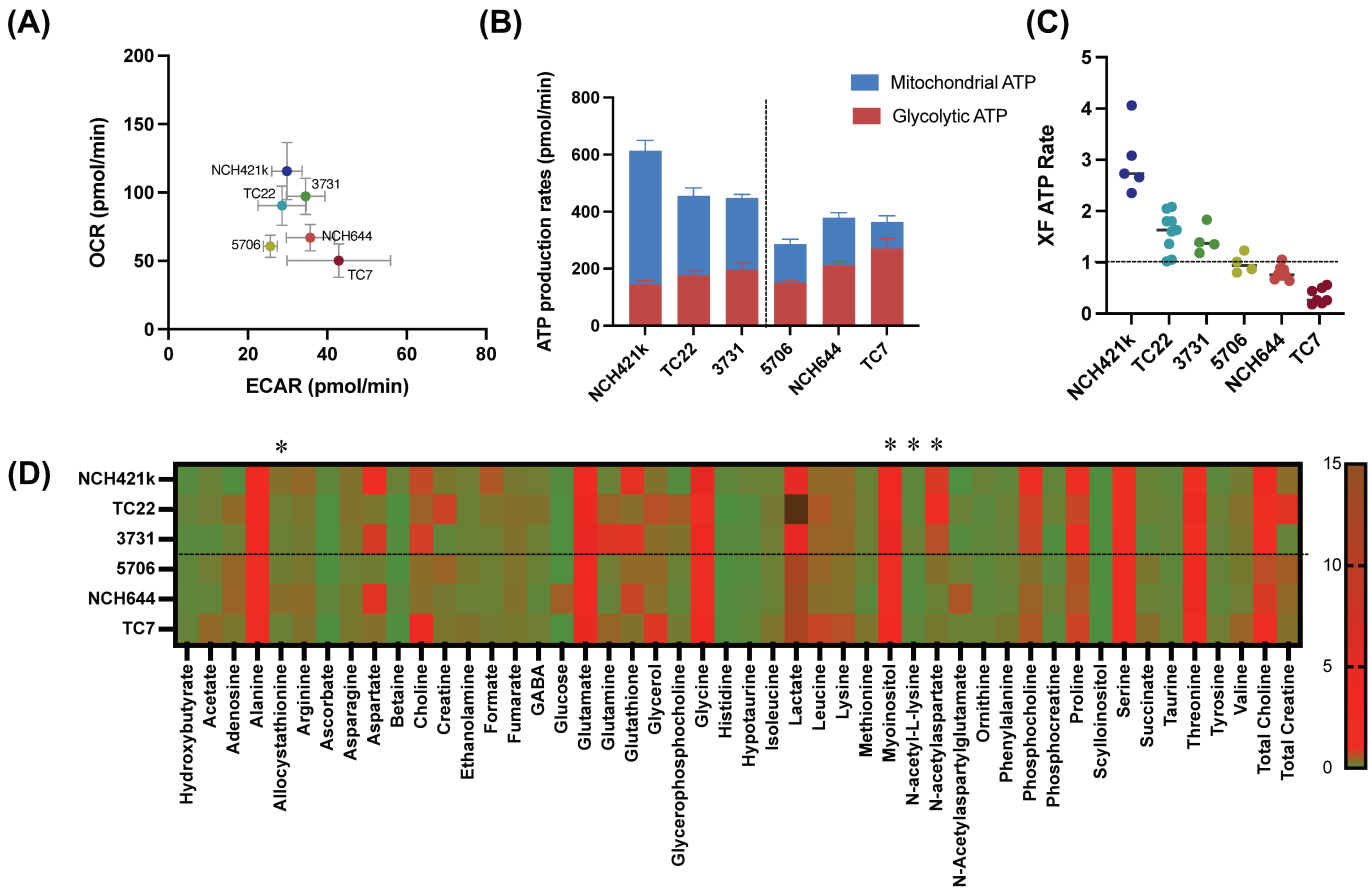
(A)
OCR (pmol/min)
ECAR (pmol/min)
NCH421k
TC22
3731
5706
NCH644
TC7
(B)
ATP production rates (pmol/min)
Mitochondrial ATP
Glycolytic ATP
(C)
XF ATP Rate
(D)
Hydroxybutyrate
Acetate
Adenosine
Alanine
Allocystathionine
Arginine
Ascorbate
Asparagine
Aspartate
Betaine
Choline
Creatine
Ethanolamine
Formate
Fumarate
GABA
Glucose
Glutamate
Glutamine
Glutathione
Glycerol
Glycerophosphocholine
Glycine
Histidine
Hypotaurine
Isoleucine
Lactate
Leucine
Lysine
Methionine
Myoinositol
N-acetyl-L-lysine
N-acetylaspartate
N-Acetylaspartylglutamate
Ornithine
Phenylalanine
Phosphocholine
Phosphocreatine
Proline
Scylloinositol
Serine
Succinate
Taurine
Threonine
Tyrosine
Valine
Total Choline
Total Creatine

Fig. 1

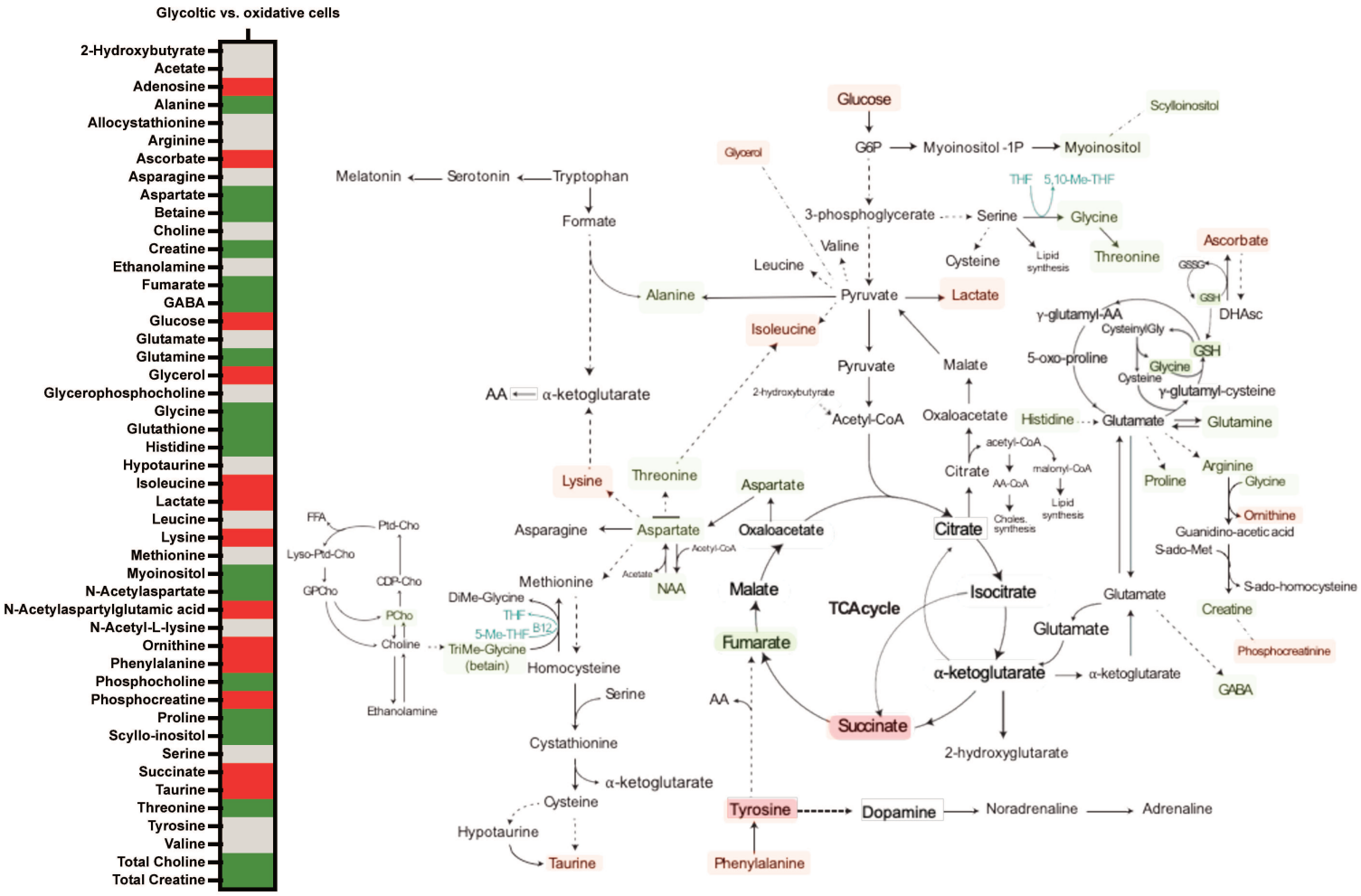
Glycoltic vs. oxidative cells
2-Hydroxybutyrate
Acetate
Adenosine
Alanine
Allocystathionine
Arginine
Ascorbate
Asparagine
Aspartate
Betaine
Choline
Creatine
Ethanolamine
Fumarate
GABA
Glucose
Glutamate
Glutamine
Glycerol
Glycerophosphocholine
Glycine
Glutathione
Histidine
Hypotaurine
Isoleucine
Lactate
Leucine
Lysine
Methionine
Myoinositol
N-Acetylaspartate
N-Acetylaspartylglutamic acid
N-Acetyl-L-lysine
Ornithine
Phenylalanine
Phosphocholine
Phosphocreatine
Proline
Scyllo-inositol
Serine
Succinate
Taurine
Threonine
Tyrosine
Valine
Total Choline
Total Creatine
Glucose
G6P
Myoinositol-1P
Myoinositol
Scylloinositol
Glycerol
3-phosphoglycerate
Serine
Glycine
THF
5,10-Me-THF
Melatonin
Serotonin
Tryptophan
Formate
Valine
Leucine
Cysteine
Lipid synthesis
Threonine
Ascorbate
GSSG
GSH
DHAsc
Alanine
Pyruvate
Lactate
γ-glutamyl-AA
CysteinylGly
5-oxo-proline
Isoleucine
Pyruvate
Malate
Glycine
Cysteine
γ-glutamyl-cysteine
AA
α-ketoglutarate
2-hydroxybutyrate
Acetyl-CoA
Oxaloacetate
Histidine
Glutamate
Glutamine
acetyl-CoA
malonyl-CoA
Citrate
AA-CoA
Lipid synthesis
Choles. synthesis
Proline
Arginine
Glycine
Ornithine
Guanidino-acetic acid
Lysine
Threonine
Aspartate
FFA
Ptd-Cho
Lyso-Ptd-Cho
Asparagine
Aspartate
Oxaloacetate
Citrate
S-ado-Met
S-ado-homocysteine
Acetyl-CoA
Acetate
NAA
CDP-Cho
GPCho
PCho
Methionine
DiMe-Glycine
THF
5-Me-THF
B12
TriMe-Glycine
(betain)
Malate
TCAcycle
Isocitrate
Glutamate
Creatine
Choline
Homocysteine
Fumarate
Glutamate
Phosphocreatinine
Ethanolamine
Serine
α-ketoglutarate
α-ketoglutarate
GABA
AA
Succinate
Cystathionine
2-hydroxyglutarate
α-ketoglutarate
Cysteine
Tyrosine
Dopamine
Noradrenaline
Adrenaline
Hypotaurine
Taurine
Phenylalanine

Fig. 2

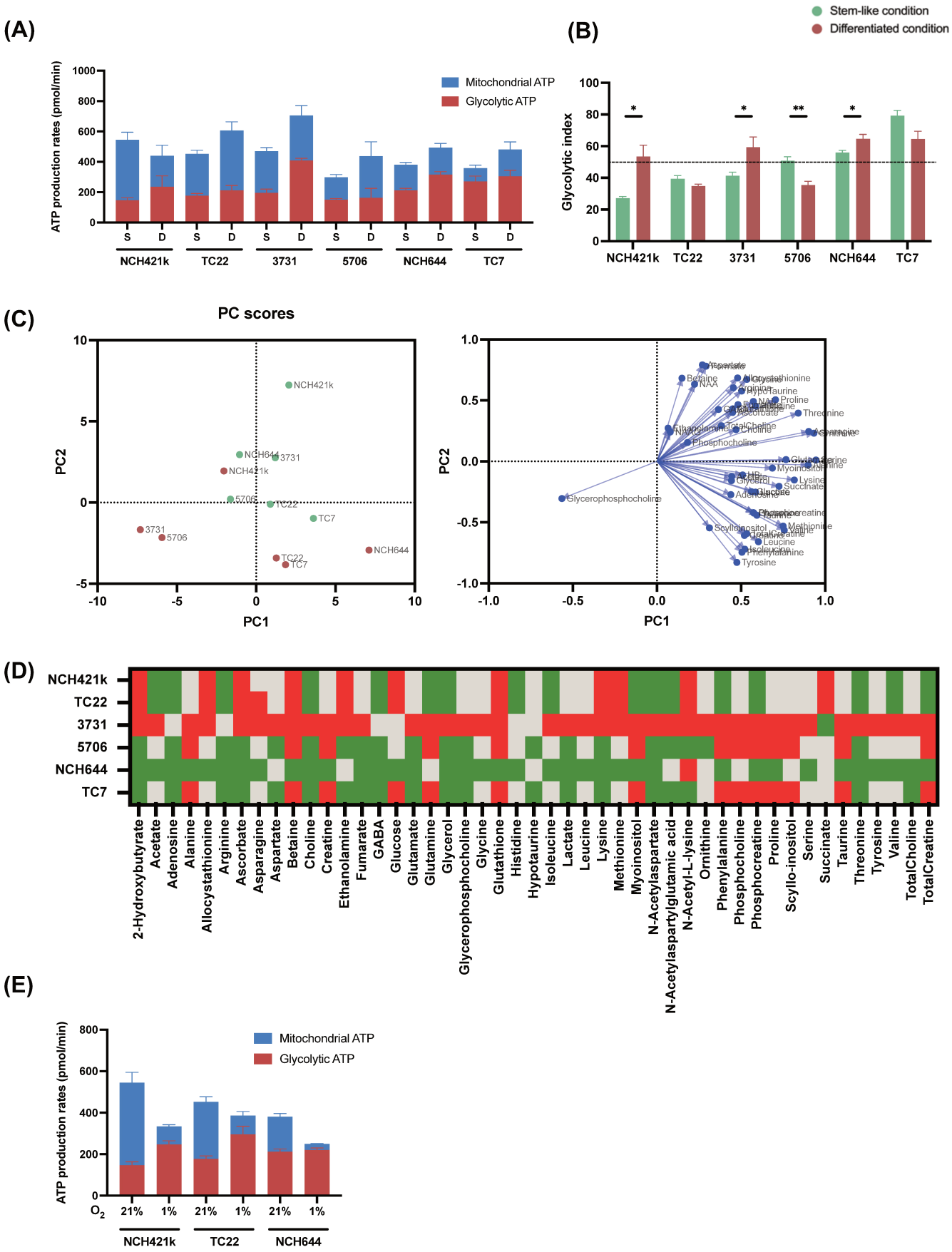
(A)
ATP production rates (pmol/min)
Mitochondrial ATP
Glycolytic ATP
S
D
NCH421k
TC22
3731
5706
NCH644
TC7
(B)
Stem-like condition
Differentiated condition
Glycolytic index
(C)
PC scores
PC1
PC2
(D)
2-Hydroxybutyrate
Acetate
Adenosine
Alanine
Allocystathionine
Arginine
Ascorbate
Asparagine
Aspartate
Betaine
Choline
Creatine
Ethanolamine
Fumarate
GABA
Glucose
Glutamate
Glutamine
Glycerol
Glycerophosphocholine
Glycine
Glutathione
Histidine
Hypotaurine
Isoleucine
Lactate
Leucine
Lysine
Methionine
Myoinositol
N-Acetylaspartate
N-Acetylaspartylglutamic acid
N-Acetyl-L-lysine
Ornithine
Phenylalanine
Phosphocholine
Phosphocreatine
Proline
Scyllo-inositol
Serine
Succinate
Taurine
Threonine
Tyrosine
Valine
TotalCholine
TotalCreatine
(E)
ATP production rates (pmol/min)
Mitochondrial ATP
Glycolytic ATP
O2
21%
1%
NCH421k
TC22
NCH644

Fig. 3

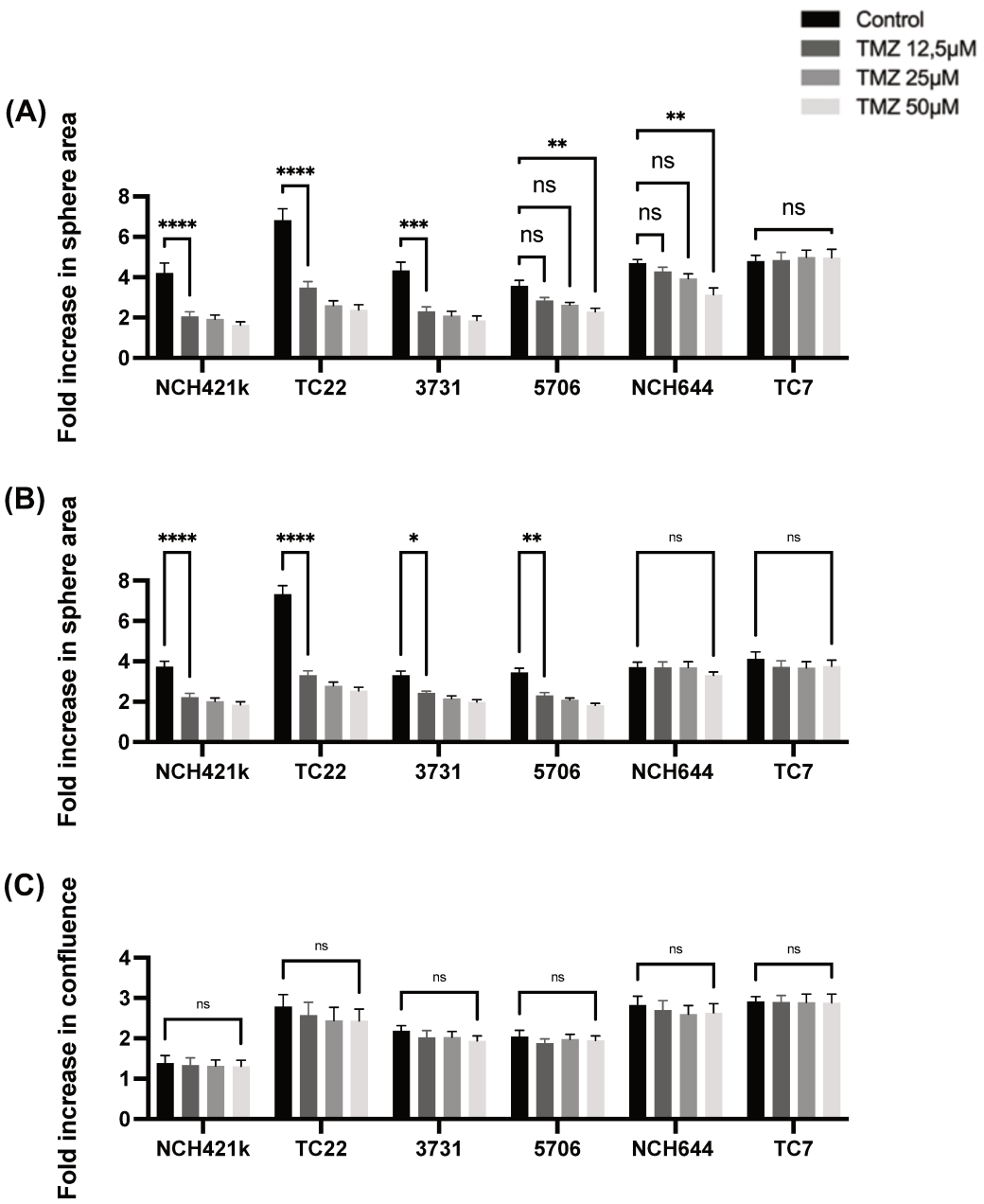
Control
TMZ 12,5μM
TMZ 25μM
TMZ 50μM
(A)
Fold increase in sphere area
(B)
Fold increase in sphere area
(C)
Fold increase in confluence
NCH421k
TC22
3731
5706
NCH644
TC7
ns

Fig. 4

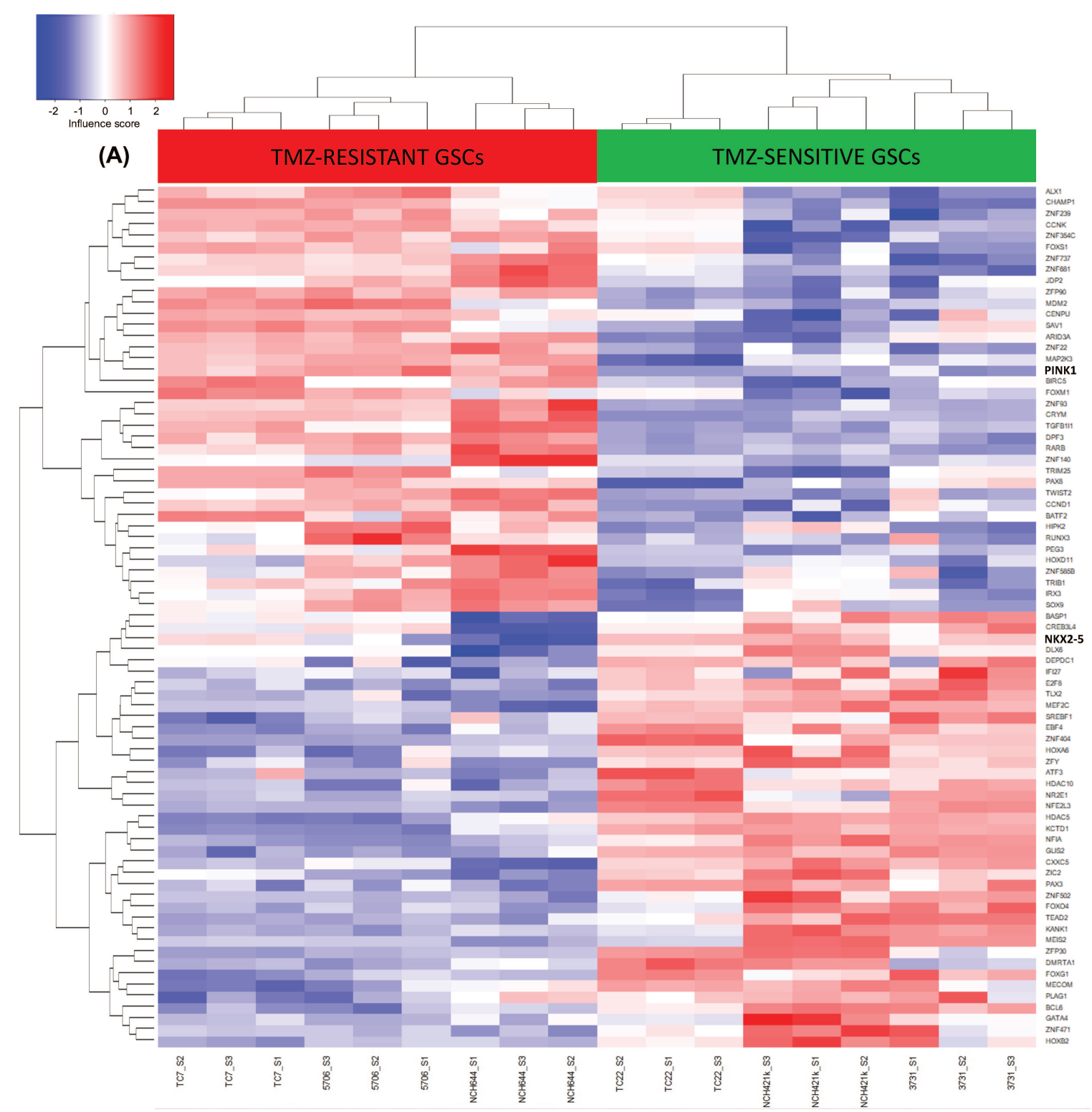
-2 -1 0 1 2
Influence score
(A)
TMZ-RESISTANT GSCs
TMZ-SENSITIVE GSCs
PINK1
NKX2-5
TC7_S2
TC7_S3
TC7_S1
5706_S3
5706_S2
5706_S1
NCH644_S1
NCH644_S3
NCH644_S2
TC22_S2
TC22_S1
TC22_S3
NCH421k_S3
NCH421k_S1
NCH421k_S2
3731_S1
3731_S2
3731_S3

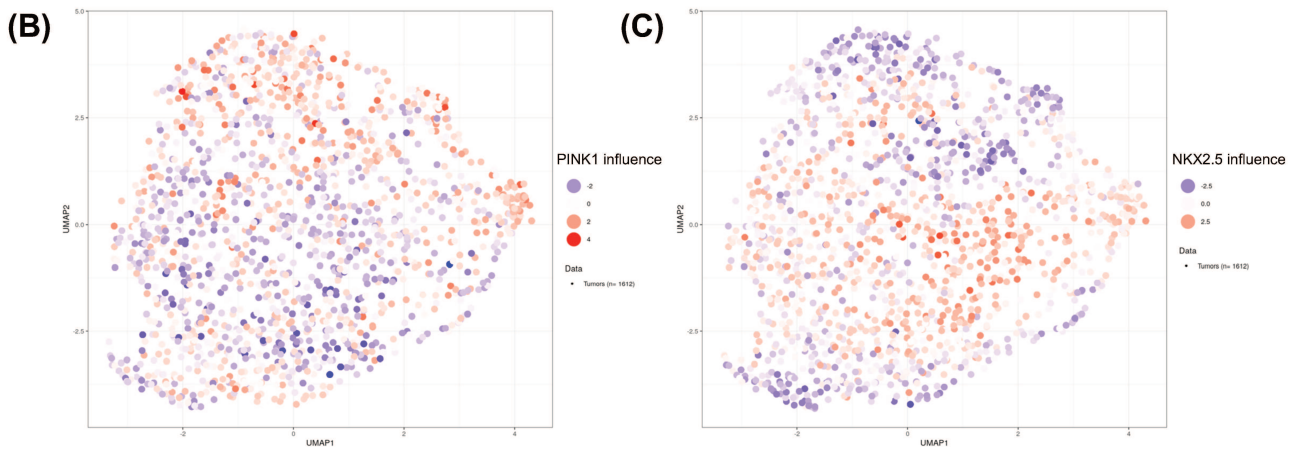
(B)
(C)
PINK1 influence
NKX2.5 influence
UMAP1
UMAP2
Data
Tumors (n= 1612)

Fig. 5

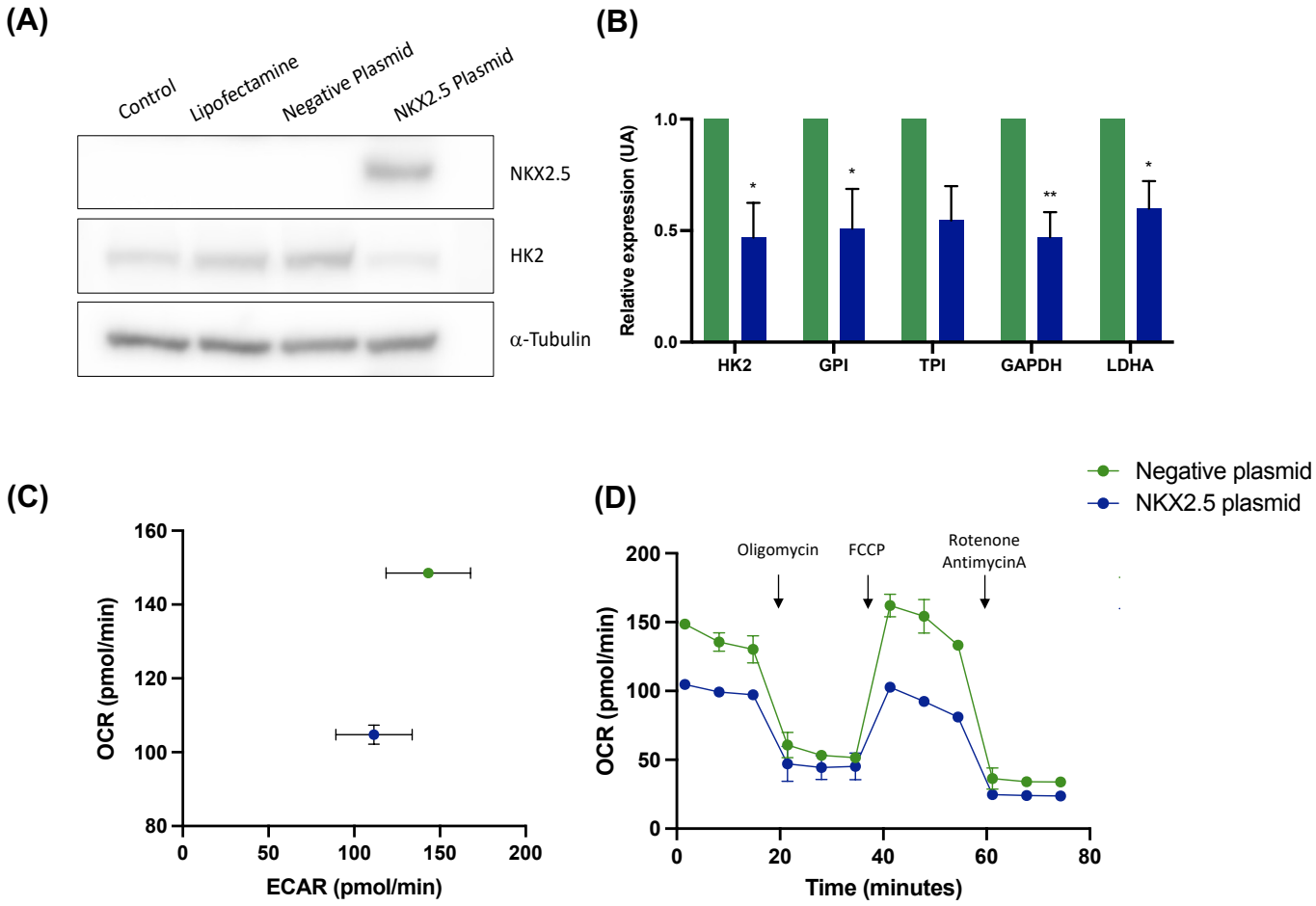
(A)
Control
Lipofectamine
Negative Plasmid
NKX2.5 Plasmid
NKX2.5
HK2
α-Tubulin
(B)
Relative expression (UA)
1.0
0.5
0.0
HK2
GPI
TPI
GAPDH
LDHA
(C)
OCR (pmol/min)
ECAR (pmol/min)
(D)
Negative plasmid
NKX2.5 plasmid
Oligomycin
FCCP
Rotenone
AntimycinA
OCR (pmol/min)
Time (minutes)

Fig. 6

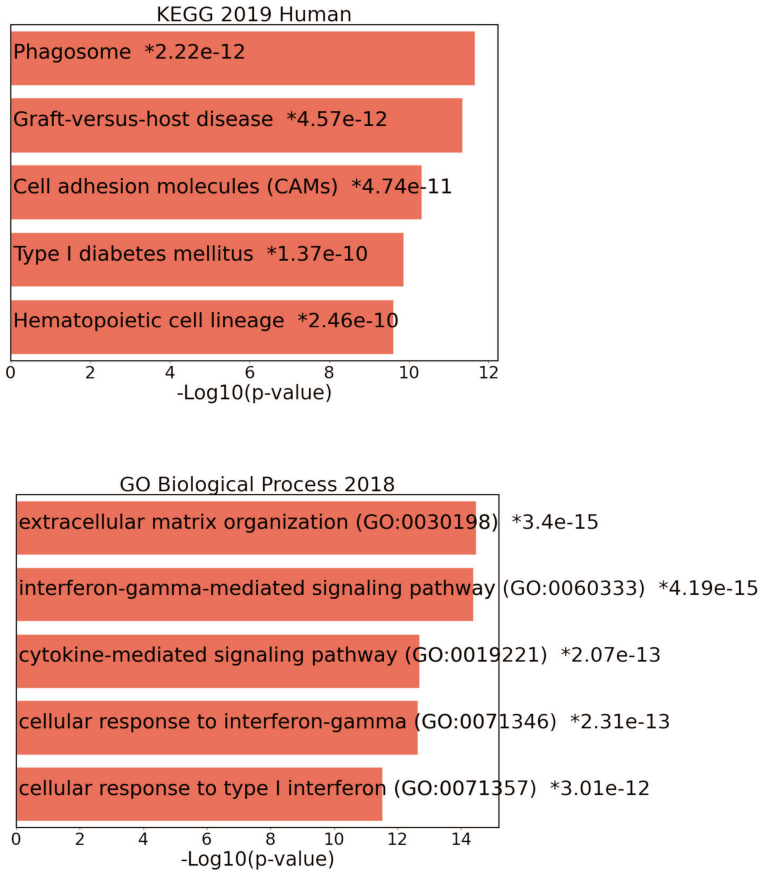
KEGG 2019 Human
Phagosome *2.22e-12
Graft-versus-host disease *4.57e-12
Cell adhesion molecules (CAMs) *4.74e-11
Type I diabetes mellitus *1.37e-10
Hematopoietic cell lineage *2.46e-10
0
2
4
6
8
10
12
-Log10(p-value)
GO Biological Process 2018
extracellular matrix organization (GO:0030198) *3.4e-15
interferon-gamma-mediated signaling pathway (GO:0060333) *4.19e-15
cytokine-mediated signaling pathway (GO:0019221) *2.07e-13
cellular response to interferon-gamma (GO:0071346) *2.31e-13
cellular response to type I interferon (GO:0071357) *3.01e-12
0
2
4
6
8
10
12
14
-Log10(p-value)

Fig. 7

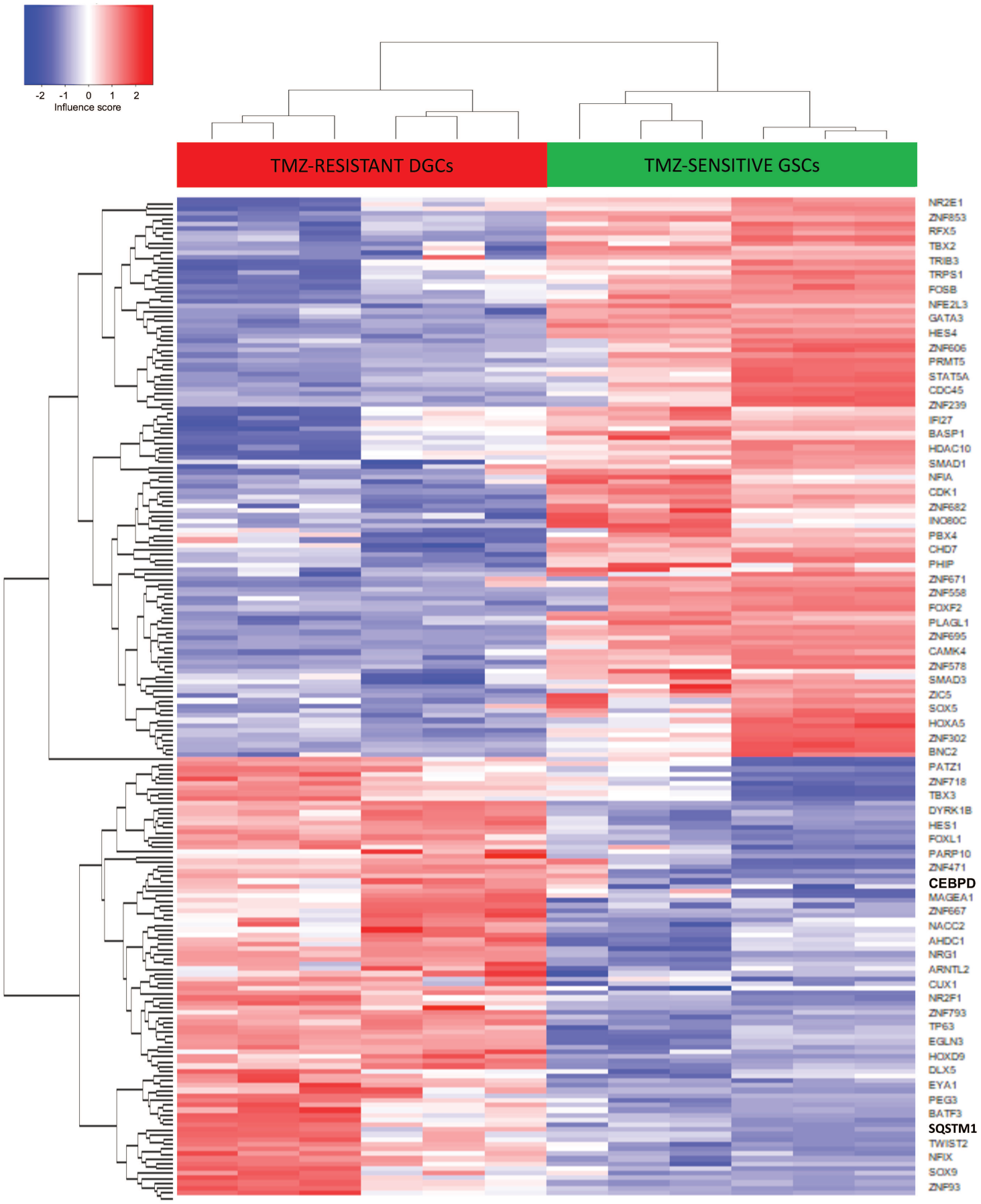
-2 -1 0 1 2
Influence score
TMZ-RESISTANT DGCs
TMZ-SENSITIVE GSCs
NR2E1
ZNF853
RFX5
TBX2
TRIB3
TRPS1
FOSB
NFE2L3
GATA3
HES4
ZNF606
PRMT5
STAT5A
CDC45
ZNF239
IFI27
BASP1
HDAC10
SMAD1
NFIA
CDK1
ZNF682
INO80C
PBX4
CHD7
PHIP
ZNF671
ZNF558
FOXF2
PLAGL1
ZNF695
CAMK4
ZNF578
SMAD3
ZIC5
SOX5
HOXA5
ZNF302
BNC2
PATZ1
ZNF718
TBX3
DYRK1B
HES1
FOXL1
PARP10
ZNF471
CEBPD
MAGEA1
ZNF667
NACC2
AHDC1
NRG1
ARNTL2
CUX1
NR2F1
ZNF793
TP63
EGLN3
HOXD9
DLX5
EYA1
PEG3
BATF3
SQSTM1
TWIST2
NFIX
SOX9
ZNF93

Fig. 8

Données supplémentaires

Variabilité de la sensibilité des CSG aux inhibiteurs métaboliques

Nous avons mené des tests de sensibilité sur les différentes lignées de CSG en utilisant la metformine (MET) et le dichloroacétate (DCA), deux médicaments disposant d'une autorisation de mise sur le marché (AMM) pour des indications autres que le cancer. La MET agit comme un inhibiteur de l'OXPHOS, tandis que le DCA est considéré comme un inhibiteur de la glycolyse, favorisant ainsi le flux de pyruvate vers les mitochondries plutôt que sa conversion en lactate. Nos tests de sensibilité (Figure 11), réalisés sur différentes lignées de CSG, ont révélé que l'utilisation individuelle de la MET ou du DCA en monothérapie présentait généralement une efficacité équivalente ou inférieure à celle du TMZ. En revanche, la combinaison de MET et DCA a montré une capacité significative à inhiber la prolifération dans toutes les lignées de CSG testées, y compris celles résistantes au TMZ. Des études antérieures ont démontré que cette combinaison thérapeutique induit une augmentation synergique du stress oxydatif dans les cellules cancéreuses, offrant ainsi une piste prometteuse pour l'éradication du GB en exploitant cette vulnérabilité [229]. Ces médicaments, bénéficiant déjà d'une AMM pour d'autres indications que le cancer, pourraient être rapidement repositionnés dans l'arsenal thérapeutique des GB.

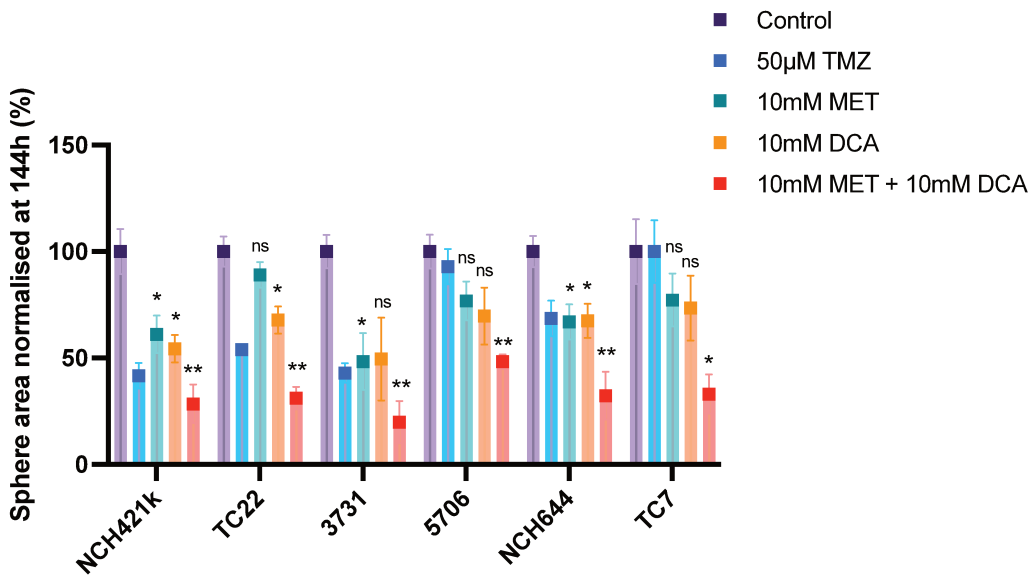

Figure 11 : La bithérapie metformine/dichloroacétate inhibe efficacement la prolifération des cellules souches de glioblastome

Des tests de sensibilité des CSG au TMZ, à la MET, au DCA, ainsi qu'à la combinaison MET-DCA, ont été réalisés sur une période de 6 jours à l'aide de la technologie Incucyte. Les histogrammes représentent l'augmentation de la taille des neurosphères entre t=0 et t=6 jours. $P < 0,05$ a été considéré comme significatif, *$P < 0,05$, **$P < 0,01$.

Effet d'un traitement prolongé du TMZ sur les CSG

Nous avons exposé différentes lignées de CSG à un traitement de 50 µM de TMZ. Les lignées sensibles à ce traitement, notamment NCH421k, TC22 et 3731, ont montré une réduction de leur viabilité après une semaine d'exposition. Les cellules survivantes ont été ensuite cultivées pendant trois semaines supplémentaires, avec un apport régulier de 50 µM de TMZ dans le milieu de culture à chaque passage. Après ces trois semaines de traitement, nous avons réévalué la sensibilité au TMZ de ces lignées en utilisant la technologie Incucyte (Figure 12 A). Nous avons constaté l'acquisition d'une résistance au TMZ dans chaque lignée. Après acquisition d'une résistance au TMZ, ces lignées ont été analysées par la technologie Seahorse, afin de comparer leur profil métabolique avant et après le traitement (Figure 12 B). Un changement métabolique notable a été observé dans les cellules NCH421k : alors que les cellules témoins non traitées (DMSO) présentaient un phénotype oxydatif, les cellules résistantes, après traitement et exposition répétée à 50 µM de TMZ, affichaient un métabolisme glycolytique. Ce résultat corrobore l'association entre un phénotype glycolytique et une résistance accrue des CSG. En revanche, pour les autres lignées TC22 et 3731 ayant développé une résistance, aucune variation significative de leur profil énergétique n'a été observée après l'exposition prolongée au TMZ.

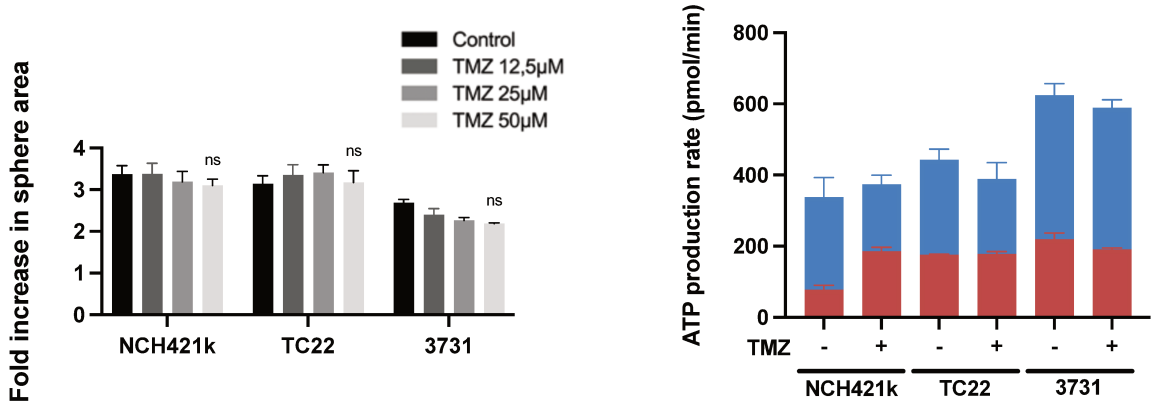

Figure 12 : Résistance au témozolomide acquise des cellules souches de glioblastome suite à un traitement prolongé
Les lignées de CSG initialement sensibles au TMZ ont été cultivées en présence de TMZ ou sans (contrôle DMSO) pendant plus de trois semaines. (A) Illustration de la croissance des neurosphères en réponse à différentes concentrations de TMZ, soulignant une résistance acquise au TMZ (B) Profils énergétiques de ces cellules résistantes. n=3.

Pour les lignées de CSG intrinsèquement résistantes au TMZ (TC7, NCH644, 5706), aucune modification significative de leur profil énergétique n'a été observée (Figure 13). Ces lignées présentaient déjà un métabolisme glycolytique avant le traitement, ce qui semble contribuer à leur résistance intrinsèque au TMZ.

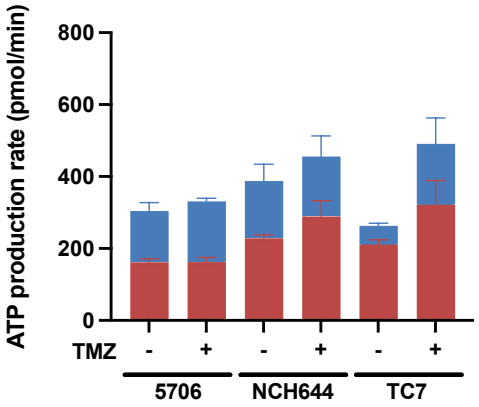

Figure 13 : Absence d'effet du témozolomide sur le profil énergétique des cellules souches de glioblastome intrinsèquement résistantes
Des analyses ATP Rate Assay ont été réalisées sur les lignées de CSG intrinsèquement résistantes au TMZ, cultivées en présence de TMZ ou sans (contrôle DMSO) pendant plus de trois semaines. n=3.

Ces résultats confirment que le traitement prolongé au TMZ conduit à une résistance dans les lignées de CSG, soulignant ainsi l'urgence de développer des stratégies thérapeutiques innovantes pour contrer cette résistance. L'acquisition de cette résistance peut s'accompagner d'un remodelage métabolique vers la glycolyse, mettant en lumière la relation étroite entre la glycolyse et la résistance au TMZ.

Étude collaborative

Alors que mes recherches portaient sur le métabolisme des CSG, une équipe dirigée par le Dr. Bellemin-Laponnaz, a développé une nouvelle molécule, le NHC-PEI30-Pt(II), qui semblait affecter spécifiquement le métabolisme mitochondrial [230]. Ce composé avait déjà démontré sa capacité à s'accumuler dans les mitochondries et à exercer une action anticancéreuse sur diverses lignées cellulaires ainsi que dans un modèle de xénogreffe. De ce fait, une collaboration a été initiée avec cette équipe afin de tester le potentiel thérapeutique de cette molécule sur les CSG.

Cette collaboration a donné lieu à une étude publiée dans la revue Cancers (IF = 6.575), intitulée « Polyethylenimine, an Autophagy-Inducing Platinum-Carbene-Based Drug Carrier with Potent Toxicity towards Glioblastoma Cancer Stem Cells » (doi: 10.3390/cancers14205057) (Annexe 2). Notre travail a exploré l'utilisation du polyéthylénimine (PEI) et du NHC-PEI30-Pt(II) en tant que stratégies anticancéreuses. Nos résultats ont révélé une sensibilité accrue des CSG à ces composés, comparativement aux cellules plus différenciées et aux cellules non cancéreuses. Le mécanisme de mort cellulaire observé présente des caractéristiques semblables à celles de la nécrose, sans marqueurs

apoptotiques, et est accompagné d'une réponse autophagique marquée, qui semble être de nature protective. Le traitement au NHC-PEI30-Pt(II) a notamment entrainé une augmentation du flux autophagique, une accumulation d'autophagosomes, une répression du phénotype souche, ainsi qu'une altération globale du métabolisme énergétique au sein des CSG.

Ces résultats mettent en lumière l'importance de la régulation de l'autophagie dans les CSG et suggèrent que des composés altérant ce processus pourraient représenter des stratégies thérapeutiques prometteuses dans la prise en charge des GB, nécessitant des investigations supplémentaires.

Discussion et perspectives

Ce travail de thèse a approfondi notre compréhension de l'hétérogénéité, de la plasticité métabolique et moléculaire, et de la résistance aux traitements des CSG, offrant ainsi de nouvelles perspectives sur la biologie des GB et leur traitement.

Hétérogénéité et plasticité métabolique

Dans notre étude portant sur une cohorte de CSG, nous avons identifié deux populations distinctes : les CSG à métabolisme principalement glycolytique et les CSG à métabolisme majoritairement mitochondrial. Cette classification est en accord avec les travaux de *Garofano et al.* [107], qui ont également identifié les sous-types : « glycolytiques plurimétaboliques » et « mitochondriaux ».

Vlashi a précédemment rapporté que les CSG sont moins glycolytiques que les cellules tumorales différenciées et qu'elles produisent plus d'ATP que ces dernières [79]. Nos résultats remettent en question cette étude, mettant en lumière une complexité accrue dans la reprogrammation métabolique en réponse à la différenciation. Nous avons constaté que certaines lignées de CSG tendent à devenir plus glycolytiques après la différentiation, alors que d'autres s'orientent vers un métabolisme plus axé sur l'OXPHOS. Par ailleurs, notre étude a révélé une tendance générale à l'augmentation des taux de production d'ATP suite à la différenciation, indiquant ainsi une activité métabolique renforcée dans les cellules différenciées par rapport à un état plus quiescent observé dans les CSG. Cette observation corrobore les études antérieures suggérant que les CSG affichent un phénotype métabolique plus quiescent comparativement aux cellules correspondantes différenciées [231].

Nos recherches ont également mis en évidence une plasticité métabolique des lignées de CSG en réponse à la chimiothérapie. En réponse au TMZ, certaines lignées oxydatives sont capables de passer à un métabolisme glycolytique, démontrant un impact significatif de la chimiothérapie sur les caractéristiques métaboliques des CSG. Cette capacité d'adaptation métabolique en réponse au traitement souligne l'importance de considérer la plasticité métabolique dans le développement de stratégies thérapeutiques ciblées pour les GB.

Résistance au TMZ

Nos observations ont mis en évidence des différences notables entre les CSG résistantes au TMZ et celles qui y sont sensibles (Figure 14).

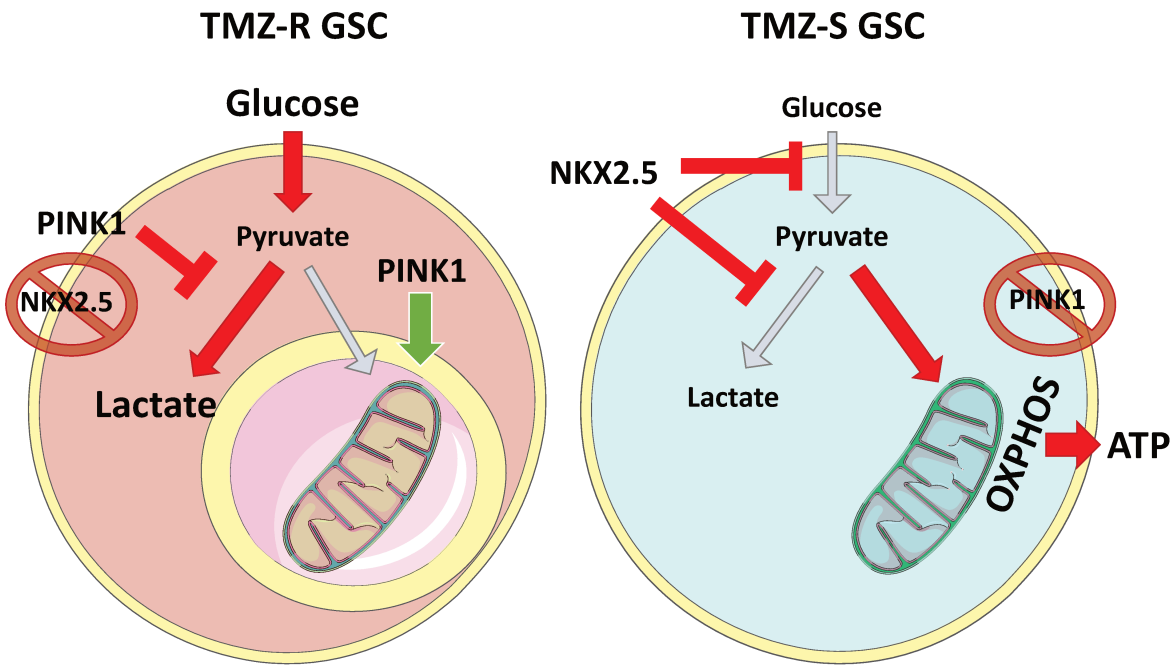

Glycolytic state
TMZ-resistant
Mitochondrial Degradation
Reduced Oxidative Metabolism
Stem Cell Quiescence
Slow Cycling, Self-Renewing State
↑ Glucose and Lactate Pathways
↓ N-Acetylaspartate-Associated Pathways
PINK1 Activity
Mitophagy
NKX2.5 Inactivity
Slow cycling, self-renewing state
p53 Turnover
↑ Capacity for Mitochondrial Reserve
More Resistant to Oxidative Stress

OXPHOS State
TMZ-sensitive
Mitochondrial Remodeling
Highly Energetic State
↓ Glucose and Lactate Pathways
↑ Glutamine and Glutathione
↑ N-Acetylaspartate-Associated Pathways
PINK1 Inactivity and Degradation
NKX2.5 Activity → Repression of Glycolysis
↑ ROS Levels
More Sensitive to Oxidative Stress

Figure 14 : Caractéristiques distinctives entre les cellules souches résistantes et sensibles au témozolomide

Nous avons constaté que les lignées à métabolisme glycolytique présentent une plus grande résistance à la chimiothérapie comparativement aux lignées à métabolisme oxydatif. Ces constatations concordent avec les résultats de *Garofano et al*., qui ont identifié que les « GB mitochondriaux » étaient associés à un meilleur pronostic. Selon leur étude, une activité mitochondriale élevée dans ces GB augmente les niveaux de ROS intracellulaires, ce qui rend ces tumeurs plus sensibles à l'irradiation et explique pourquoi les patients atteints de ce type de GB ont généralement de meilleurs résultats cliniques [107].

Au-delà du phénotype glycolytique, nous avons observé que les lignées de CSG résistantes au TMZ présentent une diminution de l'activité des voies métaboliques associées au N-acétylaspartate (NAA). Des recherches antérieures ont indiqué que le NAA, le N-acétylaspartylglutamate (NAAG), et l'aspartoacylase (ASPA) – l'enzyme responsable de la dégradation du NAA – sont significativement réduits dans les GB comparativement aux gliomes de bas grade, suggérant un rôle potentiel de la réduction du métabolisme de l'acétate dans la tumorigenèse [232]. Le NAA est généralement considéré comme un marqueur de tissu neuronal sain, et les gliomes de bas grade sont souvent caractérisés par une concentration élevée en NAA, un faible niveau de choline, et l'absence de lactate et de lipide [233]. D'autres études ont suggéré que le NAA pourrait induire un stress oxydatif ou perturber les défenses antioxydantes enzymatiques [234,235]. Il est donc plausible que dans les lignées cellulaires dépendant principalement du métabolisme OXPHOS, des concentrations élevées de NAA exacerbent le stress oxydatif induit par le TMZ, augmentant ainsi leur vulnérabilité à la chimiothérapie.

Nous avons également observé une résistance accrue au TMZ dans toutes les lignées de CSG après leur différenciation, ce qui remet en question le dogme établi selon lequel les CSG possèdent une capacité de résistance accrue aux thérapies par rapport aux cellules différenciées. L'acquisition de cette résistance a été corrélée à une reprogrammation moléculaire et métabolique profonde, suggérant l'implication de divers facteurs dans la résistance des GB. En particulier, l'analyse métabolomique des lignées de CSG ayant développé une résistance marquée au TMZ a révélé une régulation à la hausse de certains métabolites, susceptibles d'influencer cette résistance, soit par la perturbation des programmes de méthylation, soit par le renforcement des mécanismes antioxydants. Au niveau moléculaire, des altérations dans des processus clés tels que l'autophagie et la mitophagie ont été identifiées. Des modifications ont été observées dans divers processus biologiques et voies de signalisation clés, y compris la formation de phagosomes, la régulation du cytosquelette d'actine, l'adhésion focale, et la voie

de signalisation PI3K-AKT. La formation de phagosome est directement reliée au processus d'autophagie. L'augmentation de l'expression des gènes liés aux phagosomes suggère un lien potentiel avec l'autophagie. Parmi ces gènes, LAMP1 (protéine 1 associée à la membrane lysosomale) et CTSL (cathepsine L), qui sont directement impliqués dans les processus lysosomaux cruciaux pour l'autophagie [236], sont significativement surexprimés dans les deux lignées cellulaires résistantes au TMZ après différentiation. De manière générale, ces différentes voies dérégulées jouent un rôle crucial dans la modulation de la réponse cellulaire au stress et dans le maintien de l'homéostasie cellulaire, particulièrement dans la gestion du stress oxydatif. Il semble que les lignées résistantes soient plus aptes à gérer ce stress oxydatif. Ces résultats sont en accord avec une étude où l'activation du processus d'autophagie en réponse au traitement au TMZ a été observée comme contribuant à la protection des cellules contre les dommages induits par le TMZ [237]. Ces voies enrichies au cours de mon étude sont en accord avec les changements rapportés dans une étude analysant les protéines exprimées différemment après un traitement par le TMZ dans des cellules résistantes [238]. Il est donc plausible que ces processus soient des mécanismes de réponse adaptative développés par les cellules tumorales pour résister à la chimiothérapie.

De plus, des études antérieures ont souligné l'importance des dommages causés aux mitochondries par le traitement au TMZ [239]. En effet, en dehors de l'impact significatif du TMZ sur l'ADN nucléaire, le TMZ induit également des altérations au sein de l'ADN mitochondrial, notamment une réduction du nombre de copies et l'apparition de larges délétions hétéroplasmiques. Ces altérations s'accompagnent d'un remodelage profond de la chaîne respiratoire, avec une diminution des complexes I et V et une augmentation des complexes II/III et IV. De manière intéressante, cette étude a également démontré que la manipulation pharmacologique et génétique du cytochrome c oxydase (complexe IV de OXPHOS) peut restaurer la sensibilité des cellules à la chimiothérapie. Ces découvertes suggèrent que la sensibilité au TMZ pourrait être en grande partie attribuable à une réponse des mitochondries face au stress induit par le TMZ [239]. Par ailleurs, le rôle du stress oxydatif, et en particulier des niveaux de ROS, ont également démontré jouer un rôle majeur dans la sensibilité au TMZ. Une étude a montré que dans les cellules sensibles au TMZ, l'augmentation des ROS induite par le traitement active l'autophagie, entraînant la mort cellulaire. À l'inverse, dans les cellules résistantes, cette augmentation des ROS n'est pas observée, ce qui empêche l'activation de l'autophagie. En augmentant artificiellement le stress oxydatif, les auteurs de l'étude ont réussi à réactiver l'autophagie et à restaurer la sensibilité des cellules au TMZ [240].

À l'aide de l'analyse du réseau de régulateurs, nous avons mis en évidence une activité accrue de PINK1 dans les CSG résistantes au TMZ, suggérant une mitophagie renforcée. Ceci contribue à un meilleur contrôle de la qualité mitochondriale et à une résistance accrue au stress oxydatif. Les cellules cancéreuses résistantes aux traitements, semblent fortement dépendre de la mitophagie induite par PINK1. Cette dépendance offre une stratégie thérapeutique potentielle : l'utilisation de la chloroquine, un inhibiteur de la mitophagie, pourrait permettre d'éliminer ces CSG résistantes après chimiothérapie [241].

Au sein de la population de CSG étudiées, nous avons observé une divergence dans l'activité de PINK1 et NKX2.5, en fonction de leur sensibilité au TMZ. Dans les lignées résistantes, une activité accrue de PINK1 et une répression de NKX2.5 ont été observées, tandis que dans les lignées sensibles, c'est l'activité de NKX2.5 qui prédomine avec une répression de PINK1. PINK1 est particulièrement intéressant en raison de son rôle dans la mitophagie et, plus largement, dans des processus clés liés au métabolisme cellulaire, à la fonction mitochondriale et à la régulation de la réponse au stress oxydatif. Il agit également comme un régulateur négatif de l'effet Warburg et a été associé à la résistance aux traitements [241,242]. Parallèlement, notre étude a révélé le rôle de NKX2.5, un facteur de transcription initialement connu pour son implication dans le développement cardiaque, dans la répression transcriptionnelle de nombreux gènes glycolytiques dans les GB, soulignant ainsi son rôle similaire à celui de PINK1 en tant que répresseur de l'effet Warburg. Par ailleurs, NKX2.5 est activé dans un sous-type de GB particulièrement dévastateur, le sous-type CL-C (*Bernhard et al.*, BioRxiv).

Dans les CSG différenciées ayant acquis une résistance, nous avons identifié des régulateurs tels que SQSTM1 [243,244] et TFEB [245], qui sont activés de manière différentielle après la différenciation et qui sont directement impliqués dans l'autophagie.

Ainsi, que ce soit dans la population de cellules souches résistantes ou dans celle des cellules différenciées résistantes, nos différents résultats (métabolomiques, transcriptomiques, du réseau de régulateurs) soulignent particulièrement l'importance de l'autophagie dans les mécanismes de résistance.

Stratégies thérapeutiques potentielles

Étant donné que les CSG résistantes au TMZ présentent de faible niveaux de NAA, une stratégie envisagée a été une complémentation en NAA. Cependant, l'utilisation thérapeutique

du NAA ou du NAAG dans les gliomes est controversée, car ces composés ont été associés à une augmentation de la prolifération des CSG [232]. À l'inverse, la triacétine, un additif alimentaire, a été identifiée comme une source alternative d'acétate. Elle a démontré sa capacité à réduire efficacement la prolifération des CSG sans impacter les cellules saines, agissant potentiellement par un mécanisme épigénétique qui influence l'acétylation des histones et modifie l'expression génique. Cette approche a montré des effets inhibiteurs sur la croissance des CSG, particulièrement celles présentant un phénotype mésenchymateux, qui sont généralement plus glycolytiques et caractérisées par une hypoacétylation des histones [246].

Les lignées de CSG résistantes au TMZ, présentant un métabolisme glycolytique, pourraient être efficacement ciblées par l'inhibition de la glycolyse. Une stratégie prometteuse consiste à favoriser le flux de pyruvate vers les mitochondries, notamment avec le dichloroacétate (DCA). Le DCA inhibe la pyruvate déshydrogénase kinase, favorisant ainsi l'activité mitochondriale. En combinaison avec la metformine (MET), un inhibiteur du complexe I de la chaîne respiratoire mitochondriale, il a été démontré que le DCA produit un effet synergique sur les CSG, réduisant la croissance des GB *in vitro* et *in vivo* [219]. Cette combinaison a permis d'inhiber la prolifération cellulaire dans toutes les lignées étudiées, y compris celles résistantes au TMZ. En plus de cibler les deux principales voies bioénergétiques des cellules, cette combinaison MET-DCA modifie également le stress oxydatif. La MET entraîne une augmentation du stress oxydatif, notamment en modifiant l'activité de la superoxyde dismutase (SOD), qui joue un rôle de défense contre les ROS [220]. Cette modulation du stress oxydatif, en plus de cibler les deux voies bioénergétiques, pourrait donc représenter une approche thérapeutique complémentaire dans le traitement des GB [229]. D'autres approches thérapeutiques visant à induire ou augmenter le stress oxydatif au sein des GB pourraient s'avérer prometteuses [221].

Étant donné le rôle crucial de l'autophagie dans la résistance au TMZ et compte tenu de sa nature dualiste, capable de favoriser soit la survie, soit la mort cellulaire des cellules cancéreuses, la modulation de ce processus par des agents pharmacologiques semble représenter une stratégie thérapeutique prometteuse. Les mécanismes précis régissant l'impact de l'autophagie sur les cellules de GB restent à élucider [240,247,248]. Il a notamment été démontré que la modulation de l'autophagie, que ce soit par son induction ou son inhibition, affecte directement le métabolisme des cellules de GB, perturbant notamment la fonction de la chaîne respiratoire mitochondriale et la dynamique de fission-fusion mitochondriale [248]. L'utilisation d'inhibiteurs de l'autophagie, tels que la chloroquine, ou d'inducteurs, comme la

rapamycine, suscite ainsi un intérêt croissant dans la recherche sur les traitements anticancéreux [247].

Une stratégie thérapeutique en cours d'exploration au sein de notre laboratoire implique la modulation de l'équilibre entre les régulateurs PINK1 et NKX2.5. D'une part, l'inhibition de PINK1 dans les cellules résistantes au TMZ pourrait réduire la mitophagie et augmenter la vulnérabilité des cellules au stress oxydatif, conduisant potentiellement à leur mort. D'autre part, l'activation de NKX2.5 pourrait favoriser un métabolisme cellulaire moins propice à leur état de résistance.

Perspectives et conclusion

Pour approfondir notre compréhension, il serait pertinent d'étudier en détail les rôles de PINK1 et NKX2.5 en modulant leur expression, soit par surexpression *via* des plasmides, soit par répression à l'aide de siRNA. Ces études pourraient non seulement clarifier les mécanismes moléculaires à l'origine de la résistance au TMZ mais aussi ouvrir la voie à de nouvelles stratégies thérapeutiques ciblées.

Nos résultats révèlent des vulnérabilités thérapeutiques, bien que celles-ci soient influencées par de nombreux paramètres. Ces découvertes offrent un point de départ pour l'identification de cibles thérapeutiques spécifiques, adaptées à des types de tumeurs particuliers et à des stades précis de leur développement. L'objectif idéal serait de perfectionner l'outil CoRegNet et d'affiner la classification des GB en intégrant des données sur les tumeurs de patients, y compris des biomarqueurs pronostiques, diagnostiques, thérapeutiques, et des combinaisons de thérapies ciblées pour chaque sous-classe. Ceci permettrait une stratification des patients plus précise, une meilleure prédiction du pronostic et de proposer des stratégies thérapeutiques personnalisées et optimisées pour chaque type de tumeur.

En intégrant les données transcriptomiques au sein de GBM-cReg, et en combinant les différents types de données recueillis, nous avons obtenu une vue d'ensemble des processus se déroulant dans nos cellules *in vitro*. Cette approche longitudinale enrichit notre compréhension de la plasticité des GB, notamment *via* la simulation *in vitro* des conditions qui pourraient se produire *in vivo*. Cette recherche s'aligne avec un des objectifs de notre équipe, qui vise à étudier l'hétérogénéité d'expression d'une cible thérapeutique, celle de l'intégrine $\alpha5\beta1$. Un autre projet en cours dans notre laboratoire se concentre sur l'hétérogénéité moléculaire à

l'échelle intra-tumorale entre les différentes parties de la tumeur, telles que le bulk tumoral, les niches hypoxiques et les niches périvasculaires. L'objectif étant de proposer des associations thérapeutiques efficaces sur l'ensemble de la tumeur, en intégrant des cibles du bulk, des cibles des zones hypoxiques etc. Les cibles thérapeutiques potentielles identifiées *in vitro* pourront ensuite être testées sur des modèles plus pertinents, comme des organoïdes, afin d'évaluer dans un premier temps leur efficacité et leur applicabilité clinique.

En conclusion, cette deuxième partie de ma thèse a mis en lumière des aspects cruciaux de la biologie des GB, notamment l'hétérogénéité et la plasticité métabolique et moléculaire des CSG, en relation avec la résistance au TMZ. Nous avons souligné l'importance du stress oxydatif et de l'autophagie dans la résistance au TMZ et l'importance de développer des approches ciblant ces vulnérabilités. Notre travail contribue à une meilleure compréhension des mécanismes sous-jacents à la résistance des GB et met en évidence l'importance d'une approche personnalisée dans le traitement de cette maladie complexe.

CONCLUSION GÉNÉRALE

Cette thèse a exploré en profondeur l'hétérogénéité, la plasticité métabolique et moléculaire, ainsi que la résistance aux traitements des CSG, offrant de nouvelles perspectives sur la biologie complexe des GB et leur prise en charge thérapeutique.

Dans la première partie de cette thèse, notre exploration approfondie de l'hétérogénéité moléculaire des GB a révélé une diversité remarquable de sous-types tumoraux. Nous avons développé une nouvelle classification en sept sous-classes distinctes des GB, chacune associée à des caractéristiques moléculaires, des processus biologiques et des implications cliniques uniques. Cette avancée ouvre des perspectives prometteuses pour orienter la recherche vers une médecine personnalisée des GB.

La deuxième partie de cette thèse a mis en évidence des nuances complexes dans les profils métaboliques et moléculaires des CSG, ainsi que leur plasticité en réponse à la différenciation, à l'hypoxie, ou à une thérapie. Nous avons observé que les CSG glycolytiques présentent une résistance intrinsèque au TMZ, tandis que d'autres acquièrent une résistance suite à la différenciation cellulaire ou à un traitement prolongé au TMZ. Nous avons souligné l'autophagie et la gestion du stress oxydatif, comme des axes thérapeutiques potentielles pour surmonter la résistance au TMZ.

Après avoir validé des cibles thérapeutiques dans des modèles *in vitro*, il sera nécessaire de passer à des modèles expérimentaux plus représentatifs, tels que les organoïdes et les xénogreffes orthotopiques. Ces modèles, incluant le microenvironnement tumoral et les interactions cellulaires complexes, offrent des perspectives plus fidèles à la réalité *in vivo* [249]. De nombreuses cibles thérapeutiques ont d'ores et déjà été validées dans des modèles *in vitro* et *in vivo*, l'objectif est à présent d'identifier les sous-types de tumeurs pouvant bénéficier de telles thérapies.

L'objectif est de dépasser les stratégies thérapeutiques actuelles, telles que le protocole de STUPP, confrontées à des problèmes de résistance, et de surmonter les limites des thérapies ciblées qui se concentrent sur des cibles uniques sans prendre en compte l'hétérogénéité et la plasticité des tumeurs. Nous visons à une meilleure stratification des patients et à la proposition de combinaisons de thérapies ciblées, adaptées à chaque sous-classe de GB, pour une prise en charge thérapeutique plus efficace.

RÉFÉRENCES

1. Schwartzbaum, J.A.; Fisher, J.L.; Aldape, K.D.; Wrensch, M. Epidemiology and Molecular Pathology of Glioma. *Nat. Clin. Pract. Neurol.* **2006**, *2*, 494–503, doi:10.1038/ncpneuro0289.
2. Almairac, F.; Frenay, M.; Paquis, P. Maladies Génétiques et Glioblastomes. *Neurochirurgie* **2010**, *56*, 455–458, doi:10.1016/j.neuchi.2010.07.007.
3. Melin, B.S.; Barnholtz-Sloan, J.S.; Wrensch, M.R.; Johansen, C.; Il'yasova, D.; Kinnersley, B.; Ostrom, Q.T.; Labreche, K.; Chen, Y.; Armstrong, G.; et al. Genome-Wide Association Study of Glioma Subtypes Identifies Specific Differences in Genetic Susceptibility to Glioblastoma and Non-Glioblastoma Tumors. *Nat. Genet.* **2017**, *49*, 789–794, doi:10.1038/ng.3823.
4. Joseph, G.P.; McDermott, R.; Baryshnikova, M.A.; Cobbs, C.S.; Ulasov, I. V. Cytomegalovirus as an Oncomodulatory Agent in the Progression of Glioma. *Cancer Lett.* **2017**, *384*, 79–85, doi:10.1016/j.canlet.2016.10.022.
5. Moore, S.C.; Rajaraman, P.; Dubrow, R.; Darefsky, A.S.; Koebnick, C.; Hollenbeck, A.; Schatzkin, A.; Leitzmann, M.F. Height, Body Mass Index, and Physical Activity in Relation to Glioma Risk. *Cancer Res.* **2009**, *69*, 8349–8355, doi:10.1158/0008-5472.CAN-09-1669.
6. Rice, T.; Lachance, D.H.; Molinaro, A.M.; Eckel-Passow, J.E.; Walsh, K.M.; Barnholtz-Sloan, J.; Ostrom, Q.T.; Francis, S.S.; Wiemels, J.; Jenkins, R.B.; et al. Understanding Inherited Genetic Risk of Adult Glioma – a Review. *Neuro-Oncology Pract.* **2016**, *3*, 10–16, doi:10.1093/nop/npv026.
7. Louis, D.N.; Perry, A.; Wesseling, P.; Brat, D.J.; Cree, I.A.; Figarella-Branger, D.; Hawkins, C.; Ng, H.K.; Pfister, S.M.; Reifenberger, G.; et al. The 2021 WHO Classification of Tumors of the Central Nervous System: A Summary. *Neuro. Oncol.* **2021**, *23*, 1231–1251, doi:10.1093/neuonc/noab106.
8. Ostrom, Q.T.; Cioffi, G.; Waite, K.; Kruchko, C.; Barnholtz-Sloan, J.S. CBTRUS Statistical Report: Primary Brain and Other Central Nervous System Tumors Diagnosed in the United States in 2014–2018. *Neuro. Oncol.* **2021**, *23*, iii1–iii105, doi:10.1093/neuonc/noab200.
9. Miller, K.D.; Ostrom, Q.T.; Kruchko, C.; Patil, N.; Tihan, T.; Cioffi, G.; Fuchs, H.E.; Waite, K.A.; Jemal, A.; Siegel, R.L.; et al. Brain and Other Central Nervous System Tumor Statistics, 2021. *CA. Cancer J. Clin.* **2021**, *71*, 381–406, doi:10.3322/caac.21693.
10. Wang, Z.; Zhang, H.; Xu, S.; Liu, Z.; Cheng, Q. The Adaptive Transition of Glioblastoma Stem Cells and Its Implications on Treatments. *Signal Transduct. Target. Ther.* **2021**, *6*, 124, doi:10.1038/s41392-021-00491-w.
11. Louis, D.N.; Perry, A.; Reifenberger, · Guido; Von Deimling, A.; Figarella-Branger, D.; Webster, ·; Cavenee, K.; Ohgaki, H.; Otmar, ·; Wiestler, D.; et al. The 2016 World Health Organization Classification of Tumors of the Central Nervous System: A Summary., doi:10.1007/s00401-016-1545-1.
12. Yan, H.; Parsons, D.W.; Jin, G.; McLendon, R.; Rasheed, B.A.; Yuan, W.; Kos, I.; Batinic-Haberle, I.; Jones, S.; Riggins, G.J.; et al. IDH1 and IDH2 Mutations in Gliomas. *N. Engl. J. Med.* **2009**, *360*, 765–773, doi:10.1056/NEJMoa0808710.
13. Sanson, M.; Marie, Y.; Paris, S.; Idbaih, A.; Laffaire, J.; Ducray, F.; El Hallani, S.; Boisselier, B.; Mokhtari, K.; Hoang-Xuan, K.; et al. Isocitrate Dehydrogenase 1 Codon 132 Mutation Is an Important Prognostic Biomarker in Gliomas. *J. Clin. Oncol.* **2009**, *27*, 4150–4154.
14. Verreault, M.; Delattre, J.-Y.; Idbaih, A. Les Tumeurs Gliales Diffuses de l'adulte. *médecine/sciences* **2012**, *28*, 813–816, doi:10.1051/medsci/20122810005.
15. Dang, L.; White, D.W.; Gross, S.; Bennett, B.D.; Bittinger, M.A.; Driggers, E.M.; Fantin, V.R.; Jang, H.G.; Jin, S.; Keenan, M.C.; et al. Cancer-Associated IDH1

Mutations Produce 2-Hydroxyglutarate. *Nature* **2009**, *462*, 739–744, doi:10.1038/nature08617.
16. Parsons, D.W.; Jones, S.; Zhang, X.; Lin, J.C.H.; Leary, R.J.; Angenendt, P.; Mankoo, P.; Carter, H.; Siu, I.M.; Gallia, G.L.; et al. An Integrated Genomic Analysis of Human Glioblastoma Multiforme. *Science (80-.).* **2008**, *321*, 1807–1812, doi:10.1126/science.1164382.
17. Mizoguchi, M.; Yoshimoto, K.; Ma, X.; Guan, Y.; Hata, N.; Amano, T.; Nakamizo, A.; Suzuki, S.O.; Iwaki, T.; Sasaki, T. Molecular Characteristics of Glioblastoma with 1p/19q Co-Deletion. *Brain Tumor Pathol.* **2012**, *29*, 148–153, doi:10.1007/s10014-012-0107-z.
18. Galbraith, K.; Snuderl, M. Molecular Pathology of Gliomas. *Surg. Pathol. Clin.* **2021**, *14*, 379–386, doi:10.1016/j.path.2021.05.003.
19. Olympios, N.; Gilard, V.; Marguet, F.; Clatot, F.; Di Fiore, F.; Fontanilles, M. TERT Promoter Alterations in Glioblastoma: A Systematic Review. *Cancers (Basel).* **2021**, *13*, 1147, doi:10.3390/cancers13051147.
20. Koschmann, C.; Lowenstein, P.R.; Castro, M.G. ATRX Mutations and Glioblastoma: Impaired DNA Damage Repair, Alternative Lengthening of Telomeres, and Genetic Instability. *Mol. Cell. Oncol.* **2016**, *3*, e1167158, doi:10.1080/23723556.2016.1167158.
21. Verhaak, R.G.W.; Hoadley, K.A.; Purdom, E.; Wang, V.; Qi, Y.; Wilkerson, M.D.; Miller, C.R.; Ding, L.; Golub, T.; Mesirov, J.P.; et al. Integrated Genomic Analysis Identifies Clinically Relevant Subtypes of Glioblastoma Characterized by Abnormalities in PDGFRA, IDH1, EGFR, and NF1. *Cancer Cell* **2010**, *17*, 98–110, doi:10.1016/j.ccr.2009.12.020.
22. Brennan, C.W.; Verhaak, R.G.W.; McKenna, A.; Campos, B.; Noushmehr, H.; Salama, S.R.; Zheng, S.; Chakravarty, D.; Sanborn, J.Z.; Berman, S.H.; et al. The Somatic Genomic Landscape of Glioblastoma. *Cell* **2013**, *155*, 462, doi:10.1016/j.cell.2013.09.034.
23. Huang, P.H.; Xu, A.M.; White, F.M. Oncogenic EGFR Signaling Networks in Glioma. *Sci. Signal.* **2009**, *2*, re6–re6, doi:10.1126/scisignal.287re6.
24. Bettegowda, C.; Agrawal, N.; Jiao, Y.; Sausen, M.; Wood, L.D.; Hruban, R.H.; Rodriguez, F.J.; Cahill, D.P.; McLendon, R.; Riggins, G.; et al. Mutations in CIC and FUBP1 Contribute to Human Oligodendroglioma. *Science (80-.).* **2011**, *333*, 1453–1455, doi:10.1126/science.1210557.
25. Appay, R.; Dehais, C.; Maurage, C.-A.; Alentorn, A.; Carpentier, C.; Colin, C.; Ducray, F.; Escande, F.; Idbaih, A.; Kamoun, A.; et al. CDKN2A Homozygous Deletion Is a Strong Adverse Prognosis Factor in Diffuse Malignant IDH-Mutant Gliomas. *Neuro. Oncol.* **2019**, doi:10.1093/neuonc/noz124.
26. Figarella-Branger, D.; Appay, R.; Metais, A.; Tauziède-Espariat, A.; Colin, C.; Rousseau, A.; Varlet, P. La Classification de l'OMS 2021 Des Tumeurs Du Système Nerveux Central. *Ann. Pathol.* **2021**, *42*, 367–382, doi:10.1016/j.annpat.2021.11.005.
27. Yuile, P.; Dent, O.; Cook, R.; Biggs, M.; Little, N. Survival of Glioblastoma Patients Related to Presenting Symptoms, Brain Site and Treatment Variables. *J. Clin. Neurosci.* **2006**, *13*, 747–751, doi:10.1016/j.jocn.2005.10.011.
28. Larjavaara, S.; Mäntylä, R.; Salminen, T.; Haapasalo, H.; Raitanen, J.; Jääskeläinen, J.; Auvinen, A. Incidence of Gliomas by Anatomic Location. *Neuro. Oncol.* **2007**, *9*, 319–325, doi:10.1215/15228517-2007-016.
29. Fontaine, D.; Paquis, P. Glioblastomes : Facteurs Pronostiques Cliniques, Radiologiques et Biologiques. *Neurochirurgie* **2010**, *56*, 467–476, doi:10.1016/j.neuchi.2010.07.008.
30. Yang, I.; Tihan, T.; Han, S.J.; Wrensch, M.R.; Wiencke, J.; Sughrue, M.E.; Parsa, A.T. CD8+ T-Cell Infiltrate in Newly Diagnosed Glioblastoma Is Associated with Long-Term

Survival. *J. Clin. Neurosci.* **2010**, *17*, 1381–1385, doi:10.1016/j.jocn.2010.03.031.
31. Hegi, M.E.; Diserens, A.-C.C.; Godard, S.; Dietrich, P.-Y.Y.; Regli, L.; Ostermann, S.; Otten, P.; Van Melle, G.; de Tribolet, N.; Stupp, R. Clinical Trial Substantiates the Predictive Value of O-6-Methylguanine-DNA Methyltransferase Promoter Methylation in Glioblastoma Patients Treated with Temozolomide. *Clin. Cancer Res.* **2004**, *10*, 1871–1874, doi:10.1158/1078-0432.ccr-03-0384.
32. Stupp, R.; Mason, W.P.; van den Bent, M.J.; Weller, M.; Fisher, B.; Taphoorn, M.J.B.B.; Belanger, K.; Brandes, A.A.; Marosi, C.; Bogdahn, U.; et al. Radiotherapy plus Concomitant and Adjuvant Temozolomide for Glioblastoma. *N. Engl. J. Med.* **2005**, *352*, 987–996, doi:10.1056/NEJMoa043330.
33. Stupp, R.; Hegi, M.E.; Mason, W.P.; van den Bent, M.J.; Taphoorn, M.J.; Janzer, R.C.; Ludwin, S.K.; Allgeier, A.; Fisher, B.; Belanger, K.; et al. Effects of Radiotherapy with Concomitant and Adjuvant Temozolomide versus Radiotherapy Alone on Survival in Glioblastoma in a Randomised Phase III Study: 5-Year Analysis of the EORTC-NCIC Trial. *Lancet Oncol.* **2009**, *10*, 459–466, doi:10.1016/S1470-2045(09)70025-7.
34. McNamara, M.G.; Lwin, Z.; Jiang, H.; Chung, C.; Millar, B.-A.; Sahgal, A.; Laperriere, N.; Mason, W.P. Conditional Probability of Survival and Post-Progression Survival in Patients with Glioblastoma in the Temozolomide Treatment Era. *J. Neurooncol.* **2014**, *117*, 153–160, doi:10.1007/s11060-014-1368-7.
35. Friedman, H.S.; Kerby, T.; Calvert, H. Temozolomide and Treatment of Malignant Glioma. *Clin. Cancer Res.* **2000**, *6*, 2585–2597.
36. Stupp, R.; Brada, M.; van den Bent, M.J.; Tonn, J.-C.; Pentheroudakis, G. High-Grade Glioma: ESMO Clinical Practice Guidelines for Diagnosis, Treatment and Follow-Up. *Ann. Oncol.* **2014**, *25*, iii93–iii101, doi:10.1093/annonc/mdu050.
37. van Linde, M.E.; Brahm, C.G.; de Witt Hamer, P.C.; Reijneveld, J.C.; Bruynzeel, A.M.E.; Vandertop, W.P.; van de Ven, P.M.; Wagemakers, M.; van der Weide, H.L.; Enting, R.H.; et al. Treatment Outcome of Patients with Recurrent Glioblastoma Multiforme: A Retrospective Multicenter Analysis. *J. Neurooncol.* **2017**, *135*, 183–192, doi:10.1007/s11060-017-2564-z.
38. Cruz Da Silva, E.; Mercier, M.-C.; Etienne-Selloum, N.; Dontenwill, M.; Choulier, L. A Systematic Review of Glioblastoma-Targeted Therapies in Phases II, III, IV Clinical Trials. *Cancers (Basel).* **2021**, *13*, 1795, doi:10.3390/cancers13081795.
39. Castro, B.A.; Aghi, M.K. Bevacizumab for Glioblastoma: Current Indications, Surgical Implications, and Future Directions. *Neurosurg. Focus* **2014**, *37*, E9, doi:10.3171/2014.9.FOCUS14516.
40. Hamerlik, P.; Lathia, J.D.; Rasmussen, R.; Wu, Q.; Bartkova, J.; Lee, M.; Moudry, P.; Bartek, J.; Fischer, W.; Lukas, J.; et al. Autocrine VEGF–VEGFR2–Neuropilin-1 Signaling Promotes Glioma Stem-like Cell Viability and Tumor Growth. *J. Exp. Med.* **2012**, *209*, 507–520, doi:10.1084/jem.20111424.
41. Keunen, O.; Johansson, M.; Oudin, A.; Sanzey, M.; Rahim, S.A.A.; Fack, F.; Thorsen, F.; Taxt, T.; Bartos, M.; Jirik, R.; et al. Anti-VEGF Treatment Reduces Blood Supply and Increases Tumor Cell Invasion in Glioblastoma. *Proc. Natl. Acad. Sci.* **2011**, *108*, 3749–3754, doi:10.1073/pnas.1014480108.
42. Li, Z.; Bao, S.; Wu, Q.; Wang, H.; Eyler, C.; Sathornsumetee, S.; Shi, Q.; Cao, Y.; Lathia, J.; McLendon, R.E.; et al. Hypoxia-Inducible Factors Regulate Tumorigenic Capacity of Glioma Stem Cells. *Cancer Cell* **2009**, *15*, 501–513, doi:10.1016/j.ccr.2009.03.018.
43. Piao, Y.; Liang, J.; Holmes, L.; Zurita, A.J.; Henry, V.; Heymach, J. V.; de Groot, J.F. Glioblastoma Resistance to Anti-VEGF Therapy Is Associated with Myeloid Cell Infiltration, Stem Cell Accumulation, and a Mesenchymal Phenotype. *Neuro. Oncol.* **2012**, *14*, 1379–1392, doi:10.1093/neuonc/nos158.

44. Stupp, R.; Hegi, M.E.; Gorlia, T.; Erridge, S.C.; Perry, J.; Hong, Y.-K.; Aldape, K.D.; Lhermitte, B.; Pietsch, T.; Grujicic, D.; et al. Cilengitide Combined with Standard Treatment for Patients with Newly Diagnosed Glioblastoma with Methylated MGMT Promoter (CENTRIC EORTC 26071-22072 Study): A Multicentre, Randomised, Open-Label, Phase 3 Trial. *Lancet Oncol.* **2014**, *15*, 1100–1108, doi:10.1016/S1470-2045(14)70379-1.
45. Stupp, R.; Hegi, M.E.; Neyns, B.; Goldbrunner, R.; Schlegel, U.; Clement, P.M.J.; Grabenbauer, G.G.; Ochsenbein, A.F.; Simon, M.; Dietrich, P.-Y.; et al. Phase I/IIa Study of Cilengitide and Temozolomide With Concomitant Radiotherapy Followed by Cilengitide and Temozolomide Maintenance Therapy in Patients With Newly Diagnosed Glioblastoma. *J. Clin. Oncol.* **2010**, *28*, 2712–2718, doi:10.1200/JCO.2009.26.6650.
46. Weller, M.; Nabors, L.B.; Gorlia, T.; Leske, H.; Rushing, E.; Bady, P.; Hicking, C.; Perry, J.; Hong, Y.-K.; Roth, P.; et al. Cilengitide in Newly Diagnosed Glioblastoma: Biomarker Expression and Outcome. *Oncotarget* **2016**, *7*, 15018–15032, doi:10.18632/oncotarget.7588.
47. Chinot, O.L. Cilengitide in Glioblastoma: When Did It Fail? *Lancet Oncol.* **2014**, *15*, 1044–1045, doi:10.1016/S1470-2045(14)70403-6.
48. Arvind, R.; Chandana, S.R.; Borad, M.J.; Pennington, D.; Mody, K.; Babiker, H. Tumor-Treating Fields: A Fourth Modality in Cancer Treatment, New Practice Updates. *Crit. Rev. Oncol. Hematol.* **2021**, *168*, 103535, doi:10.1016/j.critrevonc.2021.103535.
49. Patel, C.B.; Beinat, C.; Xie, Y.; Chang, E.; Gambhir, S.S. Tumor Treating Fields (TTFields) Impairs Aberrant Glycolysis in Glioblastoma as Evaluated by [18F]DASA-23, a Non-Invasive Probe of Pyruvate Kinase M2 (PKM2) Expression. *Neoplasia* **2021**, *23*, 58–67, doi:10.1016/j.neo.2020.11.003.
50. Stupp, R.; Taillibert, S.; Kanner, A.; Read, W.; Steinberg, D.M.; Lhermitte, B.; Toms, S.; Idbaih, A.; Ahluwalia, M.S.; Fink, K.; et al. Effect of Tumor-Treating Fields Plus Maintenance Temozolomide vs Maintenance Temozolomide Alone on Survival in Patients With Glioblastoma. *JAMA* **2017**, *318*, 2306, doi:10.1001/jama.2017.18718.
51. Fabian, D.; Guillermo Prieto Eibl, M.; Alnahhas, I.; Sebastian, N.; Giglio, P.; Puduvalli, V.; Gonzalez, J.; Palmer, J. Treatment of Glioblastoma (GBM) with the Addition of Tumor-Treating Fields (TTF): A Review. *Cancers (Basel).* **2019**, *11*, 174, doi:10.3390/cancers11020174.
52. Singh, S.K.; Hawkins, C.; Clarke, I.D.; Squire, J.A.; Bayani, J.; Hide, T.; Henkelman, R.M.; Cusimano, M.D.; Dirks, P.B. Identification of Human Brain Tumour Initiating Cells. *Nature* **2004**, *432*, 396–401, doi:10.1038/nature03128.
53. Lathia, J.D.; Mack, S.C.; Mulkearns-Hubert, E.E.; Valentim, C.L.L.; Rich, J.N. Cancer Stem Cells in Glioblastoma. *Genes Dev.* **2015**, *29*, 1203–1217, doi:10.1101/gad.261982.115.
54. Lathia, J.D.; Gallagher, J.; Myers, J.T.; Li, M.; Vasanji, A.; McLendon, R.E.; Hjelmeland, A.B.; Huang, A.Y.; Rich, J.N. Direct In Vivo Evidence for Tumor Propagation by Glioblastoma Cancer Stem Cells. *PLoS One* **2011**, *6*, e24807, doi:10.1371/journal.pone.0024807.
55. Tang, X.; Zuo, C.; Fang, P.; Liu, G.; Qiu, Y.; Huang, Y.; Tang, R. Targeting Glioblastoma Stem Cells: A Review on Biomarkers, Signal Pathways and Targeted Therapy. *Front. Oncol.* **2021**, *11*, doi:10.3389/fonc.2021.701291.
56. Bao, S.; Wu, Q.; McLendon, R.E.; Hao, Y.; Shi, Q.; Hjelmeland, A.B.; Dewhirst, M.W.; Bigner, D.D.; Rich, J.N. Glioma Stem Cells Promote Radioresistance by Preferential Activation of the DNA Damage Response. *Nature* **2006**, *444*, 756–760, doi:10.1038/nature05236.
57. Chen, J.; Li, Y.; Yu, T.-S.S.; McKay, R.M.; Burns, D.K.; Kernie, S.G.; Parada, L.F. A

Restricted Cell Population Propagates Glioblastoma Growth after Chemotherapy. *Nature* **2012**, *488*, 522–526, doi:10.1038/nature11287.
58. Piper, K.; DePledge, L.; Karsy, M.; Cobbs, C. Glioma Stem Cells as Immunotherapeutic Targets: Advancements and Challenges. *Front. Oncol.* **2021**, *11*, doi:10.3389/fonc.2021.615704.
59. Singh, S.K.; Hawkins, C.; Clarke, I.D.; Squire, J.A.; Bayani, J.; Hide, T.; Henkelman, R.M.; Cusimano, M.D.; Dirks, P.B.; Terasaki, M.; et al. Identification of a Cancer Stem Cell in Human Brain Tumors. *Cancer Res.* **2003**, *63*, 5821–5828, doi:10.1038/nature03031.1.
60. Galli, R.; Binda, E.; Orfanelli, U.; Cipelletti, B.; Gritti, A.; De Vitis, S.; Fiocco, R.; Foroni, C.; Dimeco, F.; Vescovi, A. Isolation and Characterization of Tumorigenic, Stem-like Neural Precursors from Human Glioblastoma. *Cancer Res.* **2004**, *64*, 7011–7021, doi:10.1158/0008-5472.CAN-04-1364.
61. Wang, J.; Ma, Y.; Cooper, M.K. Cancer Stem Cells in Glioma: Challenges and Opportunities. *Transl. Cancer Res.* **2013**, *2*, 429–441, doi:10.3978/j.issn.2218-676X.2013.08.01.
62. Cheng, L.; Wu, Q.; Guryanova, O.A.; Huang, Z.; Huang, Q.; Rich, J.N.; Bao, S. Elevated Invasive Potential of Glioblastoma Stem Cells. *Biochem. Biophys. Res. Commun.* **2011**, *406*, 643–648, doi:10.1016/j.bbrc.2011.02.123.
63. Bao, S.; Wu, Q.; Sathornsumetee, S.; Hao, Y.; Li, Z.; Hjelmeland, A.B.; Shi, Q.; McLendon, R.E.; Bigner, D.D.; Rich, J.N. Stem Cell–like Glioma Cells Promote Tumor Angiogenesis through Vascular Endothelial Growth Factor. *Cancer Res.* **2006**, *66*, 7843–7848, doi:10.1158/0008-5472.CAN-06-1010.
64. Cheng, L.; Huang, Z.; Zhou, W.; Wu, Q.; Donnola, S.; Liu, J.K.; Fang, X.; Sloan, A.E.; Mao, Y.; Lathia, J.D.; et al. Glioblastoma Stem Cells Generate Vascular Pericytes to Support Vessel Function and Tumor Growth. *Cell* **2013**, *153*, 139–152, doi:10.1016/j.cell.2013.02.021.
65. Ruiz-Ontañon, P.; Orgaz, J.L.; Aldaz, B.; Elosegui-Artola, A.; Martino, J.; Berciano, M.T.; Montero, J.A.; Grande, L.; Nogueira, L.; Diaz-Moralli, S.; et al. Cellular Plasticity Confers Migratory and Invasive Advantages to a Population of Glioblastoma-Initiating Cells That Infiltrate Peritumoral Tissue. *Stem Cells* **2013**, *31*, 1075–1085, doi:10.1002/stem.1349.
66. Otvos, B.; Silver, D.J.; Mulkearns-Hubert, E.E.; Alvarado, A.G.; Turaga, S.M.; Sorensen, M.D.; Rayman, P.; Flavahan, W.A.; Hale, J.S.; Stoltz, K.; et al. Cancer Stem Cell-Secreted Macrophage Migration Inhibitory Factor Stimulates Myeloid Derived Suppressor Cell Function and Facilitates Glioblastoma Immune Evasion. *Stem Cells* **2016**, *34*, 2026–2039, doi:10.1002/stem.2393.
67. Beier, D.; Hau, P.; Proescholdt, M.; Lohmeier, A.; Wischhusen, J.; Oefner, P.J.; Aigner, L.; Brawanski, A.; Bogdahn, U.; Beier, C.P. CD133+ and CD133− Glioblastoma-Derived Cancer Stem Cells Show Differential Growth Characteristics and Molecular Profiles. *Cancer Res.* **2007**, *67*, 4010–4015, doi:10.1158/0008-5472.CAN-06-4180.
68. Kumar, V.; Vashishta, M.; Kong, L.; Wu, X.; Lu, J.J.; Guha, C.; Dwarakanath, B.S. The Role of Notch, Hedgehog, and Wnt Signaling Pathways in the Resistance of Tumors to Anticancer Therapies. *Front. Cell Dev. Biol.* **2021**, *9*, doi:10.3389/fcell.2021.650772.
69. Sharifzad, F.; Ghavami, S.; Verdi, J.; Mardpour, S.; Mollapour Sisakht, M.; Azizi, Z.; Taghikhani, A.; Łos, M.J.; Fakharian, E.; Ebrahimi, M.; et al. Glioblastoma Cancer Stem Cell Biology: Potential Theranostic Targets. *Drug Resist. Updat.* **2019**, *42*, 35–45, doi:10.1016/j.drup.2018.03.003.
70. Biserova, K.; Jakovlevs, A.; Uljanovs, R.; Strumfa, I. Cancer Stem Cells: Significance in Origin, Pathogenesis and Treatment of Glioblastoma. *Cells* **2021**, *10*, 621,

doi:10.3390/cells10030621.
71. Harder, B.G.; Blomquist, M.R.; Wang, J.; Kim, A.J.; Woodworth, G.F.; Winkles, J.A.; Loftus, J.C.; Tran, N.L. Developments in Blood-Brain Barrier Penetrance and Drug Repurposing for Improved Treatment of Glioblastoma. *Front. Oncol.* **2018**, *8*, doi:10.3389/fonc.2018.00462.
72. Wolbers, J.G. Novel Strategies in Glioblastoma Surgery Aim at Safe, Supra-Maximum Resection in Conjunction with Local Therapies. *Chin. J. Cancer* **2014**, *33*, 8–15, doi:10.5732/cjc.013.10219.
73. Trifiletti, D.M.; Alonso, C.; Grover, S.; Fadul, C.E.; Sheehan, J.P.; Showalter, T.N. Prognostic Implications of Extent of Resection in Glioblastoma: Analysis from a Large Database. *World Neurosurg.* **2017**, *103*, 330–340, doi:10.1016/j.wneu.2017.04.035.
74. Jena, L.; McErlean, E.; McCarthy, H. Delivery across the Blood-Brain Barrier: Nanomedicine for Glioblastoma Multiforme. *Drug Deliv. Transl. Res.* **2020**, *10*, 304–318, doi:10.1007/s13346-019-00679-2.
75. Shi, M.; Sanche, L. Convection-Enhanced Delivery in Malignant Gliomas: A Review of Toxicity and Efficacy. *J. Oncol.* **2019**, *2019*, 1–13, doi:10.1155/2019/9342796.
76. Chen, W.; Dong, J.; Haiech, J.; Kilhoffer, M.C.; Zeniou, M. Cancer Stem Cell Quiescence and Plasticity as Major Challenges in Cancer Therapy. *Stem Cells Int.* 2016, *2016*.
77. Cojoc, M.; Mäbert, K.; Muders, M.H.; Dubrovska, A. A Role for Cancer Stem Cells in Therapy Resistance: Cellular and Molecular Mechanisms. *Semin. Cancer Biol.* **2015**, *31*, 16–27, doi:10.1016/j.semcancer.2014.06.004.
78. Jackson, M.; Hassiotou, F.; Nowak, A. Glioblastoma Stem-like Cells: At the Root of Tumor Recurrence and a Therapeutic Target. *Carcinogenesis* **2015**, *36*, 177–185, doi:10.1093/carcin/bgu243.
79. Vlashi, E.; Lagadec, C.; Vergnes, L.; Matsutani, T.; Masui, K.; Poulou, M.; Popescu, R.; Della Donna, L.; Evers, P.; Dekmezian, C.; et al. Metabolic State of Glioma Stem Cells and Nontumorigenic Cells. *Proc. Natl. Acad. Sci. U. S. A.* **2011**, *108*, 16062–16067, doi:10.1073/pnas.1106704108.
80. Auffinger, B.; Spencer, D.; Pytel, P.; Ahmed, A.U.; Lesniak, M.S. The Role of Glioma Stem Cells in Chemotherapy Resistance and Glioblastoma Multiforme Recurrence. *Expert Rev. Neurother.* **2015**, *15*, 741–752, doi:10.1586/14737175.2015.1051968.
81. Meyer, M.; Reimand, J.; Lan, X.; Head, R.; Zhu, X.; Kushida, M.; Bayani, J.; Pressey, J.C.; Lionel, A.C.; Clarke, I.D.; et al. Single Cell-Derived Clonal Analysis of Human Glioblastoma Links Functional and Genomic Heterogeneity. *Proc. Natl. Acad. Sci. U. S. A.* **2015**, *112*, 851–856, doi:10.1073/pnas.1320611111.
82. Yabo, Y.A.; Niclou, S.P.; Golebiewska, A. Cancer Cell Heterogeneity and Plasticity: A Paradigm Shift in Glioblastoma. *Neuro. Oncol.* **2022**, *24*, 669–682, doi:10.1093/neuonc/noab269.
83. Qazi, M.A.; Vora, P.; Venugopal, C.; Sidhu, S.S.; Moffat, J.; Swanton, C.; Singh, S.K. Intratumoral Heterogeneity: Pathways to Treatment Resistance and Relapse in Human Glioblastoma. *Ann. Oncol.* **2017**, *28*, 1448–1456, doi:10.1093/annonc/mdx169.
84. Parker, J.L.; Kuzulugil, S.S.; Pereverzev, K.; Mac, S.; Lopes, G.; Shah, Z.; Weerasinghe, A.; Rubinger, D.; Falconi, A.; Bener, A.; et al. Does Biomarker Use in Oncology Improve Clinical Trial Failure Risk? A Large-Scale Analysis. *Cancer Med.* **2021**, *10*, 1955–1963, doi:10.1002/cam4.3732.
85. Martins, T.A.; Schmassmann, P.; Shekarian, T.; Boulay, J.-L.; Ritz, M.-F.; Zanganeh, S.; vom Berg, J.; Hutter, G. Microglia-Centered Combinatorial Strategies Against Glioblastoma. *Front. Immunol.* **2020**, *11*, doi:10.3389/fimmu.2020.571951.
86. Sestito, S.; Runfola, M.; Tonelli, M.; Chiellini, G.; Rapposelli, S. New Multitarget

Approaches in the War Against Glioblastoma: A Mini-Perspective. *Front. Pharmacol.* **2018**, *9*, doi:10.3389/fphar.2018.00874.
87. Yang, L.; Lin, C.; Wang, L.; Guo, H.; Wang, X. Hypoxia and Hypoxia-Inducible Factors in Glioblastoma Multiforme Progression and Therapeutic Implications. *Exp. Cell Res.* **2012**, *318*, 2417–2426, doi:10.1016/j.yexcr.2012.07.017.
88. Daubon, T.; Hemadou, A.; Romero Garmendia, I.; Saleh, M. Glioblastoma Immune Landscape and the Potential of New Immunotherapies. *Front. Immunol.* **2020**, *11*, doi:10.3389/fimmu.2020.585616.
89. Michael, J.S.; Lee, B.-S.; Zhang, M.; Yu, J.S. Nanotechnology for Treatment of Glioblastoma Multiforme. *J. Transl. Intern. Med.* **2018**, *6*, 128–133, doi:10.2478/jtim-2018-0025.
90. Bernhard, C.; Reita, D.; Martin, S.; Entz-Werle, N.; Dontenwill, M. Glioblastoma Metabolism: Insights and Therapeutic Strategies. *Int. J. Mol. Sci.* **2023**, *24*, 9137, doi:10.3390/ijms24119137.
91. Zhou, W.; Wahl, D.R. Metabolic Abnormalities in Glioblastoma and Metabolic Strategies to Overcome Treatment Resistance. *Cancers (Basel).* **2019**, *11*, 1231, doi:10.3390/cancers11091231.
92. Comba, A.; Faisal, S.M.; Varela, M.L.; Hollon, T.; Al-Holou, W.N.; Umemura, Y.; Nunez, F.J.; Motsch, S.; Castro, M.G.; Lowenstein, P.R. Uncovering Spatiotemporal Heterogeneity of High-Grade Gliomas: From Disease Biology to Therapeutic Implications. *Front. Oncol.* **2021**, *11*, doi:10.3389/fonc.2021.703764.
93. Pistollato, F.; Abbadi, S.; Rampazzo, E.; Persano, L.; Della Puppa, A.; Frasson, C.; Sarto, E.; Scienza, R.; D'avella, D.; Basso, G. Intratumoral Hypoxic Gradient Drives Stem Cells Distribution and MGMT Expression in Glioblastoma. *Stem Cells* **2010**, *28*, 851–862, doi:10.1002/stem.415.
94. Sottoriva, A.; Spiteri, I.; Piccirillo, S.G.M.; Touloumis, A.; Collins, V.P.; Marioni, J.C.; Curtis, C.; Watts, C.; Tavaré, S. Intratumor Heterogeneity in Human Glioblastoma Reflects Cancer Evolutionary Dynamics. *Proc. Natl. Acad. Sci. U. S. A.* **2013**, *110*, 4009–4014, doi:10.1073/pnas.1219747110.
95. Bonavia, R.; Inda, M.-M.; Cavenee, W.K.; Furnari, F.B. Heterogeneity Maintenance in Glioblastoma: A Social Network. *Cancer Res.* **2011**, *71*, 4055–4060.
96. Huang, S. Reconciling Non-Genetic Plasticity with Somatic Evolution in Cancer. *Trends in Cancer* **2021**, *7*, 309–322, doi:10.1016/j.trecan.2020.12.007.
97. Phillips, H.S.; Kharbanda, S.; Chen, R.; Forrest, W.F.; Soriano, R.H.; Wu, T.D.; Misra, A.; Nigro, J.M.; Colman, H.; Soroceanu, L.; et al. Molecular Subclasses of High-Grade Glioma Predict Prognosis, Delineate a Pattern of Disease Progression, and Resemble Stages in Neurogenesis. *Cancer Cell* **2006**, *9*, 157–173, doi:10.1016/j.ccr.2006.02.019.
98. Wang, Q.; Hu, B.; Hu, X.; Kim, H.; Squatrito, M.; Scarpace, L.; DeCarvalho, A.C.; Lyu, S.; Li, P.; Li, Y.; et al. Tumor Evolution of Glioma-Intrinsic Gene Expression Subtypes Associates with Immunological Changes in the Microenvironment. *Cancer Cell* **2017**, *32*, 42-56.e6, doi:10.1016/j.ccell.2017.06.003.
99. Louis, D.N.; Perry, A.; Reifenberger, G.; von Deimling, A.; Figarella-Branger, D.; Cavenee, W.K.; Ohgaki, H.; Wiestler, O.D.; Kleihues, P.; Ellison, D.W. The 2016 World Health Organization Classification of Tumors of the Central Nervous System: A Summary. *Acta Neuropathol.* 2016, *131*, 803–820.
100. Ohgaki, H.; Kleihues, P. Genetic Pathways to Primary and Secondary Glioblastoma. *Am. J. Pathol.* **2007**, *170*, 1445–1453, doi:10.2353/ajpath.2007.070011.
101. Noushmehr, H.; Weisenberger, D.J.; Diefes, K.; Phillips, H.S.; Pujara, K.; Berman, B.P.; Pan, F.; Pelloski, C.E.; Sulman, E.P.; Bhat, K.P.; et al. Identification of a CpG Island Methylator Phenotype That Defines a Distinct Subgroup of Glioma. *Cancer Cell* **2010**,

17, 510–522, doi:10.1016/j.ccr.2010.03.017.
102. Turcan, S.; Rohle, D.; Goenka, A.; Walsh, L.A.; Fang, F.; Yilmaz, E.; Campos, C.; Fabius, A.W.M.; Lu, C.; Ward, P.S.; et al. IDH1 Mutation Is Sufficient to Establish the Glioma Hypermethylator Phenotype. *Nature* **2012**, *483*, 479–483, doi:10.1038/nature10866.
103. Sturm, D.; Witt, H.; Hovestadt, V.; Khuong-Quang, D.-A.; Jones, D.T.W.; Konermann, C.; Pfaff, E.; Tönjes, M.; Sill, M.; Bender, S.; et al. Hotspot Mutations in H3F3A and IDH1 Define Distinct Epigenetic and Biological Subgroups of Glioblastoma. *Cancer Cell* **2012**, *22*, 425–437, doi:10.1016/j.ccr.2012.08.024.
104. Capper, D.; Jones, D.T.W.; Sill, M.; Hovestadt, V.; Schrimpf, D.; Sturm, D.; Koelsche, C.; Sahm, F.; Chavez, L.; Reuss, D.E.; et al. DNA Methylation-Based Classification of Central Nervous System Tumours. *Nature* **2018**, *555*, 469–474, doi:10.1038/nature26000.
105. Patel, A.P.; Tirosh, I.; Trombetta, J.J.; Shalek, A.K.; Gillespie, S.M.; Wakimoto, H.; Cahill, D.P.; Nahed, B. V.; Curry, W.T.; Martuza, R.L.; et al. Single-Cell RNA-Seq Highlights Intratumoral Heterogeneity in Primary Glioblastoma. *Science (80-.).* **2014**, *344*, 1396–1401, doi:10.1126/science.1254257.
106. Neftel, C.; Laffy, J.; Filbin, M.G.; Hara, T.; Shore, M.E.; Rahme, G.J.; Richman, A.R.; Silverbush, D.; Shaw, M.L.; Hebert, C.M.; et al. An Integrative Model of Cellular States, Plasticity, and Genetics for Glioblastoma. *Cell* **2019**, *178*, 835-849.e21, doi:10.1016/j.cell.2019.06.024.
107. Garofano, L.; Migliozzi, S.; Oh, Y.T.; D'Angelo, F.; Najac, R.D.; Ko, A.; Frangaj, B.; Caruso, F.P.; Yu, K.; Yuan, J.; et al. Pathway-Based Classification of Glioblastoma Uncovers a Mitochondrial Subtype with Therapeutic Vulnerabilities. *Nat. Cancer* **2021**, *2*, 141–156, doi:10.1038/s43018-020-00159-4.
108. Celiku, O.; Gilbert, M.R.; Lavi, O. Computational Modeling Demonstrates That Glioblastoma Cells Can Survive Spatial Environmental Challenges through Exploratory Adaptation. *Nat. Commun.* **2019**, *10*, 5704, doi:10.1038/s41467-019-13726-w.
109. Puchalski, R.B.; Shah, N.; Miller, J.; Dalley, R.; Nomura, S.R.; Yoon, J.-G.; Smith, K.A.; Lankerovich, M.; Bertagnolli, D.; Bickley, K.; et al. An Anatomic Transcriptional Atlas of Human Glioblastoma. *Science (80-.).* **2018**, *360*, 660–663, doi:10.1126/science.aaf2666.
110. Dirkse, A.; Golebiewska, A.; Buder, T.; Nazarov, P. V.; Muller, A.; Poovathingal, S.; Brons, N.H.C.C.; Leite, S.; Sauvageot, N.; Sarkisjan, D.; et al. Stem Cell-Associated Heterogeneity in Glioblastoma Results from Intrinsic Tumor Plasticity Shaped by the Microenvironment. *Nat. Commun.* **2019**, *10*, 1–16, doi:10.1038/s41467-019-09853-z.
111. Wu, Y.; Fletcher, M.; Gu, Z.; Wang, Q.; Costa, B.; Bertoni, A.; Man, K.-H.; Schlotter, M.; Felsberg, J.; Mangei, J.; et al. Glioblastoma Epigenome Profiling Identifies SOX10 as a Master Regulator of Molecular Tumour Subtype. *Nat. Commun.* **2020**, *11*, 6434, doi:10.1038/s41467-020-20225-w.
112. Chaligne, R.; Gaiti, F.; Silverbush, D.; Schiffman, J.S.; Weisman, H.R.; Kluegel, L.; Gritsch, S.; Deochand, S.D.; Gonzalez Castro, L.N.; Richman, A.R.; et al. Epigenetic Encoding, Heritability and Plasticity of Glioma Transcriptional Cell States. *Nat. Genet.* **2021**, *53*, 1469–1479, doi:10.1038/s41588-021-00927-7.
113. Rheinbay, E.; Suvà, M.L.; Gillespie, S.M.; Wakimoto, H.; Patel, A.P.; Shahid, M.; Oksuz, O.; Rabkin, S.D.; Martuza, R.L.; Rivera, M.N.; et al. An Aberrant Transcription Factor Network Essential for Wnt Signaling and Stem Cell Maintenance in Glioblastoma. *Cell Rep.* **2013**, *3*, 1567–1579, doi:10.1016/j.celrep.2013.04.021.
114. Li, Y.; Li, A.; Glas, M.; Lal, B.; Ying, M.; Sang, Y.; Xia, S.; Trageser, D.; Guerrero-Cázares, H.; Eberhart, C.G.; et al. C-Met Signaling Induces a Reprogramming Network

and Supports the Glioblastoma Stem-like Phenotype. *Proc. Natl. Acad. Sci.* **2011**, *108*, 9951–9956, doi:10.1073/pnas.1016912108.
115. Heddleston, J.M.; Li, Z.; McLendon, R.E.; Hjelmeland, A.B.; Rich, J.N. The Hypoxic Microenvironment Maintains Glioblastoma Stem Cells and Promotes Reprogramming towards a Cancer Stem Cell Phenotype. *Cell Cycle* **2009**, *8*, 3274–3284, doi:10.4161/cc.8.20.9701.
116. Bikfalvi, A.; da Costa, C.A.; Avril, T.; Barnier, J.-V.; Bauchet, L.; Brisson, L.; Cartron, P.F.; Castel, H.; Chevet, E.; Chneiweiss, H.; et al. Challenges in Glioblastoma Research: Focus on the Tumor Microenvironment. *Trends in Cancer* **2023**, *9*, 9–27, doi:10.1016/j.trecan.2022.09.005.
117. Griguer, C.E.; Oliva, C.R.; Gobin, E.; Marcorelles, P.; Benos, D.J.; Lancaster, J.R.; Gillespie, G.Y. CD133 Is a Marker of Bioenergetic Stress in Human Glioma. *PLoS One* **2008**, *3*, e3655, doi:10.1371/journal.pone.0003655.
118. Bar, E.E.; Lin, A.; Mahairaki, V.; Matsui, W.; Eberhart, C.G. Hypoxia Increases the Expression of Stem-Cell Markers and Promotes Clonogenicity in Glioblastoma Neurospheres. *Am. J. Pathol.* **2010**, *177*, 1491–1502, doi:10.2353/ajpath.2010.091021.
119. Hjelmeland, A.B.; Wu, Q.; Heddleston, J.M.; Choudhary, G.S.; MacSwords, J.; Lathia, J.D.; McLendon, R.; Lindner, D.; Sloan, A.; Rich, J.N. Acidic Stress Promotes a Glioma Stem Cell Phenotype. *Cell Death Differ.* **2011**, *18*, 829–840, doi:10.1038/cdd.2010.150.
120. Flavahan, W.A.; Wu, Q.; Hitomi, M.; Rahim, N.; Kim, Y.; Sloan, A.E.; Weil, R.J.; Nakano, I.; Sarkaria, J.N.; Stringer, B.W.; et al. Brain Tumor Initiating Cells Adapt to Restricted Nutrition through Preferential Glucose Uptake. *Nat. Neurosci.* **2013**, *16*, 1373–1382, doi:10.1038/nn.3510.
121. Meacham, C.E.; Morrison, S.J. Tumour Heterogeneity and Cancer Cell Plasticity. *Nature* 2013, *501*, 328–337.
122. Alvarado, A.G.; Turaga, S.M.; Sathyan, P.; Mulkearns-Hubert, E.E.; Otvos, B.; Silver, D.J.; Hale, J.S.; Flavahan, W.A.; Zinn, P.O.; Sinyuk, M.; et al. Coordination of Self-Renewal in Glioblastoma by Integration of Adhesion and MicroRNA Signaling. *Neuro. Oncol.* **2016**, *18*, 656–666, doi:10.1093/neuonc/nov196.
123. Ye, C.; Li, H.; Li, Y.; Zhang, Y.; Liu, G.; Mi, H.; Li, H.; Xiao, Q.; Niu, L.; Yu, X. Hypoxia-Induced HMGB1 Promotes Glioma Stem Cells Self-Renewal and Tumorigenicity via RAGE. *iScience* **2022**, *25*, 104872, doi:10.1016/j.isci.2022.104872.
124. Bhat, K.P.L.; Balasubramaniyan, V.; Vaillant, B.; Ezhilarasan, R.; Hummelink, K.; Hollingsworth, F.; Wani, K.; Heathcock, L.; James, J.D.; Goodman, L.D.; et al. Mesenchymal Differentiation Mediated by NF-KB Promotes Radiation Resistance in Glioblastoma. *Cancer Cell* **2013**, *24*, 331–346, doi:10.1016/j.ccr.2013.08.001.
125. Calabrese, C.; Poppleton, H.; Kocak, M.; Hogg, T.L.; Fuller, C.; Hamner, B.; Oh, E.Y.; Gaber, M.W.; Finklestein, D.; Allen, M.; et al. A Perivascular Niche for Brain Tumor Stem Cells. *Cancer Cell* **2007**, *11*, 69–82, doi:10.1016/j.ccr.2006.11.020.
126. Hira, V.V.V.; Aderetti, D.A.; van Noorden, C.J.F. Glioma Stem Cell Niches in Human Glioblastoma Are Periarteriolar. *J. Histochem. Cytochem.* **2018**, *66*, 349–358, doi:10.1369/0022155417752676.
127. Roos, A.; Ding, Z.; Loftus, J.C.; Tran, N.L. Molecular and Microenvironmental Determinants of Glioma Stem-Like Cell Survival and Invasion. *Front. Oncol.* **2017**, *7*, doi:10.3389/fonc.2017.00120.
128. Ishii, A.; Kimura, T.; Sadahiro, H.; Kawano, H.; Takubo, K.; Suzuki, M.; Ikeda, E. Histological Characterization of the Tumorigenic "Peri-Necrotic Niche" Harboring Quiescent Stem-Like Tumor Cells in Glioblastoma. *PLoS One* **2016**, *11*, e0147366, doi:10.1371/journal.pone.0147366.
129. Uribe, D.; Niechi, I.; Rackov, G.; Erices, J.I.; San Martín, R.; Quezada, C. Adapt to

Persist: Glioblastoma Microenvironment and Epigenetic Regulation on Cell Plasticity. *Biology (Basel).* **2022**, *11*, 313, doi:10.3390/biology11020313.
130. Vaupel, P.; Mayer, A. Hypoxia in Cancer: Significance and Impact on Clinical Outcome. *Cancer Metastasis Rev.* **2007**, *26*, 225–239, doi:10.1007/s10555-007-9055-1.
131. Evans, S.M.; Judy, K.D.; Dunphy, I.; Jenkins, W.T.; Nelson, P.T.; Collins, R.; Wileyto, E.P.; Jenkins, K.; Hahn, S.M.; Stevens, C.W.; et al. Comparative Measurements of Hypoxia in Human Brain Tumors Using Needle Electrodes and EF5 Binding. *Cancer Res.* **2004**, *64*, 1886–1892, doi:10.1158/0008-5472.CAN-03-2424.
132. Evans, S.M.; Judy, K.D.; Dunphy, I.; Jenkins, W.T.; Hwang, W.-T.; Nelson, P.T.; Lustig, R.A.; Jenkins, K.; Magarelli, D.P.; Hahn, S.M.; et al. Hypoxia Is Important in the Biology and Aggression of Human Glial Brain Tumors. *Clin. Cancer Res.* **2004**, *10*, 8177–8184, doi:10.1158/1078-0432.CCR-04-1081.
133. Evans, S.M.; Jenkins, K.W.; Jenkins, W.T.; Dilling, T.; Judy, K.D.; Schrlau, A.; Judkins, A.; Hahn, S.M.; Koch, C.J. Imaging and Analytical Methods as Applied to the Evaluation of Vasculature and Hypoxia in Human Brain Tumors. *Radiat. Res.* **2008**, *170*, 677–690, doi:10.1667/RR1207.1.
134. Semenza, G.L. Hypoxia-Inducible Factors in Physiology and Medicine. *Cell* **2012**, *148*, 399–408, doi:10.1016/j.cell.2012.01.021.
135. Uribe, D.; Torres, Á.; Rocha, J.D.; Niechi, I.; Oyarzún, C.; Sobrevia, L.; San Martín, R.; Quezada, C. Multidrug Resistance in Glioblastoma Stem-like Cells: Role of the Hypoxic Microenvironment and Adenosine Signaling. *Mol. Aspects Med.* **2017**, *55*, 140–151, doi:10.1016/j.mam.2017.01.009.
136. Zhou, Y.; Zhou, Y.; Shingu, T.; Feng, L.; Chen, Z.; Ogasawara, M.; Keating, M.J.; Kondo, S.; Huang, P. Metabolic Alterations in Highly Tumorigenic Glioblastoma Cells: Preference for Hypoxia and High Dependency on Glycolysis. *J. Biol. Chem.* **2011**, *286*, 32843–32853, doi:10.1074/jbc.M111.260935.
137. Kaur, B.; Khwaja, F.W.; Severson, E.A.; Matheny, S.L.; Brat, D.J.; Van Meir, E.G. Hypoxia and the Hypoxia-Inducible-Factor Pathway in Glioma Growth and Angiogenesis. *Neuro. Oncol.* **2005**, *7*, 134–153, doi:10.1215/S1152851704001115.
138. Kolenda, J.; Jensen, S.S.; Aaberg-Jessen, C.; Christensen, K.; Andersen, C.; Brünner, N.; Kristensen, B.W. Effects of Hypoxia on Expression of a Panel of Stem Cell and Chemoresistance Markers in Glioblastoma-Derived Spheroids. *J. Neurooncol.* **2011**, *103*, 43–58, doi:10.1007/s11060-010-0357-8.
139. Guyon, J.; Romero-Garmendia, I.; Bikfalvi, A.; Daubon, T. Fsmp-14. Metabolic Symbiosis in Glioblastoma: Lactate Dehydrogenases Take the Lead. *Neuro-Oncology Adv.* **2021**, *3*, i19–i19, doi:10.1093/noajnl/vdab024.078.
140. Monteiro, A.; Hill, R.; Pilkington, G.; Madureira, P. The Role of Hypoxia in Glioblastoma Invasion. *Cells* **2017**, *6*, 45, doi:10.3390/cells6040045.
141. Lee, G.; Auffinger, B.; Guo, D.; Hasan, T.; Deheeger, M.; Tobias, A.L.; Kim, J.Y.; Atashi, F.; Zhang, L.; Lesniak, M.S.; et al. Dedifferentiation of Glioma Cells to Glioma Stem-like Cells By Therapeutic Stress-Induced HIF Signaling in the Recurrent GBM Model. *Mol. Cancer Ther.* **2016**, *15*, 3064–3076, doi:10.1158/1535-7163.MCT-15-0675.
142. Wang, P.; Wan, W.; Xiong, S.-L.; Feng, H.; Wu, N. Cancer Stem-like Cells Can Be Induced through Dedifferentiation under Hypoxic Conditions in Glioma, Hepatoma and Lung Cancer. *Cell Death Discov.* **2017**, *3*, 16105, doi:10.1038/cddiscovery.2016.105.
143. Tejero, R.; Huang, Y.; Katsyv, I.; Kluge, M.; Lin, J.-Y.; Tome-Garcia, J.; Daviaud, N.; Wang, Y.; Zhang, B.; Tsankova, N.M.; et al. Gene Signatures of Quiescent Glioblastoma Cells Reveal Mesenchymal Shift and Interactions with Niche Microenvironment. *EBioMedicine* **2019**, *42*, 252–269, doi:10.1016/j.ebiom.2019.03.064.
144. Giese, A.; Bjerkvig, R.; Berens, M.E.; Westphal, M. Cost of Migration: Invasion of

Malignant Gliomas and Implications for Treatment. *J. Clin. Oncol.* **2003**, *21*, 1624–1636, doi:10.1200/JCO.2003.05.063.
145. Minata, M.; Audia, A.; Shi, J.; Lu, S.; Bernstock, J.; Pavlyukov, M.S.; Das, A.; Kim, S.-H.; Shin, Y.J.; Lee, Y.; et al. Phenotypic Plasticity of Invasive Edge Glioma Stem-like Cells in Response to Ionizing Radiation. *Cell Rep.* **2019**, *26*, 1893-1905.e7, doi:10.1016/j.celrep.2019.01.076.
146. Nishikawa, M.; Inoue, A.; Ohnishi, T.; Kohno, S.; Ohue, S.; Matsumoto, S.; Suehiro, S.; Yamashita, D.; Ozaki, S.; Watanabe, H.; et al. Significance of Glioma Stem-Like Cells in the Tumor Periphery That Express High Levels of CD44 in Tumor Invasion, Early Progression, and Poor Prognosis in Glioblastoma. *Stem Cells Int.* **2018**, *2018*, 1–15, doi:10.1155/2018/5387041.
147. Fedele, M.; Cerchia, L.; Pegoraro, S.; Sgarra, R.; Manfioletti, G. Proneural-Mesenchymal Transition: Phenotypic Plasticity to Acquire Multitherapy Resistance in Glioblastoma. *Int. J. Mol. Sci.* **2019**, *20*, 2746, doi:10.3390/ijms20112746.
148. Carro, M.S.; Lim, W.K.; Alvarez, M.J.; Bollo, R.J.; Zhao, X.; Snyder, E.Y.; Sulman, E.P.; Anne, S.L.; Doetsch, F.; Colman, H.; et al. The Transcriptional Network for Mesenchymal Transformation of Brain Tumours. *Nature* **2010**, *463*, 318–325, doi:10.1038/nature08712.
149. Velpula, K.K.; Rehman, A.A.; Chelluboina, B.; Dasari, V.R.; Gondi, C.S.; Rao, J.S.; Veeravalli, K.K. Glioma Stem Cell Invasion through Regulation of the Interconnected ERK, Integrin A6 and N-Cadherin Signaling Pathway. *Cell. Signal.* **2012**, *24*, 2076–2084, doi:10.1016/j.cellsig.2012.07.002.
150. Priester, M.; Copanaki, E.; Vafaizadeh, V.; Hensel, S.; Bernreuther, C.; Glatzel, M.; Seifert, V.; Groner, B.; Kogel, D.; Weissenberger, J. STAT3 Silencing Inhibits Glioma Single Cell Infiltration and Tumor Growth. *Neuro. Oncol.* **2013**, *15*, 840–852, doi:10.1093/neuonc/not025.
151. Chen, Q.; Jin, M.; Yang, F.; Zhu, J.; Xiao, Q.; Zhang, L. Matrix Metalloproteinases: Inflammatory Regulators of Cell Behaviors in Vascular Formation and Remodeling. *Mediators Inflamm.* **2013**, *2013*, 1–14, doi:10.1155/2013/928315.
152. Ortensi, B.; Setti, M.; Osti, D.; Pelicci, G. Cancer Stem Cell Contribution to Glioblastoma Invasiveness. *Stem Cell Res. Ther.* **2013**, *4*, 18, doi:10.1186/scrt166.
153. Ye, X.; Xu, S.; Xin, Y.; Yu, S.; Ping, Y.; Chen, L.; Xiao, H.; Wang, B.; Yi, L.; Wang, Q.; et al. Tumor-Associated Microglia/Macrophages Enhance the Invasion of Glioma Stem-like Cells via TGF-B1 Signaling Pathway. *J. Immunol.* **2012**, *189*, 444–453, doi:10.4049/jimmunol.1103248.
154. Torres, Á.; Erices, J.I.; Sanchez, F.; Ehrenfeld, P.; Turchi, L.; Virolle, T.; Uribe, D.; Niechi, I.; Spichiger, C.; Rocha, J.D.; et al. Extracellular Adenosine Promotes Cell Migration/Invasion of Glioblastoma Stem-like Cells through A3 Adenosine Receptor Activation under Hypoxia. *Cancer Lett.* **2019**, *446*, 112–122, doi:10.1016/j.canlet.2019.01.004.
155. Zhu, T.S.; Costello, M.A.; Talsma, C.E.; Flack, C.G.; Crowley, J.G.; Hamm, L.L.; He, X.; Hervey-Jumper, S.L.; Heth, J.A.; Muraszko, K.M.; et al. Endothelial Cells Create a Stem Cell Niche in Glioblastoma by Providing NOTCH Ligands That Nurture Self-Renewal of Cancer Stem-Like Cells. *Cancer Res.* **2011**, *71*, 6061–6072, doi:10.1158/0008-5472.CAN-10-4269.
156. Hambardzumyan, D.; Bergers, G. Glioblastoma: Defining Tumor Niches. *Trends in Cancer* **2015**, *1*, 252–265, doi:10.1016/j.trecan.2015.10.009.
157. Charles, N.; Ozawa, T.; Squatrito, M.; Bleau, A.-M.; Brennan, C.W.; Hambardzumyan, D.; Holland, E.C. Perivascular Nitric Oxide Activates Notch Signaling and Promotes Stem-like Character in PDGF-Induced Glioma Cells. *Cell Stem Cell* **2010**, *6*, 141–152,

doi:10.1016/j.stem.2010.01.001.
158. Liu, D.; Martin, V.; Fueyo, J.; Lee, O.-H.; Xu, J.; Cortes-Santiago, N.; Alonso, M.M.; Aldape, K.; Colman, H.; Gomez-Manzano, C. Tie2/TEK Modulates the Interaction of Glioma and Brain Tumor Stem Cells with Endothelial Cells and Promotes an Invasive Phenotype. *Oncotarget* **2010**, *1*, 700–709, doi:10.18632/oncotarget.101204.
159. Treps, L.; Perret, R.; Edmond, S.; Ricard, D.; Gavard, J. Glioblastoma Stem-like Cells Secrete the Pro-angiogenic VEGF-A Factor in Extracellular Vesicles. *J. Extracell. Vesicles* **2017**, *6*, doi:10.1080/20013078.2017.1359479.
160. Bao, S.; Wu, Q.; Li, Z.; Sathornsumetee, S.; Wang, H.; McLendon, R.E.; Hjelmeland, A.B.; Rich, J.N. Targeting Cancer Stem Cells through L1CAM Suppresses Glioma Growth. *Cancer Res.* **2008**, *68*, 6043–6048, doi:10.1158/0008-5472.CAN-08-1079.
161. Burgett, M.E.; Lathia, J.D.; Roth, P.; Nowacki, A.S.; Galileo, D.S.; Pugacheva, E.; Huang, P.; Vasanji, A.; Li, M.; Byzova, T.; et al. Direct Contact with Perivascular Tumor Cells Enhances Integrin Avβ3 Signaling and Migration of Endothelial Cells. *Oncotarget* **2016**, *7*, 43852–43867, doi:10.18632/oncotarget.9700.
162. Baisiwala, S.; Auffinger, B.; Caragher, S.P.; Shireman, J.M.; Ahsan, R.; Lee, G.; Hasan, T.; Park, C.; Saathoff, M.R.; Christensen, A.C.; et al. Chemotherapeutic Stress Induces Transdifferentiation of Glioblastoma Cells to Endothelial Cells and Promotes Vascular Mimicry. *Stem Cells Int.* **2019**, *2019*, 1–14, doi:10.1155/2019/6107456.
163. Deshors, P.; Toulas, C.; Arnauduc, F.; Malric, L.; Siegfried, A.; Nicaise, Y.; Lemarié, A.; Larrieu, D.; Tosolini, M.; Cohen-Jonathan Moyal, E.; et al. Ionizing Radiation Induces Endothelial Transdifferentiation of Glioblastoma Stem-like Cells through the Tie2 Signaling Pathway. *Cell Death Dis.* **2019**, *10*, 816, doi:10.1038/s41419-019-2055-6.
164. Osswald, M.; Jung, E.; Sahm, F.; Solecki, G.; Venkataramani, V.; Blaes, J.; Weil, S.; Horstmann, H.; Wiestler, B.; Syed, M.; et al. Brain Tumour Cells Interconnect to a Functional and Resistant Network. *Nature* **2015**, *528*, 93–98, doi:10.1038/nature16071.
165. Jung, E.; Osswald, M.; Ratliff, M.; Dogan, H.; Xie, R.; Weil, S.; Hoffmann, D.C.; Kurz, F.T.; Kessler, T.; Heiland, S.; et al. Tumor Cell Plasticity, Heterogeneity, and Resistance in Crucial Microenvironmental Niches in Glioma. *Nat. Commun.* **2021**, *12*, 1014, doi:10.1038/s41467-021-21117-3.
166. Wang, X.; Prager, B.C.; Wu, Q.; Kim, L.J.Y.Y.; Gimple, R.C.; Shi, Y.; Yang, K.; Morton, A.R.; Zhou, W.; Zhu, Z.; et al. Reciprocal Signaling between Glioblastoma Stem Cells and Differentiated Tumor Cells Promotes Malignant Progression. *Cell Stem Cell* **2018**, *22*, 514-528.e5, doi:10.1016/j.stem.2018.03.011.
167. Yan, K.; Wu, Q.; Yan, D.H.; Lee, C.H.; Rahim, N.; Tritschler, I.; DeVecchio, J.; Kalady, M.F.; Hjelmeland, A.B.; Rich, J.N. Glioma Cancer Stem Cells Secrete Gremlin1 to Promote Their Maintenance within the Tumor Hierarchy. *Genes Dev.* **2014**, *28*, 1085–1100, doi:10.1101/gad.235515.113.
168. Bastola, S.; Pavlyukov, M.S.; Yamashita, D.; Ghosh, S.; Cho, H.; Kagaya, N.; Zhang, Z.; Minata, M.; Lee, Y.; Sadahiro, H.; et al. Glioma-Initiating Cells at Tumor Edge Gain Signals from Tumor Core Cells to Promote Their Malignancy. *Nat. Commun.* **2020**, *11*, 4660, doi:10.1038/s41467-020-18189-y.
169. Inda, M.-M.; Bonavia, R.; Mukasa, A.; Narita, Y.; Sah, D.W.Y.; Vandenberg, S.; Brennan, C.; Johns, T.G.; Bachoo, R.; Hadwiger, P.; et al. Tumor Heterogeneity Is an Active Process Maintained by a Mutant EGFR-Induced Cytokine Circuit in Glioblastoma. *Genes Dev.* **2010**, *24*, 1731–1745, doi:10.1101/gad.1890510.
170. Xie, R.; Kessler, T.; Grosch, J.; Hai, L.; Venkataramani, V.; Huang, L.; Hoffmann, D.C.; Solecki, G.; Ratliff, M.; Schlesner, M.; et al. Tumor Cell Network Integration in Glioma Represents a Stemness Feature. *Neuro. Oncol.* **2021**, *23*, 757–769,

doi:10.1093/neuonc/noaa275.
171. Quail, D.F.; Joyce, J.A. The Microenvironmental Landscape of Brain Tumors. *Cancer Cell* **2017**, *31*, 326–341, doi:10.1016/j.ccell.2017.02.009.
172. Watson, D.C.; Bayik, D.; Storevik, S.; Moreino, S.S.; Sprowls, S.A.; Han, J.; Augustsson, M.T.; Lauko, A.; Sravya, P.; Røsland, G.V.; et al. GAP43-Dependent Mitochondria Transfer from Astrocytes Enhances Glioblastoma Tumorigenicity. *Nat. Cancer* **2023**, *4*, 648–664, doi:10.1038/s43018-023-00556-5.
173. Venkatesh, H.S.; Morishita, W.; Geraghty, A.C.; Silverbush, D.; Gillespie, S.M.; Arzt, M.; Tam, L.T.; Espenel, C.; Ponnuswami, A.; Ni, L.; et al. Electrical and Synaptic Integration of Glioma into Neural Circuits. *Nature* **2019**, *573*, 539–545, doi:10.1038/s41586-019-1563-y.
174. Sa, J.K.; Chang, N.; Lee, H.W.; Cho, H.J.; Ceccarelli, M.; Cerulo, L.; Yin, J.; Kim, S.S.; Caruso, F.P.; Lee, M.; et al. Transcriptional Regulatory Networks of Tumor-Associated Macrophages That Drive Malignancy in Mesenchymal Glioblastoma. *Genome Biol.* **2020**, *21*, 216, doi:10.1186/s13059-020-02140-x.
175. Hara, T.; Chanoch-Myers, R.; Mathewson, N.D.; Myskiw, C.; Atta, L.; Bussema, L.; Eichhorn, S.W.; Greenwald, A.C.; Kinker, G.S.; Rodman, C.; et al. Interactions between Cancer Cells and Immune Cells Drive Transitions to Mesenchymal-like States in Glioblastoma. *Cancer Cell* **2021**, *39*, 779-792.e11, doi:10.1016/j.ccell.2021.05.002.
176. Tirosh, I.; Suvà, M.L. Tackling the Many Facets of Glioblastoma Heterogeneity. *Cell Stem Cell* **2020**, *26*, 303–304, doi:10.1016/j.stem.2020.02.005.
177. Mao, P.; Joshi, K.; Li, J.; Kim, S.H.; Li, P.; Santana-Santos, L.; Luthra, S.; Chandran, U.R.; Benos, P. V.; Smith, L.; et al. Mesenchymal Glioma Stem Cells Are Maintained by Activated Glycolytic Metabolism Involving Aldehyde Dehydrogenase 1A3. *Proc. Natl. Acad. Sci. U. S. A.* **2013**, *110*, 8644–8649, doi:10.1073/pnas.1221478110.
178. Liau, B.B.; Sievers, C.; Donohue, L.K.; Gillespie, S.M.; Flavahan, W.A.; Miller, T.E.; Venteicher, A.S.; Hebert, C.H.; Carey, C.D.; Rodig, S.J.; et al. Adaptive Chromatin Remodeling Drives Glioblastoma Stem Cell Plasticity and Drug Tolerance. *Cell Stem Cell* **2017**, *20*, 233-246.e7, doi:10.1016/j.stem.2016.11.003.
179. Auffinger, B.; Tobias, A.L.; Han, Y.; Lee, G.; Guo, D.; Dey, M.; Lesniak, M.S.; Ahmed, A.U. Conversion of Differentiated Cancer Cells into Cancer Stem-like Cells in a Glioblastoma Model after Primary Chemotherapy. *Cell Death Differ.* **2014**, *21*, 1119–1131, doi:10.1038/cdd.2014.31.
180. Aulestia, F.J.; Néant, I.; Dong, J.; Haiech, J.; Kilhoffer, M.-C.; Moreau, M.; Leclerc, C. Quiescence Status of Glioblastoma Stem-like Cells Involves Remodelling of Ca2+ Signalling and Mitochondrial Shape. *Sci. Rep.* **2018**, *8*, 9731, doi:10.1038/s41598-018-28157-8.
181. Dahan, P.; Martinez Gala, J.; Delmas, C.; Monferran, S.; Malric, L.; Zentkowski, D.; Lubrano, V.; Toulas, C.; Cohen-Jonathan Moyal, E.; Lemarie, A. Ionizing Radiations Sustain Glioblastoma Cell Dedifferentiation to a Stem-like Phenotype through Survivin: Possible Involvement in Radioresistance. *Cell Death Dis.* **2014**, *5*, doi:10.1038/cddis.2014.509.
182. Liu, Y.; Shi, N.; Regev, A.; He, S.; Hemann, M.T. Integrated Regulatory Models for Inference of Subtype-specific Susceptibilities in Glioblastoma. *Mol. Syst. Biol.* **2020**, *16*, doi:10.15252/msb.20209506.
183. Eskilsson, E.; Verhaak, R.G.W. Longitudinal Genomic Characterization of Brain Tumors for Identification of Therapeutic Vulnerabilities: Table 1. *Neuro. Oncol.* **2016**, *18*, 1037–1039, doi:10.1093/neuonc/now064.
184. Aldape, K.; Amin, S.B.; Ashley, D.M.; Barnholtz-Sloan, J.S.; Bates, A.J.; Beroukhim, R.; Bock, C.; Brat, D.J.; Claus, E.B.; Costello, J.F.; et al. Glioma through the Looking

GLASS: Molecular Evolution of Diffuse Gliomas and the Glioma Longitudinal Analysis Consortium. *Neuro. Oncol.* **2018**, *20*, 873–884, doi:10.1093/neuonc/noy020.
185. Libby, C.J.; Tran, A.N.; Scott, S.E.; Griguer, C.; Hjelmeland, A.B. The Pro-Tumorigenic Effects of Metabolic Alterations in Glioblastoma Including Brain Tumor Initiating Cells. *Biochim. Biophys. acta. Rev. cancer* **2018**, *1869*, 175–188.
186. Deshmukh, R.; Allega, M.F.; Tardito, S. A Map of the Altered Glioma Metabolism. *Trends Mol. Med.* **2021**, *27*, 1045–1059.
187. Koppenol, W.H.; Bounds, P.L.; Dang, C. V. Otto Warburg's Contributions to Current Concepts of Cancer Metabolism. *Nat. Rev. Cancer* 2011, *11*, 325–337.
188. Marin-Valencia, I.; Yang, C.; Mashimo, T.; Cho, S.; Baek, H.; Yang, X.-L.L.; Rajagopalan, K.N.; Maddie, M.; Vemireddy, V.; Zhao, Z.; et al. Analysis of Tumor Metabolism Reveals Mitochondrial Glucose Oxidation in Genetically Diverse Human Glioblastomas in the Mouse Brain in Vivo. *Cell Metab.* **2012**, *15*, 827–837, doi:10.1016/j.cmet.2012.05.001.
189. Duraj, T.; García-Romero, N.; Carrión-Navarro, J.; Madurga, R.; Ortiz de Mendivil, A.; Prat-Acin, R.; Garcia-Cañamaque, L.; Ayuso-Sacido, A. Beyond the Warburg Effect: Oxidative and Glycolytic Phenotypes Coexist within the Metabolic Heterogeneity of Glioblastoma. *Cells* **2021**, *10*, 202, doi:10.3390/cells10020202.
190. Lunt, S.Y.; Vander Heiden, M.G. Aerobic Glycolysis: Meeting the Metabolic Requirements of Cell Proliferation. *Annu. Rev. Cell Dev. Biol.* **2011**, *27*, 441–464, doi:10.1146/annurev-cellbio-092910-154237.
191. DeBerardinis, R.J.; Lum, J.J.; Hatzivassiliou, G.; Thompson, C.B. The Biology of Cancer: Metabolic Reprogramming Fuels Cell Growth and Proliferation. *Cell Metab.* 2008, *7*, 11–20.
192. Dong, Z.; Cui, H. Epigenetic Modulation of Metabolism in Glioblastoma. *Semin. Cancer Biol.* **2019**, *57*, 45–51, doi:10.1016/j.semcancer.2018.09.002.
193. El Khayari, A.; Bouchmaa, N.; Taib, B.; Wei, Z.; Zeng, A.; El Fatimy, R. Metabolic Rewiring in Glioblastoma Cancer: EGFR, IDH and Beyond. *Front. Oncol.* **2022**, *12*, doi:10.3389/fonc.2022.901951.
194. Hoang-Minh, L.B.; Siebzehnrubl, F.A.; Yang, C.; Suzuki-Hatano, S.; Dajac, K.; Loche, T.; Andrews, N.; Schmoll Massari, M.; Patel, J.; Amin, K.; et al. Infiltrative and Drug-resistant Slow-cycling Cells Support Metabolic Heterogeneity in Glioblastoma. *EMBO J.* **2018**, *37*, 1–21, doi:10.15252/embj.201798772.
195. Mashimo, T.; Pichumani, K.; Vemireddy, V.; Hatanpaa, K.J.; Singh, D.K.; Sirasanagandla, S.; Nannepaga, S.; Piccirillo, S.G.; Kovacs, Z.; Foong, C.; et al. Acetate Is a Bioenergetic Substrate for Human Glioblastoma and Brain Metastases. *Cell* **2014**, *159*, 1603–1614, doi:10.1016/j.cell.2014.11.025.
196. Wang, L.-B.; Karpova, A.; Gritsenko, M.A.; Kyle, J.E.; Cao, S.; Li, Y.; Rykunov, D.; Colaprico, A.; Rothstein, J.H.; Hong, R.; et al. Proteogenomic and Metabolomic Characterization of Human Glioblastoma. *Cancer Cell* **2021**, *39*, 509-528.e20, doi:10.1016/j.ccell.2021.01.006.
197. Stadlbauer, A.; Oberndorfer, S.; Zimmermann, M.; Renner, B.; Buchfelder, M.; Heinz, G.; Doerfler, A.; Kleindienst, A.; Roessler, K. Physiologic MR Imaging of the Tumor Microenvironment Revealed Switching of Metabolic Phenotype upon Recurrence of Glioblastoma in Humans. *J. Cereb. Blood Flow Metab.* **2020**, *40*, 528–538, doi:10.1177/0271678X19827885.
198. Cabodevilla, A.G.; Sánchez-Caballero, L.; Nintou, E.; Boiadjieva, V.G.; Picatoste, F.; Gubern, A.; Claro, E. Cell Survival during Complete Nutrient Deprivation Depends on Lipid Droplet-Fueled β-Oxidation of Fatty Acids. *J. Biol. Chem.* **2013**, *288*, 27777–27788, doi:10.1074/jbc.M113.466656.

199. Guyon, J.; Fernandez-Moncada, I.; Larrieu, C.M.; Bouchez, C.L.; Pagano Zottola, A.C.; Galvis, J.; Chouleur, T.; Burban, A.; Joseph, K.; Ravi, V.M.; et al. Lactate Dehydrogenases Promote Glioblastoma Growth and Invasion via a Metabolic Symbiosis. *EMBO Mol. Med.* **2022**, doi:10.15252/emmm.202115343.
200. Shakya, S.; Gromovsky, A.D.; Hale, J.S.; Knudsen, A.M.; Prager, B.; Wallace, L.C.; Penalva, L.O.F.; Brown, H.A.; Kristensen, B.W.; Rich, J.N.; et al. Altered Lipid Metabolism Marks Glioblastoma Stem and Non-Stem Cells in Separate Tumor Niches. *Acta Neuropathol. Commun.* **2021**, *9*, 101, doi:10.1186/s40478-021-01205-7.
201. Saurty-Seerunghen, M.S.; Daubon, T.; Bellenger, L.; Delaunay, V.; Castro, G.; Guyon, J.; Rezk, A.; Fabrega, S.; Idbaih, A.; Almairac, F.; et al. Glioblastoma Cell Motility Depends on Enhanced Oxidative Stress Coupled with Mobilization of a Sulfurtransferase. *Cell Death Dis.* **2022**, *13*, 913, doi:10.1038/s41419-022-05358-8.
202. Badr, C.E.; Silver, D.J.; Siebzehnrubl, F.A.; Deleyrolle, L.P. Metabolic Heterogeneity and Adaptability in Brain Tumors. *Cell. Mol. Life Sci.* **2020**, *77*, 5101–5119, doi:10.1007/s00018-020-03569-w.
203. Agnihotri, S.; Zadeh, G. Metabolic Reprogramming in Glioblastoma: The Influence of Cancer Metabolism on Epigenetics and Unanswered Questions. *Neuro. Oncol.* **2016**, *18*, 160–172, doi:10.1093/neuonc/nov125.
204. Faubert, B.; Solmonson, A.; DeBerardinis, R.J. Metabolic Reprogramming and Cancer Progression. *Science (80-.).* **2020**, *368*, eaaw5473, doi:10.1126/science.aaw5473.
205. Saga, I.; Shibao, S.; Okubo, J.; Osuka, S.; Kobayashi, Y.; Yamada, S.; Fujita, S.; Urakami, K.; Kusuhara, M.; Yoshida, K.; et al. Integrated Analysis Identifies Different Metabolic Signatures for Tumor-Initiating Cells in a Murine Glioblastoma Model. *Neuro. Oncol.* **2014**, *16*, 1048–1056, doi:10.1093/neuonc/nou096.
206. Shibao, S.; Minami, N.; Koike, N.; Fukui, N.; Yoshida, K.; Saya, H.; Sampetrean, O. Metabolic Heterogeneity and Plasticity of Glioma Stem Cells in a Mouse Glioblastoma Model. *Neuro. Oncol.* **2018**, *20*, 343–354, doi:10.1093/neuonc/nox170.
207. Lin, H.; Patel, S.; Affeck, V.S.; Wilson, I.; Turnbull, D.M.; Joshi, A.R.; Maxwell, R.; Stoll, E.A.; Affleck, V.S.; Wilson, I.; et al. Fatty Acid Oxidation Is Required for the Respiration and Proliferation of Malignant Glioma Cells. *Neuro. Oncol.* **2017**, *19*, 43–54, doi:10.1093/neuonc/now128.
208. Knobloch, M.; Pilz, G.-A.; Ghesquière, B.; Kovacs, W.J.; Wegleiter, T.; Moore, D.L.; Hruzova, M.; Zamboni, N.; Carmeliet, P.; Jessberger, S. A Fatty Acid Oxidation-Dependent Metabolic Shift Regulates Adult Neural Stem Cell Activity. *Cell Rep.* **2017**, *20*, 2144–2155, doi:10.1016/j.celrep.2017.08.029.
209. Seliger, C.; Meyer, A.-L.; Leidgens, V.; Rauer, L.; Moeckel, S.; Jachnik, B.; Proske, J.; Dettmer, K.; Rothhammer-Hampl, T.; Kaulen, L.D.; et al. Metabolic Heterogeneity of Brain Tumor Cells of Proneural and Mesenchymal Origin. *Int. J. Mol. Sci.* **2022**, *23*, 11629, doi:10.3390/ijms231911629.
210. Janiszewska, M.; Suvà, M.L.; Riggi, N.; Houtkooper, R.H.; Auwerx, J.; Clément-Schatlo, V.; Radovanovic, I.; Rheinbay, E.; Provero, P.; Stamenkovic, I. Imp2 Controls Oxidative Phosphorylation and Is Crucial for Preservin Glioblastoma Cancer Stem Cells. *Genes Dev.* **2012**, *26*, 1926–1944, doi:10.1101/gad.188292.112.
211. Lamb, R.; Ozsvari, B.; Lisanti, C.L.; Tanowitz, H.B.; Howell, A.; Martinez-Outschoorn, U.E.; Sotgia, F.; Lisanti, M.P. Antibiotics That Target Mitochondria Effectively Eradicate Cancer Stem Cells, across Multiple Tumor Types: Treating Cancer like an Infectious Disease. *Oncotarget* **2015**, *6*, 4569–4584, doi:10.18632/oncotarget.3174.
212. Jiang, W.; Finniss, S.; Cazacu, S.; Xiang, C.; Brodie, Z.; Mikkelsen, T.; Poisson, L.; Shackelford, D.B.; Brodie, C. Repurposing Phenformin for the Targeting of Glioma Stem Cells and the Treatment of Glioblastoma. *Oncotarget* **2016**, *7*, 56456–56470,

doi:10.18632/oncotarget.10919.
213. Garnier, D.; Renoult, O.; Alves-Guerra, M.-C.C.; Paris, F.; Pecqueur, C. Glioblastoma Stem-Like Cells, Metabolic Strategy to Kill a Challenging Target. *Front. Oncol.* **2019**, *9*, doi:10.3389/fonc.2019.00118.
214. Michelakis, E.D.; Sutendra, G.; Dromparis, P.; Webster, L.; Haromy, A.; Niven, E.; Maguire, C.; Gammer, T.L.; Mackey, J.R.; Fulton, D.; et al. Metabolic Modulation of Glioblastoma with Dichloroacetate. *Sci. Transl. Med.* **2010**, *2*, 31ra34-31ra34, doi:10.1126/scitranslmed.3000677.
215. Duan, Y.; Zhao, X.; Ren, W.; Wang, X.; Yu, K.-F.; Li, D.; Zhang, X.; Zhang, Q. Antitumor Activity of Dichloroacetate on C6 Glioma Cell: In Vitro and in Vivo Evaluation. *Onco. Targets. Ther.* **2013**, *6*, 189–198.
216. Iliopoulos, D.; Hirsch, H.A.; Struhl, K. Metformin Decreases the Dose of Chemotherapy for Prolonging Tumor Remission in Mouse Xenografts Involving Multiple Cancer Cell Types. *Cancer Res.* **2011**, *71*, 3196–3201, doi:10.1158/0008-5472.CAN-10-3471.
217. Griss, T.; Vincent, E.E.; Egnatchik, R.; Chen, J.; Ma, E.H.; Faubert, B.; Viollet, B.; DeBerardinis, R.J.; Jones, R.G. Metformin Antagonizes Cancer Cell Proliferation by Suppressing Mitochondrial-Dependent Biosynthesis. *PLOS Biol.* **2015**, *13*, e1002309.
218. Zhou, G.; Myers, R.; Li, Y.; Chen, Y.; Shen, X.; Fenyk-Melody, J.; Wu, M.; Ventre, J.; Doebber, T.; Fujii, N.; et al. Role of AMP-Activated Protein Kinase in Mechanism of Metformin Action. *J. Clin. Invest.* **2001**, *108*, 1167–1174, doi:10.1172/JCI13505.
219. KORSAKOVA, L.; KRASKO, J.A.; STANKEVICIUS, E. Metabolic-Targeted Combination Therapy With Dichloroacetate and Metformin Suppresses Glioblastoma Cell Line Growth In Vitro and In Vivo. *In Vivo (Brooklyn).* **2021**, *35*, 341–348, doi:10.21873/invivo.12265.
220. Mazurek, M.; Litak, J.; Kamieniak, P.; Kulesza, B.; Jonak, K.; Baj, J.; Grochowski, C. Metformin as Potential Therapy for High-Grade Glioma. *Cancers (Basel).* **2020**, *12*, 210, doi:10.3390/cancers12010210.
221. Postovit, L.; Widmann, C.; Huang, P.; Gibson, S.B. Harnessing Oxidative Stress as an Innovative Target for Cancer Therapy. *Oxid. Med. Cell. Longev.* **2018**, *2018*, 1–2, doi:10.1155/2018/6135739.
222. Campos, B.; Wan, F.; Farhadi, M.; Ernst, A.; Zeppernick, F.; Tagscherer, K.E.; Ahmadi, R.; Lohr, J.; Dictus, C.; Gdynia, G.; et al. Differentiation Therapy Exerts Antitumor Effects on Stem-like Glioma Cells. *Clin. Cancer Res.* **2010**, *16*, 2715–2728, doi:10.1158/1078-0432.CCR-09-1800.
223. Liu, H.; Kiseleva, A.A.; Golemis, E.A. Ciliary Signalling in Cancer. *Nat. Rev. Cancer* **2018**, *18*, 511–524, doi:10.1038/s41568-018-0023-6.
224. Rajagopalan, S.; Singh, A.; Khiabanian, H. Cilium Expression Score Predicts Glioma Survival. *Front. Genet.* **2021**, *12*, doi:10.3389/fgene.2021.758391.
225. Nguyen, H.D.; Allaire, A.; Diamandis, P.; Bisaillon, M.; Scott, M.S.; Richer, M. A Machine Learning Analysis of a "Normal-like" IDH-WT Diffuse Glioma Transcriptomic Subgroup Associated with Prolonged Survival Reveals Novel Immune and Neurotransmitter-Related Actionable Targets. *BMC Med.* **2020**, *18*, 280, doi:10.1186/s12916-020-01748-x.
226. Venkataramani, V.; Yang, Y.; Schubert, M.C.; Reyhan, E.; Tetzlaff, S.K.; Wißmann, N.; Botz, M.; Soyka, S.J.; Beretta, C.A.; Pramatarov, R.L.; et al. Glioblastoma Hijacks Neuronal Mechanisms for Brain Invasion. *Cell* **2022**, *185*, 2899-2917.e31, doi:10.1016/j.cell.2022.06.054.
227. Chakraborty, C.; Nissen, I.; Vincent, C.A.; Hägglund, A.-C.; Hörnblad, A.; Remeseiro, S. Rewiring of the Promoter-Enhancer Interactome and Regulatory Landscape in Glioblastoma Orchestrates Gene Expression Underlying Neurogliomal Synaptic

Communication. *Nat. Commun.* **2023**, *14*, 6446, doi:10.1038/s41467-023-41919-x.
228. Sani, S.; Pallaoro, N.; Messe, M.; Bernhard, C.; Etienne-Selloum, N.; Kessler, H.; Marinelli, L.; Entz-Werle, N.; Foppolo, S.; Martin, S.; et al. Temozolomide-Acquired Resistance Is Associated with Modulation of the Integrin Repertoire in Glioblastoma, Impact of A5β1 Integrin. *Cancers (Basel).* **2022**, *14*, 369, doi:10.3390/cancers14020369.
229. Ward, N.P.; Poff, A.M.; Koutnik, A.P.; D'Agostino, D.P. Complex I Inhibition Augments Dichloroacetate Cytotoxicity through Enhancing Oxidative Stress in VM-M3 Glioblastoma Cells. *PLoS One* **2017**, *12*, e0180061, doi:10.1371/journal.pone.0180061.
230. Chekkat, N.; Dahm, G.; Chardon, E.; Wantz, M.; Sitz, J.; Decossas, M.; Lambert, O.; Frisch, B.; Rubbiani, R.; Gasser, G.; et al. N-Heterocyclic Carbene-Polyethylenimine Platinum Complexes with Potent in Vitro and in Vivo Antitumor Efficacy. *Bioconjug. Chem.* **2016**, *27*, 1942–1948, doi:10.1021/acs.bioconjchem.6b00320.
231. Spehalski, E.I.; Lee, J.A.; Peters, C.; Tofilon, P.; Camphausen, K. The Quiescent Metabolic Phenotype of Glioma Stem Cells. *J. Proteomics Bioinform.* **2019**, *12*, 96–103, doi:10.35248/0974-276x.19.12.502.
232. Long, P.M.; Moffett, J.R.; Namboodiri, A.M.A.; Viapiano, M.S.; Lawler, S.E.; Jaworski, D.M. N-Acetylaspartate (NAA) and N-Acetylaspartylglutamate (NAAG) Promote Growth and Inhibit Differentiation of Glioma Stem-like Cells. *J. Biol. Chem.* **2013**, *288*, 26188–26200, doi:10.1074/jbc.M113.487553.
233. Bulik, M.; Jancalek, R.; Vanicek, J.; Skoch, A.; Mechl, M. Potential of MR Spectroscopy for Assessment of Glioma Grading. *Clin. Neurol. Neurosurg.* **2013**, *115*, 146–153, doi:10.1016/j.clineuro.2012.11.002.
234. Pederzolli, C.D.; Mescka, C.P.; Scapin, F.; Rockenbach, F.J.; Sgaravatti, Â.M.; Sgarbi, M.B.; Wyse, A.T.S.; Wannmacher, C.M.D.; Wajner, M.; Dutra-Filho, C.S. N -Acetylaspartic Acid Promotes Oxidative Stress in Cerebral Cortex of Rats. *Int. J. Dev. Neurosci.* **2007**, *25*, 317–324, doi:10.1016/j.ijdevneu.2007.04.002.
235. Pederzolli, C.D.; Mescka, C.P.; Magnusson, A.S.; Deckmann, K.B.; de Souza Streck, E.; Sgaravatti, Â.M.; Sgarbi, M.B.; Wyse, A.T.S.; Wannmacher, C.M.D.; Wajner, M.; et al. N-Acetylaspartic Acid Impairs Enzymatic Antioxidant Defenses and Enhances Hydrogen Peroxide Concentration in Rat Brain. *Metab. Brain Dis.* **2010**, *25*, 251–259, doi:10.1007/s11011-010-9202-1.
236. Debnath, J.; Gammoh, N.; Ryan, K.M. Autophagy and Autophagy-Related Pathways in Cancer. *Nat. Rev. Mol. Cell Biol.* **2023**, *24*, 560–575, doi:10.1038/s41580-023-00585-z.
237. Lu, Y.; Xiao, L.; Liu, Y.; Wang, H.; Li, H.; Zhou, Q.; Pan, J.; Lei, B.; Huang, A.; Qi, S. MIR517C Inhibits Autophagy and the Epithelial-to-Mesenchymal (-like) Transition Phenotype in Human Glioblastoma through KPNA2-Dependent Disruption of TP53 Nuclear Translocation. *Autophagy* **2015**, *11*, 2213–2232, doi:10.1080/15548627.2015.1108507.
238. Yi, G.; Xiang, W.; Feng, W.; Chen, Z.; Li, Y.; Deng, S.; Guo, M.; Zhao, L.; Sun, X.; He, M.; et al. Identification of Key Candidate Proteins and Pathways Associated with Temozolomide Resistance in Glioblastoma Based on Subcellular Proteomics and Bioinformatical Analysis. *Biomed Res. Int.* **2018**, *2018*, 1–12, doi:10.1155/2018/5238760.
239. Oliva, C.R.; Nozell, S.E.; Diers, A.; McClugage, S.G.; Sarkaria, J.N.; Markert, J.M.; Darley-Usmar, V.M.; Bailey, S.M.; Gillespie, G.Y.; Landar, A.; et al. Acquisition of Temozolomide Chemoresistance in Gliomas Leads to Remodeling of Mitochondrial Electron Transport Chain. *J. Biol. Chem.* **2010**, *285*, 39759–39767, doi:10.1074/jbc.M110.147504.
240. Dico, A. Lo; Salvatore, D.; Martelli, C.; Ronchi, D.; Diceglie, C.; Lucignani, G.; Ottobrini, L. Intracellular Redox-Balance Involvement in Temozolomide Resistance-

Related Molecular Mechanisms in Glioblastoma. *Cells* **2019**, *8*, 1315, doi:10.3390/cells8111315.
241. Li, Y.; Chen, H.; Xie, X.; Yang, B.; Wang, X.; Zhang, J.; Qiao, T.; Guan, J.; Qiu, Y.; Huang, Y.-X.; et al. PINK1-Mediated Mitophagy Promotes Oxidative Phosphorylation and Redox Homeostasis to Induce Drug-Tolerant Persister Cancer Cells. *Cancer Res.* **2023**, *83*, 398–413, doi:10.1158/0008-5472.CAN-22-2370.
242. Agnihotri, S.; Golbourn, B.; Huang, X.; Remke, M.; Younger, S.; Cairns, R.A.; Chalil, A.; Smith, C.A.; Krumholtz, S.-L.; Mackenzie, D.; et al. PINK1 Is a Negative Regulator of Growth and the Warburg Effect in Glioblastoma. *Cancer Res.* **2016**, *76*, 4708–4719, doi:10.1158/0008-5472.CAN-15-3079.
243. Galavotti, S.; Bartesaghi, S.; Faccenda, D.; Shaked-Rabi, M.; Sanzone, S.; McEvoy, A.; Dinsdale, D.; Condorelli, F.; Brandner, S.; Campanella, M.; et al. The Autophagy-Associated Factors DRAM1 and P62 Regulate Cell Migration and Invasion in Glioblastoma Stem Cells. *Oncogene* **2013**, *32*, 699–712, doi:10.1038/onc.2012.111.
244. Ieni, A.; Pizzimenti, C.; Broggi, G.; Caltabiano, R.; Germanò, A.; Barbagallo, G.; Vigneri, P.; Giuffrè, G.; Tuccari, G. Immunoexpression of P62/SQSTM1/Sequestosome-1 in Human Primary and Recurrent IDH1/2 Wild-type Glioblastoma: A Pilot Study. *Oncol. Lett.* **2022**, *24*, 336, doi:10.3892/ol.2022.13456.
245. Kumar, S.; Sánchez-Álvarez, M.; Lolo, F.-N.; Trionfetti, F.; Strippoli, R.; Cordani, M. Autophagy and the Lysosomal System in Cancer. *Cells* **2021**, *10*, 2752, doi:10.3390/cells10102752.
246. Tsen, A.R.; Long, P.M.; Driscoll, H.E.; Davies, M.T.; Teasdale, B.A.; Penar, P.L.; Pendlebury, W.W.; Spees, J.L.; Lawler, S.E.; Viapiano, M.S.; et al. Triacetin-based Acetate Supplementation as a Chemotherapeutic Adjuvant Therapy in Glioma. *Int. J. Cancer* **2014**, *134*, 1300–1310, doi:10.1002/ijc.28465.
247. Yan, Y.; Xu, Z.; Dai, S.; Qian, L.; Sun, L.; Gong, Z. Targeting Autophagy to Sensitive Glioma to Temozolomide Treatment. *J. Exp. Clin. Cancer Res.* **2016**, *35*, 23, doi:10.1186/s13046-016-0303-5.
248. Kriel, J.; Müller-Nedebock, K.; Maarman, G.; Mbizana, S.; Ojuka, E.; Klumperman, B.; Loos, B. Coordinated Autophagy Modulation Overcomes Glioblastoma Chemoresistance through Disruption of Mitochondrial Bioenergetics. *Sci. Rep.* **2018**, *8*, 10348, doi:10.1038/s41598-018-28590-9.
249. Boccellato, C.; Rehm, M. Glioblastoma, from Disease Understanding towards Optimal Cell-Based in Vitro Models. *Cell. Oncol.* **2022**, *45*, 527–541, doi:10.1007/s13402-022-00684-7.

ANNEXES

ANNEXE 1 : Communications orales et posters

Communication orale :

- Bernhard C, Pawlak G, Outilfalt H, Foppolo S, Herold-Mende C, Namer I, Elati M, Dontenwill M. Hétérogénéité moléculaire et métabolique des glioblastomes. Caractériser la plasticité des cibles pour des thérapies personnalisées ?
  23e journée scientifique régionale de la ligue contre le cancer, 7 décembre 2023, Illkirch.

- Bernhard C, Messé M, Outilfalt H, Foppolo S, Herold-Mende C, Namer I, Dontenwill M. Metabolic heterogeneity and plasticity in high-grade glioma stem cells.
  Congrès ANOCEF, 1-2 juillet 2022, Rouen.

Posters :

- Bernhard C, Messé M, Outilfalt H, Foppolo S, Herold-Mende C, Namer I, Dontenwill M. Metabolic heterogeneity and plasticity in high-grade glioma stem cells
  Innovations in Delivery and Targeting, 26-27 juin 2023, Strasbourg.

- Bernhard C, Messé M, Outilfalt H, Foppolo S, Herold-Mende C, Namer I, Mohamed E, Dontenwill M. Metabolic heterogeneity and plasticity in high-grade glioma stem cells. 4th SUNRiSE Meeting, 8-9 juin 2022, Paris.

- Bernhard C, Messé M, Outilfalt H, Fuchs Q, Foppolo S, Herold-Mende C, Namer I, Elati M, Entz-Werlé N, Dontenwill M. Metabolic Heterogeneity in High-Grade Gliomas. ED days, 21-22 avril 2022, Strasbourg.

- Bernhard C, Messé M, Mercier MC, Fuchs Q, Foppolo S, Herold-Mende C, Namer I, Bund C, Elati M, Entz-Werlé. N, Dontenwill M. Heterogeneity and plasticity of integrin α5β1 expression in glioblastoma stem cells. Congrès international 16th EANO Meeting, 25-26 septembre 2021.

ANNEXE 2 : Publications parues ou soumises

Hypoxia-driven heterogeneous expression of α5β1 integrin in glioblastoma stem cells is linked to HIF-2α. Messé M, Bernhard C, Foppolo S, Thomas L, Marchand P, Jessel B, Martin S, Herold-Mende C, Idbaih A, Kessler H, Elati M, Etienne-Selloum N, Tambar UK, Entz-Werle N, Reita D, Laquerriere P, Dontenwill M.

Au cours de mon doctorat, j'ai eu la chance de m'impliquer dans un projet collaboratif complémentaire au sein de mon équipe de recherche. Ce projet était dirigé par la doctorante Mélissa Messé et portait sur l'hétérogénéité et la plasticité de l'expression de l'intégrine α5β1 au sein des CSG, notamment en réponse à l'hypoxie dans des modèles *in vitro* et *in vivo*. J'ai activement participé au suivi régulier de ce projet, en contribuant notamment à soulever des questions et à l'interprétation des données collectées tout au long du projet. Le projet a permis de soumettre l'article "Hypoxia-driven heterogeneous expression of α5β1 integrin in glioblastoma stem cells is linked to HIF-2α". Cette publication explore la corrélation entre l'expression du gène *ITGA5* et les conditions hypoxiques dans les CSG. Elle met également en lumière l'implication des facteurs HIF-1α et HIF-2α dans la modulation de l'expression de l'intégrine α5β1 et suggère une association thérapeutique efficace sur les CSG.

Hypoxia-driven heterogeneous expression of α5 integrin in glioblastoma stem cells is linked to HIF-2α.

Mélissa MESSÉ[1,2], Chloé BERNHARD[1], Sophie FOPPOLO[1], Lionel THOMAS[2], Patrice MARCHAND[2], Christel HEROLD-MENDE[3], Ahmed IDBAIH[4], Horst KESSLER[5], Nelly ETIENNE-SELLOUM[1,6], Charles OCHOA, Uttam K TAMBAR[7], Patrice LAQUERRIERE[2], Natacha ENTZ-WERLE[1,8], Sophie MARTIN[1], Damien REITA[1,9], and Monique DONTENWILL[1]*.

1. UMR7021 CNRS, Tumoral Signaling and Therapeutic Targets, Strasbourg University, Faculty of Pharmacy, Illkirch, France
2. UMR7178 CNRS, Hubert Curien Multidisciplinary Institute, Strasbourg University, 67000 Strasbourg, France.
3. Division of Neurosurgical Research, Department of Neurosurgery, Heidelberg University Hospital, 69120 Heidelberg, Germany.
4. Sorbonne University, AP-HP, Institut du Cerveau - Paris Brain Institute - ICM, Inserm, CNRS, Hôpitaux Universitaires La Pitié Salpêtrière - Charles Foix, F-75013, Paris, France.
5. Institute for Advanced Study, Department Chemie, Technical University Munich (TUM), Lichtenbergstr. 4, 85747, Garching, Germany.
6. Pharmacy department, Institut de Cancérologie Strasbourg Europe (ICANS), 67200 Strasbourg, France
7. Department of Biochemistry, The University of Texas Southwestern Medical Center at Dallas, 5323 Harry Hines Boulevard, Dallas, Texas 75390-9038, United States.
8. Pédiatrie Onco-Hématologie-Pédiatrie III, Strasbourg University Hospital, 67091 Strasbourg, France.
9. Department of Cancer Molecular Genetics, Laboratory of Biochemistry and Molecular Biology, University Hospital of Strasbourg, 67200 Strasbourg, France

*** Corresponding author**: Dr Monique DONTENWILL, UMR 7021 CNRS, LBP, Strasbourg University, Faculty of Pharmacy, 67401 Illkirch, France. Tel. (0033)368854267; Fax (0033)368854313; Email: monique.dontenwill@unistra.fr

KEYWORDS: glioma stem cells, hypoxia, integrin α5, HIF-2α

Abstract

Despite numerous molecular targeted therapies tested in glioblastoma (GBM), no significant progresses in patient survival have been achieved these last 20 years in the overall population of GBM patients. Therapy resistance is in part associated with target expression heterogeneity and plasticity between tumors and in specific tumor niches. We focused on integrin α5 which implication in aggressive GBM has already been characterized in preclinical and clinical samples. To more deeply address the characteristics of integrin α5 heterogeneity we started with patient data indicating that elevated levels of its mRNA are related to hypoxia pathways. We turned on glioma stem cells which are considered at the apex of tumor formation and

recurrence but also as they localize in hypoxic niches. We demonstrated that integrin α5 expression is stem cell line dependent and is modulated positively by hypoxia *in vitro*. Importantly, heterogeneity of expression integrin α5 is conserved *in vivo* stem cell-derived xenografted tumors in mice. In hypoxic niches, HIF-2α is preferentially implicated in integrin α5 expression which confers migratory capacity to GBM stem cells. Hence combining HIF-2α and integrin α5 inhibitors resulted in proliferation and migration impairment of integrin α5 expressing cells. Stabilization of HIF-2α is however not sufficient to control integrin α5 expression. Our results show that AHR (aryl hydrocarbon receptor) and HIF-2α expressions are inversely correlated and to integrin α5 expression suggesting a functional competition between both transcription factors. Collectively, data confirm the high heterogeneity of a GBM therapeutic target, its induction in hypoxic niches by HIF-2α and suggest a new way to attack molecularly defined GBM stem cells.

Introduction

Although clinically characterized by common histological features, accumulating data report that glioblastoma (GBM), the most aggressive brain tumors, correspond to a family of molecularly distinct entities. Integrated genomic, transcriptomic, epigenomic and proteomic analysis allowed the definition of core biological pathways and clinically relevant subtypes of GBM [1–4]. A robust gene expression-based molecular classification of GBM into four subgroups (proneural, neural, classical and mesenchymal) has been proposed in 2010 by the Cancer Genome Atlas Network [5] but neural subclass was since assigned to non tumoral cells [6]. Other layers of complexity have been characterized including the GBM stem cell (GSC) subsets and their high plasticity [7–11]. As these stem-like cells are considered to initiate brain tumors upon orthotopic implantation, to sustain tumor growth, and to escape chemo-radio-therapy-induced cell death [12], it is essential to understand their biology. Tumor cells with stem-like properties are classically cultured from GBM tumor bulk biopsies by using conditions selecting for neural stem cells. They are able to form neurospheres *in vitro* that recapitulate the histopathology of human GBM tumors when xenotransplanted in nude mice, such as pseudopalisading necrosis, nuclear pleomorphism and extensive microvascular proliferation [13]. They also maintain the clonal and genomic complexity of the parental patient tumors [9, 14, 15].

Integrins are involved in most of the hallmarks of cancer [16, 17] and their implications in brain tumor aggressiveness have been highlighted [18]. Some data exist on integrins in brain cancer stem cells [19]. Among them, the α6 integrin (ITGA6 receptor for laminin) enriches for GSC and has been involved in their self-renewal, proliferation and tumor formation capacity [20]. The α6 integrin mRNA level also negatively correlated with glioma patient survival in the REMBRANDT database [21]. Similarly, α3 integrin (ITGA3) was proposed to be overexpressed in GSC and to promote invasion [22]. More recently, α7 integrin (ITGA7) was shown to be specifically expressed in GSC compared to differentiated cells and to be a marker for aggressive and invasive tumors [23]. Finally, β8 integrin (ITGB8) similarly appeared as a marker of GSC involved in tumor initiation, progression and resistance to radiotherapy [24, 25]. We [26] and others [21, 27] have shown that patient bulk tumors express varying levels of α5 integrin (ITGA5) mRNA, negatively correlated with glioma

patient survival. Our recent data confirm that ITGA5 protein expression is effectively correlated to Stupp protocol treatment resistance [28]. No data currently support its potential role in GSC as a biomarker of aggressiveness. Starting from patient transcriptomic data (TCGA data), we show by GSEA analysis that overexpression of ITGA5 was linked to different pathways including hypoxia. We therefore investigated the expression of ITGA5 protein in GSC maintained in stem cell medium either in normoxia or in hypoxia as it is already known that GSC localize in hypoxic niches. In contrast with data on other integrins, we found that only a subpopulation of GSC is programmed to express it in normoxia and that hypoxic conditions rather increase this expression in a timely manner *in vitro*. Integrin – expressing GSC keep this property *in vivo* leading to more aggressive and invasive tumors. We demonstrated that among hypoxia-induced factors, HIF-2α predominantly modulated the expression of ITGA5. This HIF2α-driven integrin expression confers enhanced migration potency to GSC. Even if ITGA5 appeared not involved in GSC proliferation, combining HIF2α inhibitors with ITGA5 specific antagonist resulted in a clear proliferation inhibition of selected GSC. Specific HIF-2α inhibitors in addition with integrin antagonists thus represent new therapeutic options to treat ITGA5 expressing GBM. Lastly, our results support the hypothesis of an inverse relationships between HIF-2α and AHR for ITGA5 induction opening the way to new investigations on how to consider molecular heterogeneity of therapeutic targets in GBM.

Materials and methods

Gene Set Enrichment Analysis

To explore signaling pathways enrichment, Gene Set Enrichment Analysis (GSEA) [29] was performed between low and high ITGA5 expression groups using GSEA Java software (https://www.gsea-msigdb.org/gsea/index.jsp version 4.2.3) with MSigDb Hallmark gene sets [30]. Transcriptomic data are obtained from GBM cohort of TCGA. GBM samples are divided according to the median expression of ITGA5 gene into high and low expression groups. Only results from high ITGA5 expression groups are shown.

Cell lines and cell culture conditions for GSC

Six different patient-derived GBM stem cell lines were used. NCH644 and NCH421k glioma stem cells were provided by Dr. Herold-Mende (Department of Neurosurgery, University of Heidelberg, Germany). Glioma stem cells 3731 and 5706 were provided by Dr. Idbaih (Paris Brain Institute, ICM, Paris). TC7 and TC22 glioma stem cells were obtained from patient-derived heterotopic xenografts (PDX) in the Laboratory of Bioimaging and Pathology (UMR7021 CNRS, Illkirch). Cells were cultured in Dulbecco's Modified Eagle medium with nutrient Mixture F-12 and GlutaMAX™ (DMEMF12 + GlutaMAX™, Gibco™), supplemented with 20% of BSA Insulin Transferrin (BIT-100, Provitro), 20 ng/mL of EGF and 20 ng/mL β-FGF (Reliatech). All cell lines were maintained in a 37°C incubator, with 5% CO_2. Neurospheres are dissociated every 7 days with accutase (A6964, Sigma) and then put

back into culture. For the hypoxic condition, cells are cultured in a tri-gas incubator in which oxygen levels are reduced to 1% by nitrogen injection.

Western Blot analysis

Cells were directly lysed with Laemmli 2X (60mM Tris-HCl pH 6.8; 20% glycerol; 2% SDS; 0.01% bromophenol blue) (Biorad) supplemented with 5% β-mercaptoethanol (Biorad) on ice and denatured at 95°C for 13 minutes. Lysates were electrophoresed using 4-20 % SDS-PAGE polyacrylamide gels (Biorad) and then transferred to a PVDF membrane (GE Healthcare, Velizy, France). PVDF membranes were blocked in 0.1 % Tween-20 buffered saline (TBST) containing 5 % milk for 1 hour at room temperature and incubated overnight with the corresponding primary antibody (see Table 1) diluted in TBST containing 5 % milk at 4°C. Membranes were washed with TBST and incubated with horseradish peroxidase (HRP)-conjugated secondary antibodies (Table 1) diluted in TBST containing 5 % milk at room temperature for 1 hour. After washing, blots were visualized using the enhanced chemiluminescence (ECL) system (ECL™ Prime Western Blotting System, GE Healthcare Bioscience) with an ImageQuant™ LAS 4000 analyzer (GE Healthcare). Quantification of unsaturated images was performed using ImageJ software (National institutes of Health, Bethesda, MD, USA). For each experiment, 3 lysates from different cell cultures were used. Tubulin was used as a loading control for all samples. List of antibodies is provided in table 1.

RT-qPCR analysis

Cells are plated in a 6-well plate at a density of $1x10^6$ cells/well in medium alone or in the presence of 20 µM PT2977 or 20 µM compound 2 for 24h in 1% O_2 hypoxia. After 24h incubation, cells are washed with 1X PBS and lysed with 600 µL RLT plus buffer (Qiagen kit) to extract RNA. The RNA extraction step is performed using a Qiagen kit (RNEasy Plus Mini Kit). RNA concentration is then assessed using a NanoDrop™One UV-Visible spectrophotometer (ThermoFisher). Reverse transcription is performed using the "iScript™ Reverse Transcription Supermix" kit (Biorad). Samples are then placed in a thermocycler (T100, Biorad) to perform the reverse transcription reaction with the iScript program. For RT-qPCR, a reaction mixture is made for each primer (Table 3) using SYBR Green™ as reagent, and 15 µL is poured into a MicroAmp™ 96-well optical reaction plate (Applied Biosystems™). The cDNA obtained by reverse transcription is diluted 5-fold and 5 µL of DNA is added to this mixture in the 96-well plate. RT-qPCR is performed with the StepOnePlus™ real-time PCR instrument (4376357, Thermofisher) and run with StepOne™ software (v2.3). Data are then analyzed using this software. RNA18S is used as an endogenous control. List of primers is provided in table 3.

Transfection of siRNA

Cells were seeded at a density of 500,000 cells/well in a 6-well plate previously coated with 20 µg/ml cell-tak (Corning™). The cells were then transfected with the corresponding siRNA (Qiagen) at 100 nM for HIF-1α and 250 nM for HIF-2α according to the following steps. A solution of siRNA at the corresponding concentration was prepared in 250 µl of optiMEM as well as a solution of 5 µl of lipofectamine 2000 (ThermoFisher) in 250 µl of optiMEM. The solutions are then incubated at room temperature for 5 min. After incubation, the 250 µl of

lipofectamine solution is mixed with the siRNA solution. The mixture is then left to incubate at room temperature for 25 min. Finally, the lipofectamine/siRNA mixture is added to the cells in the culture medium. The cells are then placed in 1% O_2 hypoxia for 48h. After 48h, cells are recovered in 2X Laemmli (60mM Tris-HCl pH 6.8; 20% glycerol; 2% SDS; 0.01% bromophenol blue) (Biorad) supplemented with 5 % β-mercaptoethanol (Biorad) on ice and denatured at 95°C for 13 min. Samples were then subjected to western blot analysis.

Proliferation assays (Incucyte®)

3,000 stem cells/well were placed in a 96-well plate in the medium alone or with different treatments. Cells were then placed in a trigaz incubator containing the Incucyte equipment for 6 days at 37°C, 5% CO_2 in normoxia (20% O_2) or hypoxia (1% O_2). Neurosphere size (μm^2) was monitored using an IncuCyte™ Zoom live cell analysis system. IncuCyte® technology took images every 4 hours, neurosphere sizes were recorded for each time point and normalized to time zero.

Sphere evasion assays

Neurospheres were generated using the suspended drop method to get homogenous population of spheres [70]. A cell suspension of 2000 cells / 20 µl of growth medium supplemented with 1.2 % methylcellulose (Sigma Aldrich, M0262) is deposited on the inner surface of a Petri dish. After 48h, each spheroid was transferred to a 24-well plate coated with poly-L-lysine (Sigma Aldrich, P8920) or fibronectin (Promocell, C-43060) (1 sphere per well) with the medium alone or with treatments of interest. Cells were then placed in normoxia at 20% O_2 or hypoxia at 1% O_2 in a trigaz incubator. Invasion was monitored for 24h, then spheroids were fixed with 1% (vol/vol) glutaraldehyde (Thermo Fisher Scientific, 16400) for 30 minutes, followed by DAPI staining (Sigma Aldrich, D9542) at 1µg/mL for 45 minutes. An epifluorescence microscope is used to take photos. The number of migrating cells is determined by ImageJ software with the help of a dedicated in house-developed macro.

Cellular immunofluorescence

Cells were plated in a 24-well coverslip plate previously coated with poly-l-lysine (10 µg/ml). After incubation in normoxia or hypoxia for 72 h, the cells were fixed in cold methanol for 10 min at room temperature. A permeabilization step was then performed (0.2% Tween20 / PBS 1X) for 15 min, followed by a blocking step with PBS buffer containing 5% goat serum and 3% BSA for 1 h at room temperature. Specific antibodies (Table 1) were applied by incubation overnight at 4°C. After washing in PBS, cells were incubated for 1 h with the corresponding secondary antibody. Nuclei were counterstained with DAPI (10 mg/mL, Sigma-Aldrich) and coverslips were mounted using FluoreGuard aqueous mounting medium (ScyTek). Images were acquired using a Leica TCS SPEII laser scanning confocal microscope at 63X magnification with an immersion objective from the PIQ Quantum Efficiency Strasbourg platform (http://quest.igbmc.fr/). All confocal microscope settings were kept constant between each staining experiment.

Orthotopic xenograft

Eight-week-old female NUDE NMRI mice were obtained from Janvier labs. CSG lines TC22 (α5+) and NCH421k (α5-) were dissociated and injected at a density of 25 000 cells in 2 µl of culture medium into the left striatum of the mouse. Each cell line was injected into a group of 5 mice. Mice were placed in a stereotaxic frame after being anesthetized in an induction chamber with 2.5% isoflurane. The coordinates used for cell injection are : X = - 0.5 ; Y = + 1.5 ; Z = - 3 mm from the bregma. A Hamilton syringe is used to inject stem cells at 1 µl/min. A mask was placed over the muzzle of the mice to maintain anesthesia with 2.5% isoflurane. At the onset of neurological symptoms and/or weight loss (20% of mouse weight), following anesthesia, mice were sacrificed with a euthanasia agent (Euthasol®). Experiments were performed in compliance with local laws and ethics committee approval (institutional protocol approval number 26600).

Positron emission tomography (PET) imaging

Mice were evaluated by PET imaging from day 19 after stem cell injection, with weekly PET imaging sessions for 1 month. Two radiotracers were used: [^{18}F]-FLT ([^{18}F]-fluoro-thymidine) for assessing cell proliferation and [^{18}F]-FET ([^{18}F]-fluoroethyl-L-tyrosine) to monitor tumor growth. Each radiotracer was produced by the CYRCE (Cyclotron for Research and Education) platform of the pluridisciplinary Hubert Curien institute (IPHC, UMR 7178 CNRS, Strasbourg) using automated processes on AIO (Trasis®) module. Precursors and authentic references were purchased from ABX (Germany). Radiotracers were diluted in 0.9% sterile NaCl (BBraun, veterinary grade) and injected intravenously into the tail vein. Each mouse was injected with an average of 10 MBq. Once biodistribution was complete ([^{18}F]-FLT = 90 min ; [^{18}F]-FET = 45 min), the mice were anesthetized with 2.5% isoflurane and then placed in the PET/scan Inviscan® dedicated to small animals. A 10 min static acquisition was performed and the images were reconstructed using the iterative 3D ordered subset maximization algorithm (volume 201 x 201 x 120 mm^3). PET data were fully corrected for normalization, random coincidences, radioactive decay and dead time during the reconstruction process. No attenuation and scatter corrections were applied. The mice are maintained under anesthesia throughout the acquisition of the images with 2.5% isoflurane. Images were obtained using HOROS® software and tumor volume was calculated using Amide® software (http://amide.sourceforge.net/index.html). The tumor is delimited manually (ROI) then the SUVmax (Standardized Uptake Value maximum) is calculated by the software using the following formula:

$$SUV = (Volume\ activity\ ROI) \div ((Injected\ activity) \div (Mouse\ weight))$$

Tumor volume at 40% of SUVmax was calculated to exclude experimental bias in tumor delineation.

Immunohistofluorescence

Following sacrifice of the mice after reaching their endpoints, the brains were recovered and then fixed in 4% paraformaldehyde overnight. The brains were then embedded in paraffin. Slices (5 µm thick) were deparaffinized, rehydrated and subjected to an antigen unmasking protocol using Dako (Tris/EDTA) pH9 recovery solution (Agilent Technologies, Les Ulis,

France). Blocking buffer (5% goat serum, 0.1% Tween-20, PBS) was applied for 1h at room temperature. Incubation with ITGA5 specific antibodies (Table 1) was done overnight at 4°C. After washing in 0.1% PBS-Tween, the tissue sections were incubated for 1h with the corresponding secondary antibodies. Nuclei were counterstained with DAPI (10 mg/mL, Sigma-Aldrich) and coverslips were mounted using FluoreGuard aqueous mounting medium (ScyTek). Images were acquired using a Leica TCS SPEII confocal laser scanning microscope at 63X magnification with an immersion objective from the PIQ Quantum Efficiency Strasbourg platform (http://quest.igbmc.fr/, accessed July 2, 2021). All confocal microscope settings were kept constant between each staining experiment.

FACS analysis

After counting the dissociated stem cells, a pellet of 100 000 cells was made. 3 washes with PBS 1X / BSA 1% were performed and then the cell pellets were resuspended and incubated for 30 min at 4°C with the corresponding primary antibodies. the cells were then centrifuged at 2500 rpm for 1 min at 4°C and then washed twice with PBS 1X / BSA 1%. After the washes, the pellets were resuspended and incubated for 30 min at 4°C in the dark with the corresponding secondary antibodies. 2 washes with 1X PBS / 1% BSA were performed and then the cells were resuspended in 1X PBS. The samples were then run on a flow cytometer. The results were analyzed with the FCSalyzer 0.9.22-alpha software.

Subcellular fractionation

A pellet of $5x10^{6}$ cells was obtained through centrifugation. Subcellular fractionation was performed with the Qproteome cell compartment kit (Qiagen) according to the manufacturer instructions. The protein concentration was evaluated with a UV-Visible NanoDropTMOne spectrophotometer (Thermo Fisher). 10 µg of proteins from each fraction were lysed in 200 µl of 2X Laemmli (60 mM Tris-HCl pH 6.8; 20% glycerol; 2% SDS; 0.01% bromophenol blue) (Biorad) supplemented with 5% β-mercaptoethanol (Biorad) on ice and denatured at 95°C for 13 min. Each compartment was checked by Western blot with specific antibodies.

Statistics

Data are expressed as mean ± SEM, and analyzed using GraphPad Prism version 5 (GraphPad Software, California, USA). Differences between groups were analyzed using a non-paired *t*-test and $p < 0.05$ was considered statistically significant.

Results

ITGA5 expression is linked to hypoxia and Epithelial to Mesenchymal Transition (EMT) in GBM patients.

The subgrouping of GBM as high and low ITGA5 mRNA- or protein-expressing tumors already showed a clear impact of this integrin on patient survival [19, 21, 26–28]. We used publically available TCGA datasets to investigate the distribution of ITGA5 mRNA in the GBM molecular subtypes and confirmed that it was mainly associated with the mesenchymal subgroup already shown to be the most aggressive and resistant to therapies (Fig. 1A). Concerning intra-tumoral heterogeneity the IVY database pointed to an enrichment of ITGA5

mRNA expression in spatially defined regions of GBM, perinecrotic zones and perivascular zones (Fig. 1B). Gene set enrichment analysis (GSEA) was used to investigate the relationship of ITGA5 overexpression with biological processes in GBM. Transcriptomic data of 538 patients obtained from GBM cohort of TCGA were divided into 'high' and 'low' groups based on their ITGA5 expression according to the median expression of this gene. Using the Hallmark gene set, 5 pathways were highlighted in the 'high' group with TGF β signaling at the top which we already described in GBM as associated with ITGA5 [31]. Hypoxia (NES = 1.82, FDR q = 0.039) and EMT (EMT - NES = 1.76, FDR q = 0.031) were also highlighted in this analysis (Fig. 1C). At the protein level, ITGA5 expression appeared heterogeneous between patients [28] but remarkably also in an intratumoral fashion (Fig 1D). As perinecrotic and perivascular zones are proposed as GSC niches [32], we aimed to evaluate the putative expression of ITGA5 in these cells.

Heterogeneity of ITGA5 expression in GSC *in vitro* and *in vivo*.

ITGA5 protein expression was evaluated in 6 stem cell lines. Few cell lines expressed it under normoxia conditions after neurosphere dissociation (Fig. 2A left). Interestingly, hypoxia is induced in neurospheres even if the microenvironment is normoxic, as shown by increased CA9, HIF-1α and HIF-2α expression, well-known hypoxia markers (Fig. 2A middle). Although CA9 and HIF-1α expression required the formation of neurospheres, HIF-2α is constitutively present in almost all lines, even in normoxia. These results confirm others as for example those obtained for neuroblastoma [33, 34]. These markers appeared similarly expressed after 6 days under hypoxic conditions (Fig. 2A, right). In this case, ITGA5 expression increased significantly in the two already positive cell lines (3731 and TC22), but the hypoxic microenvironment also leads to ITGA5 expression in the GSC line TC7 (Fig. 2A, right). Interestingly, we observe a strong expression of HIF-1α in ITGA5-negative lines compared to ITGA5-positive lines (Fig. 2A). Low levels of HIF-1α seem necessary for HIF-2α playing its role as a transcription factor. By cell immunofluorescence labeling with anti-ITGA5 antibodies, we confirmed the absence of ITGA5 expression in the 5706 cell line but expression in the TC22 cell line in normoxia. Interestingly, hypoxia increased ITGA5 in TC22 cells but in an heterogeneous manner with about 30% of cells clearly highly positive (Fig 2B). Integrin expression occurs as expected mainly at the cell membrane as shown by FACS analysis and subcellular fractionation (Fig. S1A and B).

GSC thus express differential levels of integrin α5 exacerbated by hypoxia. To confirm these *in vitro* data, we xenografted NCH421k and TC22 GSC lines (without or with ITGA5 *in vitro* expression respectively) in the brain of Nude mice. Brains were removed and labeled with hematoxylin eosin and anti-ITGA5 specific antibodies. As shown in figure 3A, NCH421k-derived tumors were small and devoid of ITGA5 labeling. By contrast, TC22-derived tumors were large and contained integrin-labeled tumor cells. GSC thus retained their capacity to express (or not) the integrin after *in vivo* implantation. We followed the growth behavior of the tumors by PET imaging using [^{18}F]-FLT, a marker of proliferation. Interestingly, TC22-derived tumors appeared more aggressive, rapidly growing and invading tumors (Fig. 3B) in relationships with poorer mice survival, (Fig. 3C) than NCH421k- derived tumors. Results were confirmed by another radiotracer [^{18}F]-FET (Fig. S2). Data suggest that molecular

heterogeneity in GSC detected in conditions recapitulates the GSC-induced tumor heterogeneity for ITGA5 we already observed in patient tumors [28].

Impact of HIF-1α and HIF-2α on ITGA5 expression.

As hypoxia pathways appeared to be linked to expression of the integrin subunit (Fig. 1 and 2), we aimed to analyze more deeply these relationships. It is already known that the stability of HIFs is finely regulated by different oxygen levels. HIF-1α is expressed at lower levels of hypoxia compared to HIF-2α which is already present in normoxic conditions and more stable than HIF-1α [34, 35]. Therefore, we evaluated the potential relationship between HIFs and ITGA5 expression at short time points (24, 48, and 72 hours) (Fig. 4A). HIF-1α and HIF-2α behave differently in these conditions. HIF-1α increased up to 48h of hypoxia followed by a marked decrease at 72h while HIF-2α increased gradually from 24 to 72h for all cell lines. Interestingly, the temporal ITGA5 expression followed that of HIF-2α in the positive cell lines (3731 and TC22). It should also be noted that in both cell lines, HIF-2α reached a level 2.5 times higher (at 72h) than that observed in normoxia, which is not the case for ITGA5 negative cells (NCH421k and NCH644) suggesting that an HIF-2α threshold may be involved in the sustained modulation of ITGA5 expression (Fig. 4A). Stabilization of HIFs may be obtained by chemical compounds such as cobalt chloride ($CoCl_2$) or desferrioxamine (DFO). Treatments with these compounds during 72h also allowed to increase in ITGA5 expression in the TC22 positive cell line but not in the NCH421k negative cell line corroborating the impact of HIFs in specific GSC lines (data not shown). Lastly, modulation of HIFs was checked in the TC22 cells cultured 3 days in hypoxia followed by 2 days in normoxia. Here again, HIF-1α appeared unstable and finely controlled with a rapid decrease in normoxic conditions in contrast with HIF-2α remaining expressed as is the case for ITGA5 (Fig. S3).
Taken together, these results suggest a potential impact of HIF-2α on the expression of ITGA5 in GSC under hypoxia. We confirmed this hypothesis by linear regression analysis between HIF-1α or HIF-2α and ITGA5 expressions. HIF-2α and ITGA5 levels significantly correlated in TC22 and 3731 cell lines in hypoxic conditions whereas it was not the case with HIF-1α. (Fig. 4B). HIF-2α and ITGA5 expressions appeared thus linked in hypoxic conditions.

HIF-2α is preferentially linked to ITGA5 expression.

We then aimed to clarify the role of HIF-1α and HIF-2α on ITGA5 expression in hypoxia. As a first attempt to selectively inhibit expression of HIF-1α, we used irinotecan, a topoisomerase 1 inhibitor, which was shown to alter the expression of HIF-1α by inhibiting its mRNA translation [36–38]. Integrin-positive TC22 cells were treated with 2.5 µM irinotecan for 72h in hypoxia 1% O_2. In our GSC model, irinotecan not only inhibited HIF-1α but also HIF-2α expression associated with a disappearance of ITGA5 expression (Fig. 5A). To address more specifically the impact of each transcription factor, we used specific siRNA depletion. As shown in Fig. 5B, HIF-1α-siRNA specifically depleted their target gene but had no effect on ITGA5. Inversely, HIF-2α-siRNA decreased HIF-2α expression (20%) and concomitantly ITGA5 by 30% (Fig. 5B).

Finally, we checked specific HIF-2α inhibitors : PT2977 [39] and compound 2 [40]. These molecules recognize the PAS-B domain of HIF-2α and prevent its dimerization with the nuclear subunit HIF1-β also called ARNT thus inhibiting HIF-2α transcriptional activity. As PAS-B domain present a specific pocket on HIF-2α and these compounds bind to this pocket, they are highly specific for the inhibition of HIF-2α function [40, 41]. Both compounds (20 μM) proved able to decrease ITGA5 mRNA after 24h and ITGA5 protein after 72h treatment. Compound 2 also decreased HIF-2α expression perhaps explaining its better effect on ITGA5 (44% decrease with compound 2 *versus* 19% with PT2977) (Fig. 5C). Results suggest that HIF-2α is preferentially involved in the control of ITGA5 modulation particularly under hypoxia in GSC.

HIF-2α and ITGA5 as therapeutic targets in specific GSC

Based on our previous results, we hypothesized that hypoxia may affect phenotypically GSC in particular through ITGA5-dependent pathways. We already have shown that this integrin is involved in migration and therapy resistance of differentiated GBM cells [16, 42, 43]. We now investigated if hypoxia-driven expression of the integrin may affect proliferation and/or migration of GSC. First, we assessed cell proliferation, with measure of the neurosphere size as a readout, using Incucyte® technology. As shown in Figure 6A, neurosphere sizes are not linked to enhanced expression of ITGA5. As for example TC22 (ITGA5+) and NCH644 (ITGA5-) cells have a larger sphere size after 6 days in normoxia compared to the other lines. Hypoxia only affected the neurosphere sizes of two cell lines, namely 3731 and NCH644 which respectively express or not the integrin as shown before (Fig. 6A). These data suggest that ITGA5 expression does not influence stem cell proliferation either in normoxia or in hypoxia.

As a confirmation, FR248, a specific antagonist of ITGA5, does not alter neurosphere sizes either in integrin–expressing (TC22) or in non–expressing cells (NCH421k) (Fig. 6B, light to dark orange bars). We then combined FR248 with compound 2 (20 μM) which is devoid of effect when used alone. Interestingly, the combination of FR248 (20 μM) and compound 2 (20 μM) decreased the neurosphere size in the ITGA5 positive line TC22 (58% decrease) but not in the ITGA5 negative line NCH421k (Fig. 6B, light to dark blue bars). Data suggest that dual inhibition of HIF-2α and ITGA5 affects the proliferation of ITGA5-positive GSC thus providing a new therapeutic combination.

We then investigated the impact of hypoxia on stem cell migration. Spheres formed by the inverted drop technique, either with NCH421k or TC22 cells, were deposited on poly-L-lysine (a neutral substrate for adhesion) or fibronectin (the ECM ligand of ITGA5). On poly-L-lysine no cell evasion was detectable for both cell lines. By contrast, on fibronectin, cell evasion occurred for the TC22 line (ITGA5 positive) but not detectable for the NCH421k line (ITGA5 negative). Moreover, hypoxia increased this cell evasion by 30 % in the former line presumably in relationship with the increase of ITGA5 expression (Fig. 6C). To confirm this hypothesis, the spheres were treated with FR248 (20 μM) which inhibited completely the cell capacity to evade from spheres and to migrate on fibronectin either in normoxia or in hypoxia. Data confirm the impact of this integrin on cell migration out of GSC spheres.

As Compound 2 decreased ITGA5 expression by more than 40% in TC22 cell line, we evaluated its effect on stem cell migration. Interestingly, compound 2 proved able to inhibit the cell evasion and migration in hypoxia suggesting here again the interconnection between HIF-2α and ITGA5. By contrast, PT2977 did not alter cell evasion (Fig. 6D) presumably linked to its weaker capacity to decrease both HIF2α and ITGA5 expressions in the TC22 line (see Fig. 5C).

Together, these results show for the first time that combining HIF2α and ITGA5 inhibition may be an alternative therapy for GSC. In addition, data show that stem cell migration on fibronectin is dependent on ITGA5 expression as was previously demonstrated on differentiated tumoral cells. This migration is enhanced by hypoxia and HIF-2α expression specifically. These data suggest that some GSC in hypoxic niches would acquire a migratory phenotype through modulation of the integrin expression.

AHR expression is inversely correlated to HIF-2α and ITGA5 expressions in GSC

To be transcriptionally functional HIF-2α needs to heterodimerize with HIF1β/ARNT in the cell nucleus. ARNT (aryl hydrocarbon receptor nuclear translocator) also dimerizes with AHR (aryl hydrocarbon receptor). AHR plays complex roles in tumors including GBM [44] and has recently being described as a tumor suppressor-like gene in GBM whose repression induced migration and ITGA5 expression [45]. We wondered if AHR may affect the HIF-2α/ITGA5 axis in our models. AHR is strongly expressed in ITGA5 negative cell lines (NCH644, 5706, TC7) but less expressed in ITGA5 positive cells (3731, TC22) as shown by western blot (Figure 7A) and immunohistochemistry (Figure 7B). We wondered first if AHR antagonist (BAY218) may affect ITGA5 expression, but we did not observe any effect (data not shown). Following ligand binding, AHR protein is rapidly downregulated to regulate downstream signaling pathways [46]. We exploited this characteristic by subjecting TC22 and 3731 cells to the AHR agonist (compound 12a) during 72 hours in hypoxia. In these conditions, AHR protein decreased drastically compared to control and concomitantly ITGA5 increased in both cell lines. Data suggest that HIF-2α and AHR expression levels are inversely linked to ITGA5 induction.

Discussion

Integrins are implicated in different hallmarks of cancer as reviewed recently [16, 47–49]. Blocking their functions or inhibiting their expressions have been extensively studied in preclinical studies with encouraging results. Clinical trials however failed to demonstrate integrin inhibitors efficacy in different solid tumors including GBM [50]. Among others, lack of knowledge on the heterogeneity of integrin expressions in the tumor of patients may be involved in these clinical failures.

Concerning more particularly the ITGA5, its role in human cancer has been reviewed in [51]. Data confirm its role as a prognostic biomarker in solid tumors as for examples in laryngeal [52], head and neack [53], or oesophageal squamous cell carcinoma [54]. ITGA5 mediates tumor-stroma crosstalk to promote dissemination, metastasis and angiogenesis in liver, gastric, breast or pancreatic cancers [55–59]. In GBM, ITGA5 has been included in the mesenchymal subtype signature provided in the Verhaak classification [5]. Interestingly, its

prognostic and therapeutic value has been confirmed in a recent publication which also demonstrated an impact of a high integrin expression on the tumor immune microenvironment [60]. Despite all the preclinical and clinical evidence that ITGA5 may be considered as a therapeutic target, clinical trials with Volociximab (a humanized anti-α5 antibody) failed [61]. We have shown previously that TMZ chemotherapy greatly affected the integrin repertoire in GBM cells [42] suggesting that anti-integrin therapies must be adjusted to the right patient but also to the right tumor progression time. In this work, we address more particularly the question of integrin expression in glioma stem cells submitted to hypoxia as experienced in hypoxic tumor niches.

To better understand the pattern of ITGA5 expression in GBM, we analyzed patient data and found that high integrin expressing tumors were correlated with exacerbated hypoxia pathway. Hypoxia is already known to maintain a GSC phenotype, to regulate their tumorigenic capacity and to initiate a mesenchymal switch [62–64]. We therefore focused on ITGA5 expression in GSC assuming that they are at the apex of tumor development and presumably at the origin of integrin expression heterogeneity. Our data confirm that not all GSC express ITGA5 and that hypoxia enhances it in selected cell lines. Results are in line with data showing a selective impact of hypoxia on the modulation of ITGA5 expression in breast cancer [65]. The hypoxic pathway is regulated by an induction of hypoxia-induced transcription factors, HIF-1α and HIF-2α. Both HIFs bind to a consensus HIF-binding site on the ITGA5 gene promoter in breast cancer cells and both are involved in ITGA5 mRNA and protein expression in these tumors [65]. However, HIF-2α plays specific oncogenic roles in tumors [66] and particularly in GBM where it appears as a key regulator in the hypoxic niche to maintain GSC stemness [67]. Our results are in line with HIF-2α controlling ECM-GSC interactions through modulation of ITGA5 expression and ITGA5-dependent cell migration. Targeting hypoxia became an interesting way to fight hypoxic tumors such as brain tumors and specific HIFs inhibitors were developed. We focused on HIF-2α selective inhibitors in our study : PT2977 and compound 2. This later molecule was one of the first small molecule designed in the field [40]. It binds only to the PAS-B domain (Per-ARNT-Sim-B) of HIF-2α thanks to the existence of a specific druggable pocket [40]. It prevents the HIF-2α / ARNT dimerization and transcription of HIF-2α target genes. PT2977 (Belzutifan) is a second-generation inhibitor that [39, 68, 69] was approved by the Food and Drug Administration (FDA) in 2021 for the treatment of Von Hippel-Lindau disease (VHL) in patients with renal cell carcinoma, central nervous system hemangioblastoma and pancreatic neuroendocrine tumors [70]. HIF-2α inhibitors were able to decrease ITGA5 expression and to inhibit GSC migration without affecting cell proliferation. Interestingly, combination of HIF-2α inhibitor with ITGA5 antagonist results in a strong anti-proliferative effect in hypoxia sensitive ITGA5 expressing cell lines. This new therapy combination may concern subclasses of GB patient tumors and particularly GSC in hypoxic niches and deserves further preclinical studies.
HIF-2α stabilization in hypoxia is however noted in all stem cell lines studied here even if levels of HIF-2α varied between different cell lines and do not always trigger ITGA5 expression. Crosstalk between HIFs and AHR has been highlighted recently. Both are members of bHLH-PAS family of transcription factors sharing similar DNA-binding motifs

and heterodimerization with HIF1β/ARNT subunit. Stoichiometry differences in the two transcription factors are implicated in the competition for HIF1β/ARNT and crosstalk directionality in kidney carcinoma [71]. Our results are in line with this competition for the induction of ITGA5 protein but do not exclude other indirect pathways. In fact, in our hands blocking AHR transcriptional activity by antagonists did not affect ITGA5 nor AHR expressions (data not shown) whereas AHR agonist-induced activation led to AHR decrease and ITGA5 increase. Data confirm previous work in GBM cells where it was shown that AHR silencing impact positively ITGA5 expression and cell migration [45]. The role of AHR in tumors including GBM is however controversial with AHR activation related to bad prognostic [72–74] or AHR presumed to be a tumor suppressor [45, 75]. According to our results we propose a new role of AHR as a modulator of protumoral targets, such as ITGA5, in some GSC and in specific conditions. Crosstalk mechanisms between AHR and HIF-2α have to be finely characterized in the future.

Notably, our study provides novel insight into one of the mechanism by which a GBM therapeutic target, the integrin ITGA5, may be differentially expressed in some glioma stem cells and modulated in specific tumor area. Overexpression of this target confers migration advantages presumably implicated in brain dissemination of tumor cells. Targeting both HIF-2α and ITGA5 may be considered as a therapeutic option which deserves further studies in the future.

Funding

This project has received financial support from the CNRS through the 80|Prime program to support the PhD of Messe M., from Institut National du Cancer (INCA PLBIO 11527) and from ITI INNOVEC (IdEx (ANR-10-IDEX-0002), SFRI (ANR-20-SFRI-0012)).

Acknowledgements

The experimental help of Bruno Jessel for PET experiences is highly acknowledged and the CYRCé plateform.

Conflicts of Interest: The authors have no conflict of interest to declare.

References

1. Nutt CL, Mani DR, Betensky RA, et al (2003) Gene expression-based classification of malignant gliomas correlates better with survival than histological classification. Cancer Res 63:1602–1607
2. Cancer Genome Atlas Research Network (2008) Comprehensive genomic characterization defines human glioblastoma genes and core pathways. Nature 455:1061–1068. https://doi.org/10.1038/nature07385
3. Brennan CW, Verhaak RGW, McKenna A, et al (2013) The Somatic Genomic Landscape of Glioblastoma. Cell 155:462–477. https://doi.org/10.1016/j.cell.2013.09.034
4. Phillips HS, Kharbanda S, Chen R, et al (2006) Molecular subclasses of high-grade glioma predict prognosis, delineate a pattern of disease progression, and resemble stages in neurogenesis. Cancer Cell 9:157–173. https://doi.org/10.1016/j.ccr.2006.02.019
5. Verhaak RGW, Hoadley KA, Purdom E, et al (2010) Integrated genomic analysis

identifies clinically relevant subtypes of glioblastoma characterized by abnormalities in PDGFRA, IDH1, EGFR, and NF1. Cancer Cell 17:98–110. https://doi.org/10.1016/j.ccr.2009.12.020
6. Wang Q, Hu B, Hu X, et al (2017) Tumor Evolution of Glioma-Intrinsic Gene Expression Subtypes Associates with Immunological Changes in the Microenvironment. Cancer Cell 32:42-56.e6. https://doi.org/10.1016/j.ccell.2017.06.003
7. Neftel C, Laffy J, Filbin MG, et al (2019) An Integrative Model of Cellular States, Plasticity, and Genetics for Glioblastoma. Cell 178:835-849.e21. https://doi.org/10.1016/j.cell.2019.06.024
8. Patel AP, Tirosh I, Trombetta JJ, et al (2014) Single-cell RNA-seq highlights intratumoral heterogeneity in primary glioblastoma. Science 344:1396–1401. https://doi.org/10.1126/science.1254257
9. Dirkse A, Golebiewska A, Buder T, et al (2019) Stem cell-associated heterogeneity in Glioblastoma results from intrinsic tumor plasticity shaped by the microenvironment. Nat Commun 10:1787. https://doi.org/10.1038/s41467-019-09853-z
10. Mitchell K, Troike K, Silver DJ, Lathia JD (2021) The evolution of the cancer stem cell state in glioblastoma: emerging insights into the next generation of functional interactions. Neuro Oncol 23:199–213. https://doi.org/10.1093/neuonc/noaa259
11. Innes JA, Lowe AS, Fonseca R, et al (2022) Phenotyping clonal populations of glioma stem cell reveals a high degree of plasticity in response to changes of microenvironment. Lab Invest 102:172–184. https://doi.org/10.1038/s41374-021-00695-2
12. Jackson M, Hassiotou F, Nowak A (2015) Glioblastoma stem-like cells: at the root of tumor recurrence and a therapeutic target. Carcinogenesis 36:177–185. https://doi.org/10.1093/carcin/bgu243
13. Bhat KPL, Balasubramaniyan V, Vaillant B, et al (2013) Mesenchymal differentiation mediated by NF-κB promotes radiation resistance in glioblastoma. Cancer Cell 24:331–346. https://doi.org/10.1016/j.ccr.2013.08.001
14. Stieber D, Golebiewska A, Evers L, et al (2014) Glioblastomas are composed of genetically divergent clones with distinct tumourigenic potential and variable stem cell-associated phenotypes. Acta Neuropathol 127:203–219. https://doi.org/10.1007/s00401-013-1196-4
15. Idbaih A (2017) Structural and functional intratumor heterogeneities in glioblastoma: a spacetime odyssey at single-cell level. Ann Oncol 28:1415–1417. https://doi.org/10.1093/annonc/mdx217
16. Blandin A-F, Noulet F, Renner G, et al (2016) Glioma cell dispersion is driven by α5 integrin-mediated cell-matrix and cell-cell interactions. Cancer Lett 376:328–338. https://doi.org/10.1016/j.canlet.2016.04.007
17. Seguin L, Desgrosellier JS, Weis SM, Cheresh DA (2015) Integrins and cancer: regulators of cancer stemness, metastasis, and drug resistance. Trends Cell Biol 25:234–240. https://doi.org/10.1016/j.tcb.2014.12.006
18. Schaffner F, Ray AM, Dontenwill M (2013) Integrin α5β1, the Fibronectin Receptor, as a Pertinent Therapeutic Target in Solid Tumors. Cancers (Basel) 5:27–47. https://doi.org/10.3390/cancers5010027
19. Malric L, Monferran S, Gilhodes J, et al (2017) Interest of integrins targeting in glioblastoma according to tumor heterogeneity and cancer stem cell paradigm: an update. Oncotarget 8:86947–86968. https://doi.org/10.18632/oncotarget.20372
20. Lathia JD, Gallagher J, Heddleston JM, et al (2010) Integrin alpha 6 regulates glioblastoma stem cells. Cell Stem Cell 6:421–432. https://doi.org/10.1016/j.stem.2010.02.018
21. Lathia JD, Li M, Sinyuk M, et al (2014) High-throughput flow cytometry screening

reveals a role for junctional adhesion molecule a as a cancer stem cell maintenance factor. Cell Rep 6:117–129. https://doi.org/10.1016/j.celrep.2013.11.043
22. Nakada M, Nambu E, Furuyama N, et al (2013) Integrin α3 is overexpressed in glioma stem-like cells and promotes invasion. Br J Cancer 108:2516–2524. https://doi.org/10.1038/bjc.2013.218
23. Haas TL, Sciuto MR, Brunetto L, et al (2017) Integrin α7 Is a Functional Marker and Potential Therapeutic Target in Glioblastoma. Cell Stem Cell 21:35-50.e9. https://doi.org/10.1016/j.stem.2017.04.009
24. Guerrero PA, Tchaicha JH, Chen Z, et al (2017) Glioblastoma stem cells exploit the αvβ8 integrin-TGFβ1 signaling axis to drive tumor initiation and progression. Oncogene 36:6568–6580. https://doi.org/10.1038/onc.2017.248
25. Malric L, Monferran S, Delmas C, et al (2019) Inhibiting Integrin β8 to Differentiate and Radiosensitize Glioblastoma-Initiating Cells. Mol Cancer Res 17:384–397. https://doi.org/10.1158/1541-7786.MCR-18-0386
26. Janouskova H, Maglott A, Leger DY, et al (2012) Integrin α5β1 plays a critical role in resistance to temozolomide by interfering with the p53 pathway in high-grade glioma. Cancer Res 72:3463–3470. https://doi.org/10.1158/0008-5472.CAN-11-4199
27. Holmes RS, Rout UK (2011) Comparative studies of vertebrate Beta integrin genes and proteins: ancient genes in vertebrate evolution. Biomolecules 1:3–31. https://doi.org/10.3390/biom1010003
28. Etienne-Selloum N, Prades J, Bello-Roufai D, et al (2021) Expression Analysis of α5 Integrin Subunit Reveals Its Upregulation as a Negative Prognostic Biomarker for Glioblastoma. Pharmaceuticals (Basel) 14:882. https://doi.org/10.3390/ph14090882
29. Subramanian A, Tamayo P, Mootha VK, et al (2005) Gene set enrichment analysis: a knowledge-based approach for interpreting genome-wide expression profiles. Proc Natl Acad Sci U S A 102:15545–15550. https://doi.org/10.1073/pnas.0506580102
30. Liberzon A, Birger C, Thorvaldsdóttir H, et al (2015) The Molecular Signatures Database (MSigDB) hallmark gene set collection. Cell Syst 1:417–425. https://doi.org/10.1016/j.cels.2015.12.004
31. Cosset EC, Godet J, Entz-Werlé N, et al (2012) Involvement of the TGFβ pathway in the regulation of α5 β1 integrins by caveolin-1 in human glioblastoma. Int J Cancer 131:601–611. https://doi.org/10.1002/ijc.26415
32. Lathia JD, Heddleston JM, Venere M, Rich JN (2011) Deadly teamwork: neural cancer stem cells and the tumor microenvironment. Cell Stem Cell 8:482–485. https://doi.org/10.1016/j.stem.2011.04.013
33. Mohlin S, Hamidian A, von Stedingk K, et al (2015) PI3K-mTORC2 but not PI3K-mTORC1 regulates transcription of HIF2A/EPAS1 and vascularization in neuroblastoma. Cancer Res 75:4617–4628. https://doi.org/10.1158/0008-5472.CAN-15-0708
34. Holmquist-Mengelbier L, Fredlund E, Löfstedt T, et al (2006) Recruitment of HIF-1alpha and HIF-2alpha to common target genes is differentially regulated in neuroblastoma: HIF-2alpha promotes an aggressive phenotype. Cancer Cell 10:413–423. https://doi.org/10.1016/j.ccr.2006.08.026
35. Pietras A, Gisselsson D, Ora I, et al (2008) High levels of HIF-2alpha highlight an immature neural crest-like neuroblastoma cell cohort located in a perivascular niche. J Pathol 214:482–488. https://doi.org/10.1002/path.2304
36. Kummar S, Raffeld M, Juwara L, et al (2011) Multihistology, target-driven pilot trial of oral topotecan as an inhibitor of hypoxia-inducible factor-1α in advanced solid tumors. Clin Cancer Res 17:5123–5131. https://doi.org/10.1158/1078-0432.CCR-11-0682
37. Nguyen A, Moussalieh FM, Mackay A, et al (2017) Characterization of the transcriptional and metabolic responses of pediatric high grade gliomas to mTOR-HIF-1α axis

inhibition. Oncotarget 8:71597–71617. https://doi.org/10.18632/oncotarget.16500
38. Guérin E, Raffelsberger W, Pencreach E, et al (2012) In vivo topoisomerase I inhibition attenuates the expression of hypoxia-inducible factor 1α target genes and decreases tumor angiogenesis. Mol Med 18:83–94. https://doi.org/10.2119/molmed.2011.00120
39. Xu R, Wang K, Rizzi JP, et al (2019) 3-[(1S,2S,3R)-2,3-Difluoro-1-hydroxy-7-methylsulfonylindan-4-yl]oxy-5-fluorobenzonitrile (PT2977), a Hypoxia-Inducible Factor 2α (HIF-2α) Inhibitor for the Treatment of Clear Cell Renal Cell Carcinoma. J Med Chem 62:6876–6893. https://doi.org/10.1021/acs.jmedchem.9b00719
40. Scheuermann TH, Li Q, Ma H-W, et al (2013) Allosteric inhibition of hypoxia inducible factor-2 with small molecules. Nat Chem Biol 9:271–276. https://doi.org/10.1038/nchembio.1185
41. Scheuermann TH, Stroud D, Sleet CE, et al (2015) Isoform-Selective and Stereoselective Inhibition of Hypoxia Inducible Factor-2. J Med Chem 58:5930–5941. https://doi.org/10.1021/acs.jmedchem.5b00529
42. Sani S, Pallaoro N, Messe M, et al (2022) Temozolomide-Acquired Resistance Is Associated with Modulation of the Integrin Repertoire in Glioblastoma, Impact of α5β1 Integrin. Cancers (Basel) 14:369. https://doi.org/10.3390/cancers14020369
43. Renner G, Noulet F, Mercier M-C, et al (2016) Expression/activation of α5β1 integrin is linked to the β-catenin signaling pathway to drive migration in glioma cells. Oncotarget 7:62194–62207. https://doi.org/10.18632/oncotarget.11552
44. Lim TX, Ahamed M, Reutens DC (2022) The aryl hydrocarbon receptor: A diagnostic and therapeutic target in glioma. Drug Discov Today 27:422–435. https://doi.org/10.1016/j.drudis.2021.09.021
45. Jin U-H, Karki K, Cheng Y, et al (2019) The aryl hydrocarbon receptor is a tumor suppressor-like gene in glioblastoma. J Biol Chem 294:11342–11353. https://doi.org/10.1074/jbc.RA119.008882
46. Pollenz RS (2002) The mechanism of AH receptor protein down-regulation (degradation) and its impact on AH receptor-mediated gene regulation. Chem Biol Interact 141:41–61. https://doi.org/10.1016/s0009-2797(02)00065-0
47. Hamidi H, Ivaska J (2018) Every step of the way: integrins in cancer progression and metastasis. Nat Rev Cancer 18:533–548. https://doi.org/10.1038/s41568-018-0038-z
48. Bergonzini C, Kroese K, Zweemer AJM, Danen EHJ (2022) Targeting Integrins for Cancer Therapy - Disappointments and Opportunities. Front Cell Dev Biol 10:863850. https://doi.org/10.3389/fcell.2022.863850
49. Hanahan D (2022) Hallmarks of Cancer: New Dimensions. Cancer Discov 12:31–46. https://doi.org/10.1158/2159-8290.CD-21-1059
50. Cruz Da Silva E, Mercier M-C, Etienne-Selloum N, et al (2021) A Systematic Review of Glioblastoma-Targeted Therapies in Phases II, III, IV Clinical Trials. Cancers (Basel) 13:1795. https://doi.org/10.3390/cancers13081795
51. Hou J, Yan D, Liu Y, et al (2020) The Roles of Integrin α5β1 in Human Cancer. Onco Targets Ther 13:13329–13344. https://doi.org/10.2147/OTT.S273803
52. Zhou C, Shen Y, Wei Z, et al (2022) ITGA5 is an independent prognostic biomarker and potential therapeutic target for laryngeal squamous cell carcinoma. J Clin Lab Anal 36:e24228. https://doi.org/10.1002/jcla.24228
53. Zou B, Wang D, Xu K, et al (2019) Integrin α-5 as a potential biomarker of head and neck squamous cell carcinoma. Oncol Lett 18:4048–4055. https://doi.org/10.3892/ol.2019.10773
54. Xie J-J, Guo J-C, Wu Z-Y, et al (2016) Integrin α5 promotes tumor progression and is an independent unfavorable prognostic factor in esophageal squamous cell carcinoma. Hum Pathol 48:69–75. https://doi.org/10.1016/j.humpath.2015.09.029

55. Miyamoto S, Nagano Y, Miyazaki M, et al (2022) Integrin α5 mediates cancer cell-fibroblast adhesion and peritoneal dissemination of diffuse-type gastric carcinoma. Cancer Lett 526:335–345. https://doi.org/10.1016/j.canlet.2021.11.008
56. Peng Z, Hao M, Tong H, et al (2022) The interactions between integrin α5β1 of liver cancer cells and fibronectin of fibroblasts promote tumor growth and angiogenesis. Int J Biol Sci 18:5019–5037. https://doi.org/10.7150/ijbs.72367
57. Pantano F, Croset M, Driouch K, et al (2021) Integrin alpha5 in human breast cancer is a mediator of bone metastasis and a therapeutic target for the treatment of osteolytic lesions. Oncogene 40:1284–1299. https://doi.org/10.1038/s41388-020-01603-6
58. Kuninty PR, Bansal R, De Geus SWL, et al (2019) ITGA5 inhibition in pancreatic stellate cells attenuates desmoplasia and potentiates efficacy of chemotherapy in pancreatic cancer. Sci Adv 5:eaax2770. https://doi.org/10.1126/sciadv.aax2770
59. Wang T, Yang J, Mao J, et al (2022) ITGA5 inhibition in pancreatic stellate cells re-educates the in vitro tumor-stromal crosstalk. Med Oncol 40:39. https://doi.org/10.1007/s12032-022-01902-w
60. Li S, Zhang N, Liu S, et al (2022) ITGA5 Is a Novel Oncogenic Biomarker and Correlates With Tumor Immune Microenvironment in Gliomas. Front Oncol 12:844144. https://doi.org/10.3389/fonc.2022.844144
61. Bell-McGuinn KM, Matthews CM, Ho SN, et al (2011) A phase II, single-arm study of the anti-α5β1 integrin antibody volociximab as monotherapy in patients with platinum-resistant advanced epithelial ovarian or primary peritoneal cancer. Gynecol Oncol 121:273–279. https://doi.org/10.1016/j.ygyno.2010.12.362
62. Li Z, Bao S, Wu Q, et al (2009) Hypoxia-inducible factors regulate tumorigenic capacity of glioma stem cells. Cancer Cell 15:501–513. https://doi.org/10.1016/j.ccr.2009.03.018
63. Boyd NH, Tran AN, Bernstock JD, et al (2021) Glioma stem cells and their roles within the hypoxic tumor microenvironment. Theranostics 11:665–683. https://doi.org/10.7150/thno.41692
64. Cooper LAD, Gutman DA, Chisolm C, et al (2012) The tumor microenvironment strongly impacts master transcriptional regulators and gene expression class of glioblastoma. Am J Pathol 180:2108–2119. https://doi.org/10.1016/j.ajpath.2012.01.040
65. Ju JA, Godet I, Ye IC, et al (2017) Hypoxia Selectively Enhances Integrin α5β1 Receptor Expression in Breast Cancer to Promote Metastasis. Mol Cancer Res 15:723–734. https://doi.org/10.1158/1541-7786.MCR-16-0338
66. Franovic A, Holterman CE, Payette J, Lee S (2009) Human cancers converge at the HIF-2alpha oncogenic axis. Proc Natl Acad Sci U S A 106:21306–21311. https://doi.org/10.1073/pnas.0906432106
67. Seidel S, Garvalov BK, Wirta V, et al (2010) A hypoxic niche regulates glioblastoma stem cells through hypoxia inducible factor 2α. Brain 133:983–995. https://doi.org/10.1093/brain/awq042
68. Jonasch E, Plimack ER, Bauer T, et al (2019) 911PD - A first-in-human phase I/II trial of the oral HIF-2a inhibitor PT2977 in patients with advanced RCC. Annals of Oncology 30:v361–v362. https://doi.org/10.1093/annonc/mdz249.010
69. Choi WW, Boland JL, Kalola A, Lin J (2023) Belzutifan (MK-6482): Biology and Clinical Development in Solid Tumors. Curr Oncol Rep. https://doi.org/10.1007/s11912-022-01354-5
70. Deeks ED (2021) Belzutifan: First Approval. Drugs 81:1921–1927. https://doi.org/10.1007/s40265-021-01606-x
71. Lafleur VN, Halim S, Choudhry H, et al (2023) Multi-level interaction between HIF and AHR transcriptional pathways in kidney carcinoma. Life Sci Alliance 6:e202201756.

https://doi.org/10.26508/lsa.202201756
72. Sadik A, Somarribas Patterson LF, Öztürk S, et al (2020) IL4I1 Is a Metabolic Immune Checkpoint that Activates the AHR and Promotes Tumor Progression. Cell 182:1252-1270.e34. https://doi.org/10.1016/j.cell.2020.07.038
73. Panitz V, Končarević S, Sadik A, et al (2021) Tryptophan metabolism is inversely regulated in the tumor and blood of patients with glioblastoma. Theranostics 11:9217–9233. https://doi.org/10.7150/thno.60679
74. Leclerc D, Staats Pires AC, Guillemin GJ, Gilot D (2021) Detrimental activation of AhR pathway in cancer: an overview of therapeutic strategies. Curr Opin Immunol 70:15–26. https://doi.org/10.1016/j.coi.2020.12.003
75. Mavingire N, Campbell P, Liu T, et al (2022) Aminoflavone upregulates putative tumor suppressor miR-125b-2-3p to inhibit luminal A breast cancer stem cell-like properties. Precis Clin Med 5:pbac008. https://doi.org/10.1093/pcmedi/pbac008

Figure legends

Figure 1: ITGA5 expression is linked to hypoxia and Epithelial to Mesenchymal transition (**EMT) in glioblastoma (GBM) patients.**
A - Analysis of the mRNA level of ITGA5 in different GBM molecular subtypes with the TCGA database. B – IVY database analysis of ITGA5 mRNA level in intratumoral regions of GB. C – Gene set enrichment analysis (GSEA) showing the 5 top enriched biological pathways in TCGA tumors expressing high level of ITGA5 mRNA. GSEA of Hallmark Hypoxia and EMT gene sets to high expression of ITGA5 in TCGA GBM cohorts, along with normalized enrichment score (NES) and false discovery rate (FDR). D - Quantification ITGA5 protein expression level in GBM. Representative cases of immunostaining of ITGA5 intratumoral heterogeneity (magnification 40X).

Figure 2: ITGA5 protein expression in GBM stem cells in relationship with hypoxia.
A - Western blot analysis of ITGA5 and hypoxia markers (HIF-1α, HIF-2α, CA9) in 6 GBM stem cell lines after 6 days in culture. Tubulin was used as a housekeeping protein. Histograms represent the mean ± S.E.M of 3 independent experiments. Light grey bars represent dissociated neurospheres in normoxia, dark grey bars neurospheres in normoxia and red bars neurospheres in hypoxia. *p < 0.05; **p < 0.01; ***p < 0.005. B - Immunofluorescent labeling of ITGA5 under normoxia (20% O_2) and hypoxia (1% O_2) in 5706 stem cell line and TC22 stem cell line.

Figure 3: ITGA5 expression after GSC xenografts in Nude mice.
A - Hematoxylin-eosin staining and ITGA5 immunofluorescent labeling of brain sections after injection of TC22 and NCH421k GBM stem cell lines. B - Tumor growth monitoring with [^{18}F]-FLT. 2D frontal section images of mice and graphical representation of tumor volume quantification at 40% Standardized Uptake Value (SUV) as a function of time post-injection. The white arrows indicate the tumors. C - Survival curve analysis from mice implanted intracranially with TC22 (n=10 independent mice) and NCH421k cells (n=9 independent mice). Survival analysis was performed using a Kaplan-Meier plot.

Figure 4: Kinetic of HIF-1α, HIF-2α and ITGA5 expressions in GSC cells.
A - Western blot analysis of ITGA5 and hypoxia-induced factors, HIF-1**α** and HIF-2**α** expressions at 24, 48 and 72 hours of culture in indicated conditions. The relative quantification of each protein was performed according to the expression of tubulin. Histograms represent the mean ± S.E.M of 3 independent experiments with *p < 0.05; **p < 0.01; ***p < 0.005. Grey bars represent control conditions in normoxia and red bars neurospheres after 24, 48 and 72 hours of culture in hypoxia. B - Linear regression analysis of HIF-1α or HIF-2α versus ITGA5 expression by Prism software.

Figure 5: Role of HIF-1α and HIF-2α in the expression of ITGA5 in GBM TC22 stem cells in hypoxic conditions.

A - Western blot analysis of the effect of irinotecan treatment on the expression of hypoxia-induced factors and ITGA5. TC22 stem cells were treated with 2,5 μM irinotecan for 72 h in 1% O_2 hypoxia. The relative quantifications of each protein were performed according to the expression of tubulin. Histograms represent the mean ± S.E.M of 3 independent experiments with *p < 0.05; **p < 0.01; ***p < 0.005. Grey bars represent control conditions in normoxia and red bars neurospheres after 72 hours in hypoxia. B - Western blot analysis of the impact of siRNAs directed against HIF-1**α** or HIF-2**α** on ITGA5 expression. TC22 stem cells were treated with 100 nM HIF-1**α** siRNA or 250 nM HIF-2**α** siRNA for 48 h in 1% O_2 hypoxia. Relative quantifications of protein expressions were performed according to the expression of tubulin. C - Analysis of the effect of treatments with specific HIF-2**α** antagonists on ITGA5 expression. Cells were treated with 20μM PT2977 or 20μM Compound 2 for 24h (RT-qPCR analysis-left panel) or 72h (WB analysis- middle and right panels) in 1% O_2 hypoxia. Relative quantifications of the different expressions were performed based on the expression of RNA18S (RT-qPCR) or tubulin (WB). Histograms represent the mean ± S.E.M of 3 independent experiments with *p < 0.05; **p < 0.01; ***p < 0.005. Grey bars represent control conditions in normoxia and red bars neurospheres in hypoxia.

Figure 6: Impact of hypoxia and ITGA5 in GSC proliferation and migration.

A - Stem cell proliferation recorded as the neurosphere sizes by Incucyte technology. The graphs represent the fold increase versus time 0 in the size of the spheres at 144h (D6) in normoxia 20% O_2 or in hypoxia 1% O_2. Normoxia data in gray, hypoxia data in red for **α**5+ integrin lines and in blue for **α**5- integrin lines. B - Evaluation of the inhibition of ITGA5 by FR248 antagonist or HIF-2**α** by compound 2 inhibitor or both on neurosphere sizes recorded by Incucyte technology. The graph represents the size of the spheres at 144h (D6) relative to time of plating. C - Impact of ITGA5 expression on cell migration. Sphere formed for 48 hours in methylcellulose were deposited either on poly-L-lysine or on fibronectin and treated or not with ITGA5 antagonist FR248 (20 μM) in normoxia or hypoxia. Histograms represent the number of cells migrating out of the TC22 spheres after 24 hours either in normoxia or in hypoxia. D - Impact of the inhibition of HIF-2**α** on stem cell migration. Similar protocol as in B on fibronectin. PT2977 and compound 2 were applied at 20μM. Data represent the mean ± S.E.M of 4 independent experiments with *p < 0.05; **p < 0.01; ***p < 0.005; ns = non-significant.

Figure 7: AHR is inversely linked to HIF-2α for ITGA5 expression.

A - Western blot analysis of AHR and ITGA5 expressions in the 6 stem cell lines after 6 days in hypoxia**.** B. Immunochemical staining of ITGA5 and AHR in 5706 and TC22 plated on polylysine and left 3 days in hypoxia 1% O_2. Nucleus staining with DAPI. C – TC22 and 3731 cell lines were treated with compound 12a at 20μM, an agonist of AHR during 3 days in hypoxia and subjected to western blot analysis of AHR and ITGA5. Histograms represent the mean ±SEM of 3 independent experiments of the fold increase in proteins compared with the cells in normoxia.

Supplemental figure 1: FACS and subcellular fractionation analysis of ITGA5 expression in GSC (related to Figure 2).

A - FACS analysis of ITGA5 expression in two GBM stem cell lines, 5706 and TC22. In blue, ITGA5-negative stem cells and in red, ITGA5-positive stem cells. B – Subcellular fractionation of stem cell extracts and western blot analysis of ITGA5. Each subcellular fraction was identified by specific markers.

Supplemental figure 2: Evaluation of tumor growth *in vivo* with [^{18}F]-FET.

Monitoring tumor progression with [^{18}F]-FET. 3D-MIP (maximum intensity projection) frontal view of mice obtained during PET imaging sessions. White arrows indicate the tumors.

Supplemental figure 3: Persistence of ITGA5 and HIF-2α in cells submitted to normoxia after hypoxia.

Western blot analysis of ITGA5 and hypoxia-induced factors expression during 24, 48 and 72 hours in hypoxia followed by 24 or 48 hours in normoxia. Relative quantifications of ITGA5 expression were calculated according to tubulin expression. Histograms represent the mean ± S.E.M of 3 independent experiments with *$p < 0.05$; **$p < 0.01$; ***$p < 0.005$; ns = non-significant. Fold increase of ITGA5 protein level is shown *versus* the level in normoxia prior hypoxia.

A

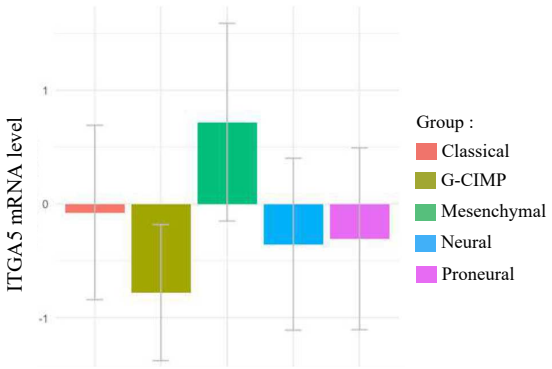

B

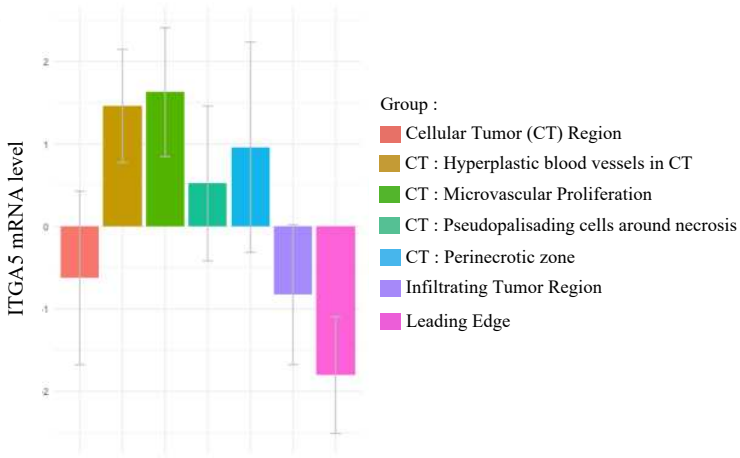

C

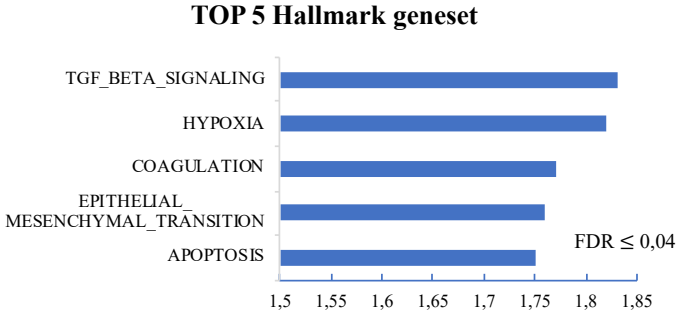

Enrichment plot :
Hallmark Hypoxia

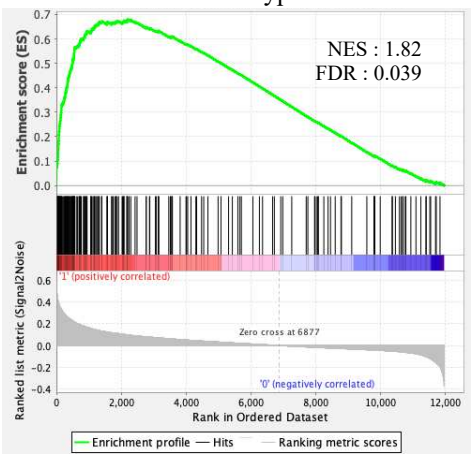

Enrichment plot :
Hallmark Epithelial Mesenchymal Transition

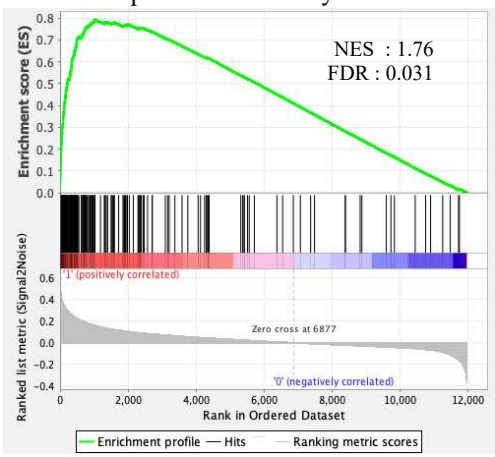

D

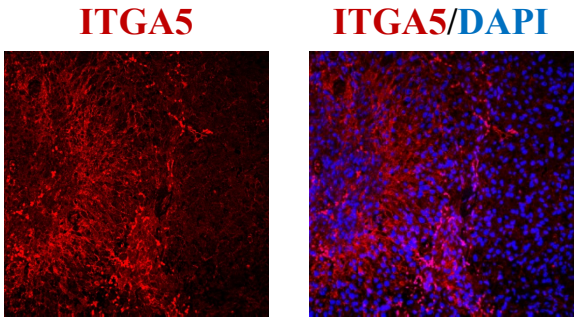

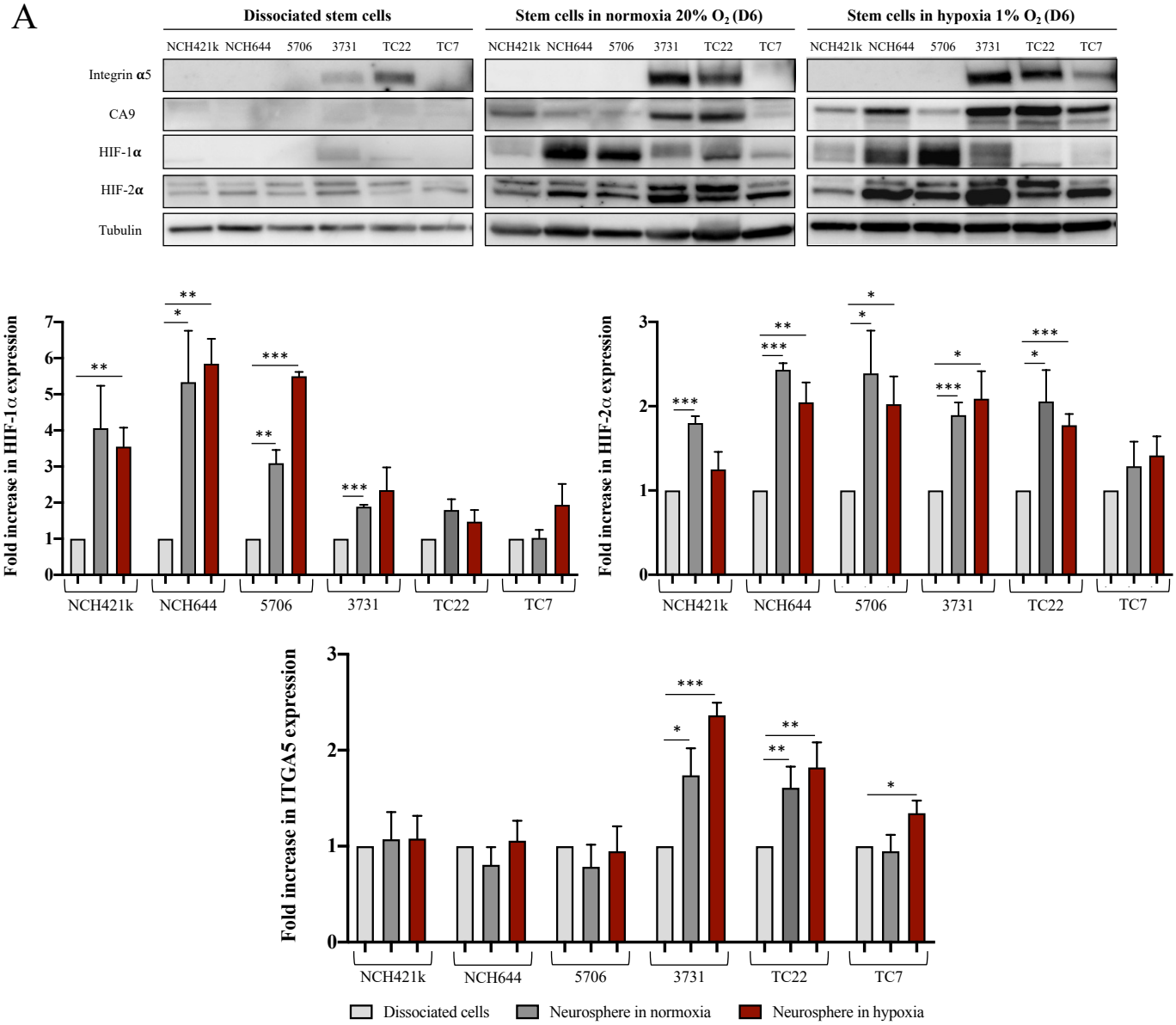
A
Dissociated stem cells
Stem cells in normoxia 20% O2 (D6)
Stem cells in hypoxia 1% O2 (D6)
NCH421k NCH644 5706 3731 TC22 TC7
Integrin α5
CA9
HIF-1α
HIF-2α
Tubulin
Fold increase in HIF-1α expression
Fold increase in HIF-2α expression
Fold increase in ITGA5 expression
NCH421k
NCH644
5706
3731
TC22
TC7
Dissociated cells
Neurosphere in normoxia
Neurosphere in hypoxia

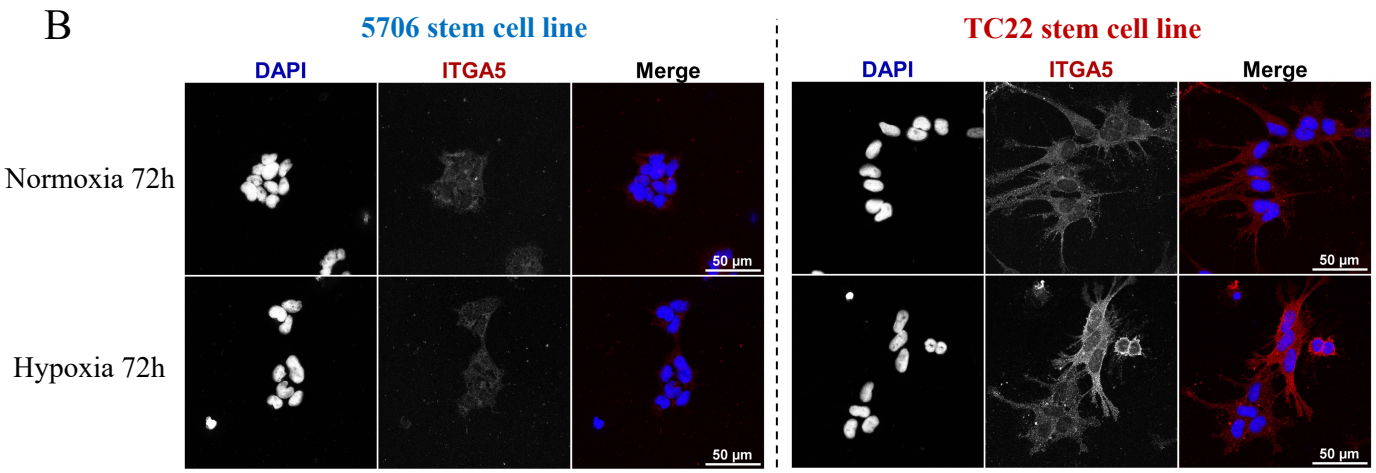
B
5706 stem cell line
TC22 stem cell line
DAPI
ITGA5
Merge
Normoxia 72h
Hypoxia 72h
50 µm

Figure 3

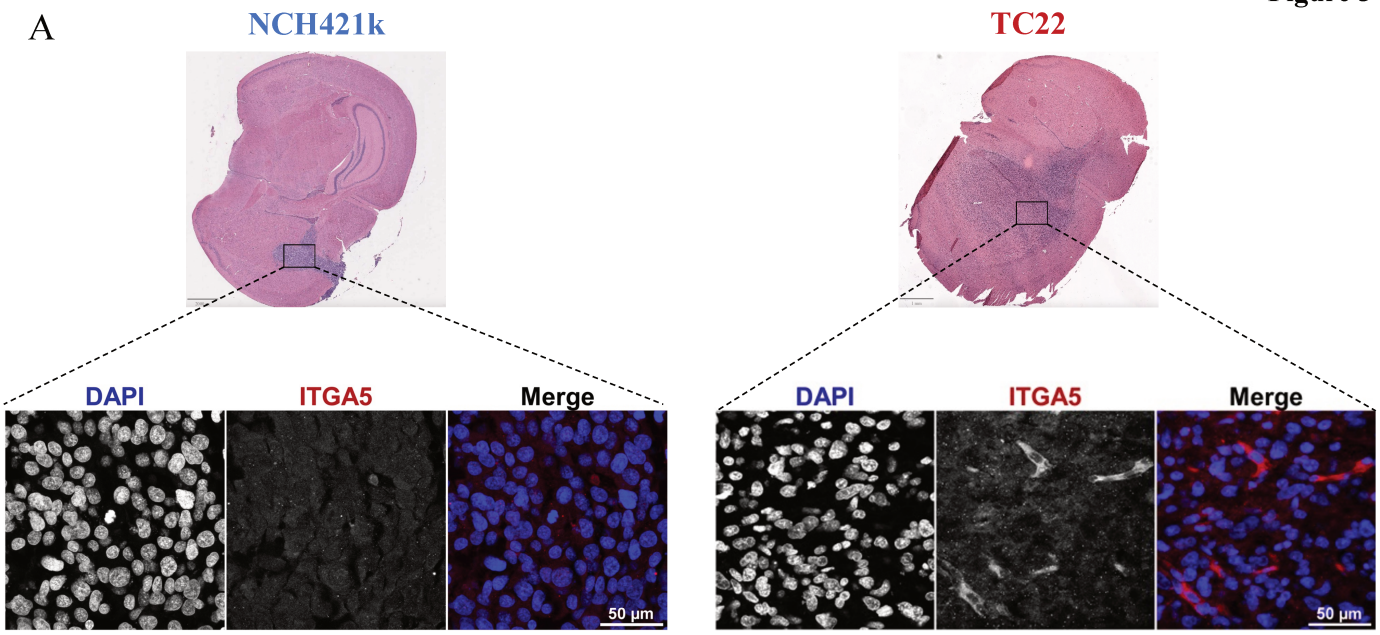
A
NCH421k
TC22
DAPI
ITGA5
Merge
50 µm
DAPI
ITGA5
Merge
50 µm

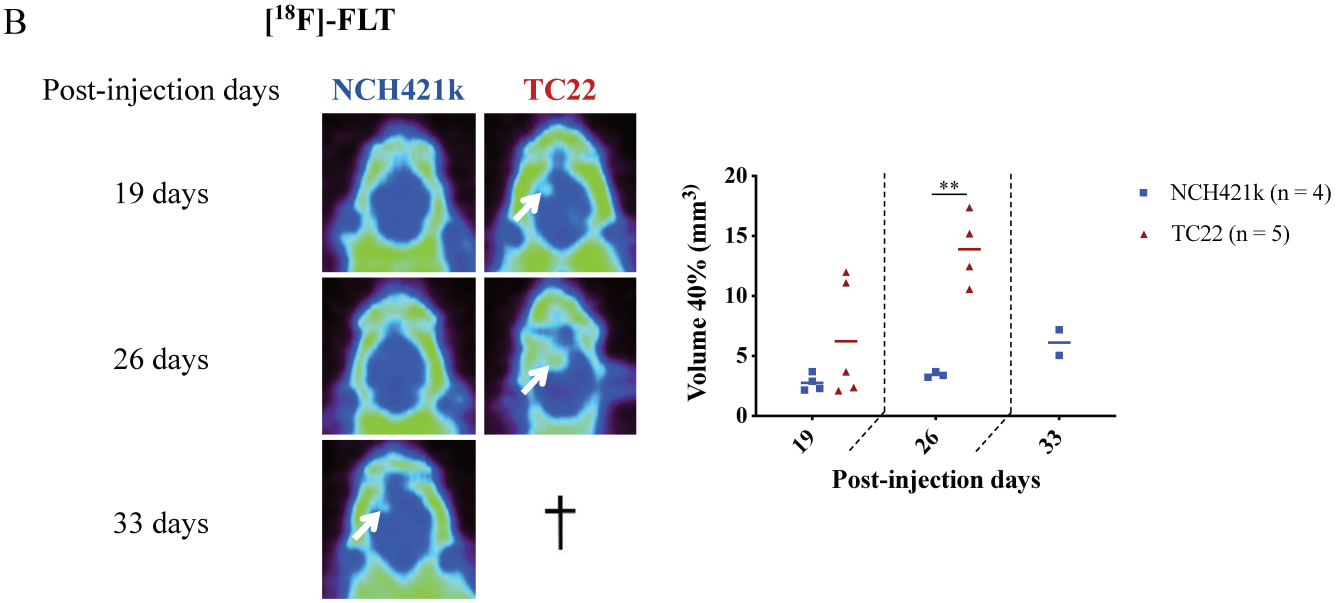
B
[18F]-FLT
Post-injection days
NCH421k
TC22
19 days
26 days
33 days
Volume 40% (mm3)
20
15
10
5
0
**
19
26
33
Post-injection days
NCH421k (n = 4)
TC22 (n = 5)

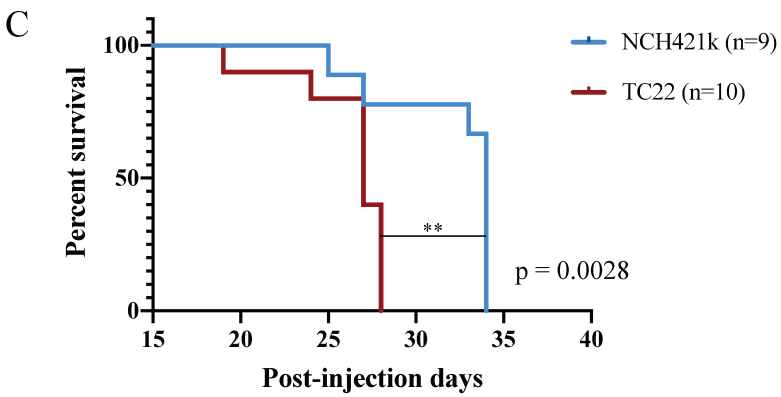
C
Percent survival
100
50
0
**
p = 0.0028
15
20
25
30
35
40
Post-injection days
NCH421k (n=9)
TC22 (n=10)

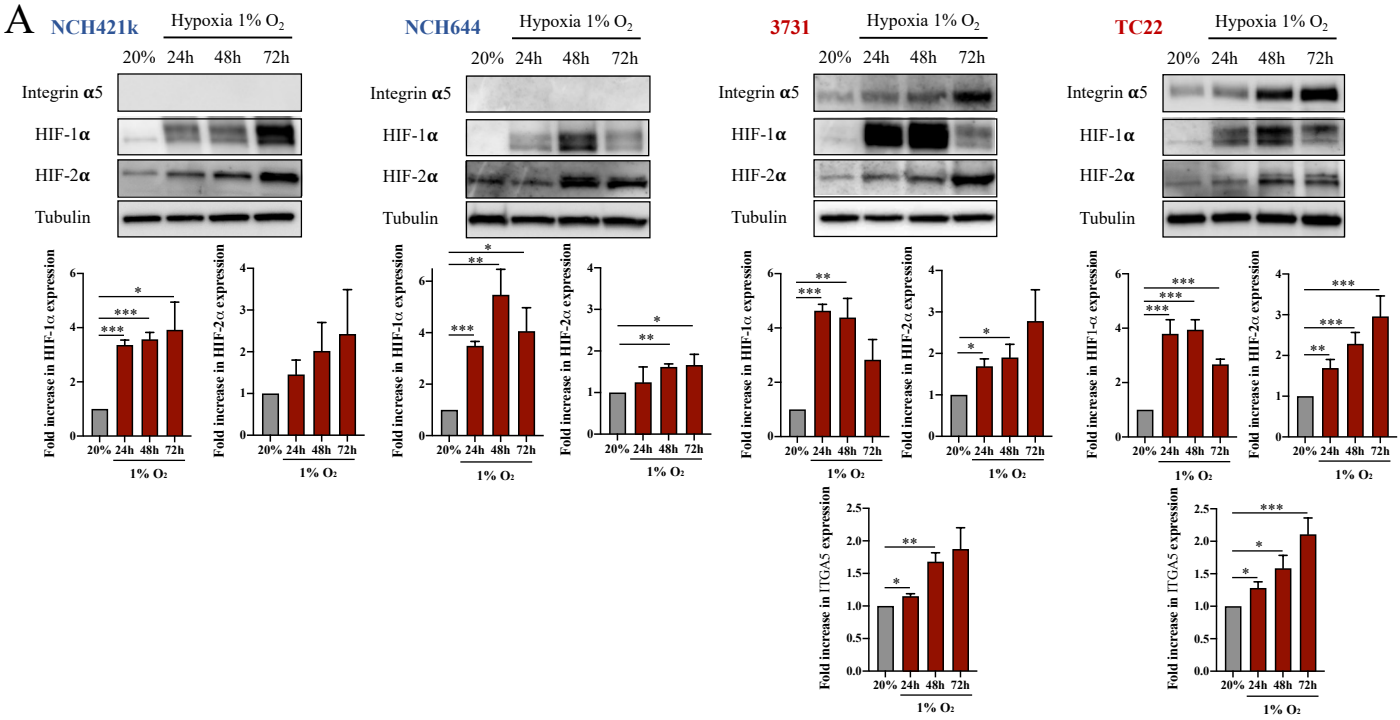
A
NCH421k
Hypoxia 1% O2
20% 24h 48h 72h
Integrin α5
HIF-1α
HIF-2α
Tubulin
Fold increase in HIF-1α expression
Fold increase in HIF-2α expression
1% O2
NCH644
Hypoxia 1% O2
3731
Hypoxia 1% O2
TC22
Hypoxia 1% O2
Fold increase in ITGA5 expression

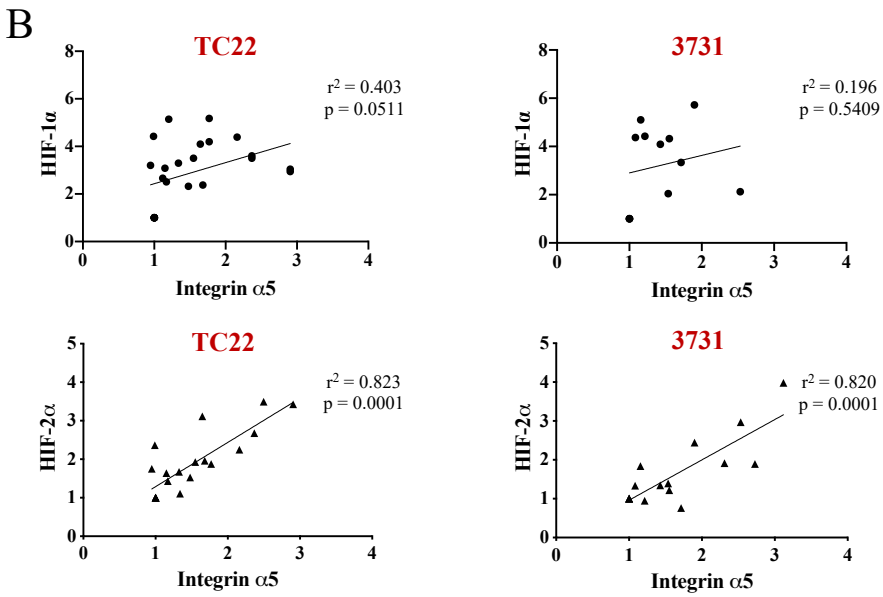
B
TC22
r2 = 0.403
p = 0.0511
HIF-1α
Integrin α5
3731
r2 = 0.196
p = 0.5409
TC22
r2 = 0.823
p = 0.0001
HIF-2α
3731
r2 = 0.820
p = 0.0001

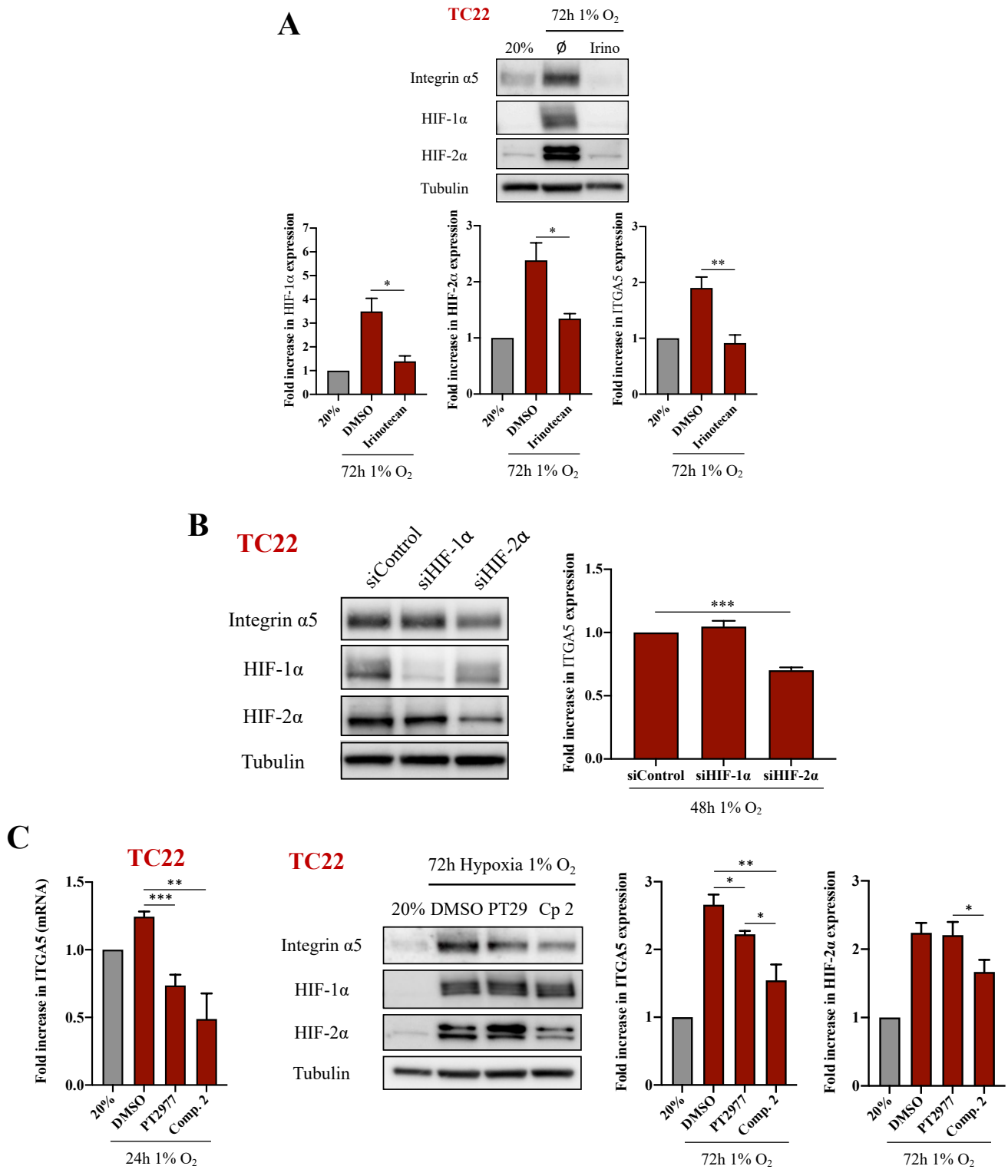
A
TC22
72h 1% O2
20%
Ø
Irino
Integrin α5
HIF-1α
HIF-2α
Tubulin
Fold increase in HIF-1α expression
Fold increase in HIF-2α expression
Fold increase in ITGA5 expression
20%
DMSO
Irinotecan
72h 1% O2
B
TC22
siControl
siHIF-1α
siHIF-2α
Integrin α5
HIF-1α
HIF-2α
Tubulin
Fold increase in ITGA5 expression
48h 1% O2
C
TC22
Fold increase in ITGA5 (mRNA)
20%
DMSO
PT2977
Comp. 2
24h 1% O2
TC22
72h Hypoxia 1% O2
20% DMSO PT29 Cp 2
Integrin α5
HIF-1α
HIF-2α
Tubulin
Fold increase in ITGA5 expression
Fold increase in HIF-2α expression
72h 1% O2

Figure 6

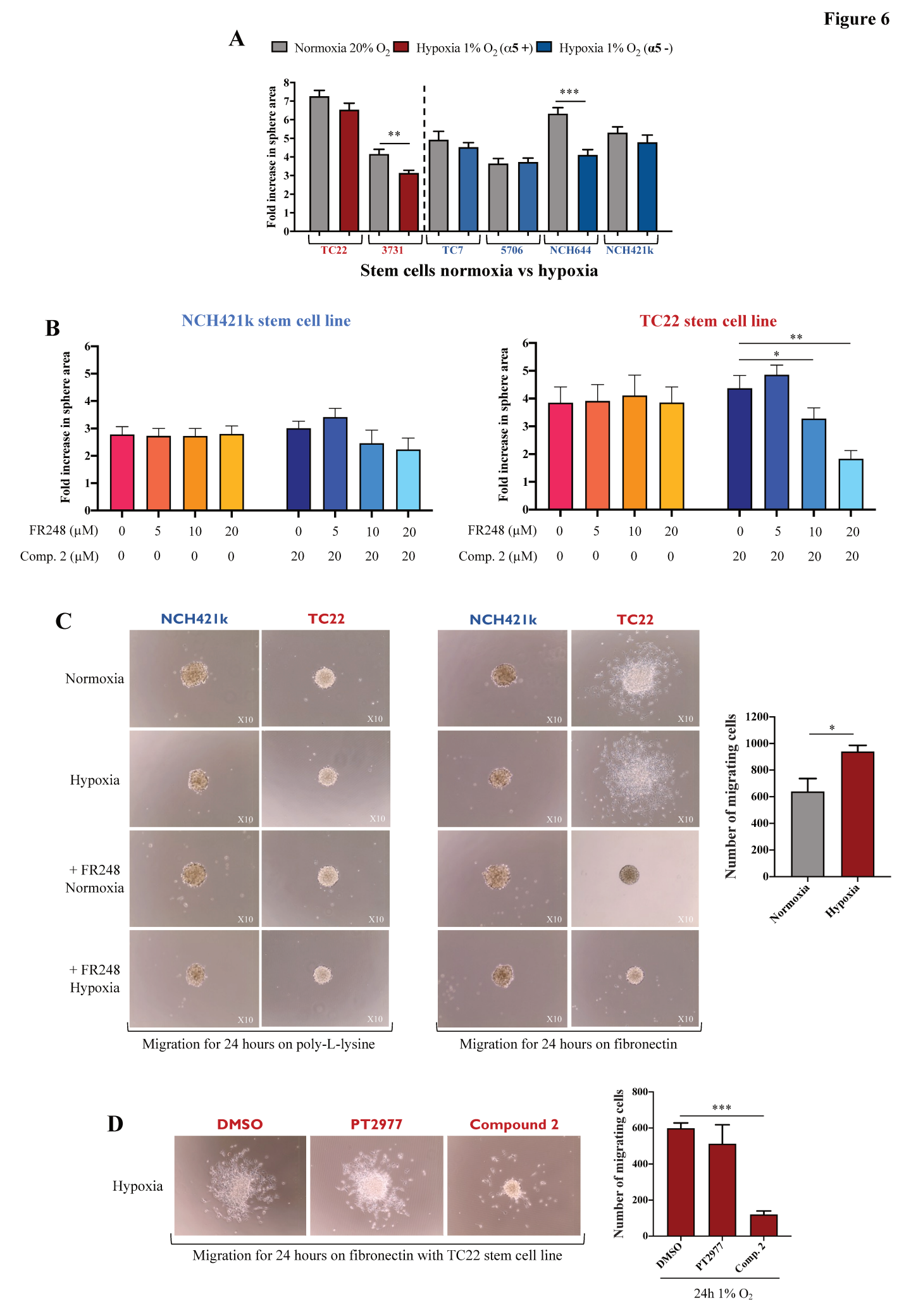
A
Normoxia 20% O2
Hypoxia 1% O2 (α5 +)
Hypoxia 1% O2 (α5 -)
Fold increase in sphere area
**
***
TC22
3731
TC7
5706
NCH644
NCH421k
Stem cells normoxia vs hypoxia
B
NCH421k stem cell line
TC22 stem cell line
Fold increase in sphere area
FR248 (μM) 0 5 10 20 0 5 10 20
Comp. 2 (μM) 0 0 0 0 20 20 20 20
C
NCH421k
TC22
Normoxia
Hypoxia
+ FR248 Normoxia
+ FR248 Hypoxia
X10
Migration for 24 hours on poly-L-lysine
Migration for 24 hours on fibronectin
Number of migrating cells
Normoxia
Hypoxia
D
DMSO
PT2977
Compound 2
Hypoxia
Migration for 24 hours on fibronectin with TC22 stem cell line
Number of migrating cells
DMSO
PT2977
Comp. 2
24h 1% O2

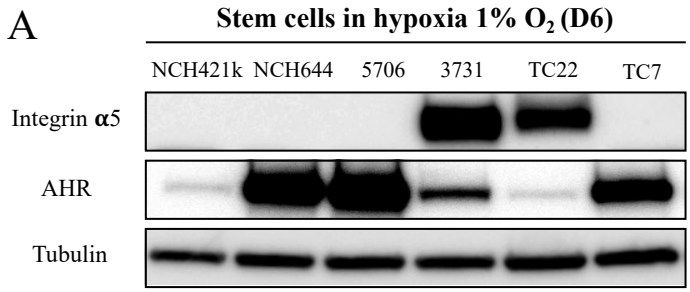
A
Stem cells in hypoxia 1% O2 (D6)
NCH421k
NCH644
5706
3731
TC22
TC7
Integrin α5
AHR
Tubulin

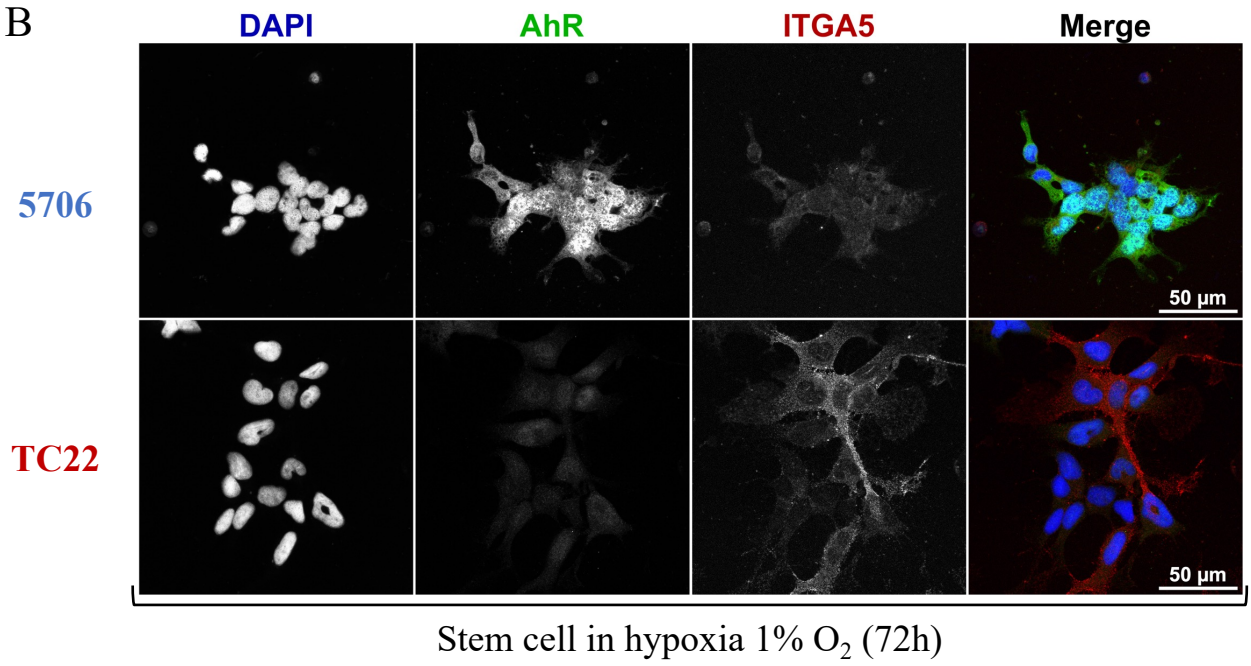
B
DAPI
AhR
ITGA5
Merge
5706
TC22
50 µm
50 µm
Stem cell in hypoxia 1% O2 (72h)

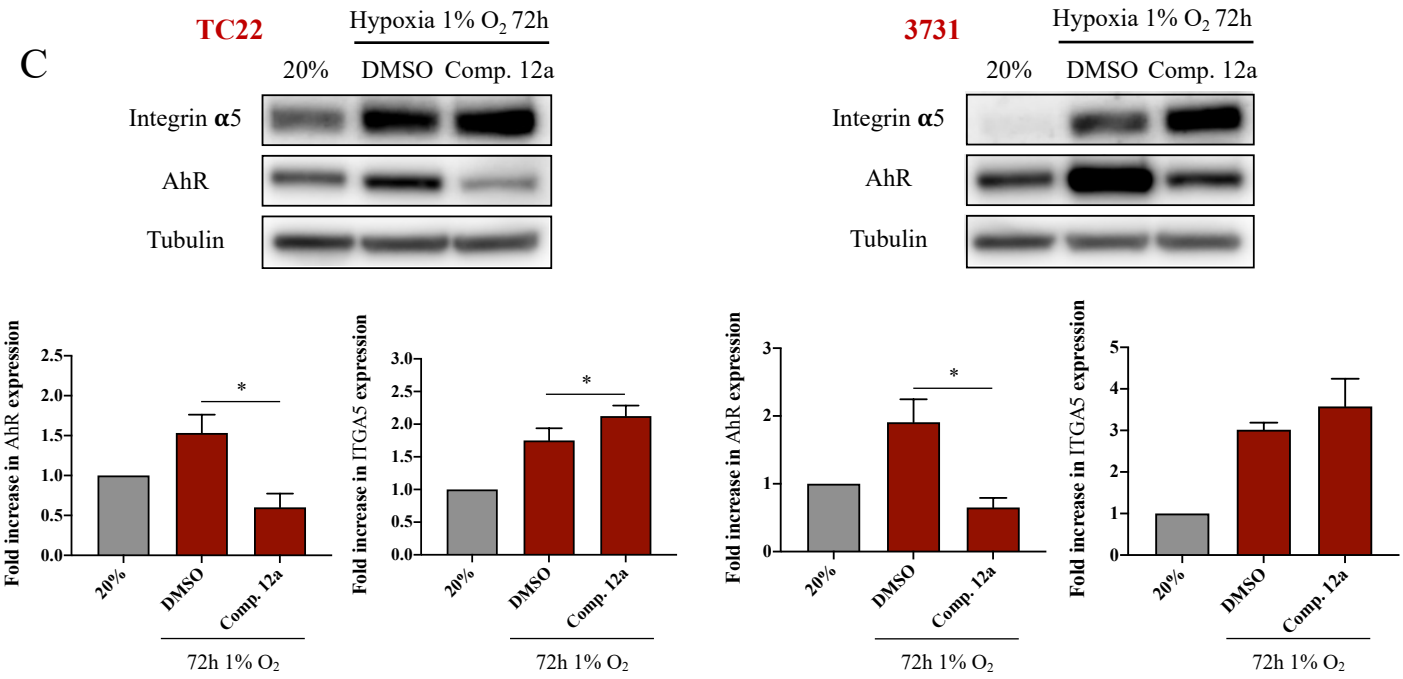
C
TC22
Hypoxia 1% O2 72h
20%
DMSO
Comp. 12a
Integrin α5
AhR
Tubulin
3731
Hypoxia 1% O2 72h
20%
DMSO
Comp. 12a
Integrin α5
AhR
Tubulin
Fold increase in AhR expression
Fold increase in ITGA5 expression
Fold increase in AhR expression
Fold increase in ITGA5 expression
20%
DMSO
Comp. 12a
72h 1% O2

Polyethylenimine, an Autophagy-Inducing Platinum-Carbene-Based Drug Carrier with Potent Toxicity towards Glioblastoma Cancer Stem Cells.

McCartin C, Dussouillez C, **Bernhard C**, Mathieu E, Blumberger J, Dontenwill M, Herold-Mende C, Idbaih A, Lavalle P, Bellemin-Laponnaz S, Kichler A, Fournel S.

Au cours de mon doctorat, j'ai eu l'opportunité de contribuer à un article collaboratif intitulé "Polyethylenimine, an Autophagy-Inducing Platinum-Carbene-Based Drug Carrier with Potent Toxicity towards Glioblastoma Cancer Stem Cells" publié dans Cancers (IF = 6.575) (doi: 10.3390/cancers14205057). Cet article a exploré l'utilisation de la polyéthylénimine (PEI) comme vecteur de médicament à base de carbène de platine, avec une toxicité potentiellement significative pour les cellules souches de GB. Ma contribution spécifique à cette publication a été centrée sur la culture CSG et la réalisation d'expériences visant à évaluer la prolifération cellulaire des CSG en réponse à des traitements au NHC-PEI30-Pt et au PEI. Ces expériences ont permis de démontrer l'efficacité de ces nouvelles thérapies sur les CSG. En outre, j'ai également mené des recherches indépendantes sur l'impact de ces drogues sur le métabolisme énergétique des CSG. Mes observations ont révélé une chute drastique du taux de consommation d'oxygène (OCR) et du taux d'acidification extracellulaire (ECAR) au fil du temps lors d'un traitement aigu avec ce composé. Ces résultats démontrent que le NHC-PEI30-Pt(II) et le PEI perturbent rapidement le métabolisme énergétique des CSG, ce qui pourrait contribuer à leur efficacité antitumorale.

cancers

MDPI

Article

Polyethylenimine, an Autophagy-Inducing Platinum-Carbene-Based Drug Carrier with Potent Toxicity towards Glioblastoma Cancer Stem Cells

Conor McCartin [1], Candice Dussouillez [1], Chloé Bernhard [2], Eric Mathieu [3,4], Juliette Blumberger [1], Monique Dontenwill [2], Christel Herold-Mende [5], Ahmed Idbaih [6], Philippe Lavalle [3,4], Stéphane Bellemin-Laponnaz [7], Antoine Kichler [1,*] and Sylvie Fournel [1,*]

1 3Bio Team, CAMB UMR7199 CNRS, Faculté de Pharmacie, University of Strasbourg, 67401 Ilkirch, France
2 Laboratoire de Bioimagerie et Pathologies UMR CNRS 7021 (LBP), Faculté de Pharmacie, University of Strasbourg, 67401 Illkirch, France
3 Institut National de la Santé et de la Recherche Médicale, Inserm UMR_S 1121 Biomaterials and Bioengineering, 67085 Strasbourg, France
4 Faculté de Chirurgie Dentaire de Strasbourg, University of Strasbourg, 67000 Strasbourg, France
5 Division of Neurosurgical Research, Department of Neurosurgery, University of Heidelberg, 69117 Heidelberg, Germany
6 AP-HP, Institut du Cerveau—Paris Brain Institute—ICM, Inserm, CNRS, Hôpitaux Universitaires La Pitié Salpêtrière—Charles Foix, DMU Neurosciences, Service de Neurologie 2-Mazarin, Sorbonne University, 75013 Paris, France
7 Institut de Physique et Chimie des Matériaux de Strasbourg (IPCMS) UMR7504 CNRS, University of Strasbourg, 67034 Strasbourg, France
* Correspondence: kichler@unistra.fr (A.K.); s.fournel@unistra.fr (S.F.)

Simple Summary: The resistance of tumours to treatment and their tendency to reoccur following successful treatment are major problems for long-term cancer patient survival. Research has identified a special subset of cells in tumours with stem-cell-like properties to be at the heart of this problem. Thus, the development of new chemotherapeutic compounds with unique characteristics that may target this subset of cancer cells is of great interest in the pursuit of more effective cancer treatments. This work describes one such compound, being a new platinum-based compound attached to a long polymer molecule in order to enhance its anti-cancer properties. Importantly, the stem-cell-like subset of cells seems to be considerably more sensitive to the toxicity of the polymer itself than the bulk of tumour cells, with an interesting mode of cell death which has characteristics different to that of more "classical" anti-cancer therapeutics.

Abstract: The difficulty involved in the treatment of many tumours due to their recurrence and resistance to chemotherapy is tightly linked to the presence of cancer stem cells (CSCs). This CSC sub-population is distinct from the majority of cancer cells of the tumour bulk. Indeed, CSCs have increased mitochondrial mass that has been linked to increased sensitivity to mitochondrial targeting compounds. Thus, a platinum-based polyethylenimine (PEI) polymer–drug conjugate (PDC) was assessed as a potential anti-CSC therapeutic since it has previously displayed mitochondrial accumulation. Our results show that CSCs have increased specific sensitivity to the PEI carrier and to the PDC. The mechanism of cell death seems to be necrotic in nature, with an absence of apoptotic markers. Cell death is accompanied by the induction of a protective autophagy. The interference in the balance of this pathway, which is highly important for CSCs, may be responsible for a partial reversion of the stem-like phenotype observed with prolonged PEI and PDC treatment. Several markers also indicate the cell death mode to be capable of inducing an anti-cancer immune response. This study thus indicates the potential therapeutic perspectives of polycations against CSCs.

Keywords: polymer–drug conjugate; polyethylenimine; N-heterocyclic carbene; platinum; cancer stem cells; autophagy; glioblastoma

Citation: McCartin, C.; Dussouillez, C.; Bernhard, C.; Mathieu, E.; Blumberger, J.; Dontenwill, M.; Herold-Mende, C.; Idbaih, A.; Lavalle, P.; Bellemin-Laponnaz, S.; et al. Polyethylenimine, an Autophagy-Inducing Platinum-Carbene-Based Drug Carrier with Potent Toxicity towards Glioblastoma Cancer Stem Cells. *Cancers* **2022**, *14*, 5057. https://doi.org/10.3390/cancers14205057

Academic Editor: Gabriella D'Orazi

Received: 23 September 2022
Accepted: 11 October 2022
Published: 15 October 2022

1. Introduction

Platinum compounds have been an integral part of the chemotherapeutic arsenal against cancer since the approval of cisplatin in the 1970s [1], with an estimated 28% of cancers being treated with a platinum-based therapeutic [2]. The current understanding of their known mechanisms indicates a general activation of apoptosis through the accumulation of DNA damage, which, along with the development of these compounds, has been extensively reviewed [3–5]. The clinical success of cisplatin has led chemists to diversify the ligands around the platinum to improve the efficacy of cisplatin while reducing its side effects. In the last decade, N-heterocyclic carbene (NHC) as a platinum stabilising ligand has demonstrated new possibilities in medicinal chemistry [6,7]. Indeed, NHC-Pt complexes exhibit superior cytotoxic activities to cisplatin or related compounds, along with high stability.

However, they still present some drawbacks such as their biocompatibility. Among the challenges in the further development and improvement of small molecule anti-cancer treatments, such as NHC-Pt molecules, are their aqueous solubility and targeted delivery/release to tumour sites [8]. This can be addressed through the development of polymer–drug conjugates (PDCs), whereby drugs with otherwise poor biological solubility may be improved by their chemical conjugation to a large hydrophilic polymer [8]. This may also have the added benefit of the potential physicochemical reformation of the disordered polymer into a nanoparticle through the organisation of the conjugated hydrophobic small molecules into a water-excluded core [8–11]. Such a trait is highly desirable due to the supposed specific accumulation of nanoparticles within solid tumours due to the enhanced permeability and retention (EPR) effect [12,13].

Polymers which have been described for the synthesis of PDCs include polyethylene glycol (PEG), dextran, N-(2-hydroxypropyl)methacrylamide (HPMA), and a variety of dendrimers [8]. With over a dozen (almost all of which are PEG-based) PDCs having market approval at the time of publishing for a variety of uses [8]. Polyethylenimine (PEI), a commonly used transfection reagent for the introduction of genetic material into mammalian cells, also has the potential as a delivery agent for drugs [14]. So far, it has mainly been described for the delivery of nucleic acids such as plasmid DNA [15] with several linear PEI-based formulations being evaluated in clinical trials [15]. However, PEI has also been used as a carrier for antitumoral drugs such as doxorubicin [16], camptothecin [17] and an NHC-platinum compound (which is elaborated in this work; [11,18]).

Of particular interest in the latest developments of the anti-cancer chemotherapeutic domain is the targeting of the so-called cancer stem cell (CSC) subpopulation (also referred to as tumour-initiating cells) [19]. These cells are characterised by their stem-like characteristics such as asymmetric division, allowing their self-renewal and differentiation [20–22]. This has led to their implication in the driving of tumour recurrence due to their known propensity to resist current chemotherapeutic treatments [23,24]. The drivers of this resistance are metabolic reprogramming relative to more differentiated tumour cells making up the bulk of the tumour mass, upregulated DNA repair, upregulated anti-apoptotic proteins and drug efflux proteins, as well as protective autophagy [25]. Autophagy is an intricate cellular mechanism used for the recycling or removal of unneeded or damaged intracellular components [26] through their sequestration (in autophagosomes) and subsequent hydrolysis via acidification of the compartment through lysosomal fusion [26], thus providing a source of nutrients such as in times of starvation or stress [27].

Among the cancers where a significant CSC population has been identified is glioblastoma [28,29]. It is a highly aggressive brain cancer, which despite an established treatment consisting of surgical resection, radiotherapy, and chemotherapy with the alkylating agent temozolomide [28], has a high rate of recurrence linked to CSCs [28], and a median survival of only 12–15 months following diagnosis [29]. Targetable characteristics of CSCs have thus come to the forefront in chemotherapeutic development, such as their observed sensitivity to mitochondrial targeting compounds linked to an upregulated mitochondrial

mass [30–33] and their upregulation of markers such as CD133 and CD44 (hyaluronic acid receptor) which may serve as cell surface targets [34,35].

Additionally, the role of the adaptive immune response against cancer has become an important aspect when considering the action and efficacy of anti-cancer chemotherapeutics [36]. The ability of a molecule to effectively and directly eliminate cancer cells is made considerably more interesting if the mode of cell death may stimulate the adaptive immune response against the tumour in question, contributing to its elimination, and potentially safeguarding against its recurrence [36]. This so-called "immunogenic cell death" (ICD), implies the release of damage-associated molecular patterns (DAMPs) from dying cells [37]. DAMPs are normally intracellular factors which are capable of stimulating the innate immune response via interaction with pattern recognition receptors (PRRs). This leads to the recruitment and maturation of professional antigen-presenting cells (APCs) such as dendritic cells, which may also phagocytose the cells [36,38], present tumour-specific or associated antigens, and thus initiate an anti-tumour T-cell response. DAMPs, of which there are several types with varying effects, include outer-membrane exposure of the normally endoplasmic reticulum localised protein calreticulin, and ATP, which serves as an immunostimulatory compound via binding to purinergic receptors which stimulate the production of pro-inflammatory cytokines [36,39].

The aforementioned NHC-platinum(II) PDC, a complex shown to form nanoparticles in aqueous solution, named NHC-Pt(II)-PEI, has been developed by our team and has already proven to be effective against several human and murine cancer cell lines in vitro and in vivo using a nude (immunodeficient) mouse tumour model [11,18]. The anti-tumour efficacy of the PDC and its accumulation within the mitochondria, associated with mitochondrial dysfunction of HCT116 cells shown in the same study led us to the hypothesis that the compound may present an even higher level of toxicity against CSCs. Thus, in this study, we wished to evaluate whether the PDC or indeed the polymer carrier itself, PEI, presented a specifically high level of toxicity towards CSCs. We also wished to evaluate the characteristics of the cell death induced, and the potential for induction of ICD.

2. Materials and Methods

2.1. Storage of Compounds

NHC-Pt(II)-PEI (22 kDa PEI with one NHC-Pt(II) coordinated every 30 repeating units; thus, 17 NHC-Pt(II), for a total molecular mass of ~30.2 kDa) and 22 kDa PEI were stored as stock solutions in absolute ethanol. Oxaliplatin (#O9512, Sigma-Aldrich, Saint-Quentin-Fallavier, France), chloroquine (#PHR1258, Sigma-Aldrich, Saint-Quentin-Fallavier, France) and 30 kDa poly-L-Lysine (#P9404, Sigma-Aldrich, Saint-Quentin-Fallavier, France) were stored as solutions in MilliQ H_2O, while all other compounds used were stored as solutions in DMSO. Stocks were stored at −20 °C or −80 °C. Prior to use, stocks were heated and sonicated briefly at 37 °C in a bath sonicator. Prior to the treatment of cells, stock compounds were diluted to desired concentrations in the culture medium of the cells being treated. The NHC-Pt(II)-PEI PDC was synthesised as described by Chekkat et al. (2016) [11]. The linear 22 kDa PEI was synthesised according to Brissault et al., 2003 [40].

2.2. Cell Culture and Treatment Conditions

2.2.1. U87-MG Cells

U87-MG (HTB-14, ATCC, Manassas, VA, USA) cells were obtained from the M. Dontenwill lab (UMR 7021 CNRS, University of Strasbourg, Faculty of Pharmacy, Illkirch, France). The cells were maintained in regular tissue culture treated T75 flasks (#658170, Greiner Bio-One, Les Ulis, France) containing Roswell Park Memorial Institute (RPMI) 1640 medium (#R2405-500 ML, Sigma-Aldrich, Saint-Quentin-Fallavier, France) medium containing 10% (*v/v*) fetal bovine serum (FBS) (#10270106, Gibco, Waltham, MA, USA), Penicillin-Streptomycin (P/S: 10 U/0.1 mg) (#P0781-100ML, Sigma-Aldrich, Saint-Quentin-Fallavier, France) in a 37 °C, 80% humidity and 5% CO_2 incubator. Once confluence reached ~80%, cultures were maintained by removal of spent culture medium, washing twice with

Dulbecco's Phosphate Buffered Saline (PBS) (#D8537-500ML, Sigma-Aldrich, Saint-Quentin-Fallavier, France), followed by treatment with trypsin-EDTA (at 0.5 mg/mL and 0.2 mg/mL, respectively) (#T3924-100ML, Sigma-Aldrich, Saint-Quentin-Fallavier, France) for 5 min at 37 °C, collection of cells, washing, resuspension in culture medium and re-seeding in a new T75 flask. Cells were counted via trypan blue (#T8154-100ML, Sigma-Aldrich, Saint-Quentin-Fallavier, France) exclusion using the Countess II FL automated cell counter (Thermo Fisher Scientific, Illkirch-Graffenstaden, France). For treatment, unless otherwise stated, cells were seeded at 18,000 cells per well in 100 µL medium in a flat-bottomed tissue culture treated 96-well culture plate (#655180, Greiner Bio-One, Les Ulis, France). Treatment was applied by aspiration of culture medium from wells and replacement with the desired dilutions of the compounds.

2.2.2. Dental Pulp Stem Cells

Dental pulp stem cells (DPSCs) were obtained from the Pr. Florent Meyer lab (INSERM 1121, Faculté de Chirurgie Dentaire, Université de Strasbourg, Strasbourg, France). The cells were maintained in regular tissue culture treated T75 flasks using Minimum Essential Medium (MEM) Alpha Medium (1×) + Glutamax (#32561-029, Gibco, Illkirch-Graffenstaden, France) medium containing 10% (*v/v*) FBS, Penicillin-Streptomycin (P/S; 10 U/0.1 mg) in a 37 °C, 80% humidity and 5% CO_2 incubator. Cells were passaged and counted in the same manner as the U87-MG cells. For treatment, unless otherwise stated, cells were seeded at 25,000 cells per well in 100µL medium in a U-bottomed 96-well suspension culture plate (#650185, Greiner Bio-One, Les Ulis, France) in order to encourage spheroid formation. Treatment was applied by the addition of 10µL medium containing the desired compound at 11× the desired final concentration.

2.2.3. Glioblastoma Stem Cells

NCH421K and NCH644 glioblastoma CSCs (GSCs) were obtained from Pr. Christel Herold-Mende (Division of Neurosurgical Research, Department of Neurosurgery, University of Heidelberg, Germany) [41]. The 3731 GSCs were obtained from Dr. A. Idbaih's group (Sorbonne Université/AP-HP/ICM, Paris, France) [42]. GSCs growing as spheroids were maintained in regular tissue culture treated T25 (#690175, Greiner Bio-One, Les Ulis, France) or T75 cell culture flasks in CSC culture medium ((Dulbecco's modified eagle medium (DMEM)/Ham's F12 (1:1) (#D6421, Sigma-Aldrich, Saint-Quentin-Fallavier, France) containing 20% (*v/v*) BIT 100 supplement (#2043100, Provitro, Berlin, Germany), 20 ng/mL basic fibroblast growth factor (FGF-2) (#130-093-842, Miltenyi Biotec, Paris, France), 20 ng/mL epidermal growth factor (EGF) (#130-097-751, Miltenyi Biotec, Paris, France), P/S (10 U–0.1 mg) and GlutaMAX supplement (#35050061, Gibco, Illkirch-Graffenstaden, France) in a 37 °C, 80% humidity and 5% CO_2 incubator. Spheroid cultures were maintained by passaging once a week via recuperation of spheroids, washing with PBS, followed by treatment with Accutase (#A6964-100ML, Sigma-Aldrich, Saint-Quentin-Fallavier, France) for 5 min at room temperature. Dissociated cells were then washed once, resuspended in culture medium, and counted in the same manner as the U87-MG cells. Cells were re-seeded at 35,000 viable cells per mL. For treatment, unless otherwise stated, GSCs were seeded at 75,000 viable cells per mL (100 µL per well) in a regular flat-bottom tissue culture treated 96-well plate and were then left to form spheres for four days prior to treatment with the tested compounds the following day. Treatment was applied in the same manner as for the DPSCs.

2.2.4. RAW Macrophages

The murine macrophage cell line RAW 264.7 (TIB-71, ATCC) (originating from BALB/c mice cells transformed with Abelson leukaemia virus [43]) was used as a model for the induction of a pro-immune or anti-inflammatory response. For facility of passaging, cells were cultured normally as a semi-adherent culture in 10 cm^2 suspension culture dishes at 37 °C, 5% CO_2 and 80% humidity in 12 mL DMEM (#D0819-500ML, Sigma-Aldrich, Saint-Quentin-Fallavier, France) medium supplemented with 5% FBS 100 U/mL penicillin and

0.1 mg/mL streptomycin (#P0781-100ML, Sigma). Cells were passaged by gentle flushing of the culture medium to remove the cells, with cells then pelleted (200 g, 3 min, RT), resuspended in medium and counted (Section 2.2.1). Cells were re-seeded at 5×10^6 cells/mL or 10×10^6 cells/mL for 2 or 3 days of growth, respectively.

For experiments, RAW 264.7 cells were seeded the day before treatment at a density of 3×10^4 cells per well (100µL medium volume) in regular adherent 96-well culture plates (#655180, Greiner Bio-One, Les Ulis, France) or 3×10^5 cells per well (300µL medium volume) in 12-well plates (#665180, Greiner Bio-One, Les Ulis, France).

2.3. Cell Viability Assay

Cell culture viability was measured by using the CelltiterGlo 3D Cell Viability Assay (#G9681, Promega, Charbonnières-les-Bains, France), which measures the quantity of ATP via luciferase activity. This decrease could be correlated with a decrease in cell viability, cell metabolism, or cell number. Treated cells were left for the desired time point prior to the addition of 110 µL CelltiterGlo 3D reagent. Wells were then periodically flushed vigorously via pipetting in order to disaggregate spheres and encourage lysis prior to transfer to a white opaque 96-well culture plate (#236105, ThermoFisher, Illkirch-Graffenstaden, France) to prevent luminescence leakage between wells during relative luminescence units (RLU) counting using a plate reader (SP2000 Safas, Monaco). Results were expressed by the subtraction of background RLU (culture medium and assay reagent) and expression of viability relative to non-treated controls (considered as 100% viability). The percentage of viability was calculated using the following equation (Equation (1)):

$$\text{Viability} = [\#\text{RLU(Treatment)}/\#\text{RLU(Non-treated)}] \times 100 \quad (1)$$

IC50 values were calculated using GraphPad Prism software from dose–response curves using non-linear regression (log(concentration) vs. %viability—variable slope (four parameters)).

2.4. Spheroid Formation Assay

In order to follow the effect of treatment on the spheroid formation capacity of the NCH421K cells, spheroid formation from individual cells was followed by the real-time microscopic assessment using Incucyte® technology (Essen BioScience, Royston Hertfordshire, UK). In total, 3000 NCH421K cells/well were seeded in a 96-well plate in medium containing the desired concentration of treatment and cultured for 6 days in an incubator at 37 °C, 5% CO_2. Cell surface area (mm^2) of the spheroids was followed with an IncuCyte Zoom Live Cell Analysis system. Images were taken every 4 h, with the size of the spheres normalised to time 0 (thus single dissociated cells) and calculated using IncuCyte Zoom 2018A software.

2.5. Annexin V/Propidium Iodide Assay

Cell death and apoptosis were investigated by double staining with APC conjugated Annexin V (AnV), a protein that binds to phosphatidylserine, an inner leaflet membrane phospholipid which is externalised during apoptosis, and propidium iodide (PI), a membrane-impermeable DNA intercalating agent that enters cells which have lost membrane integrity and fluoresces only when bound to nucleic acids. Following treatment, the cells were recovered, and the spheroids dissociated via Accutase treatment, then washed in AnV binding buffer (10 mM HEPES, 140 mM NaCl, 2.5 mM $CaCl_2$, pH 7.3–7.4). Triplicates were pooled and stained with APC-conjugated AnV (#640920, BioLegend, Amsterdam, Netherlands) diluted 1/100 with prepared AnV binding buffer which was incubated for 15 min at room temperature and sheltered from light. Cells were washed with AnV binding buffer and transferred to tubes containing 15 µM PI (#P4170-10MG, Sigma-Aldrich, Saint-Quentin-Fallavier, France), which were analysed immediately via flow cytometry (FACSCalibur, Becton Dickinson, Franklin Lakes, New Jersey, United States). APC-AnV fluorescence was detected in the FL4 channel while PI fluorescence was detected in the FL3 channel. Data were analysed using FlowJo v10 software.

2.6. Caspase 3/7 Activation Assay

Caspase 3/7 activation was investigated using the Caspase-Glo® 3/7 Assay System (#G8210 & #G8091, Promega, Charbonnières-les-Bains, France), which functions via a pro-luminescent caspase 3/7 DEVD-aminoluciferin substrate, thus generating processible luciferase substrate, and luminescence, proportional to caspase activity. Following treatment, 110 µL reagent was added to each well, which was then mixed by vigorous pipetting. After 30 min incubation at room temperature, cell-lysate was transferred to an opaque 96-well plate, with luminescence then measured using a plate reader (SP2000 Safas, Monaco).

2.7. Transmission Electron Microscopy

In order to assess in detail, the morphological effects that treatment may have on the cells, transmission electron microscopy (TEM) was carried out on treated cells. Cells were treated at the desired time point and concentration in T175 flasks (#661175, Greiner Bio-One, Les Ulis, France) in 30 mL culture volume. The spheres/cells were recovered and washed once in PBS before dissociation via Accutase treatment. Cells were then washed twice in PBS before fixation in cold 2.5% glutaraldehyde (Euromedex, Souffelweyersheim, France) in 0.05 M sodium cacodylate (Euromedex, Souffelweyersheim, France) buffer at pH 7.4. for 2.5 h. The cells were then washed three times in cold 0.175 M sodium cacodylate buffer for 10 min. The samples were then post-fixed for 1.5 h in 1% osmium tetroxide in 0.15 M sodium cacodylate buffer. The samples were washed 3 times again in the same washing buffer and dehydrated in cold graded series of ethanol (30%, 50%, 70%, 95%) for 7 min each, then twice in cold absolute ethanol and once in RT absolute ethanol for 5 min each. The composition of Spurr resin used (Sigma-Aldrich) was the following: 5.90 g of NSA (Nonenyl succinic anhydride), 4.10 g of ERL 4221 (cycloaliphatic epoxide resin), 1.59 g of DER 736 (Poly(propylene glycol) diglycidyl ether) and 0.1 g of DMAE (Dimethylethanolamine) as an accelerator. The samples were transferred successively for 30 min in 1 vol Spurr resin/1 vol absolute ethanol, 30 min in 100% Spurr resin, and twice for 1 h in the same resin. Finally, the cells were included in 250 µL polypropylene tubes and left at RT for 24 h and put in a 60 °C oven for polymerisation for 48 h. Ultra-thin sections were performed using an automatic ultra-microtome Reichert Jung Ultracut E (Leica Microsystems, Wetzlar, Germany) equipped with a diamond knife and collected on 100 mesh formvar carbon-coated grids. They were stained with 5% uranyl acetate solution for 20 min. After rinsing, the grids were stained with 4% lead citrate solution for 10 min (All of these products were purchased from Euromedex, Souffelweyersheim, France). Finally, the sections were observed using a Hitachi H-7500 instrument (Hitachi High Technologies Corporation, Tokyo, Japan) operating with an accelerating voltage of 80 kV. The images were digitally recorded with an AMT Hamamatsu digital camera (Hamamatsu Photonics, Shizuoka, Japan).

2.8. LDH Release Assay

In order to measure cell membrane permeability via the release of the metabolic enzyme lactate dehydrogenase (LDH) into the culture medium, the Pierce LDH Cytotoxicity Assay Kit (#88953, Thermo Scientific, Illkirch-Graffenstaden, France) was used. Forty-five minutes before the desired time point, 11 µL of 10× Lysis Buffer was added to a non-treated well and mixed by vigorous pipetting to serve as a maximum LDH activity control. For adherent cells, 50 µL was then removed from each well and transferred to a flat bottomed 96-well plate, with 50 µL Reaction Mixture (prepared as per the kit's instructions) added to each well and mixed. For non-adherent cells, the culture plate was centrifuged before careful removal of 50 µL medium in order to ensure that the cells were at the bottom of the plate. The mixture was then incubated for 30 min at room temperature protected from light before the addition of 50 µL Stop Solution. Absorbance was then measured at 490 nm and 680 nm using a plate reader (SP2000 Safas, Monaco). Background (680 nm) from the instrument was then subtracted from the values (490 nm), which were then

expressed as a percentage of the maximum LDH activity following subtraction of the medium-only control.

2.9. Western Blot

2.9.1. Cell Treatment, Lysis, and Protein Quantification

In order to assess the levels of the lipidated form of the protein microtubule-associated proteins 1A/1B light chain 3 (LC3), LC3-II (correlating with an accumulation of autophagosomes in the cells) and p62 (whose levels correlate inversely with autophagic flux/activation), Western blotting was carried out. Cells were treated at the desired time point and concentration in 6-well plates in a total volume of 3 mL. For LC3, all treatments were applied for 6 h except chloroquine which was treated for 3 h. For p62, all treatments were applied for 6 h. Cells were collected, washed once in PBS and either stored as pellets at −80 °C or lysed straight away. Cell lysis was carried out by resuspension of pellets in 100 µL Lysis Buffer (PBS/sodium tetrasodium pyrophosphate ($Na_4O_7P_2$) 100 mM/sodium orthovanadate (Na_3VO_4) 1 mM/sodium fluoride (NaF) 100 mM/Triton 1%), the cells were then vortexed for 10 s and left to rest on ice for 10 min. This was repeated twice more before sonication of the cells in a water bath for 10 s. Three more rounds of vortexing and resting on ice were repeated as previously, with the lysate then centrifuged for 10 min at 13,000 g (4 °C). The supernatant was removed and retained with the pellet debris discarded. Protein content was determined using the Bicinchoninic Acid (BCA) assay (#UP95425, Interchim, Montluçon, France). A standard protein curve was made using Bovine Serum Albumin (BSA), with 25 µL protein sample added to each well of a 96-well plate, to which 200 µL BCA working solution (comprised of 50 volumes Solution A (BCA solution) for 1 volume of Solution B (4% Copper (II) Sulphate Pentahydrate)) was added and incubated at 37 °C for 30 min before absorbance measurement at 560 nm using a plate reader (SP200 Safas, Monaco).

2.9.2. SDS-PAGE

Protein samples were prepared by diluting a quantity of lysate containing 20 µg of protein to a final volume of 30µL in MilliQ H_2O, to which 10 µL of 4× NuPAGE™ LDS Sample Buffer (#1610747, Bio-Rad, Marnes-la-Coquette, France) was added, with the addition of 2 µL 1 M Dithiothreitol (DTT) (#EU0006-C, Euromedex, Souffelweyersheim, France). The tubes were sealed using clips and boiled for 10 min at 95 °C in a heating block in order to denature the protein. Tubes were then briefly spun to recover the full liquid volume, with the entirety of the sample then loaded onto a pre-cast 4–20% gradient SDS-PAGE gel (Mini-PROTEAN® TGX™ Precast Protein Gels, 10-well, 50 µL, #4561094, Bio-Rad, Marnes-la-Coquette, France). A 5 µL protein ladder (PageRuler Prestained 10–180 kDa Protein Ladder, #26616, ThermoSFisher, Illkirch-Graffenstaden, France) was also loaded. The gel was run in 1× Tris/Glycine buffer (#1610734, Bio-Rad) with 0.1% (*v*/*v*) SDS (#1610416, Bio-Rad, Marnes-la-Coquette, France) at 100 V until fully resolved.

2.9.3. Western Blot

Resolved gels were immediately transferred to 0.2 µm PVDF membrane using Trans-Blot Turbo Mini 0.2 µm PVDF Transfer Packs (#1704156, Bio-Rad, Marnes-la-Coquette, France) with the semi-dry Trans-Blot Turbo Transfer System semi-dry (#1704150EDU, Bio-Rad, Marnes-la-Coquette, France), which was wet using 20% EtOH 1× Tris-Gly transfer buffer and transferred for 10 min (1.3 A up to 24 V). To quantify total protein prior to blocking, membranes were stained using Ponceau S staining solution (#A40000279, ThermoFisher, Illkirch-Graffenstaden, France) and imaged using the Amersham Imager 600. The membrane was then immediately blocked in 5% milk Tris-Buffered Saline Tween (TBST) (Tris 20 mM, NaCl 150 mM, Tween 20 0.1% (*w*/*v*)) for one hour. It was then washed thrice in roughly 15 mL TBST under gentle agitation for 5 min each time before being incubated in a sealed sachet with 1/3000 diluted anti-LC3A/B antibody (LC3A/B (D3U4C) XP® Rabbit mAb #12741, Cell signaling, Leiden, Netherlands) or 1/1000 diluted anti-p62/SQSTM1

(SQSTM1/p62 Antibody #5114, Cell signaling, Leiden, Netherlands) in 5% BSA TBST overnight under gentle agitation at 4 °C. The membrane was then thrice washed in TBST for 5 min each time, followed by incubation with roughly 30 mL 1/20,000 diluted anti-rabbit secondary (Peroxidase AffiniPure Goat Anti-Rabbit IgG (H+L), #111-035-144, Jackson) in 5% milk TBST under gentle agitation for 2 h at RT. The membrane was then thrice washed in TBST as before, with membrane signal revealed by the addition of 1 mL ECL reagent (Clarity™ Western ECL Substrate, #1705060S, Bio-Rad, Marnes-la-Coquette, France) to the membrane placed between two transparent plastic sheets. Following incubation for 5 min protected from light, the membrane was then visualised using the Amersham Imager 600. For actin normalisation of loaded protein quantity, the membrane was washed thrice in TBST and then incubated for 2 h with 1/10,000 diluted anti-β-actin (#A5441, Sigma-Aldrich, Saint-Quentin-Fallavier, France) antibody in 5% milk TBST under gentle agitation. The membrane was then washed thrice as before, and incubated with 1/200,000 anti-mouse secondary (Peroxidase AffiniPure Goat Anti-Mouse IgG + IgM (H+L), #115-035-068, Jackson Immunoresearch, Cambridgeshire, United Kingdom), which was incubated, washed and revealed in the same manner as for the anti-LC3 A/B antibody. The LC3-II/LC3-I ratio (a measure of autophagosomal accumulation) was calculated by measurement of integrated density using ImageJ. P62 intensity was measured by integrated density and normalised to total protein content measured by the Ponceau stain (quantified by integrated density).

2.10. Lysotracker Green Flow Cytometry

In order to assess the accumulation of acidic lysosomal vesicles within the cells, LysoTracker™ Green DND-26 (#L7526, ThermoFisher, Illkirch-Graffenstaden, France) staining was carried out and measured by flow cytometry. Cells were treated at the desired concentration and duration in 96-well plates before transfer to a V-bottomed 96-well plate (#651101, Greiner Bio-One). The plate was centrifuged (5 min at 350 g, 4 °C), with the supernatant removed by inversion of the plate. The cells were then resuspended in 100 µL Accutase, with the replicates pooled, and left for 5 min at RT to dissociate the spheres. The plate was then centrifuged (5 min at 350 g, 4 °C) with the supernatant eliminated. The cells were resuspended in 50 nM Lysotracker Green diluted in PBS and incubated at room temperature for 15 min protected from light. The cells were then centrifuged (350 g, 5 min, 4 °C) and resuspended in 1/200 diluted PI as a live/dead marker. Cells were run immediately on a FACS Calibur, with the Lysotracker Green analysed in the FL1 channel and PI in the FL3 channel. Live (PI−) cells were counted with dead (PI+) cells excluded from the analysis. Histograms were analysed via FlowJo v10 software.

2.11. CD133 Expression

In order to assess whether the "stemness" state of the CSCs could be affected by chemical treatment, CD133 cell surface marker (highly expressed on GSCs) expression was measured via flow cytometry. Dissociated NCH421K cells were treated with the desired concentration(s) of compound (a low/non-toxic dose) by seeding the cells at 7.5×10^4 cells/mL in a 6-well plate (#657160, Greiner Bio-One, Les Ulis, France) (3 mL per well) with the compound. The cells were then incubated for four days under standard culture conditions before recovery of the cells, washing once in PBS and repeated flushing in order to dissociate the spheres without enzymatic treatment which could affect the cell surface marker. The cells were then counted with Trypan Blue (#T8154-100ML, Sigma-Aldrich, Saint-Quentin-Fallavier, France) exclusion for viability analysis using the Countess II FL automated cell counter, with 100,000 cells then centrifuged (350 g, 5 min, 4 °C) and resuspended in 100 µL 1/20 diluted anti-CD133-APC (#17-1338-41, Thermo Fisher Scientific, Illkirch-Graffenstaden, France, Villebon-sur-Yvette, France) antibody or the corresponding isotype control (#400119, Biolegend, Amsterdam, Netherlands) in PBS (2% FBS). The cells were incubated for 1 h on ice protected from light. The cells were centrifuged (350 g, 5 min, 4 °C) and resuspended in 200 µL PBS (2% FBS). The cells were run immediately on the FACS Calibur, with CD133 fluorescence analysed in the FL4 channel. Fluorescence histograms were analysed using FlowJo v10 software.

2.12. NCH421K-RAW 264.7 Macrophage Immunogenic Cell Death Co-Culture

In order to assess whether the cell death induced by a compound in GSCs was capable of initiating an immune response, a co-culture assay of treated NCH421K cells with murine macrophage RAW 264.7 cells was carried out. The NCH421K cells were seeded as described in Section 2.2.3. in a 48-well plate (#677180, Greiner Bio-One, Les Ulis, France) format. Spheres were treated at the desired time point and concentration in 300 µL culture volume.

To easily distinguish the RAW 264.7 cells in flow cytometry, they were stained with the stable non-toxic cell membrane marker, CellBrite® NIR680 (#30070, Biotium, Fremont, CA, USA) by incubation with a dilution of 1/2000 in their culture medium at a concentration of 1×10^6 cells/mL for 45 min at 37 °C protected from light. The cells were then washed twice in PBS (200 g, 5 min, RT) before resuspension in RAW cell medium (2% FBS, as higher concentrations of serum disturbed the CSCs) at a concentration of 2×10^5 cells/mL.

In order to avoid toxicity against the immune cells, the plate was centrifuged (350 g, 5 min, RT), with the supernatant carefully aspirated (and retained for DAMPs analysis) in order to avoid disturbing the treated spheroids before replacement with 600 µL stained RAW cell suspension. The co-culture was then left overnight to allow for activation of the immune cells, with cells/supernatants then analysed for activation markers by flow cytometry.

For the sonicated control, to imitate accidental cell necrosis/DAMPs release, wells containing non-treated NCH421K cells were collected by flushing and aspiration of the CSC medium containing cells. The cells were pelleted (350 g, 5 min, RT) and resuspended in RAW cell medium (2% FBS), which was transferred to a glass test tube and sonicated on ice three times at 20 kHz for 10 s on pulsed mode with 30 s intervals using a Vibracell sonicator. A 600 µL stained RAW cell suspension was pelleted (200 g, 5 min, RT), with the supernatant eliminated and the cells resuspended in the sonicated lysate and placed in the original well of the NCH421K cells.

2.13. Phagocytosis Assay

In order to assess whether the cell death induced by a compound in GSCs was capable of inducing phagocytosis of these cells by macrophages (and thus indirectly showing the exposure of immune "eat-me" signals), a co-culture assay was carried out as described in Section 2.12. However, in order to track the phagocytosis of the CSCs by the macrophages, the NCH421K cells were also stained using a non-toxic fluorescent marker. Thus, prior to seeding (as it was unsure whether staining of spheroids would produce homogenous staining of the cells), the NCH421K cells were stained with CellTracker™ CM-DiI Dye (#C7000, Invitrogen, Villebon-Sur-Yvette, France) by incubation with a dilution of 1/1000 in their culture medium at a concentration of 5.25×10^5 cells/mL for 5 min at 37 °C protected from light, followed immediately by a further 15 min at 4 °C. The cells were then washed once in PBS and resuspended in their culture medium for seeding at 7.5×10^4 cells/mL in a 48-well plate with 300 µL total volume and left to form spheres for four days. Treatment and co-culture were then carried out as described in Section 2.12. Cells were fixed in 4% paraformaldehyde (PFA) (#47608-1L-F, Sigma-Aldrich, Saint-Quentin-Fallavier, France) PBS for 30 min at RT, centrifuged (350 g, 5 min, RT), resuspended in 200 µL PBS and stored at 4 °C until running on the FACS Canto (Becton Dickinson, Franklin Lakes, New Jersey, United States). NCH421K cells were tracked in the PE channel and RAW 264.7 cells in the APC-Cy7 channel. Fluorescence histograms were analysed using FlowJo v10 software.

2.14. ATP Release Assay

In order to assess whether the cell death induced by a compound in GSCs was capable of releasing ATP, an important DAMP in immune cell activation, a luminescence-based ATP assay was carried out in parallel on the supernatant (released ATP) and supernatant + lysed cells (total ATP) of the treated cells. NCH421K cells were treated at the desired time point and concentration in a 48-well plate format (300 µL culture volume), with the supernatant, recovered and centrifuged (500 g, 5 min, RT) in order to remove any cells

and cell debris. The supernatant was decanted to a new 1.5 mL Eppendorf containing 300 µL CellTiter-Glo® 3D Cell Viability Assay reagent (Promega, Charbonnières-les-Bains, France) which was mixed by pipetting. At the same time, 300 µL of the same reagent was added to wells containing cells which had been treated in the same manner as those from which supernatant was recovered. The solutions were removed to an Eppendorf and were vigorously mixed to ensure efficient cell lysis. Solutions (including the medium-only control) were incubated for 30 min at RT protected from light. A total of 200 µL was then removed to an opaque 96-well plate in duplicate, with measurement of luminescence emission using a plate reader (SP200 Safas, Monaco). Background luminescence of the culture medium without cells was subtracted, with values expressed as arbitrary RLU counted by the luminometer. The luminescence of the treated supernatant was compared with that of the whole well luminescence to measure the total quantity of cellular ATP in the supernatant.

2.15. MHC-II Expression

As another method of assessing immune cell activation from the ICD model described in Section 2.12, RAW 264.7 cells were analysed for their expression of MHC-II. Cells were fixed in 4% PFA PBS for 30 min at RT, centrifuged (350 g, 5 min, RT) and resuspended in 50 µL PBS (2% FBS) with 1/200 diluted MHC-II (#116418, Biolegend, San Diego, CA, USA) or the corresponding isotype controls (#17-4321-81, Thermo Fisher Scientific, Illkirch-Graffenstaden, France) for 30 min on ice. The cells were then washed once in PBS (2% FBS) and ran immediately on the FACSCanto. MHC-II was analysed in the APC fluorescence channel, while RAW 264.7 cells were distinguished and selected in the co-culture through their cell membrane marker in the APC-Cy7 channel. Fluorescence histograms were analysed using FlowJo v10 software.

3. Results and Discussion

3.1. NHC-Pt(II)-PEI and PEI Decrease CSC Viability and Spheroid Formation

In order to assess the impact of the PDC NHC-Pt(II)-PEI (see structure in Figure 1) and the linear 22 kDa PEI (noted as PEI throughout the manuscript) on CSCs, three GSC cell lines, NCH421K, NCH644 and 3731 were used. These cell lines were isolated from patients suffering from glioblastoma [41,42,44], with their stem-like state being maintained and selected for by growth in a serum-free "stem cell" medium. These cells grow in a naturally non-adherent spheroid morphology (Figure 1). The effect on viability was measured (four days following seeding to allow the formation of spheroids) via ATP decrease using the CelltiterGlo 3D cell viability assay following 24 h treatment and was compared to a more differentiated glioma cell line (U87-MG) and a primary non-cancerous stem cell culture, DPSCs (grown as spheres (Figure S1)) (Table 1 and Figures S2–S6). The commercial platinum-based anti-cancer therapeutic oxaliplatin, and the standard glioblastoma treatment, temozolomide, were used for comparison (previously published results in [45]).

In order to compare concentrations of PDC (which were expressed as the concentration of Pt, of which there are an average of 17 per polymer molecule) with that of its polymer carrier alone (PEI), the true concentration of polymer was multiplied by the average number of platinum atoms which are bound to the same polymer molecule in the PDC, giving concentrations expressed as PEI equivalent (PEI eq). The result was low micromolar IC50 values for both the PDC NHC-Pt(II)-PEI and the "naked" PEI eq against the three GSC lines, significantly lower than the IC50 values against the non-cancerous stem and more differentiated glioma controls. Interestingly, the PEI polymer itself also displayed a high level of toxicity against the GSCs, with a three to tenfold greater toxicity compared to that against the two non-CSC cultures (Table 1). The morphological effect on the spheres of both the PDC and PEI was a drastic darkening, which was accompanied by a potential shrinking, but interestingly without a major disaggregation of the spheroids after 24 h (Figure 1).

Table 1. IC_{50} values (μM) of the compounds after 24 h of treatment.

	Glioblastoma Stem Cells			Non-Cancer Stem Cells	Glioma Cells
	NCH421K	NCH644	3731	DPSC	U87
Oxaliplatin	53 ± 1.9	55 ± 1.6	55.9 ± 2	>100	>100
Temozolomide	>100	97.2 ± 15	>100	>100	>100
NHC-Pt(II)-PEI	2.6 ± 0.1	1.4 ± 0.3	2.1 ± 0.3	6.6 ± 0.9 ****, ####, xxxx	9.3 ± 0.8 ****, ####, xxxx
PEI (eq)	3.3 ± 0.4	10.6 ± 0.6	2.9 ± 0.2	32.5 ± 0.9 ****, ####, xxxx	26.3 ± 3.5 ****, ###, xxxx
PEI (nM polymer)	*(194)*	*(624)*	*(169)*	*(1912)*	*(1547)*

All IC_{50} values are the mean of at least $n = 3$ independent experiments ± one standard error of the mean (SEM), with each experiment carried out in at least a technical duplicate. IC50 values were calculated by non-linear regression of cell viability curves generated via CelltitreGlo 3D cell viability assay using Prism software. Statistics (calculated using Prism) represent one-way ANOVA tests of the three GSC lines with either DPSCs or U87 cells with a post hoc Dunnett's multiple comparisons test against DPSC or U87 values as control. * = DPSC/U87 vs. NCH421K, # = DPSC/U87 vs. NCH644 and x = DPSC/U87 vs. 3731. ### = $p \leq 0.001$; ****/####/xxxx = $p \leq 0.0001$. Distribution normality was confirmed using a Shapiro–Wilk test. NHC-Pt(II)-PEI values are expressed as the concentration of Pt.

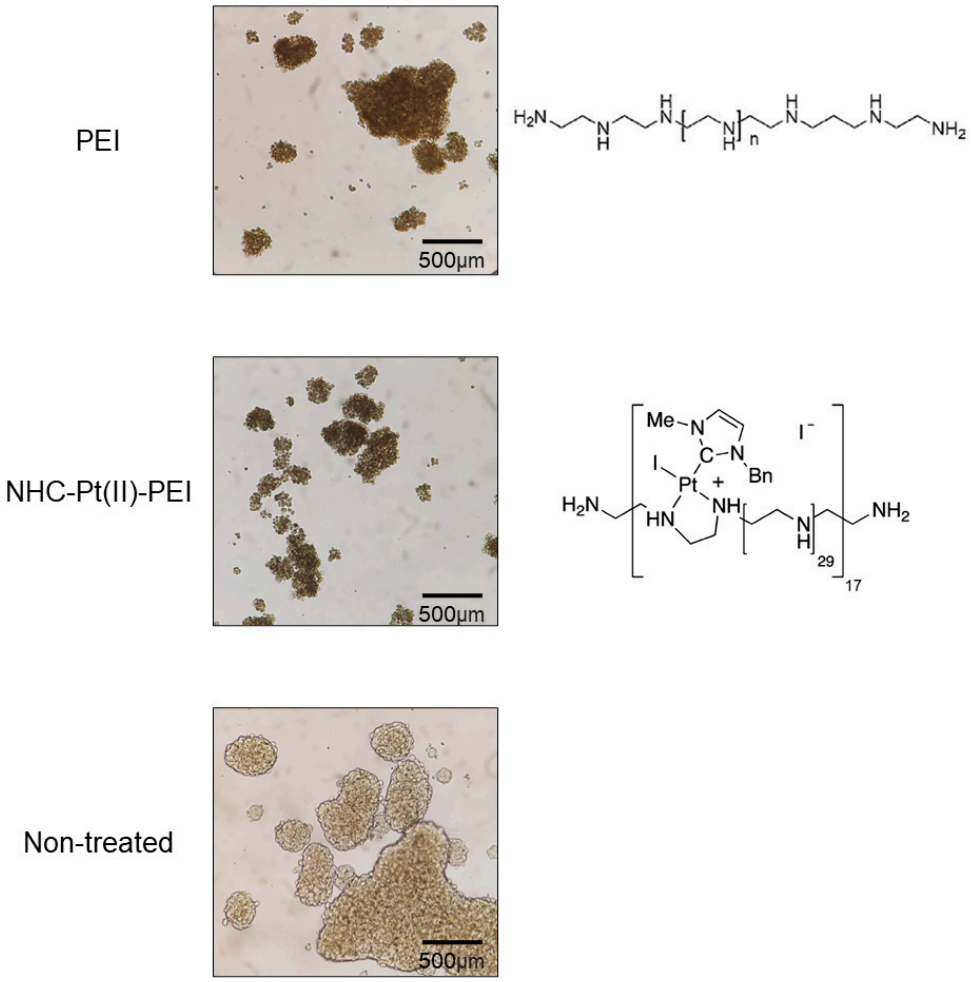

Figure 1. Light microscopy of 24 h treated PEI and NHC-Pt(II)-PEI treated NCH421K spheroids. Inverted light microscopy images at t = 24 h of 2.5 μM Platinum (or equivalent naked PEI) treated NCH421K cells at 4 × 10× = 40× magnification were taken using an Axio Vert A1 inverted light microscope (Zeiss) microscope coupled to a ProgRes C5 cool (Jenoptik, Jena, Germany) camera.

This surprising result suggested that the GSCs were specifically sensitive to PEI toxicity, which has been reported once in the literature recently by Prabhakar et al. (2021) [46], who observed that PEI-coated silica nanoparticles presented a high level of toxicity which was

seemingly selective to GSCs. A recent study by Knauer et al. (2022) [47] also suggests greater toxicity of a dendrimeric cationic polymer towards GSCs when compared to U87 cells. This is of interest as the use of such polymers as carriers for drugs (as in our case) at concentrations to which non-CSCs are not sensitive, could provide a two-pronged approach for delivering drugs which are known to be effective against bulk tumour cells, while also having a carrier-dependent or linked effect against a polymer-sensitive CSC niche. The chemical conjugation of components to the polymer may also change its physicochemical characteristics favourably by masking a portion of its positive charges, reducing interaction with serum proteins, and thus facilitating its application in vivo [48–50], an effect which could be proposed for our PDC from its successful application in vivo without visible side effects on the mice [11]. The PDC holds further promise in this respect as it has been shown to form nanoparticles in solution [11], which may allow its passive accumulation via the EPR effect, physically targeting it to the location of the polymer-sensitive CSCs [12,13].

The effect of the compounds on the capacity of the GSCs to form spheroids (an in vitro measurement of tumour proliferation capacity) was also investigated by seeding of the cells with treatment and video tracking of the formation of spheres using Incucyte technology (Figure 2).

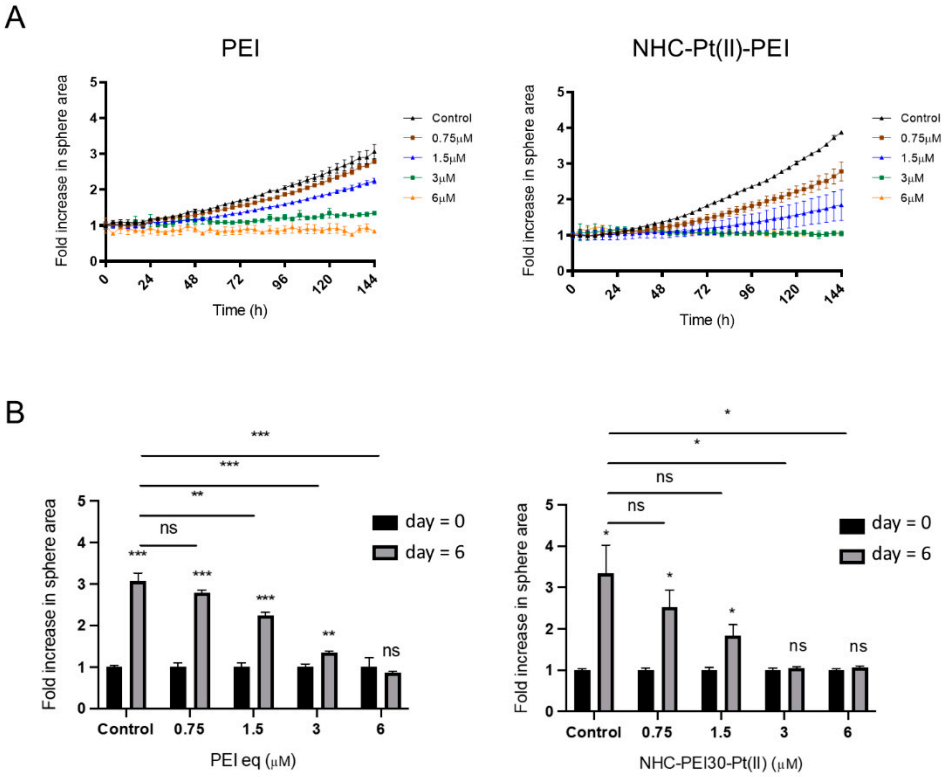

Figure 2. Effect of PEI and NHC-Pt(II)-PEI on NCH421K spheroid formation. (**A**) Scatter plots representing fold increase in spheroid area over time normalised to the time = 0 baseline. (**B**) Paired histograms showing the fold increase in area at time = 0 and time = 6 days (144 h) for each treated condition. Values represent the mean of at least $n = 3$ independent replicates ± one SEM. Control = ethanol vehicle control of the most concentrated condition (6 μM). Statistics above the bar charts represent Student's *t*-tests carried out between time = 0 and time = day 6 values for each condition. Statistics between histograms represent Student's *t*-tests of day = 6 values between conditions. ns = $p > 0.05$ * = $p \leq 0.05$, ** = $p \leq 0.01$. *** = $p \leq 0.001$. Distribution normality was confirmed using a Shapiro–Wilk test. Data collected using the IncuCyte and analysed using IncuCyte Zoom software.

The result was significant retardation in the ability of the GSCs to form spheres for both the PDC and PEI, showing the compounds may also be capable of interfering with the tumour growth capacity of these cells.

3.2. Culture Media Impacts Polymer Toxicity

As the in vitro model we used was limited with respect to the physiologically real environment and behaviour of GSCs, we particularly wished to investigate whether the serum-free nature of the CSC medium would have an impact on the physicochemical environment of the PEI such that it could change its toxicity, and potentially be responsible for the observed higher toxicity of the polymer towards CSCs. We thus treated the more differentiated glioma U87 cells for 24 h with the polymer in their classic 10% FBS medium and compared it with the treatment when applied in the FBS-free CSC medium (Figure 3).

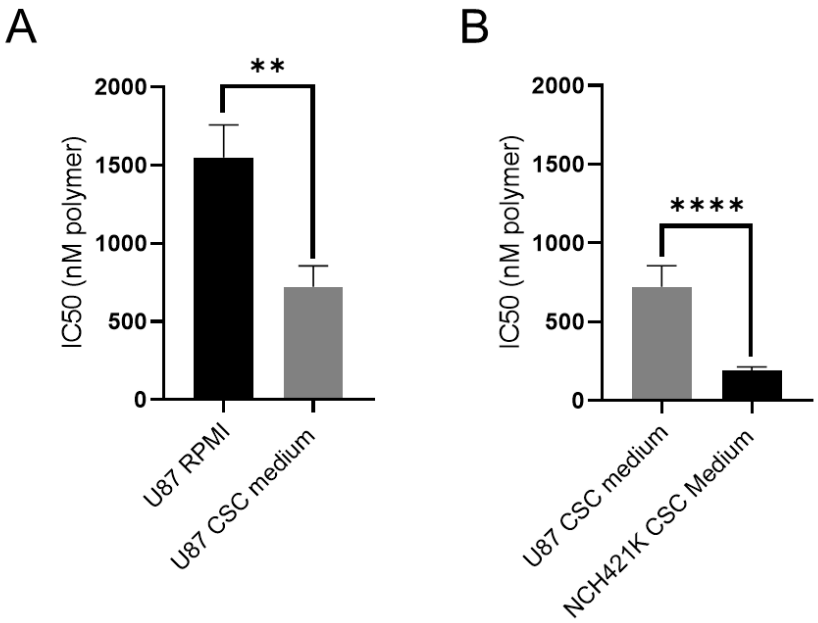

Figure 3. Effect of CSC medium on PEI toxicity on U87-MG cells. (**A**) Histograms showing 24 h IC50 values of PEI (expressed in nM of polymer) on U87-MG cells cultured in their standard medium (RPMI 10% FBS) vs. in serum-free CSC medium. (**B**) Histograms showing 24 h IC50 values of PEI (expressed in nM of polymer) on U87-MG cells cultured in CSC medium vs. NCH421K GSCs cultured in CSC medium. Values represent the mean of at least $n = 3$ independent experiments ± one SEM. Statistics represent Student's T-tests. ** = $p \leq 0.01$, **** = $p \leq 0.0001$. Distribution normality was confirmed using a Shapiro–Wilk test.

The result showed there was indeed a significant reduction of PEI's IC50 against U87 cells in the CSC medium (a roughly 800 nM difference), indicating that such difference in conditions may indeed influence the measurement of the cytotoxicity of compounds. This is an important observation for in vitro CSC studies, showing that great care should be taken in comparing toxicity between cell lines cultured in greatly different media. However, despite the impact on cytotoxicity, even when accounting for the difference in cellular medium composition, a roughly four-fold difference in IC50 remained between the GSCs and non-stem glioma (Figure 3B). This suggested that a specific sensitivity of the GSCs towards the polymer did indeed exist.

3.3. NHC-Pt(II)-PEI and PEI Induce Rapid Membrane Permeabilisation and Cytoplasm Vacuolisation in GSCs

The next step of the study was to elucidate the mechanism of cell death induced by PEI or NHC-Pt(II)-PEI. For this, an investigation into the kinetics of the GSC spheroid viability reduction of the compounds showed a rapid mechanism of action with major toxicity occurring after only 6 h of treatment, with the PDC seemingly inducing toxicity more quickly than PEI alone (Figure 4).

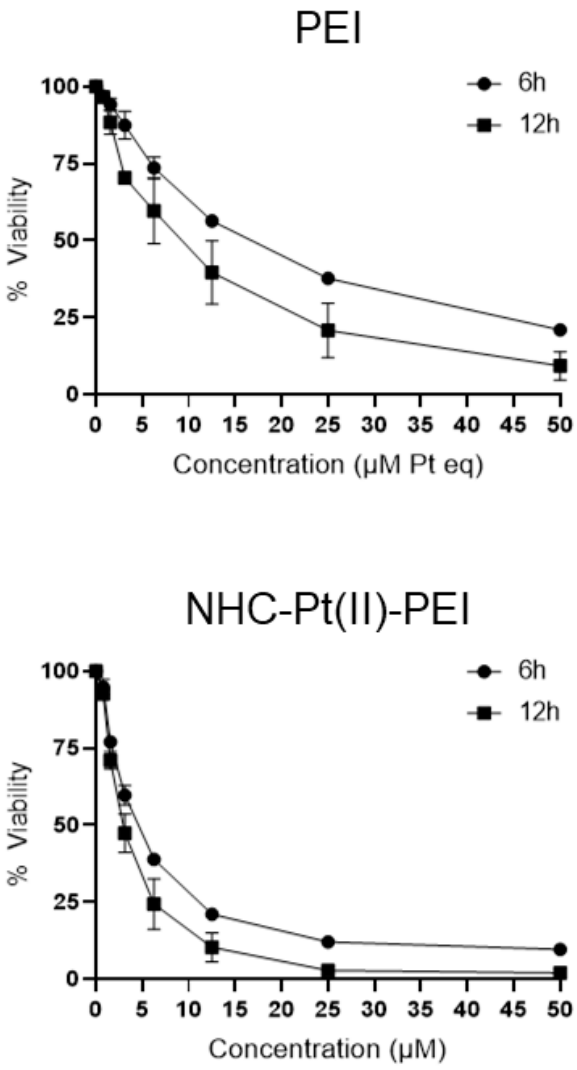

Figure 4. PEI and NHC-Pt(II)-PEI cell death kinetics. Cell viability curves of 6 h and 12 h PEI and NHC-Pt(II)-PEI treated NCH421K spheroids were measured via the CelltitreGlo 3D cell viability assay. Values are the mean of $n = 3$ independent replicates ± one SEM.

Such rapid toxicity is consistent with previous studies into the mechanisms of PEI toxicity [51], while the somewhat greater and faster toxicity of the PDC may be due to its physicochemical change into nanoparticles, or due to an implication of the platinum's chemistry.

We also wished to investigate whether the cell death mechanism induced was apoptotic, as activation of apoptotic markers has been identified in other studies and suggested as a dominant driver of cell death [52–54]. This was carried out by the measurement of caspase 3/7 activity (the terminal executioner caspases of apoptosis) and by flow cytometric measurement of early phosphatidylserine exposure on the outer cell membrane of cells which still maintain their membrane integrity AnV+/PI− cells). The result showed a clear absence of early phosphatidylserine externalisation as well as a lack of major caspase 3/7 activation for both the PDC and PEI (Figure 5A,B). This is contrary to the phosphatidylserine externalisation shown for the PDC in a previous study against the HCT116 colorectal cancer cell line [11].

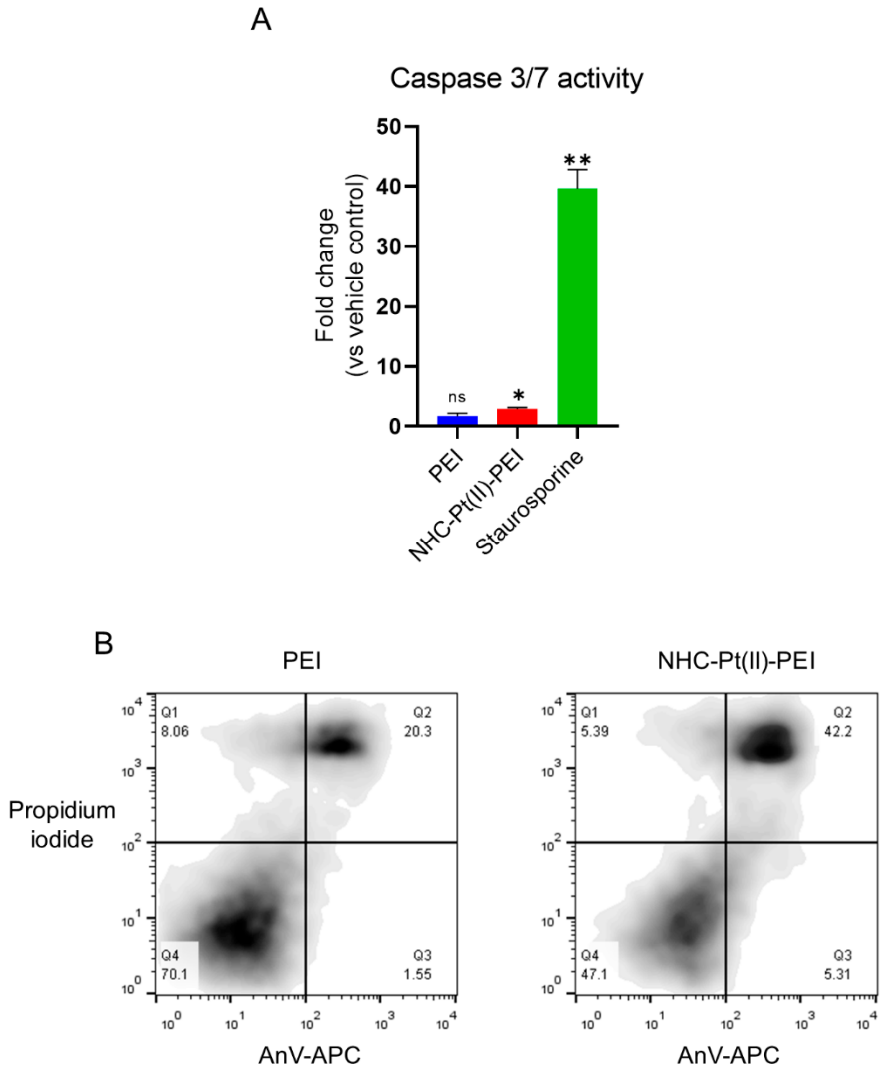

Figure 5. Absence of apoptotic markers on 24 h 2.5 μM NHC-Pt(II)-PEI and 2.5 μM PEI eq treated NCH421K spheroids. (**A**) Histograms showing fold change luminescence intensity compared to the corresponding vehicle control. Values represent the mean of at least $n = 3$ independent experiments ± one SEM. Statistics represent Student's t-tests with a Welch's correction vs. the corresponding vehicle reference. Distribution normality was confirmed using a Shapiro–Wilk test. ns = $p > 0.05$, * = $p \leq 0.05$, ** = $p \leq 0.01$. (**B**) Flow cytometry dot plots (FlowJo v10) of treated NCH421K cells stained with AnV-APC and PI. Viable cells = AnV−/PI−. Early apoptotic cells = AnV+/PI−. Late apoptotic/necrotic cells = AnV+/PI+. Early necrotic cells = AnV−/PI+.

This suggested that apoptosis was not the driver of cell death for PEI and the PDC against the GSCs, which is supported by another study where apoptotic markers were not identified and the caspase inhibitor zVAD-fmk had no effect on PEI-induced cell death [51]. We confirmed this for the PDC used in this study (Figure S7).

As other studies have shown PEI is able to induce a rapid perturbation of cell membrane integrity, resulting in necrosis [51,53], we thus wished to confirm this by treatment of NCH421K spheroids for 6 h with the compounds. This was followed by quantification of the release of LDH (an intracellular metabolic enzyme) by measurement of its enzymatic activity in the cellular supernatant and observation of cell death morphology by TEM. The result showed a significant release of total cellular LDH following 6 h (Figure 6A).

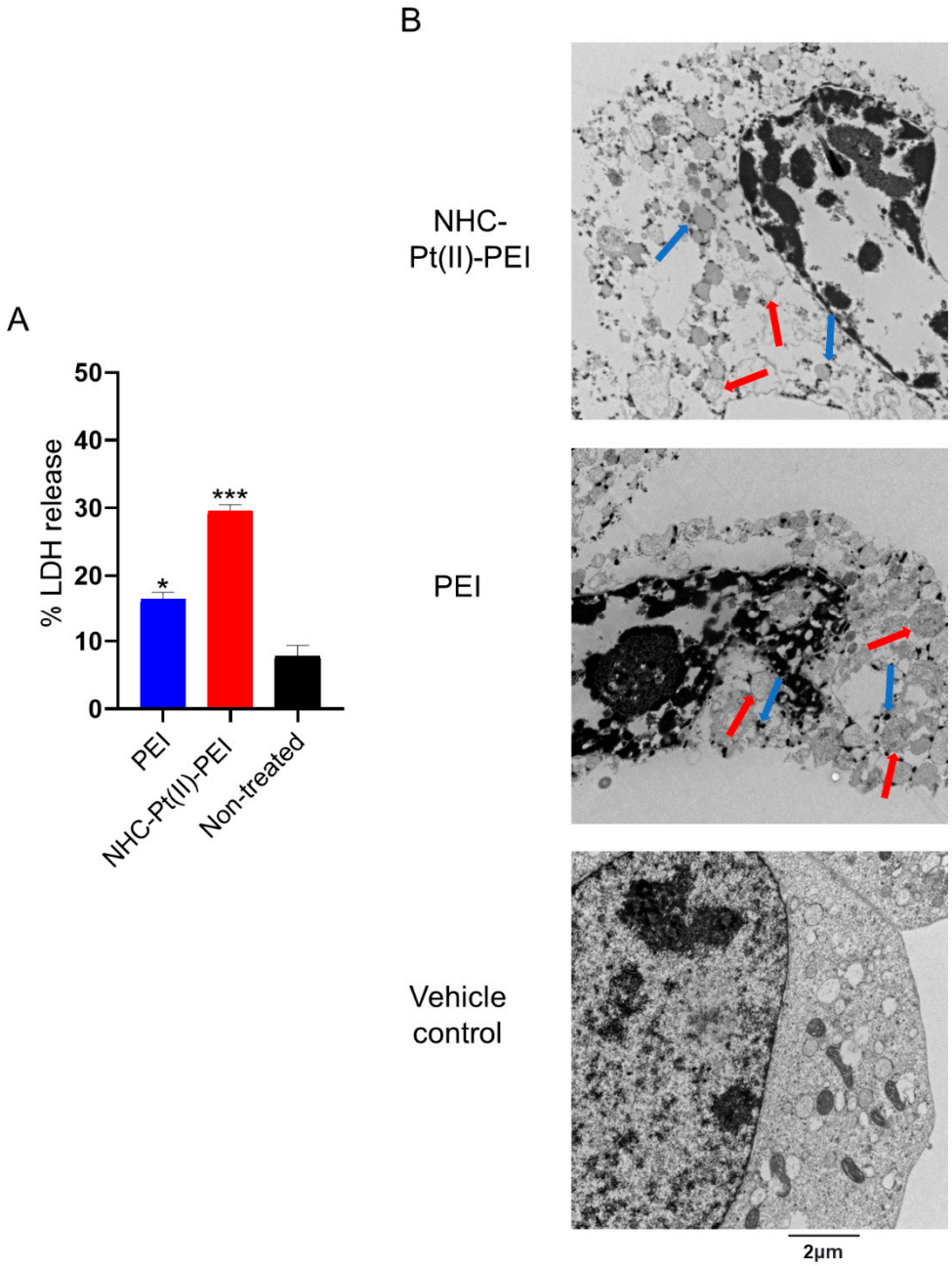

Figure 6. LDH release and necrotic, vacuolised cell death morphology of 6 h 5 µM NHC-Pt(II)-PEI and 5µM PEI eq treated NCH421K spheroids. (**A**) Histograms showing quantified LDH activity of cell supernatant as a percentage of the activity of lysed non-treated cells. Values represent the mean of at least $n = 3$ independent experiments ± one SEM. Statistics represent Student's *t*-tests versus the non-treated condition. Distribution normality was confirmed using a Shapiro–Wilk test. * = $p \leq 0.05$, *** = $p \leq 0.001$. (**B**) Representative TEM images of the treated cells at 15,000× magnification. Red arrows = Double membraned vesicles. Blue arrows = Purported lysosomes.

This membrane permeabilisation was confirmed through electron microscopy (Figure 6B), which also revealed a significant nuclear condensation and vacuolisation of the cytoplasm (Figure 6B), which was consistent with an increased granularity observed on the forward-scatter (FSC)/side-scatter (SSC) dot plots on the flow cytometer (Figure S8). This thus confirmed that the cell death (against GSCs) of PEI and the PDC proceeds via rapid membrane permeabilisation and a highly vacuolised necrosis-like cell death.

3.4. NHC-Pt(II)-PEI and PEI Induce a Protective Autophagy Response

Amongst the numerous cytoplasmic vesicles, some double-membraned vesicles could be identified, which indicated an accumulation of autophagosomes, as well as smaller dark vesicles which were likely to be lysosomes [55]. This led to the hypothesis that the observed vacuolised morphology was linked to an implication of the autophagy-lysosomal pathway, which is an important cellular turnover/recycling mechanism [26]. Either through a high level of activation of the autophagic pathway or through inhibition of autophagosome-lysosome fusion, causing their accumulation. Autophagy has been shown to be upregulated and used as a survival and drug resistance mechanism in CSCs which is highly implicated in the maintenance of their "stemness" [25,56], with therapeutics targeting this pathway, thus being of greater interest [57,58].

In order to verify whether treatment with the PDC and PEI induce an accumulation of autophagosomal vesicles, the NCH421K cells were treated for 6 h. Cells were then lysed, with total cellular lysate then analysed via SDS-PAGE Western blot for an accumulation of the protein LC3-II (lipidated LC3). LC3 is an important protein involved in autophagy and autophagosomal formation which inserts itself into the autophagosomal membrane following lipidation with the phospholipid, phosphatidylethanolamine (PE). Thus, an accumulation of autophagosomal vesicles may be detected by the differential migration of lipidated vs. non-lipidated (LC3-I) LC3. Such an accumulation may be due either to an increase in autophagic flux, and thus an increased activation of autophagy, or due to an inhibited turnover of autophagosomes, with turnover implicating the de-lipidation and degradation of LC3-II [59]. Inhibition of LC3-II turnover may be caused by an inhibition of lysosome-autophagosome fusion (the autophagolysosome), as the final degradation and turnover of the sequestered contents are dependent on this step [27,59]. The known inhibitor of lysosome-autophagosome fusion, chloroquine [60,61] was thus used as a positive control for LC3-II accumulation [59]. Treatment with the PDC and PEI showed a significant increase in the LC3-II/LC3-I ratio, indicative of autophagosome accumulation (Figure 7A,B and Figure S11).

In order to confirm whether there was also a corresponding accumulation of acidic vesicles in the cells, the treated cells were stained with the lysosomotropic dye (acidic vesicle accumulating) Lysotracker Green. Chloroquine again served as a positive control, which has been shown to increase cellular lysosome volume [60–63]. The compounds showed a clear increase in the lysotracker signal (Figure 7C,D). This suggests an accumulation of lysosomes for the PDC and PEI, as for chloroquine. However, the cellular morphology of chloroquine-treated cells observed by electron microscopy did not show the same drastic vacuolisation (Figure S9). One might suspect that the described "proton-sponge" effect of PEI [64,65] may lead to lysosomal dysfunction which prevents fusion with autophagosomes in a manner similar to chloroquine. However, a similar LC3-II accumulation we observed for poly-L-lysine (PLL)-treated cells (Figure S10), a cationic polymer whose pKa does not allow the proton-sponge effect to occur, suggested this to not be the case.

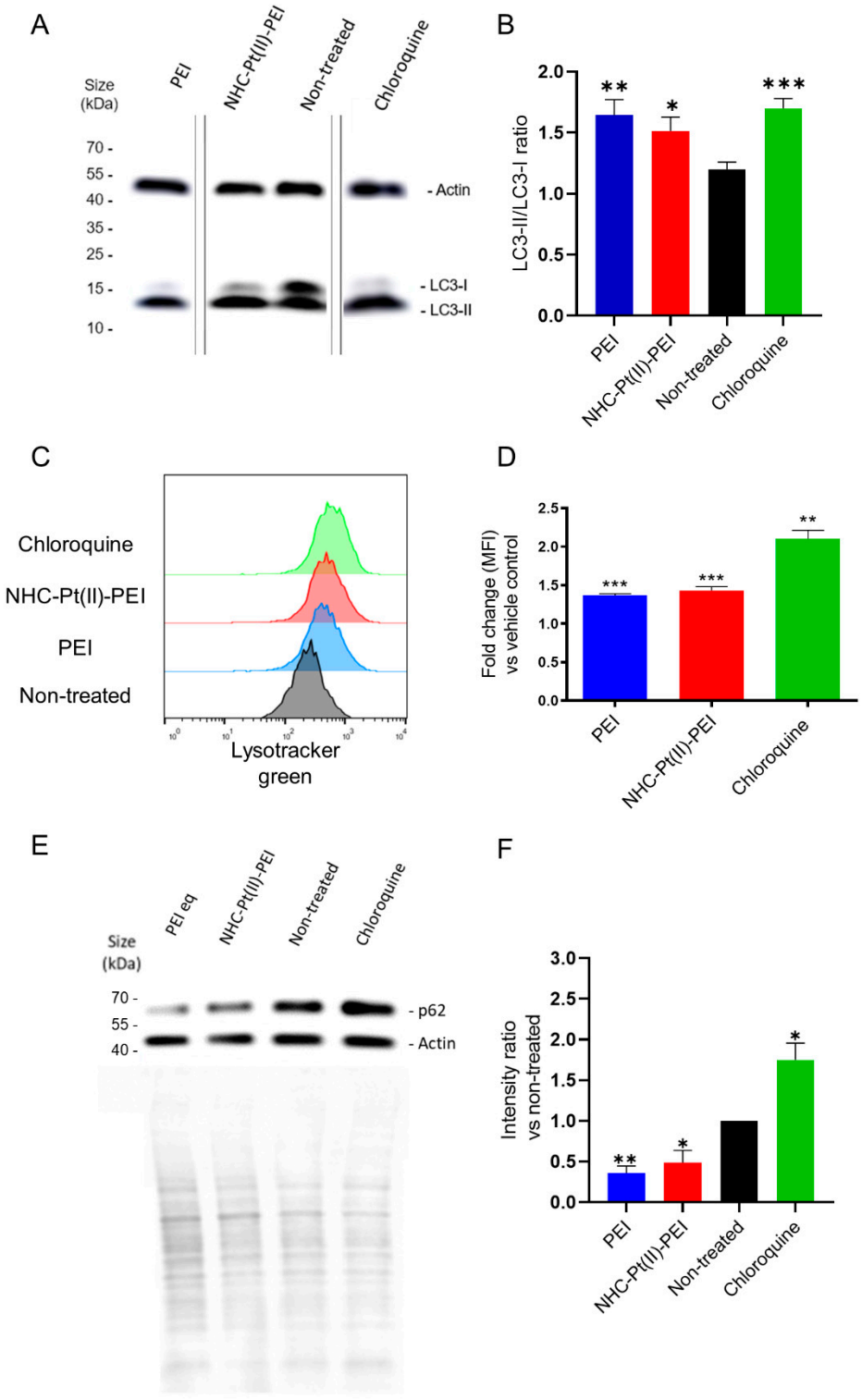

Figure 7. Accumulation of LC3-II and acidic vesicles accompanied by increased p62 degradation in 6 h 5 μM NHC-Pt(II)-PEI, 5 μM PEI eq treated NCH421K spheroids. (**A**) Representative Western blot of total cell lysate showing accumulation of LC3-II (lipid-bound) and reduction of free LC3-I. (**B**) Histograms showing LC3-II/LC3-I intensity ratio calculated from the integrated density of selected bands using ImageJ. Values represent the mean of at least $n = 3$ independent experiments ± one SEM. Statistics represent Student's *t*-tests vs. the non-treated control. Distribution normality

was confirmed using a Shapiro–Wilk test. (**C**) Representative fluorescence histograms (FlowJo v10) showing lysotracker green fluorescence of live gated NCH421K cells. (**D**) Histograms showing fold change in median lysotracker fluorescence vs. control of the treated conditions. Values represent the mean of at least $n = 3$ independent experiments ± one SEM. Statistics represent Student's T-tests with a Welch's correction vs. the corresponding vehicle reference. Distribution normality was confirmed using a Shapiro–Wilk test. * = $p \leq 0.05$, ** = $p \leq 0.01$, *** = $p \leq 0.001$. MFI = median fluorescence intensity. (**E**) Representative Western blot of total cell lysate showing changes in p62 levels. Below shows the corresponding actin and Ponceau S total protein loading controls. (**F**) Histograms showing the ratio of p62 expression (calculated from the integrated density of selected bands using Image J) versus the non-treated control, normalised for total protein loading differences by calculated Ponceau S lane intensities. Values represent the mean of $n = 4$ independent experiments + one SEM. Statistics represent Student's *t*-tests. Distribution normality was confirmed using a Shapiro–Wilk test. * = $p \leq 0.05$, ** = $p \leq 0.01$.

To confirm this, the treated cells were blotted for p62, a ubiquitin-binding protein used for the targeting of proteins for selective autophagy which is itself degraded by autophagy, and thus whose levels inversely correlate to autophagic activity [59,66]. The observation of a decrease in p62 degradation shows that the PEI and PDC-induced increase in autophagy-related vesicles is due to increased activation of the pathway, contrary to the autophagic block induced by chloroquine which increases p62 levels (Figure 7E,F and Figure S11). This is in agreement with two other studies which have shown a similar increase in autophagy due to PEI treatment [67,68] as well as another study into the effect of polystyrene nanoparticles known to cause lysosomal damage which also increased autophagic flux [69]. Interestingly, this latter study concluded that autophagy induction at the early stage is an initial pro-survival response to the treatment but also that lysosomal dysfunction eventually leads to inhibition of the pathway later on [69].

This role as a protective mechanism is also indicated in our case, as co-treatment with wortmannin (an inhibitor of the critical autophagy regulator phosphoinositide 3-kinase (PI3K)) [70] significantly increased the induced toxicity of treatment with PEI and the PDC (Figure 8).

Autophagy has been shown to be a highly important and finely regulated mechanism in CSCs, which is implicated in the maintenance of their stem-like phenotype [56,71]. Its exact role is somewhat controversial, with studies suggesting that both induction [72,73] and inhibition [74,75] are capable of interfering with the stem-like phenotype (indicating that balance, rather than activation or inhibition, may be the key to its role), which may have major therapeutic implications for their metastasis and drug-resistance [71,76]. We thus wondered whether the evident implication in the autophagic pathway displayed by PEI and our PDC could have an effect on the stem-like phenotype of the cells.

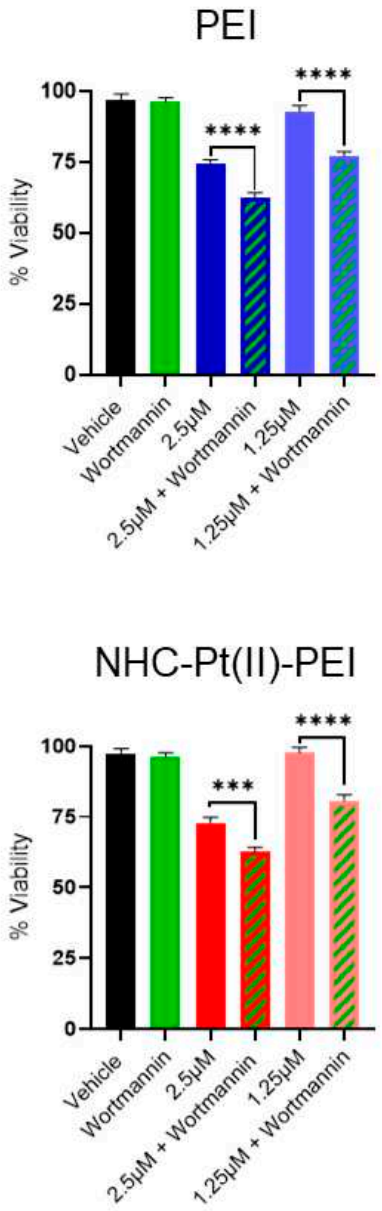

Figure 8. Increased PEI and NHC-Pt(II)-PEI toxicity with wortmannin co-treatment. CelltiterGlo 3D cell viability assay of NCH421K cells treated for 24 h with PEI or NHC-Pt(II)-PEI co-treated with 50 nM wortmannin (following 2 h pre-treatment with 50 nM wortmannin). Vehicle control corresponds to the equivalent highest amount of solvent added. Values represent the mean of at least $n = 3$ independent experiments ± one SEM. Statistics represent Student's *t*-tests. Distribution normality was confirmed using a Shapiro–Wilk test. *** = $p \leq 0.001$. **** = $p \leq 0.0001$.

3.5. NHC-Pt(II)-PEI and PEI Treatment Reduce the Expression of CSC Marker CD133

In order to evaluate whether the PDC and PEI could cause differentiation of the NCH421K GSCs, the expression of the GSC marker CD133 was evaluated using flow cytometry following treatment with low concentrations (375 nM and 375 nM PEI eq) of the compounds for four days, in order to avoid significant cell death while giving time for significant cellular expression changes to occur. Both induced a slight but significant reduction in CD133 expression (Figure 9A,B), indicating a reduction in the stem-like phenotype, as U87-MG cells did not express CD133 (Figure S12).

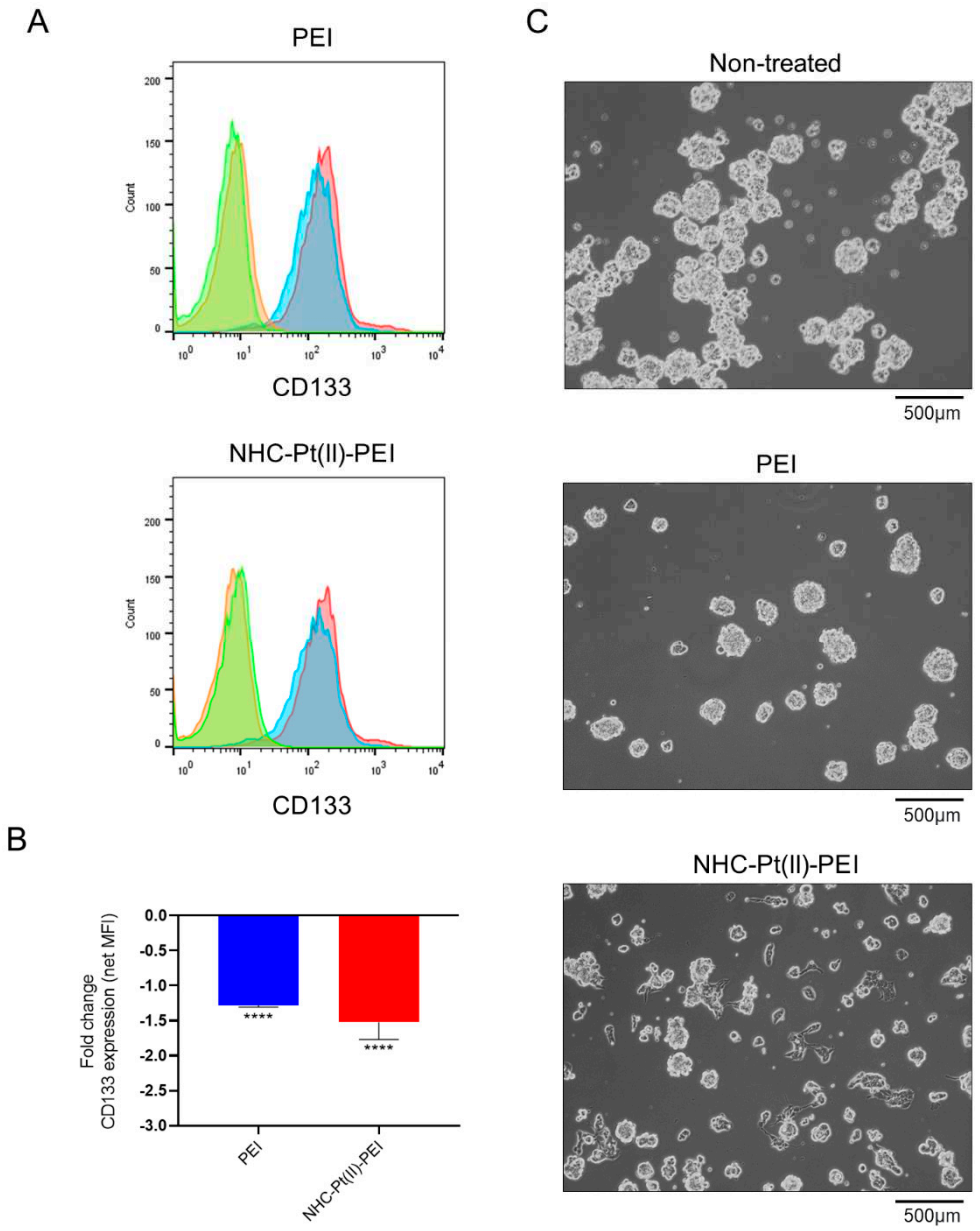

Figure 9. Loss of CD133 CSC marker and CSC morphology of NCH421K cells treated for 4 days with 375 nM NHC-Pt(II)-PEI and PEI eq. (**A**) Representative flow cytometry fluorescence histograms (FlowJo v10) showing a reduction in CD133 fluorescence on NCH421K cells. Orange = EtOH control isotype. Green = PEI or NHC-Pt(II)-PEI treated isotype. Red = Vehicle-treated CD133 stained. Blue = PEI or NHC-Pt(II)-PEI CD133 stained. (**B**) Histograms showing fold change in CD133 net geometric mean fluorescence intensity (MFI stained—MFI isotype) vs. vehicle-treated control. Values represent the mean of at least $n = 3$ independent experiments. Statistics represent Student's *t*-tests with a Welch's correction vs. the corresponding vehicle reference. Distribution normality was confirmed using a Shapiro–Wilk test. **** = $p \leq 0.0001$. (**C**) Inverted light microscopy images of treated NCH421K cells at 4 × 10× = 40× magnification were taken using an Axio Vert A1 inverted light microscope (Zeiss) microscope coupled to a ProgRes C5 cool (Jenoptik, Jena, Germany) camera.

Interestingly, this was also accompanied by a change in morphology from spheroids to a more classical adherent neural morphology for the PDC-treated condition (Figure 9C), which was less evident for the PEI-treated condition but induced an adherence of the spheroids to the culture plate (Figure 9C). This shows the great promise of PEI as a carrier for anti-CSC therapeutics, since the delivery agent itself, as well as potentially having a

specific affinity or toxicity towards the CSC population, may sensitise the cells to a cargo towards which they may otherwise be resistant, and which may be naturally effective against the rest of the bulk tumour mass [75].

3.6. NHC-Pt(II)-PEI and PEI Cell Death Induces Phagocytosis and DAMPs Release

The observed cell death mode of NHC-Pt(II)-PEI and PEI was of interest in relation to the anti-cancer immune response. This was due to its necrotic nature, which is known to be able to induce an anti-cancer immune response through the release of DAMPs [77], and also due to its activation of autophagy. As autophagy has been shown to be important for tumour immunogenicity via the secretion of the DAMP ATP [78], and the presentation of antigen on tumour cells (although autophagy's role in the anti-cancer immune response is complex, as it also seems to be important in immune evasion of established tumours) [79].

To evaluate the potential effect of NHC-Pt(II)-PEI and PEI-induced cell death on anti-tumour immune response induction, a co-culture system was used. NCH421K cells were treated for 6 h with the compound to initiate significant (but not total) cell death, with the treatment then removed from the cells and replaced with a culture of RAW 264.7 murine macrophage cells and left overnight. The removed supernatant was first dosed for a release of ATP (which is detected as a DAMP by purinergic receptors on immune cells) using the CelltiterGlo 3D assay. The result was a significant release of ATP following 6 h treatment, with roughly 12% of total cellular ATP being present in the cell supernatant (Figure 10A).

The externalisation of the phagocytotic DAMP calreticulin from the ER to the cell surface was measured via flow cytometry, which showed an externalisation of the protein to the surface of cells with an intact plasma membrane (Figure 10B,C). Expression of "eat me" signals such as calreticulin is the first step for the phagocytosis of tumour cells. Thus, we followed the active phagocytosis of these cells by RAW mouse macrophages using a flow cytometric phagocytosis assay, where the RAW cell population showed a clear uptake of the NCH421K cells (whose membranes were rendered fluorescent with a stable membrane dye prior to seeding and treatment with the compounds) for the PDC and PEI-treated conditions, but not for the sonicated control (consisting of sonicated NCH421K lysate to imitate "accidental" necrosis/DAMP release), indicating that dye uptake was indeed due to phagocytosis of whole cells and not due to non-specific pinocytosis of free or cellular debris-bound dye (Figure 11A,B).

Another important feature of ICD is the induction of APC maturation by released DAMPs that will permit the initiation of an adaptive immune response. The RAW cells also showed an upregulation of MHC-II, a marker of macrophage maturation, showing that PDC and PEI induced-cell death have the potential to activate the adaptive immune response (Figure 11C,D). This shows that the necrotic cell death type induced by the PDC and PEI against GSCs shows characteristics in line with the ability to induce an immune response, a highly desirable characteristic of anti-cancer chemotherapeutics as the activation of an adaptive immune response against tumours is well known to greatly improve clinical outcomes [36,80].

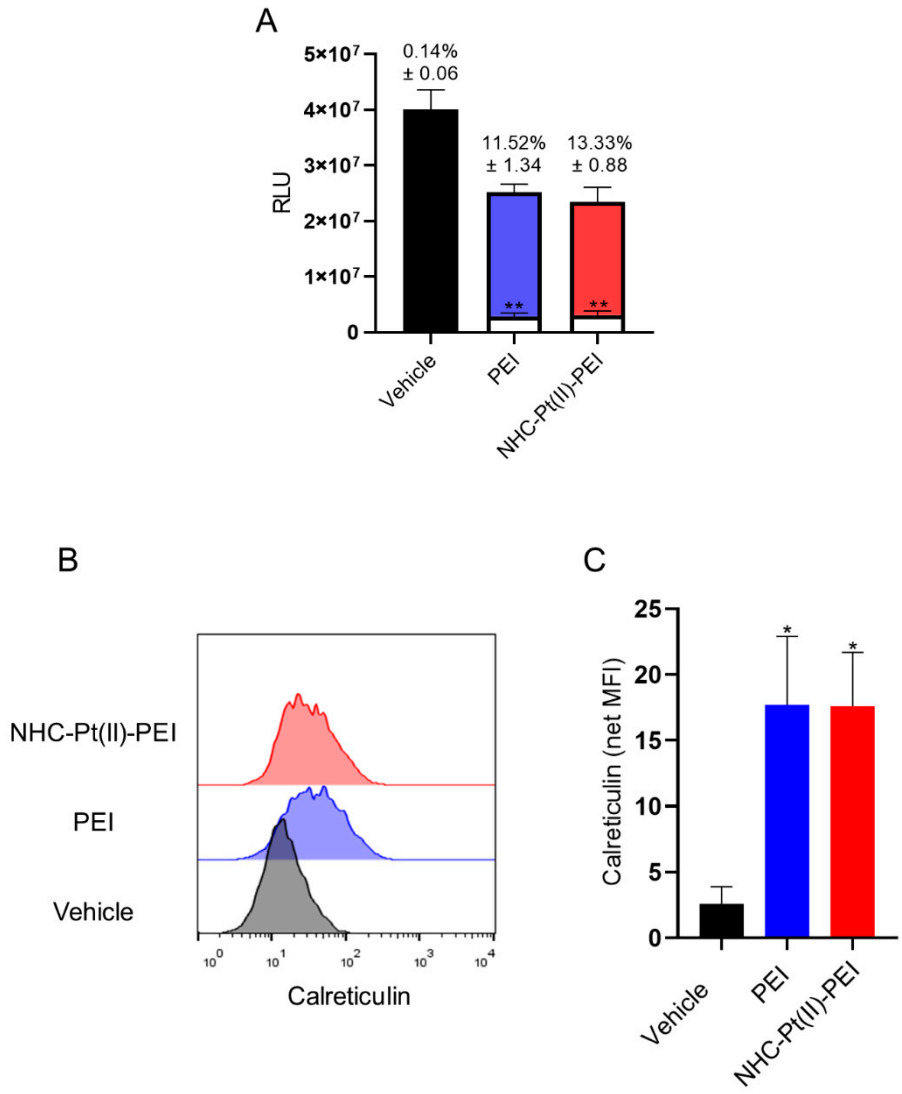

Figure 10. DAMPs release of 6 h 5µM NHC-Pt(II)-PEI and 5µM PEI eq treated NCH421K spheroids. (**A**) Overlapped histograms of ATP generated RLU using the CelltiterGlo 3D viability assay measured on the cellular supernatant (white) and the total well contents (cells + supernatant) (coloured) following treatment. The numbers above represent the percentage of ATP found in the supernatant relative to the total well contents. Values represent the mean of at least $n = 3$ independent experiments ± one SEM. Statistics represent Student's t-tests vs. the corresponding vehicle reference. Distribution normality was confirmed using a Shapiro–Wilk test. ** = $p \leq 0.01$. (**B**) Representative flow cytometry histograms (FlowJo v10) of treated live-gated (PI-) cells stained for calreticulin. (**C**) Histograms of net MFI (median) (MFI condition – MFI isotype control) of treated cells. Values represent the mean of at least $n = 3$ independent experiments ± one SEM. Statistics represent Student's T-tests vs. the corresponding vehicle reference. Distribution normality was confirmed using a Shapiro–Wilk test. * = $p \leq 0.05$.

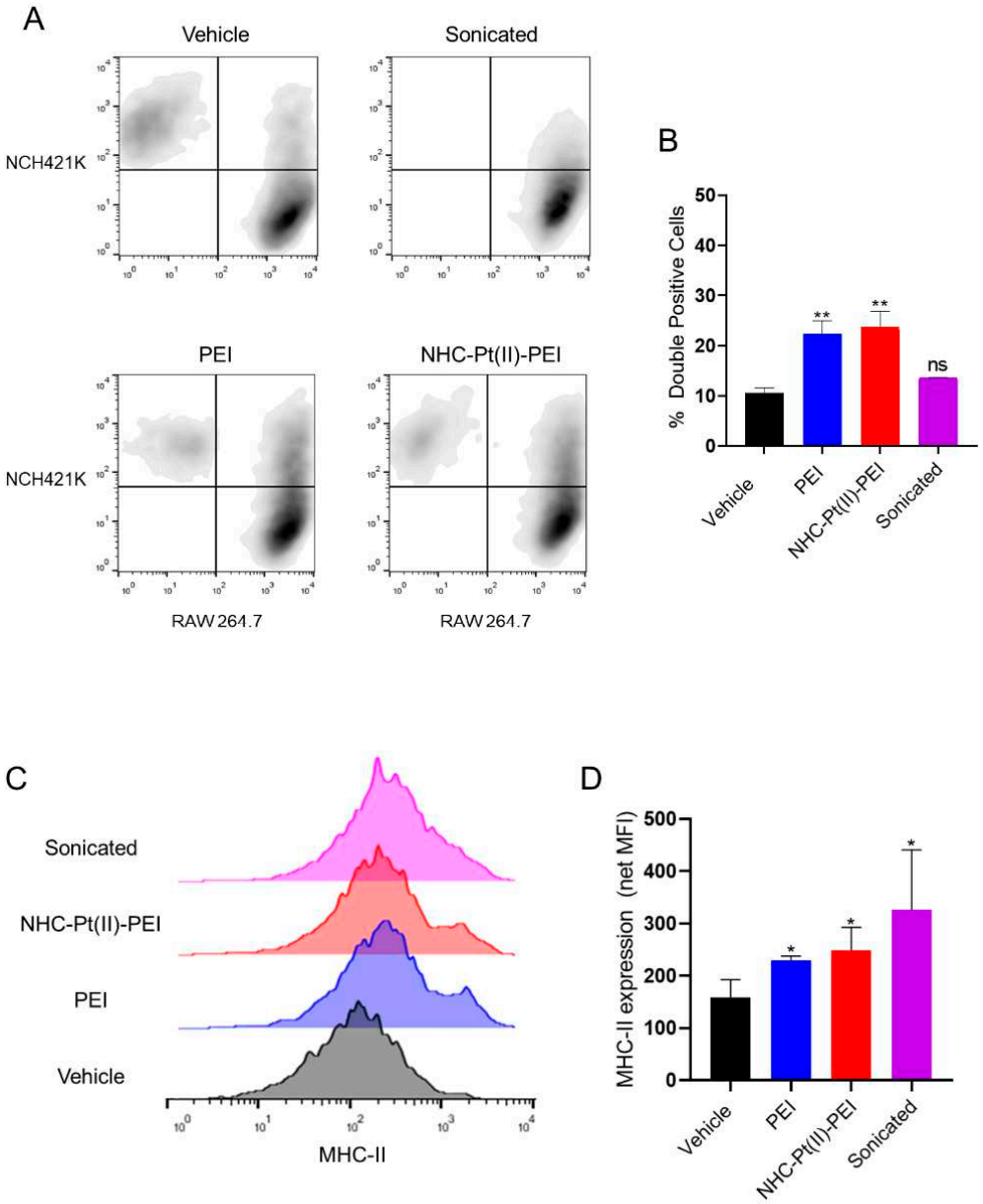

Figure 11. Phagocytosis and macrophage activation by 6 h 5μM NHC-Pt(II)-PEI and 5μM PEI eq treated NCH421K spheroid co-culture. (**A**) Representative flow cytometry dot plots (FlowJo v10) of stained NCH421K spheroids treated for 6 h prior to addition of stained RAW macrophages for overnight co-culturing. (**B**) Histograms showing the percentage of double-positive (RAW phagocytosed NCH421K) cells representing the mean of $n = 3$ independent experiments ± one SEM. Statistics represent Student's t-tests vs. the corresponding vehicle reference. Distribution normality was confirmed using a Shapiro–Wilk test. ns = $p > 0.05$, ** = $p \leq 0.01$. (**C**) Representative flow cytometry histograms (FlowJo v10) of MHC-II fluorescence. (**D**) Histograms showing net MFI (median) (MFI treatment—MFI isotype control) of treated cells. Values represent the mean of $n = 3$ independent experiments. Statistics represent Student's *t*-tests vs. the corresponding vehicle reference. Distribution normality was confirmed using a Shapiro–Wilk test. * = $p \leq 0.05$.

4. Conclusions

This work, originally intended as an evaluation of the previously described anticancer platinum PDC NHC-Pt(II)-PEI [11] against the therapeutically important CSC sub-population, may potentially be one of the first of many studies in a new paradigm within the search for effective methods of treating CSCs. The cationic polymer, linear 22 kDa PEI, may present a potent and specific toxicity toward CSCs. This effect seems to be

maintained when administered in the form of a PDC, with the physicochemical changes induced by this conjugation being potentially crucial for its pharmaceutical tolerance. The cell death was shown to be necrotic, rather than apoptotic in nature, potentially bypassing the resistance to apoptosis of CSCs and showing promise as an inducer of an anti-cancer immune response. The cell death was also shown to be accompanied by an induction of a protective autophagy response. The implication of the autophagic pathway in the compound's mechanism of action is a highly promising characteristic in its application against CSCs, as it is a pathway for which balance is key in the maintenance of their metastatic and drug-resistant phenotype. A phenotype in which we observed interference through the reduction of the CSC marker CD133. One could thus envisage the exploitation of such effects on CSCs for the delivery of a chemotherapeutic payload to which CSCs are normally resistant, with either direct toxicity or a sensitisation to the payload occurring through the action of the polymer carrier. Being, so far, one of the very few studies to suggest that CSCs possess a sensitivity to the toxicity of polycations, further attention must be paid to these observations to elaborate on why this may be the case, and to exactly which molecules it may apply. Thus bringing polymers and PDCs to the forefront of the fight against this clinically nefarious niche.

Supplementary Materials: The following supporting information can be downloaded at: https://www.mdpi.com/article/10.3390/cancers14205057/s1, Figure S1. DPSC spheroid cell culture; Figure S2. IC50 for the GSC cell line NCH421K; Figure S3. IC50 for the GSC cell line NCH644; Figure S4. IC50 for the GSC cell line 3731; Figure S5. IC50 for the non-cancerous stem cells, DPSCs; Figure S6. IC50 for the non-stem glioma cell line U87-MG; Figure S7. Cell death proportion of 24 h NHC-Pt(II)-PEI and zVAD-fmk co-treated NCH421K cells; Figure S8. The granularity of 24 h 5 μM PEI eq and NHC-Pt(II)-PEI treated NCH421K spheroids; Figure S9. Transmission electron microscopy of 6 h 60 μM chloroquine treated NCH421K cells; Figure S10. Unedited LC3 western blots; Figure S11. Unedited p62 western blots; Figure S12. U87 CD133 expression.

Author Contributions: Conceptualization, C.M., S.F. and A.K.; investigation, C.M., C.D., C.B., E.M. and J.B.; methodology, C.M., E.M., M.D., C.H.-M. and A.I.; supervision and validation, S.F. and A.K.; resources, M.D., C.H.-M., A.I., P.L. and S.B.-L.; roles/writing—original draft, C.M., S.F. and A.K.; writing—review and editing, C.D., C.B., E.M., J.B., M.D., C.H.-M., A.I., P.L. and S.B.-L.; funding acquisition, S.F., A.K. and S.B.-L. All authors have read and agreed to the published version of the manuscript.

Funding: This work was financially supported by the Fondation ARC (Association pour la Recherche sur le Cancer project Number ARCPJA32020060002306—Fournel Sylvie). This research was supported by the ITI Innovec (IdEx (ANR-10-IDEX-0002) and SFRI (ANR-20-SFRI-0012)).

Institutional Review Board Statement: Not applicable.

Informed Consent Statement: Not applicable.

Data Availability Statement: Data are contained within the article or Supplementary Material. Raw data may be made available upon request.

Acknowledgments: The authors acknowledge Cathy Royer from the In Vitro Imaging Platform (CNRS, UMR 3156, University of Strasbourg) for the technical assistance during the transmission electron microscopy observations, and Florent Meyer for his donation of the DPSCs. We acknowledge Thierry Achard, Aline Maisse-François and Emilie Couzigné for assistance with syntheses.

Conflicts of Interest: There are no conflict to declare.

Abbreviations

AnV	Annexin V
APC	Allophycocyanin/Antigen-presenting cell
CSC	Cancer stem cell
DAMP	Damage associated molecular pattern
DER	Poly(propylene glycol) diglycidyl ether
DMEM	Dulbecco's Modified Eagle Medium
DMAE	Dimethylethanolamine
DPSC	Dental pulp stem cell
EPR	Enhanced permeability and retention effect
FBS	Fetal bovine serum
FSC	Forward scatter
GSC	Glioblastoma stem cell
ICD	Immunogenic cell death
LC3	protein microtubule-associated proteins 1A/1B light chain 3
LDH	Lactate dehydrogenase
MEM	Minimum essential medium
MFI	Median/Geometric mean fluorescence intensity
NHC	N-heterocyclic carbene
NSA	Nonenyl succinic anhydride
PBS	Dulbecco's phosphate-buffered saline
PDC	Polymer–drug conjugate
PEG	Polyethylene glycol
PEI	Polyethylenimine
PI	Propidium iodide
RLU	Relative luminescence unit
RPMI	Roswell Park Memorial Institute
SEM	Standard error of the mean
SDS-PAGE	Sodium dodecyl sulphate–polyacrylamide gel electrophoresis
SSC	Side scatter
TEM	Transmission electron microscopy

References

1. Dilruba, S.; Kalayda, G.V. Platinum-Based Drugs: Past, Present and Future. *Cancer Chemother. Pharmacol.* **2016**, *77*, 1103–1124. [CrossRef] [PubMed]
2. Aggarwal, M.; Chawla, S.; Singh, K.; Rana, P. Evaluation of Anticancer Drug Utilization and Monitoring of Adverse Drug Reaction in the Indoor Patients Receiving Cancer Chemotherapy in a Tertiary Care Hospital in New Delhi. *J. Basic Clin. Pharm.* **2018**, *9*.
3. Pages, B.J.; Garbutcheon-Singh, K.B.; Aldrich-Wright, J.R. Platinum Intercalators of DNA as Anticancer Agents. *Eur. J. Inorg. Chem.* **2017**, *2017*, 1613–1624. [CrossRef]
4. Dasari, S.; Bernard Tchounwou, P. Cisplatin in Cancer Therapy: Molecular Mechanisms of Action. *Eur. J. Pharmacol.* **2014**, *740*, 364–378. [CrossRef]
5. Zhang, C.; Xu, C.; Gao, X.; Yao, Q. Platinum-Based Drugs for Cancer Therapy and Anti-Tumor Strategies. *Theranostics* **2022**, *12*, 2115–2132. [CrossRef]
6. Skander, M.; Retailleau, P.; Bourrié, B.; Schio, L.; Mailliet, P.; Marinetti, A. N-Heterocyclic Carbene-Amine Pt(II) Complexes, a New Chemical Space for the Development of Platinum-Based Anticancer Drugs. *J. Med. Chem.* **2010**, *53*, 2146–2154. [CrossRef]
7. Bellemin-Laponnaz, S. N-Heterocyclic Carbene Platinum Complexes: A Big Step Forward for Effective Antitumor Compounds. *Eur. J. Inorg. Chem.* **2020**, *2020*, 10–20. [CrossRef]
8. Ekladious, I.; Colson, Y.L.; Grinstaff, M.W. Polymer–Drug Conjugate Therapeutics: Advances, Insights and Prospects. *Nat. Rev. Drug Discov.* **2019**, *18*, 273–294. [CrossRef]
9. Wadhwa, S.; Mumper, R.J. Polymer-Drug Conjugates for Anticancer Drug Delivery. *Crit. Rev. Ther. Drug Carrier Syst.* **2015**, *32*, 215–245. [CrossRef]
10. Petros, R.A.; Desimone, J.M. Strategies in the Design of Nanoparticles for Therapeutic Applications. *Nat. Rev. Drug Discov.* **2010**, *9*, 615–627. [CrossRef]
11. Chekkat, N.; Dahm, G.; Chardon, E.; Wantz, M.; Sitz, J.; Decossas, M.; Lambert, O.; Frisch, B.; Rubbiani, R.; Gasser, G.; et al. N-Heterocyclic Carbene-Polyethylenimine Platinum Complexes with Potent in Vitro and in Vivo Antitumor Efficacy. *Bioconjug. Chem.* **2016**, *27*, 1942–1948. [CrossRef]

12. Torchilin, V. Tumor Delivery of Macromolecular Drugs Based on the EPR Effect. *Adv. Drug Deliv. Rev.* **2011**, *63*, 131–135. [CrossRef]
13. Maeda, H. Polymer Therapeutics and the EPR Effect. *J. Drug Target.* **2017**, *25*, 781–785. [CrossRef]
14. Fahira, A.I.; Abdulah, R.; Barliana, M.I.; Gatera, V.A.; Amalia, R. Polyethyleneimine (PEI) as a Polymer-Based Co-Delivery System for Breast Cancer Therapy. *Breast Cancer Targets Ther.* **2022**, *14*, 71–83. [CrossRef]
15. Neuberg, P.; Kichler, A. *Recent Developments in Nucleic Acid Delivery with Polyethylenimines*; Elsevier, 2014; Volume 88, ISBN 9780128001486.
16. Xu, C.; Wang, P.; Zhang, J.; Tian, H.; Park, K.; Chen, X. Pulmonary Codelivery of Doxorubicin and SiRNA by PH-Sensitive Nanoparticles for Therapy of Metastatic Lung Cancer. *Small* **2015**, *11*, 4321–4333. [CrossRef]
17. Zhou, Z.; Murdoch, W.J.; Shen, Y. A Linear Polyethylenimine (LPEI) Drug Conjugate with Reversible Charge to Overcome Multidrug Resistance in Cancer Cells. *Polymer* **2015**, *76*, 150–158. [CrossRef]
18. Wantz, M.; Bouché, M.; Dahm, G.; Chekkat, N.; Fournel, S.; Bellemin-Laponnaz, S. N-Heterocyclic Carbene-Polyethyleneimine (PEI) Platinum Complexes Inducing Human Cancer Cell Death: Polymer Carrier Impact. *Int. J. Mol. Sci.* **2018**, *19*, 3472. [CrossRef]
19. Neuzil, J.; Stantic, M.; Zobalova, R.; Chladova, J.; Wang, X.; Prochazka, L.; Dong, L.; Andera, L.; Ralph, S.J. Tumour-Initiating Cells vs. Cancer "stem" Cells and CD133: What's in the Name? *Biochem. Biophys. Res. Commun.* **2007**, *355*, 855–859. [CrossRef]
20. Wu, X.Z. Origin of Cancer Stem Cells: The Role of Self-Renewal and Differentiation. *Ann. Surg. Oncol.* **2008**, *15*, 407–414. [CrossRef]
21. Batlle, E.; Clevers, H. Cancer Stem Cells Revisited. *Nat. Med.* **2017**, *23*, 1124–1134. [CrossRef]
22. Ayob, A.Z.; Ramasamy, T.S. Cancer Stem Cells as Key Drivers of Tumour Progression. *J. Biomed. Sci.* **2018**, *25*, 1–18. [CrossRef]
23. Zhao, J. Cancer Stem Cells and Chemoresistance: The Smartest Survives the Raid. *Pharmacol. Ther.* **2016**, *160*, 145–158. [CrossRef]
24. Abdullah, L.; Chow, E. Chemoresistance in Cancer Stem Cells. *Clin. Transl. Med.* **2013**, *2*, 1–9. [CrossRef]
25. Najafi, M.; Mortezaee, K.; Majidpoor, J. Cancer Stem Cell (CSC) Resistance Drivers. *Life Sci.* **2019**, *234*, 116781. [CrossRef]
26. Tanida, I. Autophagy Basics. *Microbiol. Immunol.* **2011**, *55*, 1–11. [CrossRef]
27. Mizushima, N. Autophagy: Process and Function. *Genes Dev.* **2007**, *21*, 2861–2873. [CrossRef]
28. Virolle, T. Cancer Stem Cells in Glioblastoma. *Bull. Cancer* **2017**, *104*, 1075–1079. [CrossRef]
29. Seymour, T.; Nowak, A.; Kakulas, F. Targeting Aggressive Cancer Stem Cells in Glioblastoma. *Front. Oncol.* **2015**, *5*, 1–9. [CrossRef]
30. Lamb, R.; Harrison, H.; Hulit, J.; Smith, D.L.; Lisanti, M.P.; Sotgia, F. Mitochondria as New Therapeutic Targets for Eradicating Cancer Stem Cells: Quantitative Proteomics and Functional Validation via MCT1/2 Inhibition. *Oncotarget* **2014**, *5*, 11029–11037. [CrossRef]
31. Jagust, P.; De Luxán-Delgado, B.; Parejo-Alonso, B.; Sancho, P. Metabolism-Based Therapeutic Strategies Targeting Cancer Stem Cells. *Front. Pharmacol.* **2019**, *10*, 1–26. [CrossRef]
32. Farnie, G.; Sotgia, F.; Lisanti, M.P. High Mitochondrial Mass Identifies a Sub-Population of Stem-like Cancer Cells That Are Chemo-Resistant. *Oncotarget* **2015**, *6*, 30472–30486. [CrossRef] [PubMed]
33. Skoda, J.; Borankova, K.; Jansson, P.J.; Huang, M.L.H.; Veselska, R.; Richardson, D.R. Pharmacological Targeting of Mitochondria in Cancer Stem Cells: An Ancient Organelle at the Crossroad of Novel Anti-Cancer Therapies. *Pharmacol. Res.* **2019**, *139*, 298–313. [CrossRef] [PubMed]
34. Liou, G.Y. CD133 as a Regulator of Cancer Metastasis through the Cancer Stem Cells. *Int. J. Biochem. Cell Biol.* **2019**, *106*, 1–7. [CrossRef] [PubMed]
35. Thapa, R.; Wilson, G.D. The Importance of CD44 as a Stem Cell Biomarker and Therapeutic Target in Cancer. *Stem Cells Int.* **2016**, *2016*, 2087204. [CrossRef]
36. Garg, A.D.; Nowis, D.; Golab, J.; Vandenabeele, P.; Krysko, D.V.; Agostinis, P. Immunogenic Cell Death, DAMPs and Anticancer Therapeutics: An Emerging Amalgamation. *Biochim. Biophys. Acta—Rev. Cancer* **2010**, *1805*, 53–71. [CrossRef]
37. Tesniere, A.; Panaretakis, T.; Kepp, O.; Apetoh, L.; Ghiringhelli, F.; Zitvogel, L.; Kroemer, G. Molecular Characteristics of Immunogenic Cancer Cell Death. *Cell Death Differ.* **2008**, *15*, 3–12. [CrossRef]
38. Zhou, J.; Wang, G.; Chen, Y.; Wang, H.; Hua, Y.; Cai, Z. Immunogenic Cell Death in Cancer Therapy: Present and Emerging Inducers. *J. Cell. Mol. Med.* **2019**, *23*, 4854–4865. [CrossRef]
39. Pandolfi, F.; Altamura, S.; Frosali, S.; Conti, P. Key Role of DAMP in Inflammation, Cancer, and Tissue Repair. *Clin. Ther.* **2016**, *38*, 1017–1028. [CrossRef]
40. Brissault, B.; Kichler, A.; Guis, C.; Leborgne, C.; Danos, O.; Cheradame, H. Synthesis of Linear Polyethylenimine Derivatives for DNA Transfection. *Bioconjug. Chem.* **2003**, *14*, 581–587. [CrossRef]
41. Campos, B.; Wan, F.; Farhadi, M.; Ernst, A.; Zeppernick, F.; Tagscherer, K.E.; Ahmadi, R.; Lohr, J.; Dictus, C.; Gdynia, G.; et al. Differentiation Therapy Exerts Antitumor Effects on Stem-like Glioma Cells. *Clin. Cancer Res.* **2010**, *16*, 2715–2728. [CrossRef]
42. Verreault, M.; Schmitt, C.; Goldwirt, L.; Pelton, K.; Haidar, S.; Levasseur, C.; Guehennec, J.; Knoff, D.; Labussière, M.; Marie, Y.; et al. Preclinical Efficacy of the MDM2 Inhibitor RG7112 in MDM2-Amplified and TP53 Wild-Type Glioblastomas. *Clin. Cancer Res. Off. J. Am. Assoc. Cancer Res.* **2016**, *22*, 1185–1196. [CrossRef]
43. Taciak, B.; Białasek, M.; Braniewska, A.; Sas, Z.; Sawicka, P.; Kiraga, Ł.; Rygiel, T.; Król, M. Evaluation of Phenotypic and Functional Stability of RAW 264.7 Cell Line through Serial Passages. *PLoS ONE* **2018**, *13*, e0198943. [CrossRef]

44. Podergajs, N.; Brekka, N.; Radlwimmer, B.; Herold-Mende, C.; Talasila, K.M.; Tiemann, K.; Rajcevic, U.; Lah, T.T.; Bjerkvig, R.; Miletic, H. Expansive Growth of Two Glioblastoma Stem-like Cell Lines Is Mediated by BFGF and Not by EGF. *Radiol. Oncol.* **2013**, *47*, 330–337. [CrossRef]
45. McCartin, C.; Mathieu, E.; Dontenwill, M.; Herold-Mende, C.; Idbaih, A.; Bonfiglio, A.; Mauro, M.; Fournel, S.; Kichler, A. An N-Heterocyclic Carbene Iridium(III) Complex as a Potent Anti-Cancer Stem Cell Therapeutic. *Chem. Biol. Interact.* **2022**, *367*, 110167. [CrossRef]
46. Prabhakar, N.; Merisaari, J.; Le Joncour, V.; Peurla, M.; Karaman, D.Ş.; Casals, E.; Laakkonen, P.; Westermarck, J.; Rosenholm, J.M. Circumventing Drug Treatment? Intrinsic Lethal Effects of Polyethyleneimine (PEI)-Functionalized Nanoparticles on Glioblastoma Cells Cultured in Stem Cell Conditions. *Cancers* **2021**, *13*, 2631. [CrossRef]
47. Knauer, N.; Arkhipova, V.; Li, G.; Hewera, M.; Pashkina, E.; Nguyen, P.-H.; Meschaninova, M.; Kozlov, V.; Zhang, W.; Croner, R.; et al. In Vitro Validation of the Therapeutic Potential of Dendrimer-Based Nanoformulations against Tumor Stem Cells. *Int. J. Mol. Sci.* **2022**, *23*, 5691. [CrossRef]
48. Zhang, Q.F.; Wang, B.; Yin, D.X.; Zhang, J.; Wu, W.X.; Yu, Q.Y.; Yu, X.Q. Linear TACN-Based Cationic Polymers as Non-Viral Gene Vectors. *RSC Adv.* **2014**, *4*, 59164–59174. [CrossRef]
49. Kheraldine, H.; Rachid, O.; Habib, A.M.; Al Moustafa, A.E.; Benter, I.F.; Akhtar, S. Emerging Innate Biological Properties of Nano-Drug Delivery Systems: A Focus on PAMAM Dendrimers and Their Clinical Potential. *Adv. Drug Deliv. Rev.* **2021**, *178*, 113908. [CrossRef]
50. Jevprasesphant, R.; Penny, J.; Jalal, R.; Attwood, D.; McKeown, N.B.; D'Emanuele, A. The Influence of Surface Modification on the Cytotoxicity of PAMAM Dendrimers. *Int. J. Pharm.* **2003**, *252*, 263–266. [CrossRef]
51. Fischer, D.; Li, Y.; Ahlemeyer, B.; Krieglstein, J.; Kissel, T. In Vitro Cytotoxicity Testing of Polycations: Influence of Polymer Structure on Cell Viability and Hemolysis. *Biomaterials* **2003**, *24*, 1121–1131. [CrossRef]
52. Beyerle, A.; Irmler, M.; Beckers, J.; Kissel, T.; Stoeger, T. Toxicity Pathway Focused Gene Expression Profiling of PEI-Based Polymers for Pulmonary Applications. *Mol. Pharm.* **2010**, *7*, 727–737. [CrossRef]
53. Moghimi, S.M.; Symonds, P.; Murray, J.C.; Hunter, A.C.; Debska, G.; Szewczyk, A. A Two-Stage Poly(Ethylenimine)-Mediated Cytotoxicity: Implications for Gene Transfer/Therapy. *Mol. Ther.* **2005**, *11*, 990–995. [CrossRef]
54. Grandinetti, G.; Ingle, N.P.; Reineke, T.M. Interaction of Poly(Ethylenimine)-DNA Polyplexes with Mitochondria: Implications for a Mechanism of Cytotoxicity. *Mol. Pharm.* **2011**, *8*, 1709–1719. [CrossRef]
55. Novikoff, A.B.; Beaufay, H.; De Duve, C. Electron Microscopy of Lysosome-Rich Fractions from Rat Liver. *J. Cell Biol.* **1956**, *2*, 179–184. [CrossRef]
56. Smith, A.G.; Macleod, K.F. Autophagy, Cancer Stem Cells and Drug Resistance. *J. Pathol.* **2019**, *247*, 708–718. [CrossRef]
57. Arima, Y.; Nobusue, H.; Saya, H. Targeting of Cancer Stem Cells by Differentiation Therapy. *Cancer Sci.* **2020**, *111*, 2689–2695. [CrossRef]
58. El-Gowily, A.H.; Abosheasha, M.A. Differential Mechanisms of Autophagy in Cancer Stem Cells: Emphasizing Gastrointestinal Cancers. *Cell Biochem. Funct.* **2021**, *39*, 162–173. [CrossRef]
59. Mizushima, N.; Yoshimori, T.; Levine, B. Methods in Mammalian Autophagy Research. *Cell* **2010**, *140*, 313–326. [CrossRef]
60. Bik, E.; Mateuszuk, L.; Orleanska, J.; Baranska, M.; Chlopicki, S.; Majzner, K. Chloroquine-Induced Accumulation of Autophagosomes and Lipids in the Endothelium. *Int. J. Mol. Sci.* **2021**, *22*, 2401. [CrossRef]
61. Mauthe, M.; Orhon, I.; Rocchi, C.; Zhou, X.; Luhr, M.; Hijlkema, K.J.; Coppes, R.P.; Engedal, N.; Mari, M.; Reggiori, F. Chloroquine Inhibits Autophagic Flux by Decreasing Autophagosome-Lysosome Fusion. *Autophagy* **2018**, *14*, 1435–1455. [CrossRef] [PubMed]
62. Chikte, S.; Panchal, N.; Warnes, G. Use of LysoTracker Dyes: A Flow Cytometric Study of Autophagy. *Cytom. Part A* **2014**, *85*, 169–178. [CrossRef] [PubMed]
63. Lu, S.; Sung, T.; Lin, N.; Abraham, R.T.; Jessen, B.A. Lysosomal Adaptation: How Cells Respond to Lysosomotropic Compounds. *PLoS ONE* **2017**, *12*, e0173771. [CrossRef] [PubMed]
64. Kichler, A.; Leborgne, C.; Coeytaux, E.; Danos, O. Polyethylenimine-Mediated Gene Delivery: A Mechanistic Study. *J. Gene Med.* **2001**, *3*, 135–144. [CrossRef] [PubMed]
65. Akinc, A.; Thomas, M.; Klibanov, A.M.; Langer, R. Exploring Polyethylenimine-Mediated DNA Transfection and the Proton Sponge Hypothesis. *J. Gene Med.* **2005**, *7*, 657–663. [CrossRef]
66. Liu, W.J.; Ye, L.; Huang, W.F.; Guo, L.J.; Xu, Z.G.; Wu, H.L.; Yang, C.; Liu, H.F. P62 Links the Autophagy Pathway and the Ubiqutin–Proteasome System upon Ubiquitinated Protein Degradation. *Cell. Mol. Biol. Lett.* **2016**, *21*, 29. [CrossRef]
67. Gao, X.; Yao, L.; Song, Q.; Zhu, L.; Xia, Z.; Xia, H.; Jiang, X.; Chen, J.; Chen, H. The Association of Autophagy with Polyethylenimine-Induced Cytotoxity in Nephritic and Hepatic Cell Lines. *Biomaterials* **2011**, *32*, 8613–8625. [CrossRef]
68. Lin, C.W.; Jan, M.S.; Kuo, J.H.S.; Hsu, L.J.; Lin, Y.S. Protective Role of Autophagy in Branched Polyethylenimine (25K)-and Poly(L-Lysine) (30–70K)-Induced Cell Death. *Eur. J. Pharm. Sci.* **2012**, *47*, 865–874. [CrossRef]
69. Wang, F.; Salvati, A.; Boya, P. Lysosome-Dependent Cell Death and Deregulated Autophagy Induced by Amine-Modified Polystyrene Nanoparticles. *Open Biol.* **2018**, *4*, 170271. [CrossRef]
70. Pasquier, B. Autophagy Inhibitors. *Cell. Mol. Life Sci.* **2016**, *73*, 985–1001. [CrossRef]
71. Wang, X.; Lee, J.; Xie, C. Autophagy Regulation on Cancer Stem Cell Maintenance, Metastasis, and Therapy Resistance. *Cancers* **2022**, *14*, 381. [CrossRef]

72. Ryskalin, L.; Gaglione, A.; Limanaqi, F.; Biagioni, F.; Familiari, P.; Frati, A.; Esposito, V.; Fornai, F. The Autophagy Status of Cancer Stem Cells in Gliobastoma Multiforme: From Cancer Promotion to Therapeutic Strategies. *Int. J. Mol. Sci.* **2019**, *20*, 3824. [CrossRef]
73. Zhuang, W.; Long, L.; Zheng, B.; Ji, W.; Yang, N.; Zhang, Q.; Liang, Z. Curcumin Promotes Differentiation of Glioma-Initiating Cells by Inducing Autophagy. *Cancer Sci.* **2012**, *103*, 684–690. [CrossRef]
74. Lei, Y.; Zhang, D.; Yu, J.; Dong, H.; Zhang, J.; Yang, S.; Yang, S. Targeting Autophagy in Cancer Stem Cells as an Anticancer Therapy. *Cancer Lett.* **2017**, *393*, 33–39. [CrossRef]
75. Hao, C.; Liu, G.; Tian, G. Autophagy Inhibition of Cancer Stem Cells Promotes the Efficacy of Cisplatin against Non-Small Cell Lung Carcinoma. *Ther. Adv. Respir. Dis.* **2019**, *13*, 1753466619866097. [CrossRef]
76. Babaei, G.; Aziz, S.G.G.; Jaghi, N.Z.Z. EMT, Cancer Stem Cells and Autophagy; The Three Main Axes of Metastasis. *Biomed. Pharmacother.* **2021**, *133*, 110909. [CrossRef]
77. Gamrekelashvili, J.; Greten, T.F.; Korangy, F. Immunogenicity of Necrotic Cell Death. *Cell. Mol. Life Sci.* **2015**, *72*, 273–283. [CrossRef]
78. Wang, Y.; Martins, I.; Ma, Y.; Kepp, O.; Galluzzi, L.; Kroemer, G. Autophagy-Dependent ATP Release from Dying Cells via Lysosomal Exocytosis. *Autophagy* **2013**, *9*, 1624–1625. [CrossRef]
79. Luo, X.; Qiu, Y.; Dinesh, P.; Gong, W.; Jiang, L.; Feng, X.; Li, J.; Jiang, Y.; Lei, Y.L.; Chen, Q. The Functions of Autophagy at the Tumour-Immune Interface. *J. Cell. Mol. Med.* **2021**, *25*, 2333–2341. [CrossRef]
80. Wang, Y.J.; Fletcher, R.; Yu, J.; Zhang, L. Immunogenic Effects of Chemotherapy-Induced Tumor Cell Death. *Genes Dis.* **2018**, *5*, 194–203. [CrossRef]

Temozolomide-Acquired Resistance is Associated with Modulation of the Integrin Repertoire in Glioblastoma, Impact of α5β1 Integrin.

Sani S, Pallaoro N, Messe M, **Bernhard C**, Etienne-Selloum N, Kessler H, Marinelli L, Entz-Werle N, Foppolo S, Martin S, Reita D, Dontenwill M.

Cet article scientifique, publié dans Cancers (IF = 6.575) (doi : 10.3390/cancers14020369), est centré sur la caractérisation des mécanismes de résistance au TMZ dans les GB. Compte tenu du taux élevé de récidive malgré les traitements agressifs conventionnels, il est crucial de comprendre les voies moléculaires et les mécanismes sous-jacents à la résistance des cellules tumorales. Dans cette étude, nous avons mis en évidence une plasticité notable dans le répertoire des intégrines des cellules de GB, notamment en ce qui concerne l'expression de l'intégrine α5β1. Celle-ci varie significativement pendant et après le traitement au TMZ. Ces observations ouvrent la voie à des approches thérapeutiques plus ciblées. En particulier, la combinaison d'antagonistes de l'intégrine α5β1 avec des réactivateurs de p53 pourrait s'avérer potentiellement efficace dans le traitement des tumeurs récurrentes. Ainsi, cette étude contribue à une meilleure compréhension des mécanismes de résistance et suggère le développement de nouvelles combinaisons thérapeutiques.

cancers

MDPI

Article

Temozolomide-Acquired Resistance Is Associated with Modulation of the Integrin Repertoire in Glioblastoma, Impact of α5β1 Integrin

Saidu Sani [1,2], Nikita Pallaoro [1], Mélissa Messe [1], Chloé Bernhard [1], Nelly Etienne-Selloum [1,3], Horst Kessler [4], Luciana Marinelli [5], Natacha Entz-Werle [1,6], Sophie Foppolo [1], Sophie Martin [1], Damien Reita [1,7] and Monique Dontenwill [1,*]

1 Laboratoire de Bioimagerie et Pathologies (LBP), UMR CNRS 7021, Faculté de Pharmacie, Université de Strasbourg, 67401 Illkirch, France; Sanisaidu96@gmail.com (S.S.); npallaoro@unistra.fr (N.P.); melissa.messe@etu.unistra.fr (M.M.); chloe.bernhard@etu.unistra.fr (C.B.); nelly.etienne-selloum@unistra.fr (N.E.-S.); Natacha.Entz-Werle@chru-strasbourg.fr (N.E.-W.); sophie.foppolo@unistra.fr (S.F.); sophie.martin@unistra.fr (S.M.); damien.reita@gmail.com (D.R.)
2 Cancer and Diabetic Research Group, Department of Biochemistry, Faculty of Biological Science, Federal University Ndufu-Alike Ikwo, Abakaliki 482131, Nigeria
3 Department of Pharmacy, Institut de Cancérologie Strasbourg Europe (ICANS), 67200 Strasbourg, France
4 Department of Chemistry, Institute for Advanced Study, Technical University of Munich, 85748 Garching, Germany; kessler@tum.de
5 Dipartimento di Farmacia, Università degli Studi di Napoli "Federico II", 80131 Naples, Italy; lmarinel@unina.it
6 Pediatric Onco-Hematology Unit, University Hospital of Strasbourg, 67098 Strasbourg, France
7 Département de Génétique Moléculaire des Cancers, Oncologie Moléculaire & Pharmacogénétique, University Hospital of Strasbourg, 67000 Strasbourg, France
* Correspondence: monique.dontenwill@unistra.fr

Simple Summary: Glioblastomas are the deadliest brain tumours. The standard of care associates surgery, radio- and chemotherapy with Temozolomide as the reference drug. Despite this treatment, most of the tumours recur. The characterization of resistance mechanisms is of paramount importance to enable the proposal of more effective therapies. In this work we aimed to evaluate the molecular changes occurring during and after Temozolomide treatment in a glioma cell line. A high plasticity in the integrin repertoire exists in these cells. As an example, variations of the α5β1 integrin expression were observed with a reduction during the treatment and re-expression after removal of the drug. The association of integrin antagonists with p53 reactivators appears to be efficient in recurrent tumours. Specific integrins may thus be particularly targetable at different time points of glioblastoma treatment and combination therapies evaluated according to their time-dependent expression.

Abstract: Despite extensive treatment, glioblastoma inevitably recurs, leading to an overall survival of around 16 months. Understanding why and how tumours resist to radio/chemotherapies is crucial to overcome this unmet oncological challenge. Primary and acquired resistance to Temozolomide (TMZ), the standard-of-care chemotherapeutic drug, have been the subjects of several studies. This work aimed to evaluate molecular and phenotypic changes occurring during and after TMZ treatment in a glioblastoma cell model, the U87MG. These initially TMZ-sensitive cells acquire long-lasting resistance even after removal of the drug. Transcriptomic analysis revealed that profound changes occurred between parental and resistant cells, particularly at the level of the integrin repertoire. Focusing on α5β1 integrin, which we proposed earlier as a glioblastoma therapeutic target, we demonstrated that its expression was decreased in the presence of TMZ but restored after removal of the drug. In this glioblastoma model of recurrence, α5β1 integrin plays an important role in the proliferation and migration of tumoral cells. We also demonstrated that reactivating p53 by MDM2 inhibitors concomitantly with the inhibition of this integrin in recurrent cells may overcome the TMZ resistance. Our results may explain some integrin-based targeted therapy failure as integrin expressions are highly switchable during the time of treatment. We also propose an alternative way to alter the viability of recurrent glioblastoma cells expressing a high level of α5β1 integrin.

check for updates

Citation: Sani, S.; Pallaoro, N.; Messe, M.; Bernhard, C.; Etienne-Selloum, N.; Kessler, H.; Marinelli, L.; Entz-Werle, N.; Foppolo, S.; Martin, S.; et al. Temozolomide-Acquired Resistance Is Associated with Modulation of the Integrin Repertoire in Glioblastoma, Impact of α5β1 Integrin. *Cancers* **2022**, *14*, 369. https://doi.org/10.3390/cancers14020369

Academic Editors: Suzanne Ponik and Seiichiro Ishihara

Received: 25 October 2021
Accepted: 5 January 2022
Published: 12 January 2022

Publisher's Note: MDPI stays neutral with regard to jurisdictional claims in published maps and institutional affiliations.

Keywords: glioblastoma; temozolomide resistance; integrins; p53 reactivation

1. Introduction

Glioblastoma (GBM) is the most common and most aggressive malignant brain tumour in adults and is characterized by high proliferation, invasion into normal brain tissue and resistance to therapies [1,2]. Currently there is no effective long-term treatment for this killer disease, but the standard of care (Stupp protocol) is maximal surgical resection, followed by radiotherapy with concomitant and adjuvant Temozolomide (TMZ) chemotherapy [3]. However, the prognosis of patients with glioblastoma remains poor and has not improved despite numerous clinical trials on new therapeutic propositions [4]. Therefore, there is an urgent need for novel therapeutic strategies, which may be supported by a deep understanding of GBM and surrounding microenvironment crosstalk.

Primary and acquired resistances are the major challenges for the clinical use of standard and targeted therapies in GBM [5,6]. One of the mechanisms of glioblastoma resistance to TMZ involves O^6-methylguanine DNA methyl transferase (MGMT), a suicide enzyme that allows the direct repair of the lesions caused by TMZ, through the removal of a methyl group in position O^6 of guanine [7]. Previous studies have shown that intracellular accumulation of the tumour suppressor protein p53 downregulates the expression of MGMT [8,9]. The p53 protein is mutated in about 30% of glioblastomas [10], although a subtype of glioblastoma expressing mostly wild type p53 has been identified in an integrated genomic analysis [11]. However, even if wild type p53 is expressed in 70% of GBM, its functions are frequently suppressed by MDM2/MDM4, E3 ubiquitin ligases that mark and target p53 for proteasomal degradation [12–14]. MDM2, a zinc finger nuclear phosphoprotein and negative regulator of the p53 protein, is often overexpressed in GBM and has been implicated in cancer cell proliferation and survival. Inhibition of the p53–MDM2 interaction can prevent p53 degradation and restore p53 transcriptional activity, leading to the p53-mediated induction of tumour cell apoptosis, thus making the p53–MDM2 complex a promising target for glioblastoma expressing wild type p53 [15–17]. The discovery of the p53–MDM2 inhibitor Nutlin-3a represented a breakthrough in the development of p53-activators [14]. The more recent development of RG7388 (Idasanutlin), a second-generation MDM2 inhibitor with greater potency, selectivity, bioavailability and effective p53-activating ability leading to the p53-mediated induction of tumour cell apoptosis, is promising for cancers, including GBM [18,19].

Integrins have become, in the past 20 years, the subject of numerous studies because of the vital role they play in tumour progression [20,21]. The integrins are transmembrane heterodimeric cell surface receptors that mediate cell adhesion to the extracellular matrix (ECM) and support cell–cell interactions in multiple physiological and pathological conditions [22,23]. The frequent deregulation of integrin expressions and pathways in cancer cells underscores specific integrin major contributions in tumour growth and resistance to therapies [24]. The disruption of the integrin signalling pathways by integrin antagonists has been shown to inhibit tumour growth and sensitize tumours to therapies in preclinical contexts. Cilengitide [25] was the first integrin $\alpha v\beta 3/\beta 5$ antagonist to reach the clinic, but clinical trials for GBM with cilengitide in combination with the standard of care (Stupp protocol) were unsuccessful [26]. Several reasons may explain these failures, as reviewed in [27]. However, knowledge on integrin expressions and functions in GBM merits further investigations to adapt integrin-based therapies to specific subpopulations of patients. In this way, expression of $\alpha 5$ subunit of the $\alpha 5\beta 1$ integrin heterodimer is enhanced in the mesenchymal subgroup of glioblastoma patients as compared to the others [11,28], presumably conferring to these patients a better sensitivity to anti-$\alpha 5$ integrin therapy. We and others showed previously that $\alpha 5\beta 1$ integrin is an interesting therapeutic target for GBM. Its overexpression at the mRNA [29,30] or protein [31] levels define populations of patients with worse prognostics. In preclinical experiments it was shown that this integrin

is involved in survival, migration, resistance to therapies and neo-angiogenesis, all being hallmarks of GBM [32–35].

Integrin expressions in GBM vary after therapies [36]. As an example, it was shown that in tumours recurring after bevacizumab treatment, α5β1 integrin was overexpressed in a subpopulation of patients [37]. In particular, we demonstrated the existence of a negative crosstalk between α5β1 integrin and p53 pathways supporting an implication in glioma resistance to chemotherapies [30,38]. We also showed that the inhibition of the integrin concomitantly with p53 activation with Nutlin 3a in α5-overexpressing cells led to a huge increase in cell apoptosis [39].

In this study, we aimed to investigate if Temozolomide treatment affects the integrin repertory in glioma cells, taking the U87MG cell line as an example. Resistant cells were obtained that conserve the resistance even after removal of the drug. Transcriptomic analysis of non-treated U87MG cells and resistant cells cultured in the presence or absence of TMZ showed a high variation in integrin expressions. Interestingly, α5β1 integrin expression decreases in the presence of the drug but recovers after its removal, suggesting that it may represent a therapeutic target for recurrent glioblastoma. We also investigated if treatment of these recurrent TMZ-resistant cells may be sensitive to a combination of highly active and selective α5β1 integrin antagonists and p53 reactivators. Our results may add new therapeutic perspectives for recurrent glioblastoma expressing high level of α5β1 integrin.

2. Materials and Methods

2.1. Drugs

Temozolomide (TMZ), 8-carbamoyl-3-methylimidazo[5,1-d]-1,2,3,5-tetrazin (3H)-one 5 (Sigma-Aldrich), was prepared as a 100 mM stock solution in DMSO and stored at 4 °C until use. Nutlin-3a, (4-[4,5-bis-(4-chlorophenyl)-2-(2-isopropoxy-4-methoxy-phenyl)-4,5-dihydro-imidazole-1-carbonyl]-piperazin-2-one), the active enantiomer, was from Cayman chemical company (Interchim, Montluçon, France). Nutlin-3a was prepared as a 10 mM stock solution in ethanol and stored at −20 °C until use. Idasanutlin, also known as RG7388 ($C_{31}H_{29}C_{l2}F_2N_3O_4$), was from Euromedex (Souffelweyersheim, France). Idasanutlin was prepared as a 10 mM stock solution in DMSO and stored at −20 °C until use. RITA (5,5′-(2,5-furandiyl) bis-2 thiophenemethanol) was from Cayman chemical company (Interchim, France). RITA was prepared as a 10 mM stock solution in ethanol and stored at −20 °C until use. Antagonists of α5β1 integrin, 34c and 1b (respectively named K34C and FR248 in this work) were synthesized according to the procedure described in [40,41]. Their structures and binding activities for integrin α5β1 and integrin αvβ3 are shown in [34]. Compound **9** was prepared as described in [42]. They were prepared as 10 mM stock solutions in DMSO and stored at 4 °C until use.

2.2. Cell Culture

U87MG glioblastoma cell line (p53 wild type) was from American Type Culture Collection (LGC Standards Sarl, Molsheim, France). Cell lines were routinely cultured in EMEM (Minimum Essential Medium Eagle) supplemented with 10% heat-inactivated foetal bovine serum, 1% Na pyruvate and 1% non-essential amino acids at 37 °C in a humidified atmosphere containing 5% CO_2. All cells were periodically authenticated by Multiplexion GmbH and tested for the presence of mycoplasma.

2.3. Generation of Temozolomide-Resistant Glioblastoma Cells

U87MG cells (500,000) were seeded in T25 cm^2 cell culture flask containing EMEM (Eagle's minimal essential medium) supplemented with 10% serum, 1% Na pyruvate and 1% non-essential amino acids. Cells were allowed to adhere for 24 h, and the medium was replaced with a fresh medium containing 50 µM of TMZ. Cell treatment was repeated twice a week for several weeks, resulting in a sub-population of stable TMZ-resistant cells. The sub-population of resistant cells generated were continuously cultured in a medium

containing TMZ and named U87MG R50. After two months, a subpopulation of U87MG R50 cells was cultured in medium without TMZ and named U87MG R50 OFF (or U87MG OFF). The maintenance of resistance in this cell line is checked regularly (every three months) by the Incucyte technology and resistance has appeared stable for at least one year.

2.4. IncuCyte Cell Confluence Assay as an Index of Proliferation

Cells were plated (2000 cells in 100 µL per well) into 96-well culture plates. The control solvent or drugs at 2× concentration in 100 µL of 2% FBS-containing medium was added to the appropriate wells. To monitor cell growth, the plates were placed into the IncuCyte live-cell analysis system and allowed to warm at 37 °C for 30 min prior to standard scanning with 4× objective every 3 h for at least 96 h. The captured phase contrast images were analysed using the IncuCyte ZOOM software provided by the manufacturer.

2.5. Senescence Assay

The β-galactosidase activity at pH 6 was determined using the Senescence Cells Histochemical Staining Kit (Sigma-Aldrich, Saint-Quentin-Fallavier, France) according to the manufacturer's instructions. Briefly, cells were plated (2000 cells/200 µL) into a 96 well plate. The cells were washed twice with 1xPBS and fixed with 1× fixation buffer for 7 min at room temperature. The fixation buffer was aspirated and wells rinsed thrice with 1 × PBS. After washing, the cells were covered with staining mixture and incubated at 37 °C without CO_2. After 12 h of staining, light microscopy was used to identify senescent (blue-stained) cells.

2.6. Western Blotting

Cells were plated (200,000 cells per well) into 6-well culture plates and treated with the control solvent or drugs. For the basal level values of proteins of interest, cells were used 24 h after plating. Proteins were extracted from adherent and floating cells after lysis with Laemmli sample buffer (Bio-Rad, Marnes La Coquette, France) on ice and lysates heated at 95 °C for 10 min. Proteins were separated on precast gradient 4–20% SDSPAGE gels (Bio-Rad) and transferred to PVDF membrane (GE Healthcare, Velizy, France). After 1 h of blocking at room temperature, membranes were probed with appropriate primary antibodies (Table 1) overnight at 4 °C. Membranes were subsequently incubated with anti-rabbit or anti-mouse antibodies conjugated to horseradish peroxidase (Promega, Charbonnieres les- Bains, France), developed using chemoluminescence (ECL, Bio-Rad) and visualized with Las4000 image analyser (GE Healthcare, France). Quantification of non-saturated images was done using ImageJ software (National Institutes of Health, Bethesda, MD, USA). GAPDH or tubulin was used as the loading control for all samples.

Table 1. List of antibodies used in the study.

Antibody	Blocking Solution	Antibody Dilution
Anti-α5 integrin H104 (Santa Cruz)	5% milk/1 × TBS/0.1% Tween -20	1/1000
Anti-β1 integrin TS2/16 (Millipore)	5% milk/1 × TBS/0.1% Tween -20	1/1000
Anti-αv integrin (Cell signalling)	5% milk/1 × TBS/0.1% Tween -20	1/1000
Anti-β3 integrin (Cell signalling)	5% milk/1 × TBS/0.1% Tween -20	1/1000
Anti-p53 (BD Bioscience)	5% milk/1 × TBS/0.1% Tween -20	1/1000
Anti-pp53ser15 (Cell signalling)	5% BSA/1 × TBS/0.1% Tween -20	1/1000
Anti-p16 (Cell signalling)	5% milk/1 × TBS/0.1% Tween -20	1/1000
Anti-p21 (Cell signalling)	5% milk/1 × TBS/0.1% Tween -20	1/1000
Anti-MDM2 (Calbiochem)	5% milk/1 × PBS/0.1% Tween -20	1/1000
Anti-GAPDH (Millipore)	5% milk/1 × TBS/0.1% Tween -20	1/5000
Anti-tubulin (Sigma-Aldrich)	5% milk/1 × TBS/0.1% Tween -20	1/3000
Mouse HRP-conjugated secondary antibody	5% milk/1 × TBS/0.1% Tween -20	1/10,000
Rabbit HRP-conjugated secondary antibody	5% milk/1 × TBS/0.1% Tween -20	1/10,000

2.7. RNAseq Data

RNA-Seq libraries were generated from 400 ng of total RNA using TruSeq Stranded mRNA Library Prep Kit and TruSeq RNA Single Indexes kits A and B (Illumina, San Diego, CA, USA), according to manufacturer's instructions. Briefly, following purification with poly-T oligo-attached magnetic beads, the mRNA was fragmented using divalent cations at 94 °C for 2 min. The cleaved RNA fragments were copied into first-strand cDNA using reverse transcriptase and random primers. Strand specificity was achieved by replacing dTTP with dUTP during second-strand cDNA synthesis using DNA Polymerase I and RNase H. Following addition of a single 'A' base and subsequent ligation of the adapter on double-stranded cDNA fragments, the products were purified and enriched with PCR (30 s at 98 °C; (10 s at 98 °C, 30 s at 60 °C, 30 s at 72 °C) × 12 cycles; 5 min at 72 °C) to create the cDNA library. Surplus PCR primers were further removed by purification using AMPure XP beads (Beckman Coulter, Villepinte, France), and the final cDNA libraries were checked for quality and quantified using capillary electrophoresis. Libraries were then sequenced on an Illumina HiSeq4000 system as single-end 1 × 50 base reads. Image analysis and base calling were performed using RTA 2.7.7 and bcl2fastq 2.17.1.14. Reads ((Illumina, San Diego, CA, USA)) were preprocessed using Cutadapt version 1.10 in order to remove adapter, polyA and low-quality sequences (Phred quality score below 20), and reads shorter than 40 bases were discarded for further analysis. Reads mapping to rRNA were also discarded (this mapping was performed using Bowtie version 2.2.8). Reads were then mapped onto the hg38 assembly of human genome using STAR version 2.5.3a (twopassMode Basic). Gene expression was quantified using htseq-count version 0.6.1p1 and gene annotations from Ensembl release 99. Statistical analysis was performed using R 3.3.2 and DESeq2 1.16.1 Bioconductor library. Sequencing was performed by the GenomEast platform, a member of the 'France Génomique' consortium (ANR-10-INBS-0009).

Gene expression data obtained with DESeq2 were used to generate the heatmaps and dendrogram with R. Only genes expressed in all conditions (defined if normalized reads count divided by median of transcripts length in kb is greater than 1 for gene across all nine libraries) were taken into account for visualization. Hierarchical clustering method was performed according to pairwise complete-linkage method and using Pearson correlation for row clustering and Spearman correlation for column clustering. The biological significance of differentially expressed genes (DEGs) obtained was explored using ReactomePA, an R/Bioconductor package for reactome pathway analysis and visualization. |Log2 (fold change)| > 2 (|log2FC|>2) and an adjusted false discovery rate (FDR) < 0.05 (using Benjamini–Hochberg correction) were used as the cut-off criteria of DEGs samples.

2.8. Confocal Microscopy and Image Analysis

Coverslips were coated with fibronectin (20 µg/mL in DPBS), and 25,000 cells were seeded in 10% serum containing medium and cultured for 24 h. Cells were then fixed in 4% (*v*/*v*) paraformaldehyde for 12 min and permeabilized with 0.1% Triton-X100 for 2 min. After 1 h of blocking step in 3% bovine serum albumin (BSA)-PBS solution, cells were incubated with primary antibodies against integrin α5 (clone IIA1 Pharmingen, 1 µL/100 µL in 3% PBS-BSA) and β1 integrin (purified anti-human CD29, Clone:TS2/16, 1 µL/100 µL in 3% PBS-BSA) overnight at 4 °C. Cells were rinsed in 1 × PBS and incubated with appropriate secondary antibodies (Alexa fluor@ 647 goat anti-mouse (A21236) 1 µL/200 µL in 3% PBS-BSA and Alexa fluor@ 688 goat anti-mouse 1 µL/200 µL in 3% PBS-BSA) and 4′, 6-diamidino-2-phenylindole (DAPI) (1 µL/2000 µL in 3% PBS-BSA was added for nuclei staining) for 45 min. Samples were mounted on microscope slides using fluorescence mounting medium (Dako). Images were acquired using a confocal microscope (LEICA TCS SPE II, 63× magnification). For each experiment, identical background subtraction and scaling was applied to all images. Pearson correlation coefficient from 10–12 images (4–5 cells per images) from 3 independent experiments was calculated using JACoP plugin ImageJ software.

2.9. Spheroid Migration Assays

A single-cell suspension was mixed in MEM supplemented with 10% foetal bovine serum, 1% Na pyruvate, 1% non-essential amino acid containing 20% of methylcellulose. Spheroids were made by the hanging drop method with 2000 cells in a 20 µL drop as previously described [43]. Tissue culture plates were coated with fibronectin or polylysine (10 µg/mL in DPBS solution) for 3 h at 37 °C. Two-day-old spheroids were allowed to adhere to fibronectin-coated plates and migrate in complete medium (MEM, 10% FBS, 1% Na pyruvate and 1% non-essential amino acids) either with solvent or supplemented with 20 or 5 µM of K34C or FR248. Eighteen hours later, cells were fixed with glutaraldehyde 1% (Electron Microscopy Sciences) and stained with DAPI diluted at 1 µg/mL in 3% PBS-BSA (Sigma-Aldrich). Nuclei were picturized under the objective 5× in the fluorescence microscope ZEISS-Axio (ZEISS). To evaluate the number of cells that migrated out of the spheroid and the average distance of migration out of the spheroid, image analysis was performed with ImageJ software using a homemade plugin [43]. Phase-contrast images (EVOS Xl, Core10× magnification, Thermo Scientific) were also acquired.

2.10. Statistical Analysis

Statistical analyses were performed using Student's *t*-test with GraphPad Prism software. All data are presented as mean ± SEM from three or more independent experiments with *, $p < 0.05$; **, $p < 0.01$; ***, $p < 0.001$.

3. Results

3.1. Long-Term Exposure of U87MG Cells to TMZ Generates Persistent Resistant Cells

To generate TMZ-resistant cells, we subjected U87MG cells to 50 µM of TMZ for several weeks, resulting in a sub-population of stable TMZ-resistant U87MG cells. The sub-population of resistant cells was either continuously cultured in the medium containing 50 µM of TMZ (U87MG R50) or, after 2 months in the presence of TMZ, cultured in the medium without TMZ (U87MG R50 OFF). We confirmed that the parental cells were sensitive to 50 µM of TMZ and that the U87MG R50 cells were insensitive to TMZ for up to 96 h (Figure 1A). Interestingly, TMZ resistance was maintained in U87MG R50 OFF cells (Figure 1A). Furthermore, while the parental cells were dose-dependently sensitive to TMZ, the U87MG R50 and U87MG R50 OFF cells remained insensitive to varying concentrations up to 100 µM of TMZ (Supplementary Figure S1).

Phase-contrast images obtained from the IncuCyte (Figure 1B) showed that the cellular morphology of U87MG R50 cells differed from their parental cells by having a more spread, enlarged and flattened morphology. The U87MG R50 OFF cells displayed a mixed morphology, with some cells presenting the morphology of U87MG R50 cells while the others presented the morphology of the parental cells. TMZ treatment for 3 days produced a profound change in the cellular morphology of the parental cells, causing extensive branching, reduction in total cell number and confluence (Figure 1B). On the contrary, both the U87MG R50 cells and U87MG R50 OFF cells appeared healthy, with no obvious morphological changes 72 h post TMZ treatment (Figure 1B). Overall, these results demonstrate that a fraction of the U87MG cells that survived prolonged exposure to TMZ developed acquired TMZ-resistance, which was maintained even after the withdrawal of TMZ. According to the sample RNAseq data (see below), this resistance is not due to MGMT expression as no increase in MGMT mRNA was observed.

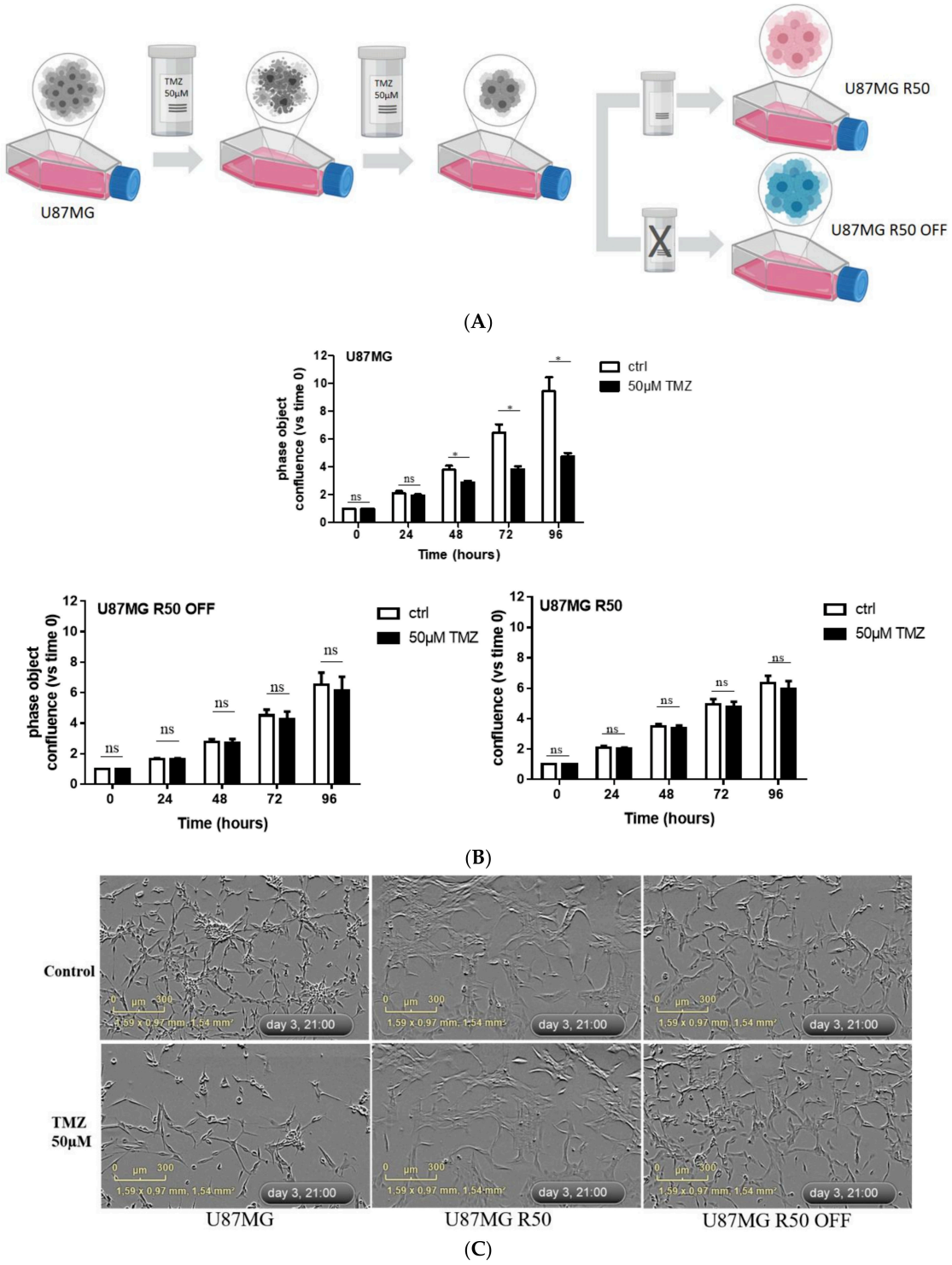

Figure 1. Confirmation of acquired TMZ resistance in U87MG GBM cells: (**A**) Generation of TMZ resistance U87MG R50 and U87MG R50 OFF cells. (**B**) Representative histograms showing the effect of TMZ (50 µM) on cell confluence of U87MG, U87MG R50 and U87MG R50 OFF cells from 0 to 96 h of treatment. Results are expressed as the relative area of plate covered versus the area covered by solvent-treated control cells. Histograms represent mean ± S.E.M. of at least three separate experiments. (**C**) Representative phase contrast images from the IncuCyte showing the cellular morphology of U87MG, U87MG R50 and U87MG R50 OFF cells 72 h post treatment with 50 µM of TMZ. Scale bar, 300 µm. *, $p < 0.05$; ns, non-significant.

3.2. TMZ Induces Senescence in U87MG Cells

Since the resistant cells showed the morphological features of senescent cells, we next tested the senescence marker SA-βGAL. Upon short incubation in 50 μM of TMZ, the remaining cells were all positive for SA-βGAL staining. Positive cells were maintained in the U87MG R50 cells but largely decreased in U87MG R50 OFF cells (Figure 2A). Accordingly, a significant increase in the expression of proteins p16 and p21, known to be involved in senescence, was observed in U87MG R50 cells as compared to the parental cells. An increase in p16 but not in p21 was recorded in U87MG R50 OFF cells (Figure 2B). Altogether, the results confirm that TMZ triggers senescence in U87MG cells, as already reported in [44], which is resumed after TMZ removal.

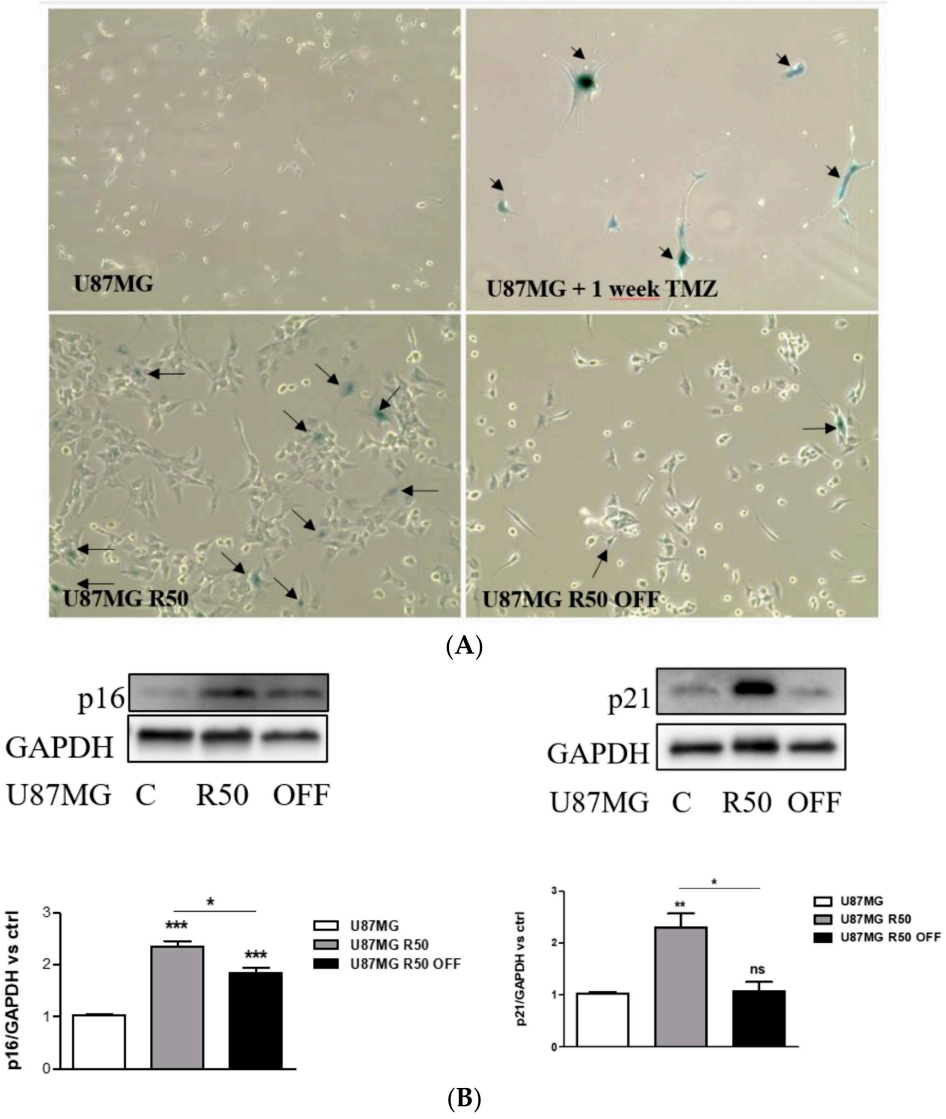

Figure 2. TMZ induces senescence in U87MG cells: (**A**) Representative photomicrographs showing cellular senescence after staining with SA-βGal. Arrows: senescent cells. (**B**). Representative Western blot analysis showing basal expression of p16 and p21 in TMZ-resistant cells (U87MG R50 and U87MG R50 OFF) compared to the parental cells. Histograms represent the mean ± S.E.M. of three separate experiments, and GAPDH expression was used as the loading control. *, $p < 0.05$; **, $p < 0.01$; ***, $p < 0.001$; ns, non-significant.

3.3. Extracellular Matrix Organization and Integrins Are Affected by TMZ

We used RNAseq analysis to compare the three cell lines. Analysis of global gene variations by unsupervized hierarchal clustering showed that profound changes occurred during TMZ treatment, with the largest differences recorded between U87MG and U87MG R50 cells (Figure 3A). U7MG R50 OFF were more closely related to the U87MG non-treated cells. The most significant genes were subjected to gene ontology analysis. Biological pathways mostly impacted by long-term Temozolomide treatment (R50 versus control cells) are extracellular matrix organization, O-linked glycosylation and integrin cell surface interactions (Figure 3B). By contrast fewer biological pathways, including neuronal system and extracellular Matrix organization, appear to be impacted in U87MG R50 OFF cells compared to non-treated cells (Figure 3C).

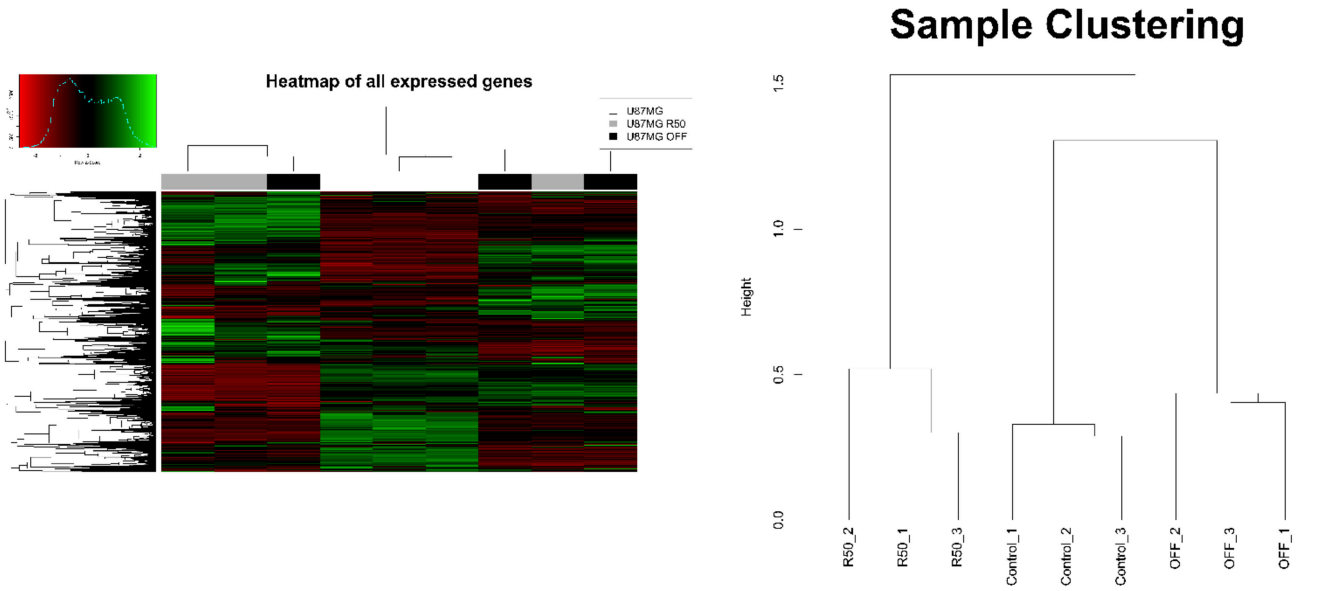

(**A**)

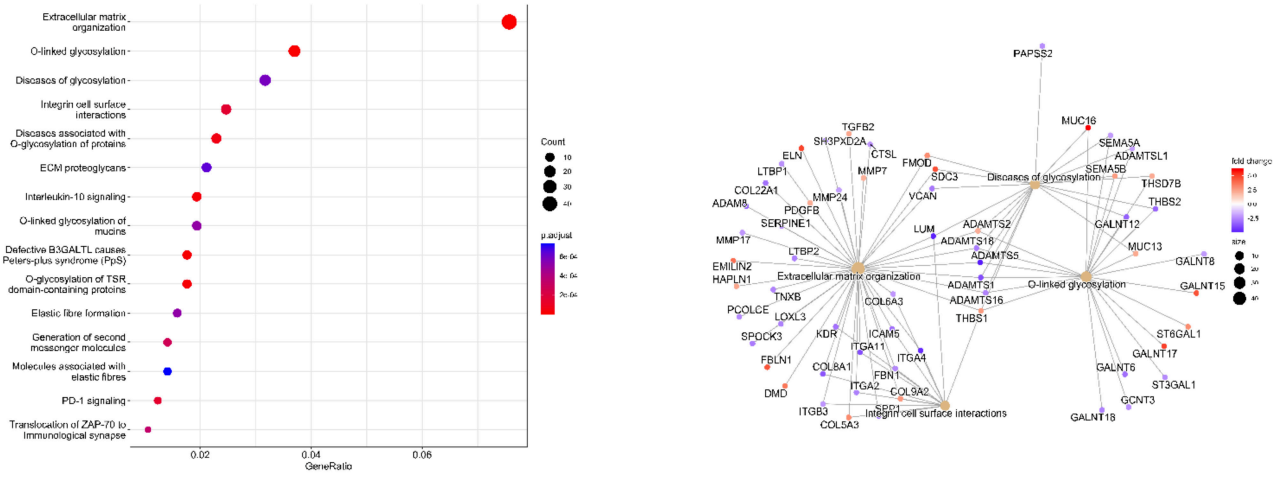

(**B**)

Figure 3. *Cont.*

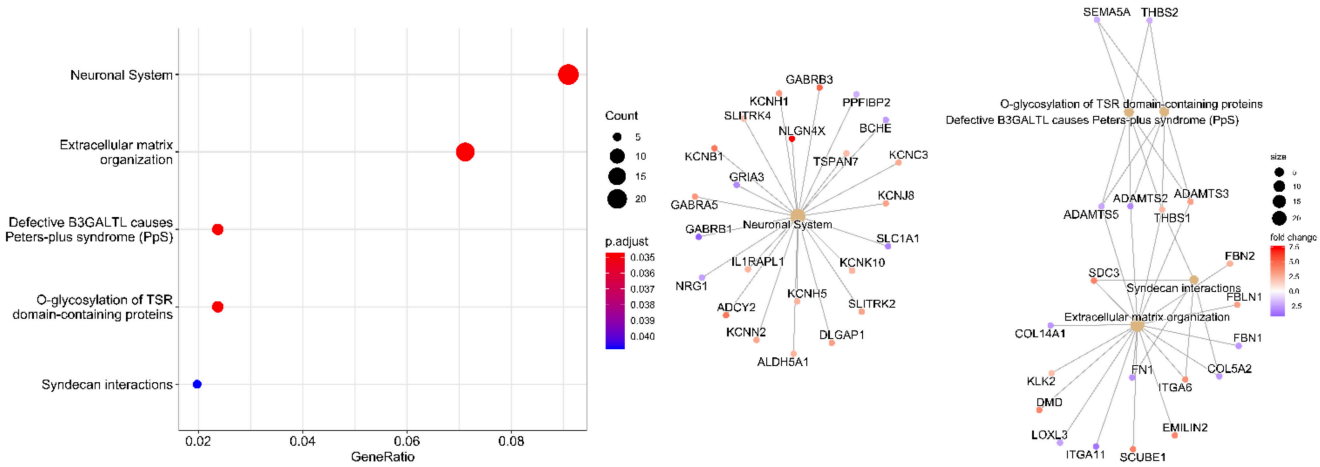

(**C**)

Figure 3. RNAseq analysis of TMZ-resistant and parental cell gene expression: (**A**) Heatmap grouped the nine samples based on the global expression profiles. Colour scale shows high and low expressions as green and red, respectively. Dendogram depicting correlation among different samples based on global expression profiles. (**B**) Top 15 enriched reactome pathways for differentially expressed genes in U87MG R50 cells versus control. Enrichment map with the inter-relation of the top three enriched reactome pathways and visualization of DEGs. (**C**) Top five enriched reactome pathways for differentially expressed genes in U87MG R50 OFF cells versus control. Enrichment map with the inter-relation of the top three enriched reactome pathways and visualization of DEGs.

Focusing on the integrin genes, profound rearrangements of integrin subunit expression levels were observed (Figure 4A). Four main clusters exist, which define particular integrin expressions in the different cell lines. Cluster 1 corresponds to integrins expressed in U87MG control cells but repressed in R50 cells and with intermediary expression in R50 OFF cells (Integrins α2, α3, α4, α5, α10, α11, αv, β1, β3). Cluster 2 involves integrins overexpressed in U87MG R50 OFF cells as compared to the two other cell lines (α6, β6 and β8), of which α6 and β8 are described as markers of glioma stem cells [36,45,46]. Cluster 3 corresponds to integrins repressed in U87MG R50 OFF cells (α7, α9, αx, αD, β5, β7). Cluster 4 includes integrins overexpressed in U87MG R50 cells (α1, αL, αM, β2, β4), including some leucocyte specific integrins. Data confirm that integrin mRNA expressions are subjected to specific variations during the time course of chemotherapy with Temozolomide.

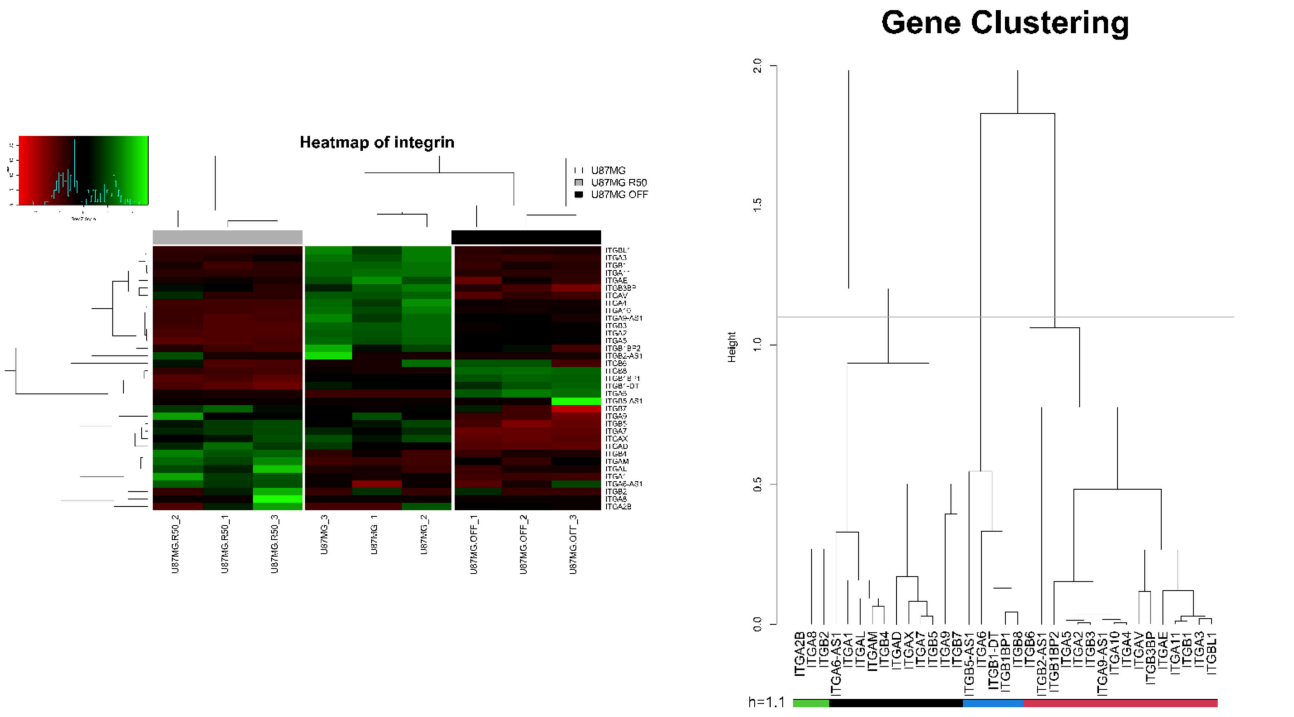

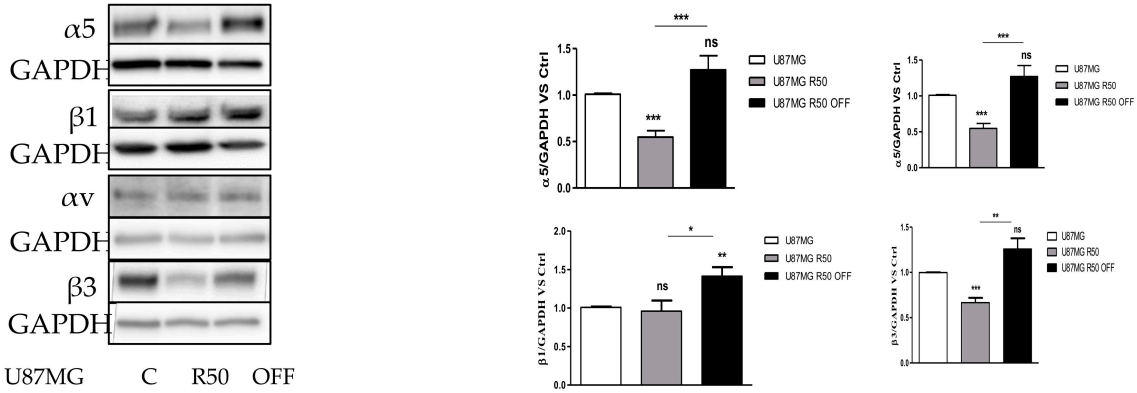

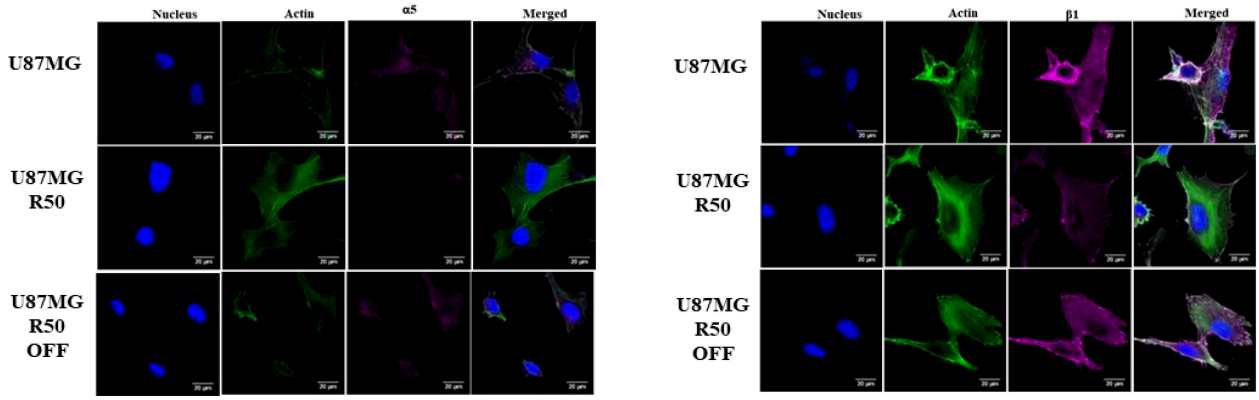

Figure 4. *Cont.*

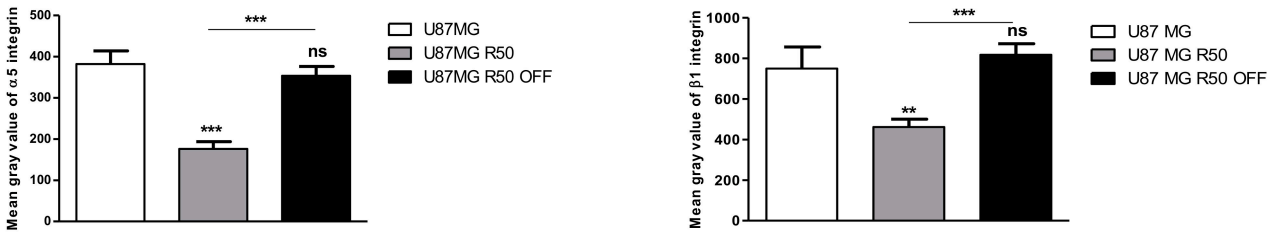

(**C**)

Figure 4. Integrin variations during TMZ treatment: (**A**) Heatmap visualization comparing expression of genes encoding integrins between samples with dendrogram to show clustering. Colour scale shows high and low expressions as green and red, respectively. (**B**) Representative Western blot analysis showing basal expression of α5, β1, αv and β3 integrins in U87MG R50 and U87MG R50 OFF cells compared to the parental cells. Histograms represent the mean ± S.E.M. of three separate experiments, and GAPDH was used as the loading control. (**C**) Representative fluorescence confocal microscopy images and mean grey value of basal α5 and β1 integrin subunits expression in TMZ-resistant U87MG R50 and U87MG R50 OFF cells compared to the parental cells. Scale bars: 20 µm. Histograms represent mean ± S.E.M. of three separate experiments. *, $p < 0.05$; **, $p < 0.01$; ***, $p < 0.001$; ns, non-significant.

As we demonstrated previously that integrin α5β1 is involved in TMZ resistance [30], we next focused on this integrin and examined its expression at the protein level in the parent and TMZ-resistant cells lines. By Western blot, we observed a clear decrease in the α5 subunit in U87MG R50 cells without a significant change in that of the β1 subunit. Interestingly, the α5 integrin level increased after removal of TMZ in the U87MG R50 OFF cells, reaching those seen in non-treated cells without changes in the β1 integrin level (Figure 4B). By contrast, the αv integrin level did not change between the three cell lines, although β3 integrin expression followed those of α5 integrin, showing that both α5β1 and αvβ3 integrins, which are largely involved in glioblastoma aggressiveness, were affected by Temozolomide treatment. As a confirmation we checked the expression changes of α5β1 integrin by immunohistochemistry. As can be seen in Figure 4C, the expression of both α5 and β1 integrins was reduced in U87MG R50 but reappeared after removal of TMZ in U87MG R50 OFF cells.

3.4. TMZ Affects Glioma Cell Proliferation and Migration through Modulation of α5β1 Integrin

The capacity to fill the culture wells as well as the proliferation index was slightly decreased for U87MG R50 cells as compared to parental and U87MG R50 OFF cells (Figure 5A) presumably due, at least in part, to the decrease in integrins. To confirm the impact of α5β1 integrin on proliferation, we used the integrin antagonists K34c and FR248, which are RGD-based peptidomimetics optimized for high affinity to α5β1 integrin with a reduced affinity to αvβ3 integrin. We already showed that both antagonists recognize α5β1 integrin and inhibit glioma cell adhesion to fibronectin and cell migration [35]. As shown in Figure 5B, K34c proved able to decrease the cell adherence for all three cell lines, inhibiting the cell spreading and forming some sphere-like structures, particularly in U87MG and U87MG R50 OFF cells. FR248 is less efficient in inhibiting cell spreading than K34c and particularly ineffective in U87MG R50 cells. A quantification of cell confluence after 3 days of treatments confirmed these morphological observations (Figure 5C). FR248, which is slightly more selective than K34c for α5β1, is inactive in U87MG R50 cells in accordance with the low level of α5β1 integrin in these cells. The data suggest that U87MG and U87MG R50 OFF cells may be similarly sensitive to α5β1 integrin antagonists at least for the inhibition of cell adherence and confluence.

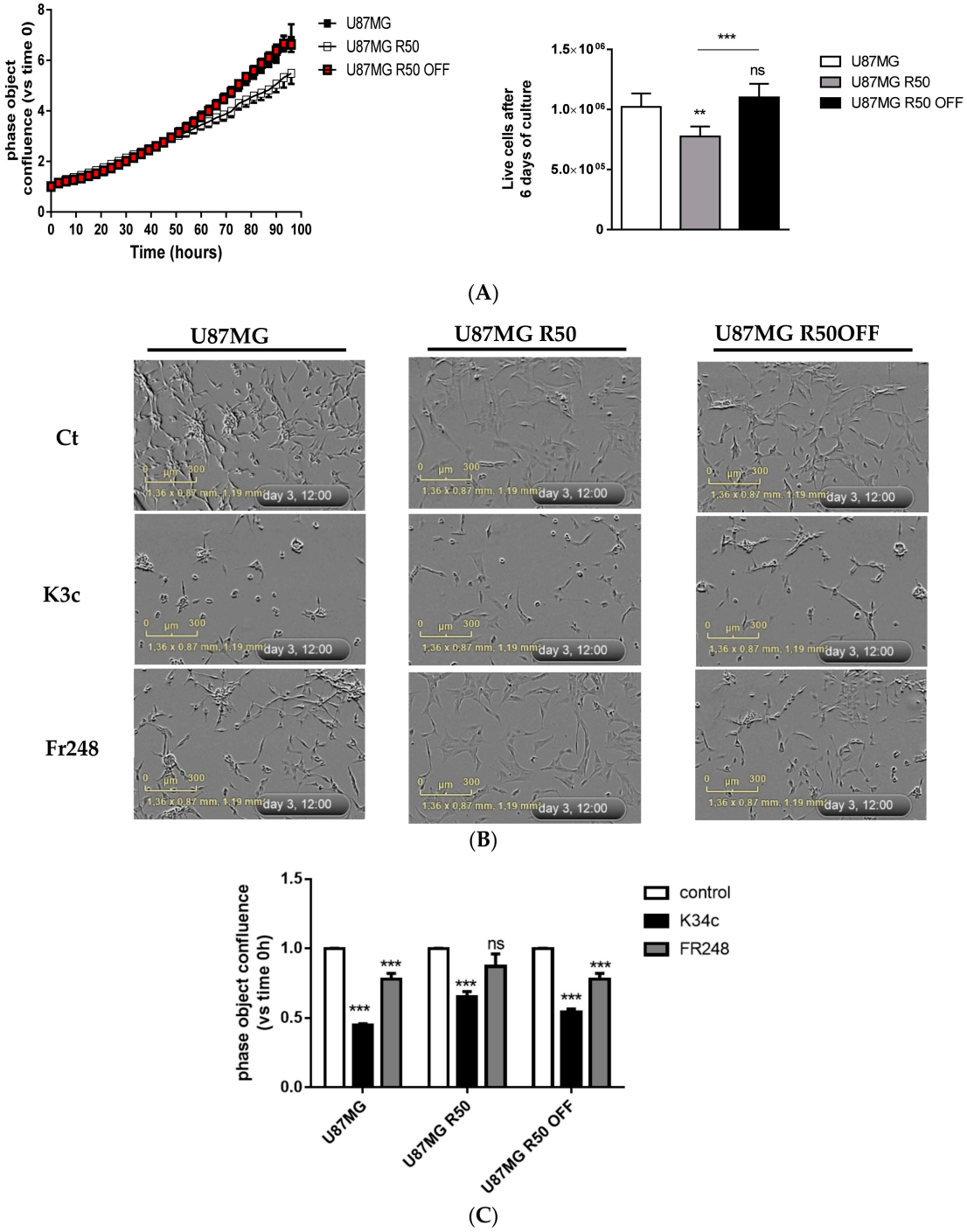

Figure 5. Proliferation and effects of integrin antagonists on TMZ-resistant and parental cells: (**A**) (left)**.** Cell confluence was calculated using IncuCyte Zoom software based on phase-contrast images of U87MG, U87MG R50 and U87MG R50 OFF cells from 0 h to 96 h. (right) Proliferation calculated as the number of viable cells after 6 days in culture compared to the number of plated cells at day 0. (**B**) Representative phase contrast images from the IncuCyte showing the cellular morphology of U87MG, U87MG R50 and U87MG R50 OFF cells 72 h post treatment with solvent, K34c (20 μM) and Fr248 (20 μM). Scale bar, 300 μM. (**C**) Cell confluence was calculated using IncuCyte Zoom software based on phase-contrast images of U87MG, U87MG R50 and U87MG R50 OFF cells at 72 h post treatment. For all panels: mean ± S.E.M. of at least three independent experiments with **, $p < 0.01$; ***, $p < 0.001$; ns, non-significant.

Integrins are largely involved in glioma cell migration, as we have shown previously for α5β1 integrin [33,34,43]. The capability of cell dispersion out of gliomaspheres in a

fibronectin-rich environment was then compared among the three cell lines. As shown in Figure 6, U87MG and U87MG R50 OFF cells were able to disseminate out of the spheres, but dissemination was blocked in U87MG R50 cells. This dissemination was clearly impacted by the expression of α5β1 integrin as it was largely inhibited by K34c and FR248 at 20 µM (Figure 6) but also at 5 µM (Supplementary Figure S2) in U87MG and U87MG R50 OFF cells. TMZ acute treatment of U87MG and U87MG R50 OFF cells did not affect cell migration, nor did TMZ removal affect U87MG R50 cells (Supplementary Figure S3). Both cell lines were unable to migrate strongly on polylysine, a nonspecific substrate, as compared to fibronectin, the privileged ECM substrate of α5β1 integrin (Supplementary Figure S4). The results show that TMZ-resistant U87MG R50 OFF cells recover their capacity not only to proliferate but also to migrate on a fibronectin-rich substrate.

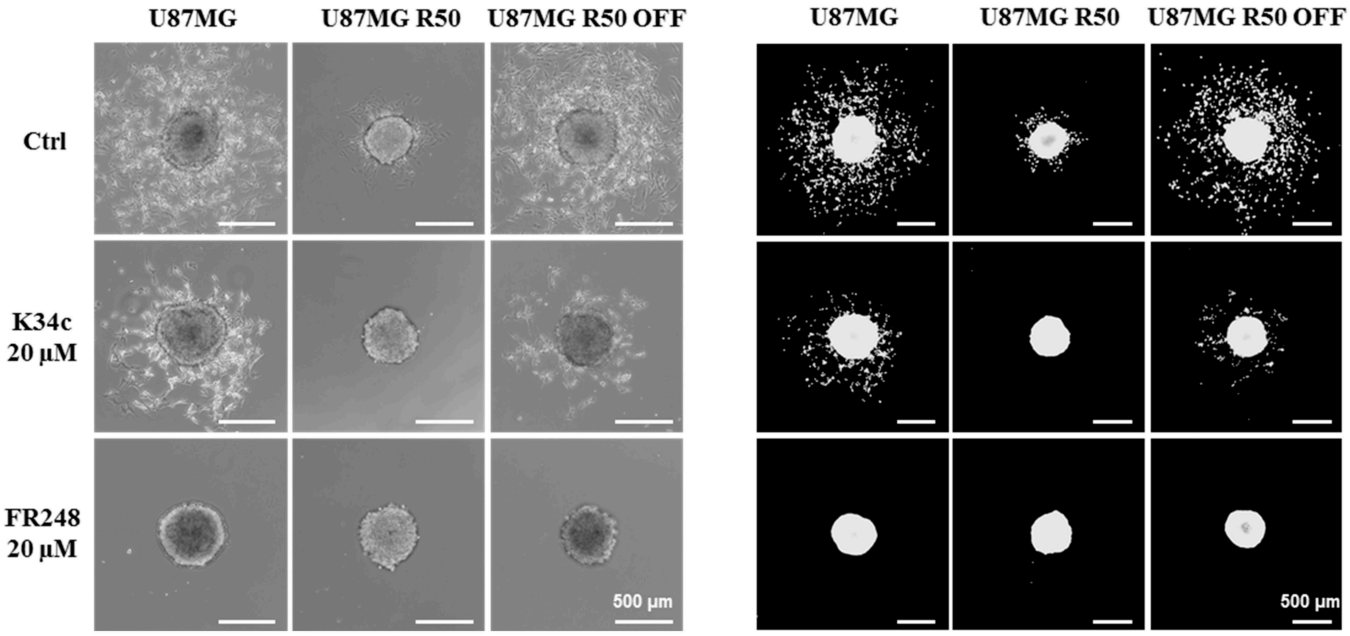

(**A**)

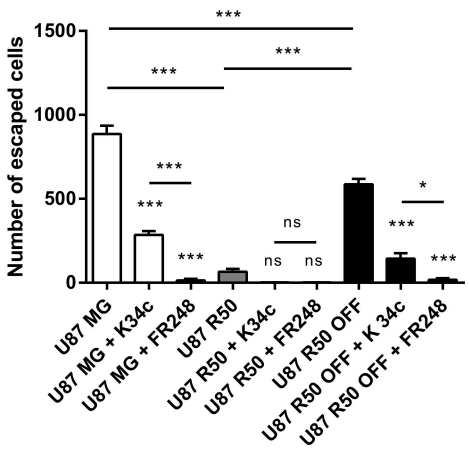

(**B**)

Figure 6. *Cont.*

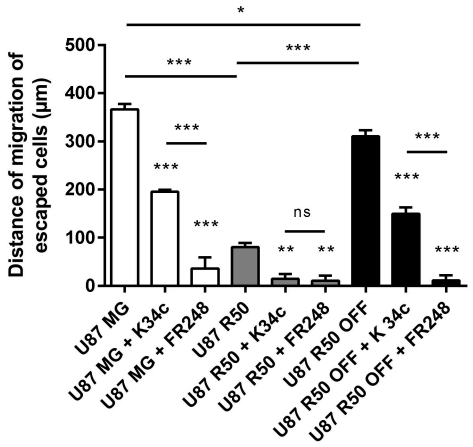

(**C**)

Figure 6. Cell evasion from spheroids and effects of integrin antagonists on TMZ-resistant and parental cells: (**A**) (left) Representative phase-contrast images of TMZ-resistant (U87MG R50 and U87MG R50 OFF) or parental cells spheroids after 18 h of migration and treatment with solvent, K34c 20 µM or Fr248 20 µM. Scale bars, 500 µm. (right) Representative fluorescence images (DAPI staining) of TMZ-resistant (U87MG R50 and U87MG R50 OFF) or parental cells spheroids after 18 h of migration and treatment with solvent, K34c 20 µM or Fr248 20 µM. Scale bars, 500 µm. (**B**) Analysis of the number of cells that migrated out of the spheroid and (**C**) analysis of the average distance of migration out of the spheroid for TMZ-resistant cells (U87MG R50 and U87MG R50 OFF) compared to parental cells, treated during 18 h with solvent, K34c 20 µM or Fr248 20 µM. Image analyses were performed with ImageJ software using a homemade plugin [43]. For all panels: mean ± S.E.M. of at least three independent experiments with *, $p < 0.05$; **, $p < 0.01$; ***, $p < 0.001$; ns, non-significant.

3.5. p53 Signalling Pathway in U87MG and TMZ-Resistant Cells

TMZ is known to activate the p53 pathway. We checked p53 stabilisation and activation in the three cell lines in the basal conditions of the culture. In U87MG R50 cells as well as in the U87MG R50 OFF cells, p53 is stabilized, and its target genes MDM2 and p21 are both increased at the mRNA level in the former cell line but only MDM2 in the latter one (Figure 7A). These data are confirmed by the protein level of both p21 (see Figure 2B) and MDM2 (Figure 7A). MDM2 may thus be used as a target in these resistant cells. We considered three inhibitors of MDM2/p53 interactions already known to reactivate p53 signalling. The different molecules used were Nutlin-3a and Idasanutlin, which bind to the MDM2 part and RITA, which binds to the p53 part of the MDM2–p53 complex. As can be seen in Figure 7B, all three drugs enhanced the stability of p53 as well as its activation (shown by the increase in MDM2 protein). No differences could be observed between control U87MG cells and their TMZ-resistant counterparts as far as the activation of p53 is concerned. In these experiments, Idasanutlin was the most efficient activator of the p53 pathway, even at 0.1 µM (a concentration 10 times lower than for Nutlin-3a and RITA), and RITA was less efficient after 24 h of treatment. The results suggest that TMZ-resistant cells may benefit from an alternative way to activate the p53 tumour suppressor pathway.

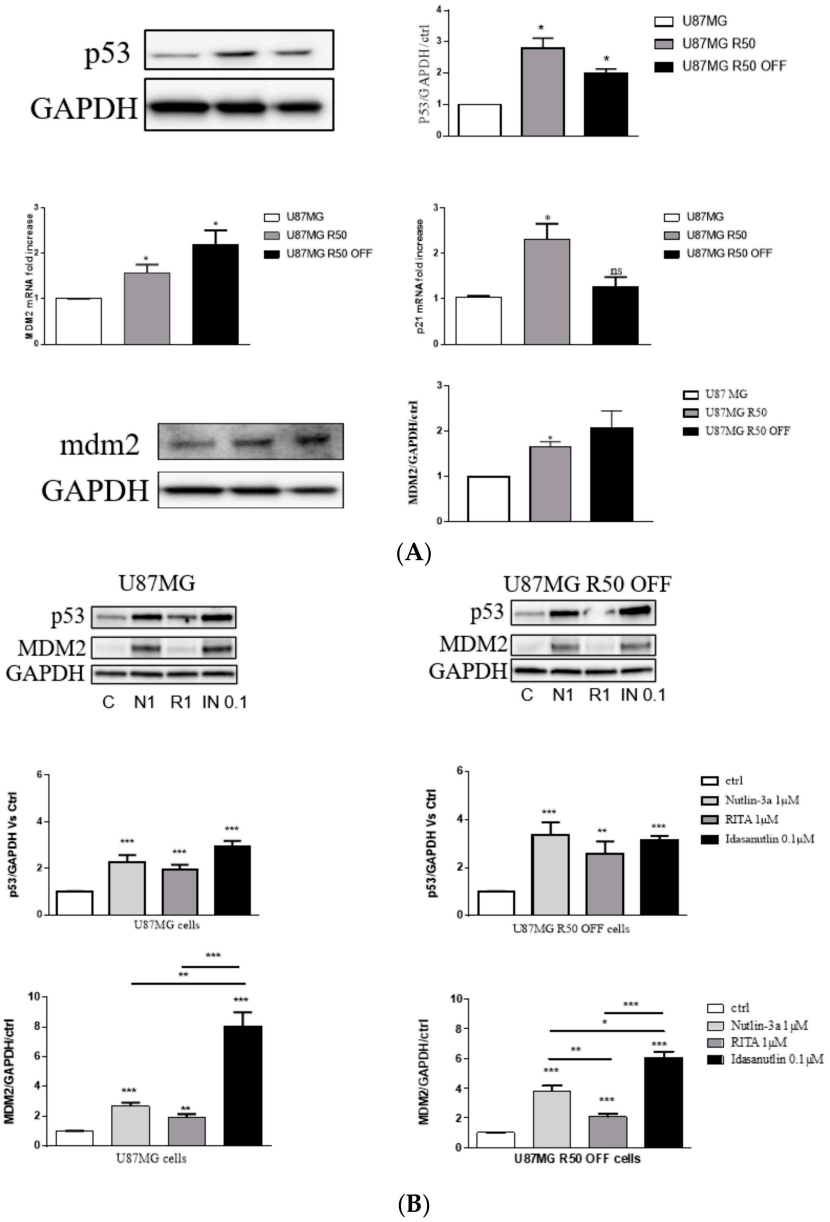

Figure 7. Modulation of the p53 pathway in U87MG, U87MG R50 and U87MG R50 OFF cells. (**A**) Representative Western blot of p53 (upper panel) and RT-qPCR analysis of p53 target genes mdm2 and p21 (middle panel) in U87MG R50 and U87MG R50 OFF compared to the parental cells. Representative Western blot of MDM2 is shown (lower panel) as well as the corresponding histograms. (**B**) Representative Western blot of p53 stabilisation and MDM2 expression 24 h post treatment with Nutlin-3a (1 μM/N1), RITA (1 μM/R1) and Idasanutlin (0.1 μM/IN 0.1) in U87MG R50 OFF cells compared to the parental cells. Histograms represent the mean ± S.E.M. of three separate experiments and GAPDH was used as the loading control. *, $p < 0.05$; **, $p < 0.01$; ***, $p < 0.001$; ns, non-significant.

3.6. p53 Activation and Integrin Inhibition as a Therapeutic Option for TMZ-Resistant Cells

We described previously negative crosstalk between α5β1 integrin and p53 signalling pathways implicated in the chemotherapy resistance of glioma cells. We showed that activating p53 concomitantly with inhibiting integrin α5β1 led to an increase in p53 signalling in α5 integrin subunit overexpressing cells [39]. We thus wondered if similar results might be obtained in TMZ-resistant cells. We investigated the association of p53 activators Nutlin-3a and Idasanutlin with the two integrin antagonists on cell confluence. Data are

summarized in Table 2. As an example, results after 72h of treatment with Idasanutlin (0.1 μM) in association with K34c (20 μM) or FR248 (20 μM) are shown in Figure 8A. In addition, the p53 signalling pathway appears over-activated in U87MG R50 OFF cells after the association of Idasanutlin with FR248 (Figure 8B).

Table 2. Summary of Incucyte experiment results at 3 days after treatment with the different drugs alone or in combination. Results are expressed as mean ± s.e.m. of 3 to 5 independent experiments. * refers to statistical comparison between control and treatment and # comparison between combination therapies and each treatment alone. * and # are indicative of $p < 0.01$. ns = non significant.

Treatment	U87MG Cells	U87MG R50 OFF Cells	U87MG R50
Control	1	1	1
TMZ	0.57 ± 0.01 *	0.94 ± 0.02 ns	-
K34c	0.44 ± 0.01 *	0.54 ± 0.03 *	0.65 ± 0.04 *
FR248	0.78 ± 0.04 *	0.78 ± 0.04 *	0.86 ± 0.09 ns
Nutlin-3a	0.35 ± 0.01 *	0.42 ± 0.02 *	0.42 ± 0.01 *
Idasanutlin	0.52 ± 0.05 *	0.45 ± 0.02 *	_
Nutlin-3a + K34c	0.21 ± 0.01 * #	0.24 ± 0.01 * #	0.25 ± 0.008 * #
Nutlin-3a + FR248	0.28 ± 0.02 * #	0.33 ± 0.01 * #	0.37 ± 0.01 * ns
Idasanutlin + K34c	0.265 ± 0.005 * #	0.244 ± 0.007 * #	-
Idasanutlin + FR248	0.399 ± 0.005 * #	0.319 ± 0.009 * #	-

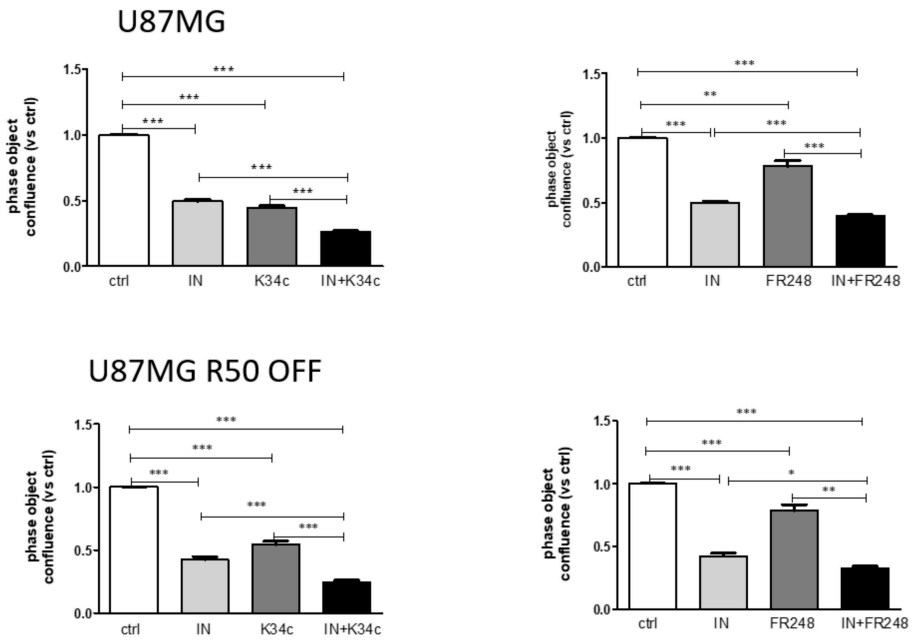

(**A**)

Figure 8. *Cont.*

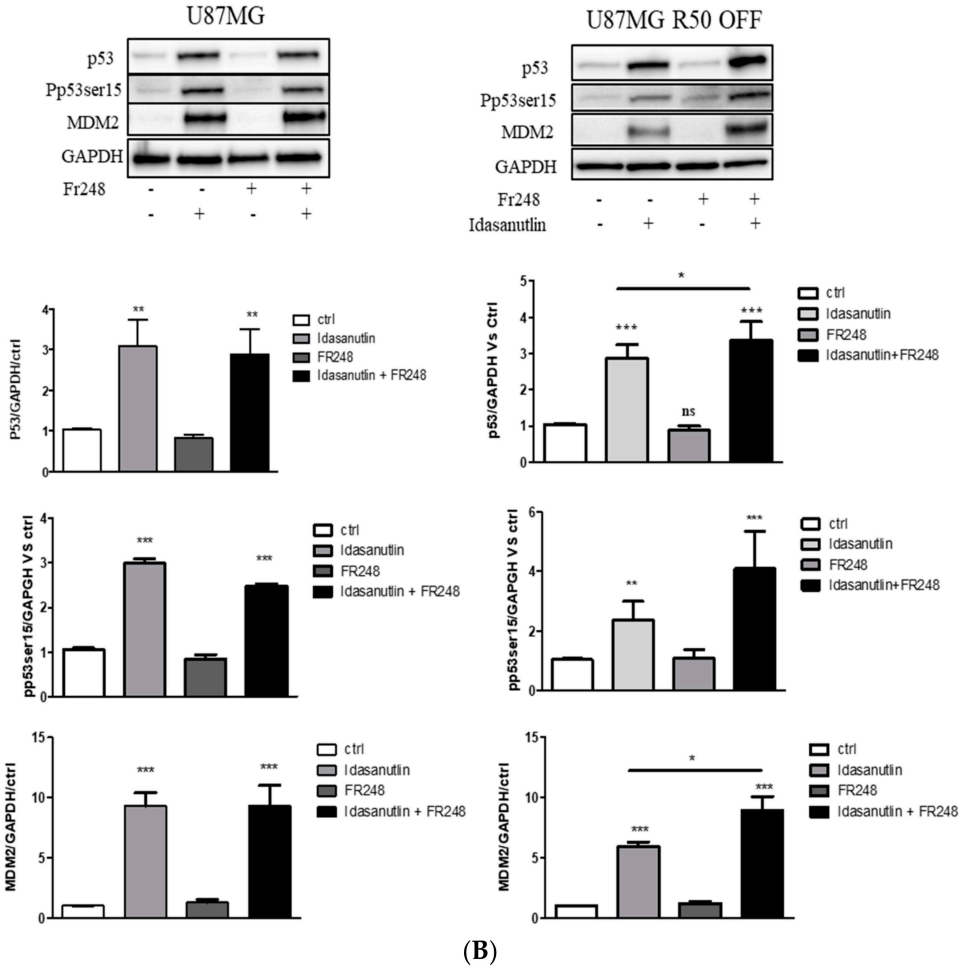

Figure 8. Effect of Idasanutlin and integrin antagonists on TMZ-resistant and parental cells. (**A**) Cell confluence was calculated using IncuCyte Zoom software based on phase-contrast images of U87MG and U87MG R50 OFF cells at 72 h after treatment with solvent, Idasanutlin (0.1 μM), K34c (20 μM) or FR248 (20 μM) alone or in combination. (**B**) Representative Western blots of p53 stability and activity (phosphorylation at ser^{15}) and the p53 target gene MDM2 expression in U87MG R50 OFF compared to the parental cells 24 h post treatment with Idasanutlin (0.1 μM) and Fr248 (20 μM) either separately or in combination. Histograms represent the mean ± S.E.M. of three separate experiments with GAPDH as the loading control. For all panels: *, $p < 0.05$; **, $p < 0.01$; ***, $p < 0.001$; ns, non-significant.

Compound **9** was described as a potent α5β1 and αvβ3 integrin inhibitor coupled with an inhibitory activity on MDM2 and MDM4, thus combining the effects we were studying [42]. We thus checked the effect of compound **9** in our cell lines. It was highly effective in inhibiting cell confluence in both U87MG and U87MG R50 OFF, cells even at low doses with 50% inhibition around 0.6 μM and profound changes on cell morphology, as shown in Figure 9A,B. Low doses of compound **9** (0.1 to 0.6 μM) hardly affected U87MG cells that were knocked down for the α5 integrin gene by the CRISPR/Cas9 technology (U87MG α5KO cells), confirming its capability to recognize this integrin (Supplementary Figure S5). Interestingly, in low doses, compound **9** (0.6 μM) behaved as integrin inhibitor K34c treatment alone but in high doses (above 5 μM), it had similar effects to the association of K34c with p53 activators in U87MG and U87MG R50 OFF cells (compare with Figure 8A). It seems that high doses are needed to activate p53 target genes (data not shown). The results suggest that compound **9** behaves as a strong inhibitor of naïve and TMZ-resistant U87MG cells through the concomitant inhibition of integrins and MDM2/MDM4.

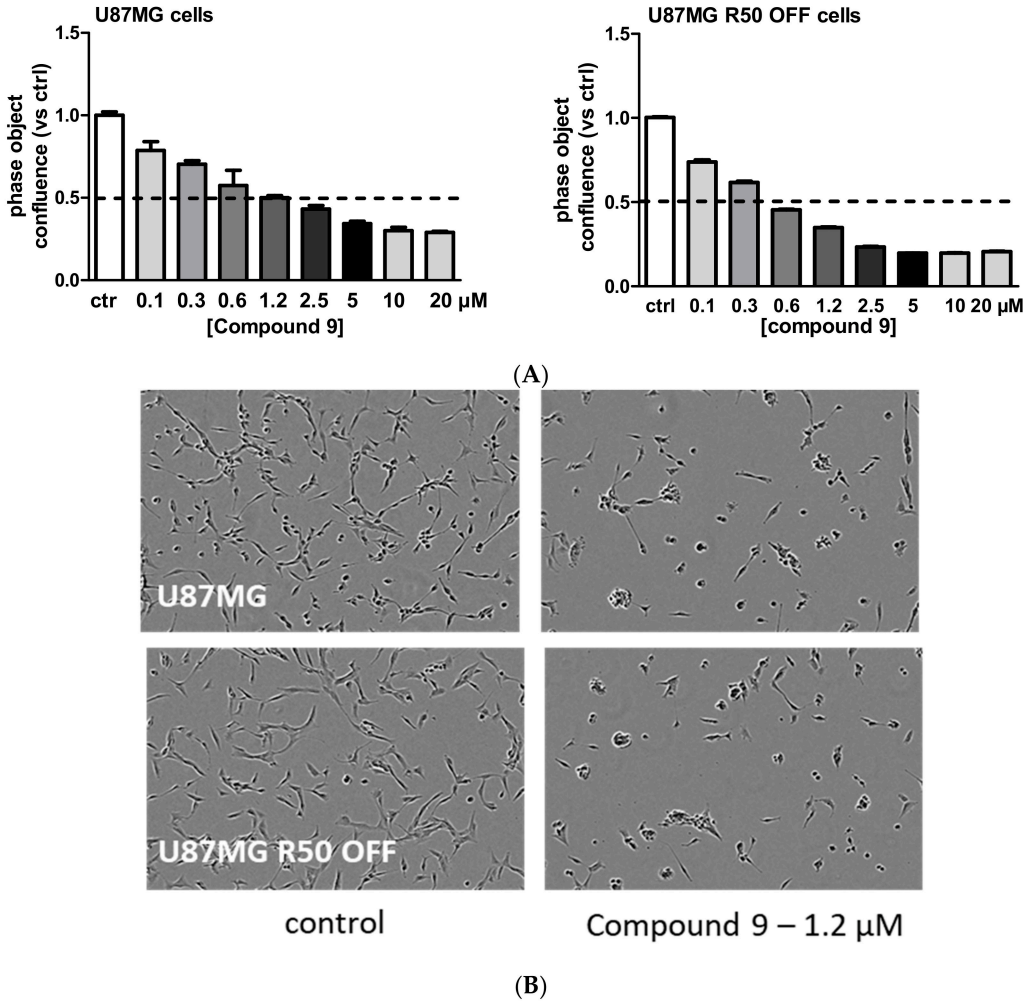

Figure 9. Effects of compound **9** on TMZ-resistant and parental cells: (**A**) Dose—response effects of compound **9** on cell confluence in U87MG and U87MG R50 OFF cells. (**B**) Representative phase contrast images from the IncuCyte showing the cellular morphology of U87MG and U87MG R50 OFF cells 72 h post treatment with compound 9 (1.2 µM). Histograms represents the mean ± S.E.M. of three separate experiments after 72 h treatment with TMZ or compound **9**.

4. Discussion

Although TMZ is currently the only approved chemotherapeutic drug known to significantly improve the overall survival of GBM patients [47,48], the development of acquired TMZ resistance leading to treatment failure remains one of the challenges to be resolved. Numerous works aimed to understand intrinsic and acquired TMZ resistance and recent reviews dedicated to this topic are available [49,50]. It appears clear that a multifaceted view is to be considered related to the high molecular heterogeneity of GBM and the plasticity of GBM cells. A consensus already exists about the role of MGMT, through which epigenetic regulation (promoter methylation or demethylation) is involved in the clinical response to TMZ. However, GBM-expressing or non-expressing MGMT can develop resistance to TMZ. Acquired resistance was also often linked to DNA damage repair pathways leading to new therapeutic avenues [51].

In this work, we generated TMZ-resistant cells by subjecting U87MG cells to TMZ 50 µM treatment as an in vitro model of MGMT-negative TMZ resistance. We aimed to compare cells continuously grown in the presence of TMZ (U87MG R50) with resistant cells growing in the absence of TMZ (U87MG R50 OFF), using this last model as a reflection of clinical recurrence. We confirmed that U87MG cells were sensitive to TMZ, resulting in large percentage of cell death at the treatment, beginning with few cells remaining alive

but exhibiting hallmarks of senescence. Senescence is considered a favourable response to chemotherapy as it blocks tumoral cell proliferation. This view has been challenged as the irreversibility of drug-induced senescence remains under debate and the pro-tumorigenic properties of the senescent-associated secretory phenotype (SASP) are clearly demonstrated [52,53]. It has already been demonstrated that TMZ induces senescence rather than apoptosis in glioma cells [44,54,55]. In line with this, we demonstrated that the few U87MG cells that remained alive after one-week incubation with TMZ were all positive for SA-βGAL staining. In our experimental conditions, the regrowth of the few surviving cell population occurred in the presence of TMZ from these stained cells, suggesting that senescence was reversible, but this point remains to be confirmed. The regrowth of U87MG cells after TMZ treatment to obtain resistant cell populations is largely described in the literature. However, treatments followed different experimental procedures (with large variations in the chosen doses, duration of treatments, time of omics or phenotypic evaluations, etc . . .) that may result in different biological outcomes [50]. The characterization of TMZ-resistant cells was generally made at the endpoint of cell treatment rather than along the treatment protocol. Recently the development of resistance was studied in a glioma cell line. Interestingly, a transient state (from day 3 to 9 after treatment) defined by slow growth and morphological and metabolic changes was characterized. Resistant cells will emerge from these transient state cells [56]. The link with senescence has not been studied in this work.

In our work we aimed to analyse another step of the TMZ resistance, i.e., how resistant cells behave after removal of the drug, to gain an understand of what may happen in patients before or at the point of recurrence. To he best of our knowledge, the molecular and phenotypic characterization of resistant cells before and after removal of the drug has not been extensively studied. Interestingly, profound changes were observed between U87MG R50 cells and the non–treated cell, whereas U87MG R50 OFF cells showed more closely related characteristics to the control cells. One of the most affected pathways was, in both cases, extracellular matrix organization, including integrin expression level modifications. Interestingly, profound changes in ECM–receptor interactions were also noted in the response of the glioma to ionizing radiation [57]. The heatmap of integrins (Figure 4) revealed particular sets of integrins overexpressed in each cell line, suggesting that anti-integrin therapeutic options have to be considered in a timely manner during therapies. As an example, U87MG R50 OFF cells overexpress α6 and β8 integrins, both known to be glioma stem cell markers [36,45]. Accordingly, a dedifferentiation of differentiated cells towards glioma stem cells has been reported in tumours after radiotherapy or TMZ chemotherapy [58,59]. Specific anti-α6 and/or β8 integrin therapies may thus be used for recurrent as well as for primary tumours.

In this work we focused on RGD-integrins such as α5β1 and αvβ3, as we demonstrated in previous studies that α5β1 integrin is involved in TMZ resistance [30]. We found that continuous treatment with TMZ decreased the expression of α5β1 integrin (as well as those of β3), while recovery of expression was found after removal of the drug. Interestingly, phenotypic alterations (proliferation and migration) are coupled with the level of this integrin. These findings portray α5β1 integrin as a promising target for recurrent GBM, as was proposed in studies examining bevacizumab-treated recurrent glioblastoma [37,60]. In our previous work [31], we showed that α5 integrin expression in primary tumours was not impacted by their MGMT status. Whether this absence of a relationship remains recurring is currently not known and deserves further studies.

Beside integrin changes, resistant cell lines exhibit p53 pathway activation with a long-lasting increase in MDM2 expression. Restoration of the tumour-suppressor function of p53 by disrupting the MDM2-p53 protein–protein interaction is considered an attractive therapeutic strategy for GBM expressing p53 wild type. Combination therapy of TMZ with Nutlin 3a, an MDM2 antagonist, was already shown to enhance the survival of mice engrafted with a GBM cell line by activating p53 and downregulating DNA repair proteins [61]. Preclinical evaluation of RG7112, another MDM2 antagonist, showed a

reduced tumour growth of p53 wild-type patient-derived cell lines with the amplification of MDM2 [17]. The significant efficacy of this drug in a subset of non-MDM2-amplified models has also been observed. We show in this work that TMZ-resistant cells remain sensitive to MDM2 inhibitors and that the p53 pathway can be over-activated in these cells by three different drugs. Our previous results point out a negative crosstalk between α5β1 integrin and p53 signalling pathways implicated in chemotherapy resistance of glioma cells. Activating p53 concomitantly with inhibiting integrin α5β1 led to an increase in p53 signalling and glioma cell death in α5 integrin subunit-overexpressing cells [30,39]. We evaluated this strategy on the TMZ-resistant U87MG R50 OFF cells, which re-express the integrin. The results obtained in experiments associating Idasanutlin (the most efficient MDM2 antagonist) with FR248 (the most specific α5β1 integrin antagonist) suggest that resistance to TMZ may be overcome by this strategy. The U87MG R50 OFF cell line appeared more sensitive than the non-treated cells, even if the expression of the α5β1 integrin was similar between the two cell lines. We cannot exclude at this point that other molecular changes participate in this phenomenon, which deserves further studies. We thus propose a new therapeutic option for recurrent GBM expressing α5β1 integrin: p53 activation along with inhibition of the integrin. This therapy may be achieved with a single molecule, compound **9**, which is able to target RGD-integrin-expressing cells and inhibit MDM2 at the same time [42]. We show here that this molecule is able to target U87MG and TMZ-resistant U87MG R50 OFF cells at lower concentrations than integrin antagonists, suggesting decreased potential side effects. Future works have to be carried out to more precisely investigate this compound, which may be very interesting to treat recurrent glioblastoma.

In conclusion, our work shows a huge impact of Temozolomide on the integrin repertoire of U87MG cells. The integrin expressions appear highly switchable during the course of temozolomide treatment. Specific integrins may be particularly targetable at different time points of glioblastoma treatment and combination therapies evaluated according to their time-dependent expression. Although confirmation in patient-derived cell lines and other preclinical models is needed, our data add new evidence that α5β1 integrin has a role to play as a therapeutic target in recurrent glioblastoma.

Supplementary Materials: The following are available online at https://www.mdpi.com/article/10.3390/cancers14020369/s1, Figure S1: Dose- dependent effect of Temozolomide on the 3 cell lines, Figure S2: Cell evasion from spheroids and effects of low dose (5 μM) of integrin antagonists on TMZ-resistant and parental cells, Figure S3: Temozolomide effect on cell migration. Figure S4: Cell evasion from spheroids on polylysine versus fibronectin Figure S5: Effect of compound **9** on U87MG-α5 integrin KO cells.

Author Contributions: Conceptualisation, N.E.-S., N.E.-W., S.M. and M.D.; Data curation, D.R.; Funding acquisition, N.E.-W., S.M. and M.D.; Investigation, S.S., N.P., M.M., C.B. and S.F.; Methodology, N.P. and D.R.; Project administration, N.E.-S., N.E.-W., S.M. and M.D.; Resources, Horst Kessler, L.M. and D.R.; Validation, S.S. and N.P.; Visualisation, S.S., N.P., M.M. and C.B.; Writing—original draft, S.S., N.P., N.E.-S., H.K., L.M., S.F., S.M., D.R. and M.D.; Writing—review and editing, S.S., N.E.-S., L.M., S.M. and M.D. All authors have read and agreed to the published version of the manuscript.

Funding: We are thankful for financial support from Institut National du Cancer (grant INCA_11527), Ligue contre le Cancer (CCIR Est), ITI Innovec (IdEx (ANR-10-IDEX-0002), SFRI (ANR-20-SFRI-0012)), Association pour la Recherche contre le Cancer, from the CNRS through the 80|Prime program, the University of Strasbourg (France), the Alex Akwueme Federal University Ndufu-Alike Ikwo (Nigeria), the Associations-charities Lyons Club de Niederbronn Les Bains, Franck Rayon de Soleil and Life Pink.

Institutional Review Board Statement: Not applicable.

Informed Consent Statement: Not applicable.

Data Availability Statement: RNAseq data will be available after request to the corresponding author.

Conflicts of Interest: The authors have no conflict of interest to declare.

References

1. Geraldo, L.H.M.; Garcia, C.; da Fonseca, A.C.C.; Dubois, L.G.F.; de Sampaio e Spohr, T.C.L.; Matias, D.; de Camargo Magalhães, E.S.; do Amaral, R.F.; da Rosa, B.G.; Grimaldi, I.; et al. Glioblastoma Therapy in the Age of Molecular Medicine. *Trends Cancer* **2019**, *5*, 46–65. [CrossRef] [PubMed]
2. Omuro, A. Glioblastoma and Other Malignant Gliomas: A Clinical Review. *JAMA* **2013**, *310*, 1842. [CrossRef] [PubMed]
3. Stupp, R.; Weller, M.; Belanger, K.; Bogdahn, U.; Ludwin, S.K.; Lacombe, D.; Mirimanoff, R.O. Radiotherapy plus Concomitant and Adjuvant Temozolomide for Glioblastoma. *N. Engl. J. Med.* **2005**, *10*, 987–996. [CrossRef] [PubMed]
4. Cruz Da Silva, E.; Mercier, M.-C.; Etienne-Selloum, N.; Dontenwill, M.; Choulier, L. A Systematic Review of Glioblastoma-Targeted Therapies in Phases II, III, IV Clinical Trials. *Cancers* **2021**, *13*, 1795. [CrossRef]
5. Khaddour, K.; Johanns, T.; Ansstas, G. The Landscape of Novel Therapeutics and Challenges in Glioblastoma Multiforme: Contemporary State and Future Directions. *Pharmaceuticals* **2020**, *13*, 389. [CrossRef]
6. Hotchkiss, K.M.; Sampson, J.H. Temozolomide Treatment Outcomes and Immunotherapy Efficacy in Brain Tumor. *J. Neurooncol.* **2020**, *151*, 55–62. [CrossRef]
7. Park, C.-K.; Kim, J.E.; Kim, J.Y.; Song, S.W.; Kim, J.W.; Choi, S.H.; Kim, T.M.; Lee, S.-H.; Kim, I.H.; Park, S.-H. The Changes in MGMT Promoter Methylation Status in Initial and Recurrent Glioblastomas. *Transl. Oncol.* **2012**, *5*, 393–397. [CrossRef]
8. Grombacher, T.; Eichhorn, U.; Kaina, B. P53 Is Involved in Regulation of the DNA Repair Gene O6-Methylguanine-DNA Methyltransferase (MGMT) by DNA Damaging Agents. *Oncogene* **1998**, *17*, 845–851. [CrossRef]
9. Harris, L.C.; Remack, J.S.; Houghton, P.J.; Brent, T.P. Wild-Type P53 Suppresses Transcription of the Human O6-Methylguanine-DNA Methyltransferase Gene. *Cancer Res.* **1996**, *56*, 2029–2032.
10. Brennan, C.W.; Verhaak, R.G.W.; McKenna, A.; Campos, B.; Noushmehr, H.; Salama, S.R.; Zheng, S.; Chakravarty, D.; Sanborn, J.Z.; Berman, S.H.; et al. The Somatic Genomic Landscape of Glioblastoma. *Cell* **2013**, *155*, 462–477. [CrossRef]
11. Verhaak, R.G.W.; Hoadley, K.A.; Purdom, E.; Wang, V.; Qi, Y.; Wilkerson, M.D.; Miller, C.R.; Ding, L.; Golub, T.; Mesirov, J.P.; et al. Integrated Genomic Analysis Identifies Clinically Relevant Subtypes of Glioblastoma Characterized by Abnormalities in PDGFRA, IDH1, EGFR, and NF1. *Cancer Cell* **2010**, *17*, 98–110. [CrossRef]
12. Crespo, I.; Vital, A.L.; Gonzalez-Tablas, M.; del Carmen Patino, M.; Otero, A.; Lopes, M.C.; de Oliveira, C.; Domingues, P.; Orfao, A.; Tabernero, M.D. Molecular and Genomic Alterations in Glioblastoma Multiforme. *Am. J. Pathol.* **2015**, *185*, 1820–1833. [CrossRef]
13. England, B.; Huang, T.; Karsy, M. Current Understanding of the Role and Targeting of Tumor Suppressor P53 in Glioblastoma Multiforme. *Tumor Biol.* **2013**, *34*, 2063–2074. [CrossRef]
14. Vassilev, L.T. In Vivo Activation of the P53 Pathway by Small-Molecule Antagonists of MDM2. *Science* **2004**, *303*, 844–848. [CrossRef]
15. Her, N.-G.; Oh, J.-W.; Oh, Y.J.; Han, S.; Cho, H.J.; Lee, Y.; Ryu, G.H.; Nam, D.-H. Potent Effect of the MDM2 Inhibitor AMG232 on Suppression of Glioblastoma Stem Cells. *Cell Death Dis.* **2018**, *9*, 792. [CrossRef]
16. Reifenberger, G.; Liu, L.; Ichimura, K.; Schmidt, E.E.; Collins, V.P. Amplification and Overexpression of the MDM2 Gene in a Subset of Human Malignant Gliomas without P53 Mutations. *Cancer Res.* **1993**, *53*, 2736–2739.
17. Verreault, M.; Schmitt, C.; Goldwirt, L.; Pelton, K.; Haidar, S.; Levasseur, C.; Guehennec, J.; Knoff, D.; Labussiere, M.; Marie, Y.; et al. Preclinical Efficacy of the MDM2 Inhibitor RG7112 in MDM2-Amplified and TP53 Wild-Type Glioblastomas. *Clin. Cancer Res.* **2016**, *22*, 1185–1196. [CrossRef]
18. Berberich, A.; Kessler, T.; Thomé, C.M.; Pusch, S.; Hielscher, T.; Sahm, F.; Oezen, I.; Schmitt, L.-M.; Ciprut, S.; Hucke, N.; et al. Targeting Resistance against the MDM2 Inhibitor RG7388 in Glioblastoma Cells by the MEK Inhibitor Trametinib. *Clin. Cancer Res.* **2019**, *25*, 253–265. [CrossRef]
19. Fishlock, D.; Diodone, R.; Hildbrand, S.; Kuhn, B.; Mössner, C.; Peters, C.; Rege, P.D.; Rimmler, G.; Schantz, M. Efficient Industrial Synthesis of the MDM2 Antagonist Idasanutlin via a Cu(I)-Catalyzed [3+2] Asymmetric Cycloaddition. *Chim. Int. J. Chem.* **2018**, *72*, 492–500. [CrossRef]
20. Nieberler, M.; Reuning, U.; Reichart, F.; Notni, J.; Wester, H.-J.; Schwaiger, M.; Weinmüller, M.; Räder, A.; Steiger, K.; Kessler, H. Exploring the Role of RGD-Recognizing Integrins in Cancer. *Cancers* **2017**, *9*, 116. [CrossRef]
21. Ludwig, B.S.; Kessler, H.; Kossatz, S.; Reuning, U. RGD-Binding Integrins Revisited: How Recently Discovered Functions and Novel Synthetic Ligands (Re-)Shape an Ever-Evolving Field. *Cancers* **2021**, *13*, 1711. [CrossRef]
22. Su, C.; Li, J.; Zhang, L.; Wang, H.; Wang, F.; Tao, Y.; Wang, Y.; Guo, Q.; Li, J.; Liu, Y.; et al. The Biological Functions and Clinical Applications of Integrins in Cancers. *Front. Pharmacol.* **2020**, *11*, 579068. [CrossRef]
23. Malric, L.; Monferran, S.; Gilhodes, J.; Boyrie, S.; Dahan, P.; Skuli, N.; Sesen, J.; Filleron, T.; Kowalski-Chauvel, A.; Cohen-Jonathan Moyal, E.; et al. Interest of Integrins Targeting in Glioblastoma According to Tumor Heterogeneity and Cancer Stem Cell Paradigm: An Update. *Oncotarget* **2017**, *8*, 86947–86968. [CrossRef] [PubMed]
24. Blandin, A.-F.; Renner, G.; Lehmann, M.; Lelong-Rebel, I.; Martin, S.; Dontenwill, M. B1 Integrins as Therapeutic Targets to Disrupt Hallmarks of Cancer. *Front. Pharmacol.* **2015**, *6*, 279. [CrossRef]
25. Mas-Moruno, C.; Rechenmacher, F.; Kessler, H. Cilengitide: The First Anti-Angiogenic Small Molecule Drug Candidate. Design, Synthesis and Clinical Evaluation. *Anticancer Agents Med. Chem.* **2010**, *10*, 753–768. [CrossRef] [PubMed]
26. Stupp, R.; Hegi, M.E.; Gorlia, T.; Erridge, S.C.; Perry, J.; Hong, Y.-K.; Aldape, K.D.; Lhermitte, B.; Pietsch, T.; Grujicic, D.; et al. Cilengitide Combined with Standard Treatment for Patients with Newly Diagnosed Glioblastoma with Methylated MGMT

Promoter (CENTRIC EORTC 26071-22072 Study): A Multicentre, Randomised, Open-Label, Phase 3 Trial. *Lancet Oncol.* **2014**, *15*, 1100–1108. [CrossRef]
27. Tucci, M.; Stucci, S.; Silvestris, F. Does Cilengitide Deserve Another Chance? *Lancet Oncol.* **2014**, *15*, e584–e585. [CrossRef]
28. Ellert-Miklaszewska, A.; Poleszak, K.; Pasierbinska, M.; Kaminska, B. Integrin Signaling in Glioma Pathogenesis: From Biology to Therapy. *Int. J. Mol. Sci.* **2020**, *21*, 888. [CrossRef]
29. Holmes, K.M.; Annala, M.; Chua, C.Y.X.; Dunlap, S.M.; Liu, Y.; Hugen, N.; Moore, L.M.; Cogdell, D.; Hu, L.; Nykter, M.; et al. Insulin-like Growth Factor-Binding Protein 2-Driven Glioma Progression Is Prevented by Blocking a Clinically Significant Integrin, Integrin-Linked Kinase, and NF- B Network. *Proc. Natl. Acad. Sci. USA* **2012**, *109*, 3475–3480. [CrossRef]
30. Janouskova, H.; Maglott, A.; Leger, D.Y.; Bossert, C.; Noulet, F.; Guerin, E.; Guenot, D.; Pinel, S.; Chastagner, P.; Plenat, F.; et al. Integrin 5 1 Plays a Critical Role in Resistance to Temozolomide by Interfering with the P53 Pathway in High-Grade Glioma. *Cancer Res.* **2012**, *72*, 3463–3470. [CrossRef]
31. Etienne-Selloum, N.; Prades, J.; Bello-Roufai, D.; Boone, M.; Sevestre, H.; Trudel, S.; Caillet, P.; Coutte, A.; Desenclos, C.; Constans, J.-M.; et al. Expression Analysis of A5 Integrin Subunit Reveals Its Upregulation as a Negative Prognostic Biomarker for Glioblastoma. *Pharmaceuticals* **2021**, *14*, 882. [CrossRef]
32. Schaffner, F.; Ray, A.; Dontenwill, M. Integrin A5β1, the Fibronectin Receptor, as a Pertinent Therapeutic Target in Solid Tumors. *Cancers* **2013**, *5*, 27–47. [CrossRef]
33. Renner, G.; Noulet, F.; Mercier, M.-C.; Choulier, L.; Etienne-Selloum, N.; Gies, J.-P.; Lehmann, M.; Lelong-Rebel, I.; Martin, S.; Dontenwill, M. Expression/Activation of A5β1 Integrin Is Linked to the β-Catenin Signaling Pathway to Drive Migration in Glioma Cells. *Oncotarget* **2016**, *7*, 62194–62207. [CrossRef]
34. Ray, A.-M.; Schaffner, F.; Janouskova, H.; Noulet, F.; Rognan, D.; Lelong-Rebel, I.; Choulier, L.; Blandin, A.-F.; Lehmann, M.; Martin, S.; et al. Single Cell Tracking Assay Reveals an Opposite Effect of Selective Small Non-Peptidic A5β1 or Avβ3/B5 Integrin Antagonists in U87MG Glioma Cells. *Biochim. Biophys. Acta BBA Gen. Subj.* **2014**, *1840*, 2978–2987. [CrossRef]
35. Dudvarski Stanković, N.; Bicker, F.; Keller, S.; Jones, D.T.; Harter, P.N.; Kienzle, A.; Gillmann, C.; Arnold, P.; Golebiewska, A.; Keunen, O.; et al. EGFL7 Enhances Surface Expression of Integrin $\alpha_5\beta_1$ to Promote Angiogenesis in Malignant Brain Tumors. *EMBO Mol. Med.* **2018**, *10*, e8420. [CrossRef]
36. Malric, L.; Monferran, S.; Delmas, C.; Arnauduc, F.; Dahan, P.; Boyrie, S.; Deshors, P.; Lubrano, V.; Da Mota, D.F.; Gilhodes, J.; et al. Inhibiting Integrin B8 to Differentiate and Radiosensitize Glioblastoma-Initiating Cells. *Mol. Cancer Res.* **2019**, *17*, 384–397. [CrossRef]
37. DeLay, M.; Jahangiri, A.; Carbonell, W.S.; Hu, Y.-L.; Tsao, S.; Tom, M.W.; Paquette, J.; Tokuyasu, T.A.; Aghi, M.K. Microarray Analysis Verifies Two Distinct Phenotypes of Glioblastomas Resistant to Antiangiogenic Therapy. *Clin. Cancer Res.* **2012**, *18*, 2930–2942. [CrossRef]
38. Martin, S.; Janouskova, H.; Dontenwill, M. Integrins and P53 Pathways in Glioblastoma Resistance to Temozolomide. *Front. Oncol.* **2012**, *2*, 157. [CrossRef]
39. Renner, G.; Janouskova, H.; Noulet, F.; Koenig, V.; Guerin, E.; Bär, S.; Nuesch, J.; Rechenmacher, F.; Neubauer, S.; Kessler, H.; et al. Integrin A5β1 and P53 Convergent Pathways in the Control of Anti-Apoptotic Proteins PEA-15 and Survivin in High-Grade Glioma. *Cell Death Differ.* **2016**, *23*, 640–653. [CrossRef]
40. Heckmann, D.; Meyer, A.; Laufer, B.; Zahn, G.; Stragies, R.; Kessler, H. Rational Design of Highly Active and Selective Ligands for the A5β1 Integrin Receptor. *ChemBioChem* **2008**, *9*, 1397–1407. [CrossRef]
41. Rechenmacher, F.; Neubauer, S.; Polleux, J.; Mas-Moruno, C.; De Simone, M.; Cavalcanti-Adam, E.A.; Spatz, J.P.; Fässler, R.; Kessler, H. Functionalizing Avβ3- or A5β1-Selective Integrin Antagonists for Surface Coating: A Method to Discriminate Integrin Subtypes In Vitro. *Angew. Chem. Int. Ed.* **2013**, *52*, 1572–1575. [CrossRef] [PubMed]
42. Merlino, F.; Daniele, S.; La Pietra, V.; Di Maro, S.; Di Leva, F.S.; Brancaccio, D.; Tomassi, S.; Giuntini, S.; Cerofolini, L.; Fragai, M.; et al. Simultaneous Targeting of RGD-Integrins and Dual Murine Double Minute Proteins in Glioblastoma Multiforme. *J. Med. Chem.* **2018**, *61*, 4791–4809. [CrossRef] [PubMed]
43. Blandin, A.-F.; Noulet, F.; Renner, G.; Mercier, M.-C.; Choulier, L.; Vauchelles, R.; Ronde, P.; Carreiras, F.; Etienne-Selloum, N.; Vereb, G.; et al. Glioma Cell Dispersion Is Driven by A5 Integrin-Mediated Cell–Matrix and Cell–Cell Interactions. *Cancer Lett.* **2016**, *376*, 328–338. [CrossRef] [PubMed]
44. Aasland, D.; Götzinger, L.; Hauck, L.; Berte, N.; Meyer, J.; Effenberger, M.; Schneider, S.; Reuber, E.E.; Roos, W.P.; Tomicic, M.T.; et al. Temozolomide Induces Senescence and Repression of DNA Repair Pathways in Glioblastoma Cells via Activation of ATR–CHK1, P21, and NF-KB. *Cancer Res.* **2019**, *79*, 99–113. [CrossRef]
45. Lathia, J.D.; Gallagher, J.; Heddleston, J.M.; Wang, J.; Eyler, C.E.; MacSwords, J.; Wu, Q.; Vasanji, A.; McLendon, R.E.; Hjelmeland, A.B.; et al. Integrin Alpha 6 Regulates Glioblastoma Stem Cells. *Cell Stem Cell* **2010**, *6*, 421–432. [CrossRef]
46. Guerrero, P.A.; Tchaicha, J.H.; Chen, Z.; Morales, J.E.; McCarty, N.; Wang, Q.; Sulman, E.P.; Fuller, G.; Lang, F.F.; Rao, G.; et al. Glioblastoma Stem Cells Exploit the Avβ8 Integrin-TGFβ1 Signaling Axis to Drive Tumor Initiation and Progression. *Oncogene* **2017**, *36*, 6568–6580. [CrossRef]
47. Stupp, R.; Hegi, M.E.; Mason, W.P.; van den Bent, M.J.; Taphoorn, M.J.; Janzer, R.C.; Ludwin, S.K.; Allgeier, A.; Fisher, B.; Belanger, K.; et al. Effects of Radiotherapy with Concomitant and Adjuvant Temozolomide versus Radiotherapy Alone on Survival in Glioblastoma in a Randomised Phase III Study: 5-Year Analysis of the EORTC-NCIC Trial. *Lancet Oncol.* **2009**, *10*, 459–466. [CrossRef]

48. Fisher, J.P.; Adamson, D.C. Current FDA-Approved Therapies for High-Grade Malignant Gliomas. *Biomedicines* **2021**, *9*, 324. [CrossRef]
49. Ortiz, R.; Perazzoli, G.; Cabeza, L.; Jiménez-Luna, C.; Luque, R.; Prados, J.; Melguizo, C. Temozolomide: An Updated Overview of Resistance Mechanisms, Nanotechnology Advances and Clinical Applications. *Curr. Neuropharmacol.* **2021**, *19*, 513–537. [CrossRef]
50. Lee, S.Y. Temozolomide Resistance in Glioblastoma Multiforme. *Genes Dis.* **2016**, *3*, 198–210. [CrossRef]
51. Lang, F.; Liu, Y.; Chou, F.-J.; Yang, C. Genotoxic Therapy and Resistance Mechanism in Gliomas. *Pharmacol. Ther.* **2021**, *228*, 107922. [CrossRef]
52. Faget, D.V.; Ren, Q.; Stewart, S.A. Unmasking Senescence: Context-Dependent Effects of SASP in Cancer. *Nat. Rev. Cancer* **2019**, *19*, 439–453. [CrossRef]
53. Putavet, D.A.; de Keizer, P.L.J. Residual Disease in Glioma Recurrence: A Dangerous Liaison with Senescence. *Cancers* **2021**, *13*, 1560. [CrossRef]
54. Martinkova, E.; Maglott, A.; Leger, D.Y.; Bonnet, D.; Stiborova, M.; Takeda, K.; Martin, S.; Dontenwill, M. A5β1 Integrin Antagonists Reduce Chemotherapy-Induced Premature Senescence and Facilitate Apoptosis in Human Glioblastoma Cells. *Int. J. Cancer* **2010**, *127*, 1240–1248. [CrossRef]
55. Li, L.; Hu, Y.; Ylivinkka, I.; Li, H.; Chen, P.; Keski-Oja, J.; Hyytiäinen, M. NETRIN-4 Protects Glioblastoma Cells FROM Temozolomide Induced Senescence. *PLoS ONE* **2013**, *8*, e80363. [CrossRef]
56. Rabé, M.; Dumont, S.; Álvarez-Arenas, A.; Janati, H.; Belmonte-Beitia, J.; Calvo, G.F.; Thibault-Carpentier, C.; Séry, Q.; Chauvin, C.; Joalland, N.; et al. Identification of a Transient State during the Acquisition of Temozolomide Resistance in Glioblastoma. *Cell Death Dis.* **2020**, *11*, 19. [CrossRef]
57. Serafim, R.B.; da Silva, P.; Cardoso, C.; Di Cristofaro, L.F.M.; Netto, R.P.; de Almeida, R.; Navegante, G.; Storti, C.B.; de Sousa, J.F.; de Souza, F.C.; et al. Expression Profiling of Glioblastoma Cell Lines Reveals Novel Extracellular Matrix-Receptor Genes Correlated with the Responsiveness of Glioma Patients to Ionizing Radiation. *Front. Oncol.* **2021**, *11*, 668090. [CrossRef]
58. Auffinger, B.; Tobias, A.L.; Han, Y.; Lee, G.; Guo, D.; Dey, M.; Lesniak, M.S.; Ahmed, A.U. Conversion of Differentiated Cancer Cells into Cancer Stem-like Cells in a Glioblastoma Model after Primary Chemotherapy. *Cell Death Differ.* **2014**, *21*, 1119–1131. [CrossRef]
59. Dahan, P.; Martinez Gala, J.; Delmas, C.; Monferran, S.; Malric, L.; Zentkowski, D.; Lubrano, V.; Toulas, C.; Cohen-Jonathan Moyal, E.; Lemarie, A. Ionizing Radiations Sustain Glioblastoma Cell Dedifferentiation to a Stem-like Phenotype through Survivin: Possible Involvement in Radioresistance. *Cell Death Dis.* **2014**, *5*, e1543. [CrossRef]
60. Carbonell, W.S.; DeLay, M.; Jahangiri, A.; Park, C.C.; Aghi, M.K. B1 Integrin Targeting Potentiates Antiangiogenic Therapy and Inhibits the Growth of Bevacizumab-Resistant Glioblastoma. *Cancer Res.* **2013**, *73*, 3145–3154. [CrossRef]
61. Wang, H.; Cai, S.; Bailey, B.J.; Reza Saadatzadeh, M.; Ding, J.; Tonsing-Carter, E.; Georgiadis, T.M.; Zachary Gunter, T.; Long, E.C.; Minto, R.E.; et al. Combination Therapy in a Xenograft Model of Glioblastoma: Enhancement of the Antitumor Activity of Temozolomide by an MDM2 Antagonist. *J. Neurosurg.* **2017**, *126*, 446–459. [CrossRef] [PubMed]

Chloé BERNHARD

Hétérogénéité métabolique des gliomes de haut grade
Applications à l'évaluation de nouvelles thérapies

Résumé

Cette thèse se concentre sur la caractérisation de l'hétérogénéité moléculaire et métabolique des glioblastomes (GB). Nous avons identifié sept sous-classes de GB se distinguant par des activités régulatrices propres, ainsi que par des caractéristiques moléculaires et biologiques spécifiques. En intégrant des analyses transcriptomiques, métabolomiques, de flux extracellulaire, et l'évaluation de l'activité de régulateurs spécifiques, nous avons caractérisé l'hétérogénéité des cellules souches de GB (CSG) et leur plasticité en fonction de leur état (souche, différencié) ou du microenvironnement (normoxie, hypoxie, chimiothérapie). L'évaluation de leur sensibilité au témozolomide a révélé une résistance intrinsèque dans les CSG glycolytiques et l'apparition d'une résistance acquise en réponse à des stimuli environnementaux. Nos découvertes soulignent l'importance de cibler l'autophagie et le stress oxydatif pour surmonter la résistance à la chimiothérapie, et renforcent la nécessité d'approches thérapeutiques personnalisées adaptées à l'hétérogénéité et à la plasticité des GB.
Mots clés : Glioblastome, Hétérogénéité, Plasticité, Métabolisme, Cellule Souche Cancéreuse.

Abstract

This thesis focuses on characterizing the molecular and metabolic heterogeneity of glioblastomas (GB). We identified seven distinct subclasses of GB, each characterized by unique regulatory activities, as well as by specific molecular and biological characteristics. Integrating transcriptomic, metabolomic and extracellular flux analyses, along with the evaluation of specific regulatory activities, we characterized the heterogeneity of GB stem cells (GSC) and their plasticity depending on their cellular state (stem, differentiated) or the microenvironment (normoxia, hypoxia, chemotherapy). The assessment of their sensitivity to temozolomide revealed an intrinsic resistance in glycolytic GSC and the emergence of acquired resistance in response to environmental stimuli. Our findings highlight the importance of targeting autophagy and oxidative stress to overcome chemotherapy resistance, and reinforce the need for personalized therapeutic approaches adapted to the heterogeneity and plasticity of GB.
Keywords: Glioblastoma, Heterogeneity, Plasticity, Metabolism, Cancer Stem Cell.